VOL.
9
1959

THE PHYSICS AND CHEMISTRY OF SOLIDS

AN INTERNATIONAL JOURNAL

VOLUME 9 1959

Editor-in-Chief HARVEY BROOKS *Cambridge, Mass*

Associate Editors H. B. G. CASIMIR *Eindhoven* · G. J. DIENES *Brookhaven* · JACQUES FRIEDEL *Paris* · E. M. LIFSHITZ *Moscow*

Editorial Advisory Board

U.S.A.: E. N. Adams, Pittsburgh · D. Alpert, Illinois · L. Apker, Schenectady · J. Bardeen, Illinois · D. S. Billington, Oak Ridge · R. G. Breckenridge, Cleveland · Leo Brewer, Berkeley, Calif. · E. Burstein, Penn. J. A. Burton, New Jersey · N. Cabrera, Virginia · C. C. Danielson, Iowa · I. Estermann, Washington, D.C. J. C. Fisher, Schenectady · F. Herman, Princeton · Conyers Herring, New Jersey · A. R. von Hippel, Cambridge, Mass. · J. H. Hollomon, Schenectady · W. V. Houston, Houston · H. B. Huntington, Troy · H. M. James, Purdue · John G. Kirkwood, Yale · C. Kittel, Berkeley, Calif. · W. Kohn, Pittsburgh · J. A. Krumhansl, Cleveland · A. W. Lawson, Chicago · H. W. Leverenz, Princeton · O. T. Marzke, Pittsburgh · B. T. Matthias, New Jersey · L. R. Maxwell, Silver Spring · Joseph E. Mayer, Chicago · E. W. Montroll, Maryland · David Pines, Princeton · H. Reiss, New Jersey · J. R. Reitz, Cleveland · A. Rose, Princeton · O. C. Simpson, Argonne R. Smoluchowski, Pittsburgh · F. H. Spedding, Iowa · D. Turnbull, Schenectady · J. H. Van Vleck, Harvard B. E. Warren, Cambridge, Mass. · Eugene P. Wigner, Princeton · B. H. Zimm, Schenectady.

Canada: R. E. Burgess, Vancouver · D. K. C. MacDonald, Ottawa.

United Kingdom: A. Charlesby, Shrivenham, Berks · W. J. Dunning and F. C. Frank, Bristol · H. K. Henisch, Reading · H. Jones, London · J. W. Mitchell, Bristol · A. B. Pippard, Cambridge · M. H. L. Pryce, Bristol R. A. Smith, Malvern · K. W. H. Stevens, Nottingham · F. C. Tompkins, London.

France: E. F. Bertaut, Grenoble · A. Guinier, Paris · Louis Néel and Louis Weil, Grenoble.

Germany: M. Born, Bad Pyrmont · Ulrich Dehlinger, Stuttgart · R. Hilsch and G. Leibfried, Göttingen E. Mollwo, Erlangen · H. Pick, Stuttgart · M. von Laue, Berlin · H. Welker, Erlangen.

Italy: F. G. Fumi, Pavia.

Czechoslovakia: J. Tauc, Praha.

Japan: Toshinosuke Muto, Tokyo.

The Netherlands: A. Michels and G. W. Rathenau, Amsterdam. *Sweden:* J. O. Linde, Stockholm · Per-Olov Löwdin, Uppsala.

Switzerland: G. Busch and P. Scherrer, Zürich. *U.S.S.R.:* G. S. Zhdanov, Moscow.

PERGAMON PRESS NEW YORK · LONDON · PARIS · LOS ANGELES

NOTES FOR CONTRIBUTORS

I. GENERAL

1. Submission of a paper to the *Journal of the Physics and Chemistry of Solids* will be taken to imply that it represents original research not previously published (except in the form of an abstract or preliminary report), that it is not being considered for publication elsewhere, and that if accepted, it will not be published elsewhere in the same form, in any language, without the consent of the editor-in-chief. It should deal with original research work in the field of the physics and chemistry of solids.

2. Papers should be submitted to the appropriate regional editor (all English-language papers to be sent to the U.S. editor).

3. Papers will be published as quickly as possible after acceptance, and, subject to space being available, should appear in the following issue, if this is due for publication not earlier than three months after the acceptance date. Short communications under the heading of "Letters to the Editors" will receive priority for publication, and will be published in the issue following receipt, if accepted not later than the beginning of the month preceding publication.

4. Fifty free reprints of each paper are supplied. Additional copies can be obtained at a reasonable cost if ordered when proofs are returned. A reprint order form will accompany first proofs.

II. SCRIPT REQUIREMENTS

1. Papers submitted should be concise and written in a readily understandable style. Scripts should be typed and double spaced and submitted in duplicate to facilitate refereeing.

It will be appreciated if authors clearly indicate any special characters used. An abstract, not exceeding 200 words, should be provided in the language of the paper. French and German papers should be submitted with English abstract and titles, but if this is not possible the abstract will be translated by the publishers. To conserve space, authors are requested to mark less important parts of the paper, such as details of experimental technique, methods, mathematical derivations, etc. for printing in small type. The technical description of methods should be given in detail only when such methods are new. Authors will receive proofs for correction when their papers are first set; page proofs will be sent only when the amount of alteration makes it advisable.

2. Illustrations should not be included in the typescript of the paper, and legends should be typed on a separate sheet. Line drawings which require redrawing should include all relevant details and clear instructions for the draughtsman. If figures are already well drawn it may be possible to reproduce them direct from the originals, or from good photo-prints if these can be provided. It is not possible to reproduce from prints with weak lines. Illustrations for reproduction should normally be about twice the final size required. Photographs should only be included where they are essential.

Tables and figures should be so constructed as to be intelligible without reference to the text. Every table and column should be provided with an explanatory heading. Units of measure must always be clearly indicated. The same data should not be published in both tables and figures. The following standard symbols should be used on line drawings since they are easily available to the printers: ○, ●, +, ×, □, ■, △, ▲, ◇, ◆, ▽, ▼.

4. References are indicated in the text by superior numbers in parentheses, and the full reference should be given in a list at the end of the paper in the following form:

1. HILL R., *J. Iron St. Inst.* **158**, 177 (1948).
2. PEARSON C., *The Extrusion of Metals*. Chapman and Hall, London (1944).

Abbreviations of journal titles should follow those given for *Physics Abstracts*. It is particularly requested that authors' initials, and appropriate volume and page numbers, should be given in every case.

Footnotes, as distinct from literature references should be indicated by the following symbols—*, †, ‡, ‡‡, commencing anew on each page; they should *not* be included in the numbered reference system.

5. Due to the international character of the journal no rigid rules concerning notation and spelling will be observed, but each paper should be consistent within itself as to symbols and units.

VOL.
9
1959

OL.
9
959

VOL
9
195

CONTENTS

NUMBER 1

ALEXEI A. MARADUDIN: Screw dislocations and discrete elastic theory 1

G. A. ALERS, J. R. NEIGHBOURS and H. SATO: Dependence of sound velocity and attenuation on magnetization direction in nickel at high fields 21

G. L. PEARSON and W. L. FELDMANN: Powder-pattern techniques for delineating ferro-electric domain structures 28

D. G. THOMAS: The diffusion and precipitation of indium in zinc oxide 31

M. J. STEPHEN and A. B. LIDARD: The Faraday effect in semiconductors 43

H. E. FARNSWORTH and JOHANNES TUUL: Influence of lattice-defect density on the chemisorption and oxide formation on a clean (100) crystal face of nickel as determined by low-energy electron diffraction 48

H. E. FARNSWORTH, R. E. SCHLIER and JOHANNES TUUL: Tests with low-energy electron diffraction for adsorbed hydrogen and nickel hydroxide formed on the (100) surface of a nickel crystal at 25°C 57

F. A. TRUMBORE, C. R. ISENBERG and E. M. PORBANSKY: On the temperature-dependence of the distribution coefficient. The solid solubilities of tin in silicon and germanium. 60

WERNER KÄNZIG and TRUMAN O. WOODRUFF: The electronic structure of an *H*-center . . 70

Letters to the Editors:

E. CORENZWIT: Superconductivity of Nb_3Al 93

M. C. STEELE: Low-field electrical breakdown in *n*-indium phosphide 93

Announcement:

Symposium on Millimeter Waves 95

Paper to be published in future issues 96

NUMBER 2

T. P. HOAR and N. F. MOTT: A mechanism for the formation of porous anodic oxide films on aluminium. 97

R. E. SCHMUNK and CHARLES S. SMITH: Pressure derivatives of the elastic constants of aluminum and magnesium 100

HARRY C. NASH and CHARLES S. SMITH: Single-crystal elastic constants of lithium . . . 113

R. T. BATE, R. K. WILLARDSON and A. C. BEER: Transverse magnetoresistance and Hall effect in *n*-type InSb 119

H. EHRENREICH: Transport of electrons in intrinsic InSb 129

N. T. MELAMED: Energy transfer in ZnS:Cu:In phosphors 149

TORMOD RISTE, KONRAD BLINOWSKI and JERZY JANIK: Spin fluctuation scattering of neutrons in magnetite 153

G. H. JONKER: Analysis of the semiconducting properties of cobalt ferrite 165

AARON WOLD and RONALD J. ARNOTT: Preparation and crystallographic properties of the systems $LaMn_{1-x}Mn_xO_{3+\lambda}$ and $LaMn_{1-x}NiO_{3+\lambda}$ JA–1106 176

Letters to the Editors:

I. BROSER und R. BROSER–WARMINSKY: Antwort auf die Bemerkung von M. BALKANSKI zu der Arbeit „Über den Mechanismus der Energiewanderung in Kadmiumsulfid-Kristallen". . 181

E. BRIAN SMITH: Phase coexistence and hysteresis. 182

A. GIANSOLDATI, J. O. LINDE and G. BORELIUS: The antiferromagnetic transformations of the alloy AuMn 183

NUMBERS 3/4

H. A. KLASENS: The temperature-dependence of the fluorescence of photoconductors . . 185

S. W. BARBER and B. MARTIN: A heat-capacity function with velocity dispersion for isotropic solids 198

H. J. HROSTOWSKI and R. H. KAISER: The solubility of oxygen in silicon 214

VOL. 9 1959

F. Moser, N. R. Nail and F. Urbach: Optical absorption studies of the volume photolysis of large silver chloride crystals 217
S. Geller and M. A. Gilleo: The effect of dispersion corrections on the refinement of the yttrium–iron garnet structure 235
Robert S. Knox: Exciton states in rare-gas crystals 238
Robert S. Knox: Exciton states in crystalline argon 265
W. F. Love: Hall effect in copper and Cu_3Au at low temperatures 281
Horst Meyer and P. L. Smith: The heat capacities of seven rare-earth ethylsulphates at low temperatures 285
Horst Meyer: Thermal and magnetic properties of praseodymium ethylsulphate below 1°K. . 296
R. J. Weiss and A. S. Marotta: Spin-dependence of the resistivity of magnetic metals. . . 302
G. J. Wolga and M. W. P. Strandberg: Hyperfine interactions in *F*-center paramagnetic-resonance spectra in LiF and NaF 309
Solomon Zwerdling, Benjamin Lax, Kenneth J. Button and Laura M. Roth: Oscillatory magneto-absorption in gallium antimonide JA–1149 320
W. D. Lawson, S. Nielsen, E. H. Putley and A. S. Young: Preparation and properties of HgTe and mixed crystals of HgTe–CdTe 325
S. Wiederhorn and H. G. Drickamer: The effect of pressure on the near-ultraviolet spectra of some fused-ring aromatic crystals 330
Letters to the Editors:
Keiji Maeda: One-dimensional configurational co-ordinate curves for luminescence centers . 335
Martin J. Arvin and Ray F. Tipsord: Hall coefficient of molybdenum disilicide 336
Book Review:
"The Physics of Rubber Elasticity", 2nd edn. (reviewed by B. H. Zimm and R. W. Kilb) . . 338
Papers to be published in future issues 339
Errata 340

VOL
9
195

AUTHOR INDEX TO VOLUME 9

(B) denotes book review

Alers, G. A. 21
Arvin, M. 336
Arnott, R. J. 176
Barber, S. W. 198
Bate, R. T. 119
Beer, A. C. 119
Blinowski, K. 153
Borelius, G. 183
Broser, I. 181
Broser–Warminsky, R. 181
Button, K. J. 320
Corenzwit, E. 93
Drickamer, H. G. 330
Ehrenreich, H. 129
Farnsworth, H. E. 48, 57
Feldman, W. L. 28
Geller, S. 235
Giansoldati, A. 183
Gilleo, M. A. 235
Hoar, T. P. 97
Hrostowski, H. J. 214
Isenberg, C. R. 60
Janik, J. 153
Jonker, G. H. 165
Kaiser, R. H. 214
Känzig, W. 70
Kilb, R. W. 338 (B)
Klasens, H. A. 185
Knox, R. S. 238, 265
Lawson, W. D. 325
Lax, B. 320
Lidiard, A. B. 43
Linde, J. O. 183
Love, W. F. 281
Maeda, K. 335
Maradudin, A. 1
Marotta, A. S. 302
Martin, B. 198
Melamed, N. T. 149
Meyer, H. 285, 296
Moser, F. 217
Mott, N. F. 97
Nail, N. R. 217
Nash, H. C. 113
Neighbours, J. R. 21
Nielsen, S. 325
Pearson, G. L. 28
Porbansky, E. M. 60
Putley, E. H. 325
Riste, T. 153
Roth, L. M. 320
Sato, H. 21
Schlier, R. E. 57
Schmunk, R. E. 100
Smith, C. S. 100, 113
Smith, E. B. 182
Smith, P. L. 285
Steele, M. C. 93
Stephen, M. J. 43
Strandberg, M. W. P. 309
Thomas, D. G. 31
Tipsord, R. F. 336
Trumbore, F. A. 60
Tuul, J. 57, 48
Urbach, F. 217
Weiss, R. J. 302
Wiederhorn, S. 330
Willardson, R. K. 119
Wold, A. 176
Wolga, G. J. 309
Woodruff, T. O. 70
Young, A. S. 325
Zimm, B. H. 338 (B)
Zwerdling, S. 320

VOL.
9
1959

VOL
9
195

J. Phys. Chem. Solids Pergamon Press 1958. Vol. 9. pp. 1–20. Printed in Great Britain.

SCREW DISLOCATIONS AND DISCRETE ELASTIC THEORY*†

ALEXEI A. MARADUDIN‡

H. H. Wills Physical Laboratory, University of Bristol, Bristol, England

(*Received* 20 *May* 1958)

Abstract—A simple model of a screw dislocation in a crystal lattice in which each atom interacts with its neighbors through Hooke's law forces is presented, and expressions for the displacement component and strain energy are obtained. Applications of the model to screw dislocations in alkali-halide crystals are discussed.

VOL. 9 1959

1. INTRODUCTION

THE usual description of the atomic displacements due to a screw dislocation in a crystal lattice is that of elastic theory, either anisotropic[1] or, more usually, isotropic.[2] The result of this theory is a z-component of displacement which is multi-valued, i.e. it increases by a lattice translation distance on completing any circuit about the dislocation line. The x- and y-components of displacement, as well as the higher-order terms in the expression for the z-component, are single-valued functions of position and can be expressed in terms of infinite series of inverse powers of distance whose coefficients are undetermined.[1,3] At large distances from the core of the dislocation (e.g. in the region where Hook's law is valid), the multi-valued term is dominant, and the higher-order terms are generally neglected.

The theory of elastic dislocations correctly gives the displacements and stresses far from the dislocation itself, but there are important differences between elastic dislocations and dislocations in crystal lattices. An elastic dislocation must necessarily be made in a multiply-connected body, viz. one from which the material at the dislocation core has been removed. For if the elastic solution is extended into the core region, it is found that the strains become infinite at the dislocation line. This is not a very serious defect in the case of elastic dislocations, since if the radius of this cylinder of exclusion is made to approach zero while the magnitude of the Burgers vector also decreases, the strains outside the cylinder can be kept arbitrarily small. In a crystal lattice, however, we are interested in the atomic displacements and strains at distances like one interatomic spacing from the dislocation line, while the Burgers vector must be a lattice translation vector. That is, we are interested in the properties of a dislocation in a region of the crystal where the strains are so large that Hooke's law no longer holds and where it is no longer valid to smear out the discrete nature of the crystal structure by a continuum approximation.

If one attempts to calculate the strain energy of an elastic dislocation, it is found that it diverges logarithmically with the radius of the external boundary of the crystal and also at the origin. The divergence at large radii is inevitable; the divergence at the origin comes from assuming the validity of Hooke's law in that region and neglecting the discrete nature of the crystal.

The difficulties of infinite stresses and infinite strain energy at the core do not exist for a

* This work is based on Chapter 2 of a thesis submitted to the University of Bristol in partial fulfillment of the requirements for the degree of Doctor of Philosophy in Physics.

† This research was partially supported by the United States Air Force through the Air Force Office of Scientific Research, Air Research and Development Command under Contract #AF18(600)1015. Reproduction in whole or in part is permitted for any purpose of the United States Government.

‡ Now at the Department of Physics, University of Maryland, College Park, Maryland.

dislocation in a crystal. This is because stresses decrease once strains exceed a certain value, and secondly because a crystal is a discrete atomic structure and not a continuum, so that at the center of a dislocation only the displacements and forces between atoms have a physical meaning, and these are always finite.

In this note we investigate the consequences of abandoning one of the unphysical assumptions of the theory of elastic dislocations—that of describing a discrete crystal lattice by an elastic continuum—by introducing a simple model of a screw dislocation in a crystal lattice in which each atom interacts with its neighbors through Hooke's law forces. We obtain expressions for the displacement component and the dislocation strain energy. It is shown that at large distances from the dislocation core the expression for the displacement component approaches that obtained by using continuum theory, while in the immediate vicinity of the core the discrete model appears to be an improvement over the continuum model. Furthermore, it is found that the strain energy in the crystal due to the dislocation increases logarithmically with the dimensions of the crystal, but due to the presence of a fundamental length, the lattice spacing, the strain energy at the dislocation core is finite, and it is not necessary to exclude the material within a cylinder of small arbitrary radius in evaluating the total strain energy as is the case in continuum calculations. Finally, the lattice anisotropy can be introduced into the calculations in a very simple and direct way.

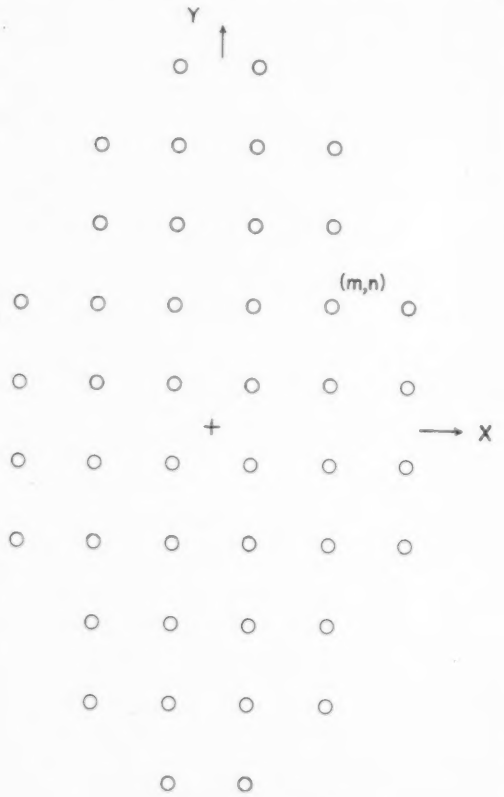

FIG. 1. Configuration I.

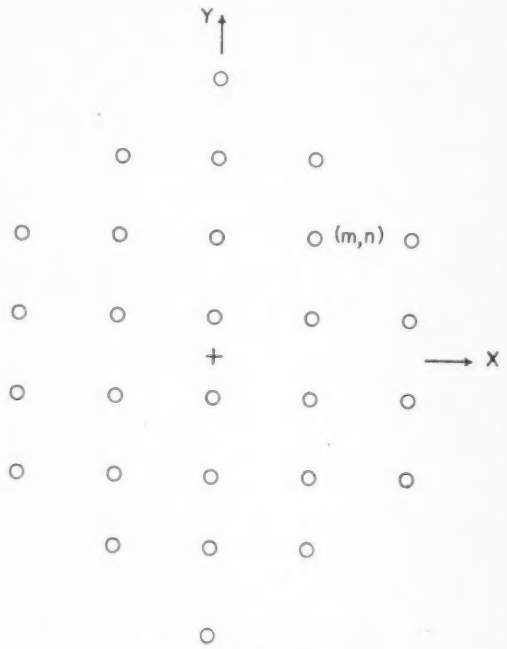

FIG. 2. Configuration II.

The calculation of the screw dislocation displacement function is carried out in a manner analogous to the continuum approach based on the theory of antiplane strain. It is a two-dimensional problem in which only displacements parallel to the direction of the Burgers vector (i.e. in the z-direction) are considered and the value of the placement of a given particle depends only on its

position in the xy-plane. We can then analyze the atoms of our crystal lattice into rows parallel to the Burgers vector. We assume that in forming the screw dislocation the spacing of the atoms in all such rows remains unchanged, so that each row effectively undergoes a rigid body translation along its length in which each atom in the row suffers the same displacement. In the present discussion we consider the co-ordinate systems given in Figs. 1 and 2, where the lattice points are to be regarded as the projections of the rows of atoms onto the xy-plane. The lattice points in these co-ordinate systems are denoted by (m, n), where m and n are half-odd integers in the case of Configuration I, and m is an integer while n is a half-odd integer in the case of Configuration II. These two configurations correspond to the two symmetric locations for the core of the dislocation as slip occurs on a $\{110\}$ plane in an alkali-halide crystal (for which the present model was originally constructed[4]).

We assume that each row of atoms interacts with only its four nearest-neighbor rows and allow the force constant for vertical displacements for rows separated along the x-direction to be different from that for rows along the y-direction.

The assumption that each row interacts with only its four nearest neighbors is not a necessary restriction in the present treatment, but it has the simplifying effect that all the displacement components can be evaluated exactly in this case. In addition, for the case of screw dislocations in the alkali-halide crystals, where the Burgers vector is in a $\langle 110 \rangle$ direction, this is also a very good approximation.[4,5] Here each ion row parallel to the Burgers vector is either a row of alkali ions only or a row of halide ions only. MADELUNG'S[6] expression for the electrostatic potential of a row of equally spaced charges of the same sign shows that the component of the force exerted by one such row on a second, parallel, row in the direction parallel to their lengths decreases faster than exponentially with the separation of the rows. Since the non-coulomb interactions between ions are of short-range type as well, the nearest-neighbor model introduced here should be applicable to the alkali-halides as long as ionic displacements parallel to the Burgers vector only are allowed.

We denote the vertical displacement of the ion at (m, n) by $w_{m,n}$ and assume that it is a multi-valued function of position, i.e. it increases by $\boldsymbol{b}$ on completing any circuit about the origin. To avoid any difficulties arising from the multi-valuedness of the displacement function we introduce a cut along the x-axis. The location of the cut is somewhat arbitrary and this particular choice is made for the sake of convenience.

2. THE SCREW DISLOCATION DISPLACEMENT FUNCTION

(a) *Configuration I*

The equation of equilibrium for the ion row at (m, n) is

$$A(w_{m+1\,n}+w_{m-1,\,n})+B(w_{m,\,n+1}+w_{m,\,n-1})- -(2A+2B)w_{m\,n}=0 \qquad (2.1)$$

where m and n are half-odd integers, and A and B are the force constants for the vertical displacement of ion rows separated along the x- and y-directions respectively. Equation (2.1) holds at all points (m, n) except at those which can be written as $(k+\frac{1}{2}, \pm\frac{1}{2})$ where $k = 0, 1, 2, 3, \ldots$ These points are on opposite sides of the cut where the discontinuity in displacement is $\boldsymbol{b}$. If we assume that we are introducing a right-hand screw dislocation, at these points equation (2.1) must be modified to

$$A(w_{k+\frac{1}{2},\,\frac{1}{2}}+w_{k-\frac{1}{2},\,\frac{1}{2}})+B(w_{k+\frac{1}{2},\,\frac{3}{2}}+w_{k+\frac{1}{2},\,-\frac{1}{2}})- -(2A+2B)w_{k+\frac{1}{2},\,\frac{1}{2}}=Bb \qquad (2.2a)$$

and

$$A(w_{k+\frac{1}{2},\,-\frac{1}{2}}+w_{k+\frac{1}{2},\,-\frac{3}{2}})+B(w_{k+\frac{1}{2},\,\frac{1}{2}}+w_{k+\frac{1}{2},\,-\frac{5}{2}})- -(2A+2B)w_{k+\frac{1}{2},\,-\frac{1}{2}}=-Bb. \qquad (2.2b)$$

Equations (2.1) and (2.2) can be combined into one equation, viz.

$$A(w_{m+1,\,n}+w_{m-1,\,n})+B(w_{m,\,n+1})+w_{m,\,n-1})- -(2A+2B)w_{m,\,n} =Bb(\delta_{m\;k+\frac{1}{2}}\delta_{n\;\frac{1}{2}}-\delta_{m,\,k+\frac{1}{2}}\delta_{n\;-\frac{1}{2}}) \qquad (2.3)$$

where the δ's are the usual Kronecker symbols.

To solve the partial-difference equation (2.3), we proceed in the following manner. We can express the δ's in the following way*

* It can be shown that the assumption of this form for the Kronecker symbol is equivalent to imposing a cyclic boundary condition on the displacement components in the limit of a large crystal.

$$\delta_{m,\,k+\frac{1}{2}}\delta_{n,\,\pm\frac{1}{2}} = \frac{1}{4\pi^2}\int_{-\pi}^{\pi}\int e^{i(m-k-\frac{1}{2})x+i(n\mp\frac{1}{2})y}\,dxdy. \quad (2.4)$$

We then introduce an auxiliary function $w_{m,\,n}(k)$ defined by

$$w_{m,\,n}(k) = \int_{-\pi}^{\pi}\int f(x, y; k)e^{imx+iny}\,dxdy. \quad (2.5)$$

We specify that $w_{m,\,n}(k)$ be a solution of equation (2.3) for each value of $k(= 0, 1, 2, \ldots)$ in turn and determine the unknown function $f(x, y; k)$ from this condition. The complete expression for the displacement function $w_{m,\,n}$ will then be obtained by summing $w_{m,\,n}(k)$ over k. Thus by equations (2.3), (2.4), and (2.5), $f(x, y; k)$ must satisfy the following equation

$$\int_{-\pi}^{\pi}\int f(x, y; k)e^{imx+iny}\times$$

$$\times[2A\cos x+2B\cos y-2A-2B]\,dxdy$$

$$=\frac{Bb}{4\pi^2}\int_{-\pi}^{\pi}\int e^{imx+iny-i(k+\frac{1}{2})x}[-2i\sin\tfrac{1}{2}y]\,dxdy \quad (2.6)$$

i.e.

$$f(x, y; k) = \frac{Bb}{4\pi^2}\cdot\frac{2i\sin\frac{1}{2}y\,e^{-i(k+\frac{1}{2})x}}{2A+2B-2A\cos x-2B\cos y}$$

and we have immediately that

$$w_{m,\,n}(k) = \frac{Bb}{4\pi^2}\int_{-\pi}^{\pi}\int\frac{2i\sin\frac{1}{2}y\,e^{-i(k+\frac{1}{2})x}e^{imx+iny}}{2A+2B-2A\cos x-2B\cos y}\,dxdy. \quad (2.7)$$

If we sum (2.7) over $k = 0, 1, 2, 3 \ldots$, we obtain the screw dislocation displacement function $w_{m,\,n}$:

$$w_{m,\,n} = \frac{Bb}{4\pi^2}\int_{-\pi}^{\pi}\int\frac{\sin\frac{1}{2}y}{\sin\frac{1}{2}x}\times$$

$$\times\frac{e^{imx+iny}}{2A+2B-2A\cos x-2B\cos y}\,dxdy.$$

The integrand must be an even function of x and y, so that

$$w_{m,\,n} = -\frac{b}{\pi^2}\int_0^{\pi/2}\int\frac{\sin y}{\sin x}\times$$

$$\times\frac{\sin 2mx\sin 2ny}{(A/B)\sin^2 x+\sin^2 y}\,dxdy. \quad (2.8)$$

As it stands equation (2.8) gives an expression for $w_{m,\,n}$ which has the y-axis as its line of zero displacement. For our purposes it is more convenient to put the line of zero displacement along the x-axis, and this is accomplished by adding $b/4$ to the values of $w_{m,\,n}$ given by (2.8). Finally we have

$$w_{m,\,n} = \frac{b}{4}-\frac{b}{\pi^2}\int_0^{\pi/2}\int\frac{\sin y}{\sin x}\times$$

$$\times\frac{\sin 2mx\sin 2ny}{(A/B)\sin^2 x+\sin^2 y}\,dxdy. \quad (2.9)$$

The evaluation of this integral is discussed in Appendix A, and values of $w_{m,\,n}$ for a number of points (m, n) are given in Table 1 for the special case $A/B = 1$. For comparison in Table 1 we also present the values of $w_{m,\,n}$ calculated from the expression given by continuum theory

$$w_{m,\,n} = \frac{b}{2\pi}\tan^{-1}\frac{n}{m} \quad (2.10)$$

on the assumption of a square lattice.

It is of interest to obtain the asymptotic expression for the integral (2.9) which is valid when (Bm^2+An^2) is large. We note that the denominator of the integral in equation (2.9) is singular at $x = y = 0$. Furthermore, for large m and n the integrand oscillates extremely rapidly with x and y except in the region $x, y \sim 0$. Hence we can expand the m- and n-independent trigonometric functions in the integrand in powers of x and y and retain only the leading terms. Also, since after this expansion has been made the major contribution to these integrals comes from the region of the origin, we should make little error in the integral (as $m, n \to \infty$) by extending the limits of integration from $(0, \pi/2)$ to $(0, \infty)$. These arguments can be made rigorous by a suitable modification of

Table 1. *Discrete screw dislocation displacement components. Configuration I. Square lattice with* $A/B = 1$. *Bracketed values are obtained from equation* (2.10) *and correspond to isotropic elastic theory*

m \ n	$\frac{1}{2}$	$\frac{3}{2}$	$\frac{5}{2}$	$\frac{7}{2}$
$\frac{1}{2}$	0·125000$\boldsymbol{b}$ (0·125$\boldsymbol{b}$)	0·193310$\boldsymbol{b}$ (0·1988$\boldsymbol{b}$)	0·216550$\boldsymbol{b}$ (0·219$\boldsymbol{b}$)	0·226644$\boldsymbol{b}$ (0·227$\boldsymbol{b}$)
$\frac{3}{2}$	0·056690$\boldsymbol{b}$ (0·0512$\boldsymbol{b}$)	0·12500$\boldsymbol{b}$ (0·125$\boldsymbol{b}$)	0·162793$\boldsymbol{b}$ (0·164$\boldsymbol{b}$)	0·184624$\boldsymbol{b}$ (0·186$\boldsymbol{b}$)
$\frac{5}{2}$	0·033451$\boldsymbol{b}$ (0·0314$\boldsymbol{b}$)	0·087207$\boldsymbol{b}$ (0·0859$\boldsymbol{b}$)	0·125000$\boldsymbol{b}$ (0·125$\boldsymbol{b}$)	0·150869$\boldsymbol{b}$ (0·151$\boldsymbol{b}$)
$\frac{7}{2}$	0·023356$\boldsymbol{b}$ (0·0226$\boldsymbol{b}$)	0·065376$\boldsymbol{b}$ (0·0645$\boldsymbol{b}$)	0·099131$\boldsymbol{b}$ (0·0987$\boldsymbol{b}$)	0·125000$\boldsymbol{b}$ (0·125$\boldsymbol{b}$)
$\frac{9}{2}$	0·017954$\boldsymbol{b}$ (0·0177$\boldsymbol{b}$)	0·051809$\boldsymbol{b}$ (0·0512$\boldsymbol{b}$)		

DUFFIN's[7] arguments; however, for our purposes these qualitative arguments suffice. Thus for (Bm^2+An^2) large

$$w_{m,n} \sim \frac{\boldsymbol{b}}{4} - \frac{\boldsymbol{b}}{\pi^2}\int_0^\infty\!\!\int \frac{y \sin 2ny}{y^2+(A/B)x^2} \cdot \frac{\sin 2mx}{x}\,dxdy$$

$$= \frac{\boldsymbol{b}}{4} - \frac{\boldsymbol{b}}{2\pi}\int_0^\infty e^{-2n\sqrt{(A/B)}x}\,\frac{\sin 2mx}{x}\,dx$$

$$= \frac{\boldsymbol{b}}{4} - \frac{\boldsymbol{b}}{2\pi}\tan^{-1}\sqrt{\frac{B}{A}}\cdot\frac{m}{n}.$$

Since

$$\frac{\pi}{2} - \tan^{-1}\frac{1}{x} = \tan^{-1}x,$$

we have finally

$$w_{m,n} = \frac{\boldsymbol{b}}{2\pi}\tan^{-1}\sqrt{\frac{A}{B}}\cdot\frac{n}{m} + O[(Bm^2+An^2)^{-1}] \qquad (2.11)$$

which is a result we would expect, knowing the corresponding expression in continuum theory. For in that case the partial-difference equation of equilibrium (2.1) becomes the partial differential equation

$$A'\frac{\partial^2 w}{\partial x^2} + B'\frac{\partial^2 w}{\partial y^2} = 0,$$

and the solution of this equation which increases by $\boldsymbol{b}$ on completing any circuit about the origin is (apart from an arbitrary single-valued function of $z = \sqrt{B'}\,x + i\sqrt{A'}\,y$)

$$w = \frac{\boldsymbol{b}}{2\pi}\tan^{-1}\sqrt{\frac{A'}{B'}}\,\frac{y}{x}.$$

(b) *Configuration II*

In this case the basic equation of equilibrium for a lattice point is again

$$A(w_{m+1,n}+w_{m-1,n}) + B(w_{m,n+1}+w_{m,n-1}) - \\ -(2A+2B)w_{m,n} = 0 \qquad (2.12)$$

where now m is an arbitrary integer while n is half an odd integer. Equation (2.12) holds at all points (m, n) except those which can be written as $(k, \pm\frac{1}{2})$ where $k = 0, 1, 2, 3, \ldots$ The points $(k \geqslant 1, \pm\frac{1}{2})$ are on opposite sides of the cut where the discontinuity in displacement is $\pm\boldsymbol{b}$, while the discontinuity in displacement at the points $(0, \pm\frac{1}{2})$ is $\pm\boldsymbol{b}/2$. If again we assume that we

are introducing a right-hand screw dislocation at these points equation (2.12) must be modified to

$$\begin{aligned} &A(w_{1,\frac{1}{2}}+w_{-1,\frac{1}{2}})+B(w_{0,\frac{1}{2}}+w_{0,-\frac{1}{2}})- \\ &\quad -(2A+2B)w_{0,\frac{1}{2}}=B(\boldsymbol{b}/2) \\ &A(w_{1,-\frac{1}{2}}+w_{-1,-\frac{1}{2}})+B(w_{0,\frac{1}{2}}+w_{0,-\frac{1}{2}})- \\ &\quad -(2A+2B)w_{0,-\frac{1}{2}}=-B(\boldsymbol{b}/2) \end{aligned} \tag{2.13a}$$

and

$$\begin{aligned} &A(w_{k+1,\frac{1}{2}}+w_{k-1,\frac{1}{2}})+B(w_{k,\frac{1}{2}}+w_{k,-\frac{1}{2}})- \\ &\quad -(2A+2B)w_{k,\frac{1}{2}}=B\boldsymbol{b} \\ &A(w_{k+1,-\frac{1}{2}}+w_{k-1,-\frac{1}{2}})+B(w_{k,\frac{1}{2}}+w_{k,-\frac{1}{2}})- \\ &\quad -(2A+2B)w_{k,-\frac{1}{2}}=-B\boldsymbol{b}. \end{aligned} \tag{2.13b}$$

We can combine equations (2.13) with equation (2.12) to give as the equation of equilibrium at any lattice point (m, n):

$$\begin{aligned} &A(w_{m+1,n}+w_{m-1,n})+ \\ &+B(w_{m,n+1}+w_{m,n-1})-(2A+2B)w_{m,n} \\ &=B\boldsymbol{b}(\delta_{m,k}\delta_{n,\frac{1}{2}}-\delta_{m,k}\delta_{n,-\frac{1}{2}})+ \\ &+B(\boldsymbol{b}/2)(\delta_{m,0}\delta_{n,\frac{1}{2}}-\delta_{m,0}\delta_{n,-\frac{1}{2}}). \end{aligned} \tag{2.14}$$

We solve the partial-difference equation (2.14) in the same manner as equation (2.3). We express the Kronecker delta's as

$$\delta_{m,k}\delta_{n,\pm\frac{1}{2}}=\frac{1}{4\pi^2}\int_{-\pi}^{\pi}\int e^{i(m-k)x+i(n\mp\frac{1}{2})y}\,dxdy. \tag{2.15}$$

If we introduce again

$$w_{m,n}(k)=\int_{-\pi}^{\pi}\int f(x,y;k)e^{imx+iny}\,dxdy, \tag{2.16}$$

then on substituting (2.15) and (2.16) into equation (2.14) we obtain for $f(x, y; k)$

$$\begin{aligned} f(x,y;k)=&\frac{B\boldsymbol{b}}{16\pi^2}\cdot\frac{2i\sin(y/2)e^{-ikx}}{A\sin^2(x/2)+B\sin^2(y/2)}+ \\ &+\frac{B\boldsymbol{b}}{32\pi^2}\cdot\frac{2i\sin(y/2)}{A\sin^2(x/2)+B\sin^2(y/2)} \end{aligned} \tag{2.17}$$

and we have that

$$w_{m,n}(k)=\frac{B\boldsymbol{b}}{16\pi^2}\int_{-\pi}^{\pi}\int\frac{2i\sin(y/2)e^{imx+iny-ikx}}{A\sin^2(x/2)+B\sin^2(y/2)}dxdy+\frac{B\boldsymbol{b}}{32\pi^2}\int_{-\pi}^{\pi}\int\frac{2i\sin(y/2)e^{imx+iny}}{A\sin^2(x/2)+B\sin^2(y/2)}dxdy. \tag{2.18}$$

If we sum the first term of equation (2.18) over the values $k = 1, 2, 3, \ldots$, we obtain the complete screw dislocation displacement function:

$$w_{m,n}=\frac{B\boldsymbol{b}}{16\pi^2}\int_{-\pi}^{\pi}\int\frac{e^{-ix}}{1-e^{-ix}}\frac{2i\sin(y/2)e^{imx+iny}}{A\sin^2(x/2)+B\sin^2(y/2)}dxdy+\frac{B\boldsymbol{b}}{32\pi^2}\int_{-\pi}^{\pi}\int\frac{2i\sin(y/2)e^{imx+iny}}{A\sin^2(x/2)+B\sin^2(y/2)}dxdy$$

The integrands must be even in x and y, so we have

$$w_{m,n}=-\frac{\boldsymbol{b}}{\pi^2}\int_0^{\pi/2}\int\frac{\sin y\sin(2m-1)x\sin 2ny}{\sin x\,(A/B)\sin^2 x+\sin^2 y}dxdy-\frac{\boldsymbol{b}}{\pi^2}\int_0^{\pi/2}\int\frac{\cos 2mx\sin y\sin 2ny}{(A/B)\sin^2 x+\sin^2 y}dxdy. \tag{2.19}$$

Again in equation (2.19) we have an expression for $w_{m,n}$ which has the line of zero displacement along the y-axis. Adding $b/4$ to (2.19) to put the line of zero displacement on the x-axis gives us

$$w_{m,n} = \frac{b}{4} - \frac{b}{\pi^2}\int_0^{\pi/2}\int \frac{\cos x \sin 2mx}{\sin x} \times$$

$$\times \frac{\sin y \sin 2ny}{(A/B)\sin^2 x + \sin^2 y}\, dx dy. \qquad (2.20)$$

This is the required displacement function. The evaluation of the integrals appearing in equation (2.20) is discussed in Appendix A, and values of $w_{m,n}$ for several points (m, n) are given in Table 2 for the special case $A/B = 1$. In Table 2 we also present the values of $w_{m,n}$ calculated for the same points (m, n) using equation (2.10).

We can also obtain the asymptotic expression for $w_{m,n}$ given by equation (2.19). The asymptotic form for the first integral was obtained in the first part of this section and is

$$-\frac{b}{2\pi}\tan^{-1}\sqrt{\frac{B}{A}}\,\frac{2m-1}{2n}. \qquad (2.21)$$

The asymptotic form of the second integral is given by

$$-\frac{b}{\pi^2}\int_0^{\infty}\int \frac{y \sin 2ny}{y^2+(A/B)x^2}\cos 2mx\, dx$$

$$= -\frac{b}{2\pi}\int_0^{\infty} e^{-2n\sqrt{(A/B)}x}\cos 2mx\, dx$$

$$= -\frac{b}{4\pi}\,\frac{\sqrt{AB}n}{(Bm^2+An^2)}. \qquad (2.22)$$

So that adding (2.21) and (2.22) we have

$$w_{m\,n} \sim \frac{b}{2\pi}\tan^{-1}\sqrt{\frac{A}{B}}\,\frac{2n}{2m-1} - \frac{b}{4\pi}\,\frac{\sqrt{AB}n}{(Bm^2+An^2)}. \qquad (2.23)$$

This expression can be reduced further yet. Since $m \geqslant 1$ we can expand the first term of (2.23) in a Taylor Series:

$$\frac{b}{2\pi}\tan^{-1}\sqrt{\frac{A}{B}}\,\frac{n}{m}\left(1+\frac{1}{2m}+\ldots\right)$$

$$= \frac{b}{2\pi}\tan^{-1}\sqrt{\frac{A}{B}}\,\frac{n}{m} + \frac{b}{4\pi}\,\frac{\sqrt{AB}n}{(Bm^2+An^2)} + \ldots \qquad (2.24)$$

Table 2. Discrete screw dislocation displacement components. Configuration II. Square lattice with $A/B = 1$. Bracketed values are obtained from equation (2.10) and correspond to isotropic elastic theory

m \ n	$\frac{1}{2}$	$\frac{3}{2}$	$\frac{5}{2}$	$\frac{7}{2}$	$\frac{9}{2}$
0	0·250000b (0·250b)	0·250000b (0·250b)	0·250000b (0·250b)	0·250000b (0·250b)	0·250000b (0·250b)
1	0·090845b (0·074b)	0·159155b (0·156b)	0·189561b (0·189b)	0·205634b (0·206b)	0·215118b (0·215b)
2	0·045070b (0·039b)	0·106103b (0·103b)	0·143897b (0·143b)	0·167746b (0·167b)	
3	0·028403b (0·026b)	0·076291b (0·074b)	0·112066b (0·111b)		
4	0·020655b (0·020b)	0·058593b (0·057b)			
5	0·016280b (0·016b)				

Combining (2.23) and (2.24) gives us finally

$$w_{m,n} \sim \frac{b}{2\pi} \tan^{-1} \sqrt{\frac{A}{B}} \frac{n}{m} + O[(Bm^2 + An^2)^{-2}]. \quad (2.25)$$

This again is a result we would expect inasmuch as the continuum theory does not take into account the detailed structure at the dislocation core.

3. STRAIN ENERGY OF THE DISCRETE SCREW DISLOCATION

Exactly as in the continuum case, we can evaluate the strain energy of a dislocated discrete lattice in two ways. We can in the first instance evaluate it by summing the bond energies pairwise between nearest neighbors over the entire lattice. This method is the discrete analogue of the volume integration method of continuum theory. However, in discrete theory as well as in continuum theory it is easier to evaluate the strain energy by recognizing the fact that it originates from the work done on the body by the applied forces that cause the strained condition.

In what follows, since we are concerned with only vertical (z-ward) displacements of ion rows in the crystal, it will be convenient to regard each row as a rigid vertical rod restricted to move only along its own length, and connected with each of its four nearest-neighbor rods by a "ladder" of parallel springs which joins two neighboring rods at regular intervals b along their length (Fig. 3a). The plane normal to the rods is the xy-plane, and the co-ordinate systems used are those of the preceding section.

We now consider the process of forming our screw dislocation. We cut all springs crossing (say) the xz-plane ($x > 0$) to the intended line of the dislocation and then apply equal and opposite vertical forces to each of the rods in the cut faces, starting from zero and increasing them until the dislocation is formed (Fig. 3b). As the dislocation forms the rods slide past each other and the forces on them do work. To obtain the total strain energy of the dislocation we must add to the work done in sliding the cut faces past each other the work done when we replace the springs across the xz-plane.

The co-ordinates of a row on the positive face of the cut are $(m, \frac{1}{2})$, while the co-ordinates of a row in the negative face of the cut are $(m, -\frac{1}{2})$, where m is half an odd positive integer in the case of Configuration I and a positive integer in the case of Configuration II. The force $F_{m,\frac{1}{2}}$ applied to the mth rod in the positive face of the cut is equal in magnitude and opposite in sign to the force $F_{m,-\frac{1}{2}}$ applied to the corresponding row in the negative face of the cut. If we assume for consistency with the results of the preceding section that we introduce a right-hand screw dislocation, then $F_{m,\frac{1}{2}}$ is directed in the negative z-direction, and the displacement it produces is also negative.

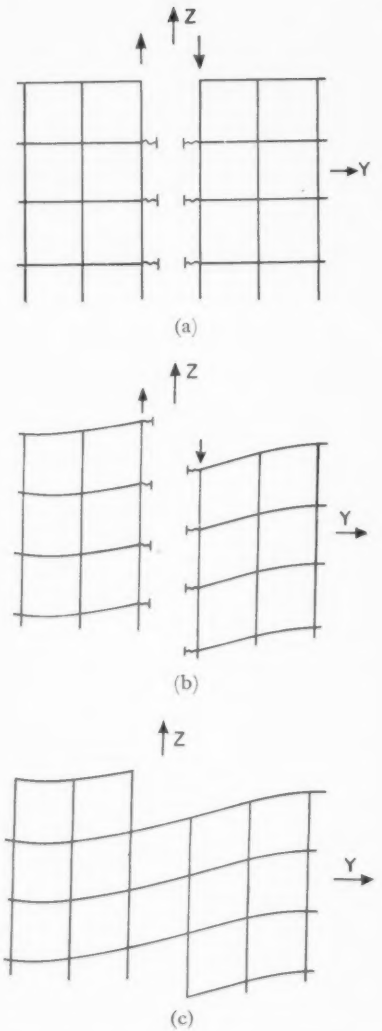

FIG. 3. Steps in forming a discrete screw dislocation.

We denote the displacement of the mth row in the positive face of the cut by $\xi_{m,\frac{1}{2}}(<0)$ and note that it satisfies the relation

$$\xi_{m,\frac{1}{2}} = -\xi_{m,-\frac{1}{2}}. \tag{3.1}$$

It is also clear from Fig. 3(b) that $\xi_{m,\frac{1}{2}}$ and $\xi_{m,-\frac{1}{2}}$ are related to the displacements $w_{m,\frac{1}{2}}$ and $w_{m,-\frac{1}{2}}$ evaluated in the preceding section through

$$\xi_{m,\frac{1}{2}} = -\left(\frac{\boldsymbol{b}}{2} - w_{m,\frac{1}{2}}\right); \quad \xi_{m,-\frac{1}{2}} = w_{m,-\frac{1}{2}} - \frac{\boldsymbol{b}}{2}. \tag{3.2}$$

The force $F_{m,\frac{1}{2}}$ satisfies the equilibrium equation

$$\begin{aligned} &A(w_{m,+1,\frac{1}{2}} - 2w_{m,\frac{1}{2}} + w_{m-1,\frac{1}{2}}) + \\ &+B(w_{m,\frac{3}{2}} - w_{m,\frac{1}{2}}) + F_{m,\frac{1}{2}} = 0 \end{aligned} \tag{3.3}$$

as it increases from zero to its final value, and a similar expression holds for $F_{m,-\frac{1}{2}}$. The final value of $F_{m,\frac{1}{2}}$ is given by equations (3.3) and (2.3) as

$$F_{m,\frac{1}{2}}(\text{final}) = -B(w_{m,\frac{1}{2}} - w_{m,-\frac{1}{2}} + \boldsymbol{b}).$$

Since the displacement of the row $(m, \frac{1}{2})$ during the formation of the dislocation is $\xi_{m,\frac{1}{2}}$, the work done in moving the row $(m, \frac{1}{2})$ to its final position is

$$-\tfrac{1}{2}B(w_{m,\frac{1}{2}} - w_{m,-\frac{1}{2}} + \boldsymbol{b})(\xi_{m,\frac{1}{2}})$$

where the factor $\frac{1}{2}$ is introduced because of the force $F_{m,\frac{1}{2}}$ in this Hookeian model builds up linearly from zero to its final value. An equal amount of work is done in displacing the row $(m, -\frac{1}{2})$ to its final position, so that the total work done in sliding the faces past each other in forming the dislocation is therefore

$$B\sum_m (2w_{m,\frac{1}{2}})\left(\frac{\boldsymbol{b}}{2} - w_{m,\frac{1}{2}}\right). \tag{3.4}$$

This is the work done *for each atom plane threaded by the dislocation.*

After the cut faces have moved past each other to their final positions, all springs crossing the xz-plane ($x > 0$) must be replaced to rejoin the two faces. We must remember now, however, that we have given each pair of rows facing each other across the cut a relative vertical displacement of very nearly a repeat distance $\boldsymbol{b}$ of the "ladder" of springs joining them together. This means that in rejoining the individual pairs of rows we do not connect with a spring two points originally on the same level across the cut, but now join a point in a rod in the positive face of the cut to a point in the corresponding row in the negative face which was originally a distance $\boldsymbol{b}$ below it (Fig. 3c). This adds an additional energy

$$\tfrac{1}{2}B\sum_m (w_{m,\frac{1}{2}} - w_{m,-\frac{1}{2}} + \boldsymbol{b})^2 = 2B\sum_m (w_{m,\frac{1}{2}})^2. \tag{3.5}$$

Adding the contributions given by (3.4) and (3.5), we obtain for the total dislocation strain energy per unit length of dislocation,

$$E_{\text{strain}} = B\sum_m w_{m,\frac{1}{2}}. \tag{3.6}$$

Alternatively, in the case of Configuration I we could make the cut along the y-axis. The expression for the strain energy in this case is

$$E_{\text{strain}} = A\sum_n \left(w_{-\frac{1}{2},n} - \frac{\boldsymbol{b}}{4}\right). \tag{3.7}$$

We now evaluate these expressions for each of Configurations I and II.

(a) *Configuration I*

In this case $w_{m,\frac{1}{2}}$ is given by equation (2.9) as

$$w_{m,\frac{1}{2}} = \frac{\boldsymbol{b}}{4} - \frac{\boldsymbol{b}}{\pi^2}\int_0^{\pi/2}\int \frac{\sin^2 y}{\sin x} \times$$

$$\times \frac{\sin 2mx}{(A/B)\sin^2 x + \sin^2 y}\,dx\,dy \tag{3.8}$$

where m is half an odd integer. This expression simplifies to (see Appendix A, equation (A.9)).

$$w_{p/2,\frac{1}{2}} = \frac{\boldsymbol{b}\sqrt{C}}{2\pi}\int_0^{\pi/2} \frac{\sin px}{\sqrt{1 + C\sin^2 x}}\,dx, \tag{3.9}$$

where we have put $(A/B) = C$, and $2m = p$, where p is an odd integer. On substituting equation (3.9) into equation (3.6) and interchanging the order of summation and integration, we obtain

$$E_{\text{strain}} = B\sqrt{C}\frac{b}{2\pi}\int_0^{\pi/2}\sum_{k=0}^{N}\sin(2k+1)x\,\frac{dx}{\sqrt{1+C\sin^2 x}}$$

$$= \frac{b}{2\pi}\sqrt{AB}\int_0^{\pi/2}\frac{\sin^2 Nx}{\sin x\sqrt{1+C\sin^2 x}}\,dx \tag{3.10}$$

$$= \frac{b}{2\pi}\sqrt{AB}\,F(N;\ C).$$

The function $F(N; C)$ is evaluated in Appendix B in the limit of large N with the result that

$$F(N;\ C) = \tfrac{1}{2}\ln 2\gamma - \tfrac{1}{4}\ln\frac{1+C}{4} + \tfrac{1}{2}\ln N + 0(1). \tag{3.11}$$

The expression for the strain energy becomes finally

$$E_{\text{strain}} = \frac{b}{4\pi}\sqrt{AB}\left\{\ln 2\gamma - \tfrac{1}{2}\ln\frac{1+C}{4} + \ln N + 0(1)\right\}. \tag{3.12}$$

To evaluate the strain energy using the expression given by equation (3.7) we need $w_{-\frac{1}{2},n}$ given by

$$w_{-\frac{1}{2},n} = \frac{b}{4} + \frac{b}{\pi^2}\int_0^{\pi/2}\int\frac{\sin y\sin 2ny}{(A/B)\sin^2 x + \sin^2 y}\,dxdy$$

where n is half an odd integer. Replacing $2n$ by p, an odd integer, (A/B) by C, and integrating over x, we obtain

$$w_{-\frac{1}{2},p/2} = \frac{b}{4} + \frac{b}{2\pi\sqrt{C}}\int_0^{\pi/2}\frac{\sin py}{\sqrt{1+1/C\sin^2 y}}\,dy. \tag{3.13}$$

Substituting this expression into equation (3.7) and again interchanging the order of summation and integration, we find that

$$E_{\text{strain}} = \frac{b}{2\pi}\frac{A}{\sqrt{C}}\int_0^{\pi/2}\sum_{k=0}^{N'}\sin(2k+1)y\,\frac{dy}{\sqrt{1+1/C\sin^2 y}}$$

$$= \frac{b}{2\pi}\sqrt{AB}\int_0^{\pi/2}\frac{\sin^2 N'y}{\sin y\sqrt{1+1/C\sin^2 y}}\,dy \tag{3.14}$$

$$= \frac{b}{2\pi}\sqrt{AB}F(N';\ C^{-1}).$$

The final expression for the strain energy in this case is

$$E_{\text{strain}} = \frac{b}{4\pi}\sqrt{AB}\left\{\ln 2\gamma - \tfrac{1}{2}\ln\frac{1+C}{4C} + \ln N' + 0(1)\right\}. \tag{3.15}$$

(b) *Configuration II*

In this case $w_{m,\frac{1}{2}}$ is given by

$$w_{m,\frac{1}{2}} = \frac{b}{4} - \frac{b}{\pi^2}\int_0^{\pi/2}\int\frac{\cos x\sin 2mx}{\sin x}\times$$

$$\times\frac{\sin^2 y}{(A/B)\sin^2 x + \sin^2 y}\,dxdy$$

$$= \frac{b}{4}\delta_{m,0} + \frac{b\sqrt{C}}{2\pi}\int_0^{\pi/2}\frac{\cos x\sin 2mx}{\sqrt{1+C\sin^2 x}}\,dx \tag{3.16}$$

where m is an integer. If we substitute this expression into equation (3.6) and interchange the order of integration and summation, we obtain

$$E_{\text{strain}} = \frac{Bb}{4} + \frac{Bb\sqrt{C}}{2\pi}\int_0^{\pi/2}\sum_{m=0}^{N}\sin 2mx\,\frac{\cos x\,dx}{\sqrt{1+C\sin^2 x}}$$

$$= \frac{Bb}{4} + \frac{b\sqrt{AB}}{4\pi}\int_0^{\pi/2}\frac{\cos x}{\sin x}\cdot\frac{\cos x - \cos(2N+1)x}{\sqrt{1+C\sin^2 x}}\,dx \tag{3.17}$$

$$= \frac{Bb}{4} + \frac{b\sqrt{AB}}{4\pi}G(N;\ C).$$

The function $G(N; C)$ is evaluated in Appendix B in the limit of large N with the result that

$$G(N; C) = \ln 2\gamma - \tfrac{1}{2}\ln\frac{1+C}{4} - \\ -\frac{1}{\sqrt{C}}\sin^{-1}\sqrt{\frac{C}{1+C}} + \ln N + 0(1). \quad (3.18)$$

The final expression for the strain energy in this case is

$$E_{\text{strain}} = \frac{Bb}{4} + \frac{b\sqrt{AB}}{4\pi}\left\{\ln 2\gamma - \tfrac{1}{2}\ln\frac{1+C}{4} - \right. \\ \left. -\frac{1}{\sqrt{C}}\sin^{-1}\sqrt{\frac{C}{1+C}} + \ln N + 0(1)\right\}. \quad (3.19)$$

(c) *Boundary Correction to Strain Energy*

There is a correction which must be added to the expressions obtained above to give the total strain energy. Since it is the same for both Configurations I and II and can adequately be treated by continuum theory, we have deferred discussion of this term until now. This contribution arises from the fact that in forming the screw dislocation work is done on the external bounding surface of the crystal, which we assume to be a cylinder of radius R, in addition to that done on the cut faces. In continuum theory, where it is customary to exclude the dislocation core by a cylinder of radius $r_0 (r_0 \lll R)$, the net work done on these two cylinders cancels out,[8] and the total strain energy is given correctly by just the integrals over the cut faces.

In the present case we have not assumed any cylinder of exclusion at the dislocation core, so that we cannot say that the work done on the external surface of the cylinder will be cancelled in any obvious way by work done at the dislocation core.

In the derivation which follows we assume that R is so large that the corrections to the expressions (2.11) and (2.25) for the displacement component are negligible.

The displacement component in this limit, equation (2.11), can be expressed in terms of the continuous variables x and y by the substitutions

$$x = m\xi, \qquad y = n\eta, \quad (3.20)$$

where ξ and η are the spacings between neighboring rows in the x- and y-directions, respectively. Thus we may write

$$w(x, y) = \frac{b}{2\pi}\tan^{-1}\frac{\kappa y}{x} \quad (3.21)$$

where

$$\kappa = \frac{\xi}{\eta}\sqrt{\frac{A}{B}} = \frac{\xi}{\eta}\sqrt{C}. \quad (3.22)$$

Then it is clear that the work (per unit length of dislocation) done on the external surface is

$$E_{\text{boundary}} = \frac{1}{2b}\int_{\theta_0}^{2\pi+\theta_0} w(R, \theta)\tau_{zr}(R, \theta)bR\, d\theta \quad (3.23)$$

where θ_0 gives the location of the cut,

$$w(R, \theta) = \frac{b}{2\pi}\tan^{-1}(\kappa \tan\theta), \quad (3.24a)$$

and

$$\tau_{zr} = \tau_{13}\cos\theta + \tau_{23}\sin\theta. \quad (3.24b)$$

The stresses τ_{13} and τ_{23} are given by ESHELBY *et al.*[1] as

$$\tau_{13} = c_{55}'\frac{\partial w}{\partial x} \\ = -c_{55}'\frac{b\kappa}{2\pi R}\cdot\frac{\sin\theta}{\cos^2\theta + \kappa^2\sin^2\theta} \\ \tau_{23} = c_{44}'\frac{\partial w}{\partial y} \\ = c_{44}'\frac{b\kappa}{2\pi R}\cdot\frac{\cos\theta}{\cos^2\theta + \kappa^2\sin^2\theta} \quad (3.25)$$

where c_{44}' and c_{55}' are the macroscopic elastic constants of the crystal referred to the co-ordinate axes of Figs. 1 and 2. With the aid of the results of Appendix C, we can express the elastic constants c_{44}' and c_{55}' in terms of A and B as

$$c_{44}' = \frac{\eta}{\xi\zeta}B, \qquad c_{55}' = \frac{\xi}{\eta\zeta}A \quad (3.26)$$

where ζ is the spacing between atoms in any row and is $\boldsymbol{b}$ in the present case. With these results the boundary strain energy becomes

$$E_{\text{boundary}} = -\frac{\boldsymbol{b}}{8\pi^2}\sqrt{AB}(\kappa^2-1)\int_{\theta_0}^{2\pi+\theta_0} \times$$

$$\times \tan^{-1}(\kappa \tan\theta)\frac{\sin\theta\cos\theta\, d\theta}{\cos^2\theta+\kappa^2\sin^2\theta}. \tag{3.27}$$

If we denote the integral in equation (3.27) by I, an integration by parts gives us

$$I = \frac{1}{2(\kappa^2-1)}\tan^{-1}(\kappa\tan\theta)\ln(\cos^2\theta+\kappa^2\sin^2\theta)\Big|_{\theta_0}^{2\pi+\theta_0} - \frac{\kappa}{2(\kappa^2-1)}\int_{\theta_0}^{2\pi+\theta_0}\frac{\ln(\cos^2\theta+\kappa^2\sin^2\theta)}{\cos^2\theta+\kappa^2\sin^2\theta}d\theta$$

$$= \frac{\pi}{\kappa^2-1}\ln(\cos^2\theta_0+\kappa^2\sin^2\theta_0) - \frac{2\kappa}{(\kappa^2-1)}\int_0^{\pi/2}\frac{\ln(\cos^2\theta+\kappa^2\sin^2\theta)}{\cos^2\theta+\kappa^2\sin^2\theta}d\theta \tag{3.28}$$

since the second term is independent of θ_0 due to the periodicity of the integrand. The evaluation of the integral is straightforward but tedious. The final result is

$$E_{\text{boundary}} = \frac{\boldsymbol{b}}{8\pi}\sqrt{AB}\ln\frac{\kappa}{\cos^2\theta_0+\kappa^2\sin^2\theta_0}. \tag{3.29}$$

In the case of the screw dislocation in Configuration I with the cut assumed to be along the x-axis ($\theta_0 = 0$), equations (3.12) and (3.29) give for the total strain energy

$$E_{\text{strain}}(\theta_0=0) = \frac{\boldsymbol{b}}{4\pi}\sqrt{AB}\times$$

$$\times\left\{\ln 2\gamma - \frac{1}{2}\ln\frac{1+C}{2} + \frac{1}{2}\ln\kappa + \ln N\right\} \tag{3.30a}$$

while for the screw dislocation with the cut assumed to be along the y-axis ($\theta_0 = \pi/2$), equations (3.15) and (3.29) give for the total strain energy

$$E_{\text{strain}}\left(\theta_0=\frac{\pi}{2}\right) = \frac{\boldsymbol{b}}{4\pi}\sqrt{AB}\times$$

$$\times\left\{\ln 2\gamma - \frac{1}{2}\ln\frac{1+C}{4} + \frac{1}{2}\ln C - \frac{1}{2}\ln\kappa + \ln N'\right\}. \tag{3.30b}$$

Since in evaluating the boundary contribution to the strain energy we have essentially normalized our results to give the energy (per unit length) stored in a right circular cylinder of external radius R concentric with the dislocation, in equations (3.30) we must have

$$N = \frac{R}{\xi}, \qquad N' = \frac{R}{\eta}. \tag{3.31}$$

With these considerations both equations (3.30) reduce to

$$E_{\text{strain}} = \frac{\boldsymbol{b}}{4\pi}\sqrt{AB}\left\{\ln 2\gamma - \frac{1}{2}\ln\frac{1+C}{4} + \right.$$

$$\left. + \frac{1}{4}\ln C + \ln\frac{R}{\sqrt{\xi\eta}}\right\} \tag{3.32}$$

so that the strain energy is independent of the location of the cut as it must be.

In the case of the screw dislocation in Configuration II, the final expression for the strain energy becomes

$$E_{\text{strain}} = \frac{\boldsymbol{b}}{4\pi}\sqrt{AB}\left\{\ln 2\gamma - \frac{1}{2}\ln\frac{1+C}{4} + \right.$$

$$\left. + \frac{1}{\sqrt{C}}\left(\pi - \sin^{-1}\sqrt{\frac{C}{1+C}}\right) + \frac{1}{4}\ln C + \ln\frac{R}{\sqrt{\xi\eta}}\right\}. \tag{3.33}$$

4. DISCUSSION AND CONCLUSIONS

We can now put on a somewhat more physical basis what up to this point has been primarily a

mathematical model by explicitly exhibiting the correspondence between our results and those obtained by continuum theory in the region in which the two approaches would be expected to overlap.

With the aid of equations (3.22) and (3.26) the expression for the displacement component $w(x, y)$ at large distances from the dislocation core, equations (3.21) becomes

$$w(x,y) = \frac{\boldsymbol{b}}{2\pi} \tan^{-1} \sqrt{\frac{c_{55}'}{c_{44}'}} \frac{y}{x} \tag{4.1}$$

in agreement with the result of ESHELBY *et al.*[1] for this case. Again using equations (3.22) and (3.26) we can rewrite the expressions (3.32) and (3.33) for the dislocation strain energy in terms of the macroscopic elastic constants as

$$E_{\text{strain}}(\text{Configuration I}) = \frac{\boldsymbol{b}^2}{4\pi} \sqrt{c_{44}' c_{55}'} \ln \frac{R}{r_0^{(1)}} \tag{4.2a}$$

$$r_0^{(1)} = \frac{\sqrt{1+C}}{4\gamma} \frac{\sqrt{\xi\eta}}{C^{\frac{1}{4}}} = \frac{1}{4\gamma} \sqrt{\xi^2 \left(\frac{c_{44}'}{c_{55}'}\right)^{\frac{1}{2}} + \eta^2 \left(\frac{c_{55}'}{c_{44}'}\right)^{\frac{1}{2}}}, \tag{4.2b}$$

and

$$E_{\text{strain}}(\text{Configuration II}) = \frac{\boldsymbol{b}^2}{4\pi} \sqrt{c_{44}' c_{55}'} \ln \frac{R}{r_0^{(2)}} \tag{4.3a}$$

$$r_0^{(2)} = \epsilon r_0^{(1)}$$

where

$$\epsilon = \exp\left\{-\frac{\xi}{\eta} \sqrt{\frac{c_{44}'}{c_{55}'}} (\pi - \phi)\right\},$$

$$\phi = \sin^{-1} \sqrt{\frac{\eta^2 c_{55}'}{\xi^2 c_{44}' + \eta^2 c_{55}'}} \tag{4.3b}$$

in agreement with the results of FOREMAN[8] for this case. However, with the aid of this model we have also been able to define unambiguously the cut off radius r_0, which appears in continuum theory, in terms of the elastic constants and lattice spacings of the crystal.

In the particular case of alkali-halide crystals where the Burgers vector of a screw dislocation lies along a $\langle 110 \rangle$ direction, the cartesian axes depicted in Figs. 1 and 2 do not coincide with the usual cubic crystal axes and the relations between the primed elastic constants and the elastic constants referred to the cubic crystal axes are (see Appendix C).

$$c_{44}' = \tfrac{1}{2}(c_{11} - c_{12}) \qquad c_{55}' = c_{44}. \tag{4.4}$$

Using these results in conjunction with the values of the low-temperature elastic constants for sodium chloride[9]

$$\begin{aligned} c_{11} &= 5{\cdot}75 \times 10^{11} \text{ erg/cm}^3 \\ c_{12} &= 0{\cdot}986 \times 10^{11} \text{ erg/cm}^3 \\ c_{44} &= 1{\cdot}327 \times 10^{11} \text{ erg/cm}^3 \\ \boldsymbol{b} &= 3{\cdot}9456 \text{ A} \end{aligned} \tag{4.5}$$

we obtain the following values for the cut-off radii and the strain energy stored inside a cylinder of 1μ radius concentric with the screw dislocation:

$$\begin{aligned} r_0^{(1)} &= 0{\cdot}13\boldsymbol{b} = 0{\cdot}513 \text{ A} \\ E_{\text{strain}}(\text{Configuration I}) &= 13{\cdot}58 \times 10^7 \text{ eV/cm} \\ &= 5{\cdot}36 \text{ eV/plane}, \end{aligned} \tag{4.6a}$$

$$\begin{aligned} r_0^{(2)} &= 0{\cdot}85 \times 10^{-3}\boldsymbol{b} = 3{\cdot}35 \times 10^{-3} \text{ Å} \\ E_{\text{strain}}(\text{Configuration II}) &= 20{\cdot}50 \times 10^7 \text{ eV/cm} \\ &= 8{\cdot}09 \text{ eV/plane}. \end{aligned} \tag{4.6b}$$

We note that the values of r_0 given by equations (4.2b) and (4.3b) are considerably smaller than the values ($r_0 \sim 2{\cdot}5$ Å) usually assumed in strain-energy calculations based on continuum theory (reference 2, pp. 29–38). However, in that case the cut-off radius usually defines the region outside which Hooke's law is valid, and to the strain energy obtained from the continuum approach must be added the (unknown) strain energy in the bad material inside this radius. With the present treatment, however, we are in fact able to obtain the total dislocation strain energy; there are no unknown energy values to be added, and it is possible to differentiate between the two configurations on the basis of their strain energies. This, however, is a consequence of the discrete nature of the present model, and the strain energies obtained through its use are probably still overestimates, since the assumption of Hooke's law forces give values for

the displacement differences (the discrete analogue of the strains) at the dislocation core which while smaller than those given by continuum theory are still too large for this approximation to be strictly valid. In addition, the present model neglects the contributions to the strain energy associated with the x- and y-components of displacement. These contributions may not be negligible in the region of the dislocation core.[4,5]

Finally we note from Tables 1 and 2 that at least in the isotropic case taking the discreteness of the lattice into account has the effect of spreading out the dislocation in both the xz-plane and the yz-plane, if we define the width of a screw dislocation as the region in which the displacement is less than one-half of its limiting value at infinity.

Acknowledgements—I should like to thank Professor M. H. L. Pryce for suggesting such a discrete model of a screw dislocation and for helpful discussions during the course of this work. I should also like to thank Professor F. C. Frank for several stimulating conversations on the subject of strain energy calculations, and Mr. G. H. Weiss for his help in the preparation of Appendix B. Finally, it is a pleasure to thank Professor Pryce for extending me the hospitality of the H. H. Wills Physical Laboratory, where the major portion of the work described in this note was carried out, and to acknowledge the financial support of a Marshall Aid Commemoration Commission Scholarship during 1954–1956.

APPENDIX A

Evaluation of Displacement Integrals

(1) We consider first the integral occurring in the expression for the displacement components for the dislocation in Configuration I:

$$w_{m,n}=\frac{b}{4}-\frac{b}{\pi^2}\int_0^{\pi/2}\int\frac{\sin y}{\sin x}\,\frac{\sin 2mx\sin 2ny}{C\sin^2 x+\sin^2 y}\,dxdy \tag{A.1}$$

where m and n are half-odd integers. The simplest way of evaluating this integral is to evaluate it in the special case $m=\frac{1}{2}$, for which it takes a relatively simple form, and obtain the off-axis values by means of the defining difference equation (2.3). In this case we have that

$$w_{\frac{1}{2},n}=\frac{b}{4}-\frac{b}{\pi^2}\int_0^{\pi/2}\int\frac{\sin y\sin 2ny}{C\sin^2 x+\sin^2 y}\,dxdy$$

$$=\frac{b}{4}-\frac{b}{2\pi}\int_0^{\pi/2}\frac{\sin 2ny\,dy}{\sqrt{(1+C)-\cos^2 y}}. \tag{A.2}$$

If we replace $2n$ by p, where p is an odd integer, we can expand $\sin py$ as follows (reference 10, p. 67):

$$\sin py=p\left\{\sin y-\frac{p^2-1^2}{3!}\sin^3 y+\right.$$

$$\left.+\frac{(p^2-1^2)(p^2-3^2)}{5!}\sin^5 y-\ldots\right\}. \tag{A.3}$$

Then, introducing the auxiliary integral

$$J_p(C)=\int_0^{\pi/2}\frac{\sin^p y\,dy}{\sqrt{(1+C)-\sin^2 y}}, \tag{A.4}$$

and using the expansion (A.3) we have finally

$$w_{\frac{1}{2},\,p/2}=\frac{b}{4}-\frac{bp}{2\pi}\left\{J_1-\frac{p^2-1^2}{3!}J_3+\right.$$

$$\left.+\frac{(p^2-1^2)(p^2-3^2)}{5!}J_5-\ldots\right\}. \tag{A.5}$$

The integral J_p has the explicit form[11]

$$J_p(C)=\frac{1}{2\sqrt{1+C}}\,\frac{\Gamma(\frac{1}{2})\Gamma\left(\frac{p+1}{2}\right)}{\Gamma\left(\frac{p+2}{2}\right)}\times$$

$$\times F\left(\frac{1}{2},\frac{1}{2};\ \frac{p+2}{2};\ \frac{1}{1+C}\right) \tag{A.6}$$

where $F(a,\,b;\,c;\,x)$ is Gauss' hypergeometric function. With the aid of the recurrence formula for the hypergeometric function (reference 12, p. 282)

$$c[c-1-(2c-a-b-1)x]F(a,b;\,c;\,x)+$$

$$+(c-a)(c-b)xF(a,b;\,c+1;\,x)$$

$$=c(c-1)(1-x)F(a,\,b;\,c-1;\,x),$$

and the relations

$$F(\tfrac{1}{2},\tfrac{1}{2};\,\tfrac{1}{2};\,x)=(1-x)^{-\frac{1}{2}}$$

$$F(\tfrac{1}{2},\tfrac{1}{2};\,\tfrac{3}{2};\,x)=\frac{\sin^{-1}\sqrt{x}}{\sqrt{x}}$$

we can establish the following recurrence formula for the J_p's

$$(p+1)J_{p+2}=p(1-C)J_p+C(p-1)J_{p-2}\quad p\geqslant 3 \tag{A.7}$$

with

$$J_1=\sin^{-1}\sqrt{\frac{1}{1+C}};\ J_3=\tfrac{1}{2}[\sqrt{C}+(1-C)J_1]. \tag{A.8}$$

Similarly we can evaluate (A.1) along the line $n=\frac{1}{2}$. Putting $2m=p$, where p is an odd integer, we have

$$w_{p/2,\,\frac{1}{2}}=\frac{b}{4}-\frac{b}{\pi^2}\int_0^{\pi/2}\!\!\int\frac{\sin px}{C\sin^2x+\sin^2y}\,\frac{\sin^2y}{\sin x}\,dxdy$$

$$=\frac{b}{4}-\frac{b}{\pi^2}\int_0^{\pi/2}\!\!\int\frac{\sin px}{\sin x}\,dxdy+$$

$$+\frac{bC}{\pi^2}\int_0^{\pi/2}\!\!\int\frac{\sin x\sin px}{C\sin^2x+\sin^2y}\,dxdy \tag{A.9}$$

$$=\frac{b}{2\pi}\int_0^{\pi/2}\frac{\sin px}{\sqrt{(1+C^{-1})-\cos^2x}}\,dx.$$

If we make use of the expansion (A.3), we can express (A.9) as

$$w_{p/2,\,\frac{1}{2}}=\frac{bp}{2\pi}\left\{J_1^*-\frac{p^2-1^2}{3!}J_3^*+\right.$$

$$\left.+\frac{(p^2-1^2)(p^2-3^2)}{5!}J_5^*-\ldots\right\} \tag{A.10}$$

where we have introduced the auxiliary integral

$$J_p^*(C)=\int_0^{\pi/2}\frac{\sin^px\,dx}{\sqrt{(1+C^{-1})-\cos^2x}}=J_p\left(\frac{1}{C}\right). \tag{A.11}$$

(2) The displacement components for the dislocation in Configuration II are given by

$$w_{m,n}=\frac{b}{4}-\frac{b}{\pi^2}\int_0^{\pi/2}\!\!\int\frac{\cos x\sin 2mx}{\sin x}\times$$

$$\times\frac{\sin y\sin 2ny}{C\sin^2x+\sin^2y}\,dxdy \tag{A.12}$$

where m is an arbitrary integer, while n is half an odd integer. This expression assumes comparatively simple forms along the lines $m=1$ and $n=\frac{1}{2}$ and can be evaluated readily in these cases. The off-axes values can be evaluated by the use of the defining difference equation (2.14).

We see immediately that $w_{0,\,n}=b/4$. Furthermore, in the special case $m=1$ equation (A.12) becomes

$$w_{1,n}=\frac{b}{4}-\frac{2b}{\pi^2}\int_0^{\pi/2}\!\!\int\frac{\cos^2x\sin y\sin 2ny}{C\sin^2x+\sin^2y}\,dxdy$$

$$=\frac{b}{4}-\frac{2b}{\pi^2}\int_0^{\pi/2}\!\!\int\frac{\sin y\sin 2ny}{C\sin^2x+\sin^2y}\,dxdy+$$

$$+\frac{2b}{\pi^2}\int_0^{\pi/2}\!\!\int\frac{\sin^2x\sin y\sin 2ny}{C\sin^2x+\sin^2y}\,dxdy.$$

This is a particularly simple expression to evaluate since the first integral has already been evaluated in the first part of this Appendix, while the second integral can be transformed as follows:

$$\frac{2b}{\pi^2}\int_0^{\pi/2}\!\!\int\frac{\sin^2x\sin y\sin 2ny}{C\sin^2x+\sin^2y}\,dxdy=\frac{2b}{\pi^2C}\int_0^{\pi/2}\!\!\int\sin y\sin 2ny\cdot dxdy$$

$$-\frac{2b}{\pi^2C}\int_0^{\pi/2}\!\!\int\frac{\sin^3y\sin 2ny}{C\sin^2x+\sin^2y}\,dxdy$$

$$=\frac{b\delta_{p,1}}{4C}-\frac{bp}{\pi C}\left\{J_3-\frac{p^2-1^2}{3!}J_5+\frac{(p^2-1^2)(p^2-3^2)}{5!}J_7-\ldots\right\}$$

where we have replaced $2n$ by p, an odd integer, and have used the auxiliary integrals defined by equation (A.4).

Thus, using the result given in equation (A.5) we have finally

$$w_{1\ p/2}=\frac{b}{4}+\frac{b}{4C}\delta_{p,1}-\frac{bp}{\pi}\Big\{(J_1+\frac{1}{C}J_3)-\frac{p^2-1^2}{3!}\times$$

$$\times\Big(J_3+\frac{1}{C}J_5\Big)+\frac{(p^2-1^2)(p^2-3^2)}{5!}\Big(J_5+\frac{1}{C}J_7\Big)-\ldots\Big\}.$$

In like manner we can evaluate the integral (A.12) along the line $n=\frac{1}{2}$. In this case

$$w_{m,\frac{1}{2}}=\frac{b}{4}-\frac{b}{\pi^2}\int_0^{\pi/2}\int\frac{\cos x\sin 2mx}{\sin x}\frac{\sin^2 y}{C\sin^2 x+\sin^2 y}dxdy$$

$$=\frac{b}{4}-\frac{b}{\pi^2}\int_0^{\pi/2}\int\frac{\cos x\sin 2mx}{\sin x}dxdy+\frac{bC}{\pi^2}\int_0^{\pi/2}\int\frac{\sin x\cos x\sin 2mx}{C\sin^2 x+\sin^2 y}dxdy$$

$$=\frac{b}{4}\delta_{m0}+\frac{b}{2\pi}\int_0^{\pi/2}\frac{\cos x\sin 2mx}{\sqrt{(1+C^{-1})-\cos^2 x}}dxdy.$$

If we replace $2m$ by p, an even integer, we can expand $\sin px$ as follows (reference 10, p. 66):

$$\sin px=p\cos x\Big\{\sin x-\frac{p^2-2^2}{3!}\sin^3 x+$$

$$+\frac{(p^2-2^2)(p^2-4^2)}{5!}\sin^5 x-\ldots\Big\}.$$

From this result it follows that

$$\cos x\sin px=p\Big\{(\sin x-\sin^3 x)-$$

$$-\frac{p^2-2^2}{3!}(\sin^3 x-\sin^5 x)+\ldots\Big\}$$

so that finally,

$$w_{p/2,\frac{1}{2}}=\frac{b}{4}\delta_{p/2,0}+\frac{b}{2\pi}p\Big\{(J_1^*-J_3^*)-\frac{p^2-2^2}{3!}\times$$

$$\times(J_3^*-J_5^*)+\frac{(p^2-2^2)(p^2-4^2)}{5!}(J_5^*-J_7^*)-\ldots\Big\}.$$

In the special case $C=1$ (the square net), $J_m=J_m^*$, and the integrals have the following values:

$$J_1=\frac{\pi}{4}\qquad J_7=\frac{1}{3}$$

$$J_3=\frac{1}{2}\qquad J_9=\frac{3\pi}{32}$$

$$J_5=\frac{\pi}{8}\qquad J_{11}=\frac{4}{15}$$

and in general

$$2J_{4k+1}=\frac{1\cdot3\cdot5\cdot7\ldots(2k-1)}{2\cdot4\cdot6\cdot8\ldots\ (2k)}\frac{\pi}{2}\quad k=1,2,3,\ldots$$

$$2J_{4k+3}=\frac{2\cdot4\cdot6\cdot8\ldots\ (2k)}{3\cdot5\cdot7\cdot9\ldots(2k+1)}\quad k=1,2,3,\ldots.$$

Values of $w_{m\ n}$ calculated by the methods of this Appendix for both Configurations I and II are given in Tables 1 and 2 respectively for the special case $C=1$.

APPENDIX B

Evaluation of The Strain Energy Integral

(1) The strain energy integral $F(N;C)$ is given by

$$F(N;C)=\int_0^{\pi/2}\frac{\sin^2 Nx}{\sin x}\frac{dx}{\sqrt{1+C\sin^2 x}}.\quad\text{(B.1)}$$

We can evaluate this integral in the limit of large N by

first evaluating

$$F'(N;\,C)=\frac{dF(N;\,C)}{dN}=\int_0^{\pi/2}\phi(x)\sin 2Nx\,dx \quad \text{(B.2)}$$

where we have assumed that N is a continuous variable, and

$$\phi(x)=\frac{x}{\sin x}\,\frac{1}{\sqrt{1+C\sin^2 x}}. \quad \text{(B.3)}$$

If now we integrate (B.2) by parts we obtain

$$F'(N;\,C)=-\phi(x)\frac{\cos 2Nx}{2N}\Big|_0^{\pi/2}+\frac{1}{2N}\int_0^{\pi/2}\phi'(x)\cos 2Nx\,dx \quad \text{(B.4)}$$

$$=-\frac{\pi}{2}\frac{\cos N\pi}{2N\sqrt{1+C}}+\frac{1}{2N}+\frac{1}{2N}\int_0^{\pi/2}\phi'(x)\cos 2Nx\,dx.$$

We now integrate both sides of equation (B.4) with respect to N in the interval $(1, N)$:

$$F(N;\,C)=F(1;\,C)+\tfrac{1}{2}\ln N-$$

$$-\frac{\pi}{4\sqrt{1+C}}\int_1^N\frac{\cos N\pi}{N}dN+$$

$$+\tfrac{1}{2}\int_1^N\frac{dN}{N}\int_0^{\pi/2}\phi'(x)\cos 2Nx\,dx, \quad \text{(B.5)}$$

and use the result that

$$\int_1^N\frac{\cos xy}{y}dy=-Ci(x)+Ci(Nx)$$

where

$$Ci(x)=-\int_x^\infty\frac{\cos t}{t}dt \quad \text{(B.6)}$$

is the cosine integral, to express equation (B.5) in the equivalent form

$$F(N;\,C)=F(1;\,C)+\tfrac{1}{2}\ln N+$$

$$+\frac{\pi}{4\sqrt{1+C}}\{Ci(\pi)-Ci(N\pi)\}+$$

$$+\tfrac{1}{2}\int_0^{\pi/2}\phi'(x)\{-Ci(2x)+Ci(2Nx)\}\,dx. \quad \text{(B.7)}$$

By repeatedly integrating equation (B.6) by parts, we find that for large x

$$Ci(x)=\frac{\sin x}{x}-\frac{\cos x}{x^2}+O(x^{-3}).$$

This means that if we neglect all terms of order N^{-1} in our expression for the strain energy, we can rewrite equation (B.7) as

$$F(N;\,C)=F(1;\,C)+\tfrac{1}{2}\ln N+\frac{\pi}{4\sqrt{1+C}}Ci(\pi)-$$

$$-\tfrac{1}{2}\int_0^{\pi/2}\phi'(x)Ci(2x)\,dx+0(1) \quad \text{(B.8)}$$

where with the aid of equation (A.11)

$$F(1;\,C)=\int_0^{\pi/2}\frac{\sin x\,dx}{\sqrt{1+C\sin^2 x}}=\frac{1}{\sqrt{C}}J_1^*(C)$$

$$=\frac{1}{\sqrt{C}}\sin^{-1}\sqrt{\frac{C}{1+C}}$$

and the terms of $0(1)$ go to zero as $N\to\infty$.

It only remains to evaluate the integral appearing in equation (B.8). This can be accomplished as follows. We write the integral as

$$I=\lim_{\epsilon\to 0}\int_{\epsilon}^{\pi/2}\phi'(x)Ci(2x)\,dx=\lim_{\epsilon\to 0}\times$$

$$\times\left\{\phi(x)Ci(2x)\Big|_{\epsilon}^{\pi/2}-\int_{\epsilon}^{\pi/2}\phi(x)\frac{\cos 2x}{x}dx\right\}$$

$$=\lim_{\epsilon\to 0}\left\{\frac{\pi}{2\sqrt{1+C}}Ci(\pi)-\phi(\epsilon)Ci(2\epsilon)-\right.$$

$$\left.-\int_{\epsilon}^{\pi/2}\frac{\cos 2x}{\sin x}\,\frac{dx}{\sqrt{1+C\sin^2 x}}\right\}. \tag{B.9}$$

The integral is readily evaluated with the result that

$$\lim_{\epsilon\to 0}\int_{\epsilon}^{\pi/2}\frac{\cos 2x}{\sin x}\,\frac{dx}{\sqrt{1+C\sin^2 x}}=-\frac{1}{2}\ln\frac{1+C}{2}-$$

$$-\frac{2}{\sqrt{C}}\sin^{-1}\sqrt{\frac{C}{1+C}}-\frac{1}{2}\ln\frac{\epsilon^2}{2}. \tag{B.10}$$

Furthermore, for small x (reference 11, p. 91)

$$Ci(x)=\ln\gamma+\ln x+0(x^2) \tag{B.11}$$

where ln γ is Euler's constant, ln $\gamma = 0{\cdot}57722$, so that finally

$$I=\frac{\pi}{2\sqrt{1+C}}Ci(\pi)+\frac{2}{\sqrt{C}}\sin^{-1}\sqrt{\frac{C}{1+C}}-$$

$$-\ln 2\gamma+\frac{1}{2}\ln\frac{1+C}{4}. \tag{B.12}$$

With this result $F(N;\,C)$ becomes

$$F(N;\,C)=\frac{1}{2}\ln 2\gamma-\frac{1}{4}\ln\frac{1+C}{4}+\frac{1}{2}\ln N+0(1). \tag{B.13}$$

In a similar manner we can obtain the large N expression for $G(N;\,C)$, which is defined by

$$G(N;\,C)=\int_0^{\pi/2}\frac{\cos x[\cos x-\cos(2N+1)x]\,dx}{\sin x\sqrt{1+C\sin^2 x}}$$

$$=2\int_0^{\pi/2}\frac{\cos^2 x\sin^2 Nx\,dx}{\sin x\sqrt{1+C\sin^2 x}}+\int_0^{\pi/2}\frac{\cos x\sin 2Nx}{\sqrt{1+C\sin^2 x}}\,dx$$

$$=2F(N;\,C)-2\int_0^{\pi/2}\frac{\sin x\sin^2 Nx}{\sqrt{1+C\sin^2 x}}+\int_0^{\pi/2}\frac{\cos x\sin 2Nx\,dx}{\sqrt{1+C\sin^2 x}}. \tag{B.14}$$

It is easily shown that in the limit as $N\to\infty$ the second integral is $O(N^{-1})$ so that we neglect its contribution to $G(N;\,c)$ in this limit. Denoting the second integral by $I(N;\,C)$, we consider N as a continuous variable to obtain

$$I'(N;\,C)=\frac{dI(N;\,C)}{dN}=\int_0^{\pi/2}\phi(x)\sin 2Nx\,dx \tag{B.15}$$

where

$$\phi(x)=\frac{x\sin x}{\sqrt{1+C\sin^2 x}}. \tag{B.16}$$

If now we integrate (B.15) by parts we find that

$$I'(N;\,C)=-\phi(x)\frac{\cos 2Nx}{2N}\Big|_0^{\pi/2}+$$

$$+\frac{1}{2N}\int_0^{\pi/2}\phi'(x)\cos 2Nx\,dx$$

$$=-\frac{\pi}{4\sqrt{1+C}}\,\frac{\cos N\pi}{N}+$$

$$+\frac{1}{2N}\int_0^{\pi/2}\phi'(x)\cos 2Nx\,dx. \tag{B.17}$$

We integrate both sides of equation (B.17) with respect to N in the interval $(1, N)$ to obtain

$$I(N;\,C)=I(1;\,C)+\frac{\pi}{4\sqrt{1+C}}\,Ci(\pi)-$$

$$-\tfrac{1}{2}\int_0^{\pi/2}\phi'(x)Ci(2x)\,dx+0(1), \qquad \text{(B.18)}$$

where the terms of $0(1)$ go to zero as $N\to\infty$.

The integral on the right-hand side of equation (B.18) is readily evaluated:

$$\int_0^{\pi/2}\phi'(x)Ci(2x)\,dx$$

$$=\phi(x)Ci(2x)\Big|_0^{\pi/2}-\int_0^{\pi/2}\phi(x)\frac{\cos 2x}{x}\,dx$$

$$=\frac{\pi}{2\sqrt{1+C}}Ci(\pi)-\int_0^{\pi/2}\frac{\sin x\cos 2x}{\sqrt{1+C\sin^2 x}}\,dx$$

$$=\frac{\pi}{2\sqrt{1+C}}Ci(\pi)-\frac{1}{\sqrt{C}}[J_1{}^*(C)-2J_3{}^*(C)] \qquad \text{(B.19)}$$

where we have used the auxiliary integrals defined by equation (A.11). Since $I(1;\,C)$ is given by

$$I(1;\,C)=\int_0^{\pi/2}\frac{\sin^3 x\,dx}{\sqrt{1+C\sin^2 x}}=\frac{1}{\sqrt{C}}J_3{}^*(C),$$

the expression for $I(N;\,C)$ becomes

$$I(N;\,C)=\frac{1}{2\sqrt{C}}J_1{}^*(C)=\frac{1}{2\sqrt{C}}\sqrt{\frac{C}{1+C}}+0(1). \qquad \text{(B.20)}$$

We finally obtain

$$G(N;\,C)=2F(N;\,C)-\frac{1}{\sqrt{C}}\sin^{-1}\sqrt{\frac{C}{1+C}}+0(1).$$

$$=\ln 2\gamma-\frac{1}{2}\ln\frac{1+C}{4}-\frac{1}{\sqrt{C}}\times \qquad \text{(B.21)}$$

$$\times\sin^{-1}\sqrt{\frac{C}{1+C}}+\ln N+0(1).$$

APPENDIX C

Relation Between Force Constants and Elastic Constants

Since we permit only vertical displacements of the rows of atoms, the total strain energy of our Hookeian lattice can be written as

$$U=\frac{NA}{2}\sum_{m,\,n=1}^{N}(w_{m+1,\,n}-w_{m,\,n})^2$$

$$+\frac{NB}{2}\sum_{m,\,n=1}^{N}(w_{m,\,n+1}-w_{m\,n})^2 \qquad \text{(C.1)}$$

where we have assumed a lattice of $N\times N$ rows, each row containing N atoms. If the spacings between neighboring rows in the x- and y-directions are ξ and η respectively, while the separation between atoms in any row is ζ, the volume per atom is $\xi\eta\zeta$. For a homogeneous pure strain we can rewrite equation (C.1) as*

$$U=2N^3[A\xi^2e_{13}{}^2+B\eta^2e_{23}{}^2] \qquad \text{(C.2)}$$

so that the energy density U/V becomes

$$u=\frac{U}{N^3\xi\eta\zeta}=2A\frac{\xi}{\eta\zeta}e_{13}{}^2+2B\frac{\eta}{\xi\zeta}e_{23}{}^2. \qquad \text{(C.3)}$$

According to the theory of elasticity (reference 13, p. 156)

$$\begin{aligned}2u=\;&c_{11}e_{11}{}^2+2c_{12}e_{12}{}^2+2c_{13}e_{13}{}^2+4c_{14}e_{11}e_{23}+\\&+4c_{15}e_{11}e_{13}+4c_{16}e_{11}e_{12}+c_{22}e_{22}{}^2+\\&+2c_{23}e_{22}e_{33}+4c_{24}e_{22}e_{23}+4c_{25}e_{22}e_{13}+\\&+4c_{26}e_{22}e_{12}+c_{33}e_{33}{}^2+4c_{34}e_{33}e_{23}+\\&+4c_{35}e_{33}e_{13}+4c_{36}e_{33}e_{12}+4c_{44}e_{23}{}^2+\\&+8c_{45}e_{23}e_{13}+8c_{46}e_{33}e_{12}+4c_{55}e_{13}{}^2+\\&+8c_{56}e_{13}e_{12}+4c_{66}e_{12}{}^2. \qquad \text{(C.4)}\end{aligned}$$

so that comparing the two expressions we find that

$$A=\frac{\eta\zeta}{\xi}e_{55} \qquad B=\frac{\xi\zeta}{\eta}c_{44} \qquad \text{(C.5)}$$

where the macroscopic elastic constants, c_{44} and c_{55},

* In writing equation (C.2) we have used the tensor strain components defined by

$$e_{ij}=\frac{1}{2}\left[\frac{\partial u_i}{\partial x_j}+\frac{\partial u_j}{\partial x_i}\right] \quad (i,j=1,2,3)$$

so that our final results can be compared directly with those obtained by ESHELBY *et al.*[1] and by [illegible]

are those appropriate to the co-ordinate systems shown in Figs. 1 and 2.

In the case of alkali-halide crystals for which the cartesian axes depicted in Figs. 1 and 2 do not coincide with the cubic crystal axes, we can express the elastic constants c_{44} and c_{55} in equation (C.5) in terms of the elastic constants referred to the cubic crystal axes as

$$c_{55}' = c_{44} \qquad c_{44}' = \tfrac{1}{2}(c_{11} - c_{12}). \tag{C.6}$$

We have affixed primes to the elastic constants calculated in the co-ordinate systems corresponding to Configurations I and II and have left unprimed the elastic constants referred to the cubic crystal axes. The elastic constants in a new (primed) co-ordinate system can be obtained in terms of the elastic constants in the old (unprimed) co-ordinate system by means of the relations[1]

$$c'_{pqrs} = \sum_{ijkl} \cos(x_i, x_p') \cos(x_j, x_q') \cos(x_k, x_r') \times \cos(x_l, x_s') c_{ijkl}, \tag{C.7}$$

where, in order to express the transformation simply, the tensor nature of the elastic constants has been employed. (The fourth rank tensor c_{ijkl} can be transformed into the conventional notation $c_{11}, c_{12}, \ldots c_{66}$, by replacing the pair of subscripts 11 by 1, 22 by 2, 33 by 3, 23 by 4, 13 by 5, and 12 by 6.)

Furthermore, for the case of alkali-halide crystals the lattice spacings ξ, η, ζ are given in terms of the magnitude of the Burgers vector, $\boldsymbol{b}$, by

$$\xi = \frac{\boldsymbol{b}}{\sqrt{2}}, \qquad \eta = \frac{\boldsymbol{b}}{2}, \qquad \zeta = \boldsymbol{b}, \tag{C.8}$$

so that finally for this case

$$A = \frac{1}{\sqrt{2}} \boldsymbol{b} c_{55}' = \frac{1}{\sqrt{2}} \boldsymbol{b} c_{44}$$
$$B = \sqrt{2} \boldsymbol{b} c_{44}' = \frac{1}{\sqrt{2}} (c_{11} - c_{12}). \tag{C.9}$$

REFERENCES

1. Eshelby J. D., Read W. T., and Shockley W., *Acta Met.* **1,** 251 (1953).
2. Cottrell A. H., *Dislocations and Plastic Flow in Crystals*, p. 36. Clarendon Press, Oxford (1953).
3. Read W. T., *Dislocations in Crystals*, p. 213. McGraw-Hill Book Co., New York (1953).
4. Maradudin A. A., Ph.D. Thesis, University of Bristol (1956).
5. Huntington H. B., Dickey J., and Thomson R., *Phys. Rev.* **100,** 1117 (1955).
6. Madelung E., *Phys. Z.* **19,** 524 (1918).
7. Duffin R. J., *Duke Math. J.* **20,** 233 (1953).
8. Foreman A. J. E., *Acta Met.* **3,** 322 (1955).
9. Overton W. C. and Swim R. T., *Phys. Rev.* **84,** 758 (1951).
10. Adams E. P., *Smithsonian Mathematical Formulae and Tables of Elliptic Functions*. Smithsonian Institute, Washington (1947).
11. Gröbner W. and Hofreiter N., *Integraltafel* Vol. 2, p. 103. Springer-Verlag, Vienna and Innsbruck (1949).
12. Whittaker E. T. and Watson G. N., *A Course of Modern Analysis*. Cambridge University Press (1922).
13. Green A. and Zerna W., *Theoretical Elasticity* p. 156. Clarendon Press, Oxford (1954).

J. Phys. Chem. Solids Pergamon Press 1958. Vol. 9. pp. 21–27. Printed in Great Britain.

DEPENDENCE OF SOUND VELOCITY AND ATTENUATION ON MAGNETIZATION DIRECTION IN NICKEL AT HIGH FIELDS

G. A. ALERS, J. R. NEIGHBOURS and H. SATO

Scientific Laboratory, Ford Motor Company, Dearborn, Michigan

(*Received* 2 *July* 1958)

VOL. 9 1959

Abstract—The velocity and attenuation of 10-Mc/s sound waves in a nickle single crystal have been measured as a function of magnetic field orientation and intensity at room temperature and at 77°K. Changes in the velocity of transverse waves of the order of 0·1 per cent were observed when the crystal was rotated about a crystallographic axis in a magnetic field high enough to allow saturation of the elastic constants. Attenuation changes were also observed, but showed a different angular dependence than the velocity changes. The measurements can be explained by a phenomenological theory based on magneto-elastic coupling. Using this theory, it was possible to estimate the magnetostriction constants at 77°K. The resulting value for λ_{100} ($\lambda_{100} = -30 \times 10^{-6}$) supports previous measurements which show that it goes through a minimum near 173°K.

1. INTRODUCTION

It is well known that the application of a magnetic field to a ferromagnetic material gives rise to a net increase in the effective elastic modulus of the material. This effect, called the ΔE effect, has been adequately explained in terms of the magnetostriction associated with the magnetization processes of domain wall motion and domain rotation.[1–3] At high magnetic fields, where the magnetization is saturated, these mechanisms are not effective, and the elastic moduli are observed to reach a saturation value independent of the magnetic field. However, very accurate measurements[4] show that this saturation value of the elastic modulus of a nickel single crystal depends upon the direction of magnetization with respect to the crystallographic axes. This variation with direction is of the order of a few tenths of 1 per cent.

These measurements have been interpreted[5] in terms of a "morphic effect" which is based on the fact that magnetostriction changes the crystal symmetry, giving rise to an apparent change in the measured elastic constants. Since these measurements were made with the magnetization only along a few particular crystallographic directions and since several other explanations are conceivable, it was felt worth while to repeat the experiment, using a more accurate technique, and to obtain measurements for a variety of magnetization directions.[6] If the predominant mechanism could be established, the experimental results might then be used to yield new information about ferromagnetic substances.

2. EXPERIMENTAL PROCEDURE

Since the effect is small, the measurement technique must be capable of detecting very small changes in the elastic constants. The ultrasonic-pulse technique is well suited to such measurements, since changes in the arrival time of an echo which has travelled through the specimen several times can be very easily and accurately detected. Furthermore, this method allows the specimen to be held firmly and moved about during the course of the measurement.

A $\frac{7}{8}$ in.-diameter nickel ingot containing several large crystals was grown by the Bridgman technique. The orientation of one crystal was determined by the back-reflection Laue method, and a circular cylinder with its faces normal to a [110] direction was cut out, using a thin liquid-cooled

abrasive wheel. The (110) faces were polished and lapped until flat and parallel, making the final cylinder height 1·5077 cm. After lapping, the specimen was placed in a small copper pillbox and held there with sealing wax. This pillbox and the necessary electrical connections were supported between the pole faces of an A.D.L. electromagnet by a micarta rod which was capable of being turned through several revolutions. By changing the attachment of the crystal holder to the micarta rod, it was possible to rotate the nickel crystal about the [001], [110], and [$\bar{1}$10] directions.

In any of these positions, the velocity of the sound was measured by the pulsed ultrasonic method described elsewhere.[7] For waves propagating in a [110] direction, the longitudinal velocity is determined by $\frac{1}{2}(C_{11}+C_{12}+2C_{44})$ and the transverse wave velocities by $C = C_{44}$ (for polarizations parallel to [001]) and $C' = \frac{1}{2}(C_{11}-C_{12})$ (for polarizations parallel to [$\bar{1}$10]). For convenience, these three waves are here designated as the longitudinal, C, and C' modes. By observing the time of arrival of a particular echo as either the field intensity or the orientation of the crystal was changed, it was possible to detect changes in time of arrival of 0·01 μsec out of a total time of about 100 μsec. Thus, relative velocity changes of approximately 1 part out of 10^4 could be detected. Changes in the height of the echo were also measured in order to determine the changes in attenuation accompanying the velocity changes. This could be done to an accuracy of 2×10^{-4} nepers/cycle.

The experimental procedure was to observe the changes in arrival time and height at constant field intensity with changes in field orientation and also the changes accompanying field-intensity changes at constant orientation. At room temperature, the maximum field used was usually 15·0 kOe (sometimes 20·0 kOe). At liquid-nitrogen temperature (77°K), the maximum field was also 15·0 kOe. In all cases, the magnetic field in the gap of the electromagnet was measured with a Rotating Coil Component Gaussmeter made by Rawson Electric Instrument Company. The measurements at 77°K were obtained by simply placing a small Dewar filled with liquid nitrogen between the magnet pole faces and immersing the crystal holder into the liquid.

The absolute values of the room-temperature elastic constants for a 15·0 kOe magnetic field applied in the [001] direction are, in units of 10^{12} dynes/cm^2:

$$C_{11} = 2{\cdot}507 \qquad C_{44} = 1{\cdot}230 \qquad C' = 0{\cdot}500$$

which are in agreement with previous results.[4,8,9] At 77°K the absolute values are, in the same units:

$$C_{11} = 2{\cdot}609 \qquad C_{44} = 1{\cdot}313 \qquad C' = 0{\cdot}548$$

3. RESULTS

Below the practical saturation of magnetization (occurring at about 2 kOe), the magnetic effects on the velocity and attenuation were not studied, because they are associated with the redistribution of domains and are adequately treated elsewhere.[1–3] At fields much greater than were necessary for saturation, the velocity of sound was observed to change with the intensity of the applied magnetic field. The amount and manner of this change

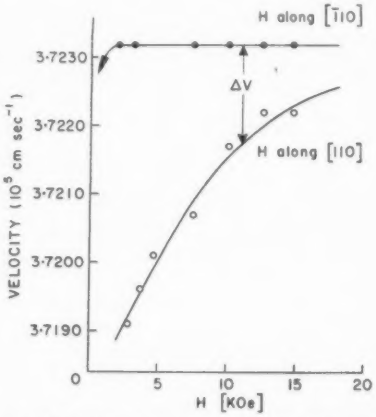

FIG. 1. Variation in sound velocity with intensity and orientation of applied magnetic field H of a transverse sound wave propagating in the [110] direction and polarized parallel to [001].

depended upon the orientation of the field. Fig. 1 shows the effect for the C mode (polarized parallel to [001]) as a function of applied magnetic field for the field parallel to two different directions: [110] and [$\bar{1}$10]. When the applied field is parallel to [$\bar{1}$10], the observed velocity rapidly approaches a limiting value, while the approach to this limiting value when the applied field is along [110] is more gradual.

In Fig. 1 and in subsequent figures and discussions, no correction has been made for the

changes in echo transit time caused by magnetostrictive changes of the sample dimensions. Such effects are easily shown to be at least one order of magnitude less than the smallest velocity changes observed. Furthermore, these dimension changes would effect all modes by the same amount, while the observations show widely different effects on each mode.

If the nickel crystal is rotated in a constant applied magnetic field H, the velocity is observed to change. For rotation of the previously mentioned [001] polarized sample about [001], the maximum change in velocity is the difference between the values for H parallel to [110] and H parallel to [$\bar{1}$10]. For intermediate orientations of H, the change is less. The observed velocity is highest for H parallel to [$\bar{1}$10] and is a minimum for H parallel to [110]. The deviation of the velocity from its maximum value at a certain orientation and magnitude of field is denoted by Δv. For example, the Δv associated with a field of 11 kOe applied in the [110] direction is marked on Fig. 1 as the difference of the curves.

As noted above, the velocity changes with the orientation of a constant applied magnetic field. Polar diagrams in which the radial co-ordinate is the quantity $\Delta v/v$ and the angle co-ordinate is the orientation of a constant 10·0-kOe applied magnetic field are shown in Figs. 2 and 3. Measured points are denoted by circles and their scatter is indicative of the precision of the measurements. Fig. 2 is for the C' mode, [$\bar{1}$10] particle motion, and Fig. 3 is for the C mode, [001] particle motion. The curves drawn through the points are simple angular functions which describe the results reasonably well. The three graphs in each figure are for rotations about the three mutually perpendicular directions: [110], [$\bar{1}$10], and [001]. The small cube shows in perspective the relation of these three polar plots to each other and to the direction of propagation K and the direction of polarization u. Fig. 1 is consistent with the upper left part of Fig. 3, in which $\Delta v/v$ is zero for the magnetic field in the [$\bar{1}$10] direction and is a maximum for H along the [110] direction. It is worth noticing that as defined here the values of Δv and $\Delta v/v$ are negative, since they are measured from the maximum value.

From Figs. 2 and 3, it is seen that the observed effect is in general small, being of the order of 0·1 per cent. For both modes, the zeroes in the twofold figures are in a direction perpendicular to the plane defined by the direction of propagation and the

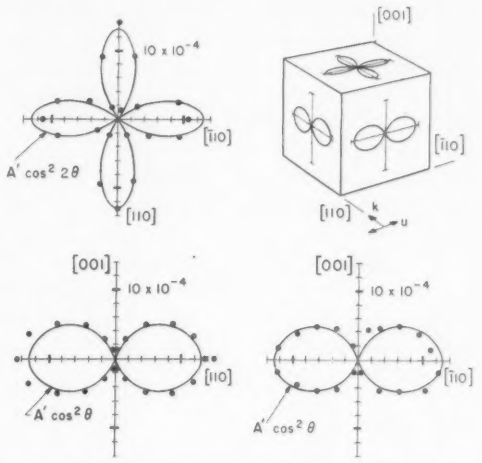

FIG. 2. Polar diagrams of the relative change in sound velocity (radial co-ordinate) of the C' mode with direction of magnetization (angular co-ordinate) for a constant field of 10·0 kOe. The propagation direction is [110] and the direction of polarization is [$\bar{1}$10]. The curves are the functions noted which best fit the experimental points. The small cube shows, in perspective, the relation of the polar plots. $A' = 12{\cdot}5 \times 10^{-4}$.

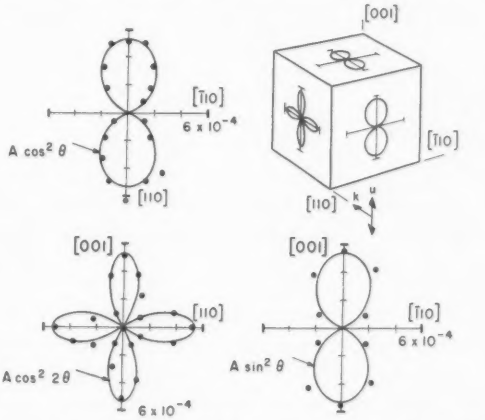

FIG. 3. Polar diagrams of the relative change in sound velocity (radial co-ordinate) of the C mode with direction of magnetization (angular co-ordinate) for a constant field of 10·0 kOe. The propagation direction is [110] and the direction of polarization is [001]. The curves are the functions noted which best fit the experimental points. The small cube shows, in perspective, the relation of the polar plots. $A = 5{\cdot}3 \times 10^{-4}$.

direction of polarization. The fourfold figures lie in the above-defined plane for both modes. For longitudinal waves, the changes in velocity were too small to be detected. This result supports the assumption that the effects of dimensional changes in the sample were negligibly small.

As the magnetic field is increased, Δv_{max} decreases for both the C and C' modes, and at room temperature the magnitude of Δv_{max} is greater for the C' mode. When the temperature is decreased to 77°K, the relative magnitudes of Δv_{max} for the two shear modes are reversed, and Δv_{max} is larger for the C mode. These effects of temperature and field are shown graphically in Fig. 4, where the

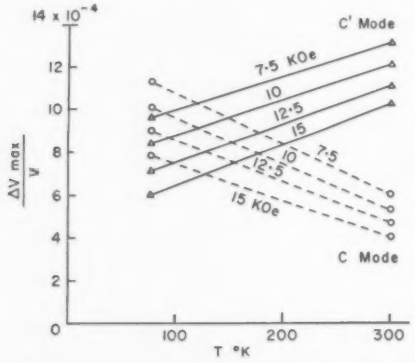

FIG. 4. Maximum relative changes in velocity for the C and C' modes at 77 and 300°K as a function of magnetic field intensity. The straight lines serve only to connect the points.

maximum fractional change in velocity is plotted as a function of temperature for different values of the applied field. The straight lines between the data points at 300 and 77°K serve only to connect the points and so do not show the detailed variation of $\Delta v_{max}/v$ with temperature.

Along with changes in velocity, the observed echo heights also change with orientation of the magnetic field. These changes, expressed in terms of changes in the logarithmic decrement of the sound waves, are plotted in Fig. 5 for a field of 15 kOe for the C' mode. Changes in attenuation were also detected for the longitudinal and the C modes, but they were too small to be measured accurately. It is interesting to note that the angular dependence of the attenuation and that of the corresponding velocity changes (shown in Fig. 2) are different. As a function of magnetic field, the maximum change in attenuation was found to decrease from approximately 20×10^{-4} nepers/cycle

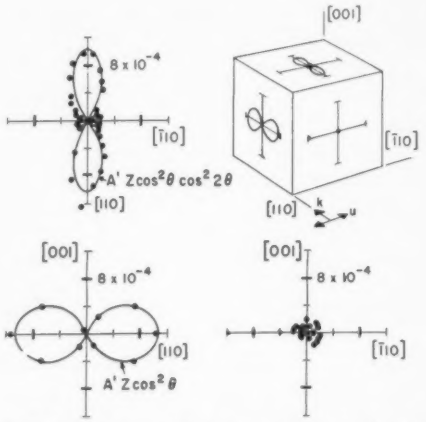

FIG. 5. Polar diagrams of changes in attenuation (radial co-ordinate) of the C' mode with direction of magnetization (angular co-ordinate) at 15·0 kOe. The units are those of the logarithmic decrement and $A'Z = 10{\cdot}4\times10^{-4}$ nepers/cycle. The small cube shows, in perspective, the relation of the polar plots.

at 10 kOe to $8{\cdot}7\times10^{-4}$ nepers/cycle at 20 kOe. At 77°K, the attenuation changes were too small to be measured accurately for all modes, being of the order of 2×10^{-4} nepers/cycle at most.

4. DISCUSSION

The results presented here show that the morphic effect cannot explain all of the observations. An alternative explanation based on a magneto-elastic coupling model was considered, but it was discarded because such an effect was thought to give rise to an attenuation variation corresponding exactly to the velocity variation. As a third explanation, it has been noted[10] that since the total energy of a ferromagnetic crystal depends upon the direction of magnetization through the anisotropy energy, a variation of the elastic constants with magnetization direction is to be expected, as the elastic constants are second derivatives of the total energy with respect to a strain. The analysis of the data in terms of this explanation was not completely satisfactory because of the many simplifying assumptions required. It was, however, the only available solution until it was

shown by SIMON* that a detailed analysis of the magneto-elastic coupling model might give rise to effects of the observed magnitude and that the attenuation changes need not correspond exactly to the velocity changes. In view of these many possible explanations for the effect, it is felt that a less cursory comparison of the results of the measurements with the predictions of the above mechanisms is worth while.

The morphic effect has been discussed in detail by MASON[5] in order to explain the velocity of sound measurements on a single crystal of nickel by BOZORTH *et al.*[4] Their measurements were made with the magnetic field only along certain directions, so that the details of the angular dependence predicted by the morphic effect could not be determined. The present measurements give the angular dependence and show several discrepancies between theory and experiment. As an example, the morphic effect predicts that C' is independent of the direction of magnetization when the field lies in the plane defined by the propagation direction and the polarization direction, i.e. the [001] plane. Reference to Fig. 2 shows that the measurements are clearly in disagreement with this prediction. For this reason, it was concluded that the morphic effect is not the major contributor to the observed velocity variations.

Another possible contributor is the intrinsic effect associated with the magnetic anisotropy energy. If a magnetic moment can be associated with each lattice point, then there is a non-central, pseudo-multipole interaction which contributes to the cohesive energy and hence the elastic constants of a magnetically saturated metal. Such a contribution could make the elastic constants depend upon the angle between the deformation and the magnetization. SATO[10] has shown that the total free energy F of a ferromagnetic material can be considered in three parts $(F_n+F_m+F_k)$. F_n is the sum of all the contributions of non-magnetic origin; (F_m+F_k) describes the magnetic contribution and is written in two parts in order to separate the anisotropic contributions which depend upon the direction of magnetization relative to the crystallographic axis, F_k, and the isotropic contributions which are independent of the magnetization direction, F_m. In this way, the dependence of a particular elastic constant upon the direction of magnetization can be discussed by examining the second derivative of only F_k with respect to the appropriate strain. The same derivative of F_m yields the dependence of the elastic constant upon the state of magnetization. By assuming that the non-central magnetic interaction is short range (i.e. only nearest neighbors need be considered), that the material is magnetically saturated, and that the lattice is cubic, it is possible to write F_k as a sum of terms having the form

$$r^{-m}\cos^n\theta$$

where θ is the angle between the line joining the pair of nearest neighbors and the magnetization direction and r is the interatomic spacing. Symmetry dictates that only even powers of $\cos\theta$ appear, so that $n = 2, 4, 6 \ldots$ The value of m was considered as an adjustable parameter. With this model, it was found impossible to describe the form of the experimental polar plots of $\Delta v/v$ using only a $\cos^2\theta$ term. By using $F_k = D(\cos^2\theta/r^p)+E(\cos^4\theta/r^q)$, the model was able to give a fair description if certain values were chosen for p, q, and D/E. These parameters can be related, in principle, to the magnetostriction and anisotropy constants, &c., but since it is possible to get a good description of the results from the simpler, phenomenological theory based on magneto-elastic coupling, the further elaboration of this atomic description was considered unwarranted.

The magneto-elastic coupling mechanism is based on the fact that magnetostriction allows the stress to change slightly the direction of magnetization, which in turn produces a slight additional strain that makes the effective elastic modulus, and hence the wave velocity, appear reduced. Such additional strains will depend upon the relative directions of the external stress and the magnetization in the crystal, and therefore the reduction in velocity will depend upon the relative orientation of the stress and magnetization. Since the angular dependence of the attenuation did not follow the symmetry of Δv, it was felt at first that this mechanism was incapable of explaining the observations. However, detailed calculations by SIMON[11] reveal that this mechanism can well reproduce the measured results. He shows that, for nickel in a large

* We are indebted to GERHARD SIMON of Justus Liebig University, Giessen, Germany, for communicating the results of his calculations before publication.[11]

applied field, the relative change in velocity, $\Delta v/v$, and the logarithmic decrement, δ, will be given as a function of field direction by the following equations:

(a) Field in the (110) plane, making an angle θ with the $[\bar{1}10]$ direction

$$\frac{\Delta v}{v} = A' \cos^2\theta \qquad \delta = 0 \qquad (C' \text{ mode})$$

$$\frac{\Delta v}{v} = A \sin^2\theta \qquad \delta = 0 \qquad (C \text{ mode})$$

(b) Field in the $(\bar{1}10)$ plane, making an angle θ with the [110] direction

$$\frac{\Delta v}{v} = A' \cos^2\theta \qquad \delta = A' Z \cos^2\theta \qquad (C' \text{ mode})$$

$$\frac{\Delta v}{v} = A \cos^2 2\theta \qquad \delta = A Z \cos^2 2\theta \cos^2\theta \qquad (C \text{ mode})$$

(c) Field in the (001) plane, making an angle θ with the [110] direction

$$\frac{\Delta v}{v} = A' \cos^2 2\theta \qquad \delta = A' Z \cos^2 2\theta \cos^2\theta \qquad (C' \text{ mode})$$

$$\frac{\Delta v}{v} = A \cos^2\theta \qquad \delta = A Z \cos^2\theta \qquad (C \text{ mode})$$

The magnitude of the effects are determined by A, A', and Z. These are defined in terms of the magnetostriction constants λ_{111} and λ_{100}, the saturation magnetization I_s, a characteristic frequency $\omega_0 = \sigma\mu_0 V^2$ (where σ is the electrical conductivity, μ_0 the absolute permeability, $4\pi\times10^{-7}$ H/m, and V the wave velocity), and susceptibility χ, which can be approximated by I_s/H, where H is the applied field. The parameters are, for $\chi \ll 1$,

$$A = \frac{9}{2}\frac{C_{44}\lambda_{111}^2}{I_s^2}\chi,$$

$$A' = \frac{9}{2}\frac{C'\lambda_{100}^2}{I_s^2}\chi,$$

and

$$Z = 2\pi\chi\frac{\dfrac{\omega}{\omega_0}}{1+\left(\dfrac{\omega}{\omega_0}\right)^2}$$

These parameters may be calculated from magnetic and elastic data. Using the measurements of CORNER and HUNT,[12] which give $\lambda_{111} = -19\times\times10^{-6}$, $\lambda_{100} = -50\times10^{-6}$, and $I_s = 484$ cgs units at room temperature, the values of C and C' measured here, and taking $\sigma = 1{\cdot}6\times10^5$ mho/cm, the theoretical values appearing in Table 1 were calculated. By choosing the curves which best fit the data of Figs. 2, 3, and 5, the observed parameter values were obtained. The observed and theoretical values are seen to agree to within an order of magnitude, with the observed parameters always larger.

Table 1. *Comparison of the predicted values of the magneto-elastic parameters with values obtained from wave-velocity measurements. The theoretical values are computed using the magnetostriction constants of* CORNER *and* HUNT.[12] *The observed values are chosen to fit best the data of Figs.* 2, 3, *and* 5.

	Theory	Observed
A	$4{\cdot}1\times10^{-4}$	$5{\cdot}3\times10^{-4}$
A'	$11{\cdot}6\times10^{-4}$	$12{\cdot}5\times10^{-4}$
Z (C' mode)	0·08	0·83
Z (C mode)	0·04	0·5

5. CONCLUSIONS

From Figs. 2, 3, and 5, it may be concluded that the observed angular variation of the shear wave velocities and attenuation with orientation of the applied magnetic field are well predicted by the magneto-elastic coupling theory. It may also be concluded that the model not only predicts the correct angular dependence but also gives the proper magnitude for the velocity effect.

In view of this agreement, it is most probable that the observed effect can be interpreted on the basis of this mechanism, and it must then be concluded that the contributions to $\Delta v/v$ from the morphic effect and from the intrinsic effect are smaller than 1×10^{-4}. The small deviations which might exist between the experimental points and the predicted curves may arise from these other contributions, but until more accurate measurements are made, it is not worth while to attach much significance to the deviations. The observed

attenuation, reflected in the Z parameter, seems to be much too large to be explained by inaccuracies in measurement or over-simplification of the theory. The apparent failure of this one aspect of the theory cannot be explained and should receive further attention.

Since the magneto-elastic coupling calculation describes the observations at room temperature very well, it seems worth while to use the 77°K measurements with the theory to obtain some information about the magnetostriction constants of nickel at liquid-nitrogen temperature, where they have not yet been measured. By using the ratio of $\Delta v_{max}/v$ for the two modes, it is possible to eliminate all of the magnetic parameters except the magnetostriction constants. The measured ratio A/A' was used with the ratio C'/C to obtain $\lambda_{100}/\lambda_{111} = 1{\cdot}38$ at 77°K, as compared to 2·63 at room temperature. The magnetostriction measurements of CORNER and HUNT[12] show that λ_{111} varies slowly enough with temperature to allow a reasonable extrapolation to 77°K. This extrapolated value is $\lambda_{111} = -22\times10^{-6}$ and when used with the ratio $\lambda_{100}/\lambda_{111}$ gives $\lambda_{100} = -30\times10^{-6}$ at 77°K. This value of λ_{100} is a reasonable extrapolation of the CORNER–HUNT measurements and is in agreement with their finding that λ_{100} goes through a minimum at a temperature of approximately 173°K with a minimum value of $-55\times\times10^{-6}$.

REFERENCES

1. BOZORTH R. M., *Ferromagnetism*, p. 684. Van Nostrand Co., New York (1951).
2. BECKER R. and DÖRING W., *Ferromagnetismus*, p. 336. Springer, Berlin (1938).
3. LEE E. W., *Rep. Progr. Phys.* **18,** 184 (1955).
4. BOZORTH R. M., MASON W. P., and MCSKIMMIN H. J., *Bell Syst. Tech. J.* **30,** 970 (1951).
5. MASON W. P., *Phys. Rev.* **82,** 715 (1951).
6. NEIGHBOURS J. R., ALERS G. A., and SATO H., *Bull. Amer. Phys. Soc.* **2,** 118 (1957).
7. ALERS G. A. and NEIGHBOURS J. R., *J. Phys. Chem. Solids* **7,** 58 (1958).
8. LEVY S. and TRUELL R., *Rev. Mod. Phys.* **25,** 140 (1953).
9. NEIGHBOURS J. R., BRATTEN F. W., and SMITH C. S., *J. Appl. Phys.* **23,** 389 (1952).
10. SATO H., *J. Appl. Phys.* **29,** 456 (1958).
11. SIMON G., *Z. Naturf.* **13A,** 84 (1958).
12. CORNER W. D. and HUNT G. H., *Proc. Phys. Soc.* **A68,** 133 (1955).

J. Phys. Chem. Solids Pergamon Press 1958. Vol. 9. pp. 28–30. Printed in Great Britain.

POWDER-PATTERN TECHNIQUES FOR DELINEATING FERROELECTRIC DOMAIN STRUCTURES

G. L. PEARSON and W. L. FELDMANN

Bell Telephone Laboratories, Inc., Murray Hill, N.J.

(*Received* 4 *June* 1958)

Abstract—Colloidal suspensions in insulating organic liquids have been found which produce powder patterns on polarized domains in ferroelectric crystals. Sulfur (yellow) in hexane deposits on negative dipole ends, while lead oxide (red Pb_3O_4) deposits on positive dipole ends. This technique delineates domain structures in great detail and can be used on a wide variety of ferroelectric crystals in which a domain structure has not been detected by other means. Ferroelectric crystals which have been studied by this technique include barium titanate, Rochelle salt, glycine sulfate, guanidinium aluminum sulfate hexahydrate, and numerous isomorphs. New etching techniques for barium titanate and glycine sulfate are described. Similar domain structures are revealed by etching and by powder deposit in those materials where both techniques can be used.

VOL
9
195

1. INTRODUCTION

THE domain structure in certain ferroelectric crystals can be observed either by optical means or by special etching techniques.[1] Neither of these methods has proved effective, however, when applied to some recently discovered ferroelectric crystals (for example, glycine sulfate and guanidinium aluminum sulfate hexahydrate) so that little is known regarding their domain structures.

CADY[2] describes a technique for observing surface charges on insulating crystals. It consists of dusting electrostatically charged powders onto the surface and noting the resulting patterns. Although this technique was developed some 50 years ago, it has been used very little because of its poor delineating qualities. It occurred to the present authors that greatly improved patterns might be obtained if electrostatically charged powders could be held in colloidal suspension and applied directly to the crystal surface. This paper describes procedures which have given excellent results on a wide variety of ferroelectric crystals. The procedures are such that they should also apply to piezoelectric and pyroelectric charged surfaces.

2. POWDER-PATTERN TECHNIQUES

Studies on the electrokinetics of colloids[3] show that, although the colloid as a whole is neutral, individual particles acquire a diffuse double-layer charge when brought in contact with the liquid. Under the influence of an electric field, the colloidal particles are attracted to either the anode or the cathode, depending on the orientation of their dipole layers.

For our purpose we desire an insulating liquid of low viscosity and low dielectric constant, so that the charged colloidal particles will be free to move toward the ferroelectric domains under maximum electrostatic attraction. Although many organic liquids meet these requirements, we found hexane ($\epsilon = 1{\cdot}87$) to be the most satisfactory. After trying a variety of powders, we concluded that sulfur deposits best on negatively charged domains and that lead oxide (Pb_3O_4) deposits satisfactorily on positively charged domains. The sulfur was commercial-grade spray powder having particle sizes between 3 and 4 μ. Flowers of sulfur is unsatisfactory, since it reacts chemically with hexane to form crystallites. The lead oxide was CP grade with approximately the same particle sizes.

Separate colloidal solutions were prepared (1 cc of powder per 100 cc of hexane) and stored in glass bottles with medicine drop stoppers. The sulfur colloid maintains its positive charge indefinitely. The red lead colloid may lose its negative charge

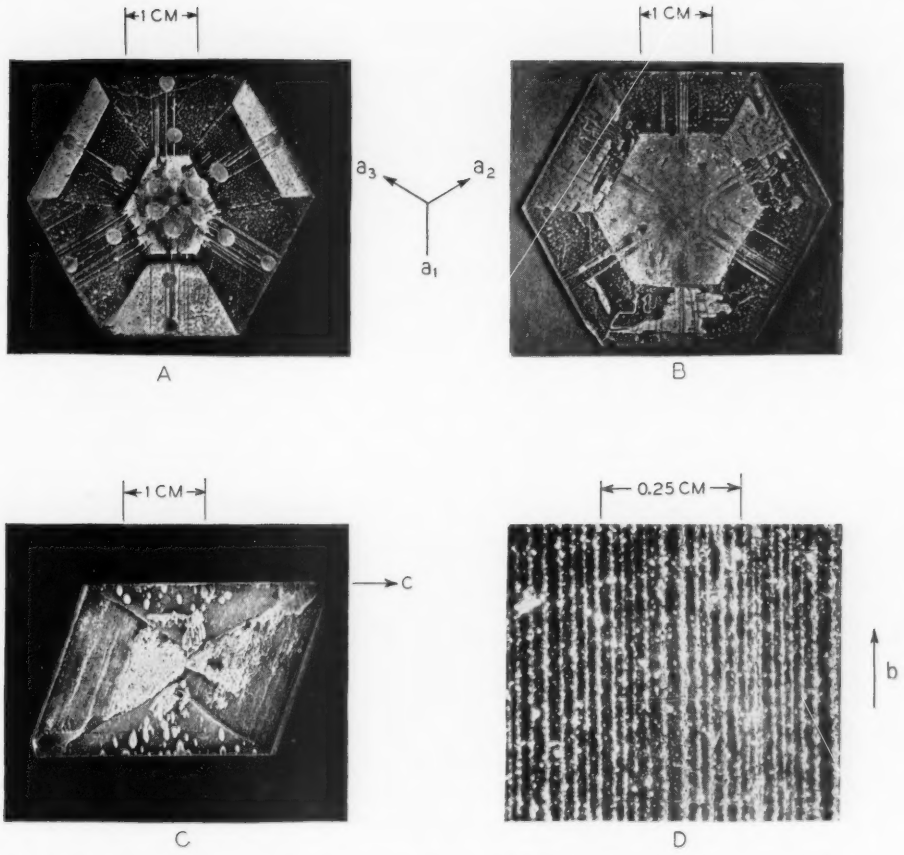

FIG. 1. Powder patterns on surfaces perpendicular to the ferroelectric axis of various crystals.

A. (0001) surface of guanidinium aluminum sulfate hexahydrate (GASH).
B. (0001) surface of the isomorph, guanidinium gallium selenate hexahydrate.
C. (010) surface of glycine sulfate.
D. (100) surface of monoclinic Rochelle salt.

[*facing p.* 28

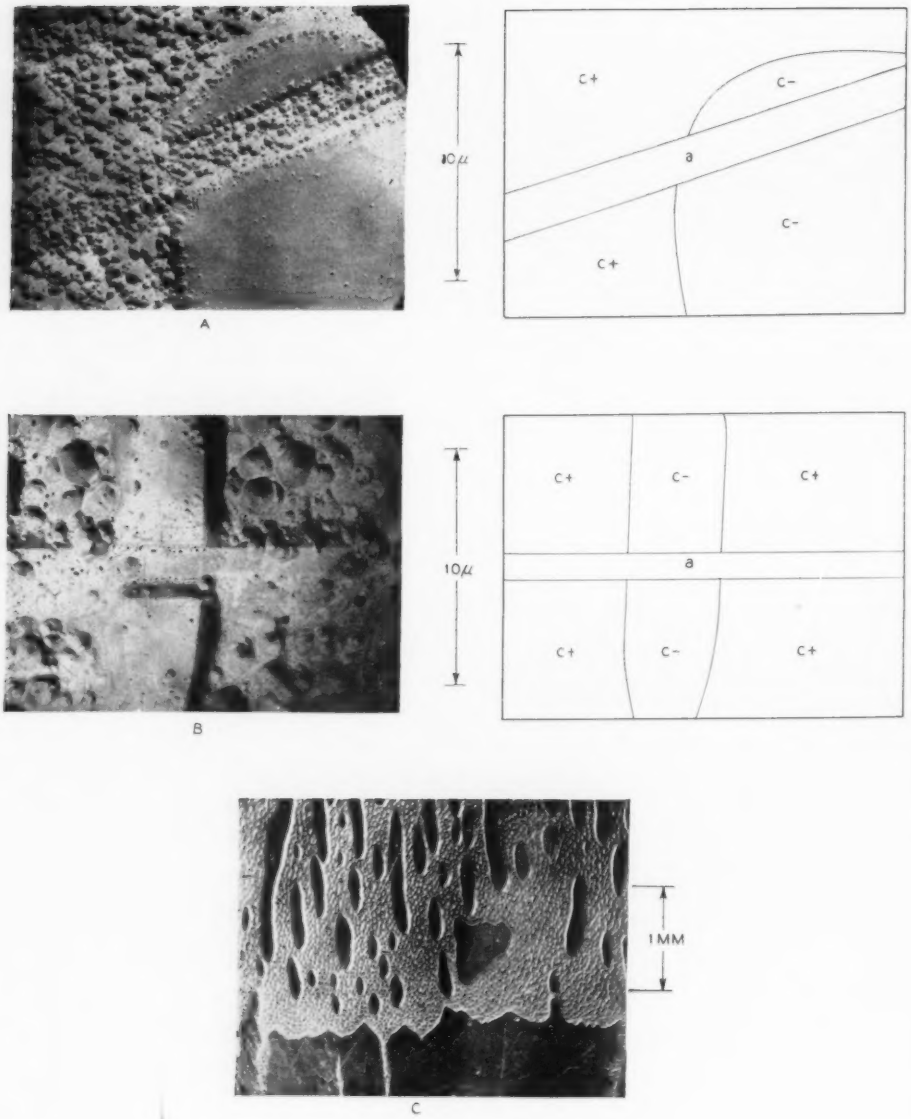

FIG. 2. Etch patterns on ferroelectric crystals.

A. Electron micrograph of $BaTiO_3$ etched 4 min in HCl. Domain structure shown at right.
B. Electron micrograph of $BaTiO_3$ etched 10 sec in HF. Domain structure shown at right.
C. Photomicrograph of glycine sulfate etched in H_2O. Smooth portions are positive domains and pebbled portions negative domains.

VOL.
9
959

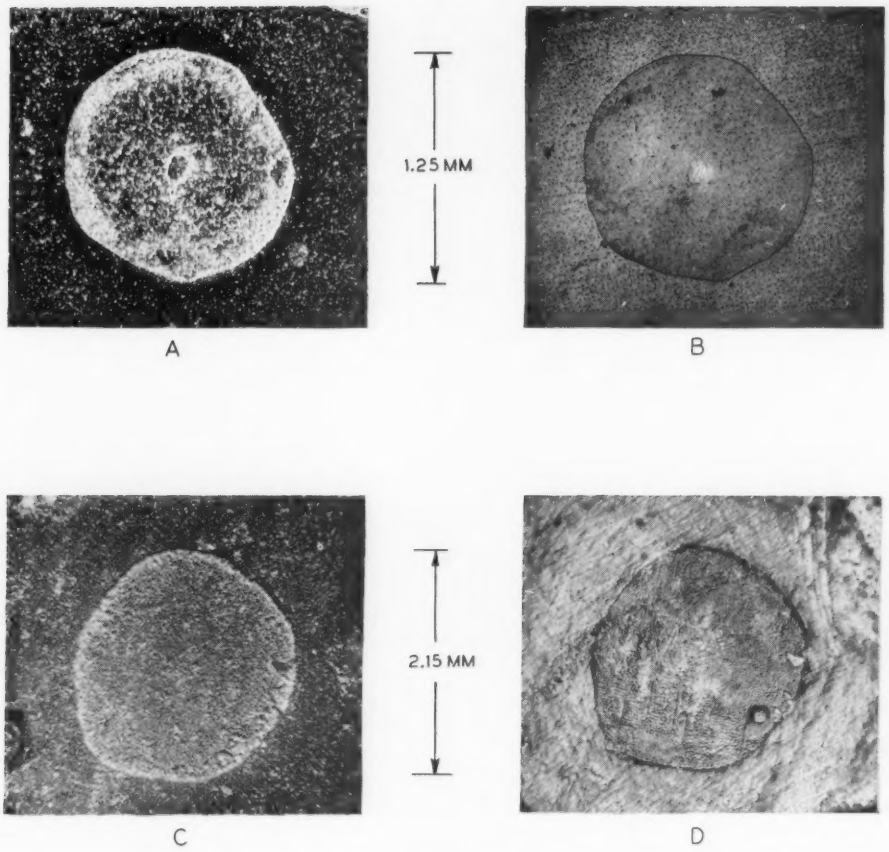

FIG. 3. Comparison of powder and etch patterns on $BaTiO_3$ and glycine sulfate crystals. Circular areas are negative domains.

A. Sulfur powder on $BaTiO_3$.
B. Same $BaTiO_3$ crystal etched in HF.
C. Sulfur powder on glycine sulfate.
D. Same glycine sulfate crystal etched in H_2O.

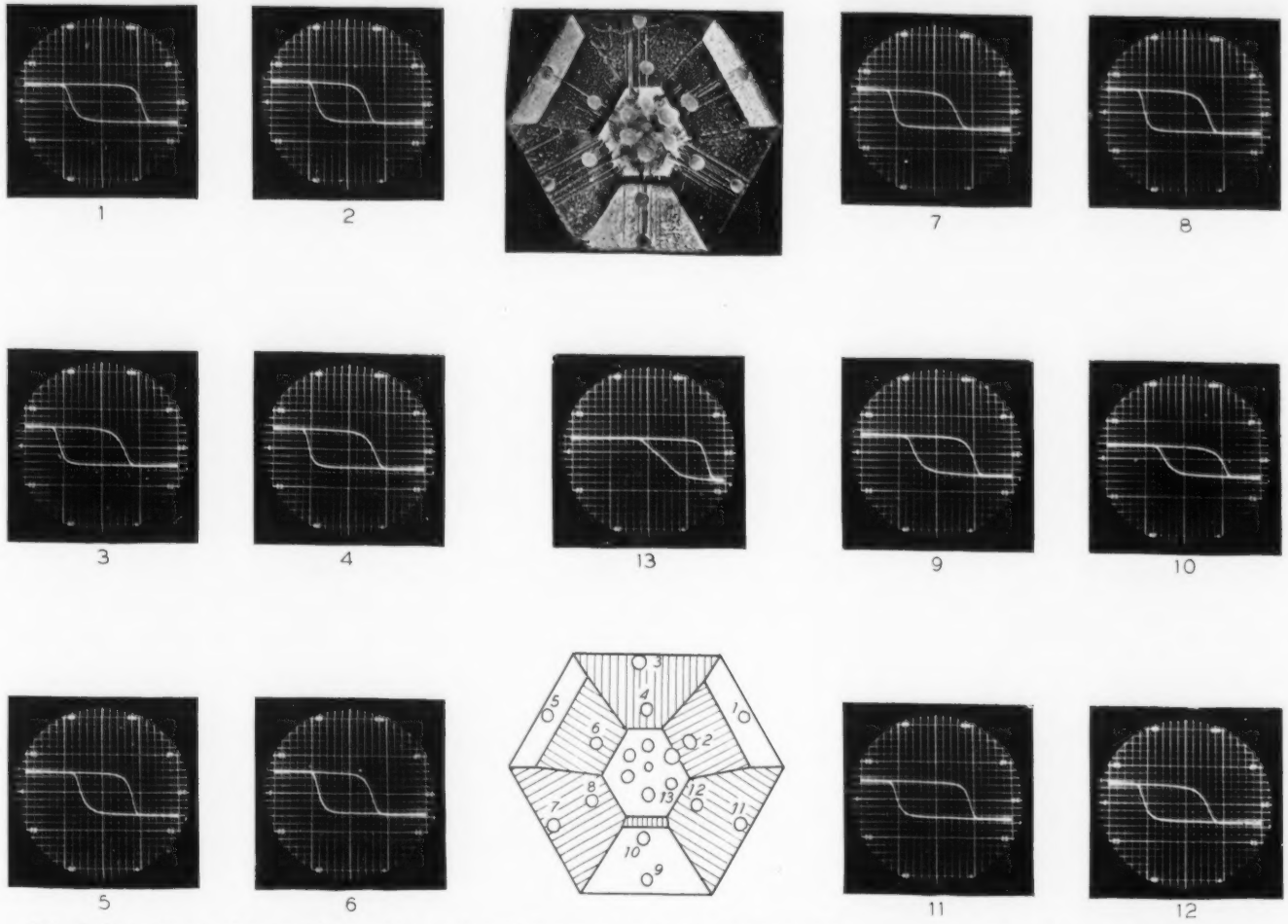

FIG. 4. Dependence of hysteresis loop bias on domain structures in GASH. Numbered traces were obtained at the electrodes indicated.

VOL 9 1957

after several hours and possibly reverse sign eventually. For this reason a freshly mixed solution of the red lead is recommended. The charge polarity can be checked in a cataphoresis cell. An alternative negatively charged colloid which has been found satisfactory consists of the cross-linked polymer of polystyrene in hexane. This may be made any desired color by adding an oil-soluble dye.

Powder patterns are produced by placing a few drops of colloid solution on the crystal surface. The charged powder is immediately attracted to ferroelectric domains carrying opposite sign of charge and covers their entire areas. For example, the yellow powder in the sulfur colloid deposits on negatively charged domains and leaves the positively charged domains vacant. These latter may be filled in with red powder by putting a few drops of the lead oxide colloid on the surface. The second solution must not be added until after the hexane has evaporated from the first; otherwise the powders loose their charges and no pattern is formed. After the hexane has evaporated, the powders are fixed in place indefinitely by the electrostatic charges.

If, in place of sulfur or lead oxide, we use a colloid of finely divided barium titanate in hexane, the resulting powder patterns are of an entirely different nature. The $BaTiO_3$ particles carry no net electrical charge, but they do have a very high dielectric constant. When placed on the surface of a ferroelectric crystal containing plus and minus domains, the particles polarize in the external electrostatic fields and are deposited at domain boundaries where large field gradients exist. The resulting powder patterns outline the domain boundaries but do not differentiate the sign of charge.

3. POWDER PATTERNS ON FERROELECTRIC CRYSTALS

Powder patterns have been placed on a number of typical ferroelectric crystals using the techniques described above. Fig. 1 exhibits the results obtained on four such crystals. In each case the powder patterns are on surfaces perpendicular to the ferroelectric axis, and the domain structures are those grown into the mother crystal rather than due to applied electric fields. Fig. 1A shows powder patterns on the cleaved (0001) surface of a guanidinium aluminum sulfate hexahydrate (abbreviated GASH) crystal. The yellow sulfur powder (white in this figure) covers negatively charged domains and the red lead oxide powder (black in this figure) covers positively charged domains. The domain structure is related to the hexagonal symmetry of the crystal, being negative in the center hexagon and also near the outer edges of each *a* segment. Patterns on the back side of the crystal are similar excepting that the colors are reversed. The round white dots are silver paste electrodes used for obtaining the hysteresis loops to be discussed later. Notice that there are a large number of small domains of reversed polarity in both the plus and minus areas.

Fig. 1B exhibits powder patterns on the (0001) cleaved surface of the isomorph, guanidinium gallium selenate hexahydrate. This ferroelectric has the same crystal structure as GASH and shows an analogous domain structure.

Fig. 1C is a photograph of powder patterns on the (010) cleaved surface of a monoclinic glycine sulfate crystal. The *c*-axis is as shown. It can be seen that the domain structure is intricate in this as-grown crystal. More will be said about the switching properties of these domains in the following section.

The patterns on the (100) ground surface of a monoclinic Rochelle salt crystal are shown in Fig. 1D. Rochelle salt was the first ferroelectric crystal to be discovered, and optical studies have been made in order to reveal its domain structure.[4] The close-spaced striations parallel to the *b*-axis shown in this figure are in accordance with optical results.

4. NEW ETCHING TECHNIQUES FOR BARIUM TITANATE AND GLYCINE SULFATE

Etching procedures have been described by HOOTON and MERZ[1] for delineating domain structure in barium titanate. The crystal is placed in concentrated HCl for several minutes at room temperatures. Etching takes place over the entire crystal, but is faster on positively poled *c*-domains than on negatively poled *c*-domains and is intermediate on *a*-domains. Fig. 2A is an electron micrograph of a tetragonal barium titanate crystal after etching for 4 min in concentrated HCl. The domain structure is indicated on the right.

We have found that a dilute solution of hydrofluoric acid (1 drop of 48 per cent HF in 5 cc of

water) is superior to concentrated HCl for bringing out the domain structure in barium titanate. The rate of etch is much greater, only a few seconds being required at room temperature, and the pebble structure on positive *c*-domains and *a*-domains is much less than that obtained with HCl. Fig. 2B is an electron micrograph of a tetragonal barium titanate crystal after etching for 10 sec in dilute HF. Etch patterns on orthorhombic barium titanate form in dilute HF after a few minutes at 0°C, while HCl requires several hours.

To the best of our knowledge, no preferential etch has been described for glycine sulfate ferroelectric domains. We find that water is excellent when used in the following manner: Place a thin cloth on a flat plate and put a few drops of water at one corner. Rub the (010) surface of the crystal in a circular manner on the cloth, so that it passes successively over wet and dry portions. After about 10 passes the domain structure is delineated as shown in Fig. 2C. The pebbled areas are negative domains and the smooth areas are positive domains.

A comparison between etch and powder domain delineation in switched barium titanate and glycine sulfate crystals is shown in Fig. 3. A barium titanate crystal was completely poled in one direction by an electric field, after which its polarity was reversed in a small circular area. A few drops of sulfur–hexane colloid were placed on that surface which had been poled positive and subsequently switched partly negative. The powder pattern is shown in Fig. 3A. Sulfur powder covers the negatively poled circular area, excepting for a small hole at its center. The powder was then removed and the entire crystal was etched for 10 sec in HF. The etch pattern, shown in Fig. 3B, has precisely the same shape as the powder pattern, even including the small unswitched island at the center.

Similar processing was given a glycine sulfate crystal. The powder pattern is shown in Fig. 3C, and the etch pattern formed by the water treatment described above is shown in Fig. 3D. The correlation between powder and etch patterns is complete.

5. POWDER PATTERNS AND HYSTERESIS LOOPS

HOLDEN *et al.*[5] have shown that the hysteresis loops obtained from GASH crystals are often biased and that the shape of the loop is dependent on the location of the electrodes on the [0001] faces of the crystal. Fig. 4 shows a direct correlation between loop biases and powder patterns on a given crystal. Each trace is numbered, corresponding to the electrode location sketched in the lower center, and the powder patterns are shown in the upper center. The 60 c/s peak-to-peak voltage (horizontal axis) was 1000 V for all traces excepting No. 13, which was 1500 V. It can be seen that all electrodes in sulfur powder areas (1, 5, 9, 10, and 13) give traces which are shifted to the right, while the remainder, which are in lead oxide powder areas, give traces which are shifted to the left. By inserting a d.c. voltage into the circuit, it was shown that a negative charge on the top surface of the crystal produces a shift to the right, and this agrees with the charge distribution determined from the powder patterns. It is interesting to note that electrode No. 13 has a bias of about 250 V.

Acknowledgements—We wish to thank J. P. REMEIKA for supplying the ferroelectric crystals, E. A. WOOD for determining the crystal orientations, E. E. THOMAS for the photomicrographs, and S. E. KOONCE for the electron micrographs.

REFERENCES

1. HOOTON J. A. and MERZ W. J., *Phys. Rev.* **98,** 409 (1955).
2. CADY W. G., *Piezoelectricity*, p. 703. McGraw-Hill Book Company, New York (1946).
3. VERWEY E. J. W. and OVERBEEK J. Th. G., *Theory of the Stability of Lyophobic Colloids*. Elsevier Publishing Company, New York (1948).
4. MITSUI T. and FURUICHI J., *Phys. Rev.* **90,** 193 (1952).
5. HOLDEN A. N., MERZ W. J., REMEIKA J. P., and MATTHIAS B. T., *Phys. Rev.* **101,** 962 (1956).

J. Phys. Chem. Solids Pergamon Press 1958. Vol. 9. pp. 31–42. Printed in Great Britain.

THE DIFFUSION AND PRECIPITATION OF INDIUM IN ZINC OXIDE

D. G. THOMAS

Bell Telephone Laboratories, Inc., Murray Hill, N.J.

(*Received* 10 *June* 1958)

Abstract—Indium has been dissolved in ZnO single crystals by coating crystals with a solution of indium nitrate and firing at temperatures between 800 and 1300°C. The diffusion rate may be obtained by following the increase of conductivity produced by the indium as a function of time. The conductivity of a crystal supersaturated with respect to indium falls at a rate which indicates internal precipitation of a new phase occurring along lines. These lines are tentatively identified as dislocations, and the results, interpreted according to a treatment given by H. L. FRISCH, indicate that crystals grown in the laboratory have a dislocation density near 10^7 cm^{-2}, while some commercial crystals have a density near 10^6 cm^{-2}. The diffusional behavior around the new phase is highly reproducible and in air gives:

$$D \approx 2{\cdot}5 \times 10^2 \exp\left(-\frac{3{\cdot}16}{kT}\right) \text{cm}^2/\text{sec}.$$

D is found to increase with increasing oxygen pressure with $D \propto P_{O_2}{}^{1/4}$, indicating that zinc vacancies control diffusion. The solubility of indium varies approximately as $P_{O_2}{}^{-1/8}$, as is to be expected if the indium dissolves in ZnO without being associated with a comparable concentration of vacancies. Hall-effect measurements give solubilities in the range 10^{17} to 2×10^{19} cm^{-3} and show that the precipitated phase materially lowers the electron mobility.

1. INTRODUCTION

ZINC oxide is an *n*-type semiconductor. It can be grown as single crystals.[1] The identity of the donor centers in the crystals as grown is not known; however interstitial zinc,[2,3] hydrogen,[4] and lithium[5] have been found to act as donors with well-defined properties. Substitutional impurities from Group III, such as an indium atom at a zinc site, should behave as donors since they have one more valence electron than zinc. Provided that these impurities are not accompanied by compensating centers such as zinc vacancies, the conductivity of the crystals should increase. This situation has been discussed by HAUFFE and VIERK,[6] who showed that the conductivity of sintered ZnO was considerably increased by adding 1–2 molecular per cent of Al_2O_3, or Cr_2O_3. They reported that the conductivity of the sample containing chromium varied with oxygen pressure according to $P_{O_2}{}^{-1/5{\cdot}5}$. WAGNER[7] similarly found that Ga_2O_3 increased the conductivity of sintered ZnO, and HEILAND[8] reported that indium included in single crystals during growth gave blue crystals of high conductivity. In this paper we will report more quantitative results concerning the behavior of substitutional indium as a donor in single crystals of ZnO.

2. EXPERIMENTAL

ZnO crystals were grown in this laboratory using SCHAROWSKY's method,[1] and also using a modification of this procedure[5] in which the necessity of evaporating metallic zinc is avoided. By passing a mixture of hydrogen and nitrogen over excess ZnO at 1100–1200°C and then mixing these gases with oxygen, also in a region of high temperature, single crystals can be produced. This is a somewhat simpler technique than the original one and yields similar results. The diameter of the hexagonal, needle-like crystals used were about

2×10^{-2} cm. Some larger crystals were obtained from a commercial source (The American Zinc Company of Illinois, P.O. Box 489, Hillsboro, Illinois).

The crystals were doped with indium by allowing a film of indium nitrate solution to dry on the surface. Heating then produced a coating of In_2O_3 from which indium diffused into the crystals. The indium nitrate solutions were made by dissolving indium in nitric acid, evaporating and adding water.

The conductivities of the crystals were measured above room temperature in the apparatus previously described,[2] in which the atmosphere could be controlled. Experiments were always made at 1 atm pressure, the partial pressure of oxygen being controlled by mixing appropriate proportions of oxygen and nitrogen measured with flow gauges. This method was simpler than using a low-pressure system, allowed better temperature control, and helped to prevent evaporation of the crystals at high temperatures. Temperatures up to 1100°C were attained in this apparatus and were measured with a Pt/Pt–Rh thermocouple with its hot junction strapped to the platform holding the crystal. For diffusion runs lasting many hours, a recorder was used to measure the probe voltage while the current through the crystal was held constant. The temperature, which was also recorded, was maintained sufficiently constant by adjusting a controlled power supply. The oven materials consisted of high-purity sintered alumina, and there was no evidence that aluminum from this source entered the crystal and behaved as a donor.

Hall measurements were made at room temperature in a holder similar to that described by HUTSON,[3] using a permanent magnet and a Kintel microvoltmeter. The number of carriers, n, was determined from the Hall coefficient, R_H, by means of the relation

$$R_H = \frac{3\pi}{8}\frac{1}{ne}.$$

The mobility, μ, was then obtained from the conductivity, σ, using:

$$\sigma = ne\mu.$$

Because of the uncertainty in the mechanism of electron scattering, it is likely that the factor $3\pi/8$ is inapplicable over the whole range of electron concentrations covered. If it is omitted, the mobility values quoted should be increased by 18 per cent.

3. RESULTS

It was found that if a crystal of conductivity 1 $(\Omega\ \text{cm})^{-1}$ or less, which is the normal product of the growing process, was coated with a solution of indium nitrate, dried, and then fired in air to a temperature of 1000°C or higher for some time, conductivities of up to 200 $(\Omega\ \text{cm})^{-1}$ at room temperature were produced. Equilibrium could be attained at a particular firing temperature after a sufficient length of time, and the solubility was found to increase with increasing temperature. Crystals uncoated with indium solution and heated similarly do not change their conductivities by comparable amounts. To check whether sodium might be acting as an electronically active contaminant, a crystal which had a conductivity near 3 $(\Omega\ \text{cm})^{-1}$ arising from indium doping at 812°C, was coated with NaOH solution and refired at 812°C. The conductivity remained practically unchanged, so that it appears that sodium at least was not important in the process.

The highest-conductivity crystals had a faint blue-green color to be ascribed to free-carrier absorption which becomes appreciable in the red end of the visible spectrum at these concentrations. No obvious effects were apparent in dark-field illumination after internal precipitation of the new phase (see below).

Experiments to be described showed that all the donors were ionized at or above room temperature; thus the conductivity could be related to the number of donor centers present and so the diffusion and solubility of the donors were investigated as follows.

4. DIFFUSION

(a) *Initial diffusion*

Crystals coated with indium solution were heated for appropriate time intervals and then quenched to room temperature. It was found that equilibrium solubilities were reached in less than 1 hr at 1250°C, but took nearly 100 hr at 900°C. This method of observing the fraction diffused as a function of time can be used to estimate the diffusion coefficients if allowance is made for the

variation of mobility with impurity content at room temperature, and if the size of the crystal is known and if simple diffusion into a cylinder is assumed. Fig. 10 gives data for the mobility as a function of crystal conductivity which were used to obtain the quantity of donors present at, and before, saturation was reached. (In the latter case allowance was made for the fact that most of the donors were not at the average electron concentration.) The results of these experiments performed on a large number of crystals were not particularly consistent, and for a series of time intervals with

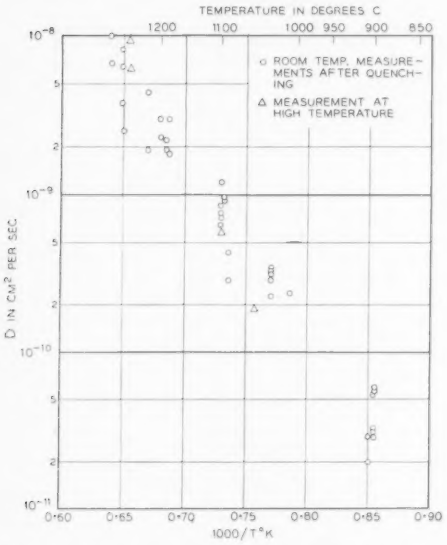

FIG. 1. Diffusion of indium into ZnO in air as a function of temperature, as determined from the first diffusion into the crystals.

the same crystal did not obey simple diffusion laws very well. The data calculated from results involving between 20 and 60 per cent of saturation are represented by circles in Fig. 1. Experiments on two crystals were also performed, in which the approach to equilibrium was measured by following the conductivity at one temperature, and then the process was repeated with the same crystal at a higher temperature. In this way diffusion coefficients at the two temperatures could be calculated for each crystal. Again ideal diffusion behavior was not observed, and the approximate results are indicated by triangles in Fig. 1.

The reason for the scatter in these diffusion data is not definitely known, but subsequent experiments showed that the crystals were by no means perfect and the imperfections may have affected the diffusion process. It is, however, necessary to use these data to obtain an absolute value of the diffusion coefficient for use in subsequent calculations. A value of $D = 8\times10^{-10}$ cm^2/sec at 1100°C was chosen. As will be shown, a value of $D = 10^{-9}$ cm^2/sec may then be expected in 1 atm of oxygen at 1100°C.

(b) *Subsequent diffusion*

If a crystal coated with indium solution was brought to equilibrium at a high temperature and then annealed at a lower temperature, the conductivity fell to the new equilibrium value as though the excess indium had diffused out of the crystal. However the process was much faster (by factors of 10–100) than was expected. Furthermore subsequent diffusion in was similarly fast; thus the initial diffusion to equilibrium at 1250°C took about 1 hr, but any later diffusion at this temperature was complete in 5 min or less. These observations suggested that if a crystal becomes supersaturated with indium, precipitation of the excess indium occurs within the crystal, and since the indium diffuses a smaller distance, the process is faster. This was confirmed by bringing a crystal to equilibrium at 1100°C (which required several hours) so that its room-temperature conductivity became 41 $(\Omega\ \text{cm})^{-1}$. Precipitation at 890°C then gave a conductivity of 3·2 $(\Omega\ \text{cm})^{-1}$. At this stage the crystal was etched with hydrofluoric acid so that 0·001–0·002 in. of the surface was removed, and presumably if the excess indium had diffused to the surface it too would have dissolved or been removed. However, heating for 15 min at 1100°C restored the conductivity to 38 $(\Omega\ \text{cm})^{-1}$, showing that the indium had come from within the crystal.

The kinetics of the precipitation were studied by equilibrating a crystal at 1250°C, quenching it, and then heating it quickly to a temperature below 1250°C in the crystal holder and observing the conductivity decrease as a function of time as precipitation occurred. The experiment was repeated for as many as fifteen times on a single crystal under a variety of conditions of temperature and atmosphere. The behavior was highly reproducible, a run at the end of the series being, within

experimental error, identical with a similar run at the beginning.

Examples of the behavior of a single crystal at different temperatures and in 1 per cent oxygen are shown in Fig. 2. The conductivity observed at the temperature of diffusion is plotted, for convenience

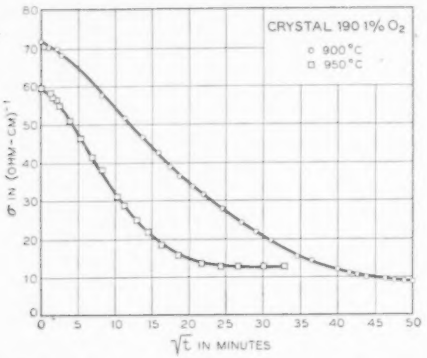

FIG. 2. Conductivity measured at the indicated temperatures versus $\sqrt{\text{time}}$ for the precipitation of indium in ZnO.

against the square root of the time. The conductivities at zero time are slightly different, partly because the conductivity varies with temperature for a fixed donor concentration and partly because the quenching process does not always yield precisely the same conductivity. The conductivities at the end of the runs are also different because of the mobility variation with temperature, and also because the solubility varies with temperature and oxygen pressure. These plots, showing an absence of an initial linear section, indicate that ordinary cylindrical diffusion is not taking place. If, however, $\log_{10}(\sigma_t - \sigma_\infty)$ is plotted against t, where σ_t is the conductivity after time t, and σ_∞ is the conductivity at the end of the precipitation, a straight line is obtained for at least 90 per cent of the precipitation, as is shown in Figs. 3 and 4. The final 5–10 per cent of the precipitation usually did not fall on a straight line, deviating sometimes upward and sometimes downwards. Whether these deviations are significant or whether they arose from experimental uncertainties in the determination of the end-point is not clear. At these high temperatures lattice scattering is likely to predominate in determing the mobility, so the assumption that σ_t is proportional to the average

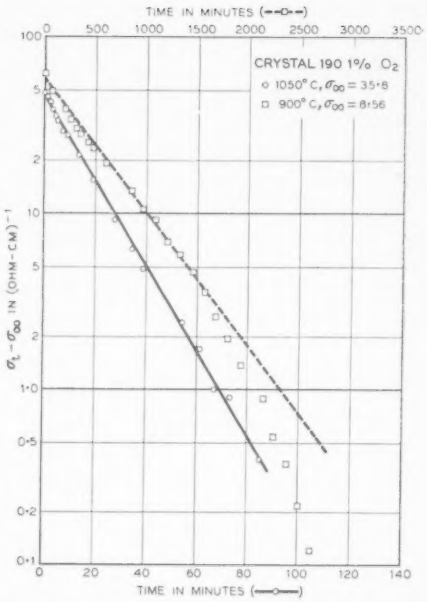

FIG. 3. Log $(\sigma_t - \sigma_\infty)$ versus time at different temperatures for the precipitation of indium in ZnO. Note the different time scales. The σ_∞ values are the constant values reached after precipitation and are obtained from curves such as those in Fig. 2.

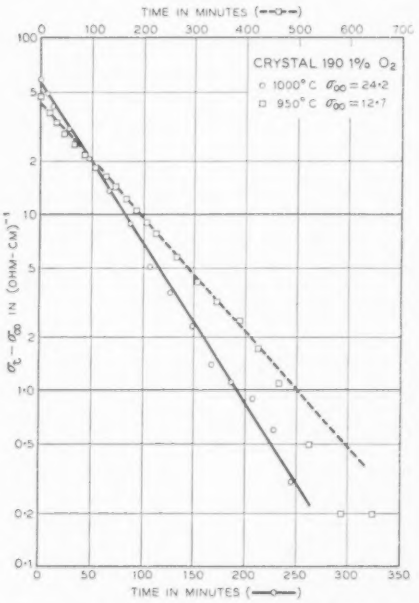

FIG. 4. Similar to Fig. 3, except for different temperatures. Again notice the different time scales.

concentration, $\bar{c}$, of indium in the crystal at time t will be made.

(c) *Interpretation of precipitation data*

ZENER[9] has discussed internal precipitation of a new phase and concluded that if nucleation and growth of the new phase take place around a long line of constant length, and the cylinders so formed do not grow so large that they overlap, then the following relation should be obeyed:

$$\frac{\bar{c}-c_\infty}{c_0-c_\infty}=\exp(-\alpha t^\beta) \qquad (1)$$

with $\beta=1$; c_0 and c_∞ being the initial and final concentrations of the precipitating component. For nucleating centers of different shape, β had values greater than unity. Recently HAM[10] has corrected some of this work, but he still agrees that for cylindrical precipitation $\beta=1$. HAM has pointed out that $\beta=1$ regardless of shape after 50 per cent precipitation has occurred, so that to be sure that lines are involved it must be shown that $\beta=1$ for the first half of the process. The present data show a small deviation from a straight line, but there is no doubt that for the first 50 per cent of the reaction β is much closer to 1 than 3/2. MORIN and REISS[11] observed precipitation of interstitial lithium in germanium and found that equation (1) was obeyed when $\beta=3/2$. From this and other evidence they concluded that precipitation of the new phase occurred around isolated lattice vacancies. TWEET[12] found that interstitial copper precipitated in germanium according to equation (1) when $\beta=1$, and from this, and from a correlation of the precipitation rate with the dislocation etch-pit density, he concluded that the nucleating centers were dislocation lines which ranged in density from 10^4 to 10^7/cm^2.

It seems likely therefore that indium in ZnO precipitates on long cylinders. The author is greatly indebted to H. L. FRISCH for a detailed derivation of equation (1) for cylindrical precipitation which follows from previous results given by FRANK and by FRISCH and COLLINS.[13] As before, β is unity and

$$\alpha=\pi NlD\frac{s^2}{v(c_0-c_\infty)} \qquad (2)$$

where Nl is the total length of nucleating line/cc (and also the line density/cm^2 if the lines are straight and perpendicular to the surface considered), D is the diffusion coefficient, and $v(c_0-c_\infty)$ is the total volume/cc of the precipitated phase; s is a parameter which depends on the total volume of the new phase precipitated and is given by:

$$\frac{s^2}{v(c_0-c_\infty)}=\frac{2}{2{\cdot}3\exp\left(\frac{s^2}{4}\right)\log_{10}\left(\frac{1{\cdot}5}{s}\right)}, \text{ for } s<1. \qquad (3)$$

Equation (3) has been used to determine some values of $s^2/v(c_0-c_\infty)$ as a function of $v(c_0-c_\infty)$, and these are plotted in Fig. 5. The values of s

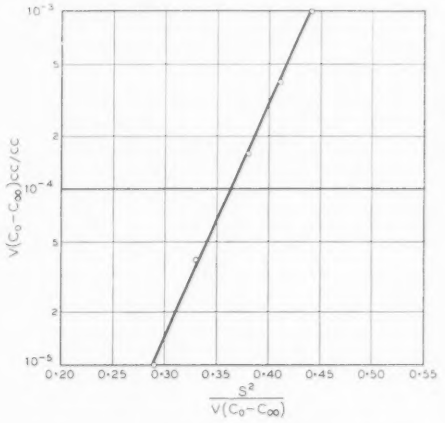

FIG. 5. Log $v(c_0-c_\infty)$ as a function of $s^2/v(c_0-c_\infty)$, as calculated from equation (3).

corresponding to the limits used are $1{\cdot}5\times10^{-3}$ to 2×10^{-2}, and so the condition $s<1$ is satisfied. It will be noticed that a change in $v(c_0-c_\infty)$ by a factor of 100 changes $s^2/v(c_0-c_\infty)$ by only about 50 per cent. This is a fortunate circumstance, for although (c_0-c_∞) can be determined quite well from the room-temperature conductivity before and after precipitation, v, the volume of precipitate containing 1 atom of indium, is known much less precisely. In this paper it is assumed that $v=2\times10^{-23}$ cc, which is the volume per Zn ion in ZnO. But even if the value were ten times this, the value of Nl to be calculated would only be about 20 per cent too high.

If τ sec is the time required for $\bar{c}-c_\infty/c_0-c_\infty$ to have fallen to $1/e$ of its original value, then

$$\alpha = \frac{1}{\tau}. \qquad (4)$$

Values of τ can be read off curves such as those in Figs. 3 and 4 (c_0-c_∞ is, of course, constant for any particular run). Using the value of D at 1100°C mentioned above, together with a determination of τ at the same temperature, Nl may now be calculated for the crystal from equation (2). The reproducibility of the results show that Nl remains constant for any particular crystal. The

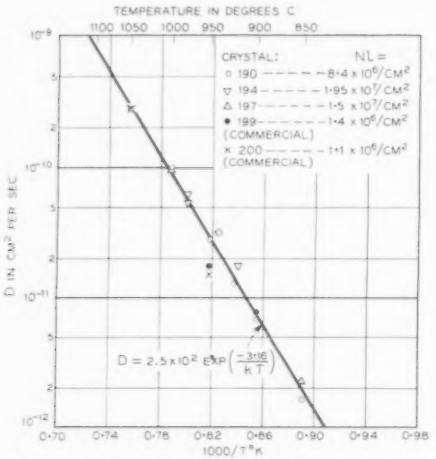
TEMPERATURE IN DEGREES C
1100 1050 1000 950 900 850
CRYSTAL: Nl =
○ 190 8·4 x 10⁶/CM²
▽ 194 1·95 x 10⁷/CM²
△ 197 1·5 x 10⁷/CM²
• 199 1·4 x 10⁶/CM²
(COMMERCIAL)
× 200 1·1 x 10⁶/CM²
(COMMERCIAL)
D IN CM² PER SEC
D = 2·5 x 10² EXP(−3·16/kT)
1000/T °K

FIG. 6. Diffusion coefficient of indium in ZnO as a function of temperature obtained from precipitation data in air with the Nl values chosen as indicated, so that the line drawn passes through $D = 8\times10^{-10}$ at 1100°C. For two other crystal Nl values of $1{\cdot}1\times10^{7}$ and $3{\cdot}2\times$ $\times10^{7}$ were found.

value of Nl is now used with τ values to obtain D at different temperatures. The results obtained in air with several different crystals are shown in Fig. 6. In effect Nl values have been chosen for each crystal so that the straight line through the D values as a function of temperature passes through $D = 8\times10^{-10}$ cm²/sec at 1100°C. For the crystals grown in these laboratories, the Nl values are not very different, being near 10^7 cm/cc. Measurements were also made on two rather larger crystals obtained from commercial sources and for these the Nl values were approximately ten times smaller. The straight line in Fig. 6 is given by

$$D = 2{\cdot}5\times10^{2}\exp\left(-\frac{3{\cdot}16}{kT}\right)\text{cm}^2/\text{sec}. \qquad (5)$$

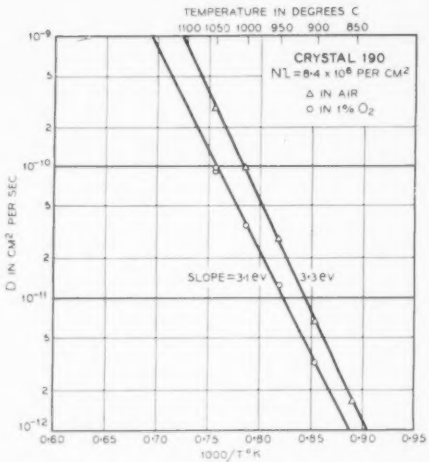

FIG. 7. D as obtained from precipitation for crystal 190 in two different oxygen partial pressures.

(d) *Oxygen pressure-dependence of D*

In addition to the variation of D with temperature, there was also a variation with oxygen pressure. Consequently, the same precipitation experiments were repeated at various oxygen pressures.

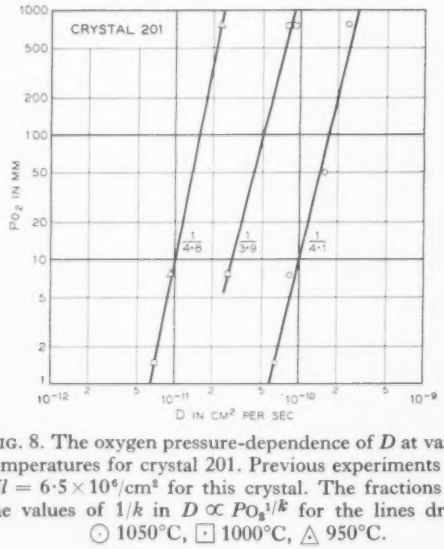

FIG. 8. The oxygen pressure-dependence of D at various temperatures for crystal 201. Previous experiments gave $Nl = 6{\cdot}5\times10^{6}$/cm² for this crystal. The fractions give the values of $1/k$ in $D \propto P_{O_2}^{1/k}$ for the lines drawn. ⊙ 1050°C, ⊡ 1000°C, △ 950°C.

Fig. 7 shows diffusion data at two different oxygen pressures for crystal No. 190. The two lines drawn are almost parallel; if there is a change in the activation energy between 100 and 1 per cent oxygen, it is less than 10 per cent and almost within experimental error. Very similar results were obtained for a second crystal, No. 201. Fig. 8 illustrates the dependence of D at various temperatures, on oxygen pressure at various temperatures. The slopes of the lines are indicated on the graph. At a constant temperature, it is found that approximately

$$D \propto P_{O_2}^{\frac{1}{6}} \tag{6}$$

the diffusion rate *increasing* with increasing pressure.

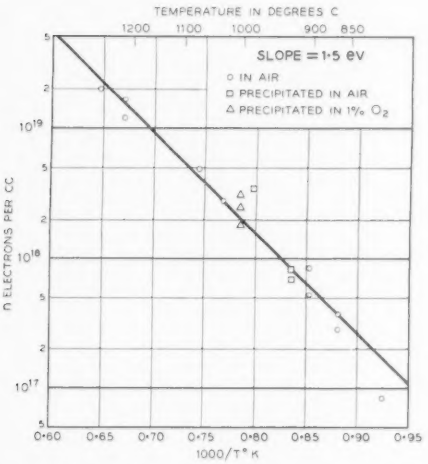

FIG. 9. The solubility of indium in ZnO as obtained from Hall measurements of the electron concentration at room temperature. Equilibrium was attained under the various conditions indicated and the crystals were then quenched.

(e) *Solubility*

Solubilities of indium in ZnO could be determined by equilibrating in air at a high temperature, quenching, and measuring the conductivity and Hall coefficient at room temperature. The results, which show some scatter, are given in Fig. 9. Included are points obtained by saturating the crystals at 1250°C and then precipitating to the equilibrium condition at a lower temperature, and these points fall near the other points. Fig. 10 shows the mobility as a function of conductivity. It is clear that the added impurities are important in determining the mobility. This is particularly true of those crystals in which precipitation has occurred, since these show unusually small mobilities. This confirms that precipitation occurs within the crystal.

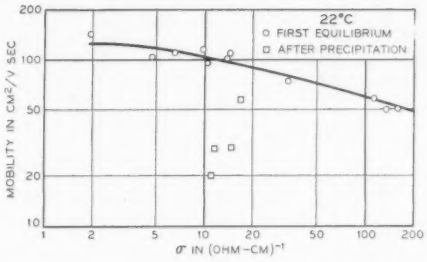

FIG. 10. The electron mobility as a function of crystal conductivity at room temperature for crystals doped with indium and for crystals containing in addition the precipitated indium phase.

The solubility, like the diffusion rate, is dependent on the oxygen pressure. This was observed by precipitating indium in a crystal and measuring conductivity changes at constant temperature brought about by changes in oxygen pressure. The equilibrium values reached were taken to be proportional to the solubility. Fig. 11 is

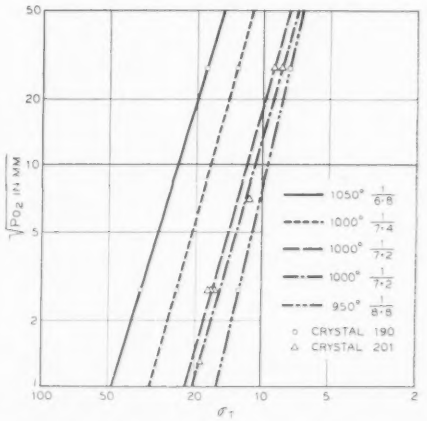

FIG. 11. The oxygen pressure-dependence of the conductivity measured at the temperatures indicated due to dissolved indium for two crystals. The fractions give the values of $1/k$ in $\sigma \propto P_{O_2}^{-1/k}$ for the lines drawn.

a log–log plot of $\sqrt{P_{O_2}}$ against σ for two crystals at different temperatures. The lines drawn have an average slope indicating

$$\sigma \propto P_{O_2}^{-1/7.6} \tag{7}$$

which is close to

$$\sigma \propto P_{O_2}^{-\frac{1}{8}}. \tag{8}$$

Although the kinetics of the change of conductivity with oxygen pressure were not analyzed in detail, it is interesting that the times taken for these changes were comparable to that for the initial precipitation. Table 1 shows the τ values for a series of such changes:

Table 1. τ *values for crystal No.* 201

Change at 1000°C	τ (min)
Initial precipitation in 1 per cent O_2	80
1 per cent → 100 per cent O_2	18
100 per cent → 6·5 per cent O_2	12
6·5 per cent → 0·2 per cent O_2	30
0·2 per cent → 1 per cent O_2	45

At this temperature in 100 per cent O_2, τ for the initial diffusion may be estimated to be 3000 min. It is clear that a change in the oxygen pressure at the surface is rapidly reflected in a change at the nucleating centers. This will be considered below.

(f) *Conductivity as a function of temperature*

Figs. 12(a) and (b) show how the conductivities of various crystals with different equilibrium concentrations of indium vary with temperature. Ionization is complete at room temperature. On cooling the more conductive crystals, the conductivity hardly changes, probably because the impurity orbits overlap at these concentrations. Hall measurements at low temperatures are necessary to determine the mobility variation with temperature and the magnitude of the ionization energy of the donors.

(g) *Doping with interstitial zinc*

A crystal was treated with indium so that its room-temperature conductivity was 11·9 $(\Omega\ \text{cm})^{-1}$. It was then doped with interstitial zinc at 650°C for 1 min, and then for 5 min, according to the procedure previously described.[2] After both experiments, the room-temperature conductivity was raised to 13 $(\Omega\ \text{cm})^{-1}$, showing that some interstitial zinc had entered the crystal. On heating for

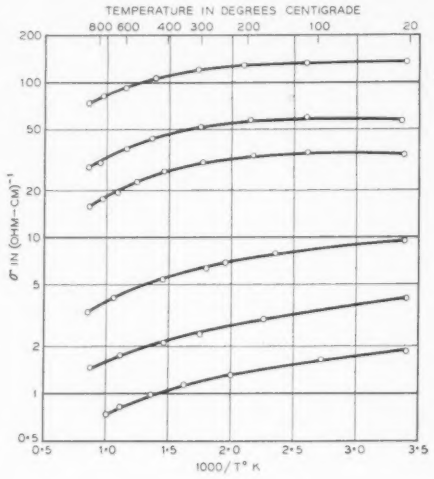

(a)

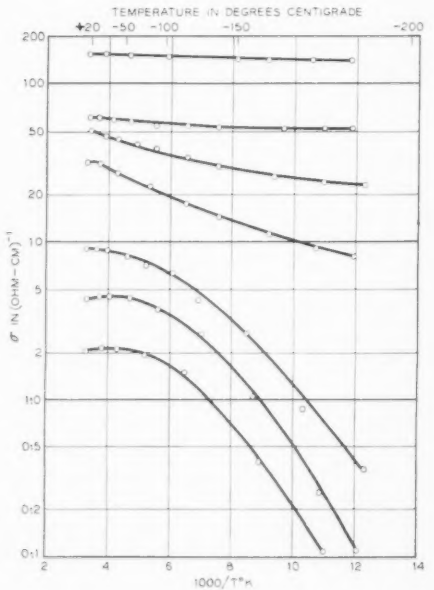

(b)

FIG. 12. The conductivity of crystals with different equilibrium concentrations of indium as a function of temperature above (*a*) and below (*b*) room temperature.

a few minutes in air at 600°C, the conductivity fell to 11·9 $(\Omega\ \text{cm})^{-1}$, as expected if the interstitial zinc diffused out. Very similar results were obtained if the crystal was held for ½ hr at 1000°C in the same pressure of zinc. These experiments strongly indicate that the indium is not incorporated in the lattice together with a comparable number of zinc vacancies which act as acceptors, for if this were the case, the interstitial zinc should fall into these vacancies and permanently increase the conductivity by a factor of about two.

5. DISCUSSION

(a) *Solubility of indium*

Equation (5) shows that the diffusion of indium in ZnO has an activation energy of about 3·2 eV. This value is in marked contrast to the values for the diffusion of interstitial zinc[2] and lithium[5], which are 0·55 and 1·0 eV respectively. Such a contrast suggests that there is a different diffusion mechanism involved, and it is therefore assumed that indium occupies substitutional lattice sites. It is also assumed that association of defects is not important at the elevated temperatures (> 900°C) used. Since indium causes an increase of conductivity, it clearly cannot enter the lattice accompanied by a compensating zinc vacancy, as indicated in the following equation

$$(In_2O_3)_{surface} \rightleftharpoons 2In_{Zn}^{+} + 3O_O + V_{Zn}^{=}. \quad (9)$$

(Here the "atomic" system of notation has been used, in which normal charges at a lattice point have been neglected. Thus O_O represents an $O^=$ ion at a normal oxygen site. $V_{Zn}^{=}$ represents a vacancy at a zinc site which has accepted two electrons.)

It is possible that the zinc vacancy may only accept one electron

$$(In_2O_3)_{surface} \rightleftharpoons 2In_{Zn}^{+} + 3O_O + V_{Zn}^{-} + e^-, \quad (10)$$

but this reaction may be discounted, since it gives no oxygen pressure-dependence of the conductivity. The absence of zinc vacancies in concentrations comparable to the indium concentrations was strongly indicated by the experiments mentioned above in which, on doping indium-containing crystals with interstitial zinc, there was little or no permanent increase of conductivity.

The reaction

$$(In_2O_3)_{surface} \rightleftharpoons 2In_{Zn}^{+} + 2O_O + V_{Zn}^{-} + e^- + \tfrac{1}{2}O_2 \quad (11)$$

can be excluded, since it adds three positive ion sites and only two negative ion sites to the crystal.

Of the simple possibilities, all that remains is

$$(In_2O_3)_{surface} \rightleftharpoons 2In_{Zn}^{+} + 2O_O + 2e^- + \tfrac{1}{2}O_2. \quad (12)$$

Since the indium is the only significant source of electrons, equation (12) gives

$$N_{In^+} = n, \quad (13)$$

where N_{In^+} is the number of indium ions/cc and n is the number of free electrons/cc. Applying the law of mass action to equation (12), and using equation (13)

$$K_1 = N_{In^+}^2 n^2 P_{O_2}^{\frac{1}{2}}$$

$$\therefore \quad n = K_1^{\frac{1}{2}} P_{O_2}^{-\frac{1}{4}}. \quad (14)$$

Assuming that at the high temperatures the conductivity is proportional to n, it is expected that

$$\sigma \propto P_{O_2}^{-\frac{1}{4}} \quad (15)$$

and, as Fig. 11 showed, this is approximately so, confirming that equation (12) is indeed the mechanism of solution at the oxygen pressures used.

Fig. 9, and other results, show that the solubility of the precipitated phase is approximately the same as that of the surface phase. The nature of the precipitated phase cannot be definitely inferred, although it is presumably a mixed ZnO–In_2O_3 compound. There is some evidence from X-ray diffraction patterns[14] that two compounds exist with about 1 indium atom for every 2 or 4 zinc atoms. A dilute mixture seems reasonable, as its molecular volume might not be very different from that of the parent ZnO lattice, thus allowing internal precipitation without undue lattice strain.

Since precipitation occurs along lines, it is likely that the lines are dislocations, that is a row of Zn and O ions which are missing from the lattice. The dislocation density is then equal to the Nl values quoted in Fig. 6. The values, ranging from 10^6 to $10^7/cm^2$, are high but not unreasonably so. Thus the highest dislocation density quoted by TWEET[12]

for germanium was about $10^7/cm^2$. THEIMER,[15] from light-scattering data, has concluded that Harshaw sodium chloride crystals have a dislocation density between 10^7 and $10^9/cm^2$. AMELINCKX[16] has decorated the dislocations in rock-salt crystals with sodium, and from his photographs one can deduce that the dislocation density was of the order of 5×10^6 cm^{-2}. DOREMUS[17] has estimated that strained KCl crystals contained about 3×10^7 dislocation cm/cc and this was confirmed by etch-pit counts. It is interesting that the commercial ZnO crystals, which are presumably grown at a lower temperature and at a much lower rate than the others, have a lower dislocation count.

Although temperatures up to 1400–1500°C have been employed, it has not been possible to deform ZnO crystals plastically,[18] indicating that the dislocations are not mobile and so do not facilitate the permanent bending of the crystals. This constancy of the dislocations would account for the reproducibility of our diffusion results, but would make difficult the proof that dislocations are the centers of precipitation, for there is no means of introducing dislocations at will. At present there seems to be no other information concerning dislocations in ZnO. It would be interesting to look for a correlation between etch-pit patterns and the *Nl* values reported here. Crystals containing precipitated indium were examined under a microscope using dark-field illumination. No decorated dislocation lines were apparent, perhaps because the refractive index and absorption of the precipitated phase are not very different from those of ZnO.

(b) *Diffusion of indium*

It has been shown from the precipitation data that the diffusion rate at constant temperature increases with increasing oxygen pressure. It is therefore concluded that the diffusion is controlled by a defect the concentration of which increases with oxygen pressure. The only such simple defect is a zinc vacancy. Since zinc vacancies are not involved in the indium solution process, their concentration must be low compared to the indium concentration; and, as they control the diffusion of the latter, they must move rapidly through the lattice. As a consequence, the simplifying assumption is made that they come to equilibrium in a time short compared to the diffusion times. A zinc vacancy is expected to be an acceptor for one or possibly two electrons; the latter will be assumed.

There is then a rapidly established equilibrium with the atmosphere as follows

$$2e^- + \tfrac{1}{2}O_2 + Zn_{Zn} = V_{Zn}^{=} + ZnO \qquad (16)$$

which leads to

$$X_{V_{Zn}=} N_{Zn} = N_{V_{Zn}=} = K_2 n^2 P_{O_2}^{\frac{1}{2}} \qquad (17)$$

where $X_{V_{Zn}=}$ is the atom fraction of zinc vacancies, and N_{Zn} is the number of zinc sites/cc.

REISS[19] has shown that for the present circumstances the diffusion coefficient of indium, D_{In}, may be represented

$$D_{In} = X_{V_{Zn}=} \frac{\omega_{In}}{\omega_{Zn}} D_v, \qquad (18)$$

where ω_{In} is the frequency with which an indium atom jumps into a vacancy next to it, and ω_{Zn} is the corresponding frequency for a zinc atom next to a vacancy. D_v is the diffusion coefficient of vacancies, and if the correlation factor which is not very different from unity is neglected, then D_v may be approximated by

$$D_v = \omega_{Zn} \lambda^2 \qquad (19)$$

where λ is the jumping distance. Combining equations (18) and (19) yields the following

$$D_{In} = X_{V_{Zn}=} \omega_{In} \lambda^2. \qquad (20)$$

Substituting (17) into (20) gives

$$D_{In} = \frac{K_2 n^2 P_{O_2}^{\frac{1}{2}}}{N_{Zn}} \omega_{In} \lambda^2. \qquad (21)$$

In the precipitation experiments, the crystals were always quenched from the same temperature of 1250°C, so that they all have approximately the same uniform electron concentration. After precipitation the final electron concentration is controlled both by the oxygen pressure and by the temperature. If equation (21) is true, then D_{In} should vary during the reaction and this might be expected to invalidate equation (1) with $\beta = 1$. However, H. L. FRISCH has demonstrated that, in fact, an equation of the form of (1) will still be obeyed, albeit with a different value of α. At present this point has been ignored.

If the oxygen pressure-dependence of n in equation (21) is controlled by the indium solubility represented by equation (14), one finds that

$$D_{\mathrm{In}} = \frac{K_2 K_1^{\frac{1}{2}}}{N_{\mathrm{Zn}}} P_{\mathrm{O}_2}^{\frac{1}{2}} \omega_{\mathrm{In}} \lambda^2. \qquad (22)$$

Thus D_{In} should vary as $P_{\mathrm{O}_2}^{\frac{1}{2}}$, as was approximately found to be the case. However, the situation is more complicated than this, for again the electron concentration starts by being the same no matter what the oxygen pressure, and it is only at the end of the precipitation that equation (14) is obeyed. Thus equation (6) is predicted as a limiting law, and until more detailed calculations have been made of the rate at which the charged indium diffuses in the presence of a varying electron concentration, one can only say that experiment indicates that equation (6) is approximately obeyed over the major part of the precipitation. It may be that diffusion is controlled by the region at which the diffusion coefficient has its lowest value. This will occur at the surface of the precipitated phase, and at this point equation (14) is obeyed.

It is interesting to notice that the energy of activation for the diffusion involved in precipitation is 3·2 eV, which is practically identical with the values for the activation energy reported for the self-diffusion of zinc in ZnO at high temperatures. These are 3·19 eV for diffusion in air[20] and 3·17 eV for diffusion in zinc vapor.[21] This agreement suggests that the temperature variation of the concentration of the same defect is responsible for the temperature variation of the diffusion of both zinc and indium. Again, however, if this defect interacts with the electrons present, it is not obvious that the agreement should be as simple as it appears to be. It might be useful to study the self-diffusion of zinc in ZnO at various oxygen pressures in crystals which contain equilibrium amounts of indium.

Using the model of diffusion presented above, an estimate of the zinc-vacancy concentrations may be made as follows. Suppose that the energy of activation for the jump of an indium atom into an adjacent vacancy is small, so that ω_{In} in equation (20) is nearly equal to the lattice vibration frequency. COLLINS[22] has recently found a lattice-absorption peak leading to a lattice frequency of $1{\cdot}25 \times 10^{13}$ sec^{-1}. In ZnO, λ has a value near 3·3 Å. Now at 1100°C in 1 atm of oxygen $D \approx 10^{-9}$ cm^2/sec.

Thus, using these values in equation (20), one finds

$$10^{-9} = X_{V_{\mathrm{Zn}}=} \times 1{\cdot}25 \times 10^{13} \times (3{\cdot}3 \times 10^{-8})^2$$

$$\therefore \quad N_{V_{\mathrm{Zn}}=} = X_{V_{\mathrm{Zn}}=} \times N_{\mathrm{Zn}}$$

$$= 7{\cdot}4 \times 10^{-8} \times 4{\cdot}1 \times 10^{22}$$

$$N_{V_{\mathrm{Zn}}=} = 3 \times 10^{15}. \qquad (23)$$

This is a lower limit, for if ω_{In} is less than the lattice frequency, then $N_{V_{\mathrm{Zn}}=}$ must be proportionately larger. At 1100°C in oxygen the indium solubility is about 6×10^{18}. Presumably the vacancy concentration is at least ten times smaller than this. Assuming

$$\omega_{\mathrm{In}} = 1{\cdot}25 \times 10^{13} \exp(-E_{\mathrm{In}}/kT), \qquad (24)$$

where E_{In} is the energy of activation for an indium to jump into an adjacent vacancy, one finds for a maximum value for E_{In},

$$\frac{3 \times 10^{15}}{6 \times 10^{17}} = \exp(-E_{\mathrm{In}}/kT) \qquad (25)$$

$$\therefore \quad E_{\mathrm{In}}(\mathrm{max}) = 0{\cdot}63 \text{ eV}.$$

Further experiments are necessary to check these limits, but it seems clear that the diffusion of a vacancy occurs with small activation energy, so that the overall activation energy for diffusion is dominated by the energy term which controls the variation of the defect concentration with temperature.

The diffusing zinc vacancies may provide the mechanism whereby the effect of changing the oxygen pressure is rapidly reflected at the dislocation lines (see above). There is also, however, the possibility that the oxygen may diffuse down the lines rapidly, whereas the indium does not.

Acknowledgement—Thanks are due to Mr. E. A. SADOWSKI for his competent assistance in this work.

REFERENCES

1. SCHAROWSKY E., *Z. Phys.* **135,** 318 (1953).
2. THOMAS D. G., *J. Phys. Chem. Solids* **3,** 229 (1957).
3. HUTSON A. R., *Phys. Rev.* **108,** 222 (1957).
4. THOMAS D. G. and LANDER J. J., *J. Chem. Phys.* **25,** 1136 (1956).
MOLLWO E., *Z. Phys.* **138,** 478 (1954).

5. LANDER J. J. To be published.
6. HAUFFE K. and VIERK A. L., *Z. phys. Chem.* **196,** 160 (1950).
7. WAGNER C., *J. Chem. Phys.* **18,** 62 (1950).
8. HEILAND G., *Z. Phys.* **148,** 15 (1957).
9. ZENER C., *J. Appl. Phys.* **20,** 950 (1949).
10. HAM F. S., *Bull Amer. Phys. Soc.* **3,** 70 (1958); and work to be published.
11. MORIN F. J. and REISS H., *J. Phys. Chem. Solids* **3,** 196 (1957).
12. TWEET A. G., *Phys. Rev.* **106,** 221 (1957).
13. FRANK F. C., *Proc. Roy. Soc.* A**201,** 586 (1950).
FRISCH H. L. and COLLINS F. C., *J. Chem. Phys.* **20,** 1797 (1952); **21,** 2158 (1953).
14. READ (Mrs.) M., private communication.
15. THEIMER O., *Bull Amer. Phys. Soc.* **3,** 60 (1958).
16. AMELINCKX S., *Phil. Mag.* **1,** 269 (1956).
17. DOREMUS R. H., *J. Phys. Chem.* **61,** 1677 (1957).
18. PEARSON G. L., READ W. T. and FELDMAN W. L., *Acta Met.* **5,** 181 (1957).
19. REISS H., *Z. Elektrochem.* **61,** 79 (1957).
20. LINDNER R., *Acta Chem. Scand.* **6,** 457 (1952).
21. SECCO E. A. and MOORE W. J., *J. Chem. Phys.* **26,** 942 (1957).
22. COLLINS R. J., private communication.

VOL
9
195

J. Phys. Chem. Solids Pergamon Press 1958. Vol. 9. pp. 43–47. Printed in Great Britain.

THE FARADAY EFFECT IN SEMICONDUCTORS

M. J. STEPHEN

Department of Theoretical Chemistry, University of Cambridge

and

A. B. LIDARD

Department of Physics, University of Reading

(*Received* 30 *June* 1958)

VOL. 9 1959

Abstract—A general expression for the Faraday rotation, θ, in a semiconductor is derived and applied to the case of free carriers. At low magnetic field strengths and low frequencies, θ is determined by the d.c. conductivity σ_0 and the Hall coefficient R_0 and is proportional to $\sigma_0^{3/2}R_0$. At high frequencies θ depends on the electron distribution and on the shape of the energy surfaces but is independent of the relaxation mechanism. Explicit expressions are given for particular cases, and it is shown how measurements of θ at high frequencies will lead to information about energy surfaces. At low temperatures and high magnetic field strengths, resonances should appear in the rotation at the cyclotron-resonance frequencies.

1. INTRODUCTION

THE rotation of the plane of polarization of a plane polarized electromagnetic wave passing through a substance under the influence of a static magnetic field along the direction of propagation is known as the Faraday rotation. This rotation has been observed at microwave frequencies in germanium by RAU and CASPARI[1] and at infrared frequencies in indium antimonide by SMITH and MOSS.[2] In both experiments the rotation is due to the free charge carriers, and RAU and CASPARI have analysed their results in terms of a simple free-electron model having a relaxation time of the carriers independent of energy. MITCHELL[3] has pointed out that measurements of the Faraday rotation at high frequencies will yield information about the effective mass parameters of the charge carriers.

The purpose of this paper is to examine how the Faraday rotation will vary with frequency and magnetic field strength in semiconductors and to provide a general theory of the effect for arbitrary energy surfaces. In favourable cases interesting information about energy surfaces may be obtained from measurements of the Faraday rotation.

2. THEORY

The main features of the Faraday rotation and its dependence on frequency and magnetic field strength can be illustrated simply for free electrons and this case will be considered first. In the second part of this section the Faraday effect is formulated for semiconductors having arbitrarily shaped energy surfaces and either degenerate or non-degenerate electron distributions. In the third part these general equations are applied to some special situations in germanium and indium antimonide.

(a) *Free Electrons*

We choose a system of axes such that the direction of propagation of the electromagnetic radiation (which is parallel to the static magnetic field H) is along the z-direction. Only the x- and y-components of the electric vector $\mathbf{E}$ of the radiation are non-zero, and it is convenient to use the complex quantities

$$E_{\pm} = E_x \pm iE_y;$$

for, by setting

$$E_+ = E_{0+}(z)\exp(i\omega t)$$

we represent circularly polarized radiation rotating anti-clockwise (observer looking towards the radiation) and by setting

$$E_- = E_{0-}(z)\exp(i\omega t)$$

we represent radiation rotating clockwise. The

problem will be analyzed in terms of E_+ and E_-. Both situations can be described by the single equation, derived from Maxwell's equations

$$\nabla^2 E_\pm = \frac{-\omega^2 \epsilon E_\pm}{c^2} \pm \frac{4\pi i \omega J_\pm}{c^2}, \qquad (2.1)$$

in which ϵ is the dielectric constant and $J_\pm$ is the complex current density $J_x \pm i J_y$.

From a consideration of the classical equation of motion of a free electron in combined electric and magnetic fields, we may write the current density as[1]

$$J_\pm = (A_\pm - iB_\pm)E_\pm, \qquad (2.2)$$

where

$$A_\pm = \frac{\sigma_0}{1+(\omega\tau \mp \omega_c\tau)^2}; \quad B_\pm = \frac{\sigma_0(\omega\tau \mp \omega_c\tau)}{1+(\omega\tau \mp \omega_c\tau)^2};$$

$$\omega_c = \frac{eH}{mc}; \quad \sigma_0 = \frac{Ne^2\tau}{m}, \qquad (2.3)$$

in which N is the number of electrons in unit volume, and τ is the relaxation time. Substitution from (2.2) into (2.1) gives

$$\frac{\partial^2 E_\pm}{\partial z^2} = \left[\frac{-\omega^2\epsilon}{c^2} + \frac{4\pi i\omega}{c^2}(A_\pm - iB_\pm)\right]E_\pm \qquad (2.4)$$

with solutions

$$E_\pm = a_\pm \exp(-\mu_\pm z + i\omega t), \qquad (2.5)$$

in which $a_\pm$ are independent of z and where

$$\mu_\pm^2 = \frac{\omega^2}{c^2}\left[-\epsilon + \frac{4\pi i}{\omega}(A_\pm - iB_\pm)\right]. \qquad (2.6)$$

It is well known that the real and imaginary parts of the $\mu_\pm$ are simply related to the extinction coefficients $k_\pm$ and the refractive indices $n_\pm$. Refractive index is the significant parameter for the present discussion, since the rotation of the plane of polarization of *plane polarized* light is easily shown to be

$$\theta = \frac{\omega l}{2c}(n_- - n_+), \qquad (2.7)$$

in which l is the path length through the specimen. The rotation is positive when it is clockwise for a wave propagating along the direction of the magnetic field towards the observer. The equation for the refractive indices is

$$n_\pm = \frac{c}{\omega}(\mathrm{Im}\mu_\pm), \qquad (2.8)$$

where Im stands for "imaginary part of", leading to

$$n_\pm^2 = \frac{1}{2}\left[\left(\epsilon - \frac{4\pi B_\pm}{\omega}\right) + \sqrt{\left(\epsilon - \frac{4\pi B_\pm}{\omega}\right)^2 + \left(\frac{4\pi A_\pm}{\omega}\right)^2}\right]. \qquad (2.9)$$

The Faraday rotation may then be obtained from equations (2.7) and (2.9). In order to illustrate how the rotation varies with frequency and magnetic field strength, θ has been computed as a function of ω and H for the case $(\epsilon/4\pi) = 1{\cdot}0$, $\sigma_0 = 10^{11}$ esu and $\tau = 10^{-11}$ sec (typical values for n-type germanium). The results are shown in Fig. 1. The frequency range considered corresponds to the region where the sample will not be strongly absorbing or reflecting.

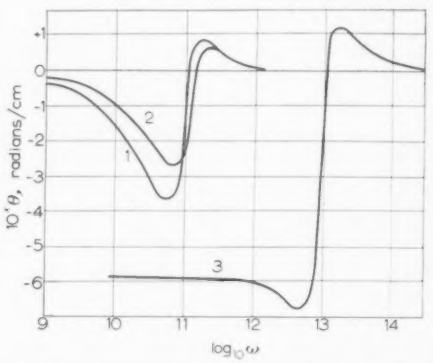

FIG. 1. Faraday rotation $10^x\theta$ in radians/cm for a free electron gas as function of frequency (logarithmic scale); $\sigma_0 = 10^{11}$ esu, $\tau = 10^{-11}$ sec and $\epsilon = 4\pi$ esu. Curve 1 is for $\omega_c\tau = 10^{-2}(x = 2)$, curve 2 is for $\omega_c\tau = 1{\cdot}0(x = 0)$ and curve 3 is for $\omega_c\tau = 10^2(x = 2)$.

The general behaviour of θ over the entire range of ω differs according as $\omega_c\tau < 1$ or $\omega_c\tau > 1$. The first inequality corresponds to a situation in which the electron scattering prevents the observation of

cyclotron resonance. Here θ first decreases as $\omega^{\frac{1}{2}}$, then increases to zero and changes sign at $\omega\tau \sim 1$, and finally approaches zero as ω^{-2}. The change in sign on passing through the natural frequency (τ^{-1}) of the system is equivalent to a change in phase of the current and is a well-known result for a system undergoing forced oscillations. When $\omega_c\tau > 1$ on the other hand the magnetic force on the electrons is more important than the relaxation effect. θ is almost constant for $\omega\tau < 1$ and now changes in sign at $\omega \sim \omega_c$ corresponding to the cyclotron resonance. The rotation is also greatly reduced in magnitude. At high frequencies θ is again proportional to ω^{-2}. Indeed, when ω is much greater than both ω_c and τ^{-1}, θ is independent of the magnitude of $\omega_c\tau$; from equations (2.7) and (2.9) we have

$$\frac{\theta}{lH} = \frac{2\pi Ne^3}{c^2nm^2\omega^2}, \quad \omega \gg \omega_c, \tau^{-1}.$$

This equation was previously obtained by MITCHELL.[3] The independence of this result from $\omega_c\tau$ is important, since it means that studies of Faraday rotation can be employed under conditions in which the cyclotron resonance cannot be observed.

(b) *General Equations for a Cubic Crystal*

In this part we formulate the Faraday rotation for arbitrary energy surfaces for the case of small magnetic fields, i.e. $\theta \propto H$. This limitation only excludes situations close to cyclotron-resonance conditions and is not therefore serious in practice. An advantage of small fields is that quantization of the electron orbits can be neglected and a quasi-classical wave-packet approach may be used (average electron energy $\gg \hbar\omega_c$).

For small magnetic fields we may write the current density in a tensor notation (ABELES and MEIBOOM[4])

$$J_i = \Sigma_{ij}E_j + \Sigma_{ijk}E_jH_k. \tag{2.10}$$

In cubic crystals symmetry requires

$$\Sigma_{ij} = \sigma\delta_{ij}; \quad \Sigma_{ijk} = \sigma'\epsilon_{ijk}, \tag{2.11}$$

where δ_{ij} is the Kronecker symbol and ϵ_{ijk} the substitution tensor. To the approximation in (2.10) the Faraday rotation will be independent of crystal orientation. Substitution of (2.11) and (2.10) into (2.1) gives an equation with solutions again of the form (2.5), where now

$$\mu_\pm^2 = \frac{-\omega^2\epsilon}{c^2} + \frac{4\pi i\omega\sigma}{c^2} \pm \frac{4\pi\omega\sigma' H}{c^2}. \tag{2.12}$$

The Faraday rotation is now obtained by application of (2.7) and (2.8). If we bear in mind that σ and σ' are complex quantities (on account of the phase difference between $E_\pm$ and $J_\pm$) so that

$$\sigma = \sigma_r + i\sigma_i, \quad \sigma' = \sigma_r' + i\sigma_i', \tag{2.13}$$

we find after some manipulation that

$$\theta = \frac{2\pi lH}{c} \frac{(\sigma_r'n - \sigma_i'k)}{(n^2+k^2)}, \quad \text{(low fields)} \tag{2.14}$$

in which n and k are respectively the refractive index and the extinction coefficient in the absence of H. In terms of quantities already defined, they are given by

$$\left.\begin{matrix} 2n^2 \\ 2k^2 \end{matrix}\right\} = \left[\left(\epsilon + \frac{4\pi\sigma_i}{\omega}\right)^2 + \left(\frac{4\pi\sigma_r}{\omega}\right)^2\right]^{\frac{1}{2}} \pm \pm\left(\epsilon + \frac{4\pi\sigma_i}{\omega}\right), \tag{2.15}$$

the plus sign to be taken with n and the minus with k.

These equations can only be applied to particular cases when the quantities σ and σ' have been obtained, for example by solving the Boltzmann transport equation (see, e.g., WILSON[5] or ABELES and MEIBOOM[4]). It is necessary to generalize the results of these authors to the case of alternating fields, but this is very simply done by replacing the relaxation time τ by $(\tau^{-1}+i\omega)^{-1}$ (in addition to the collision term as usually written, $(f_0-f)/\tau$, there will be the time derivative $-\partial f/\partial t = -i\omega(f-f_0)$ in the complex representation).

(c) *Particular Results*

At low frequencies, $\omega\tau \ll 1$, the term in σ_r' in (2.14) is the most important, and it is easily shown that θ is proportional to the Hall coefficient R_0 and varies with frequency as $\omega^{\frac{1}{2}}$. Thus

$$\frac{\theta}{lH} = \left(\frac{\pi\omega\sigma_0^3}{2}\right)^{\frac{1}{2}} \frac{R_0}{c}, \tag{2.16}$$

where σ_0 is the d.c. conductivity. This result is independent of the relaxation mechanism and of the form of the energy surfaces and is valid for both degenerate and non-degenerate semiconductors.

For high frequencies ($\omega\tau \gg 1$), the term in σ_r' in (2.14) is again predominant and θ decreases as ω^{-2} and is independent of the relaxation time. By using the Boltzmann equation to provide expressions for σ_r', the Faraday rotation may be formulated in terms of the energy surfaces of the conduction electrons and their number N per unit volume. If, in addition, the relaxation mechanism is known, N may be related to the Hall coefficient R_0. For example, if we take the energy-band model of n-type germanium used by ABELES and MEIBOOM[4] with four ellipsoids of revolution along the (111) directions, then for the case of lattice scattering (τ proportional to $\mathscr{E}^{-\frac{1}{2}}$) and non-degenerate statistics, (2.14) reduces to

$$\frac{\theta}{lH} = -\frac{3\pi^2 e^2 K^2 (K+2)^2}{4R_0 c^3 \omega^2 \epsilon^{\frac{1}{2}} m_3^2 (2K+1)^2}, \qquad (2.17)$$

where $K = m_3/m_1$ and m_3 and m_1 are the longitudinal and transverse effective masses referred to the principal axes of the ellipsoid. The change in sign of θ between (2.16) and (2.17) corresponds to the change in sign illustrated in Fig. 1.

The general expression for σ_r' for a single energy surface having cubic symmetry is

$$\sigma_r' = \frac{e^3}{4\pi^3 \hbar^4 c \omega^2} \int \frac{\partial f_0}{\partial \mathscr{E}} \frac{\partial \mathscr{E}}{\partial k_x} \times$$

$$\times \left[\frac{\partial \mathscr{E}}{\partial k_y} \frac{\partial^2 \mathscr{E}}{\partial k_x \partial k_y} - \frac{\partial \mathscr{E}}{\partial k_x} \frac{\partial^2 \mathscr{E}}{\partial k_y^2} \right] d\boldsymbol{k},$$

where $\mathscr{E}$ and $\boldsymbol{k}$ are the energy and wave-vector of the conduction state $\exp(i\boldsymbol{k}\cdot\boldsymbol{r})u_{\boldsymbol{k}}(\boldsymbol{r})$ and where f_0 is the equilibrium Fermi distribution function. An interesting special case is that of a degenerate semiconductor having energy surfaces which are spherically symmetrical—though not necessarily quadratically dependent on k (e.g. InSb). We then find that the Faraday rotation is given by an expression similar to that obtained by MITCHELL[3] using the Drude–Zener theory, namely

$$\frac{\theta}{lH} = \frac{2\pi N e^3}{c^2 \omega^2 \epsilon^{\frac{1}{2}}} \left[\frac{1}{\hbar^2 k} \cdot \frac{d\mathscr{E}}{dk} \right]_F^2, \qquad (2.18)$$

but in which the inverse effective mass is replaced by

$$\left(\frac{1}{\hbar^2 k} \cdot \frac{d\mathscr{E}}{dk} \right)$$

evaluated at the Fermi surface. The Fermi radius k_F is given by $k_F^3 = 3\pi^2 N$. Thus for non-parabolic energy bands the Faraday rotation measures $(d\mathscr{E}/dk)$ rather than the second derivative $d^2\mathscr{E}/dk^2$ as one might at first suppose. It should be noted that under the same conditions the Hall coefficient is $-1/Nec$. When the statistics are non-degenerate, the rotation may be evaluated for simple assumed forms of energy surface. Interesting information about the dependence of energy $\mathscr{E}$ on k may be obtained in this way.[2]

At frequencies such that $\omega\tau \sim 1$ (with $\omega_c\tau < 1$) the Faraday rotation, as in the free-electron case, decreases to zero and changes sign. However it does not appear possible to obtain a useful expression for θ in this region when the relaxation time is energy dependent.

3. CONCLUSIONS

The important results are:

(i) At low frequencies and low magnetic field strengths, measurement of the Faraday rotation will lead to a value of the Hall coefficient.

(ii) At high frequencies and low magnetic field strengths, measurement of the Faraday rotation can provide interesting information about the shapes of energy surfaces provided that sufficient additional information is available to determine the number of electrons, e.g. from the Hall coefficient.

(iii) At high magnetic field strengths ($\omega_c\tau > 1$), resonances should appear in the Faraday rotation at exactly the cyclotron-resonance frequencies, but here the experiment differs only in detail from a cyclotron-resonance experiment.

In the above theory the contribution of interband transitions has been omitted. This would be negligible when the energy of the radiation is much smaller than the energy gap between the valence and conduction bands. However, when the frequency of the radiation is comparable to the energy gap, interband transitions will be important. In this case it is possible to develop a theory using the methods of LUTTINGER and KOHN.[6] This

indicates that the Faraday rotation should show oscillations at the absorption edge corresponding to allowed transitions between the Landau levels in the valence and conduction bands and very similar to the oscillations observed in magneto-absorption experiments by ZWERDLING *et al.*[7] When the frequency of the radiation is such that the effect of the absorption edge is not negligible, it may be approximately allowed for by an expression of the form

$$AH/(\omega^2-\omega_g^2)^2,$$

where A is a constant and ω_g is the frequency corresponding to the energy gap. This correction will then yield the total rotation due to free carriers.

Acknowledgement—The authors are much indebted to Dr. S. D. SMITH and Dr. T. S. MOSS for interesting and stimulating discussions on the topic of this paper.

REFERENCES

1. RAU R. R. and CASPARI M. E., *Phys. Rev.* **100,** 632 (1955).
2. SMITH S. D. and MOSS T. S., *Proc. Brussels Conference of Semiconductors* 1958, in the press.
3. MITCHELL E. W. J., *Proc. Phys. Soc.* B68, 973 (1955).
4. ABELES B. and MEIBOOM S., *Phys. Rev.* **95,** 31 (1954).
5. WILSON A. H., *The Theory of Metals* Second Edition. University Press, Cambridge (1953).
6. LUTTINGER J. M. and KOHN W., *Phys. Rev.* **97,** 869 (1955).
7. ZWERDLING S., LAX B. and ROTH L. M., *Phys. Rev.* **108,** 1402 (1957).

Phys. J. Chem. Solids Pergamon Press 1958. Vol. 9. pp. 48–56. Printed in Great Britain.

INFLUENCE OF LATTICE-DEFECT DENSITY ON THE CHEMISORPTION AND OXIDE FORMATION ON A CLEAN (100) CRYSTAL FACE OF NICKEL AS DETERMINED BY LOW-ENERGY ELECTRON DIFFRACTION*

H. E. FARNSWORTH and JOHANNES TUUL

Barus Research Laboratory, Brown University, Providence, R.I.

(*Received* 20 *May* 1958; *revised* 16 *July* 1958)

VOL
9
195

Abstract—An atomically clean, carbon-free, (100) single-crystal face of nickel was obtained by outgassing in high vacuum, argon-ion bombardment, and subsequent annealing. As the exposure to oxygen was increased from 10^{-6} mm Hg-min at 25°C, adsorption occurred first in a double-spaced, face-centered, crystalline lattice, then in a single-spaced, simple-square lattice, and finally in a nickel-oxide lattice. The intensities of the diffraction patterns from the adsorbed structures were much greater for a surface having a high defect density than for one having a low defect density, although the exposures required to produce detectable amounts of the structures were approximately independent of the defect density. These intensities from the chemisorbed lattice structures were much greater when the exposures were made at 150 than at 25°C, and the structures were stable for higher exposures at the higher temperature. Consequently, *larger* oxygen exposures were required to form a detectable amount of oxide at 150 than at 25°C. The exposures required to produce detectable amounts of chemisorbed lattice structures did not vary appreciably with temperature in this range. Most of the adsorption and oxidation measurements were made in the exposure range 10^{-6} to 10^{-4} mm Hg-min. Certain exposures and subsequent heat treatments resulted in additional lattice structures.

1. INTRODUCTION

RECENT reviews of fundamental concepts on chemisorption and oxidation of metals have been presented by EHRLICH[1] and by CABRERA.[2] These include considerations of grain boundaries, lattice steps, and dislocations. Other fundamental aspects of the adsorption problem have also been discussed recently by HIGUCHI *et al.*[3] and by MATSEN *et al.* and by BRODD.[4]

The present paper contains an extension of work reported previously on oxygen chemisorption and oxidation using the low-energy electron-diffraction method,[5] and is closely related to other work in this laboratory on catalysis.[6] In the previous report[5] no consideration was given to the influence of lattice-defect density on the adsorption and oxidation problems. Measurements were made for a given state of anneal of a clean (100) nickel face at room temperature. It was shown that, as the oxygen exposure (pressure × time) was increased, the oxygen first formed a chemisorbed layer of definite lattice structure and finally a true nickel oxide appeared.

In the first experiments, the nickel was found to be covered with a double-spaced, face-centered monolayer of carbon subsequent to heat treatment at temperatures as high as 1100°C. An atomically clean (100) crystal surface was produced by argon-ion bombardment and subsequent anneal,[7] although further high-temperature heat treatment caused more carbon to diffuse from the interior to the surface until many cyclings over several days depleted the carbon density near the surface. The presence of the carbon prevented the chemisorption of oxygen, but the formation of the oxide on

* Assisted by Office of Ordnance Research, U.S. Army, and by the National Science Foundation.

the surface appeared to be independent of the presence of the carbon.*

Although the present work is exploratory in nature, it does furnish information on some of the fundamental questions regarding chemisorption and initial oxide formation on an atomically clean crystal face. It also indicates the capabilities of the low-energy electron-diffraction method in this field and suggests further experiments which should yield additional information.

2. APPARATUS AND PROCEDURE

The low-energy electron-diffraction apparatus and the method of producing and maintaining an atomically clean surface of nickel have been described elsewhere.[7] Residual pressures of less than 10^{-9} mm Hg were obtained by two mercury diffusion pumps in series and a liquid-nitrogen trap. Mercury cutoffs between the pumps made it possible to use one pump occasionally to evacuate gas storage volumes without degrading the vacuum in the experimental tube. Precautions were taken to eliminate all probable sources of contamination and blank runs were taken as checks. A renewable, evaporated, molybdenum getter was attached to the experimental tube through a Pyrex ball-and-socket valve to reduce the residual pressure of oxygen and any other active gases still further. This valve was of the type described by DECKER;[8] it could be outgassed by baking and, of course, was operated without any lubricant. The conductance of the dry valve when closed was small enough for the present purpose. During oxygen exposure the valve was closed to protect the getter.

(a) *Control and determination of the oxygen pressure*

Spectroscopically pure oxygen in a 1-l. Pyrex flask with break-off tip was used to supply oxygen at a reduced pressure in a Pyrex storage volume. The oxygen passed from this storage volume to the experimental tube through a porous porcelain-tube leak and a liquid-nitrogen trap; the leak was adjusted by a mercury column. An equilibrium pressure was maintained in the tube, which was continuously connected to the vacuum system.

The presence of oxygen in the experimental tube was determined from a calibration of the adjustable leak for nitrogen gas. This calibration was made with the ionization gauge as a pressure reference. Thus, it was assumed that a given leak setting resulted in the same pressures of oxygen and nitrogen in the experimental tube. Direct measurement of the oxygen pressure by the ionization gauge was impossible owing to pumping of oxygen by the gauge and the formation of Co.[9] An error in pressure determinations due to the gettering action of an active nickel film on the glass envelope, produced by ion bombardment or evaporation, was kept small whenever possible.† This was accomplished by saturation of any freshly produced film with oxygen. The accompanying contamination of the crystal was then removed by a subsequent *short* ion bombardment or heating to keep the amount of active film small. It was impossible to eliminate this error completely. It was greatest for the initial exposures, with the indicated values being larger than the true values. However, this error did not affect the main features of the results to be discussed.

(b) *Production of defects*

The defects for most of the observations were introduced by argon-ion bombardment under the conditions used to clean the surface, and hence consisted of both vacancies and interstitials. To reduce the defect density, this treatment was followed by varying amounts of anneal (both temperature and time). No attempt was made to determine the defect density.

(c) *Method of making observations as a function of exposure*

These observations were obtained by recording colatitude curves and noting the peak deflections of certain typical diffraction beams as a function of exposure.‡ Starting with a clean crystal which had been subjected to a desired anneal, the adjustable leak was opened for a certain pressure and time.

* The identification of carbon was made by bombarding the clean nickel surface with positive ions in a CO discharge. Following a short anneal, the characteristic diffraction beam which previously had been associated with a carbon monolayer was observed from the carbon deposited during the discharge.

† See captions for Figs. 2 and 3.

‡ The product of pressure and time was found to be a reliable measure of exposure in the pressure range of the observations (10^{-8} to 2×10^{-5} mm Hg).

The exposures were usually of 10 min duration. After closing the leak, the pressure dropped quickly to a negligible value, so that observations on each of several diffraction beams could be made. This procedure was then repeated for similar or larger exposures. More than one day was required to obtain a complete set of data. However, the stability was such that after an interruption of many hours the observations could be duplicated and continued. The current in the gun filament was reduced to a low value during the exposure to prevent formation of CO by the filament.[9]

(d) *Procedures for adsorption at elevated temperatures*

Two procedures were used. (1) The crystal could be withdrawn by a magnetic control into a side tube which was surrounded by a small oven. This oven was maintained at a fixed temperature throughout a set of exposures with the associated observations. In the observation position the crystal was outside the oven at a distance of 2 to 3 in. and hence it must have been near room temperature. The maximum feasible temperature of the oven was 150°C. At higher temperatures, difficulties were encountered due to liberation of gases from the walls, and the appearance of electrical leakage in the movable collector circuit. (2) Some exposures were made at higher temperatures by first heating the crystal to 800°C by electron bombardment, removing the power, admitting the oxygen at a fixed time after the end of heating, and determining the temperature range during exposure from a cooling curve which was obtained when a thermocouple was attached to the crystal. Because of the varying temperature, observations of the type discussed in sub-section (c) above could not be obtained, but some significant observations on changes in structure were made.

3. EFFECTS OF ANNEAL AND TEMPERATURE

Colatitude curves for the five diffraction beams, which were observed as a function of exposure, are shown in Fig. 1. These beams consist of two typical beams from the nickel lattice, one in each of the two principal azimuths,[7] one beam which is characteristic of a double-spaced, face-centered (d–s, f–c) chemisorbed oxygen lattice, one for a single-spaced, simple-square (s–s, s–s) chemisorbed oxygen lattice, and one for a nickel-oxide lattice with the rock-salt type of structure.* Plots of the peak values of these colatitude curves† as a function of $\log_{10}$ of exposure are shown in Figs. 2 and 3 for different annealing conditions. These

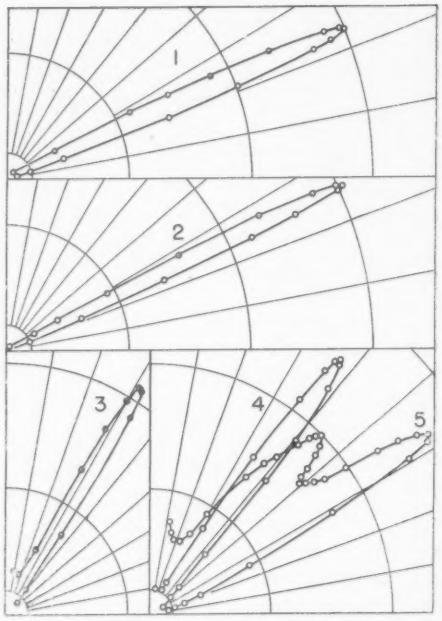

FIG. 1. Colatitude curves (diffraction-beam current against colatitude angle) for five diffraction beams. *Curve* 1: Typical beam from the clean nickel lattice in the (110) azimuth at 27 V. Multiply the current scale by 10. *Curve* 2: Typical beam from the clean nickel lattice in the (100) azimuth at 56 V. Multiply the current scale by 20. *Curve* 3: Typical beam from a double-spaced, face-centered lattice of chemisorbed oxygen in the (110) azimuth at 17 V. Multiply the current scale by 6. *Curve* 4: Typical beam from a single-spaced, simple-square lattice of chemisorbed oxygen in the (100) azimuth at 27 V. Multiply the current scale by 10. *Curve* 5: Typical beam from a nickel-oxide lattice on the crystal surface in the (110) azimuth at 22 V. Multiply the current scale by 5. *Curves* 3, 4, and 5 were obtained after various oxygen exposures at room temperature.

* The oxide had a rock-salt structure; the lattice spacing was the same as the X-ray value and the [110] direction of the oxide lattice was parallel to the [110] direction of the nickel lattice.

† The areas under these curves (when plotted on rectangular co-ordinates) have also been plotted as a function of log of exposure. There are no significant differences between these results and those obtained with the peak values.

VOL 9 195

plots are of the type shown in Fig. 1 of reference (3) except that the previous observations were not made in the (100) azimuth and hence the single-spaced oxygen lattice was not observed. Because

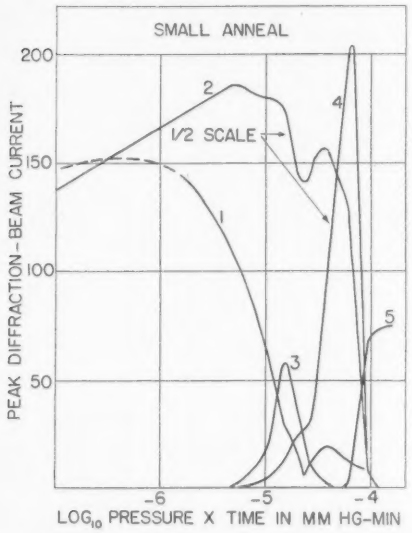

FIG. 2. Peak current versus $\log_{10}$ (pressure $\times$ time) for the five diffraction beams shown in Fig. 1 after ion bombardment of the crystal surface followed by a small anneal. The discrepancies between the positions of the curves on the exposure axis compared with the positions in Figs. 4 and 5 are attributed to the presence of an active nickel film on the inner surface of the glass envelope when the results for this figure were obtained. The positions in Figs. 4 and 5 are, therefore, more nearly correct.

of more detailed observations in the later results, certain characteristics appeared which were not noted previously.

Referring to Fig. 2, the small anneal was produced by heating the crystal to not more than 400°C and cooling to room temperature during a time of 35 min. The following features are noted in the curves of Fig. 2. Beginning with a clean surface in a high vacuum, the peak values of the beams from the nickel lattice increased with exposure, passed through a maximum, decreased rapidly, passed through a weaker second maximum, and then dropped to zero. By taking a blank run with no oxygen exposure, the initial increase was shown to be due to an annealing out of defects at room temperature, and hence an improvement in the degree of perfection of the lattice. The subsequent decrease was caused by adsorption of oxygen which shielded the nickel lattice. The second maxima in the two curves are explained in the following manner. The one for the 57-V curve in the (100) azimuth was caused by the superposition of a second-order beam from the s–s, s–s oxygen lattice on the first-order diffraction from the nickel lattice. The second maximum in the 27-V curve in the (110) azimuth was caused by the superposition of a first-order beam from the s–s, s–s oxygen lattice which maximized at 38-V in the (110) azimuth but which overlapped and was superimposed on the 27-V beam from the nickel lattice.

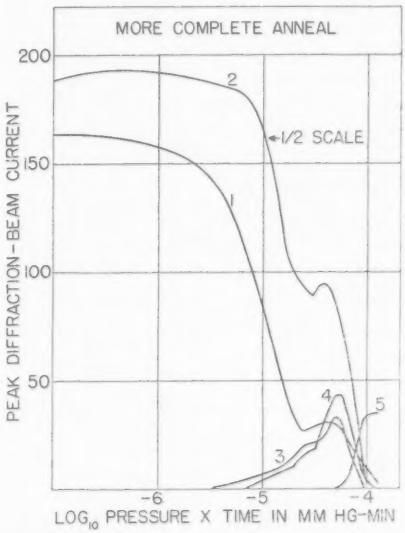

FIG. 3. Curves, similar to those for Fig. 2, obtained after a more complete anneal. The discrepancies between the positions of the curves on the exposure axis compared with the positions in Figs. 4 and 5 are attributed to the presence of an active nickel film on the inner surface of the glass envelope when the results for this figure were obtained. The positions in Figs. 4 and 5 are, therefore, more nearly correct.

The first indication of oxygen adsorption was the decrease in intensity of the 27-V beam in the (110) azimuth. With increasing exposure, the 17-V beam from the d–s, f–c oxygen lattice was detected; it then increased to a maximum value and decreased to zero with further exposure. Concurrently, the formation of the s–s, s–s structure was observed, as indicated by the 27-V beam in the

(100) azimuth. The intensity of this beam increased rapidly with further exposure, passed through a maximum, and decreased to zero while the NiO structure made its appearance, as indicated by the 22-V beam in the (110) azimuth. The intensity of this beam increased rapidly until an exposure of about 10^{-4} mm Hg-min was reached.

The more complete anneal for Fig. 3 was produced by heating the crystal at 750°C for 14 hr and cooling to room temperature over a period of 90 min. A comparison of the corresponding curves in Figs. 2 and 3 shows the large influence of the amount of anneal on certain adsorption characteristics. The maximum for the 27-V beam in the (100) azimuth from the oxygen lattice was reduced to about 10 per cent of its former value by the more complete anneal. The beams from the other two structures were reduced by smaller amounts. However, the exposures at which these beams were rst detected were approximately the same after he two different anneals.

To obtain curves of the type shown in Figs. 4 and 5, illustrating the influence of temperature on the adsorption and oxidation processes, it was necessary to reduce the effect of annealing. Hence, an intermediate state of anneal was chosen which was large enough to keep further anneal at 150°C small during the time of observations, but which was small enough to result in appreciable adsorption effects. Fig. 4 shows such a set of curves for adsorption at room temperature and Fig. 5 is for adsorption at 150°C and approximately the same state of anneal. Comparison of the corresponding curves in these two figures shows the following:

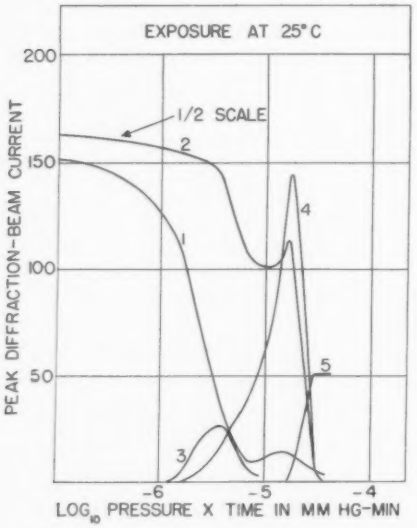

FIG. 4. Curves, similar to those for Fig. 2, obtained after an intermediate anneal. Oxygen adsorption occurred at 25°C.

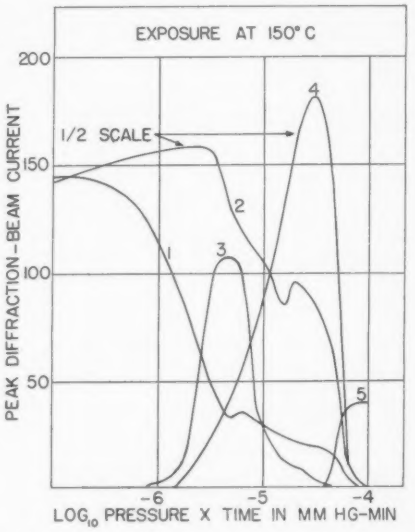

FIG. 5. Curves, similar to those for Fig. 4, obtained at room temperature after oxygen adsorption at 150°C.

(1) The smallest exposures at which the two characteristic structures of chemisorption could be detected were approximately the same at the two temperatures.

(2) The diffraction beams from these two structures were much more intense for the exposure at the higher temperature.

(3) The chemisorbed structures were present over a wider range of exposure, and hence at higher values, for the exposure at 150°C.

(4) The smallest exposure for which the oxide appeared was larger for the exposure at 150°C.

(5) The largest beam intensity from the oxide structure was less for the exposure at 150°, although this result may have been due to the occurrence of some annealing as indicated by the positive slope at the left of curve 2, Fig. 5.

VOL. 9 1959

4. DISCUSSION

In earlier work[5] it was suggested that the maximum in the curve for the 17-V beam corresponded to the completion of one monolayer. This interpretation is now seen to be incorrect, since the height of the maximum for this curve varied with defect intensity, as determined by the amount of anneal, and with the temperature during adsorption. It appears that the heights of the maxima for the 17-V, the 27-V ((100) azimuth), and the 22-V curves all correspond to less than complete coverage of the surface. Since the diffraction beams from all of the other structures were reduced to zero intensity when the NiO beam reached its maximum values, independently of this maximum value, it appears necessary to conclude that the remainder of the surface, which was not covered with an oriented oxide layer, was, nevertheless, covered with an amorphous or disarranged layer of oxygen or oxide.

It is noted that the diffraction-beam current for the nickel lattice, which is shown in curve 1, Fig. 2, decreased before any evidence of a chemisorbed lattice structure was observed in curve 3. This might be considered to suggest that some adsorption occurred in the form of an amorphous or disarranged crystalline layer of oxygen in addition to chemisorption in a lattice structure. However, some or all of this difference may be attributed to the greater sensitivity of the 27-V beam to a small surface coverage which would be expected if one assumes that the diffracted intensity is proportional to the square of the surface coverage (the amplitude is proportional to surface coverage). It is also to be noted that the ordinates of curves 1 and 2 in Fig. 3 both decrease in approximately the same exposure range as in the cases of curves 1 and 2 of Fig. 2, even though the intensities (and hence the shielding actions) from the oxygen structures were less in the former case. Thus the formations of the oxygen lattices do not appear sufficient to account for the decreases in the beams from the nickel lattice. An assumption of some adsorption in an amorphous or disarranged structure would account for this observation.

The amounts of chemisorbed oxygen which formed in the two monolayer crystal lattices over the most perfect parts of the crystal facets increased with an increase in the numbers of lattice imperfections. Hence it appears that the lattice defects acted as nuclei for this oxygen lattice growth and that the total area of growth increased as the number of defect centers was increased. It is assumed that this growth occurred during the exposure and not subsequent to it, the favorable areas of growth being those immediately adjacent to the defects. The initiation of this growth appears to have been approximately independent of temperature in the range 25–150°C. However, the maximum diffracted intensities (and hence areas of growth) showed a strong temperature-dependence, and both chemisorbed structures were stable for higher exposures at 150 than at 25°C. As a consequence, it is noted that *larger* oxygen exposures were required to form a detectable amount of oxide at 150 than at 25°C.

There are certain unresolved discrepancies between the present observations and those of GOMER[10] using the field-emission technique. GOMER states that only adsorption takes place below 400°C. He also states that "the patterns seemed to appear almost instantly without subsequent changes", although photographs for three pressures 2×10^{-6}, 10^{-5}, and 10^{-3} mm Hg, show different patterns. From our observations it is difficult to understand how GOMER's results can be independent of time.

5. STICKING COEFFICIENT

An approximate value for the sticking coefficient for oxygen of 0·01 was obtained from curve 1 in Fig. 4, using the portion of the curve with the greatest slope. This was done by assuming that the coverage $\theta = 1-\sqrt{I/I_0}$, where I is the variable diffraction-beam intensity and I_0 is the value for the clean surface. It was assumed that there was one oxygen atom per surface nickel atom and that the diffraction beam was extinguished by one layer of oxygen. While the accuracy of this computation is not great, the order of magnitude is believed to be correct.

6. ADDITIONAL OBSERVATIONS UNDER CERTAIN CONDITIONS OF TEMPERATURE AND EXPOSURE

After completing the exposures required to produce an oxide layer, this oxide could be removed by heating. With progressive heat treatment, the oxide was replaced by a single-spaced, simple-square structure, and this structure was

subsequently replaced by the double-spaced, face-centered one. Further heating resulted in a clean surface.* However, the intensities and, in some cases, the shapes of the diffraction beams for these structures differed from those of the beams which were formed by adsorption at room temperature. In some cases certain heat treatments resulted in new structures. Although the interpretations of all of the observations have not been completed, the following results are given to indicate the complexity of the data which have been obtained. Fig. 6 shows colatitude curves for some representative diffraction beams. Curve 1 shows the development of the high-angle component of the 22-V oxide (see curve No. 5 of Fig. 1) with the low-angle component suppressed. This result was obtained after heating the NiO-covered nickel at 400°C for 5–10 min. Curve 2 shows a colatitude curve of the 80-V oxide beam which was obtained in the (100) azimuth under the same conditions. Both of these curves correspond to the NiO surface spacing, within the experimental error, as determined by X-rays.

Curve 3 was obtained after the clean nickel surface had been exposed to 4×10^{-5} mm Hg-min of oxygen while the crystal cooled from 190 to 115°C. The observations were made with the crystal at room temperature. This exposure was sufficient to form the two-component oxide structure when the crystal was at room temperature, but that structure was not found in the present case. Curve 3 was not found when the exposure was made above 300°C or below 115°C. This curve corresponds to a large surface-lattice spacing which is approximately three times the nickel-lattice spacing in this azimuth and to nearly 2·5 times the nickel-to-nickel spacing for the NiO lattice in this azimuth. Because of this large spacing, other possible beams associated with it fall outside the angular range of observations. It is not known whether this large lattice is associated with a chemisorbed layer or an oxide structure. Computations for NiO planes other than the (100), such as the (110), which might form on the surface and yield the necessary spacing have been unsuccessful in accounting for this beam.

After observing this structure, the crystal was heated at about 400°C for 5–10 min. This treatment caused curve 3 to disappear and curves 4 and 5 were then observed in the (110) and (100) azimuths, respectively. Curve 4 coincides closely with

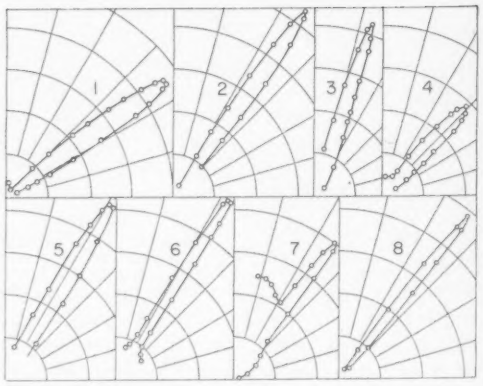

FIG. 6. Colatitude curves (diffraction-beam current against colatitude angle) for selected diffraction beams obtained after certain oxygen exposures and thermal treatments of the crystal. *Curve* 1: High-angle component of a nickel-oxide beam in the (110) azimuth at 22 V. Multiply the current scale by 10. *Curve* 2: A nickel-oxide beam in the (100) azimuth at 80 V, under the same conditions as those for Curve 1. Multiply the current scale by 5. *Curve* 3: A low-angle beam, in the (110) azimuth at 20 V, from an oxygen structure having a lattice spacing about three times that of nickel in this azimuth. Multiply the current scale by 20. *Curve* 4: Low-angle component of the nickel-oxide beam in the (110) azimuth at 22 V. Multiply the current scale by 10. *Curve* 5: Low-angle oxide beam in the (100) azimuth at 80 V. Multiply the current scale by 2. *Curve* 6: Beam from the double-spaced, face-centered oxygen lattice, in the (110) azimuth at 17 V, produced by an oxygen exposure of $2{\cdot}5\times10^{-5}$ mm Hg-min followed by heating at 150°C for 1 min. Multiply the current scale by 10. *Curve* 7: Similar to Curve 6, but obtained after heating an oxide-covered crystal at 750°C for 5–10 min. Multiply the current scale by 3. *Curve* 8: Intense beam from a single-spaced, simple-square lattice of chemisorbed oxygen in the (100) azimuth at 27 V, with the adsorption occurring at 190–340°C. Multiply the current scale by 60.

* In the later stages of outgassing, the surface was not completely cleaned of the d–s, f–c structure by heating, although the change from oxide to this structure was readily accomplished. It has been observed that metal oxides, when heated to a few hundred °C *in vacuo*, may be removed from supporting metal surfaces by reaction of the surface oxide with carbon in the metal to form CO.[11] In the present case, it is possible that small amounts of carbon were present on some surfaces of the crystal or its mounting even when the (100) face was free of carbon. Then, as the amount of available carbon was decreased, it became more difficult to clean the surface by heating.

VOL. 9 1959

the low-angle component of the oxide curve No. 5 of Fig. 1. Curve 5 is similar to the oxide curve No. 2, Fig. 6, but it is weaker and at a smaller colatitude angle. Both curves 4 and 5 correspond to an oxide lattice having a surface spacing approximately 15–20 per cent greater than the X-ray spacing. The beam in the (110) azimuth (curve 4, Fig. 6) was present over a wide range of voltage from 12 to 90, maximizing at 22 V and with a second maximum at 45 V. When these beams were observed, the crystal surface was also partly covered with the s–s, s–s surface oxygen structure. Heating the crystal at 530–600°C caused this oxide lattice to weaken and its surface lattice spacing to decrease a few per cent. Since the lattice spacing of this oxide structure is greater than that for NiO, it may be associated with NiO_2 or Ni_2O_3.[12]

Curve 6 is for the beam from the d–s, f–c oxygen lattice, in the (110) azimuth at 17 V. This beam was obtained after an exposure of $2{\cdot}5\times10^{-5}$ mm Hg-min at room temperature, followed by heating at 150°C for only 1 min. This beam was considerably more intense than the corresponding beam from the d–s, f–c lattice which was formed at room temperature under optimum conditions, thus indicating the improvement of this lattice which could be effected by suitable exposure and heat treatment. Curve 7 is for the corresponding beam which was observed after formation of an oxide structure at 25°C, followed by heat treatment at 750°C for 5–10 min. This beam was weaker than the one represented by curve 6 and its colatitude angle was at 37° instead of at 33°, thus indicating that a slightly smaller lattice constant resulted from heating at the higher temperature. Curve 8 is for an intense beam from the s–s, s–s lattice of chemisorbed oxygen in the (100) azimuth at 27 V after adsorption of oxygen at an exposure of 4×10^{-5} mm Hg-min at 190–340°C. This was the most intense beam that was observed from this nickel crystal face.

7. SUMMARY AND CONCLUSIONS

The low-energy electron-diffraction method has furnished information on chemisorption and oxidation which has not been available in other methods. In particular, it has provided a criterion for an atomically clean surface and has made possible the determination of conditions necessary for the initial formation of at least two chemisorbed lattice structures and an oxide structure on the (100) nickel crystal face. The formation of nickel oxide on the (100) face was always preceded by the formation of double-spaced, face-centered and single-spaced, simple-square monolayer structures, in sequence. The chemisorbed oxygen lattice structures remained stable at larger exposures when the temperature was increased. This resulted in a requirement of a *larger* oxygen exposure to form the oxide at the higher temperature. There is evidence for at least two other structures which were produced under certain temperature and exposure conditions.

The following observations appear of special significance. (1) Chemisorption in the form of a crystal lattice and oxidation at room temperature were strongly dependent on the density of lattice defects at the surface. (2) The amount of crystalline chemisorption increased rapidly with the temperature. (3) The extinction of the diffraction pattern from nickel (and hence the sticking coefficient) did not appear to depend on the area of the chemisorbed crystalline layer. (4) Subsequent heating of the crystal, after formation of either one of the crystalline chemisorbed layers at 25°C, caused a decrease in the amount of this chemisorption. (5) The smallest exposures at which the chemisorbed crystal lattice structures were first detected were approximately independent of the defect density and temperature.

Further details concerning a possible model to account for the above observations will be given at a later date.

Because the present work was exploratory in nature, several questions remain which this method is capable of answering. There has been no indication that the uptake of oxygen was proportional to the square root of the oxygen pressure rather than the first power of the pressure, as is usually assumed to be the case. The product of pressure and time was found to be a reliable measure of exposure in the range used. However, a more careful study is desirable of the possible influence of pressure on the transition from a chemisorbed structure to an oxide structure. The observations should also be extended to a larger temperature range. In addition, a study of the photoelectric yield and work function for the observed structures should furnish significant information.

Acknowledgements—The experimental tube and auxiliary apparatus used in these investigations were assembled by Dr. R. E. SCHLIER for use in a previous investigation.[1] We are indebted to Dr. SCHLIER for certain experimental adjustments and assistance and the discussion of the results.

REFERENCES

1. EHRLICH G., *J. Phys. Chem. Solids* **1,** 3 (1956).
2. CABRERA N., *Semiconductor Surface Physics* p. 327. Univ. of Penn. Press, Philadelphia (1957).
3. HIGUCHI I., REE T. and EYRING H., *J. Amer. Chem. Soc.* **79,** 1330 (1957).
4. MATSEN F. A., MAKRIDES A. C. and HACKERMAN N., *J. Chem. Phys.* **22,** 1800 (1954).
   BRODD R. J., *J. Phys. Chem.* **62,** 54 (1958).
5. SCHLIER R. E. and FARNSWORTH H. E., *Advances in Catalysis* Vol. 9, p. 434. Academic Press, Inc., New York (1957).
6. FARNSWORTH H. E. and WOODCOCK R. F., *Industr. Engrg. Chem.* **49,** 258 (1957); *Advances in Catalysis* Vol. 9, p. 123. Academic Press, Inc., New York (1957).
7. FARNSWORTH H. E., SCHLIER R. E., GEORGE T. H. and BURGER R., *J. Appl. Phys.* **29,** 1150 (1958).
8. DECKER R. W., *J. Appl. Phys.* **25,** 1441 (1954).
9. SCHLIER R. E., *J. Appl. Phys.* **29,** 1162 (1958).
10. GOMER R., *J. Chem. Phys.* **21,** 293 (1953).
11. HOLM V. C. F., *J. Res. Nat. Bur. Stand.* **28,** 569 (1942).
    GULBRANSEN E. A. and ANDREW K. F., *J. Phys. Colloid Chem.* **53,** 690 (1949).
    UHLIG H. H. Private communication.
12. VAINSHTEIN E. E., *Zh. eksp. teor. fiz.* **20,** 442 (1950).

VOL
9
195

Phys. Chem. Solids Pergamon Press 1958. Vol. 9. pp. 57–59. Printed in Great Britain.

TESTS WITH LOW-ENERGY ELECTRON DIFFRACTION FOR ADSORBED HYDROGEN AND NICKEL HYDROXIDE FORMED ON THE (100) SURFACE OF A NICKEL CRYSTAL AT 25°C*

H. E. FARNSWORTH, R. E. SCHLIER and JOHANNES TUUL

Barus Research Laboratory, Brown University, Providence, R.I.

(*Received* 20 *May* 1958; *revised* 16 *July* 1958)

Abstract—A low-energy electron-diffraction pattern from a chemisorbed double-spaced monolayer was observed subsequent to an exposure to hydrogen, only when a hot filament was present during the exposure, thus indicating adsorption of atomic hydrogen or water vapor or both. Evidence is presented which indicates that this double-spaced structure was due to water vapor. Adsorption of hydrogen on some parts of the surface, with no hot filament present during exposure, was confirmed by consecutive exposures of the clean nickel surface to hydrogen and oxygen to form $Ni(OH)_2$.

THE results reported here were obtained during an investigation of the chemisorption of gases on the clean (100) face of a nickel crystal,[1,2] using the method of low-energy electron diffraction. This method and the method of obtaining an atomically clean crystal surface in high vacuum have been described elsewhere.[2,3] The same procedures and precautions for obtaining a high vacuum and clean surfaces were observed in the present work.

In our first attempts to observe the structure of adsorbed hydrogen, the pressure was measured with an ion gauge *using a hot tungsten filament*. After exposures of 10^{-5} to 10^{-1} mm Hg-min on the clean nickel surface at room temperature, a diffraction pattern was observed from a chemisorbed monolayer having a face-centered lattice structure with twice the spacing of nickel. A typical diffraction beam in the (110) azimuth is shown in Fig. 1, curve 1. Beginning with a clean surface, it was then observed that no diffraction pattern from a double-spaced lattice was present subsequent to hydrogen exposure, *unless the gauge filament* (*or some other filament*) *was hot during the exposure*. This was true for all exposures made (up to 25 mm Hg-min).

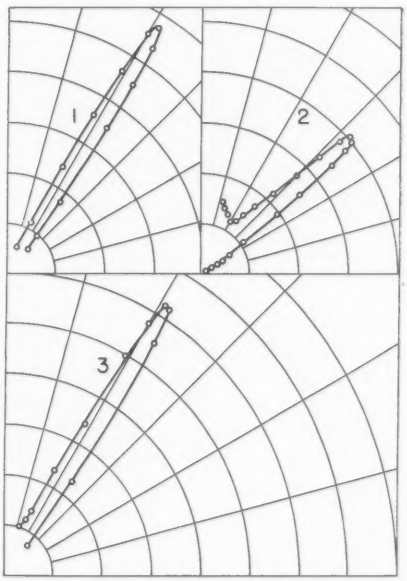

FIG. 1. Typical colatitude curves obtained after the following treatments: (1) hydrogen exposure of a clean surface in the presence of a hot filament, (2) consecutive exposures to hydrogen (in the presence of a hot filament) and oxygen to form nickel hydroxide, and (3) oxygen exposure of a clean surface sufficient to form a double-spaced lattice.

* Assisted by Office of Ordnance Research, U.S. Army, and by the National Science Foundation.

Thus the observed structure caused by the presence of the hot filament must have been due to atomic hydrogen[4] or water vapor.* It is also evident that any hydrogen which was chemisorbed when no hot filaments were present was not detected by electron diffraction.

The following evidence indicates that, after the hydrogen exposure in the presence of a hot filament, the resulting diffraction pattern from the double-spaced lattice was due to water vapor (formed by interaction of atomic hydrogen with oxygen on neighboring surfaces) rather than atomic hydrogen, CO, or oxygen contamination, the diffraction being produced by the oxygen atoms in the adsorbed molecules rather than by hydrogen atoms. (It does not, of course, exclude the adsorption of atomic hydrogen in addition to water vapor.) (1) This pattern was not observed after a blank run with no hydrogen present, and hence it could not have been due to background oxygen contamination in the tube with the filament hot. (2) This pattern was not due to oxygen contamination in the hydrogen, since it was not observed after a hydrogen exposure with no hot filament present. (3) This pattern is similar to that of double-spaced chemisorbed oxygen, and may be attributed to oxygen atoms in the water molecules. The corresponding diffraction beam from a double-spaced oxygen lattice is shown in Fig. 1, curve 3. (4) The diffraction beams from this double-spaced structure do not resemble those obtained after CO† exposures; hence they are not due to CO. (5) The diffraction beams from the nickel lattice were insensitive to the hydrogen adsorbed at room temperature (with no hot filament present), thus indicating negligible scattering (and hence negligible diffraction) by the hydrogen. It will be shown below that hydrogen was adsorbed under these conditions. (6) The intensities of the beams from the nickel lattice were decreased by about the same amount due to the following: (*a*) formation of a double-spaced oxygen layer, or (*b*) formation of a double-spaced structure by exposure to hydrogen in the presence of a hot filament, thus indicating that the double-spaced structure was not atomic hydrogen. However, it is to be noted that the double-spaced structure, resulting from the hydrogen exposure in the presence of the hot filament, was not replaced by another structure with increased exposures, while in the case of oxygen the double-spaced structure was replaced by a single-spaced, simple-square structure and then by an oxide structure as the exposure was increased.[2] These differences in the two structures are attributed to the presence of hydrogen in the water molecule.

It was also of interest to attempt to verify the chemisorption of hydrogen[6] on the (100) nickel crystal face when the exposure was made in the absence of a hot filament. This was done by making the following observations. After consecutive exposures of the clean (100) nickel surface at 25°C to hydrogen and oxygen, with thorough evacuation after each exposure, a surface nickel hydroxide structure was observed. This was true both with and without the presence of a hot tungsten filament during exposure of the hydrogen. The second observation indicates that hydrogen must have been present on the surface. The first observation does not distinguish between hydrogen and water vapor. The $Ni(OH)_2$ structure was not observed if the order of the above exposures was reversed, thus indicating that when oxygen was first chemisorbed on the surface, the exposure to hydrogen or water vapor did not alter the positions of the adsorbed oxygen atoms. A characteristic beam from the $Ni(OH)_2$ lattice which was observed in the (110) azimuth at 33 V is shown in Fig. 1, curve 2. The lattice of this structure was hexagonal; the (0001) plane of the $Ni(OH)_2$ was parallel to the (100) plane of nickel, and the $[10\bar{1}0]$ direction was parallel to the [110] direction of nickel. Diffraction beams were observed in the (110) azimuths as well as in azimuths differing from this by 60° intervals. Because there are four (110) azimuths, beams were observed in adjacent azimuths differing by only 30°.‡

* Observations with an omegatron mass spectrometer on another experimental system in this laboratory have shown that water vapor is formed in appreciable quantity during a hydrogen exposure in the presence of a hot filament.

† HICKMOTT[5] has recently reported the production of large amounts of CO due to the presence of a hot filament in a hydrogen ambient. The fact that this was not true in the present case may have been due to a different experimental arrangement and pumping speed.

‡ In the case of exposures in the *absence of a hot filament*, the observed lattice constant was somewhat smaller. The reason for this is not apparent.

VOL 9 195

Effects similar to those described above due to the presence of a hot filament during hydrogen exposure to germanium and silicon surfaces have been observed in this laboratory by both electron diffraction[7] and work-function[8] measurements. In these cases, no changes in the diffraction pattern and work functions were observed due to hydrogen exposures with no hot filament present (except that no observation was made on the work function of germanium after hydrogen exposure with no hot filament present) up to 10^{-2} mm Hg-min, but in all cases changes were observed when a hot filament was present during the exposure. More recently, LAW[9] has reported the observation of a similar effect in measurements of the adsorption of hydrogen on silicon. He attributes the result to atomic hydrogen rather than water vapor.

VOL. 9 1959

REFERENCES

1. SCHLIER R. E. and FARNSWORTH H. E., *Advances in Catalysis* Vol. 9, p. 434. Academic Press, Inc., New York (1957).
2. FARNSWORTH H. E. and TUUL J., *J. Phys. Chem. Solids* **8**, 48 (1959).
3. FARNSWORTH H. E., SCHLIER R. E., GEORGE T. H. and BURGER R., *J. Appl. Phys.* **29**, 1150 (1958).
4. LANGMUIR I., *J. Amer. Chem. Soc.* **37**, 417 (1915).
5. HICKMOTT T. W., *Bull. Amer. Phys. Soc.* **3**, 259 (1958).
6. BAKER M. McD., JENKINS G. I. and RIDEAL E. K., *Trans. Faraday Soc.* **51**, 1593 (1955).
   BEECK O., SMITH A. E. and WHEELER A., *Proc. Roy. Soc.* **A177**, 62 (1940).
7. *Air Force Cambridge Research Center, Sci. Rep.* No. 2, p. 5 (March 1957), AFCRC-TN-58-135 ASTIA Document No. AD 146897; also unreported data on germanium.
8. *Air Force Cambridge Research Centre, Sci. Rep.* No. 3, p. 6 (June 1957); *Bull. Amer. Phys. Soc.* **3**, 31 (1958); *J. Appl. Phys.* **28**, 179 (1957).
9. LAW J. T., *J. Chem. Phys.* **28**, 511 (1958).

J. Phys. Chem. Solids Pergamon Press 1958. Vol. 9. pp. 60–69. Printed in Great Britain.

ON THE TEMPERATURE-DEPENDENCE OF THE DISTRIBUTION COEFFICIENT

THE SOLID SOLUBILITIES OF TIN IN SILICON AND GERMANIUM*

F. A. TRUMBORE, C. R. ISENBERG and E. M. PORBANSKY

Bell Telephone Laboratories, Inc., Murray Hill, N.J.

(*Received* 4 *June* 1958)

VOL
9
195

Abstract—The solid solubility of tin in silicon has been determined in the range from 800°C to the melting point of silicon, using crystal-pulling and thermal-gradient crystallization techniques. The distribution coefficient, k, of tin in silicon falls from 0·016 at the melting point of silicon to about $6{\cdot}5 \times 10^{-4}$ at 800°C. Earlier work on the tin–germanium system has also been extended. The form of the temperature-dependence of k is similar for both systems and does not fit into the correlation recently proposed by HALL (*J. Phys. Chem. Solids* **3**, 63 (1957)). For these two systems the observed temperature-dependence of k can be explained as being due in a large measure to departures from ideality in the liquid state. Binding energies of tin in germanium and silicon calculated from the solid-solubility data compare favorably with binding energies calculated using ALLEN's reciprocal mean postulate for covalent bond energies (*J. Chem. Phys.* **27**, 810 (1957)).

1. INTRODUCTION

IN a recent paper HALL[1] suggested that the distribution coefficient, k, of a solute having a low solid solubility should vary with temperature according to an equation of the type $\log k = B - A/T$. More recently ORIANI and HALL[2] have pointed out that HALL's original statistical treatment was an oversimplification,† and a more involved treatment, based on an equation due to THURMOND and STRUTHERS,[3] was presented. The fact remains, however, that HALL did find a striking correlation for a number of elements in germanium and silicon. Specifically, plots of $\log k$ versus $1/T$ gave a family of straight lines intersecting at common points for germanium and silicon. This correlation proved quite valuable in predicting that the previously published data on the solubility of lithium in silicon were considerably in error.

However, the published solid-solubility data for a number of systems are totally inconsistent with the above correlation. For example, one of the authors[4,5] found from thermal-gradient crystallization experiments that, for the tin–germanium system, k is relatively temperature-independent at low temperatures. However, a relatively rapid change in k near the melting point of germanium was indicated. THURMOND *et al.*[5] obtained similar results for the aluminum–, gallium–, and indium–germanium systems from analyses of crystals recovered from slowly cooled melts and for the antimony–germanium system from diffusion measurements. In view of the apparent inconsistencies, HALL questioned the validity of the thermal-gradient and slow-cooling measurements and suggested that the presence of occluded solute in the crystals leads to high values of k. In support of this view experimental evidence was presented which

* Presented in part at the Electrochemical Society Meeting, New York, N.Y., 28 April, 1958.

† Hall's original treatment was in error in that it purported to show that a linear dependence of $\log k$ on $1/T$ was consistent with a linear variation of the heat of solution with temperature. Specifically, his equation (2) with C independent of temperature holds only if ΔH is also temperature-independent, as can be shown by integrating a form of the Gibbs–Helmholtz equation.

indicated that the slow-cooling data for the indium–germanium system were in error by an order of magnitude or more.*

In the present paper, further work on the tin–germanium system is reported in support of the previous data. In addition, the results of crystal-pulling and thermal-gradient experiments on the tin–silicon system are presented. Because of the electrical neutrality of tin in germanium and silicon, the interpretation of the solid-solubility behavior in these systems should be simpler than for electrically active impurities where electron-hole interactions may be present, as discussed by REISS.[7] Considerable attention will be paid to the effects of non-ideality in the liquid alloys, whereas in the work of HALL[1] and ORIANI and HALL[2] it was essentially assumed that these effects were negligible.

VOL. 9 1959

2. EXPERIMENTAL

(a) *Crystal-pulling experiments*

Conventional crystal-pulling techniques were used to grow germanium and silicon crystals from melts containing up to 10 and 35 atomic per cent tin, respectively. The tin used in these experiments was zone-refined material, stated to be of $> 99{\cdot}999$ per cent purity, obtained from the Vulcan Detinning Co., while the germanium and silicon were very high-purity materials used in growing high-resistivity single crystals. A variety of pull rates, rotation rates, seed orientations, and other growth parameters were used in order to detect any effect of these parameters on the observed distribution coefficients. One factor which appeared to affect the apparent solid solubility to a significant extent was the presence of a non-uniform crystal diameter. In order to promote uniform growth, seed crystals of the same diameter as the resulting grown crystals were used. In the present work considerably greater care was taken than in the previous work[4] in the growth of the crystals and in the selection of the samples for chemical analysis.

Because of the volatility of tin near the melting point of silicon, the tin–silicon melts remaining in the crucibles were analyzed chemically for tin at the end of the experiments. In most cases the amount of tin lost was only about 1 or 2 per cent of the original amount added to the melt. There was also a very small loss of silicon via the volatile SiO species, which was on the order of 1 per cent or less.

One set of crystal-pulling experiments deserves special mention. Attempts were made to pull silicon single crystals from melts containing 25 and 35 atomic per cent tin. These experiments were prompted by the work of JOHN,[8] who pulled single crystals of germanium from very heavily doped melts several hundred degrees below the melting point of germanium. In the present experiments, a pull rate of only 0·1 cm/hr was used in conjunction with a rotation rate of 60 rev/min. The crystal pulled from the 35 per cent tin melt was polycrystalline though with relatively large grains. In the case of the 25 per cent tin melt, etching and X-ray tests showed the sample to be a single crystal, although an infrared photo-image tube in conjunction with polarized light revealed the presence of strain patterns suggesting the presence of occluded tin. The imperfect nature of this crystal was not surprising, however, in view of the fact that it was a crystal of sharply increasing diameter. Prior to chemical analysis, both of these crystals were crushed and digested in HCl in an attempt to remove any occluded tin. The chemical analyses were very helpful in providing upper limits on the solid solubility in an intermediate temperature range.

(b) *Thermal-gradient experiments*

Two additional thermal-gradient experiments were performed on the tin–germanium system. In addition, one sample from a previous thermal-gradient experiment[4] was reanalyzed by the spectrophotometric technique for comparison with the previous spectroscopic analyses. The thermal-gradient experiments were performed using essentially the same technique as that described previously for the tin–germanium system.[4] A modified design of the tube used in growing the crystals is shown in Fig. 1. In this arrangement silicon or germanium dissolves in the upper, hotter portion of the melt, diffuses down through the melt, and precipitates, it is hoped, in the lower capillary portion of the tube. The object of the capillary section is to permit a single grain to predominate, thus yielding a single crystal as growth continues as in various modifications of the Bridgman technique. This design has been moderately successful in yielding single or near-single crystals of relatively large size, as indicated in Fig. 1.

Four thermal-gradient experiments were run on the tin–silicon system. Lattice constants were determined on one set of these crystals, using X-ray diffraction techniques.

(c) *Chemical analyses*

In the previous work on the tin–germanium system,[4] a spectroscopic technique was used for the determination of the tin concentrations. This technique was later found to give somewhat erratic results. The present samples of both silicon and germanium were analyzed for tin, using spectrophotometric techniques which are more reliable

* TRUMBORE and PORBANSKY[6] have performed crystal-pulling and thermal-gradient experiments on the aluminum– and gallium–germanium systems which indicate that the slow-cooling results are also significantly in error for these systems. However, the log k versus $1/T$ plots in both cases retain the same general characteristics and the departures from HALL's correlation are even greater. It should be pointed out that aluminum and gallium have relatively large distribution coefficients and perhaps should not be considered as slightly soluble impurities from HALL's viewpoint.

and reproducible than the spectroscopic method. The techniques used were modifications of the method discussed by LUKE.[9] The accuracy of these analyses is believed to be better than ±10 per cent of the tin concentration.

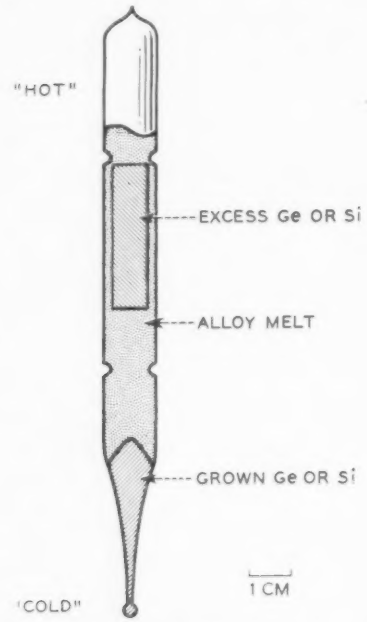

FIG. 1. Sketch of tube used for thermal-gradient crystal growth.

(d) *Electrical measurements*

Resistivity and lifetime measurements on some of the tin–silicon crystals were made, using conventional four-point-probe and photoconductivity-decay techniques, respectively.

3. RESULTS

(a) *Effect of various growth parameters on k*

In Fig. 2 are plotted the results of chemical analyses of sections of ten germanium–tin and four silicon–tin crystals all grown from melts containing initially 0·5 atomic per cent tin, but at different pull rates. Except for the silicon crystals pulled from 25 and 35 per cent tin melts, these were the only crystals pulled at a rate other than 0·5 cm/hr. From the results on the tin–germanium crystals, grown under two sets of rotation and orientation conditions, it is apparent that the pull rate of 0·5 cm/hr is sufficiently low to yield equilibrium values of k within the limits of experimental error. A similar conclusion is evident for the tin–silicon case, although the data are much less extensive.

The results for the tin–germanium system are in agreement with the theory of BURTON *et al.*[10] on

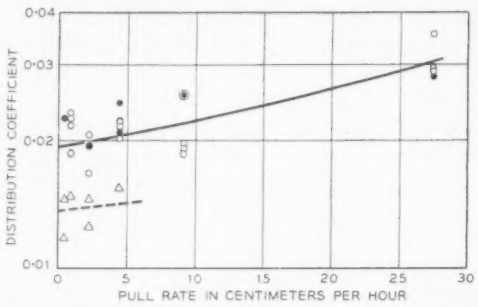

FIG. 2. Effect of pull rate on the observed distribution coefficients of tin in germanium and silicon. The melts all contained initially 0·5 atomic per cent tin. ○ = [211] direction, 288 rev/min; ● = [100] direction, 60 rev/min; △ = [100], 60 rev/min. The symbols ○ and ● represent tin in germanium; △ tin in silicon.

the effect of growth rate on k. BRIDGERS and KOLB[11] have shown that linearity of a plot of $\log(1/k-1)$ versus growth rate is a good test of the

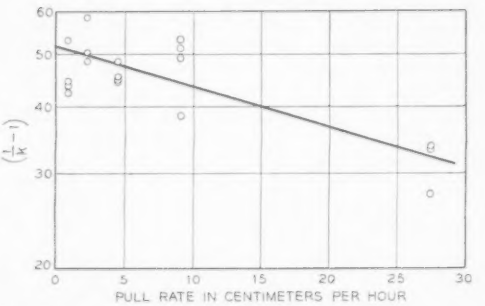

FIG. 3. Plot of $\log[(1/k)-1]$ versus pull rate for one set of tin–germanium crystals grown in the [211] direction at 288 rev/min.

validity of this theory. Such a plot is shown in Fig. 3 for one set of crystals.* The equilibrium distribution coefficient obtained by extrapolating

* Strictly speaking, the true growth rate instead of the pull rate should be used. However, in most cases the pull and growth rates differed by less than 5–10 per cent, and in view of the precision of the analytical data the tedious corrections were not deemed necessary.

to zero pull rate, using a least-squares fit, is $0{\cdot}0194 \pm 0{\cdot}0006$ at an average melt concentration of 0·55 atomic per cent tin. The probable error is quoted.

Concerning the effect of rotation rate on k, experiments were performed on both the tin–silicon and tin–germanium systems in which the rotation rate was varied from 60 to 144 rev/min, all other growth parameters being similar. Within experimental error, no effect on k was observed at the 0·5 cm/hr pull rate. A number of different growth directions were used, but no significant effect on k could be detected. This result is in agreement with the work of BURTON *et al.*[10] who found differences of less than 10 per cent for different crystal orientations.

(b) *Effect of melt concentration in crystal-pulling experiments*

The results of the crystal-pulling experiments in which the melt concentrations were varied are summarized in Table 1, where x_L is the atomic fraction of tin in the melt.

The distribution coefficient, k, is defined here as $k = x_S/x_L$, where x_S is the atomic fraction of tin in the crystal. The figures for the two silicon crystals corresponding to 25 and 35 atomic per cent tin in the melt are to be considered as representing maximum values of k in view of the rather drastic growth conditions discussed earlier.

Table 1. Effect of melt concentration on the distribution coefficient in crystal-pulling experiments

x_L	k	x_L	k
	*Tin in Silicon**		
$0{\cdot}0058_3$	$0{\cdot}011_8$	$0{\cdot}036_4$	$0{\cdot}009_8$
$0{\cdot}0073_5$	$0{\cdot}014_5$	$0{\cdot}041_5$	$0{\cdot}008_6$
$0{\cdot}0099_1$	$0{\cdot}013_4$	$0{\cdot}042_1$	$0{\cdot}010_1$
$0{\cdot}0104_8$	$0{\cdot}015_3$	$0{\cdot}042_5$	$0{\cdot}008_9$
$0{\cdot}0104_9$	$0{\cdot}016_2$	$0{\cdot}25_1$	$< 0{\cdot}003_9$†‡
$0{\cdot}021_2$	$0{\cdot}012_3$	$0{\cdot}34_9$	$< 0{\cdot}002_9$†‡§
	*Tin in Germanium**		
$0{\cdot}005_5$	$0{\cdot}019_4$‖	$0{\cdot}0638$	$0{\cdot}017_3$
$0{\cdot}0158$	$0{\cdot}019_9$	$0{\cdot}0691$	$0{\cdot}017_7$
$0{\cdot}0184$	$0{\cdot}019_3$	$0{\cdot}1091$	$0{\cdot}018_5$
$0{\cdot}0198$	$0{\cdot}018_8$	$0{\cdot}1128$	$0{\cdot}018_5$

* Unless noted otherwise, the silicon crystals were pulled at 0·5 cm/hr at 60 rev/min in the [100] direction, while the germanium crystals were pulled at 0·5 cm/hr at 144 rev/min in the [111] direction.

† Pulled at 0·1 cm/hr.

‡ Probably contained occlusions.

§ Polycrystalline.

‖ From results of pull-rate experiments shown in Figs. and 3.

(c) *Thermal-gradient results*

The results of the chemical analyses of the thermal-gradient crystals are summarized in Table 2. The temperatures are believed to be accurate to about $\pm 10°C$.

Table 2. Thermal-gradient results

System	Temp(°C)	x_S	k
Si–Sn	810	$7{\cdot}4 \times 10^{-4}$	$7{\cdot}5 \times 10^{-4}$
Si–Sn	878	$7{\cdot}1 \times 10^{-4}$	$7{\cdot}2 \times 10^{-4}$
Si–Sn	878	$6{\cdot}3 \times 10^{-4}$	$6{\cdot}3 \times 10^{-4}$
Si–Sn	998	$1{\cdot}0_2 \times 10^{-3}$	$1{\cdot}0_5 \times 10^{-3}$
Si–Sn	1066	$1{\cdot}0_2 \times 10^{-3}$	$1{\cdot}0_8 \times 10^{-3}$
Si–Sn	1066	$8{\cdot}5 \times 10^{-4}$	$9{\cdot}0 \times 10^{-4}$
Ge–Sn	619	$8{\cdot}6 \times 10^{-3}$*	$1{\cdot}1_3 \times 10^{-2}$
Ge–Sn	706	$6{\cdot}6 \times 10^{-3}$	$1{\cdot}1_0 \times 10^{-2}$
Ge–Sn	709	$8{\cdot}3 \times 10^{-3}$	$1{\cdot}4_0 \times 10^{-2}$
Ge–Sn	799	$5{\cdot}7 \times 10^{-3}$	$1{\cdot}5_3 \times 10^{-2}$

* This result compares well with the previous value of $8{\cdot}8 \times 10^{-3}$ obtained spectroscopically as reported in reference (4).

For the tin–silicon crystals grown at 810°C, the X-ray measurements revealed an expansion of the silicon lattice by the tin of $0{\cdot}00080 \pm 0{\cdot}00036$ Å. Assuming Vegard's law, the expansion predicted from the lattice constants of silicon and grey tin and from the chemical analyses is about 0·00075 Å. The agreement with the observed value is good evidence against the presence of occluded tin. Similar evidence was obtained for the tin–germanium system.[4]

(d) *Temperature-dependence of k*

In Figs. 4 and 5 plots of log k versus the reciprocal of the absolute temperature are given for the tin–silicon and tin–germanium crystal-pulling results, respectively. The tin–silicon points were obtained from the data of Table 1, assuming ideal liquid solutions, a melting point for silicon of 1412°C,[12] and a heat of fusion for silicon of 12·1

kcal/g-atom[12] corresponding to a freezing-point lowering constant of 4·7°C per atomic per cent impurity in the melt. For the crystals pulled from the 25 and 35 per cent tin melts, the temperature was

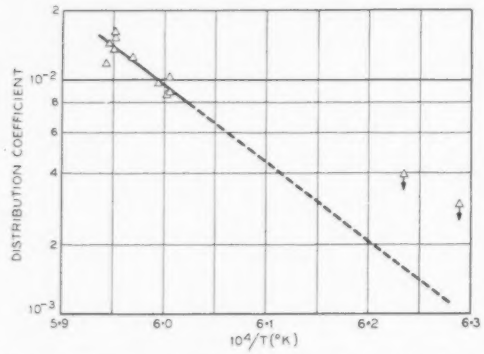

FIG. 4. Temperature-dependence of the distribution coefficient of tin in silicon from crystal-pulling experiments. The straight line corresponds to least-squares fit of data excluding maximum points.

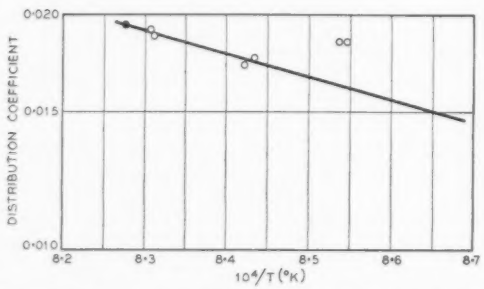

FIG. 5. Temperature-dependence of the distribution coefficient of tin in germanium from crystal-pulling experiments. The solid point ● was obtained from the pull-rate data of Fig. 3 extrapolated to zero pull-rate and was weighted more heavily in the least-squares fit of the data. The two points corresponding to crystals pulled from melts containing about 10 atomic per cent tin were not included in the least-squares fit because of the possibility of occluded material or non-equilibrium conditions during growth from these heavily doped melts.

determined from the liquidus curve of THURMOND *et al.*[13] The tin–germanium points were based on similar calculations, assuming a melting point of 937°C[14] and a heat of fusion of 8·1 kcal/g-atom[15] corresponding to a freezing-point lowering constant of 3·6°C per atomic per cent impurity in the melt. Extrapolations of these data, assuming linear behavior and using the method of least squares, yield values of k^0, the distribution coefficient at the melting points of germanium and silicon, of $0{\cdot}019_6 \pm 0{\cdot}003_0$ and $0{\cdot}015_7 \pm 0{\cdot}002_2$, respectively, in good agreement with earlier work.[4,16] The estimated errors quoted here are about 3–4 times larger than the least-squares probable errors.

The results of both crystal-pulling and thermal-gradient experiments are summarized in Figs. 6 and 7, which are smaller-scale plots of log k versus $1/T$. In these plots the crystal-pulling points have been omitted, but the curves near the melting points of silicon and germanium correspond to those in Figs. 4 and 5, respectively. The dotted lines correspond to the behavior predicted from HALL's correlation,[1] using his points of intersection and the values of k^0 at the silicon and germanium melting points from the present study.

(e) *Electrical properties*

Room-temperature resistivities of a number of pulled tin–silicon crystals ranged from 25 to 140 Ω-cm, p-type, with p–n junctions occurring frequently. Lifetimes were on the order of 5–10 μsec. Since the tin concentrations in these crystals were on the order of 10^{19} atoms/cc, it is reasonably certain that tin has neither donor nor acceptor properties in silicon and furthermore that it is not an effective recombination center for holes and electrons. This electrical neutrality is consistent with the similar behavior of tin in germanium.[4]

4. DISCUSSION

(a) *Temperature-dependence of k*

From Figs. 6 and 7 it is seen that not only are the forms of the log k versus $1/T$ plots non-linear, but also the tin–silicon data lie *below* the straight line expected from HALL's correlation over a wide temperature range. This is, of course, the opposite effect to that to be expected if occlusions played an important role in these experiments.

In the following discussion it will be shown that the form of the temperature-dependence of k for the tin–germanium and tin–silicon systems is quite reasonable and can be accounted for in a large measure by considering the effect of departures from ideality in the liquid state. The influence of interactions in the liquid state on k is illustrated in the following treatment, which is essentially that

of THURMOND and STRUTHERS[3] from a slightly different viewpoint. In the present treatment a parameter is introduced which is very convenient for the discussion and comparison of solid solubilities in general.

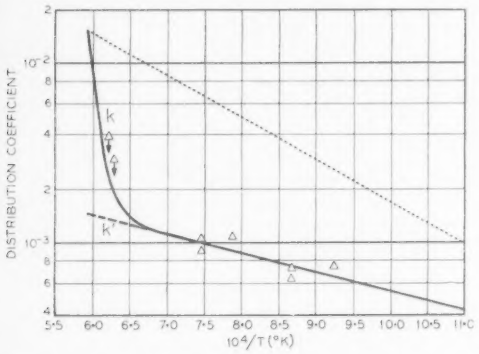

FIG. 6. Variation of the distribution coefficient of tin in silicon with temperature. The curve near the melting point of silicon corresponds to the line in Fig. 4. Plotted points are thermal-gradient results except for the two maximum values. The dashed line is an extrapolation of least-squares fit to thermal-gradient data. The dotted line represents behavior predicted from HALL's correlation.

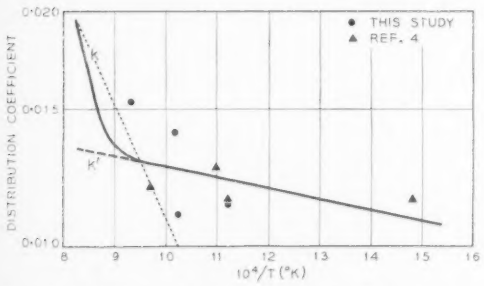

FIG. 7. Variation of the distribution coefficient of tin in germanium with temperature. The curve near the melting point of germanium corresponds to the line in Fig. 5. Plotted points are thermal-gradient results. The dashed line is an extrapolation of least-squares fit to thermal-gradient data. The dotted line represents behavior predicted from HALL's correlation.

If we arbitrarily take as our standard state for both solid and liquid solutions the pure liquid solute element (tin in the present case), it follows that

$$a_S = a_L \tag{1}$$

where a_S and a_L are the activities of the impurity element in the solidus and liquidus alloys respectively. We may introduce activity coefficients as follows

$$a_S = \gamma_S x_S = \gamma_L x_L = a_L, \tag{2}$$

where γ_S and γ_L are the activity coefficients and x_S and x_L are the atomic fractions of the impurity element in the solidus and liquidus solutions. From the definition of the distribution coefficient it follows that

$$k = \frac{x_S}{x_L} = \frac{\gamma_L}{\gamma_S}. \tag{3}$$

Thus, the distribution coefficient is essentially the ratio of a measure of the departure from ideality of the liquidus alloy to a measure of the departure from ideality of the solidus alloy.* In view of the fact that k involves both solid and liquid interactions, it is not a good measure of solid solubility in the strictest sense. By the same token the frequent use of maximum solid solubilities in comparing solubilities of various solutes in a given solvent is to be regarded as only very qualitative, since the solid phases interact with other liquid or solid phases.

An obvious way of separating out the effect of interactions in the liquid alloys on solid solubility is to divide equation (3) by γ_L to give a new parameter k' defined by

$$k' = k/\gamma_L = x_S/a_L = 1/\gamma_S. \tag{4}$$

Here, k' is essentially a solid solubility per unit activity of the impurity element in the melt and is simply the reciprocal of γ_S, a measure of the departure from ideality in the solidus solution. It should be noted that equations (1)–(4) remain unchanged for standard states other than the pure liquid solute element as long as the standard state is taken to be the same for both solidus and liquidus alloys. Perhaps the most fundamental form of k' would be based on the element in the form of the monatomic gas at a given pressure. In such a case

* A more appropriate standard state for expressing departures from ideality of the solidus alloy would be the pure solid solute. The parameter γ_S, based on a standard state of pure liquid solute, is related to γ_S', based on pure solid solute, by the relation $RT \ln(\gamma_S/\gamma_S') = T\Delta S_f - \Delta H_f$, where ΔH_f and ΔS_f are the heat and entropy of fusion of the pure solute at the temperature T.

k' would depend only on the properties of the solid solution and of the free impurity atom and not on the pure solid or liquid phases of this element. However, for the purposes of this paper it is more convenient to retain the pure liquid solute as the standard state, and the equations following are based on this choice.

It can be shown[22] that

$$\left(\frac{\partial \ln \gamma_S}{\partial 1/T}\right)_{x_S} = \frac{\overline{\Delta H}}{R} \tag{5}$$

where R is the gas constant and $\overline{\Delta H}$ is the differential heat of solution corresponding to the transfer of 1 g-atom of solute element from the pure liquid state to an infinite amount of the solid solution. This equation, which is valid at constant composition, is also true at varying compositions if γ_S is independent of composition at a given temperature, i.e. if Henry's law is obeyed. Since tin is electrically neutral in germanium and silicon, thus barring any significant mass-action effects,[7] and the solid solutions are reasonably dilute ($x_S \lesssim 0{\cdot}01$ or $0{\cdot}001$ for tin in germanium or silicon) Henry's law should hold rather well. Thus, from equations (4) and (5)

$$\frac{\partial \ln k'}{\partial 1/T} \approx -\frac{\overline{\Delta H}}{R}. \tag{6}$$

At relatively low temperatures the liquidus alloys are rich with respect to tin and Raoult's law is a good approximation. Hence, at low temperatures $\gamma_L \approx 1$ and, from equation (4), $k' \approx k$, so that equation (6) becomes

$$\frac{\partial \ln k}{\partial 1/T} \approx -\frac{\overline{\Delta H}}{R}. \tag{7}$$

If $\overline{\Delta H}$ is assumed to be independent of temperature, it follows that at low temperatures a log k versus $1/T$ plot should be linear. The low-temperature data for both tin–germanium and tin–silicon systems were fitted to least-squares straight lines, as shown in Figs. 6 and 7. The values of $\overline{\Delta H}$ corresponding to these lines are $0{\cdot}6 \pm 0{\cdot}3$ and $4{\cdot}7 \pm \pm 1{\cdot}2$ kcal/g-atom for the tin–germanium and tin–silicon systems, respectively. Probable errors are quoted. The values of k' at higher temperatures can be estimated by extrapolation of the low-temperature k data, as shown by the dashed lines in Figs. 6 and 7.

We have seen that k rises relatively sharply near the melting points of germanium and silicon, with the variation in the case of silicon being about an order of magnitude larger than that for germanium. This type of behavior can be explained in terms of the values of k and k' at the melting points of germanium and silicon and the departures from ideality in the liquid alloys. It follows from equation (4) that $\gamma_L{}^0 = k^0/k'^0$, where the superscripts indicate the values of the parameters at the melting point of germanium or silicon. Since $k^0 > k'^0$, it follows that $\gamma_L{}^0$ is greater than unity for both systems. That is, positive departures from ideality are indicated in the liquidus alloys at higher temperatures. Unfortunately, there are no experimental measurements of γ_L for either of the systems. However, an estimate of γ_L can be obtained from the liquidus-curve studies of THURMOND *et al.*,[13,24] who found that germanium and silicon follow a relatively simple type of solution behavior along the liquidus curves for a large number of systems. Specifically, departures from the regular solution behavior postulated earlier[24] have been noted, and the parameter b now appears to be a linear function of temperature. The more recent studies[13] indicate values of $b = 1680 - -1{\cdot}08T$ and $b = 9030 - 2{\cdot}24T$ cal for tin in germanium and silicon respectively. By assuming that this simple behavior extends into the homogeneous liquid solution range, the Gibbs–Duhem equation can be used to obtain estimates of γ_L for the second component. In Table 3 the values of $\gamma_L{}^0$ obtained from the liquidus curves are compared with the values of $\gamma_L{}^0$ calculated from the distribution-coefficient data. The estimate of the uncertainty in $\gamma_L{}^0$ (dist. coeff.) is very rough in view of the precision and number of the data points. Unfortunately, no estimate of the uncertainty in the values of $\gamma_L{}^0$ (from the liquidus) can be given.

Table 3. Predicted values of γ_L from distribution-coefficient and liquidus data

System	$\gamma_L{}^0$ (dist. coeff.)	$\gamma_L{}^0$ (liquidus)
Sn–Si	11 ± 2	5
Sn–Ge	$1{\cdot}5 \pm 0{\cdot}2$	1·2

VOL 9 195

Qualitatively, however, the general behavior is as expected. First, both systems show positive departures from ideality and, secondly, the magnitude of γ_L is appreciably greater in silicon than in germanium.

(b) *Binding energy of tin in germanium and silicon*

The binding energies of tin in germanium and silicon can be estimated from the preceding equations as follows. The quantity $\overline{\Delta H}$ can be written as the sum of the heats associated with the reactions:

$$M(\text{liq.}) = M(\text{g}) \qquad \Delta H_v \qquad (8)$$

$$M(\text{g}) \quad = M(\text{in sol. soln.}) \quad -\text{B.E.} \qquad (9)$$

$$M(\text{liq.}) = M(\text{in sol. soln.}) \quad \overline{\Delta H} = \Delta H_v - \text{B.E.} \qquad (10)$$

where ΔH_v is the heat of vaporization of pure liquid tin to the monomeric vapor species and B.E. is the term commonly known as the binding energy of tin in the solid germanium or silicon solution. Thus, from the heat of vaporization of tin, the binding energy of tin in germanium and silicon can be calculated. Using a value of ΔH_v of 70 kcal/g-atom[17] and values of 0·6 and 4·7 kcal/g-atom for $\overline{\Delta H}$, the binding energies of tin in germanium and silicon are about 69 and 65 kcal/g-atom, respectively.

(c) *Calculation of binding energy from bond energies*

An independent estimate of the binding energy is possible from a consideration of bond energies. If the solid solutions are dilute enough, the sublimation process may be assumed to involve simply the breaking of 4 Sn–Si or Sn–Ge bonds, followed by the formation of 2 Si–Si or Ge–Ge bonds. From this common argument it follows that, using Sn–Ge as an example,

$$\text{B.E.} = 4D_{\text{Sn–Ge}} - 2D_{\text{Ge–Ge}}, \qquad (12)$$

where $D_{\text{Sn-Ge}}$ and $D_{\text{Ge-Ge}}$ are the appropriate bond energies.* The value of $D_{\text{Ge-Ge}}$ is simply one-half the heat of sublimation of germanium.

A number of proposals have been made for the calculation of covalent bond energies. Recently, ALLEN[18] suggested a reciprocal mean as having a firmer basis in chemical theory than the additivity or geometric-mean postulates of PAULING.[19] We have calculated bond energies involving the Group IV elements carbon, silicon, germanium and tin from the reciprocal-mean postulate and the recent electronegativities proposed by ALLRED and ROCHOW.[20] For bonds in compounds such as CH_4, $GeBr_4$, $SnCl_4$ &c., the agreement between calculated and experimental bond energies is usually very good. Therefore, the value of $D_{\text{Sn–Ge}}$ was calculated from the heat of sublimation of gray tin, using the reciprocal-mean expression and the electronegativity correction, i.e.

$$D_{\text{Sn–Ge}} = \frac{2D_{\text{Sn–Sn}}D_{\text{Ge–Ge}}}{D_{\text{Sn–Sn}} + D_{\text{Ge–Ge}}} + 23{\cdot}060(\Delta X)^2(\text{kcal}), \qquad (13)$$

where ΔX is the difference in electronegativity between tin and germanium. The heats of sublimation of gray tin and germanium to the monatomic vapor species were obtained from the compilation of HONIG.[21] Using the value of $D_{\text{Sn–Ge}}$ from equation (13), the binding energy of tin in germanium was calculated from equation (12) to be 71 kcal, in good agreement with the value of 69 kcal obtained from the distribution-coefficient data in Fig. 7. A similar calculation for the tin–silicon system gives a value of the binding energy of 64 kcal,† in good agreement with the value of 65 kcal obtained from the distribution-coefficient data of Fig. 6.

(d) *Entropy of solution of tin in germanium and silicon*

The distribution coefficient can be related to the entropy of solution of the solute element through the equation

$$\ln k' = -\frac{\overline{\Delta H}}{RT} + \frac{\overline{\Delta S^x}}{R}, \qquad (14)$$

which is a modified form of a relation derived by

* WEISER[25] has recently made theoretical calculations involving solid solubilities of impurity elements in germanium and silicon. He considered the strain energies as contributing significantly to the heat of solution in the solid. In the present paper no direct attempt is made to calculate strain energies. However, the agreement between the calculated and "experimental" binding energies is good, indicating that the strain energies calculated by WEISER may be too large.

† The value for the heat of sublimation of silicon is at present very uncertain.[21] In these calculations a value of 113 kcal/g-atom was used. Actually, this value may still be too low as pointed out by A. SEARCY (private communication).

THURMOND and STRUTHERS.[3] Here $\overline{\Delta S^x}$ is the differential excess entropy of solution, i.e. the entropy change corresponding to equation (10) less the ideal entropy of mixing term. Thus,

$$\overline{\Delta S^x} = \bar{S} - S^0, \tag{15}$$

where $\bar{S}$ is the partial molar entropy of tin in the solid solution and S^0 is the absolute entropy of pure liquid tin. Since $k' \approx k$ at low temperatures, the low-temperature distribution-coefficient data can be used to estimate $\overline{\Delta H}$ and k', as discussed above, and $\overline{\Delta S^x}$ can be calculated from equation (14). It is of interest to compare the values at a given temperature for germanium and silicon. At 1100°K the values of $\overline{\Delta S^x}$ are $-8{\cdot}_1$ and $-10{\cdot}_2$ eu/g-atom for tin in germanium and silicon, respectively. Using the value for S^0 at 1100°K,[17] the values of $\bar{S}$ can be obtained from equation (15). These are summarized in Table 4, together with the values of k', $\overline{\Delta S^x}$, $S_{Ge}{}^0$ and $S_{Si}{}^0$. It is seen that the values of $\bar{S}$ are approximately the same as the values of $S_{Ge}{}^0$ or $S_{Si}{}^0$, the absolute entropies of germanium or silicon at 1100°K. That is, the effect of adding an atom of tin to the solid solution is very similar to adding an atom of germanium or silicon. In view of the similarities between tin, germanium, and silicon, the fact that the $\bar{S}_{Sn}$ values are of the same order as the values of $S_{Ge}{}^0$ or $S_{Si}{}^0$ lends confidence to the validity of the distribution-coefficient data.

Table 4. *Thermodynamic properties at* 1100°K

Element	k'	$\overline{\Delta S^x}$(eu/g-atom)	$\bar{S}$(eu/g-atom)	$S^0{}_{\text{Ge or Si}}$ (eu/g-atom)
Ge	0·013	$-8{\cdot}_1$	$16{\cdot}_9$	15·6
Si	$6{\cdot}_9\times10^{-4}$	$-10{\cdot}_2$	$14{\cdot}_8$	12·0

The entropy change is due to at least two factors. The silicon or germanium lattice is expanded by the introduction of the tin atom which crowds the silicon or germanium atoms together in its immediate vicinity. This effect would lead to reduced entropy due to decrease of vibrational freedom. If the introduction of the tin atoms were accompanied by an appreciable number of vacancies, this effect would be diminished. A second effect is the loosening of the lattice through the introduction of Sn–Ge and Sn–Si bonds. That is, the bond energies of the Sn–Ge and Sn–Si bonds are not as large as the Ge–Ge and Si–Si bond energies. With "looser" bonds, the silicon or germanium atoms would be less tightly bound, resulting in lower vibrational frequencies and higher entropies. If the reciprocal-mean postulate is applied, the percentage decrease in bond energy is greater for silicon than for germanium, which might account for the slightly larger difference, $2{\cdot}_8$ eu, between $\bar{S}$ and $S_{Si}{}^0$ compared to the $1{\cdot}_3$ eu difference between $\bar{S}$ and $S_{Ge}{}^0$. Whether or not these slight differences are real can only be determined by more precise experimental data.

5. CONCLUDING REMARKS

The linear plots of log k versus $1/T$ observed by HALL may perhaps be explained on the basis that the liquidus ranges in some, though not all, of the systems are limited and the value of γ_L may not change appreciably. Where a long liquidus range occurs, a straight line could result if the liquidus alloys were nearly ideal ($\gamma_L \approx 1$). The most striking feature of HALL's correlation is the common point of intersection of the log k versus $1/T$ plots. Such behavior indicates the possibility of a linear relationship between the heats and excess entropies of solution.[23,2] The heats and entropies of solution obtained from a log k versus $1/T$ plot correspond, under certain assumptions, to the transfer of the impurity element from the liquidus to the solidus alloy. Only if the liquidus solutions are ideal are these quantities equal to the heats and entropies of solution considered in this paper. It would be of considerable interest to determine experimentally values of the activities of impurity elements along liquidus curves, so that one might deal with k' rather than k. An interesting possibility is that by eliminating the effect of liquid interactions one might find that log k' versus $1/T$ plots were linear with a common point of intersection, which would imply a simple relation between heats and entropies of solution in these dilute solid solutions. In the case of the liquidus alloys of germanium and silicon a monotonic relation has been observed between the heats and entropies of solution of germanium and silicon.[13]

VOL 9 195

Acknowledgements—The authors are especially indebted to Miss M. E. CAMPBELL and C. L. LUKE for the spectrophotometric analyses. Thanks are also due Mrs. M. H. READ for the lattice-parameter determination, to W. L. BOND for the infrared observations, and to M. KOWALCHIK, D. WINTERS, Miss A. MILLS and A. A. TARTAGLIA for technical assistance at various stages of this work. Numerous stimulating and helpful discussions with C. D. THURMOND have contributed significantly to this work. The comments of M. TANENBAUM are also appreciated.

REFERENCES

1. HALL R. N., *J. Phys. Chem. Solids* **3,** 63 (1957).
2. ORIANI R. A. and HALL R. N., *J. Phys. Chem. Solids* **6,** 97 (1958).
3. THURMOND C. D. and STRUTHERS J. D., *J. Phys. Chem.* **57,** 831 (1953).
4. TRUMBORE F. A., *J. Electrochem. Soc.* **103,** 597 (1956).
5. THURMOND C. D., TRUMBORE F. A. and KOWALCHIK M. *J. Chem. Phys.* **25,** 799 (1956).
6. TRUMBORE F. A. and PORBANSKY E. M., Electrochemical Soc. Meeting, New York, N.Y., 28 Apr., 1958 (to be published).
7. REISS H., *J. Chem. Phys.* **21,** 1209 (1953).
8. JOHN H. F., Electrochemical Soc. Meeting, Cleveland, Ohio, Oct., 1956.
9. LUKE C. L., *Analyt. Chem.* **28,** 1276 (1956).
10. BURTON J. A., PRIM R. C. and SLICHTER W. P., *J. Chem. Phys.* **21,** 1987 (1953).
    BURTON J. A., KOLB E. D., SLICHTER W. P. and STRUTHERS J. D., *J. Chem. Phys.* **21,** 1991 (1953).
11. BRIDGERS H. and KOLB E., *J. Chem. Phys.* **25,** 648 (1956).
12. OLETTE M., *C.R. Acad. Sci., Paris* **244,** 1033 (1957).
13. THURMOND C. D., HASSION F. X. and KOWALCHIK M., *J. Phys. Chem.* (to be published).
14. GREINER E. S. and BREIDT P., Jr., *J. Metals, N.Y.* **7,** 187 (1955).
    HASSION F. X., THURMOND C. D. and TRUMBORE F. A., *J. Phys. Chem.* **59,** 1076 (1955).
15. GREINER E. S., *J. Metals, N.Y.* **4,** 1044 (1952).
16. BURTON J. A., *Physica* **20,** 845 (1954).
17. STULL D. R. and SINKE G. C., *Thermodynamic Properties of the Elements.* American Chemical Society (1956).
18. ALLEN T. L., *J. Chem. Phys.* **27,** 810 (1957).
19. PAULING L., *The Nature of the Chemical Bond* Chap. 2. Cornell University Press (1945).
20. ALLRED A. L. and ROCHOW E. G., American Chemical Society Meeting, New York, N.Y., Sept. 1957.
21. HONIG R. E., *RCA Rev.* **18,** 195 (1957).
22. See, for example, PRIGOGINE I. and DEFAY R., *Chemical Thermodynamics* Chap. 24. Longmans Green and Co., New York (1954).
23. THURMOND C. D. Private communication.
24. THURMOND C. D., *J. Phys. Chem.* **57,** 827 (1953).
25. WEISER K., *J. Phys. Chem. Solids* **7,** 118 (1958).

J. Phys. Chem. Solids Pergamon Press 1958. Vol. 9, pp. 70–92. Printed in Great Britain.

THE ELECTRONIC STRUCTURE OF AN H-CENTER

WERNER KÄNZIG and TRUMAN O. WOODRUFF

General Electric Research Laboratory, Schenectady, New York

(*Received* 14 *July* 1958)

Abstract—The electronic structure of a new type of color center, which is produced in KCl, KBr, and LiF crystals by X-irradiation at low temperatures, has been determined by electron-spin-resonance experiments. Crudely, this center can be described as a halogen$_2^-$ molecule-ion located in a halide-ion vacancy. The unpaired electron interacts strongly with the two nuclei of the molecule-ion and weakly with two more halogen nuclei. All four nuclei lie in a straight row along a [110] axis. This paramagnetic center may be identical with the center that gives rise to the optical *H*-band, since in KCl it has the same production, bleaching, and symmetry characteristics.

VOL
9
195

1. INTRODUCTION

It is known that X-rays produce in alkali halides a number of optical absorption bands on the short-wavelength side of the *F*-band; for example, the *V*-bands and the *H*-band. The relative intensities of these bands depend strongly upon the temperature at which the crystal is held during and after the exposure to X-rays. The *V*-bands, as well as the *H*-band, were attributed by SEITZ[1] to holes (electron deficiencies) trapped at vacancies or simple vacancy aggregates, whereas VARLEY[2] proposed models involving interstitials, as well as models involving halogen atoms occupying alkali vacancies. All these models are highly speculative. Prior to the present work, there was only one electron-deficiency center not involving an impurity, the structure of which had been determined by electron spin resonance[3,4] and the optical absorption of which had been identified unambiguously:[5] the *V*-center described in our previous work. This center is essentially a halogen$_2^-$ molecule-ion. It is not closely associated with any imperfection and probably may be regarded as a "self-trapped hole".* Its weak optical absorption band (which was overlooked for a long time) is close to the V_1-band.[5] The structures of two more types of trapped-hole centers in LiF have been determined recently;[6] however, the optical absorption bands due to these centers have not been identified as yet.

This article contains a study of a *new* paramagnetic resonance spectrum which has been observed in X-rayed KCl, KBr, and LiF.† For KCl the production and bleaching characteristics of this paramagnetic center are the same as those of the optical *H*-band.[8] Also the symmetry of the paramagnetic center is compatible with the optical symmetry of the *H*-center.[9] Thus, for KCl the identification of the optical *H*-center with our paramagnetic center seems to be fairly well established, and we shall call the paramagnetic center throughout this paper an *H*-center. It appears, however, that the paramagnetic center in KBr with the same structure has rather different production and bleaching characteristics than the optical *H*-band in KBr which DUERIG and MARKHAM[10] discovered and called the *H*-band. However, a recent reinvestigation of the optical *H*-band by MARKHAM and KONITZER[10a] indicates that there is no discrepancy with our data.

First, a description and an analysis of the paramagnetic resonance spectra will be given. The hyperfine splitting can be resolved to a high degree with conventional paramagnetic-resonance techniques, and the structure of the center can be deduced entirely from the magnetic-resonance spectrum. The hyperfine splitting of the *H*-center is closely related to the hyperfine splitting of the *V*-center (self-trapped hole) described previously;[3,4] i.e. the *H*-center consists also of a

* In this paper we refer to this center as a *V*-center or self-trapped hole.

† The results of a preliminary study of this spectrum for KCl have been reported previously.[7]

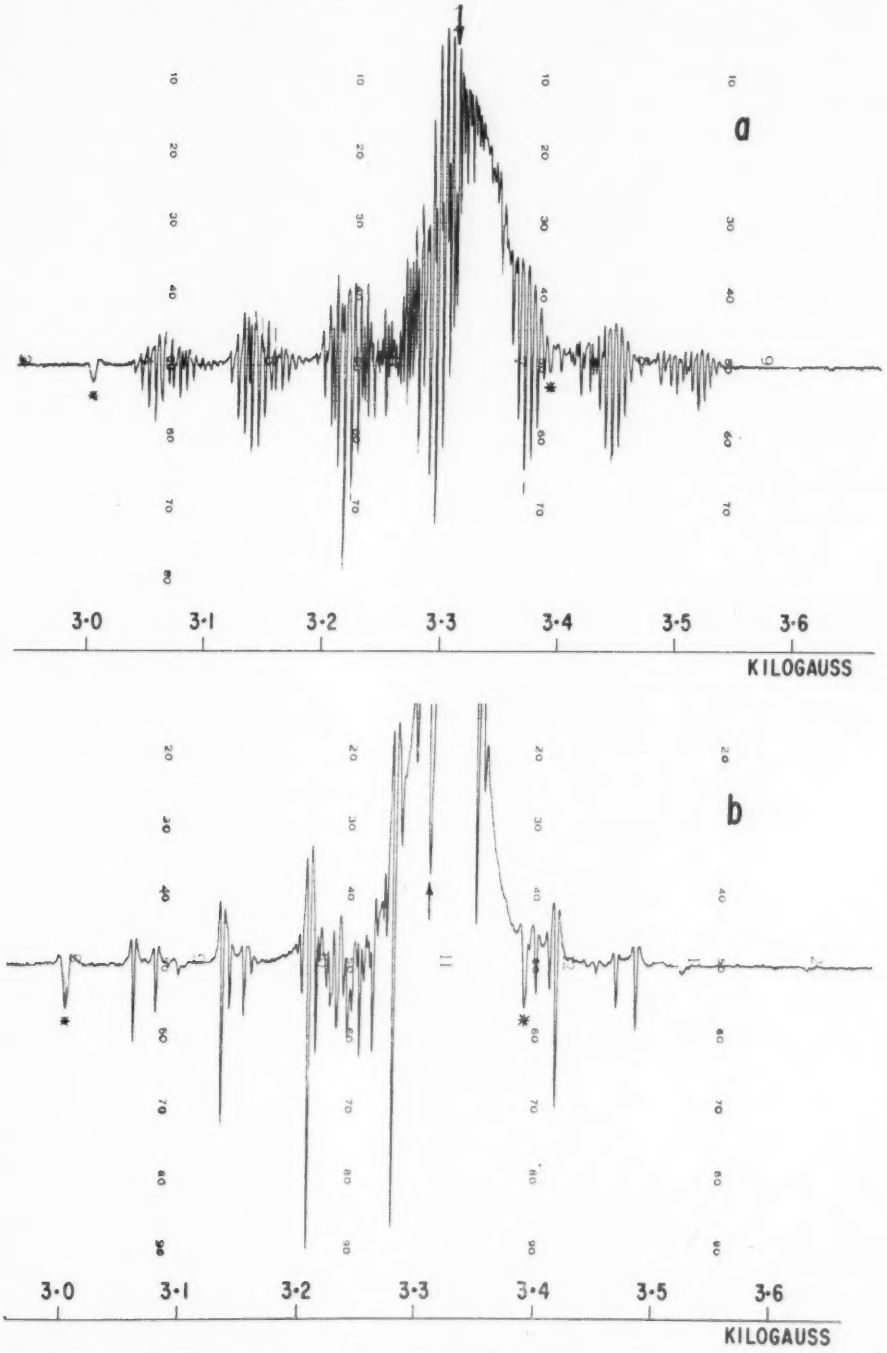

FIG. 1. Paramagnetic-resonance spectrum of KCl crystals at liquid-hydrogen temperature with $H \| [100]$. (a) H-center resonance + F-center resonance. (b) V-center resonance + F-center resonance. The asterisks indicate the resonance due to an impurity and the arrows the position of the resonance line due to α,α-diphenyl β-picryl hydrazyl. Derivative of dispersion measured at 9277 Mc/s.

halogen$_2^-$ molecule-ion.* However, in contrast to the V-center, the H-center involves *interstitial halogen*, and thus is genetically very different from the V-center. The structure differs from those proposed by SEITZ[1] and by VARLEY[2] for the H-center. However, it may lend some support to VARLEY's ideas about the mechanism of color-center production by energetic radiation.

In the last part of this paper, the magnetic-resonance experiments will be correlated with the optical investigations of previous authors through a study of the generation and bleaching characteristics of the H-center resonance in KCl and KBr. Finally, a model will be proposed which explains the magnetic-resonance spectrum, as well as some of the generation and bleaching characteristics.

2. DESCRIPTION AND QUALITATIVE INTERPRETATION OF THE PARAMAGNETIC RESONANCE SPECTRA

(a) *The Hyperfine Splitting*

(i) *Potassium chloride*

Fig. 1 compares the H-center resonance with the V-center resonance discussed in reference (3). Both spectra show the derivative of the dispersion and were taken at liquid-hydrogen temperature (20·3°K) with the d.c. magnetic field along a [100] axis of the crystal.†

The similarity between the H-center spectrum and the V-center spectrum is striking. To every line in the V-center spectrum corresponds a *group* of lines in the H-center spectrum. We shall call the splitting within the groups "secondary splitting" and the intervals between the centers of the different groups "primary splitting". The primary splitting in the H-center spectrum is about 10 per cent larger than the splitting of the corresponding V-center spectrum and shows the same orientation-dependence, as can be seen by comparing Fig. 2 of this paper with Fig. 4 of reference (3). The complete analogy of the orientation effects for the H-center spectra to those for the V-center spectra indicates that the axis of the major hyperfine interaction is the same for both types of centers; namely a [110] axis of the crystal. All six [110] axes are equally populated with H-centers (unless the crystal has been exposed to polarized H-light). Hence, for a general orientation of the crystal in the d.c. magnetic field, one observes the superposition of six different basic spectra. This number degenerates to two for $\boldsymbol{H}\|[100]$ and $\boldsymbol{H}\|[111]$ and to three for $\boldsymbol{H}\|[110]$.

The nature of the *secondary* splitting in the H-center spectrum is illustrated in Fig. 3, which shows a detailed recording of the groups of lines encircled in Fig. 2. With the help of Fig. 2 of reference (3), one finds now that the basic H-center spectrum can be derived from the basic V-center spectrum by splitting every line of the V-center spectrum into a miniature (secondary) spectrum of the same kind. Even the lines arising from the different possible isotope combinations are partially resolved in the miniature pattern.

The interpretation of this complex spectrum is almost obvious on the basis of the known interpretation of the V-center spectrum.[3] The V-center spectrum arises from the strong interaction of an electron deficiency with two *equivalent* halide ions; i.e. it is the hyperfine spectrum of a Cl_2^- molecular ion. Since the primary splitting in the H-center spectrum is entirely analogous to the splitting in the V-center spectrum, we conclude that in the H-center the unpaired spin interacts strongly with two *equivalent* halide ions (1 and 2), just as in the V-center. Thus the H-center is basically also a Cl_2^- molecule-ion. However, the secondary splitting indicates that the unpaired electron spin interacts in addition more weakly with two other halide ions (3 and 4) which are again equivalent to each other. The hyperfine

---

* The present paper should be read in conjunction with the earlier work on the halogen$_2^-$ molecule-ion.[3,4]

† Note that three more spectra are superposed on the H-center resonance and on the V-center resonance in Fig. 1. The intense broad resonance in the center of the spectra is due to F-centers. Fast passage effects make it look like an absorption curve rather than like the derivative of a dispersion curve. The narrow resonance line marked by an arrow is due to α,α-diphenyl β-picryl hydrazyl and served as reference for the measurement of the g-factor. The weak resonance lines marked by a star were already present in the virgin crystals. They are due to an impurity, possibly O_2^- molecular ions. If the spectrometer is tuned to measure pure *absorption*, the H-center resonance, the V-center resonance, and the F-center resonance are completely saturated at 20°K by a microwave magnetic field of a few hundreths of a gauss. The V-center resonance is, however, readily detectable in absorption at 78°K, whereas the F-center resonance is still saturated because of its longer relaxation time. For this reason the F-center resonance did not appear in our previous work on the V-center.[3,4]

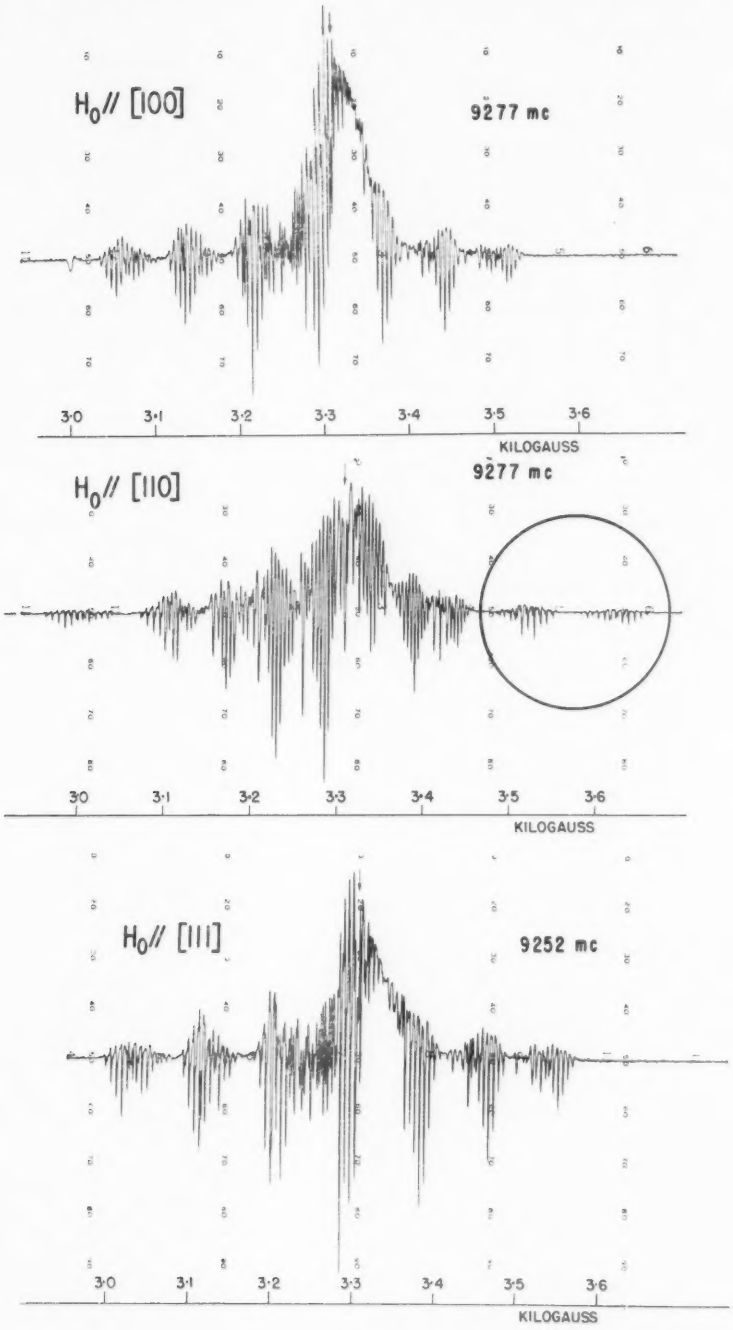

FIG. 2. Illustration of the anisotropy of the hyperfine interaction in the *H*-center in KCl. Derivative of the dispersion of the paramagnetic resonance measured at liquid-hydrogen temperature. (Compare with Fig. 4 of reference (3).)

spectra show that this equivalence holds for any orientation of the d.c. magnetic field with respect to the axis defined by the nuclei 1 and 2. Therefore, the nuclei 3 and 4 must lie on a straight line passing through the midpoint of the line 1–2 and they are equally distant from this midpoint. Since the axis 1–2 is exactly a [110] axis of the crystal, and since the nuclei 1 and 2 are in equivalent positions, the angle between the axes 1–2 and 3–4 must be either zero or a right angle. The first case is unique. In the second case two possibilities are compatible with the qualitative features of the observed spectra. If we choose [110] for the axis 1–2, then the line 3–4 must be either $[1\bar{1}0]$ or [001]. All other axes perpendicular to [110] can be excluded on the basis of the observation that the secondary hyperfine pattern consists always of a *single* basic pattern. The reasoning goes as follows: If the line 3–4 were along a more general direction, there would be for symmetry reasons two equivalent possible orientations for 3–4 for every given line 1–2. These would be equally occupied. However, they are nonequivalent with respect to a general direction of the external d.c. magnetic field $\boldsymbol{H}$. Since the secondary hyperfine splitting is strongly anisotropic, one would observe for a general orientation (as well as for a few special orientations) a secondary pattern that consists of *two* different basic patterns. This is contrary to our observations, which show only one basic pattern. At this stage we can only conclude that the principal axes of the tensor of the hyperfine interaction* are the same for all four nuclei: namely [110] = axis (1–2) = x', $[\bar{1}10] = x'$, [001] = y'; i.e. the center is orthorhombic and has these principal axes. The question whether the line 3–4 is perpendicular to 1–2 or whether it

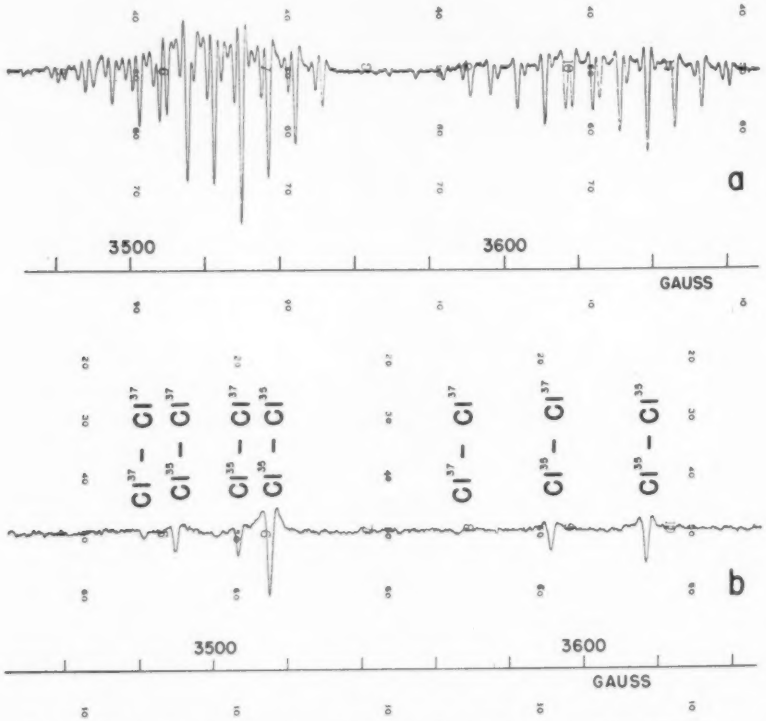

FIG. 3. Illustration of the nature of the secondary splitting for KCl. $\boldsymbol{H}\|[110]$.
(a) Detailed recording of the groups of lines encircled in Fig. 2.
(b) Corresponding lines in the V-center spectrum. Frequency 9277 Mc/s.

* This tensor is discussed in Section 3(a).

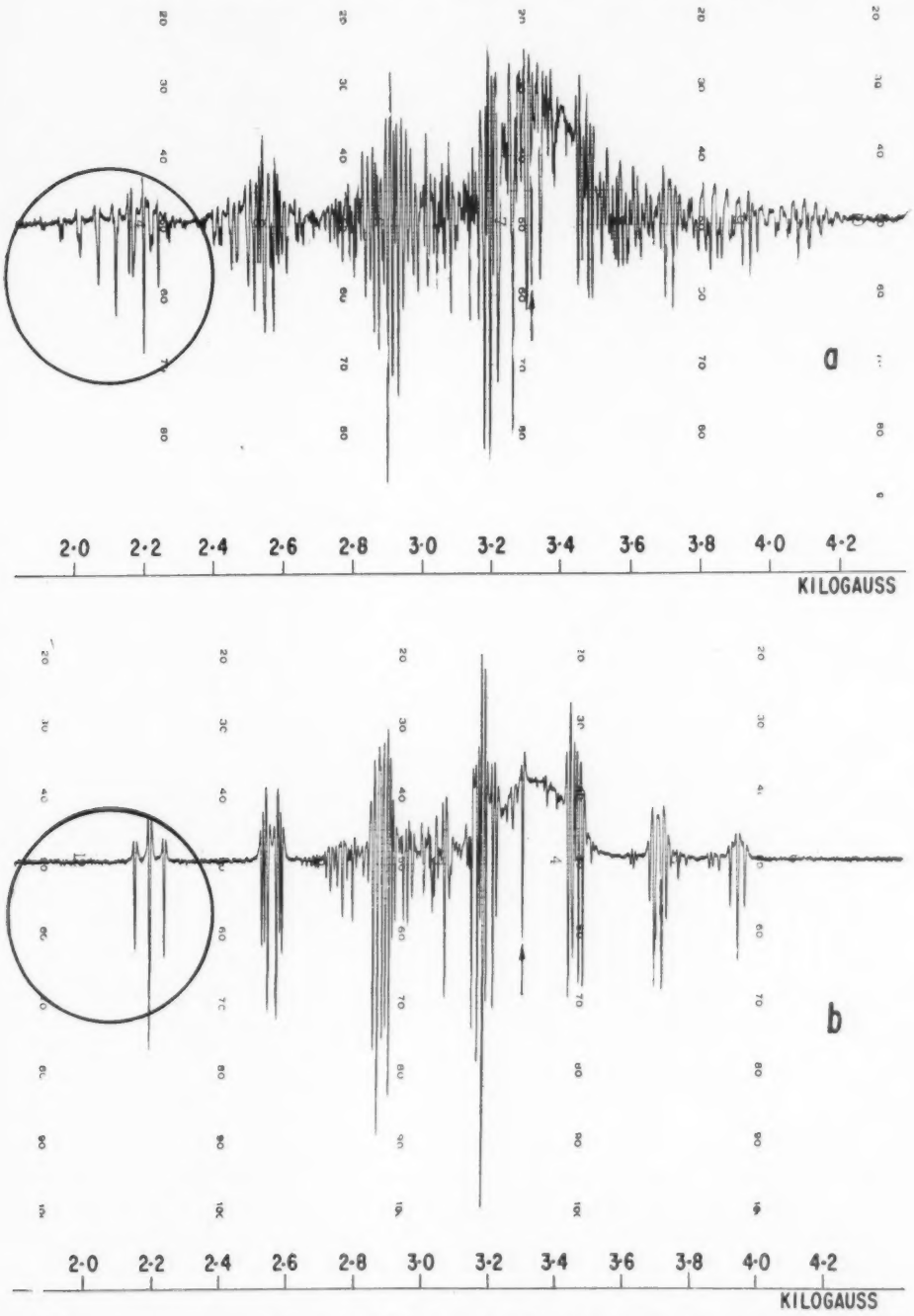

FIG. 4. Paramagnetic-resonance spectrum of KBr crystals at liquid-hydrogen temperature with $H \| [100]$.
(a) H-center + V-center + F-center. (b) V-center + F-center.
The arrows indicate the position of the resonance line due to α,α-diphenyl β-picryl hydrazyl. Derivative of dispersion measured at 9260 Mc/s. Recording time 1hr.

coincides with 1–2 will be answered in the course of the quantitative analysis (see Section 3(a)).

(ii) *Potassium bromide*

In KBr a hyperfine spectrum is found which is the complete analogue of the spectrum just discussed, and thus is due to a *center with the same structure*. The analogy is, however, not very obvious for the following reasons.

miniature pattern of the same kind as the primary pattern) is exceedingly complex. Moreover, in contrast to the case of KCl, it was not possible to get rid of the V-center resonance (see Section 5(b)), which, therefore, was always superposed on the H-center resonance. Fig. 4 illustrates this superposition, which, in addition, contains the F-center resonance, an impurity resonance (possibly due to O_2^- molecular ions) and the resonance of α,α-

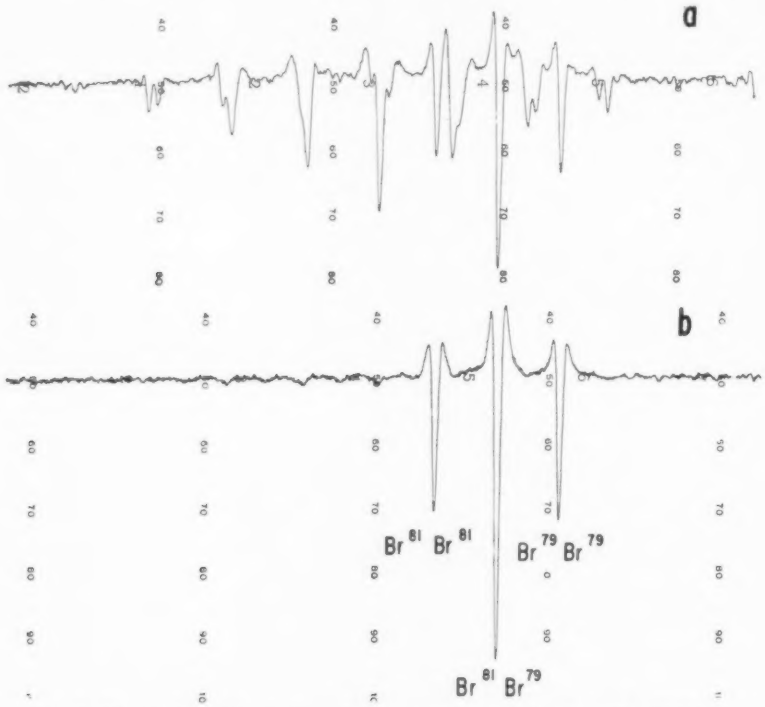

FIG. 5. Illustration of the nature of the secondary splitting for KBr. $H \parallel [100]$.
(a) Detailed recording of the group of lines in the H-center + V-center spectrum encircled in Fig. 4a.
(b) Detailed recording of the corresponding group in the V-center spectrum encircled in Fig. 4b.

It was shown in reference (3) that the hyperfine spectrum of the V-center (self-trapped hole) in KBr is already very complicated, mainly because of the existence of two bromine isotopes (^{79}Br and ^{81}Br) which are almost equally abundant, and because of additional splittings due to second-order hyperfine and quadrupole effects. Hence, the H-center resonance (which again can be derived from the V-center resonance by splitting every line into a

diphenyl β-picryl hydrazyl (DPPH). Fig. 5 shows a detailed recording of the group of lines encircled in Fig. 4. The splitting due to different isotope combinations of nuclei 3 and 4 is not resolved, in contrast to the case of KCl. It is only evident that the secondary pattern consists of seven broadened lines with the intensity ratio 1 : 2 : 3 : 4 : 3 : 2 : 1, indicating that the nuclei 3 and 4 are in equivalent positions and have spin 3/2. Since the ratio of

primary splitting to secondary splitting is about the same as for KCl, it can be concluded that the nuclei 3 and 4 are also Br nuclei. The dependence of the hyperfine spectrum upon the orientation of the crystal in the d.c. magnetic field shows that the orientation and the symmetry of this center in KBr are exactly the same as in KCl.

(iii) *Lithium fluoride*

The center with the *same structure* exists in LiF. We shall call it also an *H*-center, although there is no optical absorption band in LiF that has been labelled an *H*-band.

Unfortunately, it was not possible to prepare a crystal containing *H*-centers only and no *V*-centers (self-trapped holes), so that the two spectra were always superposed. Fig. 6 illustrates this superposition and compares it with the pure *V*-center spectrum.†

(b) *The Spectroscopic Splitting Factor*

The observed spin resonance is due to a hole in the otherwise filled *p*-shells of the halide ions. Therefore, the spectroscopic splitting factor is larger than for the free electron. However, the orbital moment is quenched through the formation of a molecular bond, so that the excess over the free electron value is small, just as for the *V*-center.[3] Table 1 gives the components of the *g*-tensors for the *H*-center referred to the axes x', y', and z', and compares them to the corresponding quantities for the *V*-center. For $\boldsymbol{H}$ parallel to the axis z' (defined by the nuclei 1 and 2), one measures a value that is very close to the free-electron value (the very small negative shift is a higher-order effect), whereas for $\boldsymbol{H}$ perpendicular to z' the *g*-shift is larger and positive. Axial symmetry about z' is again a good approximation. The *g*-shifts for the *H*-center are about half the *g*-shifts for the *V*-center. This indicates that the molecular bond of the halogen$_2^-$ molecular ion is more tight in the *H*-center than in the *V*-center (see Section 4).

Table 1. *Components of the g-tensors measured at* 9·3 *kMc/s, referred to polycrystalline DPPH* ($g = 2{\cdot}0034$). *The data for the V-center are taken from ref.* (3). *The temperature variation of the g-shift between* 20 *and* 78°K *is within the experimental errors.*

	LiF		KCl		KBr	
	H-center 78°K	*V*-center 78°K	*H*-center 20°K	*V*-center 78°K	*H*-center 20°K	*V*-center 78°K
$g_{x'}$	2·014	2·023	2·0227	2·0428	2·078	2·179
$g_{y'}$	2·012	2·023	2·0219	2·0447	2·070	2·175
$g_{z'}$	2·001	2·003	2·0023	2·0010	1·993	1·980
Error	±0·002	±0·001	±0·0005	±0·0001	±0·003	±0·001

Since there is only one fluorine isotope in the crystal, ^{19}F, with the nuclear spin 1/2, the hyperfine spectrum of the *H*-center is rather simple. The strong interaction of the unpaired electron spin with two equivalent fluorine nuclei 1 and 2 would give rise to three hyperfine lines with the intensity ratio 1 : 2 : 1.*

The weak interaction with the fluorine nuclei 3 and 4 (which are also *equivalent* to each other) splits every one of these lines into a miniature (secondary) pattern of 3 lines with the intensity ratio 1 : 2 : 1.

* This is true if the angle θ between the axis defined by the two nuclei and the d.c. magnetic field does not exceed about 70°. For larger angles the line with the intensity 2 splits into its two components. This splitting was explained in quantitative detail in ref. (4). For the sake of brevity, we discuss here only the spectra for $\theta < 70°$.

† Fig. 6 represents the derivative of *absorption* in contrast to the preceding figures. The *F*-center resonance is completely saturated.

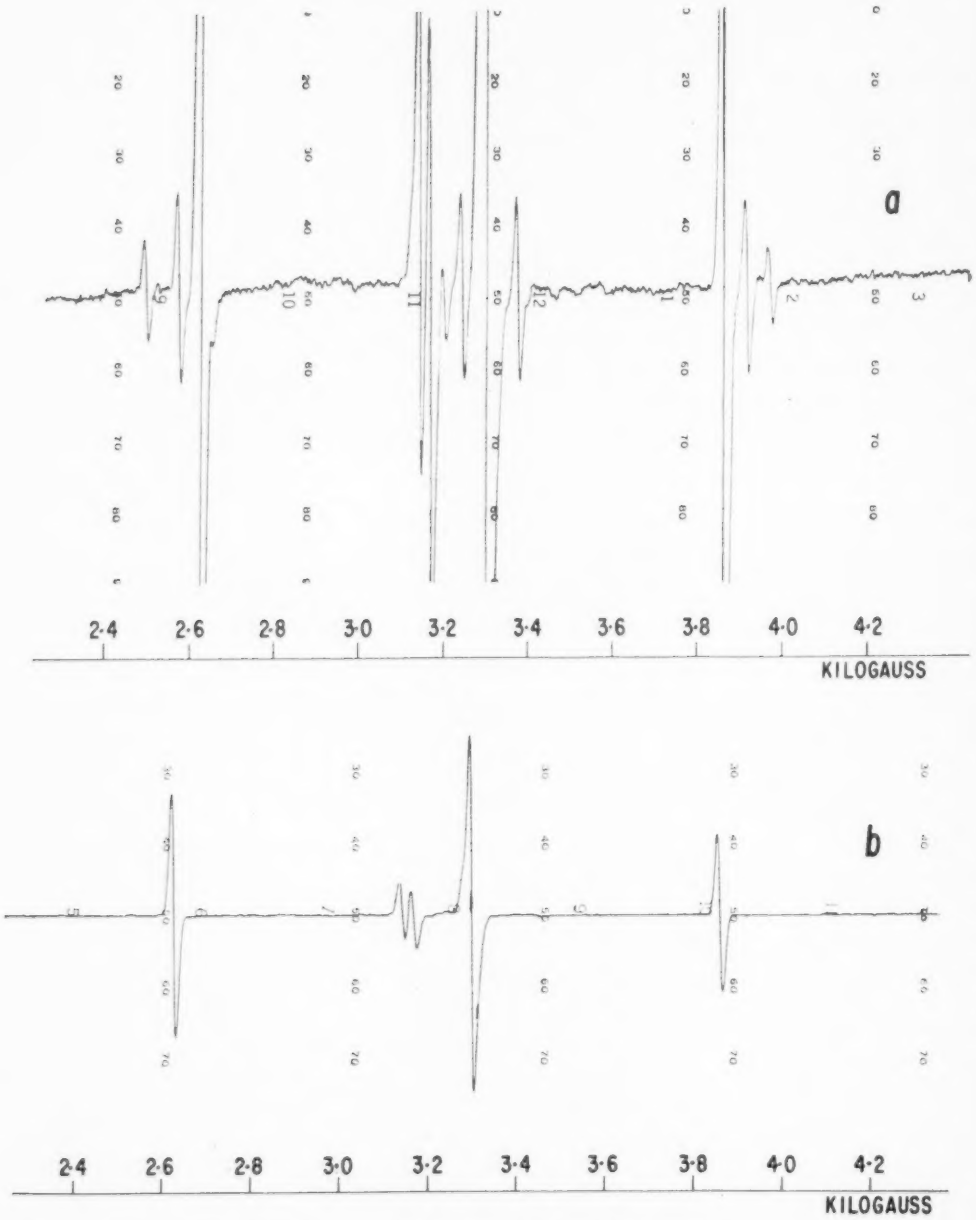

FIG. 6. Paramagnetic-resonance spectrum of LiF crystals at liquid-nitrogen temperature with $H \| [100]$.
(a) H-center resonance + V-center resonance (the V-center resonance goes off the scale).
(b) V-center resonance only (reduced gain).
Derivative of absorption measured at 9322 Mc/s.

(c) *Line Width and Saturability*

The line width of the H-center resonance is mainly due to unresolved hyperfine interaction. Hence the absorption spectrum saturates much more easily than the dispersion spectrum. At 20°K the absorption spectrum is completely saturated by a microwave magnetic field of a few hundredths of an oersted, whereas the dispersion spectrum is readily observable. The H-center resonance saturates somewhat less easily than the V-center resonance. The static line widths are 0·8 Oe for the H-center in KCl and 11 Oe for the H-center in LiF. The corresponding values for the V-center are 1·35 and 12·3 Oe.[3] In the case of KBr, the secondary pattern is not sufficiently resolved to permit a determination of the line width.

3. ANALYSIS OF THE HYPERFINE SPECTRUM

(a) *The Spin Hamiltonian*

The spatial wavefunction of the unpaired electron is now to be thought of as expanded in spherical harmonics referred to co-ordinate systems centered on four halogen nuclei $i = 1, 2, 3, 4$, in the case of the H-center and on two nuclei $i = 1, 2$ in the case of the V-center. The spin Hamiltonian can be written as

$$\mathscr{H} = g_0\beta_0\left\{\frac{g}{g_0}S_zH_z + \boldsymbol{S}\cdot\sum_i \boldsymbol{T}^{(i)}\cdot\boldsymbol{I}^{(i)}\right\}. \qquad (1)$$

Here g_0 is the spectroscopic splitting factor of the free electron and g that of the H-center for a particular orientation of the center in the magnetic field. β_0 is the Bohr magneton, $\boldsymbol{S}$ and $\boldsymbol{I}^{(i)}$ are the spin operators of the electron and of the nuclei respectively, and z is the axis of the externally applied d.c. magnetic field. Each tensor $\boldsymbol{T}^{(i)}$ can be represented as a sum of tensors each of which corresponds to a term in the expansion of the wave-function in spherical harmonics about the nucleus i.

The *accurate* determination of the tensors $\boldsymbol{T}^{(i)}$ from the observed hyperfine splitting is not straightforward, because the hyperfine splitting is not very small compared to the externally applied d.c. magnetic field, so that a rigorous diagonalization of the spin energy matrix would be required.[4] In this paper we restrict ourselves to an *approximate* solution. We begin by observing that in first-order approximation the hyperfine splitting in gauss is given by the eigenvalues of the projection on the z-axis of $\Sigma\boldsymbol{T}^{(i)}\cdot\boldsymbol{I}^{(i)}$. The first-order approximation is, however, clearly inadequate because the observed hyperfine splittings are non-uniform, except for $\boldsymbol{H}\|z'$. However, if the angle θ between the d.c. magnetic field $\boldsymbol{H}$ and the axis z' of the color center does not exceed about 60°, the experimental hyperfine spectra of the H-center and of the V-center in KCl are adequately (although not accurately) described by a second-order expression of the form

$$H - H_0 \approx A[(m_1+m_2)+a(m_3+m_4)]+ \\ +B[(m_1+m_2)+b(m_3+m_4)]^2. \qquad (2)$$

The magnetic quantum numbers of the nuclei are denoted by m_i. H_0 is the position of the center line, and the coefficients A, a, B, and b depend upon the orientation of the d.c. magnetic field with respect to the axes x', y', z' of the color center. For the V-center the hyperfine splitting due to nuclei other

Table 2. Experimental values of the coefficients of equation (2) *for the H-center and V-center in* KCl. *The data for the V-center are taken from ref.* (3).

Direction of $\boldsymbol{H}$ referred to crystal axes	Direction cosines of $\boldsymbol{H}$ in x', y', z' system $\alpha\ \beta\ \gamma$	Angle between $\boldsymbol{H}$ and z', θ (degrees)	H-center ^{35}Cl				V-center ^{35}Cl	
			A	B	a	b	A	B
[110]	0, 0, 1	0	108·8	0·00	0·067	—	101·4	0·00
[111]	0, $\sqrt{\frac{1}{2}}$, $\sqrt{\frac{1}{2}}$	35·26	88·7	0·564	0·069	0·064	81·8	0·527
[100]	$\sqrt{\frac{1}{2}}$, 0, $\sqrt{\frac{1}{2}}$	45	76·8	0·842	0·072	0·056	70·7	0·751
[101]	$\frac{1}{2}$, $\sqrt{\frac{1}{2}}$, $\frac{1}{2}$	60	55·0	1·23	0·081	0·038	49·9	1·163

than $i = 1, 2$ is small and not resolved. It will not be considered here; i.e. for the V-center we put $a \approx b \approx 0$.

As an example, the measured values of the coefficients of equation (2) are listed in Table 2 for the ^{35}Cl H-center and V-center in KCl. Approximate values of the components of the hyperfine tensors follow from the first-order terms in equation (2). Since the tensors are diagonal in the $x'y'z'$ system (see Section 2(a)), we can write for the primary splitting ($i = 1, 2$):

$$A(\alpha,\beta,\gamma) \approx \frac{g_0}{g}\sqrt{\alpha^2\left(T^{(i)}_{x'x'}\right)^2+\beta^2\left(T^{(i)}_{y'y'}\right)^2+\gamma^2\left(T^{(i)}_{z'z'}\right)^2}, \quad (3)$$

where α, β, γ are the direction cosines of the d.c. magnetic field in the $x'y'z'$ system. A corresponding expression is valid for the secondary splitting Aa. The data in Table 2 provide four equations for three tensor components. The internal consistency is satisfactory when we consider the crudeness of the approximation. For KBr and for LiF this approach is considerably less accurate, because the hyperfine interaction is much larger than for KCl. Table 3 summarizes the results of this approximate determination of the hyperfine tensors for the H-center in each of the three salts and compares them with the corresponding results for the V-center. It appears that axial symmetry about z' is a good approximation for the interaction of the electron spin not only with the nuclei 1 and 2 but also with the nuclei 3 and 4. Therefore, it is most likely that the axis 3–4 coincides with the axis 1–2; i.e. *the four nuclei lie in a straight row along a* [110] *axis*.

Note that the interactions considered here do not permit the determination of the signs of the tensor components.

(b) *Interpretation of the Hyperfine Tensors*

The relation between the hyperfine tensor of an unpaired electron and its wavefunction is simple if one ignores the polarization of the ion core by this electron. For an s-electron we have then the well-known expression

$$T_{x'x'} = T_{y'y'} = T_{z'z'} = \frac{8\pi}{3}\frac{\mu}{I}|\psi(0)|^2 \quad (4)$$

where μ and I are the magnetic moment and the spin of the nucleus respectively, and $|\psi(0)|$ is the amplitude of the s-function at the nucleus. For a $p_{z'}$-function one obtains

$$-T_{x'x'} = -T_{y'y'} = \frac{1}{2}T_{z'z'} = \frac{2}{5}\frac{\mu}{I}\left(\overline{\frac{1}{r^3}}\right) \quad (5)$$

(off-diagonal elements vanish in the $x'y'z'$ system) where $\overline{(1/r^3)}$ is an average over the $p_{z'}$ function.

Table 3. Approximate values of the components of the hyperfine tensors. The data for the V-centers are taken from ref. (3). The meaning of $T_{x'x'} \approx T_{y'y'} \sim 0$ *is* $T_{x'x'} \approx T_{y'y'} \ll T_{z'z'}$.

Crystal	Isotope	Center	$T_1 = T_2$			$T_3 = T_4$		
			$\lvert T_{x'x'}\rvert$	$\lvert T_{y'y'}\rvert$	$\lvert T_{z'z'}\rvert$	$\lvert T_{x'x'}\rvert$	$\lvert T_{y'y'}\rvert$	$\lvert T_{z'z'}\rvert$
LiF	^{19}F	H-center	~ 0	~ 0	956	26	24	89·8
		V-center	59	59	887	.....	.....	.....
KCl	^{35}Cl	H-center	~ 0	~ 0	109	2·9	2·8	7·3
		V-center	~ 9	~ 9	101	.....	.....	.....
KBr	^{81}Br	H-center	~ 0	~ 0	498	~ 0	~ 0	59·5
		V-center	~ 80	~ 80	455	.....	.....	.....

Higher-order functions will not be considered here, since the unpaired electron in the *H*-center and *V*-center is essentially a *p*-electron (2*p* for the fluorides, 3*p* for the chlorides, and 4*p* for the bromides). The orbital degeneracy of the *p*-functions is lifted through the formation of the molecular bond, so that the ground-state wave function has mainly $p_{z'}$ character. Table 3 shows, however, that the traces of the experimental hyperfine tensors do *not* vanish. This may be due to hybridization; that is, to the admixture of *s*-function to the $p_{z'}$-function, but it may also be a manifestation of *core polarization*. The interaction of the unpaired electron with the nucleus through the ion core can be considerable, as is indicated by the calculations of STERNHEIMER,[11] PRATT,[12] and HEINE.[13] There is considerable need for more work along these lines. The analysis given in the present paper is based on the assumption of hybridization, and core polarization is neglected.

We assume that the ground-state orbital of the unpaired electron is a linear combination of hybridized atomic wavefunctions centered on the nuclei *i*. Each atomic wave function has a certain amount η_i^2 of *s*-character and a certain amount ζ_i^2 of *p*-character. If there were no overlap, normalization would require that

$$\sum_i (\eta_i^2+\zeta_i^2) = 1. \tag{6}$$

According to equations (4) and (5) the components of the hyperfine tensors of the hybridized atomic wavefunctions are*

$$T^{(i)}_{x'x'} = T^{(i)}_{y'y'} = \frac{\mu_i}{I_i}\left[\frac{8\pi}{3}\eta_i^2|\psi_i(0)|^2 - \frac{2}{5}\zeta_i^2\left(\overline{\frac{1}{r^3}}\right)\right] \tag{7}$$

$$T^{(i)}_{z'z'} = \frac{\mu_i}{I_i}\left[\frac{8\pi}{3}\eta_i^2|\psi_i(0)|^2 + \frac{4}{5}\zeta_i^2\left(\overline{\frac{1}{r^3}}\right)\right]. \tag{8}$$

We shall now analyze the experimental hyperfine tensors (Table 3) in terms of equations (7) and (8). Axial symmetry is a good approximation, so that we can use the average of $T_{x'x'}$ and $T_{y'y'}$. The decomposition of the experimental hyperfine tensors into an *s*-part and a *p*-part is ambiguous (unless $T_{x'x'} = T_{y'y'} = 0$) because the sign of $T_{x'x'} = T_{y'y'}$ is unknown. The analysis will be carried out for both signs.

We now solve equations (7) and (8) for the normalization factors η_i^2 and ζ_i^2 (neglecting overlap effects), by inserting the experimental values for the tensor components and plausible values for $|\psi_i(0)|^2$ and $(\overline{1/r^3})$. The $(\overline{1/r^3})$ values for the halogen *np* functions are taken from STERNHEIMER's[14] calculations. The values for $|\psi(0)|^2$ which should be inserted are somewhere between the values for an

* The relation between the notation of this paper and the notation used in ref. (3) is as follows:

This paper (for $i = 1, 2$)	$T_{x'x'} \approx T_{y'y'}$	$T_{z'z'}$	$\sum_i \eta_i^2$	$\sum_i \zeta_i^2$	I_1+I_2
Ref. (3)	a	$a+b$	β^2	α^2	I

Also note the misprints in equations (9), (10), and (11) of ref (3). The correct equations are:

$$a = \frac{\mu_I}{I}\left[\frac{8\pi}{3}\beta^2|\psi(0)|^2 - \frac{2}{5}\alpha^2\left(\overline{\frac{1}{r^3}}\right)\right] \tag{9}$$

$$b = \frac{\mu_I}{I}\left[\frac{6}{5}\alpha^2\left(\overline{\frac{1}{r^3}}\right)\right] \tag{10}$$

$$\beta^2 = \frac{(a/b+\frac{1}{2})}{(a/b+\frac{1}{3})+\dfrac{20\pi|\psi(0)|^2}{9\left(\overline{\frac{1}{r^3}}\right)}} \tag{11}$$

ns function and an $(n+1)s$ function. The calculations will be carried out for both limits.* For the $(n+1)s$ function we use the estimate of $|\psi(0)|^2$ given in ref. (3). The $|\psi(0)|^2$ values for the fluoride $2s$ function and for the chloride $3s$ function are taken from HARTREE's calculations.[15,16] The $4s$-function for Br^- was interpolated by W. W. PIPER between HARTREE's[15] $4s$-function for Rb^+ and PIPER's[17] $4s$-function for germanium. The numerical values used in this paper are listed in Table 4, and the resulting values for η_i^2 and ζ_i^2 are contained in Table 5. This table also includes the data for the V-center in order to facilitate comparison.

three crystals, the reduction of $\Sigma(\eta_i^2+\zeta_i^2)$ in the case of KBr suggests that an important factor has been neglected in the analysis. It is conceivable that *core polarization* has quite a different influence in KBr than in the chlorides and fluorides. On the other hand, it should be kept in mind that the numbers in Table 5 depend upon approximate calculations of $\overline{(1/r^3)}$ values.†

(5) The values of $\sum_{i=1}^{3}(\eta_i^2+\zeta_i^2)$ tend to be higher for the H-center than for the V-center in all three alkali halides under investigation.‡ This difference most probably indicates increased overlap in the H-center; i.e. a reduced internuclear distance 1–2.

Table 4. Numerical values of wavefunctions used in the analysis of the hyperfine tensors.

Ion	np function	$\overline{(1/r^3)}$ (cm^{-3})	Ref. No.	ns function	$\lvert\psi(0)\rvert^2$ (cm^{-3})	Ref. No.	$(n+1)s$ function	$\lvert\psi(0)\rvert^2$ (cm^{-3})	Ref. No.
F^-	$2p$	$60{\cdot}0\times10^{24}$	14	$2s$	74×10^{24}	15	$3s$	$3{\cdot}32\times10^{24}$	3
Cl^-	$3p$	$55{\cdot}6\times10^{24}$	14	$3s$	69×10^{24}	16	$4s$	$5{\cdot}72\times10^{24}$	3
Br^-	$4p$	163×10^{24}	14	$4s$	143×10^{24}	15, 17	$5s$	$14{\cdot}2\times10^{24}$	3

The contents of Table 5 can be summarized roughly as follows:

(1) In the H-center the unpaired spin spends about 4–10 per cent of its time on the ions 3 and 4 together.

(2) If admixture of the ns function to the np function is assumed, then 3–8 per cent s-character is needed to account for the anisotropy of the hyperfine interaction with the nuclei 1 and 2 and the nuclei 3 and 4.

(3) If admixture of $(n+1)s$ function is assumed, then 23–52 per cent s-character is necessary to account for the anisotropy of the hyperfine interaction with the nuclei 1 and 2, and between 10 and 60 per cent s-character to account for the anisotropy of the hyperfine interaction with the nuclei 3 and 4.

(4) The sum $\Sigma(\eta_i^2+\zeta_i^2)$ deviates from unity. For LiF and KCl it tends to be larger than unity, whereas for KBr the tendency seems to be opposite. Since one would expect that overlap gives about the same *positive* contribution to this sum in all

4. THE EXCITED STATES AND THE SHIFT OF THE SPECTROSCOPIC SPLITTING FACTOR

Since the unpaired electron of the H-center spends only a small fraction of its time on the ions 3 and 4, we can regard the H-center as a halogen$_2^-$ molecule-ion, just as we did the V-center. The excited states of this system were discussed in earlier work.[3,18] Here only the differences between the

* In ref. (3) we considered only admixture of an $(n+1)s$ function with the np function.

† *Note added in proof:* Dr. J. OWEN (Oxford) pointed out to the authors that STERNHEIMER's[14] calculated $\overline{(1/r^3)}$ value for the $4p$ function of Br is about twice the value obtained from atomic beam experiments,[24] whereas the calculations for F and Cl agree much better.[25,26] Thus the low values of $\sum_i(\eta_i^2+\zeta_i^2)$ for KBr in Table 5 are merely a manifestation of the fact that we used too large a $\overline{(1/r^3)}$ value for Br. If we insert $\overline{(1/r^3)}$ values deduced from atomic beam experiments, the numbers for KBr in Table 5 do not differ significantly from those for LiF and KCl.

‡ This effect manifests itself most clearly when one compares directly an H-center spectrum with the corresponding V-center spectrum. The primary splitting of the H-center spectrum always exceeds the splitting of the V-center spectrum for $\theta < 70°$.

Table 5. Result of the calculation of η_i^2 and ζ_i^2 by means of equations (7) and (8), using the measured hyperfine tensors (Table 3) and the information on the wavefunctions listed in Table 4. Core polarization and overlap effects are neglected.

Crystal	Center	s-admixture	Nuclei 1 and 2			Nuclei 3 and 4			$\sum_i(\eta_i^2+\zeta_i^2)$
			Sign $T_{x'x'}$	η^2 (s-function)	ζ^2 (p-function)	Sign $T_{x'x'}$	η^2 (s-function)	ζ^2 (p-function)	
LiF	H	2s	~ 0	0·019	0·500	+	0·003	0·034	1·112
						−	0·001	0·060	1·160
		3s	~ 0	0·431	0·500	+	0·063	0·034	2·056
						−	0·018	0·060	2·018
	V	2s	+	0·020	0·433		.....	.....	0·906
			−	0·016	0·494		.....	.....	1·020
		3s	+	0·474	0·433		.....	.....	1·814
			−	0·362	0·494		.....	.....	1·712
KCl	H	3s	~ 0	0·022	0·586	+	0·002	0·023	1·266
						−	0·000	0·056	1·328
		4s	~ 0	0·272	0·586	+	0·032	0·023	1·826
						−	0·004	0·056	1·836
	V	3s	+	0·025	0·499		.....	.....	1·048
			−	0·017	0·597		.....	.....	1·228
		4s	+	0·300	0·499		.....	.....	1·598
			−	0·209	0·597		.....	.....	1·612
KBr	H	4s	~ 0	0·018	0·335	~ 0	0·002	0·040	0·790
		5s	~ 0	0·184	0·335	~ 0	0·022	0·040	1·162
	V	4s	+	0·022	0·252		.....	.....	0·548
			−	0·011	0·359		.....	.....	0·740
		5s	+	0·226	0·252		.....	.....	0·956
			−	0·108	0·359		.....	.....	0·934

H-centers and the *V*-center will be elucidated. One essential difference is the increased overlap in the *H*-center. A qualitative idea of the changes of the level scheme with decreasing internuclear distance can be obtained from HERZBERG's book.[19] The situation is depicted schematically in Fig. 7 for axial symmetry. The transitions corresponding to optical absorption are represented by full arrows (E_{violet}, E_{red}) and the optically forbidden transitions that produce the $g_\perp$-shifts by dotted arrows (E_g). This scheme leads us to expect that the *H*-center violet absorption should be shifted somewhat to the violet side of the *V*-center violet absorption. For KCl this seems to be true. The *V*-center absorption peak lies at 3700 Å,[5] whereas the center of the *H*-band is at 3450 Å.[8,10]

For the shift of $g_\perp$ (which is roughly proportional to $1/E_g$), one expects a larger change, since E_g increases considerably faster than E_v with decreasing internuclear distance. This explains why the *g*-shift of the *H*-center is only about half the *g*-shift of the *V*-center for all three alkali halides that were investigated, and thus represents additional evidence for crowding of the nuclei in the

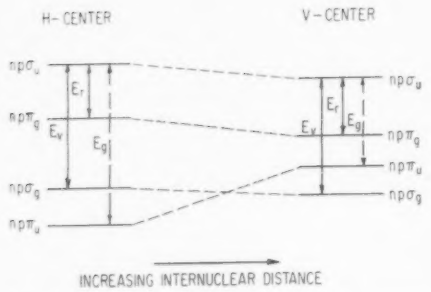

FIG. 7. Shift of the energy levels of a halogen$_2^-$ moleculeion with increasing internuclear distance. Schematic. Axial symmetry is assumed so that the degeneracy of the π-levels is not lifted. The full arrows indicate the optical transitions and the broken arrows the transitions that produce the shift of the spectroscopic splitting factor. (Compare with Fig. 8 of reference (3).)

H-center. However, it is important to note that the *H*-center and the *V*-center can be compared on the basis of HERZBERG's scheme only because the admixture of *s*-function to the *p*-function is about the same for these two centers (see Table 5).

5. GENERATION AND BLEACHING OF THE H-CENTER

(a) *Potassium Chloride*

(i) *The magnetic resonance spectrum after X-irradiation at* 20·3 and 4·2°K

Three different paramagnetic-resonance spectra due to color centers are predominant after X-irradiation of pure KCl at 20·3°K if the crystal is kept at this temperature:

(1) The *H*-center resonance just described.

(2) The *V*-center (self-trapped hole) resonance of ref. (3).

(3) The *F*-center resonance.

The composite spectrum is shown in Fig. 8a for $H \| [111]$.* The *F*-centers and the *V*-centers have similar generation characteristics. The concentration of these centers (measured by paramagnetic resonance) grows rapidly at first; electrons are trapped at already existing traps (for example, halide vacancies) and the holes are "self-trapped". When the electron traps are filled, the growth rate becomes smaller (Fig. 9). In contrast to this, the concentration of the *H*-centers grows slowly at the beginning of the irradiation and faster as the radiation damage proceeds. This production characteristic is typical for a defect which is produced entirely by the ionizing radiation, and which does not involve imperfections present prior to the irradiation. Consequently, the production rate of *H*-centers should not be determined by the concentration of unfilled electron traps, in contrast to the production rate of *V*-centers (self-trapped holes). This was confirmed by experiments with a KCl crystal doped with 0·1 mole per cent TlCl. The initial *V*-center production is enhanced by a factor of about 10^3, whereas the *H*-center production is almost the same as in a pure KCl crystal.

The ratio of the *V*-center concentration to the *H*-center concentration measured in pure KCl crystals at 20·3°K after 64 hr of (weak) X-irradiation at 20·3°K is about 0·7, according to Fig. 9. The same ratio, however, drops to about 0·46 when the crystal is irradiated at 4·2°K and then measured at 20·3°K. In contrast to this the ratio of *F*-center concentration to *H*-center concentration (again measured at 20·3°K) is almost unaffected when the temperature of X-irradiation is lowered from 20·3 to 4·2°K, although the absolute concentration of each of these centers is about 20 per cent smaller after irradiation at 4·2°K. These results suggest that *at very low temperatures F-centres and H-centers are created in pairs* and that the production of other traps becomes less important as the temperature is lowered.

(ii) *Thermal bleaching*

When, after X-irradiation at 20·3°K, the pure KCl crystal is warmed to 42°K for a few minutes and then remeasured at 20·3°K, the *V*-center resonance has disappeared and the *F*-center resonance is roughly 15 per cent weaker. The *H*-center resonance, however, has grown by about 40 per cent (Fig. 8b). This change is probably closely connected with the charge release observed by TEEGARDEN and MAURER[8] near 40°K in KCl crystals X-rayed at 35°K. The charges released are very probably electrons, because they annihilate the positively charged *V*-centers (self-trapped holes), which otherwise can be stable up to

* Note that the *V*-center resonance is not present in the spectra shown in Figs. 1a, 2, and 3a. These spectra were taken after bleaching of the *V*-centers (see Section 5(a) (ii)).

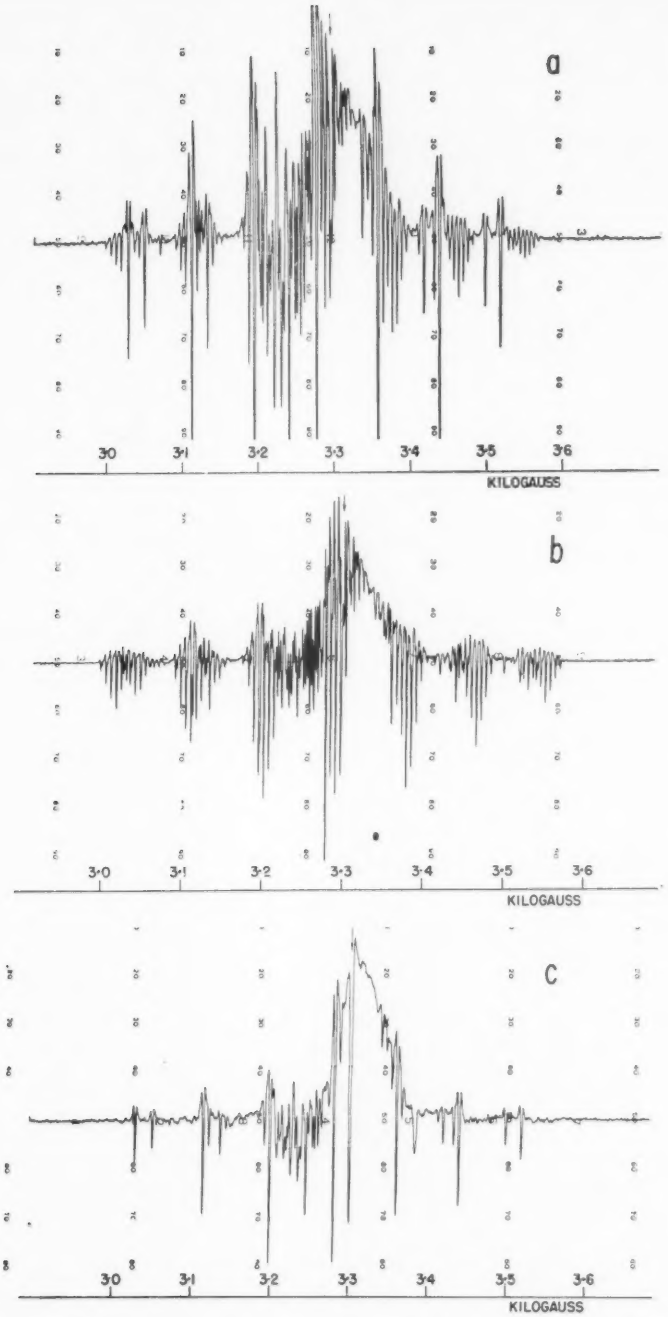

FIG. 8. Paramagnetic-resonance spectrum of a KCl crystal measured at liquid-hydrogen temperature with $H \| [111]$.

(a) After X-irradiation at liquid-hydrogen temperature prior to warming up: H-center + V-center + F-center.

(b) After subsequent warming to 42°K for a few minutes: H-center + F-center. (Gain approximately as in (a).)

(c) After subsequent warming to 58°K for a few minutes: V-center + F-center. (Higher gain than in (a) and (b).)

Derivative of dispersion measured at 9252 Mc/s.

205°K.[3,5]* The fact that the *H*-centers are not annihilated may indicate that they have no net positive charge. The increase of the *H*-center resonance, on the other hand, suggests that the trap that releases the electron is converted into an *H*-center in this process. A possible mechanism, of *H*-centers that have disappeared, whereas the decrease of the number of *F*-centers is possibly of the same order of magnitude.†

It seems that these changes coincide with the charge release observed by TEEGARDEN and MAURER[8] near 58°K. The fact that the optical

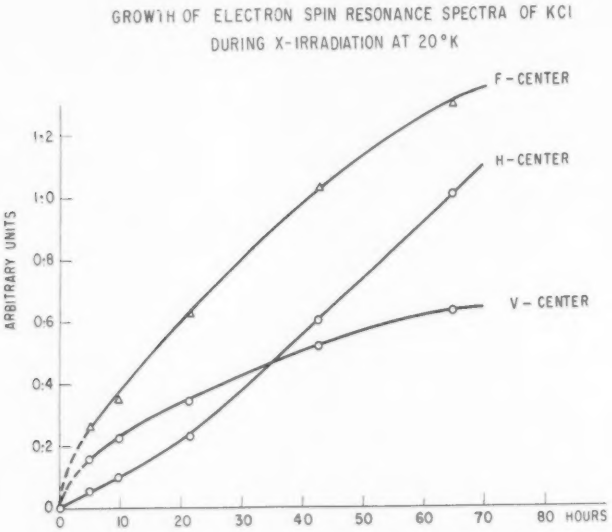

FIG. 9. Growth of the paramagnetic-resonance dispersion of the *F*-centers, *V*-centers, and *H*-centers upon X-irradiation of a virgin KCl crystal at liquid-hydrogen temperature. Arbitrary units. The scale factor is about the same for the *H*-centers and for the *V*-centers whereas the scale for the *F*-centers is compressed. Data for X-ray source: W-target 10 cm from crystal, filtering equivalent of 4 mm Al, 70 kV, 8 mA.

based on a model of the *H*-center, will be discussed in Section 6.

If the crystal is warmed up to 60°K for a few minutes and cooled again to 20·3°K, one finds that the *H*-center resonance has bleached completely. The *F*-factor resonance is reduced in intensity by roughly 15 per cent by this annealing process, but the *V*-center (self-trapped hole) resonance reappears with about one-sixth of its original intensity (see Fig. 9c). The number of these *V*-centers is, however, only about one-twelfth of the number

H-band bleaches near the same temperature suggests that our paramagnetic *H*-center might be identical with the optical *H*-center of these authors. It is known that the thermal bleaching of the optical *H*-band is connected with the growth of the V_1-band.[8,10] However, no new paramagnetic-resonance spectrum shows up after the *H*-center has been bleached thermally.

Another charge release was observed near 68°K.[8] We did not find a measurable change of the paramagnetic-resonance spectrum at this temperature.

* A similar situation was encountered in pure KCl X-rayed at 78°K.[3] In this case the *V*-centers (self-trapped holes) are annihilated at about 140°K by electrons released from some electron trap (possibly *F'*-centers).

† The saturation characteristics of the *F*-center resonance and of the *H*-center resonance are so different that we were unable to measure the concentration ratio of these two types of centers.

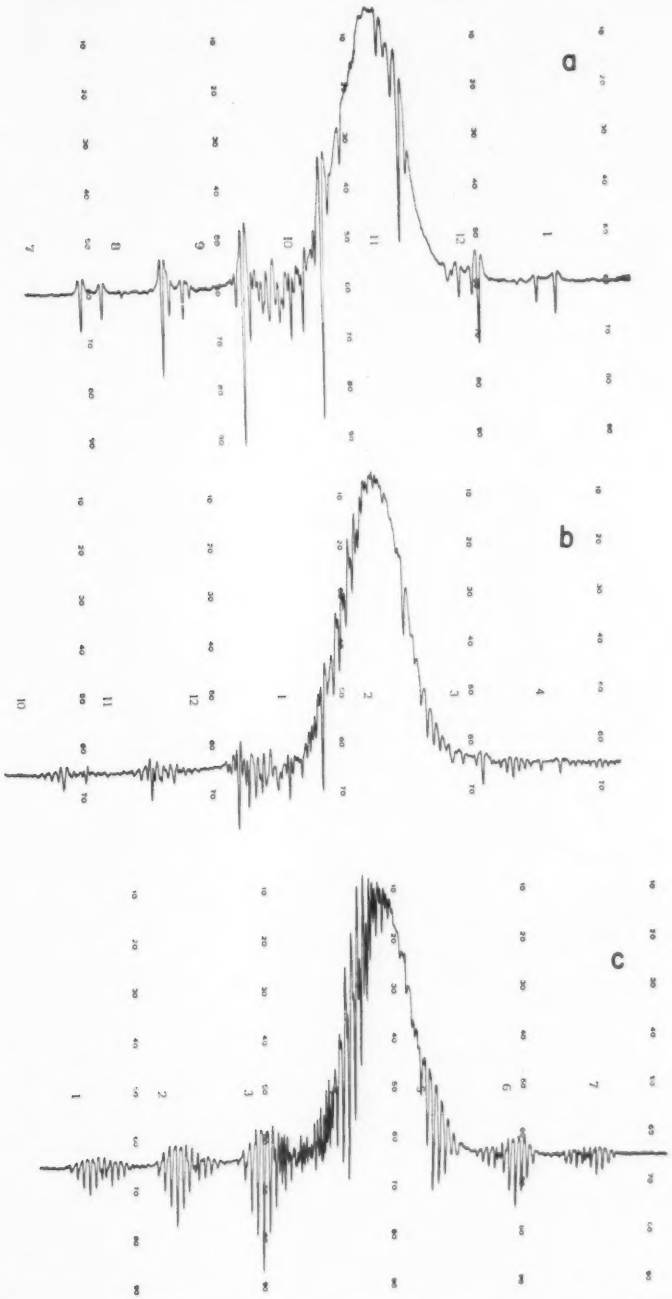

FIG. 10. Paramagnetic-resonance spectrum of a KCl crystal X-rayed at liquid-nitrogen temperature and then cooled to liquid-hydrogen temperature $H \| [100]$.

(a) Prior to irradiation with 3650 Å light.
(b) After irradiation with 3650 Å light for 400 sec.
(c) After total irradiation with 3650 Å light for 11,600 sec.

(iii) *Production of H-centers by light absorbed in the V_1-band*

TEEGARDEN and MAURER[8] discovered that the optical H-band can be generated in a KCl crystal containing V_1-centers* by light absorbed in the V_1-band at 35°K. In order to test whether our paramagnetic H-center has the same property, we creases at the same time, because the optical absorption of these centers is also close to 3650 Å (see Fig. 10b). However, the H-center resonance still grows at the same rate after all the V-centers (self-trapped holes) have been bleached, and finally, when saturation is reached, the concentration of H-centers is about three times the original con-

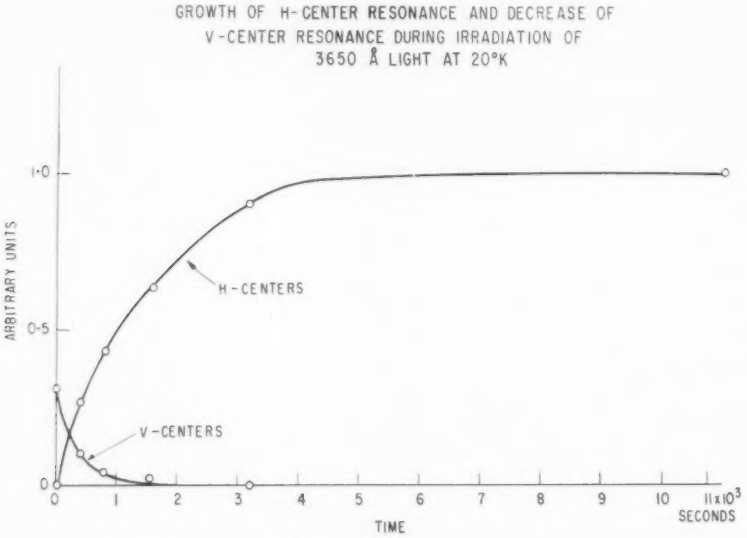

FIG. 11. Influence of 3650 Å light at liquid-hydrogen temperature on a KCl crystal that has been X-rayed at liquid-nitrogen temperature and then cooled to liquid-hydrogen temperature; measured by means of para-magnetic resonance. The H-center and V-center concentrations are plotted on roughly the same scale.

X-rayed KCl crystals at 78°K so that they contained V_1 centers[1] and then cooled them to 20·3°K. The paramagnetic-resonance spectrum shows the presence of V-centers (self-trapped holes) and F-centers after this treatment (Fig. 10a). (An electron spin resonance which might be due to V_1-centers was not found in the course of our work, although most experimental parameters were varied over a wide range. This suggests that the V_1-center may be diamagnetic.) If the crystal is then irradiated with light absorbed in the V_1-band (we used the 3650 Å light from a H 100-BL 4 lamp), the H-center resonance begins to appear. The V-center (self-trapped hole) resonance decentration of self-trapped holes (see Figs. 10c and 11). Thus it is not the self-trapped holes that are converted into H-centers by 3650 Å light, but another center, the V_1 center according to TEEGARDEN and MAURER.[8] The F-center resonance is not affected by this conversion.

The H-centers produced through this optical conversion bleach thermally at the same temperature ($\approx$ 58°K) as the H-centers produced by X-irradiation at 20·3°K. After this bleaching and recooling to 20·3°K, the H-centers can be regenerated by 3650 Å light, no matter whether they were produced originally by optical conversion or by X-irradiation at 20·3°K. Roughly 40 per cent are lost in every regeneration-bleaching cycle. At least part of this loss is due to the fact that the H-centers themselves bleach somewhat under irradiation by

* Note that the V_1-center is not identical with the previously mentioned V-center (self-trapped hole).[5,20] The structure of the V_1-center has not been established.

3650 Å light. Thus their optical absorption must be considerable at 3650 Å.

The influence of 3650 Å light is different for a crystal that has been X-rayed at 20·3°K and is kept at this temperature. The *H*-center resonance (which is already present under these conditions) does not grow upon irradiation of this light, but rather decreases (Fig. 12). This indicates that no V_1 centers are present in such a crystal, in agreement with optical investigations.[8,10] The *V*-centers (the optical absorption of which has a peak at 3700 Å)[5] bleach also, but not as rapidly as in the experiment summarized in Fig. 11.

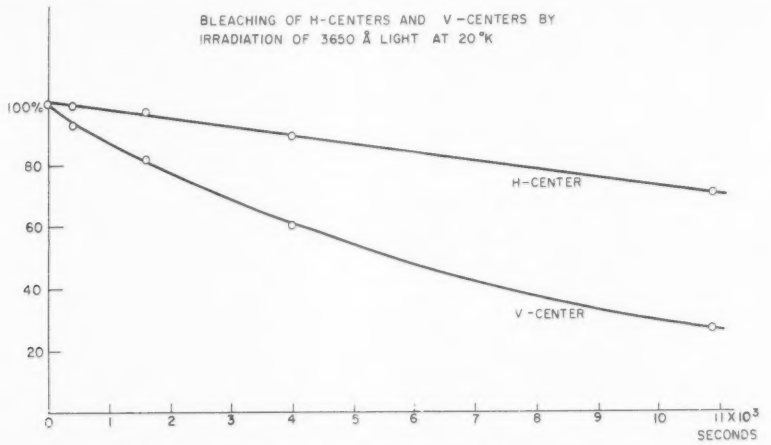

FIG. 12. Influence of 3650 Å light at liquid-hydrogen temperature on a KCl crystal that has been X-rayed and kept at liquid-hydrogen temperature; measured by means of paramagnetic resonance.

The results of all these resonance experiments parallel perfectly the results of the optical experiments of TEEGARDEN and MAURER.[8] *Thus the identity of our paramagnetic H-center with the optical H-center appears to be well established.*

The convertibility of V_1-centers into *H*-centers by 3650 Å light at 20·3°K provides the basis for a sensitive test for the presence of V_1-centers by means of paramagnetic resonance. This test is more sensitive than the detection of the optical absorption band, which is rather broad and overlaps other optical absorption bands. We used this test to find out whether or not all the *V*-centers bleach thermally during the charge burst observed by DUTTON and MAURER at 128°K.[21] It was found that about 80–90 per cent of the V_1-centers bleach if the crystal (X-rayed at 78°K) is kept near 128°K for about 30 min. Some V_1-centers, however, survive even after the crystal has been warmed up to 240°K. This result suggests that the thermal bleaching of V_1-centers at 128°K is not due to the thermal instability of the V_1-center as such, but involves also other kinds of centers.

(iv) *The influence of irradiation with F-light*

MARKHAM *et al.*[22] found that the irradiation with *F*-light of KBr crystals X-rayed and kept at 5°K bleaches not only the *F*-band but also the *H*-band. We have investigated a similar effect in KCl crystals X-rayed and kept at 20·3°K. Fig. 13 illustrates the decrease of the *F*-center, *V*-center, and *H*-center resonances upon irradiation with weak* *F*-light at 20·3°K. It is interesting to note that this effect was not present in KCl X-rayed at 4·2°K and then warmed to 20·3°K. Thus it is somewhat doubtful that the simultaneous bleaching of *F*-, *V*-, and *H*-centers by *F*-light is due to a mechanism involving tunneling between these centers. In crystals irradiated at a lower temperature, one would expect that *F*-type and *V*-type centers should be closer together, so that tunneling

* We used a 50-W incandescent lamp with a 5400 Å interference filter at a distance of about 10 cm from the crystal.

should become more probable as the temperature of X-irradiation is lowered.

(b) *Potassium Bromide*

The paramagnetic-resonance spectrum of pure KBr X-rayed and kept at 20·3°K reveals the presence of F-centers, H-centers, and V-centers (self-trapped holes), just as for KCl. If the crystal is X-rayed at 4·2°K instead of at 20·3°K, the ratio of V-center concentration to H-center concentration is reduced, as for KCl.

If the crystal is subsequently warmed to 40°K for a few minutes and then recooled to 20·3°K, the H-center resonance has completely disappeared. This behavior seems to contrast with the behavior of the optical absorption in the region of the H-band described by DUERIG and MARKHAM.[10] These authors warmed the crystal up to 78°K and observed at this temperature a slow decay of the optical absorption in the region of the H-band. However, a recent investigation by MARKHAM and KONITZER[10a] revealed that the H-band proper bleaches very fast below 40°K in *agreement* with our resonance experiments.

The thermal bleaching of the H-center between 20·3 and 40°K is connected with a decrease in the F-center concentration by about 15 per cent. After a further warm up to 78°K, the F-center concentration drops again by about 15 per cent, whereas the V-center concentration remains unaffected.

After annealing at 40°K, the H-centers can be regenerated by V_1-light* at 20·3°K. These regenerated H-centers bleach thermally between 20·3 and 40°K, just as do the H-centers originally generated by X-irradiation at 20·3°K. Regeneration of H-centers by V_1-light at 20·3°K is no longer possible after the temperature of the crystal has been raised to 78°K, in contrast to the case of KCl. Also V_1-light produces (at 20·3°K) no H-centers in KBr that has been X-rayed at 78°K. Thus it appears that the center in KBr that can be converted by V_1-light into the H-center bleaches thermally between 40 and 78°K. In contrast to this, the V_1-band produced by X-irradiation at 78°K bleaches thermally near 115°K.[21] There appear to be essentially two possibilities for explaining this discrepancy.

(a) The V_1-center obtained by thermal bleaching of H-centers is a different center than the V_1-center produced by X-irradiation at 78°K.

(b) The two types of V_1-centers are essentially the same; however, they are associated in different ways with some other center. The V_1-center obtained by thermal bleaching of the H-center is *very closely* associated with this other center. This close association makes possible the regeneration of H-centers by optical excitation of the V_1-center

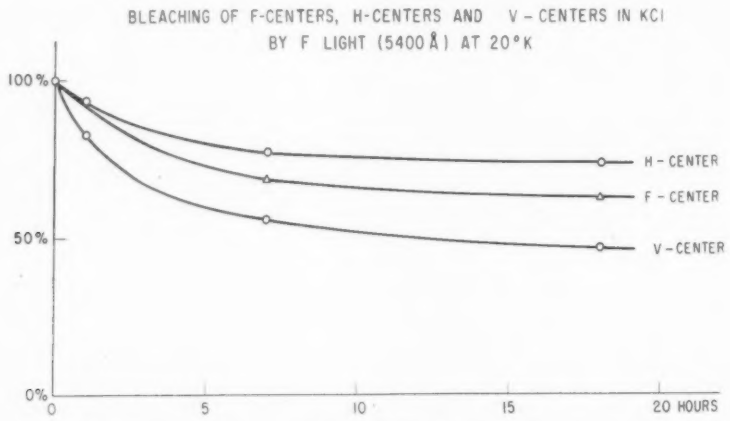

FIG. 13. Influence of weak F-light (5400 Å) at liquid-nitrogen temperature on a KCl crystal that has been X-rayed and kept at liquid-hydrogen temperature; measured by means of paramagnetic resonance.

* A-H6 mercury arc with Corning filter # 3389 and 4400 Å interference filter was used.

VOL.
9
1959

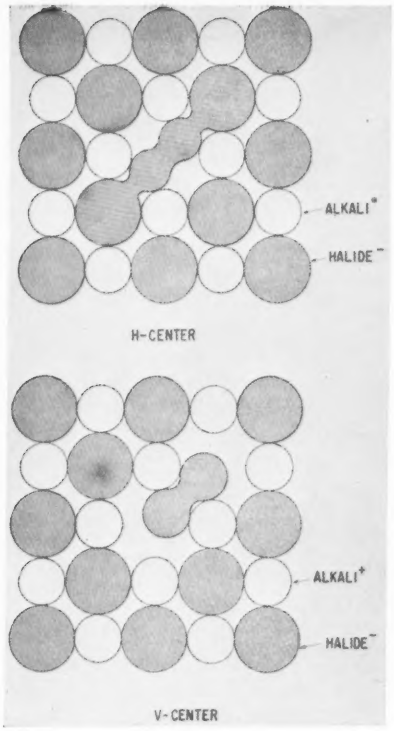

FIG. 14. Schematic models for the *H*-center and for the *V*-center (self-trapped hole). The ratio of the ionic radii in the figure corresponds to KCl.

[*facing p.* 90

VOL
9
195

at 20·3°K, but it is also responsible for the lower bleaching temperature of this V_1-center. The V_1-center produced by X-irradiation at 78°K, on the other hand, is less closely associated with this other center.

The explanation (b) appears more reasonable, because it does not require an essential difference in the behavior of KBr as compared to KCl.

(c) *Lithium Fluoride*

In LiF the *H*-center resonance is present after prolonged X-irradiation at 78°K, together with the *V*-center resonance and the *F*-center resonance.* The ratio of *H*-centers to *V*-centers depends upon the sample. But always it increases with increasing exposure to X-rays, as in KCl and KBr. Thermal bleaching occurs between 78 and 130°K. We have not made attempts to regenerate the *H*-center by light.

6. A MODEL FOR THE H-CENTER

(a) *Description of the Model*

The most important facts that an acceptable model of our paramagnetic *H*-center must explain can be summarized as follows:

(1) The *H*-center is essentially a halogen$_2^-$ molecular ion. The unpaired electron spin interacts strongly with two halogen nuclei 1 and 2, but in addition it interacts more weakly with two more halogen nuclei 3 and 4.

(2) The nuclei 1 and 2 are in positions equivalent to each other and so are nuclei 3 and 4.

(3) All four nuclei lie on a straight line along [110]. The center has orthorhombic symmetry with the axes $[110] = z'$, $[\bar{1}10] = x'$, and $[001] = y'$. Axial symmetry about z' is a good approximation for the hyperfine interaction with all four nuclei.

(4) The distance between the nuclei 1 and 2 is smaller for the *H*-center than for the *V*-center (self-trapped hole).

(5) The production of the *H*-center by X-rays does not involve traps that are present in the crystal prior to X-irradiation, but involves defects that are produced by the X-rays. Presumably *H*-centers and *F*-centers are produced in pairs.

(6) Electrons released in the crystal leave the *H*-center unaffected.

These facts lead us to propose the model for the *H*-center which is depicted very schematically in Fig. 14 and also is compared with the model for the *V*-center (self-trapped hole). The *H*-center can be described as a halogen$_2^-$ molecule-ion located in a halide vacancy. The resulting crowding accounts not only for the reduced internuclear distance as compared to the *V*-center, but also for the additional interaction of the unpaired electron with two more halide ions. The configuration might also be characterized as a "crowdion† stabilized by a hole". Chemically, the *H*-center is equivalent to an interstitial halogen *atom*. The *H*-center and the *F*-center are *complementary centers*; i.e. a region of undamaged crystal is restored if an *H*-center and an *F*-center are brought together.

(b) *Speculations Based on the H-center Model*

(i) *Production mechanism*

Our model for the *H*-center suggests that one of the mechanisms proposed by VARLEY[2] may be operative in the production of color centers by ionizing radiation at very low temperatures. For example, an *F*-center–*H*-center pair might be produced as follows. A halide ion becomes multiply ionized and, since it is now positively charged, it will be expelled from its original site. It can migrate because of its small size. Finally, it becomes neutralized, settles in an interstitial position, and thus forms an *H*-center. The electron which remains is trapped at the halide vacancy left behind; i.e. an *F*-center is formed together with each *H*-center. At very low temperatures this may be a predominant process. However, other processes cannot be neglected, as is indicated, for example, by the interesting release of charge in KCl near 42°K. On the basis of the observations described in Section 5(a) (ii) of this paper, one might speculate that below 42°K interstitial chloride *ions* are also present. These become unstable at 42°K and release an electron. Thus the interstitial ion transforms into an *H*-center, and the released electron annihilates a self-trapped hole. A corresponding process was not observed either in KBr or in LiF. It is to be expected that interstitial halide ions would be less stable in these salts than in KCl because of their relatively large size.

* The *F*-center resonance does not show up in the absorption spectra because of saturation.

† The term "crowdion" was introduced by PANETH.[22]

(ii) *Bleaching and regeneration*

The experiments with KCl and KBr indicate that the *H*-center transforms upon warming into another center, which appears to be non-paramagnetic and presumably gives rise to the optical V_1-band. This V_1-center is closely related to the *H*-center, since through an optical-excitation process it can be reconverted at 20·3°K into the *H*-center. Thus, on the basis of the model of the *H*-center, it should be possible to guess the structure of the V_1-center.

As a possible mechanism for the thermal bleaching of the *H*-center, one might visualize the following. The thermal instability of the *H*-center is partially due to the strains associated with the crowding. The strain energy, however, can be reduced substantially through the release of an electron from this center, because the resulting halogen$_2$ molecule is smaller than the halogen$_2^-$ molecular ion. In KCl, for example, a Cl_2 molecule fits into a negative-ion vacancy without straining the lattice. The molecule can even rotate without much hindrance. Therefore, this center is unlikely to give rise to dichroic effects except perhaps at very low temperatures. LAMBE and WEST[20] found no dichroic effects in the V_1-band at 77°K. Since the *H*-center can be regenerated by optical excitation of the V_1-center, we must assume that the electron that was released from the *H*-center was trapped only a few lattice spacings away. The resonance spectrum of the *H*-center does not indicate a lowering of the symmetry due to the proximity of the empty trap. Hence, it is likely that this trap is *neutral*. The decrease of the *F*-center resonance which seems to be connected with the thermal bleaching of the *H*-center suggests that the trap close to the *H*-center is an *F*-center, which converts into an F'-center by capturing the electron released from the *H*-center. According to this picture the regeneration of *H*-centers by V_1-light should be connected with an increase of the *F*-center concentration, which was not observed. In KCl the *F*-center resonance is almost unaffected by the regeneration process, and in KBr it even decreases somewhat. This, however, may be due to the overlap of the V_1-band with other absorption bands (e.g. with the band due to the self-trapped holes). Thus the process described above may not be the only one occurring when the crystal is exposed to V_1-light.

Acknowledgements—We thank W. D. COMPTON and C. C. KLICK for communicating to us prior to publication the results of their optical investigation of the *H*-center.[9] It was their work which led us to undertake the research described in this paper.

We are also indebted to W. W. PIPER for access to the results of his computation of the Br^- wavefunctions, and to J. J. MARKHAM for communication of experimental results concerning the thermal bleaching of the *H*-band in KBr.

REFERENCES

1. SEITZ F., *Rev. Mod. Phys.* **26,** 7 (1954).
2. VARLEY J. H. O., *J. Nuclear Energy* **1,** 130 (1954).
3. CASTNER T. G. and KÄNZIG W., *J. Phys. Chem. Solids* **3,** 178 (1957).
4. WOODRUFF T. O. and KÄNZIG W., *J. Phys. Chem. Solids* **5,** 268 (1958).
5. DELBECQ C. J., SMALLER B. and YUSTER P. H., to be published.
6. COHEN M. H., KÄNZIG W. and WOODRUFF T. O., *Phys. Rev.* **108,** 1096 (1957).
7. KÄNZIG W. and WOODRUFF T. O., *Phys. Rev.* **109,** 220 (1958).
8. TEEGARDEN K. and MAURER R. J., *Z. Phys.* **138,** 284 (1954).
9. COMPTON W. D. and KLICK C. C., *Phys. Rev.* **110,** 349 (1958).
10. DUERIG W. H. and MARKHAM J. J., *Phys. Rev.* **88,** 1043 (1952).
10a. MARKHAM J. J. and KONITZER J. D., private communication.
11. STERNHEIMER R., *Phys. Rev.* **86,** 316 (1952).
12. PRATT G. W., *Phys. Rev.* **102,** 1303 (1956).
13. HEINE V., *Phys. Rev.* **107,** 1002 (1957).
14. STERNHEIMER R., *Phys. Rev.* **84,** 244 (1951).
15. HARTREE D. R., *Proc. Roy. Soc.* **A151,** 96 (1935).
16. HARTREE D. R. and HARTREE W., *Proc. Roy. Soc.* **A156,** 45 (1936).
17. PIPER W. W. To be published.
18. CASTNER T. G., KÄNZIG W. and WOODRUFF T. O., *Suppl. Nuovo Cim.* **7,** 612 (1958).
19. HERZBERG G., *Spectra of Diatomic Molecules* p. 239. New York (1950).
20. LAMBE J. and WEST E. J., *Phys. Rev.* **108,** 634 (1957).
21. DUTTON D. and MAURER R., *Phys. Rev.* **90,** 126 (1953).
22. MARKHAM J. J., PLATT R. T. and MADOR I. L., *Phys. Rev.* **92,** 579 (1953).
23. PANETH H. R., *Phys. Rev.* **80,** 708 (1950).
24. KING J. G. and JACCARINO V., *Phys. Rev.* **94,** 1610 (1954).
25. RADFORD H. E., *Bull. Amer. Phys. Soc.* **3,** 325 (1958).
26. DAVIS L., FELD B. T., ZABEL C. W. and ZACHARIAS J. R., *Phys. Rev.* **76,** 1076 (1949).

VOL
9
195

Superconductivity of Nb_3Al

(*Received* 30 *June* 1958; *in revised form* 19 *September* 1958)

A NUMBER of intermetallic compounds crystallizing in the β-Wolfram structure have been discovered in recent years. Many of these are superconducting and include almost all of the known superconductors whose transition temperature is greater than 15°K.[1,2]

The only reported β-Wolfram compound which contains Al is Mo_3Al.[3] It is not superconducting above 1°K, but a search for β-Wolfram compounds between other transition metals and Al resulted in the discovery of two compounds of Nb and Al which are superconducting, Nb_3Al which has the β-Wolfram structure, and a compound of Nb and Al which has been tentatively identified as a sigma phase.

The ingots were made in a small helium arc furnace using various compositions between 20 and 30 at. per cent of Al. The loss of weight during melting averaged about 3·5 per cent, a sizeable fraction if the loss were all Al, since Nb_3Al contains only 8·8 per cent Al by weight. However, chemical analyses of four of the ingots which yielded the β-Wolfram structure gave the following atomic percentages of Al—22·57, 24·89, 25·06, and 25·38 per cent $\pm$ 1 per cent. The sigma phase compounds are believed to have higher percentages of Al and were not analysed in detail.

The β-Wolfram materials had a range of superconducting transition temperatures from 16·8° to 18°K while the σ phase materials ranged from 7° to 12°K.

It is a great pleasure to thank Dr. E. A. WOOD and Mrs. V. B. COMPTON for their X-ray diffraction work, which is separately reported[4] and Dr. B. T. MATTHIAS for help with the superconductivity measurements, as well as all three for much helpful discussion.

Bell Telephone Laboratories E. CORENZWIT
Murray Hill
New Jersey

REFERENCES

1. HARDY G. F. and HULM J. K., *Phys. Rev.* **89**, 884 (1953).
2. MATTHIAS B. T., GEBALLE T. H., GELLER S., and CORENZWIT E., *Phys. Rev.* **95**, 1435 (1954).
3. NORTHCOTT L., *Metallurgy of the Rarer Metals*, Vol. 5 *Molybdenum*. Academic Press Inc., New York (1956).
4. WOOD E. A., COMPTON V. B., MATTHIAS B. T., and CORENZWIT E., *Acta Cryst.* **11**, 604 (1958).

Low-field electrical breakdown in *n*-indium phosphide

(*Received* 27 *August* 1958)

A REVERSIBLE low-field electrical breakdown has been observed at 4·2°K in *n*-type InP crystals. The *I–V* characteristic of a typical crystal exhibiting the effect is shown in Fig. 1. It is seen that at V_c the

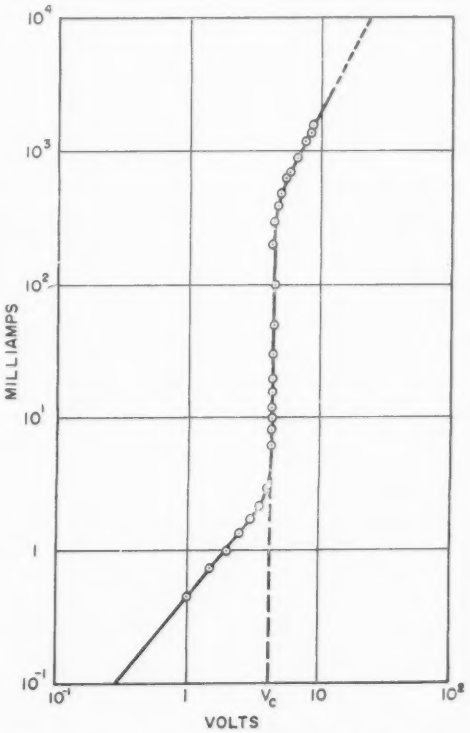

FIG. 1. Current/voltage characteristic of an *n*-InP single crystal at 4·2°K. The electric field corresponding to V_c is 9·1 v/cm.

current increases by two orders of magnitude without any further increase in voltage. This behavior is interpreted as the impact-ionization phenomenon previously found in germanium[1] and p-InSb.[2] The electric field corresponding to the voltage V_c was 9·1 V/cm. Measurements were made by a pulse technique* in order to avoid heating effects that occurred when the continuous power dissipation in the crystal exceeded about 5 mW. At the lower values of current (pre-breakdown region), d.c. measurements confirmed the pulse values. Data taken in the reversed current direction gave completely similar results to those shown in Fig. 1.

Prior to the breakdown there is already a marked departure from Ohm's law. The data in Fig. 1 show that $I \propto V^{1.22}$ in the pre-breakdown region. Such behavior is probably the result of the energy-dependence of the ionized-impurity scattering, which probably controls the mobility at 4·2°K.

For currents above 3×10^2 mA, the voltage began to increase to values greater than V_c. This is qualitatively attributed to the strong recombination processes which become dominant when the free-carrier concentration becomes high. In order to increase the current further, more energy would have to be supplied to the carriers. In that region (extended as a dashed line in Fig. 1) $I \propto V^2$. Such a departure from Ohm's law might be due to ionized-impurity scattering causing an increasing mobility as the carriers became "hotter".

Impact ionization was observed in both polycrystalline and single-crystal specimens of n-InP. One crystal of n-InP did not show impact ionization at 4·2°K. It had an electron concentration of 3×10^{16}/cc and a mobility of 3400 cm²/V-sec at 290°K. For this sample the resistance increased only by a factor of three as the temperature was decreased to 4·2°K. It is believed that it was degenerate at the low temperature. The data shown in Fig. 1 were taken with a single crystal of material† that had a net electron concentration of 6×10^{15}/cc and a Hall mobility of 4500 cm²/V-sec at 290°K. At 77°K the mobility was 2×10^4 cm²/V-sec, while the electron concentration was $5 \times \times 10^{15}$/cc. From resistivity (ρ) versus temperature (T) data taken down to 25°K, there appeared to be an impurity activation energy of $2{\cdot}2 \times 10^{-2}$ eV. However, Hall measurements were taken only at 77 and 4·2°K. At 4·2°K the Hall coefficient gave an electron concentration of 2×10^{15}/cc and a Hall mobility of 100 cm²/V-sec. This is indicative of impurity-band effects such as have been observed in germanium[3] and p-InSb.[4] Further support for this was obtained from the change to a smaller slope of the log ρ versus $1/T$ curve at temperatures below 25°K. The apparent activation energy from the temperature region 4·2—25°K was $1{\cdot}9 \times 10^{-3}$ eV.

At 4·2°K, in the pre-breakdown region, this crystal showed a negative magnetoresistance which was independent of the direction of the magnetic field. A field of 6400 Oe increased the breakdown voltage by only about 5 per cent.‡ These characteristics are similar to those found in p-InSb.[2] It seems that in the III–V compound semiconductors there is an intimate connection between impact-ionization and impurity-band effects. Details of that connection are not yet clearly understood. It is hoped that future experiments with purer crystals may reveal a specific model to explain the existing results.

RCA Laboratories M. C. STEELE
Princeton, N.J.

VOL. 9 1959

REFERENCES

1. SCLAR N., BURSTEIN E., TURNER W. J., and DAVISSON J. W., *Phys. Rev.* **91**, 215A (1953).
2. BRAY R., *Phys. Rev.* **100**, 1262A (1955).
3. FRITZSCHE H., *Phys. Rev.* **99**, 406 (1955).
4. FRITZSCHE H. and LARK-HOROVITZ K., *Phys. Rev.* **99**, 400 (1955).

* Pulses of 2 μsec duration and 50 c/s repetition rate were used for most of the data. In order to ensure that heating effects were absent, the repetition rate was increased to 500 c/s without any change in the results being observed.

† All the InP used was supplied by K. WEISER. The author wishes to thank him for making these experiments possible.

‡ The author wishes to thank M. GLICKSMAN for having made these magnetoresistance measurements at 4·2°K.

ANNOUNCEMENT

SYMPOSIUM ON MILLIMETER WAVES

March 31 and April 1, 2, 1959

Millimeter Waves will be the subject of the ninth international symposium of the Polytechnic Institute of Brooklyn, Microwave Research Institute, to be held in New York City on March 31, April 1, 2, 1959, under the co-sponsorship of the Air Force Office of Scientific Research, U.S. Army Signal Research and Development Laboratory, Office of Naval Research, and the Institute of Radio Engineers. The symposium is intended to highlight the present state of research in, and applications of, millimeter wave technology. Accordingly, the program will be devoted to invited and contributed papers treating the generation, transmission, control, measurement, and detection of millimeter wave energy. In addition, source material and significant advances in basic supporting fields will be summarized in tutorial papers chosen from appropriate fields in physics and engineering. A more detailed indication of topics which fall within the scope of the symposium is given below.

Interaction of millimeter waves and materials

Hall effect circuits, circuits utilizing ferromagnetic and paramagnetic resonances, cryogenic circuits, ferrite devices, equivalent circuit representations for active and anisotropic structures.

Solid state active millimeter circuits

Maser and parametric amplifiers and oscillators, solid state mixers and frequency multipliers, duplexing and switching circuits, active matching elements, discontinuities in active systems.

Millimeter electron tubes

Oscillators and amplifiers such as klystrons, magnetrons, backward wave oscillators, etc., Cerenkov millimeter sources, relativistic electron beam harmonic generators and radiators, millimeter-wave interaction with plasmas.

Radiating circuits and antennas

Antennas for millimeter waves, equivalent circuits for radiating discontinuities, radio astronomy.

Coupled line, multimode, and non-conventional transmission systems

Periodic structures in multimode waveguide, anisotropic media, surface waveguides, quasi-optic techniques, equivalent circuits for discontinuities in multimode or non-conventional waveguides.

Millimeter components

Filters, transformers, directional couplers, rotary joints quasi-optic component techniques.

Millimeter circuit measurement techniques

New measurement methods, measurement techniques for non-reciprocal and active circuits, diagnostic measurements of plasmas with millimeter waves.

The closing date for submission of papers and/or 100 word abstracts is January 30, 1959. All correspondence should be addressed to:

Professor HERBERT J. CARLIN
Microwave Research Institute
55 Johnson Street
Brooklyn 1, New York

PAPERS TO BE PUBLISHED IN FUTURE ISSUES

T. Riste, K. Blinowski and J. Janik: Spin fluctuation scattering of neutrons in magnetite.

H. C. Nash and C. S. Smith: Single crystal elastic constants of lithium.

R. I. Bate, R. K. Willardson and A. C. Beer: Transverse magnetoresistance and Hall effect in N-type InSb.

N. T. Melamed: Energy transfer in ZnS : Cu : In phosphors.

G. H. Jonker: Analysis of the semiconducting properties of cobalt ferrite.

T. P. Hoar and N. F. Mott: A mechanism for the formation of porous anodic oxide films on aluminium.

A. Wold and R. J. Arnott: Preparation and crystallographic properties of the systems $LaMn_{1-x}Mn_xO_{3+\lambda}$ and $LaMn_{1-x}Ni_xO_{3+\lambda}$.

R. E. Schmunk and C. S. Smith: Pressure derivatives of the elastic constants of aluminium and magnesium.

H. Ehrenreich: Transport of electrons in intrinsic InSb.

H. A. Klasens: The temperature dependence of the fluorescence of photoconductors.

S. W. Barber and B. Martin: A heat capacity function with velocity dispersion for isotropic solids.

H. J. Hrostowski and R. H. Kaiser: The solubility of oxygen in silicon.

S. Geller and M. A. Gilleo: The effect of dispersion corrections on the refinement of the yttrium–iron garnet structure.

W. F. Love: Hall effect in Cu and Cu_3Au at low temperatures.

H. Meyer and P. L. Smith: The heat capacities of seven rare earth ethylsulphates at low temperatures.

H. Meyer: Thermal and magnetic properties of praseodymium ethylsulphate below 1°K.

F. Moser, N. R. Nail and F. Urbach: Optical absorption studies of the volume photolysis of large silver chloride crystals.

R. S. Knox: Exciton states in rare gas crystals.

R. S. Knox: Exciton states in crystalline argon.

G. J. Wolga and M. W. P. Strandberg: Hyperfine interactions in *F*-center paramagnetic-resonance spectra in LiF and NaF.

R. J. Weiss and A. S. Marotta: Spin dependence of the resistivity of magnetic metals.

S. Zwerdling, B. Lax, K. J. Button and L. M. Roth: Oscillatory magneto-absorption in gallium antimonide.

W. D. Lawson, S. Nielsen, E. H. Putley and A. S. Young: Preparation and properties of HgTe and mixed crystals of HgTe–CdTe.

A. W. Hornig, R. C. Rempel and H. E. Weaver: Electron paramagnetic resonance in single crystals of $BaTiO_3$.

A. Michels, J. van Eck, S. Machlup and C. A. ten Seldam: Pressure dependence of the resistivity of germanium.

S. Wiederhorn and H. G. Drickamer: The effect of pressure on the near ultraviolet spectra of some fused ring aromatic crystals.

H. Sato, A. Arrott and R. Kikuchi: Remarks on magnetically dilute systems.

VOL
9
195

J. Phys. Chem. Solids Pergamon Press 1959. Vol. 9. pp. 97–99. Printed in Great Britain.

A MECHANISM FOR THE FORMATION OF POROUS ANODIC OXIDE FILMS ON ALUMINIUM

T. P. HOAR* and N. F. MOTT†

* Department of Metallurgy, University of Cambridge

† Department of Physics, University of Cambridge

(*Received* 18 *August* 1958)

Abstract—It is shown that, in order to account for the formation of porous anodic oxide films on aluminium, it is necessary to assume that oxygen as well as aluminium is capable of diffusing through the compact part of the film. A detailed discussion of the mechanism is given.

VOL. 9 959

THE purpose of this note is to propose a mechanism for the formation of anodic oxide films on aluminium in an acid bath, under conditions such that a thick porous film is produced. The discussion is based on the review of the experimental evidence given by HOAR.[1]

When aluminium is treated anodically in solutions of sulphuric, chromic and certain other acids, a film of the form shown in Fig. 1 is formed. A

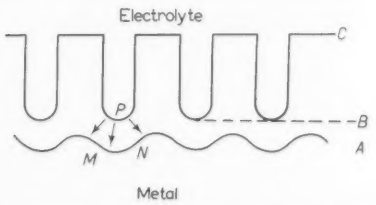

FIG. 1. Arrows show the path of oxygen through compact film.

compact film AB, of about the same thickness as that formed at the same bath voltage in non-acid (e.g. borate) solutions, is formed initially, after which a much thicker porous film BC continues to grow while a proportion of the metal oxidized appears as Al^{3+}_{aq} in the acid solution.

A theory of the compact film was proposed by VERWEY[2] and discussed further by CABRERA and MOTT,[3] DEWALD,[4–6] BEAN, FISHER and VERMILYEA[7] and others. All agree that aluminium ions pass through the film and neutralize oxide ions formed at the interface between oxide and electrolyte. It is generally agreed, too, that the probability per unit time that an ion makes a jump (i.e. moves into an interstitial position in the oxide, or from one interstice to another) is of the form

$$\nu \exp\{-(W-qaF)/kT\}, \qquad (1)$$

where ν is its vibration frequency, W is an activation energy, q the ionic charge, a of the order of 2A and F the field in the oxide film where the jump is made. There is uncertainty (DEWALD[6]) about whether the rate-determining step of the overall process is that of pulling the ion out of the metal into an interstitial position in the oxide, or pulling an ion out of the oxide lattice itself, leaving a mobile vacancy and a mobile interstitial ion, or pulling an interstitial ion from one interstice to another. This need not concern us here.

In a borate bath the formation of an oxide film at constant voltage proceeds only until F drops so that the rate given by (1) is very small. In the acid bath the essential points that have to be explained are:

(a) From the bottom of the pores some *oxygen* must pass through the film. Only thus can we explain a reaction initiated at the bottom of the pores which makes the porous film *as a whole* grow thicker, so that there is an increasing separation between the metal and the surface A in Fig. 1. The suggested path of the oxygen is shown in Fig. 1 (PM, PN).

(b) At the same time the acid must dissolve the oxide at the bottom of the pores, keeping the thickness of the compact film constant. Various authors have suggested that this may occur at a sufficient rate because the base of the pore will become hot; we shall offer an alternative explanation.

Our explanation of both (a) and (b) is based on the following consideration. If Al_2O_3 is in contact with an acid, solution of the oxide involves the passage of the Al^{3+} ions into the electrolyte and the combination of the oxide ions with hydrogen ions to form water. This process, as has been pointed out by many authors, is slow at ordinary temperatures but could be accelerated if the electrolyte is hot; but, as we have stated above, it is in any case not sufficient to explain the observed phenomena. We suggest the following. Fig. 2

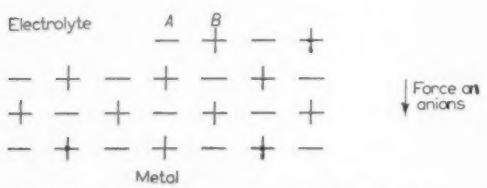

FIG. 2. Oxide surface in contact with electrolyte.

shows schematically a portion of the oxide in contact with the electrolyte; we represent it as crystalline, so that the process of solution involves the successive removal from a kink site of anions (A) and cations (B). We consider that the (large) anion O^{2-} cannot normally move in the reverse direction—i.e. into an interstitial position in the oxide and thence through the film. But at the base of the pores there are two factors that will aid the transfer of oxygen through the film:

(a) A high field pulling the anions in this direction.

(b) The presence in the acid of hydrogen ions, which may well lead to the production at A of a hydroxyl ion instead of an oxide ion,

$$O^{2-}+H^{+} \rightleftharpoons OH^{-}.$$

The energy for movement into an interstitial position and thence through the oxide is likely to be much smaller for the small singly charged hydroxyl ion than for the large doubly charged oxide ion. Under the influence of the high field, it will move through the oxide and neutralize Al^{3+} formed at the metal/film interface. If oxide rather than hydroxide is the final product, positive hydrogen ions could then be released and move back to the electrolyte, perhaps by proton transfer between the lattice O^{2-} ions (FEITKNECHT *et al.*[8–11]; HOAR[12]; JONES and WYNNE-JONES[13]).

During the growth of the porous film, then, two processes are going on in the region of P in Fig. 1 at such a rate as to keep the compact film thickness constant there. These are:

(1) Aluminium ions from the area MN move towards P and neutralize O^{2-} as in the formation of compact films in a non-acid bath.

(2) Aluminium ions go into solution at P and the corresponding anions move through the oxide film as OH^{-}, neutralizing Al^{3+} ions formed from the metal at the interface MN (Fig. 1). This will tend to make the bottom of the pore approach *closer* to the metal, because the oxide ions from the bottom of the pore are spread over a bigger area MN.

The rates of the two processes will depend on the thickness of the film in different ways. If the field F were constant through the oxide film, we should have for the rate of process (1), since $q = 3e$,

$$\nu \exp\{-(W_1-3ea_1F)/kT\},$$

where W_1, a_1 are the relevant quantities for the interstitial aluminium ions; while for the rate of transfer of the singly charged OH^{-} we should similarly have

$$\nu \exp\{-(W_2-ea_2F)/kT\}.$$

If $W_2 < W_1$ and $a_2 \simeq a_1$, then for some value of the field, and hence (for given applied voltage) for some value of the film thickness, these two rates will be equal. It should be emphasized that both these processes give the rate of transfer of an ion across an interface, and that once so transferred it moves through the oxide comparatively easily, so that no space charge is set up.

Any quantitative analysis, however, will be complicated by the fact that, as Fig. 1 shows, the field strength must be greater at P than at MN. In fact the proposed mechanism will keep the pores open; if the curvature of the bottom of a pore becomes too great, the field will increase there and as a consequence oxide will be decomposed more

quickly, the metal ions going into solution and the OH^- ions into the oxide.

REFERENCES

1. HOAR T. P., "The anodic behaviour of metals", *Modern Aspects of Electrochemistry* (Edited by J. O'M. BOCKRIS) Vol. II, in press. Butterworths, London (1958).
2. VERWEYE J. W., *Physica* **2,** 1059 (1935).
3. CABRERA N. and MOTT N. F., *Rep. Progr. Phys.* **12,** 163 (1948).
4. DEWALD J. F., *Acta Met.* **2,** 340 (1954).
5. DEWALD J. F., *J. Electrochem Soc.* **102,** 1 (1955).
6. DEWALD J. F., *J. Phys. Chem. Solids* **2,** 55 (1957).
7. BEAN C. P., FISHER J. C., and VERMILYEA D. A., *Phys. Rev.* **101,** 551 (1956).
8. FEITKNECHT W. and MARTI W. *Helv. Chim. Acta.* **28,** 129 (1945).
9. FEITKNECHT W. and KELLER G., *Z. anorg. Chem.* **262,** 61 (1950).
10. FEITKNECHT W. and ZBINDEN H, *Chimia* **5,** 110 (1950).
11. CHRISTEN H. R., FEITKNECHT W., and STUDER H. *Z. anorg. Chem.* **283,** 88 (1956).
12. HOAR T. P., *J. Inst. Met.* **72,** 436 (1946).
13. JONES E. and WYNNE-JONES W. F. K., *Trans. Faraday Soc.* **52,** 1260 (1956).

VOL.
9
1959

J. Phys. Chem. Solids Pergamon Press 1959. Vol. 9. pp. 100–112. Printed in Great Britain.

PRESSURE DERIVATIVES OF THE ELASTIC CONSTANTS OF ALUMINUM AND MAGNESIUM

R. E. SCHMUNK* and CHARLES S. SMITH

Case Institute of Technology, Cleveland, Ohio

(*Received* 19 *September* 1958)

Abstract—The pressure derivatives of the elastic stiffness constants of aluminum and magnesium have been measured over a pressure range from 0 to 6500 bars, by a modified ultrasonic pulse-echo method. The values found are:

	dC/dP	dC'/dP	dB_s/dP
Al	2·31	1·62	5·19

	dC_{11}/dP	dC_{33}/dP	dC/dP	dC'/dP	dC_H/dP
Mg	6·11	7·22	1·58	1·36	13·7

The notation $C = C_{44}$, $C' = (C_{11}-C_{12})/2$, $B_s = (C_{11}+2C_{12})/3$, and $C_H = C_{11}+C_{12}+2C_{33}-4C_{13}$ has been used. The pressure data for aluminum have been interpreted in terms of LEIGH's theory for the elastic stiffnesses themselves, and the magnesium data in terms of the similar theory of REITZ and SMITH. Variation of the effective charge density at the boundary of the atomic polyhedron under volume strain causes the electrostatic contribution to the shear stiffnesses to vary approximately as r^{-5} instead of r^{-4} for both metals. Electron transfer from states overlapping one type of Brillouin-zone face to states overlapping another type of face under volume strain contributes appreciably to the variation of the Fermi shear-stiffness contribution with pressure.

1. INTRODUCTION

CONTRIBUTIONS to the fundamental shear stiffnesses of aluminum have been suggested by LEIGH[1] in a theoretical calculation which accounts for the observed values of the shear stiffnesses in that metal. The anisotropy ratio of the electrostatic contribution to the shear stiffnesses, $\{2C_{44}/(C_{11}-C_{12})\}_{el}$, has a value of 8·9, the same as for face-centered cubic monovalent metals. Because of the large separation between ion-cores in the crystal, the short-range repulsive interaction makes a negligible contribution to the shear stiffnesses. The low value of the anisotropy ratio of the observed shear stiffnesses, 1·22, is accounted for by the Fermi contribution, which, in fact, has a negative anisotropy ratio.

REITZ and SMITH[2] extended LEIGH's calculation to include crystals of lower symmetry, and their results were used to account for the observed values of the shear stiffnesses of pure magnesium. Contributions to the shear stiffness of magnesium arise from changes in the electrostatic and Fermi energies of the crystal as a function of strain, in the same way as for aluminum.

It is expected that contributions to the pressure derivatives of the elastic stiffnesses would arise from the same two sources. The theoretical electrostatic and Fermi contributions to the shear stiffnesses contain electron parameters which were adjusted in physically plausible ways to account for the stiffnesses and for other physical data. These contributions, as well as the parameters, must depend on the volume of the crystal in a plausible way. Thus, measurement of the pressure derivatives of the elastic stiffnesses of aluminum and

* Now at Phillips Petroleum Company, Atomic Energy Division, Idaho Falls, Idaho.

magnesium enables one to test further the models of LEIGH and of REITZ and SMITH, and to shed further light on the location of the electrons in real and crystal momentum space.

Previous measurements had been made on the pressure variation of the elastic stiffnesses of aluminum by LAZARUS.[3] These measurements have been repeated, using the ultrasonic pulse-echo method with modifications, and arranging to measure *directly* both of the shear stiffnesses of theoretical interest, which LAZARUS was not able to do. The pressure variations of the five elastic stiffnesses of magnesium have also been measured, again with the experimental arrangement emphasizing the quantities of theoretical interest.

2. EXPERIMENTAL PROCEDURE

(a) *Aluminum*

The high-pressure system that was used for the present experiment was developed by W. B. DANIELS of this laboratory.[4,5] There have been no changes in the system since the previously reported work.

The aluminum single crystal on which measurements have been made was purchased from the Virginia Institute for Scientific Research. This crystal was 6 in long by $\frac{5}{8}$ in. in diameter and was oriented to within 2° of [110]. Specimens of desired length were cut by means of a water-cooled abrasive wheel, with the crystal held close to the point of cut-off in a brass collet chuck. Acoustic surfaces were prepared on the specimens by means of the lapping technique used previously in this laboratory.[5,6] Cold work on the acoustic surfaces was reduced as much as possible by etching.

The 10-mc quartz transducers used for the ultrasonic measurements were cemented to the acoustic surface of the aluminum specimens by polythylene used in the manner described by DANIELS.[5] An electrode was painted directly on the transducer with du Pont 4817 silver conducting paint. The differential compressibility between the quartz transducer and the crystal specimen is small in the case of aluminum. This was confirmed experimentally by the fact that the quartz transducers did not crack with the application of hydrostatic pressure as they had done in previous work with copper, silver, and gold, where the differential compressibility is large.[5]

The velocities and their changes with pressure were measured for the longitudinal wave and two shear waves in aluminum, using the ultrasonic pulse-echo method. The ultrasonic gear had been modified previously[7] in such a way that the unrectified echo pulses were observed on the oscilloscope. By identifying a particular cycle in the 10-mc structure of an echo pulse, as one went from one echo to the next, and measuring the time difference between these cycles, it was possible to obtain a transit time for which no end correction was necessary. This procedure is not unambiguous, but the velocities determined were verified by measurements on crystals of different length. The measurements are also in agreement with determinations made in this laboratory some time ago on aluminum in which rectified echo pulses were used, for which a transit-time correction was necessary.[8]

The method used to take data on the change of transit time with pressure was to measure the

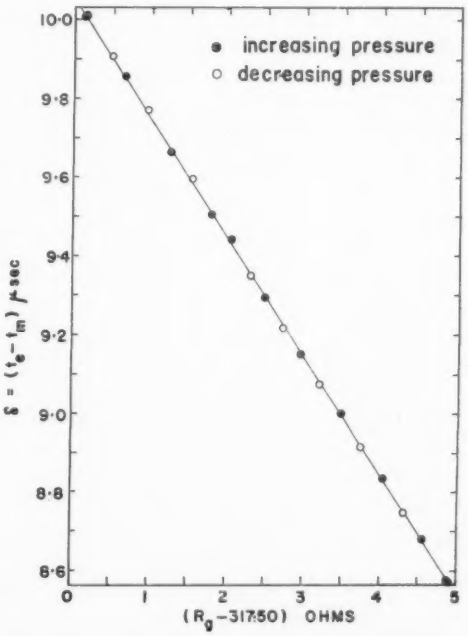

FIG. 1. Typical data plot showing the difference between the time, t_e, of arrival of one of the maxima of echo No. 7 of the longitudinal wave in a 3·164-cm-long aluminum crystal and a fixed time-marker, t_m, as a function of pressure-gauge coil resistance, R_g.

Table 1. *Pressure data for the longitudinal wave for two aluminum crystals. The echo number is n, and the echo arrival time is* T_n. T_0 *is the zero pressure transit time and* R_g *the pressure-gauge resistance. Units of* $(1/nT_0)(dT_n/dR_g)$ *are* 10^{-3} *ohm*$^{-1}$. *Experiment* 3′ *on crystal A was performed with the same cementing of the quartz on the specimen as experiment* 3. *The same statement applies to crystal C for experiments* 2, 2′, *and* 2″.

Crystal *A* (length 3·164 cm)				Crystal *C* (length 2·205 cm)			
Experiment No.	n	Run No.	$-\frac{1}{nT_0}\frac{dT_n}{dR_g}$	Experiment No.	n	Run No.	$-\frac{1}{nT_0}\frac{dT_n}{dR_g}$
1	6	1	4·38	1	9	1	4·62
		2	4·40			2	4·67
		3	4·33			3	4·60
		4	4·39			4	4·54
2	7	1	4·38	2	8	1	4·47
		2	4·41			2	4·51
		3	4·36			3	4·58
		4	4·43			4	4·57
3	7	1	4·53	2′	2	1	4·53
		2	4·51			2	4·33
		3	4·52			3	4·66
						4	4·55
3′	4	1	4·45	2″	5	1	4·55
		2	4·48			2	4·56
		3	4·43			3	4·61
		4	4·43			4	4·56
Average			4·43				4·56

change in time of arrival of a particular maximum of the 10-mc echo structure, relative to a fixed time-marker, as the pressure was cycled up and then down several times. A typical data plot is given in Fig. 1, showing the difference between time of arrival of one of the maxima of echo No. 7 of the longitudinal wave in a 3·164-cm-long aluminum crystal and a fixed time-marker, as a function of pressure-gauge coil resistance. The pressure range of these data is about 6400 bars. Data points were taken about 5 min after each pressure change in order that the system be near thermal equilibrium. Absence of hysteresis justifies the time interval chosen. In some cases the data plots showed a slight departure from linearity, the departure always being concave upward. However, this was not observed consistently for any given wave, and the slope for the full range of data as computed by a least-squares method did not show any marked difference from slopes computed where the data did plot as a straight line. The pressure range for an experiment was generally about 6500 bars, and the full range of data was used in computing a least-squares slope, although, strictly speaking, we are interested in this paper only in the initial slope of these curves. This slope, together with the measured zero-pressure transit time, T_0, enables one to compute the quantity $(nT_0)^{-1}\,dT_n/dR_g$, where n is the number of the echo under observation, T_n is the observed time of arrival of the nth echo, and R_g is the pressure-gauge coil resistance. Since one can express the pressure-gauge coil calibration as $dP = kdR_g$, and $T_n(P) = nT(P)$, the quantity $(nT_0k)^{-1}$

dT_n/dR_g represents the fractional change of transit time with pressure, $(T_0)^{-1}\,dT/dP$.

A series of data points taken for ΔP of a given sign will be called a run, and four runs, or two pressure cycles, constitute an experiment. A quartz transducer was generally in place for one experiment and then changed for the next. A value of $(T_0)^{-1}\,dT/dP$ was computed for each pressure run, and the arithmetic mean of such numbers was used to obtain a result for the experiment.

Measurements were made on three aluminum crystals of different lengths: A 3·164 cm, B 1·349 cm and C 2·205 cm. Crystals A and B were used in measuring the elastic stiffnesses at zero pressure and their pressure derivatives. Because of the difficulty of obtaining consistent data for the pressure derivative of the longitudinal wave in crystal B, further pressure measurements on the longitudinal wave were made with crystal C, of intermediate length, to compare with data taken on crystal A. All pressure-run data for the longitudinal wave in crystal C are compared, in Table 1, with similar measurements made on crystal A. The average deviation of the quantity $(T_0)^{-1}\,dT/dP$, computed for a given run, from the arithmetic mean of the same quantity for all pressure runs on the longitudinal wave is 1 per cent for crystal A and 1·1 per cent for crystal C. These numbers are also representative of the reproducibility for crystals A and B of pressure data taken for the shear stiffnesses.

For cubic crystals with orientation near [110], the elastic stiffnesses Y are given by:

$$\left.\begin{aligned} Y_2 &= B_S+4(\tfrac{1}{3}-\Gamma)C'+4\Gamma C,\\ Y_4 &= C+2a_1(C'-C),\\ Y_5 &= C+2a_2(C'-C). \end{aligned}\right\} \qquad (1)$$

Y_2 refers to the longitudinal wave, while Y_4 and Y_5 refer to the slow shear and fast shear waves, respectively. The notation $C = C_{44}$, $C' = (C_{11}-C_{12})/2$, and $B_S = (C_{11}+2C_{12})/3$ has been used, B_S being the adiabatic bulk modulus. The orientation functions Γ, a_1, and a_2[9] are independent of pressure for cubic crystals. The stiffness Y is expressed experimentally as the product of density times velocity squared. This enables us to write:

$$\frac{1}{Y}\cdot\frac{dY}{dP} = (3B_T)^{-1} - \frac{2}{T}\cdot\frac{dT}{dP}, \qquad (2)$$

where B_T is the isothermal bulk modulus and all derivatives are to be evaluated at zero pressure. The zero pressure values for Y and the results of the pressure measurements enable one to compute dY/dP for each of the three waves in aluminum. These values are then introduced into the pressure derivatives of equations (1) to determine the pressure variation of C, C', and B_S. For a crystal of exactly [110] orientation, C and C', and their pressure derivatives, are determined directly, whereas B_S is derived from a combination of all three measurements.

After all measurements had been made on a given crystal, one of the acoustic surfaces was etched and a back-reflection Laue X-ray pattern taken to determine the orientation of the crystal. The aluminum specimens measured were all within 2° of [110].

(b) *Magnesium*

Magnesium was handled in the same way as aluminum though with certain variations, arising principally in the lower symmetry. The magnesium specimens that were measured were grown in this laboratory by Mr. T. R. Long. An acid string saw was used to cut the specimens to size and length. Because of the agreement of pressure data taken on aluminum crystals of different lengths, end effects were considered negligible in making pressure measurements on magnesium. In the case of magnesium there are five elastic constants,[6] and hence more than one direction of measurement was necessary. One crystal was oriented for wave propagation along the c-axis of the specimen. This crystal was used to determine C_{33} and C_{44} and their pressure derivatives directly, C_{33} from the longitudinal wave velocity and C_{44} from the shear wave. A second magnesium specimen was prepared with two pairs of acoustic surfaces. One pair of surfaces was oriented for wave propagation perpendicular to the c-axis. In this case C_{11} and its pressure derivative were measured directly with the longitudinal wave, while $C' = (C_{11}-C_{12})/2$ was determined by using a shear wave with particle vibration in the basal plane. The second pair of acoustic faces on this crystal was oriented perpendicular to the first pair, with a direction of propagation at an angle of 41° to the c-axis. A shear wave with particle motion in the plane containing the c-axis, for this direction of

propagation, provided the fifth independent measurement. This shear stiffness is denoted by C'' which is given in terms of the conventional stiffness constants by:

$$C'' = (C_{11}-2C_{13}+C_{33})n^2\alpha^2+(\alpha^2-n^2)^2C_{44}. \quad (3)$$

The direction cosine for the angle between the c-axis and the direction of wave propagation is denoted by n, and $n^2+\alpha^2 = 1$.

The pressure data for magnesium were interpreted by the general equation:

$$\frac{1}{Y}\cdot\frac{dY}{dP} = 2k_T(a)-k_T(c)+ \\ +2\sin^2\theta[k_T(c)-k_T(a)]-\frac{2}{T}\cdot\frac{dT}{dP}, \quad (4)$$

where $k_T(c)$ and $k_T(a)$ are the isothermal linear compressibilities along the c-axis and directions perpendicular to that axis respectively, and the direction of wave propagation is at an angle θ to the c-axis. The pressure data for C'' were combined with the other pressure data to evaluate the derivative of the shear stiffness $C_H = (C_{11}+C_{12}+2C_{33}-4C_{13})$. C_H corresponds to a strain which changes the c/a ratio at constant volume, leaving the symmetry of the crystal unchanged.

3. RESULTS

(a) *Aluminum*

It is felt that the present reported values of the elastic stiffnesses of aluminum represent the best determinations of these constants to date. The only previously reported pulse-echo determination for aluminum is that of LAZARUS,[3] who was not able to measure separately the Y_4 or C' velocity. The data given in Table 2 for the elastic stiffnesses C, C', and C'_{11} were directly determined; C'_{11} refers to the longitudinal stiffness which is given by $\frac{1}{2}(C_{11}+C_{12}+2C_{44})$. The adiabatic bulk modulus was determined from a combination of the three experimental quantities using equations (1), while the isothermal bulk modulus was determined by means of the equation:

$$B_S \cong B_T(1+TV\beta^2B_T/C_P) \quad (5)$$

where β, the cubical coefficient of thermal expansion, equals $7{\cdot}11\times10^{-5}$ (°C)$^{-1}$ and the specific heat is $C_P = 5{\cdot}70$ cal (mole deg)$^{-1}$.[10] V is the molar volume and T is room temperature, taken as 298°K. The internal agreement of the data for the two crystals is excellent, particularly for the directly determined stiffnesses. As indicated previously, crystals A and B, for which data are reported, are considerably different in length. The value 2·699 g cm^{-3} for the density of aluminum, as calculated from the value 4·050 Å for the lattice parameter,[11] has been used to obtain the elastic stiffnesses.

The average values given in Table 2 were used in computing Table 3. The adiabatic compliances, S_{ij}, were determined from the adiabatic stiffnesses, C_{ij}, using the relations:

$$\left.\begin{aligned}(S_{11}-S_{12}) &= (C_{11}-C_{12})^{-1},\\ S_{44} &= C_{44}^{-1},\\ (S_{11}+2S_{12}) &= (C_{11}+2C_{12})^{-1}.\end{aligned}\right\} \quad (6)$$

The adiabatic compliances were corrected to isothermal by means of the thermodynamic relation:

$$S_{ij}^T-S_{ij}^S = T\gamma_i\gamma_jC_p^{-1}. \quad (7)$$

Table 2. Adiabatic elastic stiffnesses and isothermal bulk modulus of aluminum at 25°C. ZENER's notation for the fundamental shear stiffnesses $C = C_{44}$ and $C' = (C_{11}-C_{12})/2$ has been used. C'_{11} is the longitudinal stiffness given by $(C_{11}+C_{12}+2C_{44})/2$. Units are 10^{12} dyne cm^{-2}.

Crystal	Length (cm)	C	C'	C'_{11}	B_s	B_T
A	3·164	0·2832	0·2319	1·1242	0·7637	0·7269
B	1·349	0·2831	0·2319	1·1248	0·7644	0·7275
Average		0·2832	0·2319	1·1245	0·764	0·727

The value of γ_i, the coefficient of linear expansion, is determined from β above. Isothermal stiffnesses were then computed from the isothermal compliances, using the conversion relations (6).

Table 3. *Values at* 25°C *for pure aluminum of the average adiabatic elastic stiffnesses* C^s, *the computed adiabatic compliances* S^s, *the isothermal compliances,* S^T, *and the isothermal stiffnesses* C^T. *Units are* 10^{12} dyne cm^{-2} *for* C *and* 10^{-12} dyne^{-1} cm^2 *for* S.

Term Subscript	C^s	S^s	S^T	C^T
11	1·073	1·582	1·589	1·039
12	0·609	−0·573	−0·566	0·575
44	0·283	3·533	3·533	0·283

Values of the pressure derivatives of the elastic stiffnesses of aluminum in Table 4 were obtained from the experimental data as described in the previous section. The average deviation from the mean for all pressure-run data on aluminum was 1·9 per cent for the longitudinal wave and 1·1 and 1·2 per cent for the slow shear and fast shear waves, respectively. The latter two numbers are felt to represent the accuracy of the measurements on the shear stiffnesses, whereas the uncertainty of the pressure derivative of the bulk modulus is placed at 4 per cent.

The average value for dC/dP was used in calculating $dC/d\ln r$, which is given by the relation:

$$dC/d\ln r = -3B_T dC/dP. \tag{8}$$

This relation holds similarly for C' and B_S.

BRIDGMAN's compressibility data are usually expressed as the coefficients a and b in the equation:

$$\Delta V/V_0 = -ap + bp^2, \tag{9}$$

where a is the reciprocal of the isothermal bulk modulus and b is related to the pressure derivative of the bulk modulus by:

$$b = \frac{1}{2B_T{}^2}\left(\frac{dB_T}{dP} + 1\right). \tag{10}$$

The value of a quoted from the present results was determined from the average value of B_T as given in Table 2. The coefficient b was computed by means of equation (10), where the pressure derivative of the bulk modulus was first corrected from adiabatic to isothermal by means of the exact form of equation (5) and standard thermodynamic data. The comparison with BRIDGMAN's[12,13] coefficient a in Table 5 is good, the values differing by 0·5 per cent. The 20 per cent difference in the b coefficients is outside the statistical uncertainty of the present experiments and is in the same direction as the differences encountered for copper and silver and also, according to a recent analysis[14] of BRIDGMAN's data, for gold. The results of the analysis by GILVARRY[14] on some of BRIDGMAN's latest data[15] for aluminum to 30,000 bars are also given for comparison in Table 5. This systematic discrepancy is not understood, but we feel we must stand on the present method. It should be pointed out that the value of b quoted from the present results comes from the slope of a raw-data plot, while in BRIDGMAN's method it comes essentially from the curvature. Also it is probably significant that the present value of the b coefficient is based on closely spaced data to the relatively low pressure

Table 4. *Pressure derivatives of the elastic stiffnesses of aluminum. The average values given have been weighted according to the amount of data taken on each crystal.*

	C	C'	B_s	Remarks
dC/dP	2·308	1·620	5·13	Crystal *A*, 298°K
dC/dP	2·329	1·614	—	Crystal *B*, 298°K
dC/dP	—	—	5·32	Crystal *C*, 298°K
dC/dP	2·31	1·62	5·22	Average
$dC/d\ln r$	− 5·04	− 3·53	−11·4	Units of 10^{12} dyne/cm^2
$d\ln C/d\ln r$	−17·8	−15·2	−14·9	—

Table 5. Comparison of present values of compressibility data for aluminum with the BRIDGMAN *values. The values are expressed as the constants a and b in the equation* $\Delta V/V_0 = -ap+bp^2$.

	BRIDGMAN*	GILVARRY†	Present work	Units
a	13·40	13·58	13·48	10^{-7} cm^2—kg^{-1}
b	4·64	4·86	5·62	10^{-12} cm^4—kg^{-2}

* See references 12, 13.
† See references 14, 15.

of 6500 bars, whereas the b coefficient of BRIDGMAN describes the dependence of volume on pressure over a much wider pressure range. Another systematic difference is that BRIDGMAN's measurements are for polycrystalline materials. Finally, we do not ignore the possibility of an undiscovered systematic error in our longitudinal wave-velocity measurements, on which the bulk modulus depends heavily. These velocities are always more difficult to measure than the shear velocities with which we are principally concerned here.

In Table 6 a comparison is made of the present pressure measurements on aluminum with measurements made by LAZARUS.[3] Values of the elastic stiffnesses at different pressures were calculated from the data given in LAZARUS's Table 1, and a least-squares slope calculated from these data gave the values quoted for the pressure derivatives of the longitudinal stiffness c'_{11} and the shear stiffness C. The values for the shear stiffness appear to be in good agreement; however, they are not consistent with the value $7{\cdot}49\times10^{-6}$ bars^{-1} which LAZARUS specifically quotes for $(\partial \ln C/\partial P)_T$ in his paper. Comparison of the pressure derivatives of the longitudinal stiffness shows a considerable difference. For this reason they are the data for just this stiffness which are illustrated in Fig. 1 and given in full in Table 1.

Table 6. Comparison of the pressure derivatives for the shear stiffness $C = C_{44}$ *and the longitudinal stiffness* $C'_{11} = \frac{1}{2}(C_{11}+C_{12}+2C_{44})$ *of aluminum with values calculated from* LAZARUS's *table of data. These stiffnesses were directly measured in both experiments.*

	LAZARUS[3]	Present work
dC'_{11}/dP	6·23	7·91
dC/dP	2·33	2·31

(b) *Magnesium*

Measurements made by the present investigators on the zero-pressure elastic stiffnesses of magnesium are in good agreement with the values of LONG and SMITH,[6] which are quoted in Table 7. With the exception of C_H, all of the pressure derivatives of the elastic stiffnesses given in Table 7 were directly measured. The average deviation from the mean of all pressure run data, in per cent,

Table 7. Adiabatic elastic stiffnesses of magnesium and their pressure derivatives at 25°C. The values of the stiffnesses are those of LONG *and* SMITH.[6] C_H *is the shear stiffness* $(C_{11}+C_{12}+2C_{33}-4C_{13})$.

	C_{11}	C_{33}	C	C'	C_H	Units
C	0·5974	0·617	0·1639	0·168	1·226	10^{12} dyne—cm^{-2}
dC/dP	6·13	7·22	1·58	1·36	13·7	—
$dC/d\ln r$	− 6·33	− 7·45	−1·63	−1·40	−14·2	10^{12} dyne—cm^{-2}
$d\ln C/d\ln r$	−10·6	−12·1	−9·92	−8·37	−11·6	—

for the different stiffnesses are as follows: C_{11}1·3, C_{33}0·6, C2·7, C'0·6, C''0·5. By the propagation of errors this leads to an uncertainty for the pressure derivative of C_H of about 5 per cent. Equation (8) was used to calculate $dC/d\ln r$ for the elastic stiffnesses of magnesium. This relation does not strictly apply, since $d\ln V = 2d\ln(a)+d\ln(c) \neq 3d\ln r$. However, the approximation $d\ln V \cong 3d\ln r$ and hence $dC/d\ln r \cong -3B_T dC/dP$ is rather good, the linear compressibilities in the c- and a-directions differing by only 6 per cent. The value of the isothermal compressibility which was used was computed from LONG and SMITH's values of the linear compressibility.

VOL. 9 1959

4. INTERPRETATION

(a) *Aluminum*

The elastic stiffness of a crystal can be expressed as the second derivative of the crystal binding energy with respect to the appropriate strain. For monovalent metals it is generally assumed that there are two important contributions to the elastic shear-strain energy of the crystal: (1) a purely electrostatic term representing the difference of electrostatic energy of the ion-cores in the strained and unstrained geometry, and (2) a term arising from the change in the short-range repulsive interaction of the ion-cores. The Fermi surface is approximately a sphere lying wholly in the first Brillouin zone, and movements of the zone boundaries as the metal is sheared have little effect on the Fermi energy. For metals of higher valence, however, the Fermi energy is affected by shear and therefore contributes to the elastic stiffness of the crystal.

LEIGH[1] proposed a theory which accounts for the observed shear stiffnesses in aluminum. Before speculating about the pressure derivative of the shear stiffnesses, the details of LEIGH's theory will be examined. In aluminum the ion-cores are small and the short-range repulsive interaction is negligible. Contributions to the shear-strain energy then are the electrostatic and Fermi terms.

For the electrostatic contribution LEIGH modified FUCH's[16] terms,

$$\Omega C'_E = 0{\cdot}1058e^2/2a$$

$$\Omega C_E = 0{\cdot}9479e^2/2a \text{ per atom,}$$

which had been evaluated for monovalent metals, to fit the case of trivalent aluminum. Ω represents the atomic volume and a is the lattice parameter. The modified electrostatic terms are

$$C_E = Z^2_{\text{eff}}(1{\cdot}639\times 10^{11}) \text{ dyne cm}^{-2} \tag{11}$$

and

$$C'_E = Z^2_{\text{eff}}(0{\cdot}183\times 10^{11}) \text{ dyne cm}^{-2},$$

where Z_{eff} is the effective charge density at the boundary of the atomic polyhedron.

In Fig. 2 is shown the first Brillouin zone for

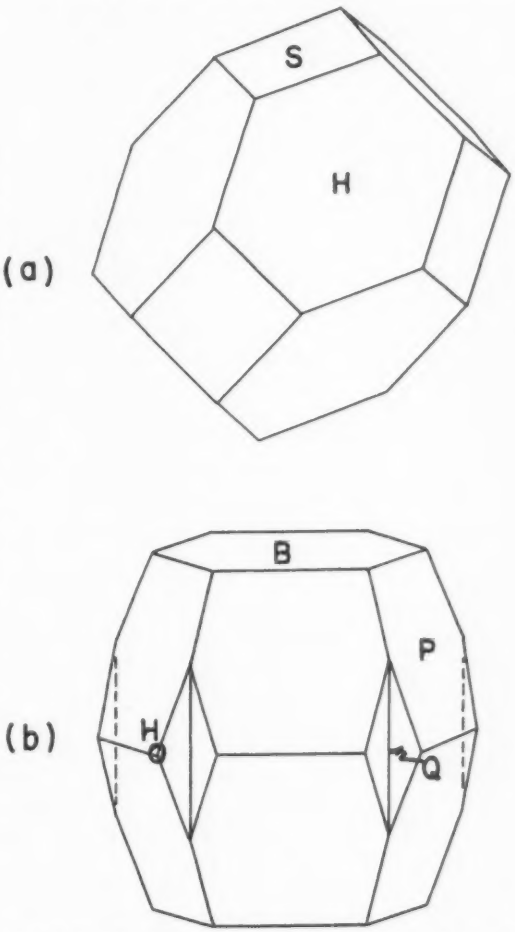

FIG. 2. (*a*) The Brillouin zone of aluminum, showing the positions of electron overlap. (*b*) The Brillouin zone of magnesium, showing the positions of electron overlap and holes.

aluminum, a truncated octahedron. The first zone has sufficient states for two electrons per atom with each state doubly occupied. The remaining electron occupies states overlapping the hexagonal and square faces. LEIGH divided the Fermi contribution into two parts: a contribution from the first or filled zone and contributions from overlap electrons. The full zone contributions to C and C' are

$$\frac{\alpha_0 h^2}{ma^5} \text{ and } \frac{\alpha_0 h^2}{3ma^5} \tag{12}$$

respectively, where α_0 is the reciprocal effective mass ratio, and a is the lattice parameter. General expressions for the overlap contributions to the shear stiffnesses are

$$\left.\begin{aligned} &\frac{1}{\Omega}\left(\frac{8}{3}n_h E_h - \frac{16}{9}N_h E_h^2 + 2n\ E_s\right) \\ &\frac{1}{\Omega}\left(\frac{8}{3}n_h E_h + 2n_s E_s - 2N_s E_s^2\right), \end{aligned}\right\} \tag{13}$$

for C and C', respectively. The number of electrons per atom overlapping a pair of hexagonal or square faces is given by n_h or n_s. N_h and N_s are the corresponding contributions to the density of states per atom at the Fermi level, and E_h and E_s are the equilibrium-position energies at the centers of the Brillouin-zone faces in the second zone. The positive terms in equations (13) arise from the shift of the energy surfaces as a whole with the zone faces during shear, and the negative terms result from electron transfer between zone faces during shear. This latter effect is displayed in Fig. 3 for both C and C'.

The sum of terms for C or C' in equations (11), (12), and (13) gives the total contribution to each shear stiffness. In order to assess the relative contributions of the various terms for C and C', LEIGH made use of four pieces of experimental information to fit parameters in his theory: (i) and (ii) the observed values of the two shear stiffnesses, (iii) the density of states, $N(\zeta_0)$, at the Fermi level as determined from electronic specific-heat data, and (iv) the value of the energy at the Fermi level, ζ_0, from the width of the soft X-ray emission spectrum. The value of $N(\zeta_0)$ is used in the normalization condition

$$4N_h + 3N_s = N(\zeta_0), \tag{14}$$

and, assuming that all states in the first Brillouin zone are occupied, we have in addition

$$4n_h + 3n_s = 1. \tag{15}$$

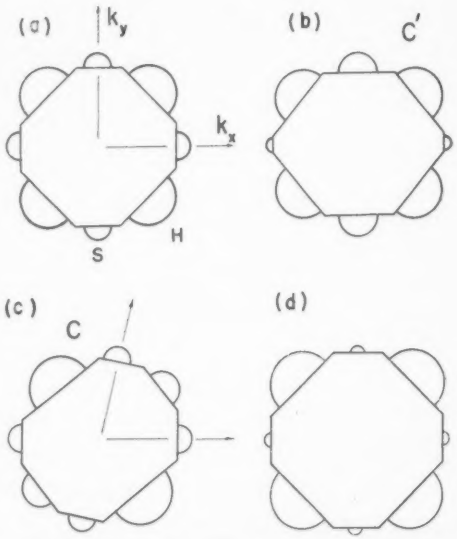

FIG. 3. Schematic representation of the Brillouin zone and overlap electron populations of aluminum in various strain states. Electron-overlap populations for the square and hexagonal faces are denoted by S and H respectively. (*a*) Unstrained, (*b*) C' shear strain, (*c*) C shear strain, and (*d*) negative volume strain.

Experimental values of the shear stiffnesses used by LEIGH were those of LAZARUS.[3] Since one of these stiffnesses C' had been determined indirectly and differed from the present reported value by 10 per cent, LEIGH's model was fitted to the present values of the shear stiffnesses of aluminum, as given in Table 2. This revision was necessary before an evaluation of the pressure derivatives of the shear stiffnesses was made. Contributions to the shear stiffnesses based on LEIGH's model and the present reported values for C and C' are given in Table 8. The parameters E_h, E_s, and α_0 with values of 9·2 eV, 11·2 eV, and 1, respectively, were not altered in the present fitting. Parameters for which small adjustments have been made and their new values are $Z_{\text{eff}}^2$6·75, n_h0·233 per atom, n_s0·022 per atom, N_h0·134 per eV atom, and N_s0·026 per eV per atom.

The pressure derivative of the shear stiffness

Table 8. Constitution of the present observed shear stiffnesses of aluminum as explained by LEIGH's *model. Units are* 10^{12} dyne cm^{-2}.

Contribution	C		C'	
Coulomb (C_E)		1·106		0·1235
Fermi: Full zone	0·450		0·1500	
Hexagonal overlap	−1·320		0·5400	
Square-face overlap	0·047		−0·5817	
Net Fermi (C_F)		−0·823		0·1083
Total (observed) (C_E+C_F)		0·283		0·232

may be expressed in terms of the quantity π, which is defined by the first equality of

$$\pi = -d\ln C/d\ln r = \frac{\pi_E C_E + \pi_F C_F}{C_E + C_F} \qquad (16)$$

where $\pi_E = -d\ln C_E/d\ln r$, $\pi_F = -d\ln C_F/d\ln r$ and $C = C_E + C_F$. The quantity π' is defined by the same relations, where C, C_E, and C_F are replaced by C', C_E', and C_F'. The electrostatic contributions (11) to C and C' may be written in the form:

$$C_E = KZ_{\text{eff}}^2/r^4 \text{ and } C_E' = K'Z_{\text{eff}}^2/r^4, \qquad (11')$$

which according to equation (16) gives $\pi_E = \pi'_E = 4$, assuming Z_{eff}^2 constant. Noting that C_F, the net Fermi term, is given by the sum of equations (12) and (13), we can assign a value of 5 to the coefficient π_F where it is assumed that α_0 in equation (12) is independent of pressure and that the atomic volume, in equation (13) is differentiated as well as E, but that N_h and N_S are treated as constants. That is,

$$dC/d\ln r = \frac{1}{\Omega}\cdot\frac{d(\Omega C)}{d\ln r} - 3C$$

applies for the differentiation of equation (13), and the differentiation of E is assumed to be the same as for the free electron case. It is convenient here to express N_h and N_s in terms of n_h and n_S, as it is expected that $N_i = \text{const.}\ \Omega^{2/3}n_i^{1/3}$. Substitution of the values 4 and 5 for π_E and π_F in the defining equation (16) for π, where the values of C_E and C_F given in Table 8 are used, one obtains values of 1·1 and 4·5 for π and π', respectively, in contrast to the observed values of 17·8 and 15·2.

Examination of the second equality of equation (16),

$$\pi = \sum_i \pi_i C_i / \sum_i C_i,$$

in the case of the stiffness C for which C_F *is large and negative*, according to Table 8, shows that there are two possibilities of achieving a large value of π. One possibility is $\pi_E > \pi_F > 0$, the second is $\pi_E > 0 > \pi_F$. Recalling that for C' both C'_E and C'_F are greater than zero, the condition $\pi_E > > \pi_F > 0$ would give a weighted value for π', $\pi_E > \pi' > \pi_F$, whereas the second possibility, $\pi_E > 0 > \pi_F$, would give a smaller value for π' and would seem less probable. Thus, to have both π and π' large implies the condition $\pi_E > \pi_F > 0$.

The possibility of having a large value for π_E does not seem unreasonable, as Z_{eff}, the effective charge density at the boundary of the atomic polyhedron, undoubtedly depends on r. In any case, recent measurements of the pressure derivative of the shear stiffnesses of monovalent sodium,[17] a metal for which the shear stiffness is given almost entirely by the electrostatic contribution, have in fact suggested a value for π_E of about 7·3 in contrast to the value of 4 one might predict from simple theory, and we may logically expect a similarly large value in aluminum.

Taking $\pi_F = 5$, it is possible to obtain the observed value of either π or π' by adjusting π_E, but not both of them simultaneously. Some adjustment of π_F is necessary, and it should be recalled that in assigning a value of 5 to π_F for the overlap Fermi terms it was assumed that the overlap populations, n_h and n_s, did not change. The large negative contributions to C and C' due to electron transfer, as exhibited in Table 8, suggest that electron transfer under volume strain would make a significant contribution to the pressure derivative of the shear stiffnesses. Such an effect is indicated in Fig. 3(d).

Assuming such an effect, the complete contribution from overlap electrons to the pressure derivative of the shear stiffness is given by:

$$dC_F^{II}/d\ln r = (\partial C_F^{II}/\partial \ln r)_n + \\ +(\partial C_F^{II}/\partial n)_r (dn/d\ln r), \qquad (17)$$

where C_F^{II} represents the overlap contribution to the Fermi shear stiffness as given by equation (13) for C and C'. The first term in equation (17) contributes $-\pi_F C_F^{II}$, where $\pi_F = 5$ as was assumed previously, and the second term is the effect of electron transfer under volume strain. The complete expression for π in the case of the shear stiffness C, where C_F^{II} as given by equation (13) is introduced, is given by:

$$\pi = \frac{1}{C}\left\{\pi_E C_E + \pi_F C_F - \frac{1}{\Omega}\left[\left(\frac{8}{3}n_h E_h - \frac{16}{27}N_h E_h^2\right)\right]\times \right. \\ \left. \times \frac{d\ln(n_h)}{d\ln r} + 2n_S E_S \frac{d\ln(n_s)}{d\ln r}\right\}. \qquad (18)$$

In differentiating N_h, the relation $N_h = \text{const.}\ \Omega^{2/3} n_h^{1/3}$ has been used. A similar expression can be written for π' and the shear stiffness C', and from equation (15) we obtain the relation:

$$dn_s/d\ln r = -\frac{4}{3}dn_h/d\ln r. \qquad (15')$$

By assuming the values of C_E, C_F, C_E', and C_F' indicated in Table 8, the observed values of π and π' and $\pi_F = 5$, the two equations (18) for π and π' and equation (15) were solved simultaneously for the variables π_E, $dn_h/d\ln r$, and $dn_s/d\ln r$. Values obtained in this way are π_E 8·73, $dn_h/d\ln r$ −0·159, and $dn_S/d\ln r$ 0·212 per atom per pair of zone faces. Introducing these values back in equation (18) for π and π' gives the contributions to $(-d\ln C/d\ln r)$ shown in Table 9. The value of 8·73 obtained for π_E is satisfied if Z_{eff} varies with r according to:

$$Z_{\text{eff}} = Z_0(r/r_0)^{-4.73/2}, \qquad (19)$$

where the subscript zero refers to the equilibrium values at zero pressure. This dependence of Z_{eff} on r is not a very strong one and is therefore not unreasonable. The values quoted for $dn_h/d\ln r$ and $dn_s/d\ln r$ correspond to approximate fractional changes of 0·002 and −0·03 respectively in n_h and n_s for a pressure of 10^4 bars. As hydrostatic pressure is applied to the specimen, part of the electrons in states overlapping the square faces of the Brillouin zone transfer to states overlapping the hexagonal faces. Such an effect is important for the stiffness C', which is quite sensitive to the amount of square-face overlap, but less important for the stiffness C, as evidenced in Table 9.

A recent paper by HEINE[18] suggests that there are hole pockets in the first Brillouin zone, at the corner points, in addition to the electron overlap for the hexagonal and square faces. According to LEIGH, this would have only a small effect on the details of the contributions to the shear stiffnesses. Adding holes in the first Brillouin zone would cause some change in our description of the pressure derivative of the shear stiffnesses. Equations (15′) and (18) would then involve another variable of the type $dn/d\ln r$ giving three equations in terms

Table 9. Values for aluminum of the contributions $(-dC_i/d\ln r)/C$ to the derivatives $(-d\ln C/d\ln r)$ of the shear stiffnesses C and C'. The quantities, $(-dC_i/d\ln r)/C$ arise from the contributions, $\sum_i C_i$ which are named.

Contribution	C	C'
Coulomb term	34·13	4·65
Net Fermi term assuming n's constant	−14·52	2·32
Contributions from electron transfer with volume strain:		
Hexagonal overlap	− 0·17	1·59
Square-face overlap	− 1·62	6·63
Total (and observed)	17·8	15·2

of four unknowns. A solution could then be achieved by arbitrarily setting the value of one unknown and solving the equations for the other three. It is expected that the values of the parameters π_E, $dn_h/d\ln r$, and $dn_s/d\ln r$ would not change significantly by adding holes in the first Brillouin zone.

(b) *Magnesium*

REITZ and SMITH[2] accounted for the shear stiffnesses C_H and C' in magnesium by using a model similar to that of LEIGH. Magnesium has the close-packed hexagonal structure, is divalent, and therefore has just enough electrons to fill the combined first and second Brillouin zones. Being a metal, it must have holes in the second zone and an equal number of electron overlaps in higher zones. The combined first and second Brillouin zone of magnesium is shown in Fig. 2b with the overlap and hole positions indicated.

The details of the shear stiffness C were not given in the paper of REITZ and SMITH, due to the difficulty of calculating the full zone contribution to the Fermi stiffness. In addition, there is some question about the value of the electrostatic contribution to this stiffness as calculated previously.[19] In magnesium the atoms are not all at lattice points nor are they in a center of symmetry, and for the shear stiffness C it does not seem that the motion of all the ions under shear strain follows the displacements given by that strain. With these uncertainties in the contributions to the shear stiffness C, it is hardly worthwhile to estimate what the contributions to the pressure derivative of C might be.

Electrostatic contributions to the shear stiffnesses C_H and C' for magnesium can be thought of in the same way as the electrostatic contributions to the shear stiffnesses of aluminum in equation (11′), that is:

$$C_E = \frac{KZ_{\text{eff}}^2}{r^4}.$$

The electrostatic contributions used by REITZ and SMITH correspond to a Z_{eff}^2 value of 1·8, compared to the maximum possible value of 4 for divalent magnesium.

Contributions from the Fermi energy to the shear stiffnesses were expressed as a full zone contribution and contributions from overlaps and holes. REITZ and SMITH assumed overlap at the B and P points indicated in Fig. 2, but no overlap at points Q. The assumption of B overlaps was necessary in order to ensure stability with respect to a deformation which changes the c/a ratio at constant volume. It should be noted that the *net* Fermi contributions to the shear stiffnesses C_H and C' are positive but very small.

As for aluminum, the separation of the ion-cores in magnesium is large enough that the short-range repulsive interaction is negligible.

In discussing the pressure derivative of the shear stiffnesses of magnesium in terms of the quantity $\pi = -d\ln C/d\ln r$, the arguments used previously for aluminum apply here also. With $C_E \cong \cong C$ for both C_H and C', it is expected that $\pi_E \cong \cong \pi$ for both shear stiffnesses. Thus again π_E is bound to turn out large, but it is necessary to invoke some electron transfer in order to account for the *difference* between π_H and π'. The details of the pressure derivative for C_H and C' were worked out by writing the equation, equivalent to equation (15′), which applies for magnesium

$$dn_b/d\ln r + 6dn_p/d\ln r + 6dn_h/d\ln r = 0, \quad (20)$$

and two equations of the form of equation (18), one for C_H and one for C'. The parameter π_E was allowed to vary in the last two mentioned equations, $\pi_F = 5$ was assumed, and the terms giving the contributions from electron transfer under volume strain were evaluated by using equation (16) of REITZ and SMITH and the data from their Tables II and III. We have then three equations in terms of the four variables: π_E, $dn_b/d\ln r$, $dn_p/d\ln r$, and $dn_h/d\ln r$. A solution was obtained by arbitrarily setting $dn_p/d\ln r$ equal to zero and solving the three simultaneous equations for the other three variables. Values obtained in this way are π_E 7·57, $dn_b/d\ln r$ 0·347 and $dn_h/d\ln r$ −0·058 per atom per spheroid. This solution yields the contributions to π for C_H and C' as given in Table 10.

Finally, the numerical work has been analyzed for the effect that the participation of p electrons in the volume transfer mechanism would have. Because it is essentially the transfer under pressure of B electrons out of the B overlap positions that accounts for $\pi_H > \pi'$, it does not really matter

Table 10. *Values for magnesium of the contributions* $(-dC_t/d\ln r)/C$ *to the derivatives* $(-d\ln C/d\ln r)$ *of the shear stiffnesses* C_H *and* C'. *The quantities* $(-dC_t/d\ln r)/C$ *arise from the contributions,* C_t, *which are named. The number of overlap electrons for the P faces of the Brillouin zone is assumed to be independent of pressure.*

Contribution	C_H	C'
Coulomb term	7·08	6·11
Net Fermi term assuming n's constant	0·32	0·98
Additional contributions from electron transfer with volume strain:		
B overlap	3·42	—
H holes	0·76	1·28
Total (and observed)	11·58	8·37

much where they go. Equation (20) holds and it turns out that non-zero $dn_p/d\ln r$ has little effect. A positive value of $dn_p/d\ln r$ would give a lower value for π_E than the number quoted in Table 10 and a negative value for $dn_p/d\ln r$ would give a larger value for π_E.

5. SUMMARY

It has been possible to account for the pressure derivative of the shear stiffnesses of both aluminum and magnesium in terms of the pressure variation of their electrostatic and Fermi contributions. The electrostatic contribution to the shear stiffnesses of both metals varies approximately as r^{-8}, the same as for sodium. The value $\pi_E \cong 8$ instead of $\pi_E = 4$ is presumably due to the variation of the effective charge density at the boundary of the atomic polyhedron, Z_{eff}, under volume strain. Changes in overlap and hole populations by electron transfer under volume strain contribute appreciably to the pressure variation of the Fermi shear stiffnesses of these metals.

Acknowledgements—This research was supported by The Office of Naval Research and The National Carbon Company. Suggestions by Professor J. R. REITZ were helpful in interpreting the results, and discussions with Dr. W. B. DANIELS concerning the operation and maintenance of the high-pressure system were invaluable.

REFERENCES

1. LEIGH R. S., *Phil. Mag.* **42,** 139 (1951).
2. REITZ J. R. and SMITH C. S., *Phys. Rev.* **104,** 1253 (1956).
3. LAZARUS D., *Phys. Rev.* **76,** 545 (1949).
4. DANIELS W. B. and HRUSCHKA A. A., *Rev. Sci. Instrum.* **28,** 1058 (1957).
5. DANIELS W. B. and SMITH C. S., *Phys. Rev.* **111,** 713 (1958).
6. LONG T. R. and SMITH C. S., *Acta Met.* **5,** 200 (1957).
7. EROS S. and REITZ J. R., *J. Appl. Phys.* **29,** 683 (1958).
8. LONG T. R., Master's Thesis, Case Institute of Technology (1953).
9. NEIGHBOURS J. R., BRATTEN F. W., and SMITH C. S., *J. Appl. Phys.* **23,** 389 (1952).
10. LANDOLT–BÖRNSTEIN, *Physikalish-Chemische Tabellen,* Supp. 2, pp. 1151, 1233. Julius Springer, Berlin (1931).
11. *American Institute of Physics Handbook* pp. 2–48 McGraw-Hill, New York (1957).
12. BRIDGMAN P. W., *Proc. Amer. Acad. Arts Sci.* **70,** 285 (1935).
13. BRIDGMAN P. W., *Rev. Mod. Phys.* **16,** 1 (1946).
14. GILVARRY J. J., *J. Chem. Phys.* **23,** 1925 (1955).
15. BRIDGMAN P. W., *Proc. Amer. Acad. Arts Sci.,* **77,** 187 (1949).
16. FUCHS K., *Proc. Roy. Soc.* A**153,** 622 (1936); A**157,** 444 (1936).
17. DANIELS W. B. To be published.
18. HEINE V., *Proc. Roy. Soc.* A**240,** 340 (1957).
19. HUNTINGTON H. B., *Phys. Rev.* **57,** 60 (1940).

VOL
9
195

J. Phys. Chem. Solids Pergamon Press 1959. Vol. 9. pp. 113–118. Printed in Great Britain.

SINGLE-CRYSTAL ELASTIC CONSTANTS OF LITHIUM

HARRY C. NASH and CHARLES S. SMITH

Case Institute of Technology, Cleveland, Ohio

(*Received* 29 *July* 1958)

Abstract—The elastic constants of single-crystal lithium have been measured by the ultrasonic pulse-echo technique. The results, in units of 10^{11} dyn cm^{-2}, are:

Temperature (°K)	C_{44}	$(C_{11}-C_{12})/2$	B_s
78	1·08	0·116	1·33
155	1·00	0·111	1·25
195	0·96	0·109	1·20

where B_s is the adiabatic bulk modulus. These results are compared with FUCHS's theoretical calculation of the Coulomb contribution to the shear stiffness of the alkali metals, which in lithium is the only significant contribution. Extrapolation of the experimental values to absolute zero gives values for both C_{44} and $(C_{11}-C_{12})/2$ which are lower than the corresponding theoretical values. The extrapolated anisotropy, $C_{44}/(C_{11}-C_{12})/2$, is higher than the value predicted by the theory.

INTRODUCTION

FUCHS[1] has calculated theoretical values for the shear elastic constants of the alkali metals lithium, sodium, and potassium. In these calculations the dominant term is the long-range electrostatic, or Coulomb, stiffness. Since this same physical term occurs as a contribution to the stiffness of all metals, it is desirable to verify these calculations experimentally to the fullest extent possible. Lithium is most suitable for this purpose because the electrostatic stiffness is relatively a more important contribution in lithium than in any other metal; all other contributions to its shear constants are small. Other investigators[2,3] have measured the single-crystal elastic constants of sodium and potassium. One of these, BENDER,[3] attempted to produce single crystals of lithium, but the various methods he employed were unsuccessful. This paper describes a method of growing single crystals of lithium, and the results of elastic-constant determinations at three temperatures by the ultrasonic pulse-echo technique.

EXPERIMENTAL PROCEDURE

Lithium single crystals were grown from a melt of commercial-grade lithium in a crucible of special design shown in Fig. 1. The unusual feature of this crucible is that the nucleation tip is formed at the top of the melt, and solidification proceeds downward from the surface

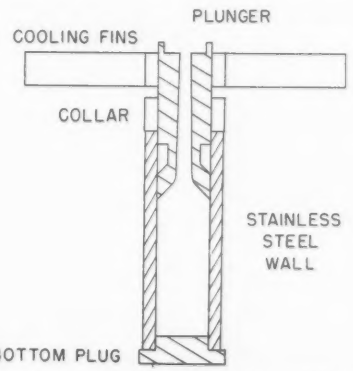

FIG. 1. Crucible used in growing lithium crystals. The crucible is heated by a hot plate at the bottom and nucleation starts at the top.

of the melt. This crucible form was developed when attempts to produce single crystals with crucibles of the usual shape were unsuccessful. The usual crucible shape has a small-diameter nucleation tip at the apex of a conical bottom, and is suitable for growing crystals of many metals by freezing upward from the bottom. However, the high surface tension and low density of lithium do not allow it to flow into a bottom nucleation tip when the ingot is melted. Also, some of the surface contamination on the ingot settles to the bottom of the melt, producing spurious nucleations. With the crucible of special design, impurities which tend to settle are at the end of the melt which solidifies last, and therefore have no effect on the part of the crystal to be used. Impurities which rise to the surface are skimmed off before crystal growth begins.

The entire growing process was carried out in an argon atmosphere. The sample and all surfaces touching it were lightly coated with petroleum jelly. This coating was found necessary to control chemical reactions at the surface of the sample.

Briefly, the growing procedure was the following. The lithium stock was melted and cast into a cylindrical ingot. This ingot was melted in the cup of the growing crucible and heated at 315°C for 1 hr on a hotplate. The plunger, preheated to 315°C, was then lowered into the crucible, forcing the molten lithium up through the center channel, until a bead of lithium formed at the top. The adjustable collar held the plunger at this position while the bead of molten lithium with any surface contamination was removed. Next the cooling fins were attached to the top of the plunger. By manual control, the hotplate temperature was lowered at a rate of 30 C°/hr until solidification was complete.

Under these conditions the crystal nucleated at the top of the plunger bore, and growth continued downward. A large temperature gradient, initially about 20 C°/cm, was produced by the combined effect of the controlled hotplate at the bottom, the copper cooling fins at the top, and a stainless-steel crucible wall. The crucible bottom plug and the plunger were made of mild steel.

After cooling, the sample was examined for grain boundaries. The coating of petroleum jelly remaining after the growing process was removed by rinsing the sample in xylene. Methanol proved to be a suitable etchant. Best results were obtained by etching for a few seconds and then rinsing in xylene, repeating this process four or five times. If either the sample or the etchant became too warm, the resulting vigorous etching action led to very poor grain-boundary definition. This operation and all succeeding ones were carried out in air, the sample being protected with a coating of petroleum jelly except during etching. (The reaction of the air with the sample between etching in methanol and rinsing in xylene is an essential part of the etching technique. Attempts to follow the same procedure in an argon atmosphere were completely unsuccessful. A white crust covered the sample as soon as it was removed from the methanol. This crust was not soluble in xylene.)

If no grain boundaries were brought out by the etching, the sample was examined by X-ray diffraction techniques. The back-reflection Laue diffraction method used on the heavier metals is not applicable to lithium because of the low scattering power of lithium atoms and the effects of thermal agitation. However, transmission Laue diffraction patterns can be viewed directly on a fluorescent screen. These have been observed satisfactorily through the 4-cm length of a single-crystal specimen. The X-ray examination of the sample was performed by placing the sample on a travelling stage and translating it through the X-ray beam in such a way that the orientation of the sample with respect to the X-ray beam did not change. In this way each sample was examined throughout its volume. Whenever the X-ray beam crossed a grain boundary, easily observable changes in the diffraction pattern occurred.

The crystal-growing method which has been described was used until a sufficient stock of single crystals was in hand. Roughly 50 per cent success was encountered. The crystals were free from mosaic structure as judged by visual examination of the etched crystals and of the Laue patterns. The ingots showed no evidence of frozen-out impurities, and spectroscopic analysis of the crystals showed no major impurities. Soluble magnesium in particular analyzed at 0·01 per cent.

In measuring the elastic constants of a cubic material by the ultrasonic pulse-echo technique, it is advantageous to have the direction of wave propagation along a [110] direction.[4] It is then possible to determine each of the elastic shear constants by an independent measurement. In lithium the anisotropy of the shear constants is large (approximately 9). Because of this, the experimental measurement of both shear constants on one single-crystal sample is feasible only for propagation directions very close to [110].

Each single-crystal sample was cut to produce two parallel faces perpendicular to a [110] direction. To accomplish this, the sample was mounted in a two-circle goniometer in the X-ray beam, and the angle between the sample axis and the nearest [110] direction was measured by rotating the sample until a [110] Laue pattern was observed on the fluorescent screen. A lapping ring was made to hold the sample at this angle. The specimen ends were cut off parallel to the lapping-ring faces by means of a string saw charged with methanol; about 2 hr were required for one cut through a $\frac{1}{2}$ in-dia. sample. The surfaces obtained were somewhat irregular, and therefore the cut was positioned to leave about 0·05 in. of material to be removed by lapping. The faces of the sample were finished by lapping them flat and coincident with the lapping-ring faces. The lap used consisted of paper toweling placed on a plate-glass backing and moistened liberally with methanol.

A transmission Laue diffraction photograph taken with the sample face perpendicular to the X-ray beam provided the orientation of the finished sample. All samples were within 2° of [110]. The proper polarization directions for the slow and fast shear waves were also noted from this film to facilitate positioning of the shear-wave transducers.

The elastic constants were measured by the ultrasonic pulse-echo method. The appropriate 10-Mc quartz transducer was cemented to one end of the single-crystal

VOL 9 195

sample. At 195 and 155°K, petroleum jelly was a suitable cement. The transducer was attached to the single-crystal sample at room temperature with a thin layer of petroleum jelly. The sample was enclosed in an aluminum cartridge and cooled to the measuring temperature. When cooled, the cement transmitted both shear and longitudinal waves satisfactorily. Attempts to use this cement at 78°K were unsuccessful because the quartz transducers cracked. A small amount of rubber dissolved in the petroleum jelly produced a cement which was satisfactory at this temperature if the sample was not cooled too rapidly.

The electronic equipment used to produce the pulses and measure the transit times has been described previously.[6]

RESULTS

The primary data are the transit-time measurements. The longitudinal and the two transverse acoustic-wave velocities propagated in the [110] direction as found from these transit times are shown in Table 1 for the lithium crystal designated

Table 1. *Acoustic-wave velocities in the* [110] *direction. Results are expressed in units of* 10^5 *cm sec*$^{-1}$ *and are for lithium crystal I*

Temp. (°K)	Slow shear	Fast shear	Longitudinal
78	1·46	4·44	6·69
155	1·43	4·29	6·50
195	1·42	4·22	6·37

as "I" below. To obtain these values, the length of the sample was measured at 298°K, and the lengths at the measuring temperatures were calculated with the aid of PEARSON's measurements of the lattice parameter of lithium at these temperatures.[6] The lattice parameter values used were: 3·510, 3·494, 3·489, and 3·482 Å at 298, 195, 155, and 78°K, respectively.

The single-crystal adiabatic elastic constants of lithium were calculated from the velocity data. These constants at 195°K are shown in Table 2, where ZENER's notation for the two shear constants $C = C_{44}$ and $C' = (C_{11} - C_{12})/2$ has been used, and B_s denotes the adiabatic bulk modulus, $(C_{11} + 2C_{12})/3$. Table 2 also compares the results for three samples of different lengths and slightly different orientations as measured at 195°K. The agreement of the three specimens is seen to be good. Crystal I was considered to be the most

Table 2. *Comparison of the elastic constants of three lithium samples at* 195°K. *Results are expressed in units of* 10^{11} *dyne cm*$^{-2}$

Sample	C'	C	B_s	Length (cm)
I	0·1086	0·960	1·197	1·11
II	0·1054	0·969	1·205	0·98
III	0·1064	0·959	1·193	1·40
Mean	0·1068	0·963	1·198	

reliable of the three for experimental reasons; the results for it are quoted in the remainder of the paper.

The lengths of the three crystals are also given in Table 2. The range of lengths used is not large, but there appears to be no systematic dependence of elastic constant on length such as would arise if a "transit time error"[5] were present. This error would not be expected to be large, since the acoustic mismatch between lithium and the quartz transducers is large. Extensive experiments with dummy transducers showed no error from this source.

The results for the three measuring temperatures are given in Table 3. Also shown in this table

Table 3. *Values of the adiabatic elastic constants of lithium and of the density. Elastic constants expressed in units of* 10^{11} *dyne cm*$^{-2}$, *and the density in g cm*$^{-3}$

Temp. (°K)	C'	C	B_s	ρ
78	0·116	1·08	1·33	0·5454
155	0·111	1·00	1·25	0·5421
195	0·109	0·96	1·20	0·5398

are the values of the density which have been used in the calculation of the elastic constants. The densities were obtained from PEARSON's lattice-parameter measurements[6] and HUTCHISON's atomic-weight determination.[7]

The values shown in Tables 2 and 3 have been corrected for the difference between the actual direction of propagation of the acoustic waves and the [110] direction. This difference was only a few degrees in the worst case, and less than $\frac{1}{2}°$ for

Crystal I. Perturbation corrections[4] are zero for the [110] direction and were found to be negligible for the actual orientations.

Because BARRETT[8] has reported that a transformation from body-centred cubic to face-centred cubic can be induced in lithium at 78°K by plastic deformation, the elastic constants were measured at 195°K both before and after the measurements at 78°K. No change in the elastic constants was observed.

in the form:

$$C = 0{\cdot}7422\frac{e^2}{a^4}, \qquad C' = 0{\cdot}0997\frac{e^2}{a^4}, \qquad (1)$$

where a is the cubic lattice constant and e is the electronic charge. The theory can conveniently be compared with the experimental values by plotting the dimensionless quantity a^4C/e^2 against temperature, placing the common theoretical value for all alkali metals at $T = 0$°K and the experimental

Table 4. (a) *The values for lithium of the measured adiabatic elastic stiffnesses* C^S, *and the computed adiabatic compliances* S^S. (b) *Isothermal stiffnesses and compliances. Units are* 10^{11} *dyne cm*$^{-2}$ *for* C *and* 10^{-11} *cm*^{2} *dyne*$^{-1}$ *for* S

T (°K)	C_{11}	C_{12}	C_{44}	S_{11}	S_{12}	S_{44}
			(a) *Adiabatic*			
78	1·481	1·248	1·077	2·948	−1·348	0·929
155	1·401	1·179	0·997	3·094	−1·414	1·003
195	1·342	1·125	0·960	3·162	−1·442	1·042
			(b) *Isothermal*			
78	1·476	1·243	1·077	2·948	−1·348	0·929
155	1·384	1·162	0·997	3·096	−1·413	1·003
195	1·320	1·102	0·960	3·164	−1·440	1·042

Finally in Table 4 are given the adiabatic stiffnesses, C_{ij}, and compliances, S_{ij}, for the three temperatures, and then the isothermal stiffnesses and compliances. Isothermal quantities have been computed from auxiliary data.[6,9]

DISCUSSION

This problem was undertaken to test the validity of the FUCHS theory[1] of the electrostatic shear stiffness. In the one previous case where a comparison can be made, that of sodium, the calculated values of C and C' at absolute zero are lower than the extrapolated experimental values.[10] But since the exact form of the extrapolation is somewhat uncertain, it is difficult to evaluate the degree of disagreement.

The FUCHS theory gives the electrostatic contribution to the shear constants of the alkali metals values of individual metals at the measurement temperatures. The reader may then make his own extrapolation.

Fig. 2 presents the experimental findings of this work, those of QUIMBY and SIEGEL[2] for sodium, and a single point for potassium due to BENDER,[3] together with the theoretical values of FUCHS, for the two shear constants C and C'. (The lattice constant of potassium has been estimated rather crudely from the room-temperature values to be 5·248 Å at 78°K.) It is seen that there is rough agreement between the experimental values for these three alkali metals and those calculated from equations (1).

The experimental values for both C and C' for lithium increase as the temperature decreases, but the increase is not sufficient to bring the extrapolated values up to the predictions of equations

(1). On the other hand, the experimental values for sodium at 80°K are already higher than the theoretical values, and extrapolation increases the discrepancies. The same statement holds for potassium if a curve similar to those for lithium and sodium is passed through the single point which is available.

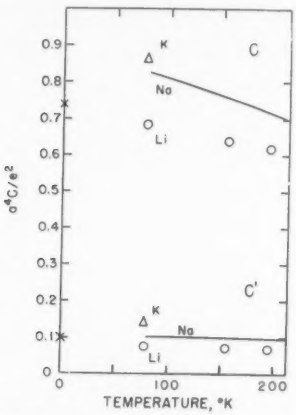

FIG. 2. The elastic shear constants C and C', expressed in the dimensionless form a^4C/e^2, plotted as a function of temperature for lithium, sodium, and potassium. The crosses at $T = 0$ are the theoretical values of the Coulomb contribution.

The elastic shear constants of lithium, sodium and potassium fall in a monotonic sequence in Fig. 2 which is the same as their sequence in the Periodic Table. The number of nodes in the actual s wave function for the three metals follows the same sequence. In FUCHS's calculations the effect of shear strain on the wave function in the region of these nodes is neglected, equations (1) being obtained by considering a constant valence-electron charge density. These two facts taken together suggest that a more sophisticated treatment of the "electrostatic" term may be all that is necessary to bring about more detailed agreement between theory and experiment for all the alkali metals. However, we consider here some other possibilities.

As FUCHS points out, equations (1) may be modified on reasonable grounds by the introduction of a common factor f^2 on the right side of each, f being physically the electron density at the boundary of the unit polyhedron in the metal. FUCHS gives the factor f as unity in the case of sodium and potassium. Its value is uncertain for lithium.

Because of the uncertainty in the f value for lithium, the theory and experiment can better be compared by inspecting the anisotropy, C/C', in the elastic constants, which is independent of the value of f. The anisotropies have been plotted in Fig. 3. Again there is basic agreement with the theoretical values, but detailed disagreement in a monotonic sequence as noted in connection with Fig. 2. We note that the small uncertainty in the lattice constant of potassium present in Fig. 2 has also cancelled out in the anisotropy. It is apparent that the differences between experiment and equations (1) shown in these two figures cannot be resolved by the simple device of introducing f.

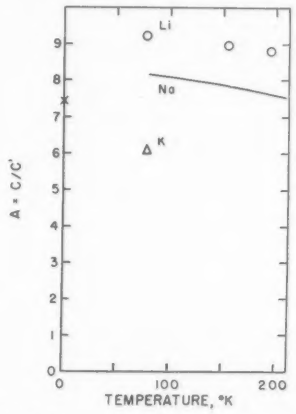

FIG. 3. The elastic anisotropy C/C' plotted as a function of temperature for lithium, sodium, and potassium. The cross at $T = 0$ is the theoretical anisotropy.

In addition to the electrostatic contribution to the shear constants, FUCHS, in his original papers, includes a term for the repulsive interaction of the closed-shell ion cores and a van der Waals term. We regard the theoretical values of these terms as exceedingly questionable, but the effect of introducing them may be considered in empirical terms. For this purpose the van der Waals term may be grouped with the repulsive interaction, since both are short-range and operate only between nearest-neighbor ions. If $W(r)$ is the short-range interaction energy per ion pairs, or "bond" (such that $4W(r)$ is the energy per atom in these body-centred cubic metals), the contribution of W to the

shear constants may be written:

$$\Omega C_R = \frac{4}{9} r_0^2 W'' + \frac{8}{9} r_0 W', \quad \Omega C_R' = \frac{4}{3} r_0 W', \quad (2)$$

where Ω is the atomic volume, r_0 is the equilibrium separation of the nearest neighbors, and differentiation with respect to r is indicated by a prime. For a net repulsive interaction we have $W'' > 0$ and $W' < 0$, and for a short-range interaction $|r_0^2 W''| \gg |r_0 W'|$. Thus these contributions to the theoretical values will be positive for C, and negative and smaller in magnitude for C'. Inspection of Figs. 2 and 3 shows that the agreement of theory and experiment for lithium cannot be improved for both C and C' by the introduction of such a term alone. The theory and experiment can be brought into detailed agreement in the case of lithium by assuming reasonable values for C_R and C_R' and combining these with a suitable value of f^2, but this process amounts to satisfying two experimental numbers by three free parameters and we do not feel justified in pursuing the point.

BARDEEN[11] has calculated the bulk modulus of lithium at absolute zero. This value is shown in Table 5, together with the values determined in the present work. The order-of-magnitude agreement is good. Also shown in this table is the room-temperature adiabatic bulk modulus obtained from BRIDGMAN's data by the following approximate relation:

$$B_s \cong B_T \left(1 + \frac{9T\alpha^2 B_T}{\rho C_p}\right)$$

where $\rho = 0{\cdot}532$ g cm^{-3}, and $\alpha = 46{\cdot}6 \times 10^{-6}$ deg^{-1} were taken from PEARSON,[6] $C_p = 0{\cdot}816$ cal gm^{-1} deg^{-1},[11] and $B_T = 1{\cdot}127 \times 10^{11}$ dyne cm^{-2}.[12] The agreement is regarded as satisfactory considering the inherent difficulties in BRIDGMAN's method of measuring B_T of lithium.

Table 5. Experimental and theoretical values of the adiabatic bulk modulus of lithium. Results are expressed in units of 10^{11} *dyne cm*$^{-2}$

Temperature (°K)	B_s	Source
0 (theoretical)	1·19	BARDEEN[11]
78 (experimental)	1·33	This paper
155 (experimental)	1·25	This paper
195 (experimental)	1·20	This paper
303 (experimental)	1·17	BRIDGMAN[12]

Acknowledgements—This research was supported by the Office of Naval Research, and by the National Carbon Company. The work was performed while H. C. NASH was on leave of absence from John Carroll University and he is indebted to the National Carbon Company for a scholarship for this period. We thank our colleague, W. B. DANIELS, for much advice on the experiments, and A. A. HRUSCHKA for the support of his excellent machine shop.

REFERENCES

1. FUCHS K., *Proc. Roy. Soc.* **A153,** 622 (1936); **A157,** 444 (1936).
2. QUIMBY S. L. and SIEGEL S., *Phys. Rev.* **54,** 293 (1938).
3. BENDER O., *Ann. Phys.* **34,** 359 (1939).
4. NEIGHBOURS J. R. and SMITH CHARLES S., *J. Appl. Phys.* **21,** 1338 (1950).
5. EROS S. and REITZ J. R., *J. Appl. Phys.* **29,** 683 (1958).
6. PEARSON W. B., *Canad. J. Phys.* **32,** 708 (1954).
7. HUTCHISON D. A., *J. Amer. Chem. Soc.* **76,** 967 (1954).
8. BARRETT C. S., *Phys. Rev.* **72,** 245 (1947).
9. *American Institute of Physics Handbook,* Table 4e McGraw-Hill, New York (1957).
10. MOTT N. F., *Progr. Metal Phys.* **3,** 76 (1952).
11. BARDEEN J., *J. Chem. Phys.* **6,** 367 (1938).
12. BRIDGMAN P. W., *The Physics of High Pressures* p. 160. Bell and Sons, London (1952).

VOL 9 195

J. Phys. Chem. Solids Pergamon Press 1959. Vol. 9. pp. 119–128. Printed in Great Britain.

TRANSVERSE MAGNETORESISTANCE AND HALL EFFECT IN *N*-TYPE InSb*

R. T. BATE, R. K. WILLARDSON and A. C. BEER

Battelle Memorial Institute, Columbus, Ohio

(*Received* 14 *July* 1958)

Abstract—Data on the transverse magnetoresistance and Hall effect are given for fixed temperatures between 50 and 200°K, covering the range from the weak-magnetic-field region to the strong-field quantum limit in InSb samples of high mobility and sufficient purity that classical statistics are applicable. At weak fields, results are in semiquantitative agreement with the predictions of theory based on a simple mixed-scattering mechanism and a spherical conduction band. At the highest fields, the transverse-magnetoresistance data approach the H/T behavior expected on the basis of the quantum treatment of ARGYRES and ADAMS (*Phys. Rev.* **104,** 900 (1956)), and the result in the quantum limit for the purest specimen shows good agreement with the theory for reasonable values of the electron effective mass.

1. INTRODUCTION

IN recent years, analyses of the magnetic-field dependence of galvanomagnetic effects in germanium and silicon have contributed significantly to an understanding of the influence of band structure and crystalline imperfections on conductivity.[1,2] This method of investigation can also be helpful in studies of many other semiconducting materials.

Indium antimonide is particularly well suited for such investigations because of its very small electron effective mass and consequent high electron mobility. Since galvanomagnetic coefficients depend on the dimensionless parameter $\mu^0 H$, where μ^0 is the carrier drift mobility in electromagnetic units and H is the magnetic field intensity, one can observe in indium antimonide at moderate magnetic fields those effects which would require much higher fields in other semiconductors.

FREDERIKSE and HOSLER[3] have made an extensive study of galvanomagnetic effects in *n*-type InSb between 1 and 78°K for samples with excess donor concentrations in the range 9×10^{14} to 7×10^{15} cm^{-3}. At 78°K, the electron concentration for which the Fermi level is $2kT$ from the edge of the conduction band is about 7×10^{14} cm^{-3}, so that, strictly speaking, galvanomagnetic data on InSb with electron concentrations greater than this should be analyzed using Fermi–Dirac statistics for temperatures as low as that of liquid nitrogen. The behavior of the galvanomagnetic coefficients for such material may be quite complex, since the Fermi energy depends on the magnetic field, and the variation can be appreciable at large fields.[3,4] Also, ionized-impurity scattering is probably the major scattering mechanism in such material below 78°K. In order to simplify analysis, it is therefore desirable to obtain data on samples of higher purity in a temperature range where classical statistics apply and impurity scattering is not predominant.

High-field measurements are of particular interest in InSb because of the quantum effects in strong magnetic fields. As was originally pointed out by LANDAU,[5] the motion of a conduction electron is quantized in a strong magnetic field. The effects of this quantization on the galvanomagnetic coefficients should be most pronounced at low temperatures and high fields, such that $\omega\tau \gg 1$ and $\hbar\omega/kT \gg 1$ (when classical statistics apply, and where ω is the cyclotron resonance

* This work was supported by the U.S. Air Force through the Air Force Office of Scientific Research of the Air Research and Development Command.

frequency and τ is the relaxation time), since the quantized energy levels will be widely separated and the motion of the electrons will be characterized by small quantum numbers. The condition for which $\hbar\omega/kT \gg 1$, so that all carriers are in the lowest quantum state in the magnetic field, has been called the "quantum limit" by ARGYRES and ADAMS.[6] On the other hand, when $\hbar\omega/kT \ll 1$, the motion is characterized by large quantum numbers and, by virtue of the correspondence principle, a quantum treatment should give the same results as the semiclassical treatment, which ignores the quantization.

For high-purity n-type InSb at 77°K, the condition $\omega\tau > 1$ is satisfied for magnetic fields above 200 G, and the quantity $\hbar\omega/kT$, which is approximately equivalent to 0·01 H/T, becomes unity at about 8000 G. Thus, n-type InSb is an ideal material for the study of quantum effects.

2. METHOD OF ANALYSIS

The analysis of the data is carried out using the simplest possible model. At low fields, ionized-impurity scattering is introduced following the treatment by JOHNSON and WHITESELL,[7] which assumes that the Rutherford scattering and acoustical-mode lattice scattering (or, more generally, a scattering mechanism for the second process characterized by a relaxation time proportional to $\epsilon^{-\frac{1}{2}}$) are the dominant mechanisms, that the energy surfaces are spherical, that quantum effects are unimportant, and that classical statistics apply.

The high-field data are analyzed by means of the quantum procedure developed by ARGYRES,[4] which assumes spherical energy surfaces and acoustical-mode lattice scattering only.

The treatment of JOHNSON and WHITESELL yields the following expressions for the Hall coefficient and transverse magnetoresistance:

$$|R| = \frac{3\pi}{8}\left[\frac{L}{K^2+(\pi/4)\gamma L^2}\right]\frac{1}{ne}$$

$$\frac{\Delta\rho}{\rho_0} = \frac{K^0 K}{K^2+(\pi/4)\gamma L^2} - 1,$$

where

$$K \equiv K(\beta,\gamma) \equiv \int_0^\infty \frac{x^3 e^{-x}(x^2+\beta)\,dx}{(x^2+\beta)^2+\gamma x^3}$$

$$L \equiv L(\beta,\gamma) \equiv \frac{2}{\sqrt{\pi}}\int_0^\infty \frac{x^{9/2}e^{-x}\,dx}{(x^2+\beta)^2+\gamma x^3}$$

$$\gamma \equiv \frac{9\pi}{16}(\mu_L{}^0 H)^2,\ \beta \equiv \mu_L{}^0/\mu_I{}^0$$

$$K^0 \equiv K(\beta,0) \equiv K(\beta),\ \mu^0 = \mu_L{}^0 K(\beta),$$

where R is the Hall coefficient, ρ is the resistivity, $\mu_L{}^0$ and $\mu_I{}^0$ are the carrier drift mobilities for the respective cases of scattering only by lattice vibrations and by ionized impurities in the absence of a magnetic field. The integrals $K(\beta, \gamma)$ and $L(\beta, \gamma)$ have recently been evaluated over a wide range of values of β and γ by BEER *et al.*[8]

Analysis of the expressions reveals that the Hall coefficient approaches the field-independent value $1/ne$ at strong fields regardless of the value of β, and it approaches a β-dependent value at weak fields. The transverse magnetoresistance, $\Delta\rho/\rho_0$, is proportional to H^2 at low fields, and becomes field-independent at high fields, but is dependent on β at all fields.

ARGYRES[4] has taken into account the quantization of the electron motion to calculate the strong-field magnetoresistance and Hall coefficient of a semiconductor with spherical energy surfaces for which acoustical-mode lattice scattering is the only important scattering mechanism. His results, which apply as long as $\omega\tau \gg 1$ and $\hbar\omega/kT \gg 1$, can be simplified when classical statistics apply and when $kT\tau \gg \hbar$ to yield:

$$|R| \simeq \frac{1}{ne}(1+\sqrt{\pi}\Gamma^{\frac{1}{2}})$$

$$\frac{\rho_H}{\rho_0} \simeq \frac{2}{3\pi}\left(\frac{\hbar\omega}{kT}\right)(\log\Gamma^{-1} - 0{\cdot}577)$$

$$\simeq \frac{4}{3\pi}\,\frac{m}{m^*}\,\frac{\mu_B H}{kT}(\log\Gamma^{-1} - 0{\cdot}577),$$

where

$$\Gamma \equiv \left(\frac{\hbar}{2kT\tau_0(kT)}\right)^2 = \left(\frac{m}{m^*}\,\frac{\mu_B}{kT}\,\frac{4}{3\sqrt{\pi}\mu_L{}^0}\right)^2$$

and μ_B is the Bohr magneton. For high-purity InSb at 80°K, $\Gamma \simeq 10^{-6}$, so that the predicted strong-field Hall coefficient agrees with the classical

value $1/ne$ to within about 0·1 per cent for this case. On the other hand, the behavior of the transverse magnetoresistance is quite different, the magnetoresistance being roughly proportional to H/T at high fields and low temperatures (as long as classical statistics apply), instead of saturating as the classical theory predicts.

Several objections to the above model can be raised, and it would be well at this point to examine the limitations. KANE[9] has calculated the structure of the conduction band in InSb and has found that the relation between energy and wave number is nonparabolic for sufficiently large energies above the bottom of the band. In our case, however, this consideration causes no difficulty because of the small carrier concentrations and low temperatures of measurements. Hence, the assumption of spherical energy surfaces appears quite well justified. It is interesting to note that in germanium the warped heavy mass band is responsible for a minimum in the magnetic-field variation of the Hall coefficient[2] similar to that observed in InSb (see Fig. 2).

Recently EHRENREICH[10] has shown that polar scattering is the dominant scattering mechanism in InSb above 200°K. Since the Debye temperature for the polar modes in InSb is approximately 290°K, we would expect them to be somewhat less important at low temperatures, but a rough extrapolation of EHRENREICH's calculations shows that the mobility contribution from polar-mode scattering still predominates over that from acoustical modes at 80°K. In addition, HARRISON[11] has pointed out that piezoelectric scattering should be important in InSb at low temperatures. Therefore, a truly satisfactory treatment should incorporate both of these scattering mechanisms. This would be quite complicated, especially in the case of polar scattering, inasmuch as one cannot define a relaxation time in the temperature range of interest.

In view of these complications, it is obvious that the analysis adopted here can be expected to give only a semiquantitative description of the situation, and that any magnitude quoted for lattice mobility must be considered as only an approximation to the true mobility. However, as will be apparent, the treatment presented here does indicate the importance of considering a mixed scattering mechanism rather than a single process. This conclusion is based on the fact that our development appears to account better for the experimental data than does a treatment where the relaxation time is determined only by polar scattering or by Rutherford scattering.

3. EXPERIMENTAL PROCEDURE

The specimens used in this investigation were high-purity single crystals of InSb cut from ingots which had been given many zone-refining passes. Ultrasonic cutting was used to fabricate "bridge" samples. Current and potential leads and thermocouples were welded

Table 1. *Electric characteristics of n-type* InSb *samples*

Sample	Temperature (°K)	Hall coefficient, R_{min} (cm^3/C)	Resistivity, ρ (Ω-cm)	Mobility, μ^0 (cm^2/V-sec)	Impurity-scattering parameter, $\beta \equiv 6(\mu_L{}^0/\mu_I{}^0)$	Excess-donor concentration, $N_D - N_A$ (cm^{-3})	Estimated ionized-impurity concentration, N_I(est.) (cm^{-3})
1	195	$=8{\cdot}8\times10^{3}$	$6{\cdot}0\times10^{-2}$	$1{\cdot}46\times10^{5}$	0·3	$7{\cdot}8\times10^{13}$	8×10^{14}
	77	$=8{\cdot}0\times10^{4}$	$1{\cdot}70\times10^{-1}$	$4{\cdot}9\times10^{5}$	4·5		
	55	$=8{\cdot}0\times10^{4}$	$1{\cdot}56\times10^{-1}$	$5{\cdot}1\times10^{5}$	12		
2	195	$=9{\cdot}1\times10^{3}$	$6{\cdot}0\times10^{-2}$	$1{\cdot}51\times10^{5}$	0·3	$1{\cdot}0\times10^{14}$	5×10^{14}
	77	$=6{\cdot}2\times10^{4}$	$1{\cdot}38\times10^{-1}$	$4{\cdot}6\times10^{5}$	3		
	55	$=6{\cdot}2\times10^{4}$	$1{\cdot}20\times10^{-1}$	$5{\cdot}2\times10^{5}$	8		
3	195	$=7{\cdot}5\times10^{3}$	$4{\cdot}8\times10^{-2}$	$1{\cdot}57\times10^{5}$	0·3	$1{\cdot}7\times10^{14}$	$1{\cdot}7\times10^{14}$
	77	$=3{\cdot}7\times10^{4}$	$6{\cdot}0\times10^{-2}$	$6{\cdot}2\times10^{5}$	1		
	55	$=3{\cdot}7\times10^{4}$	$5{\cdot}0\times10^{-2}$	$7{\cdot}4\times10^{5}$	2·5		

to the samples, which were then sealed in Pyrex tubes in a helium atmosphere. Voltage measurements were made with an L & N K−2 potentiometer and an L & N White double potentiometer.

Measurements of the Hall coefficient were done at fixed temperatures for magnetic fields in the range 20–20,000 G. Fields of 50 G and below were obtained from Helmholtz coils. The constant-temperature baths and the associated temperatures were: dry ice and acetone, 195°K; liquid nitrogen, 77°K; pumping of vapor from liquid nitrogen containing oxygen, approximately 55°K.

In taking the measurements, the sample current and magnetic field were reversed independently and the readings averaged to eliminate thermomagnetic and thermoelectric voltages.

4. RESULTS AND DISCUSSION

(a) *Mobility data and determination of degree of impurity scattering*

Table 1 lists the Hall coefficients, resistivities, and mobilities of three samples at the fixed temperatures employed. The mobilities were obtained by assuming that $|R|_{\min} = 1/ne$, where $|R|_{\min}$ is the absolute value of the Hall coefficient measured at the magnetic field for which it is minimum (see Fig. 1).

Before the galvanomagnetic data can be interpreted, it is necessary to determine the appropriate values of β,

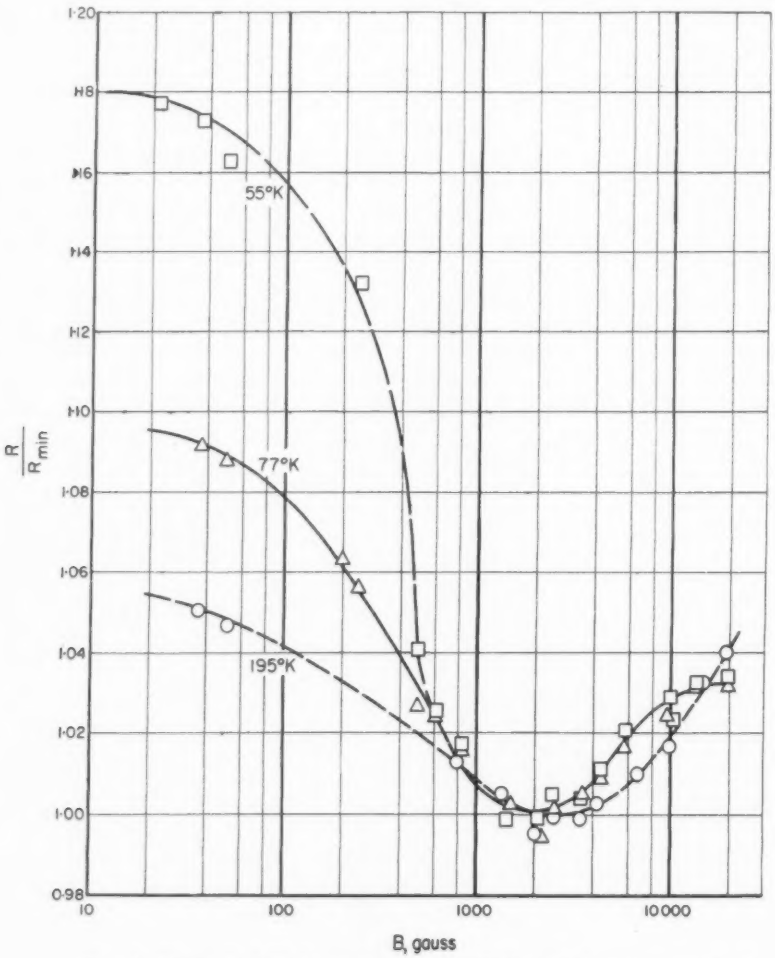

FIG. 1. Magnetic-field dependence of the Hall coefficient in n-type InSb (Sample 1, $N_D - N_A = 7{\cdot}8 \times 10^{13}$ cm^{-3}).

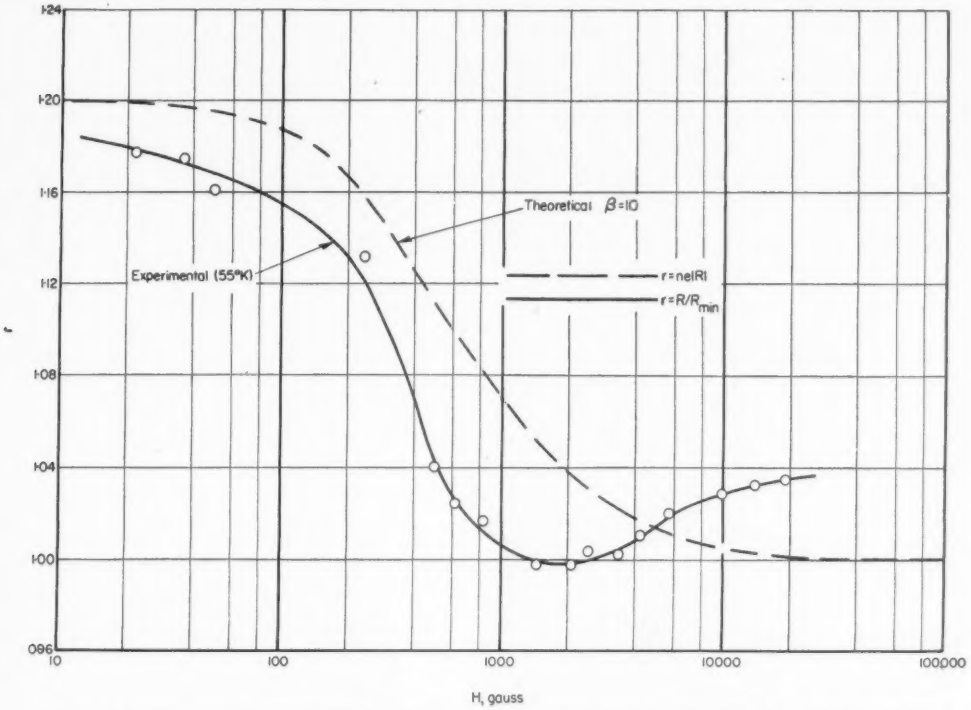

FIG. 2. Comparison of experimental and theoretical magnetic-field dependence of the Hall coefficient (Sample 1, $N_D - N_A = 7{\cdot}8 \times 10^{13}$ cm^{-3}).

the impurity-scattering parameter. A self-consistent way of doing this is as follows: according to the JOHNSON and WHITESELL treatment,[7] which is based on the simplified mixed-scattering mechanism previously discussed, the mobility at a temperature T_1 in the extrinsic region is

$$\mu_1{}^0 = \mu_{L1}{}^0 K(\beta_1) = aT_1{}^{-3/2} K(bT_1{}^{-3}).$$

Thus, if $\mu_2{}^0$ is the mobility at another temperature T_2 in the extrinsic range, then:

$$\frac{\mu_1{}^0}{\mu_2{}^0} = \left(\frac{T_1}{T_2}\right)^{-3/2} \frac{K(bT_1{}^{-3})}{K(bT_2{}^{-3})},$$

an equation which may be solved graphically for b when the ratios $\mu_1{}^0/\mu_2{}^0$ and T_1/T_2 are known. Then,

$$\beta(N_I, T) = bT^{-3}.$$

This procedure, which employs only the ratios of measured mobilities at different temperatures, avoids the use of absolute magnitudes of total impurity content and lattice mobilities required when a direct calculation is made of μ_L/μ_I. The method thus eliminates errors due to compensation effects and those resulting from measurements of sample geometry. Results are summarized in Table 1.

In calculating the β values in the intrinsic region, hole conduction and electron-hole scattering must also be taken into account. Since the effective mass of holes in InSb is much greater than that of the electrons, electron-hole scattering can, in first approximation, be treated like ionized-impurity scattering, taking into account the temperature-dependence of the hole concentration. Thus, the chief effect of electron-hole scattering is to modify the temperature-dependence of β in the intrinsic region, and this modification has been taken into account in the calculation of β at 195°K.

As a consequence of the large mobility ratio in InSb, the effect of hole conduction on the conductivity and on the galvanomagnetic coefficients below 1000 G is quite small in the intrinsic region. However, the effects of the holes on the strong-field galvanomagnetic effects may be significant, and these will be discussed.

(b) *The Hall coefficient*

Fig. 1 shows the magnetic-field dependence, at

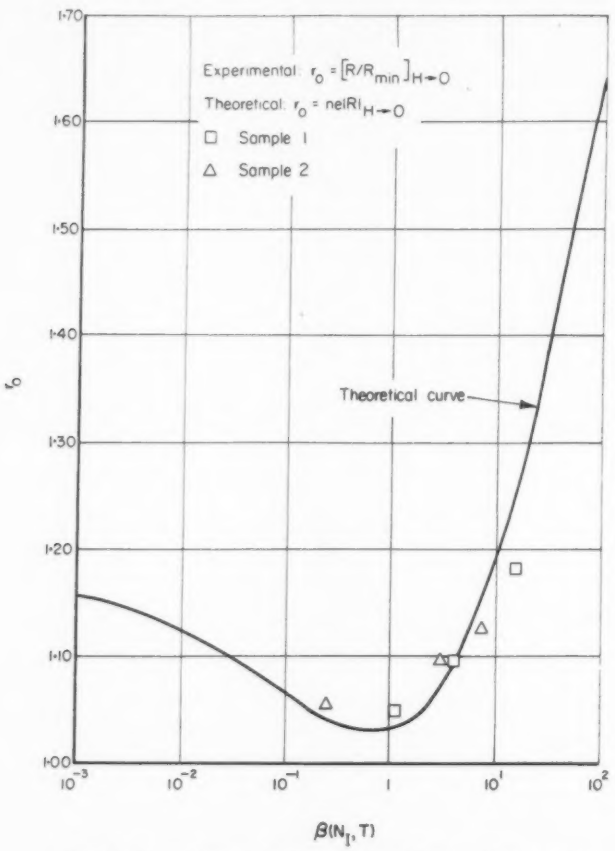

FIG. 3. Dependence of the weak-field Hall coefficient on the impurity-scattering parameter $\beta(\beta \equiv 6\mu_L{}^0/\mu_I{}^0)$.

three fixed temperatures, of the Hall coefficient for a typical specimen of high-purity n-type InSb. It will be noted that a minimum occurs in the high-field region, and the Hall coefficient has been arbitrarily normalized to unity at this minimum to facilitate comparison. (The values of R at the minimum are given in Table 1.) Note that there appears to be little evidence of the oscillatory or "sinuous" variation reported for samples with larger conduction-electron concentrations.[3]

In Fig. 2 the experimental data at 55°K are compared with calculated values. Although the appropriate value of β is 12, a value of 10 was used, since $K(\beta, \gamma)$ and $L(\beta, \gamma)$ are tabulated[8] for this value. The lattice mobility used in determining γ was found by applying the relation $\mu_L{}^0 = \mu^0/K(\beta)$ to the mobility data on several samples. The agreement is seen to be fairly good at low fields, but at higher fields the data exhibit a fine structure not accounted for by the theoretical curve.

The increase in the absolute value of the extrinsic Hall coefficient at strong fields seems rather difficult to explain. As has already been pointed out, the warped heavy-mass valence band in germanium leads to such a behavior. Although the present case is somewhat different due to the absence of the band degeneracy, we are not inclined to rule out anisotropy as a point for consideration before directional effect studies are completed.* Another possible cause is the magnetically-induced

* In this connection, GOLD and ROTH[13] have shown how anisotropy introduced via combinations of ellipsoidal energy surfaces can also lead to minima in R_H as a function of magnetic field.

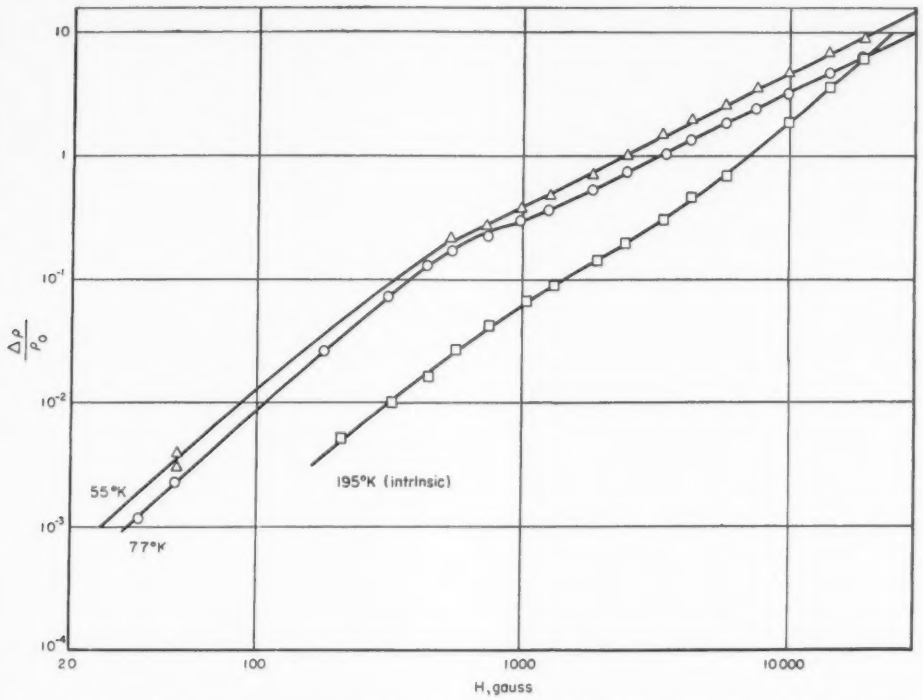

FIG. 4. Typical magnetoresistance data for n-type InSb (Sample 3, $N_D - N_A = 1{\cdot}7 \times 10^{14}$ cm^{-3}).

impurity banding investigated by KEYES and SLADEK.[12]

For the measurements at 200°K, an increase in Hall coefficient at large fields is to be expected as a result of contributions from hole conduction.

Fig. 3 shows a comparison of a theoretical plot of the normalized weak-field Hall coefficient as a function of β, with experimental points for two samples. Note that the agreement is quite good, although it must be remembered that the data were rather arbitrarily normalized. It is significant, however, that the minimum occurs in the predicted range of β values.

(c) *Weak-field magnetoresistance*

Transverse magnetoresistance data for one sample of n-type InSb at three fixed temperatures are shown in Fig. 4. The transverse magnetoresistance increases with decreasing temperature, because of the increased mobility, and it is proportional to H^2 at low fields. At high fields, the magnetoresistance is proportional to H in the extrinsic region, whereas it increases more rapidly with H when intrinsic. Fig. 5 shows the data for 77°K replotted along with the theoretical curve for the appropriate value of β. Although the agreement with the simple theory is fairly good at low fields, the magnetoresistance begins to deviate when $\omega\tau$ becomes of the order of unity, and approaches a linear dependence on H at high fields, whereas the semiclassical theory predicts saturation. This high-field behavior is evidently a quantum effect, but the initial deviation occurs at a rather small value of $\hbar\omega/kT$ to be attributed to quantization, and may result from some other mechanism as, for example, a delayed saturation due to polar scattering.[14]

A plot of the weak-field magnetoresistance analogous to that of Fig. 3 for the weak-field Hall coefficient is shown in Fig. 6, where the parameter,

$$\left[T^3 \frac{\Delta\rho}{\rho_H H^2}\right]_{H\to 0},$$

is plotted as a function of β. The theoretical variation, assuming

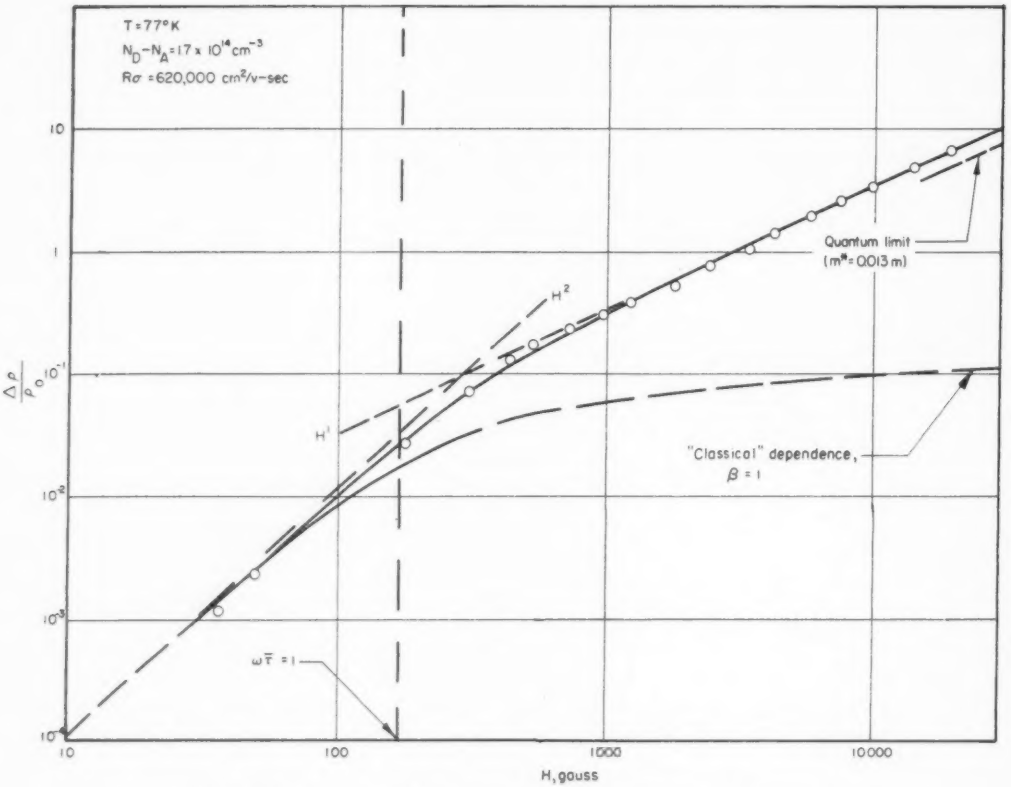

FIG. 5. Comparison of experimental magnetoresistance with theory.

$$\mu_L{}^0(77°\text{K}) = 1{\cdot}2\times10^6 \frac{\text{cm}^2}{\text{V-sec}},$$

is shown for comparison. Note that the theoretical low-field magnetoresistance is extremely sensitive to impurity scattering (and electron-hole scattering), the relative change in resistance having been reduced two orders of magnitude when $\mu_I = 10\mu_L$. The agreement here is not so good as in the case of the Hall coefficient, although, in most cases, the deviation is less than 50 per cent. Note that there seems to be a correlation of the deviation from theory with the degree of compensation.

(d) *Strong-field magnetoresistance*

Turning now to the strong-field region, the quantum treatment suggests a transverse magnetoresistance proportional to H at high fields, and the predicted high-field behavior is shown by the broken line in Fig. 5. However, this calculation was made for acoustical-mode lattice scattering only and for $\hbar\omega/kT \gg 1$; and neither of these conditions has been completely satisfied experimentally.

It is interesting to note that the values of $\hbar\omega/kT$ for the maximum field of 20,000 G are 2·6 at 77°K and 3·5 at 55°K. To investigate the effects of impurity scattering and to illustrate the approach to the quantum limit, the dimensionless parameter

$$\frac{\rho_H}{\rho_0}\cdot\frac{kT}{\mu_B H}$$

has been plotted in Fig. 7 as a function of magnetic field for three samples at two different temperatures. The theory predicts that for the acoustic-phonon scattering, this parameter should have the approximate value

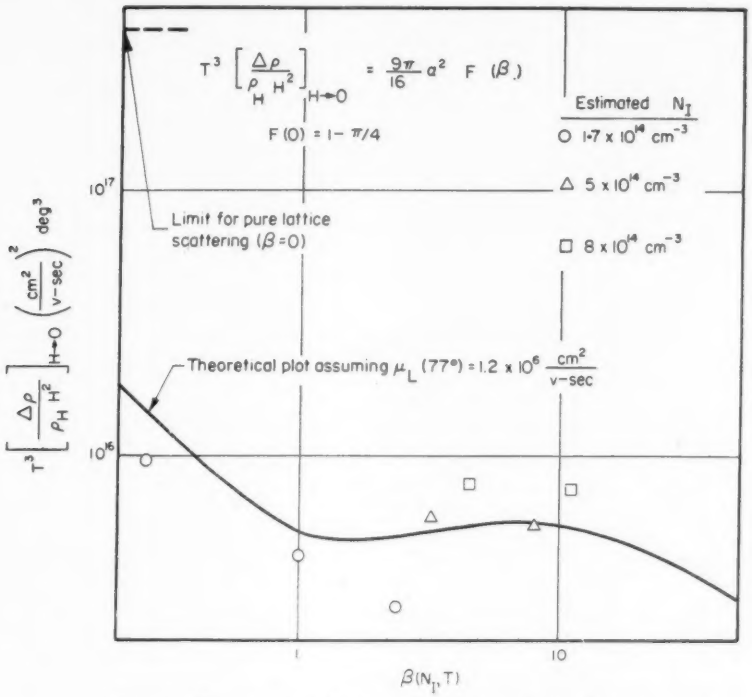

FIG. 6. Dependence of the weak-field magnetoresistance on the impurity-scattering parameter $\beta(\beta \equiv 6\mu_L{}^0/\mu)$

$$\frac{4}{3\pi}\frac{m}{m^*}(\log \Gamma^{-1} - 0{\cdot}577),$$

an expression which is relatively independent of temperature between 50 and 80°K, and equals about 350 for m^*/m of 0·013.[15] Note that according to our data this parameter does seem to be approaching a constant value for each sample, but the value appears to be a function of the total ionized-impurity concentration, with the result for the purest sample approaching most nearly the theoretical value for pure lattice scattering. Unfortunately, it is not possible at this time to continue the analysis further, because the quantum treatment has not been extended to encompass the case of mixed scattering.

5. SUMMARY

The experimental data tend to support the hypothesis of nearly spherical energy surfaces in the conduction band of InSb, and to confirm the predicted influence of impurity scattering and electron-hole scattering on the Hall coefficient and magnetoresistance. The existence of quantum effects for nondegenerate material in strong magnetic fields has been verified, and the data show that the strong-field magnetoresistance and Hall coefficient are in semiquantitative agreement with the quantum treatment.

Acknowledgements—The authors are grateful to Dr. P. N. ARGYRES for sending us his manuscript before publication, and to Dr. E. N. ADAMS, Jr., Dr. H. EHRENREICH, and Dr. C. HERRING for helpful comments. Thanks are also due to Miss M. E. TANNER, who produced some of the material, to G. L. KENDALL, who prepared the bridge-type samples, and to J. SCHROEDER of Ohio Semiconductors Inc., who supplied the highest-purity sample.

Note added in proof: Experiments are now being carried out on specimens taken from *pulled crystals*. Although this material is slightly less pure than that cut

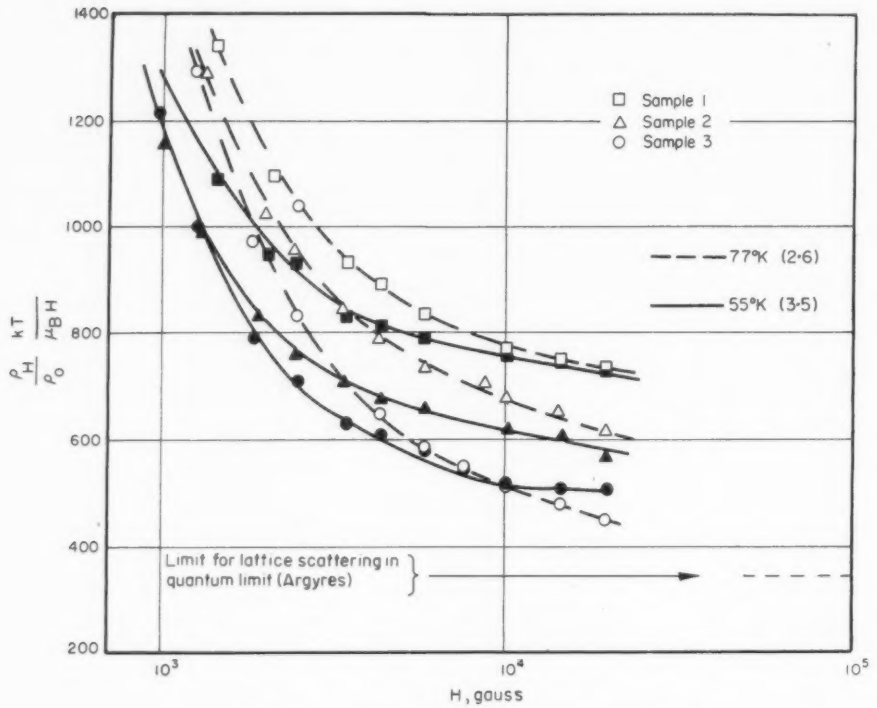

FIG. 7. Strong-field magnetoresistance in *n*-type InSb.

from zone-refined ingots ($N_D - N_A \sim 5 \times 10^{14}$, $\mu_{77°K} \sim$ $\sim$ 310,000), etch-pit densities are negligible compared to the $10^4/cm^2$ count for the zone-refined material. The behavior of R_H is substantially different from that shown in Fig. 1. After plastic bending, however, the difference disappears. It may be possible that dislocations exert a significant influence on the weak-field behavior of R_H. This problem is now being investigated by JULES DUGA.

REFERENCES

1. ABELES B. and MEIBOOM S., *Phys. Rev.* **95,** 31 (1954). SHIBUYA M., *Phys. Rev.* **95,** 1385 (1954). WILLARDSON R. K., HARMAN T. C. and BEER A. C., *Phys. Rev.* **96** 1512 (1954).
2. BEER A. C. and WILLARDSON R. K., *Phys. Rev.* **110,** 1286 (1958).
3. FREDERIKSE H. P. R., and HOSLER W. R., *Phys. Rev.* **108,** 1136 (1957).
4. ARGYRES P. N., *Phys. Rev.* **109,** 1115 (1958).
5. LANDAU L., *Z. Phys.* **64,** 629 (1930).
6. ARGYRES P. N. and ADAMS E., *Phys. Rev.* **104,** 900 (1956).
7. JOHNSON V. A. and WHITESELL W. J., *Phys. Rev.* **89,** 941 (1952).
8. BEER A. C., ARMSTRONG J. A. and GREENBERG I. N., *Phys. Rev.* **107,** 1506 (1957).
9. KANE E. E., *J. Phys. Chem. Solids* **1,** 249 (1957).
10. EHRENREICH H., *J. Phys. Chem. Solids* **2,** 131 (1957).
11. HARRISON W. H., *Phys. Rev.* **100,** 903 (1956).
12. KEYES R. K. and SLADEK R. J., *J. Phys. Chem. Solids* **1,** 143 (1956).
13. GOLD L. and ROTH L. M., *Phys. Rev.* **107,** 358 (1957).
14. LEWIS B. F. and SONDHEIMER E. H., *Proc. Roy. Soc.* A**227,** 241 (1955).
15. DRESSELHAUS G., KIP A. F., KITTEL C. and WAGONER G., *Phys. Rev.* **98,** 556 (1955).

J. Phys. Chem. Solids Pergamon Press 1959. Vol. 9. pp. 129–148. Printed in Great Britain.

TRANSPORT OF ELECTRONS IN INTRINSIC InSb†

H. EHRENREICH

General Electric Research Laboratory, Schenectady, New York

(*Received* 3 *July*; *revised* 15 *September* 1958)

Abstract—The mobility, thermoelectric power, Hall coefficient, and far infrared reflectivity of InSb are calculated, taking account of the non-parabolic conduction band as well as the correct wave functions of the electrons. Lattice scattering by polar modes and electron-hole scattering, previously shown to be the dominant mechanisms between 200 and 700°K, are properly combined in a variational transport calculation. Screening effects of the intrinsic carriers on the electron–phonon interaction are considered explicitly. A modified form of KOHLER's variational principle is introduced, and the sensitivity of the calculated transport properties to several choices of trial functions is investigated. The Hall coefficient for weak magnetic fields is obtained from a new variational principle, the results being used to correct the experimental Hall mobility. The calculated mobility and thermoelectric power for the effective ionic charge determined from optical experiments agree well with experiment. The theory in its present form contains no adjustable parameters. Finally, the Boltzmann equation for high-frequency conduction is solved by means of a perturbation technique. The reflectivity minimum of InSb in the far infrared is calculated and found to agree well with experiment.

1. INTRODUCTION

IN a previous paper[1]‡ the problem of determining the important scattering mechanisms in intrinsic InSb was considered. It was shown that polar scattering is the dominant mechanism in the temperature range between 200 and 500°K and that electron–hole scattering becomes comparably important at 500°K and dominates at higher temperatures. Deformation potential scattering was seen to be small over this entire temperature range. The calculations were based on the 0°K conduction-band structure calculations of KANE,[2] which showed an appreciable deviation from the parabolic relationship between energy and wave number, $E = \hbar^2k^2/2m^*$, that is found in simple bands. These calculations were extended heuristically by the use of results from pressure experiments[3] to give the conduction-band curvature at finite temperatures as well. The transport calculations were then formulated to be applicable to non-parabolic bands. The final results thus reflected in a quantitative way the actual conduction-band structure of InSb.

There were, however, several aspects of the problem that were not given detailed consideration in I. The first deals with the neglect of conduction-electron screening of the interaction between an electron and the vibrating polar lattice. This point will be discussed briefly in Section 2 and taken into account in the subsequent calculations. The second aspect deals with the electron wave function which has pure *s*-symmetry at the band edge but acquires an increasing amount of *p*-function admixture as one moves away from the band edge. This admixture was neglected in I and will be considered quantitatively in Section 3 of the present paper. It will be seen to alter the angular dependence of the scattering cross-sections. Further, both screening and the *p*-function admixture will be shown to decrease the scattering probabilities and hence to increase the mobility.

Since the relaxation-time approximation fails for polar scattering, the transport calculations must be performed with the aid of a variational principle due to KOHLER.[4] A third aspect not considered in I concerns this variational principle, in particular the sensitivity of the various transport properties to the choice of the trial function, as well as the problem of combining different scattering

† A preliminary account of this work has been presented at the meeting of the American Physical Society in Boulder, Colorado (*Bull. Amer. Phys. Soc.* **2**, 313 (1957).

‡ To be denoted as I throughout.

mechanisms. A modified form of KOHLER's variational principle will be introduced in Section 6 determining the corrections to some known function which by itself should already represent a good approximation to the solution of the problem. This procedure is most useful when the solution of the Boltzmann equation is known over some energy range, or alternatively when a scattering process for which the relaxation-time approximation applies dominates the polar scattering. The variational procedure is so formulated as to permit consideration of the combined effect of two scattering mechanisms, a generalization which is necessary in applying this technique to InSb, since both polar and electron–hole scattering are important over part of the temperature range of interest here. A fourth unsatisfactory aspect of I was the treatment of the effective ionic charge e^* as an adjustable parameter. As a result of the modifications introduced by the present theory, we find that proper conversion of the experimental Hall mobility[5] to a drift mobility, using the theory for the Hall effect to be presented in Section 7, leads to good agreement with the calculated mobility between 200 and 700°K for the effective ionic charge $e^* = 0{\cdot}13$ computed from the experimental data of SPITZER and FAN.[6] Although this value of e^* may not be completely accurate because of its dependence on the small difference between the static and dynamic dielectric constants, its use removes from the theory all adjustable parameters. The thermoelectric power is also seen to agree closely with experiment[7] over the specified range of temperatures.

Since the proper interpretation of the Hall coefficient to obtain the carrier concentration and the drift mobility is important in a quantitative calculation, we present a variational technique for its calculation in the limit of weak magnetic fields in Section 7 and apply it to InSb. Between 200 and 700°K we find that $1 < (nec)R_H < 3\pi/8$.

Section 8 considers the closely related problem of conduction in rapidly oscillating electric fields for the case of polar scattering. It is seen that the Boltzmann equation has the same form as in the presence of a magnetic field. However, in the present case we consider a limit corresponding to the condition $\omega\tau \gg 1$ arising in simple theories where a relaxation time τ is valid. The Boltzmann equation can now be solved by a perturbation technique. The classical solution is valid for incident light waves provided that the photon energy is considerably smaller than KT. The results are applied to the far infrared reflectivity minimum observed by YOSHINAGA and OETJEN.[8] The calculated position of the minimum is seen to coincide with the experimentally observed minimum at the two temperatures ($T = 298$ and 313°K) considered. The results depend most sensitively on the band structure, and to a considerably lesser degree on the scattering mechanism. They therefore provide a good confirmation of the non-parabolic conduction-band structure[2] used in these calculations.

As an aid to the reader, an appendix defining the principal symbols used in the equations to follow has been included.

2. SCREENED POLAR INTERACTION

As already pointed out in I, when the density of conduction electrons is appreciable, the interaction between a given electron and the vibrating polar lattice must be modified. An approximate method for taking these effects into account was outlined in the earlier paper (cf. Section 4). In the simple case of Boltzmann statistics and parabolic bands, the Fourier components $V_q^{\pm}$ and $v_q^{\pm}$ of the electron-phonon interaction energy in the presence and absence of screening electrons, respectively, are related by the equation:

$$V_q^{\pm} = \{1 + (q\lambda_D)^{-2}\}^{-1} v_q^{\pm} \qquad (1)$$

where λ_D is the Debye length. The $\pm$ signs refer to right and left traveling waves.

In evaluating $v_q^{\pm}$, a continuum approximation is ordinarily made. It can be shown, however, that it is legitimate to neglect the effects of the atomic structure provided that the phonon wavelength is much larger than the interatomic spacing. This condition is ordinarily satisfied for the phonons involved in scattering processes with electrons in semiconductors. Accordingly, we may use the result previously derived by FRÖHLICH[9] and CALLEN[10] which was also used in I:

$$v_q^{\pm} = \mp(4\pi iee^*/G^3 v_a)(\hbar/2M\omega_l)^{\frac{1}{2}} q^{-1} a_q^{(*)}, \qquad (2)$$

where G^3 is the number of unit cells in volume V, v_a is the volume of the unit cell, M is the reduced mass of the atoms in the unit cell, ω_l is the longitudinal optical frequency assumed independent of

q, and a_q, a_q^* respectively are the annihilation and creation operators for phonons. The symbol $a_q^{(*)}$ is to be understood as a_q for the upper sign and a_q^* for the lower sign. The effective ionic charge e^* appearing in equation (2) is defined and discussed in Section 4 of I.

In the present calculations we shall for the most part introduce the screening effects via equation (1) with the Debye length modified as in equation (I, 52) to take into account the InSb band structure as well as Fermi statistics. However, this result is not general. It fails to take into account two classes of effects that may be categorized as 'time-dependent' and 'quantum-mechanical' respectively. The time-dependent effects are most pronounced for lattice waves having small wave numbers q. The screening of such lattice waves which have a phase velocity larger than the typical electron velocity, corresponding to an energy KT in the case of Boltzmann statistics, is somewhat reduced from that obtained by use of equation (1). In this case the distance travelled by the electron during one period of the lattice vibration in question is smaller than its wavelength and the electron experiences a time-dependent field. Quantum-mechanical effects become important when q is larger than the typical electron wave number. The Uncertainty Principle then does not permit the electron to be as localized as is required by classical considerations. The Debye length is therefore increased and the screening effect reduced.

These results are obtained from a self-consistent treatment of the quantum-mechanical Liouville and Poisson equations. A generalization of equation (1) that is valid for phonons having wave numbers which influence the transport properties most significantly can be shown to be:

$$V_q^{\pm} = \{1 + A_q^{(s)}(q\lambda_s)^{-2}\}^{-1} v_q^{\pm}, \qquad (3)$$

where $A_q^{(s)}$ is a function of the wave number q, and the index s indicates the type of statistics. For parabolic bands, λ_s is the Debye length in the case of Boltzmann statistics and the Thomas–Fermi length for Fermi statistics.

A detailed discussion of equation (3) will be given in a later publication.[11] Since A_q is a very complicated function of q for the band structure and statistics under consideration here, we shall be content to estimate the effect on our results when $A_q \neq 1$ by considering the classical limit with A_q evaluated at $q = (2m_n KT)^{1/2}/\hbar$ but assumed constant. This assumption is equivalent to a redefinition of the screening length. Table 1, to be discussed below, presents some typical values of this parameter.

Unless otherwise indicated, we shall set $A_q = 1$ in the present calculations. A brief discussion of the more general case just described is given at the conclusion of Section 6.

3. ELECTRON–PHONON SCATTERING

In this section we shall give the results for the scattering functions, proportional to the probability per unit time that an electron emits or absorbs a phonon, which will be required to evaluate the collision term of the Boltzmann equation. The conduction-band wave functions for InSb given by KANE[2] will be used. These wave functions have pure s-symmetry at the band edge, and acquire some p-function admixture as one moves away from $k = 0$ into the band. This admixture was neglected in I. It was shown in Section 6 of I, however, that this approximation is not really justified at temperatures greater than about 400°K. We shall find that when the p-function admixture is included, the probability of scattering an electron from a state k to k' no longer depends on the angle of scattering alone, but in addition on the direction of the initial state. In order to obtain tractable results we shall consider the scattering from an initial state k taken along one of the principal cubic axes of the crystal to some other state k' as typical of the scattering from initial states k along other directions as well. The approximation that the energy Δ, associated with spin-orbit splitting, which is of the order of 1 eV, is much greater than the band gap E_g and kP will also be made. The matrix element P is defined by equation (3) of I. This approximation is valid for electrons in the conduction band having energies $E < E_g$.

In addition to the effects of the p-function admixture on the scattering probabilities, we shall also include the screening effects considered in the preceding section.

In order to evaluate the matrix elements for scattering, let

$$\psi_{k\mu} = G^{-\frac{1}{2}} \psi_{k\mu} e^{ik\cdot r} \qquad (4)$$

be one of the doubly degenerate cell-periodic wave

function of an electron in the conduction band having wave number k. The degeneracy, expressed by the index $\mu = 1, 2$, is due to spin. For phonon emission and absorption, respectively, one finds

$$H_{k'\mu',k\mu} = \sum_q \int \Psi_{k'\mu',n'} V_q^{\pm} e^{\pm iq\cdot r} \Psi_{k\mu,n} d^3r$$

$$= \mp \frac{4\pi iee^*}{v_a} \left(\frac{\hbar}{2MG^3\omega_l}\right)^{\frac{1}{2}} q^{-1} \begin{Bmatrix} \sqrt{n} \\ \sqrt{n+1} \end{Bmatrix} \times$$

$$\times \{1 + A_q^{(s)}(q\lambda_s)^{-2}\}^{-1} \int_0 \chi^*_{k'\mu'} \chi_{k\mu} d^3r \quad (5)$$

where Ψ is a product of electron and phonon wave functions, $V_q^{\pm}$ is given by equation (3), and n is the number of phonons of wave number q in the field. The integral in equation (5) extends over a single unit cell. The square of the matrix element is proportional to the transition probability per unit time. Since the collision term of the Boltzmann equation does not distinguish between the degenerate states μ, we sum over the degenerate final states and average over the initial states. In terms of notation that will prove useful later on, we obtain for a transition from a state k to $k_\pm \equiv$ $\equiv k(E \pm \hbar\omega_l)$:

$$|H_{k\pm,k}|^2 = |\mathscr{H}|^2 \begin{pmatrix} n \\ n+1 \end{pmatrix} \mathscr{F}(q_\pm) \mathscr{G}_\pm(\beta), \quad (6)$$

where

$$\left.\begin{aligned} \mathscr{H} &= \mp (4\pi iee^*/v_a)(\hbar/2MG^3\omega_l)^{\frac{1}{2}} k^{-1} \\ \mathscr{F}(q_\pm) &= (k/q_\pm)^2 \{1 + A_q^{(s)}(q_\pm\lambda_s)^{-2}\}^{-2} \\ \mathscr{G}_\pm(\beta) &= \frac{1}{2} \sum_\mu \sum_{\mu'} \left| \int_0 \chi^*_{k'\mu'} \chi_{k\mu} d^3r \right|^2. \end{aligned}\right\} \quad (7)$$

The quantity $\mathscr{F}(q_\pm)$ represents the dependence of $|H_{k'k}|^2$ on the phonon wave number

$$q_\pm = \{k_\pm^2 + k^2 - 2k_\pm k \cos\beta\}^{\frac{1}{2}} \quad (8)$$

where β is the angle between k and $k_\pm$. The quantity $\mathscr{G}_\pm(\beta)$ contains the angular dependence of scattering due to the p-function admixture in the wave function. $\mathscr{G}_\pm(\beta)$ is unity for s-functions alone. This value was assumed in I. We note again the fact that in general $\mathscr{G}_\pm$ depends on the direction of k in addition to β, and that we circumvent this difficulty here simply by calculating it for an initial state taken along one of the principal axes of the crystal, assuming subsequently that this result holds for all other initial directions as well.

To calculate $\mathscr{G}_\pm(\beta)$, we use KANE's[2] results for the cell-periodic part of the conduction-band wave functions as given by equation (5) of I. Here:

$$\sigma_\lambda{}^\mu(\theta,\phi) = iA_{\mu\lambda}$$

$$\pi_{\nu\lambda}{}^1(\theta,\phi) = -(6)^{\frac{1}{2}}(B_{1\nu} + iB_{2\nu})A_{2\lambda} + (2/3)^{\frac{1}{2}} B_{3\nu} A_{1\lambda}$$

$$\pi_{\nu\lambda}{}^2(\theta,\phi) = (6)^{\frac{1}{2}}(B_{1\nu} - iB_{2\nu})A_{1\lambda} + (2/3)^{\frac{1}{2}} B_{3\nu} A_{2\lambda}, \quad (9)$$

and the matrices $\|A_{\mu\lambda}\|$ and $\|B_{\mu\lambda}\|$ are the ones given in KANE's equation (6) and (7), respectively. The angles θ, ϕ are the same polar angles as those used by KANE, the z-axis of the crystal being the polar axis to which k is referred. The assumption that the initial state lies along the z-axis implies that the polar angle θ', corresponding to the final state k', equals β. The azimuthal angle ϕ' drops out of the calculation. Using the conventional orthogonality relations for the basis functions S, X_ν, α_ν, we find that

$$\mathscr{G}_\pm(\beta) = g_1{}^\pm - (1 - \cos\beta)\{g_2{}^\pm + (1 + \cos\beta) g_3{}^\pm\} \quad (10)$$

where

$$\left.\begin{aligned} g_1{}^\pm &= \{(1-\epsilon^2)^{\frac{1}{2}}(1-\epsilon_\pm^2)^{\frac{1}{2}} + \epsilon\epsilon_\pm\}^2 \\ g_2{}^\pm &= 2\epsilon\epsilon_\pm(1-\epsilon^2)^{\frac{1}{2}}(1-\epsilon_\pm^2)^{\frac{1}{2}} \\ g_3{}^\pm &= 3\epsilon^2\epsilon_\pm^2/4. \end{aligned}\right\} \quad (11)$$

The $\pm$ signs refer to final states having wave numbers $k_\pm$. In addition

$$\epsilon_\pm = [\{1 + 4s_\pm^2(1-\mu)\}^{\frac{1}{2}} - 1]^{\frac{1}{2}} / \times$$

$$\times [2\{1 + 4s_\pm^2(1-\mu)\}^{\frac{1}{2}}]^{\frac{1}{2}}, \quad (12)$$

where $s_\pm = s(\xi_\pm)$, $\xi_\pm = E_\pm/E_g{}^*$, and $\mu = m_n/m_0$ in the notation of I. One obtains ϵ from equation (12) simply by deleting all $\pm$ subscripts. It can be shown that

$$0 \leqslant \mathscr{G}_\pm(\beta) \leqslant 1. \quad (13)$$

Since we recall that $\mathscr{G}_\pm(\beta) = 1$ in the absence of p-function admixture, it follows that the scattering probability is *reduced* by this admixture.

Equation (7) shows that the scattering probability is also reduced by the screening effect. It is seen that the large scattering probability for small q associated with the q^{-2} dependence of $|H_{k'k}|^2$ in the simple case is greatly reduced by screening. The resultant effect on the mobility is, however, not as great as it might seem, since scattering in the forward direction does not alter appreciably the motion of the electrons with respect to the direction of the electric field.

It will be helpful to show the effects of the p-function admixture and screening on the absolute square of the matrix element for scattering as a

function of angle for a particular case. We consider an electron in the conduction band of InSb having wave number k associated with an energy KT, $T = 400°K$, absorbing or emitting a phonon having energy $K\Theta$. For InSb, $\Theta = 290°K$. The results are shown in Fig. 1. We have decomposed the results for the absorption process, represented by solid lines, into three cases. The curve labeled (1) corresponds to the unscreened interaction and assumes that the wave function has pure s-symmetry. The curve labeled (2) results from including screening effects, while maintaining the assumption of s-symmetric wave functions. Curve (3) combines the effects of screening and p-function admixture. The dashed curve shows the composite result (corresponding to curve (3)) for the emission process. It is to be noted that the nonparabolic nature of the conduction band is used here, since k and k' are related to KT by equations (10) and (11) of I.

Comparing curves (1) and (2), we see that the scattering in the forward direction is considerably reduced by the screening effects. For scattering larger than about 60°, on the other hand, the screening effect is rather small. Curve (3) illustrates the conclusion of equation (13), that the p-function admixture reduces the scattering through all angles. Moreover, it is seen that the scattering in the backward direction is principally affected. Such scattering anisotropies have the most sensitive

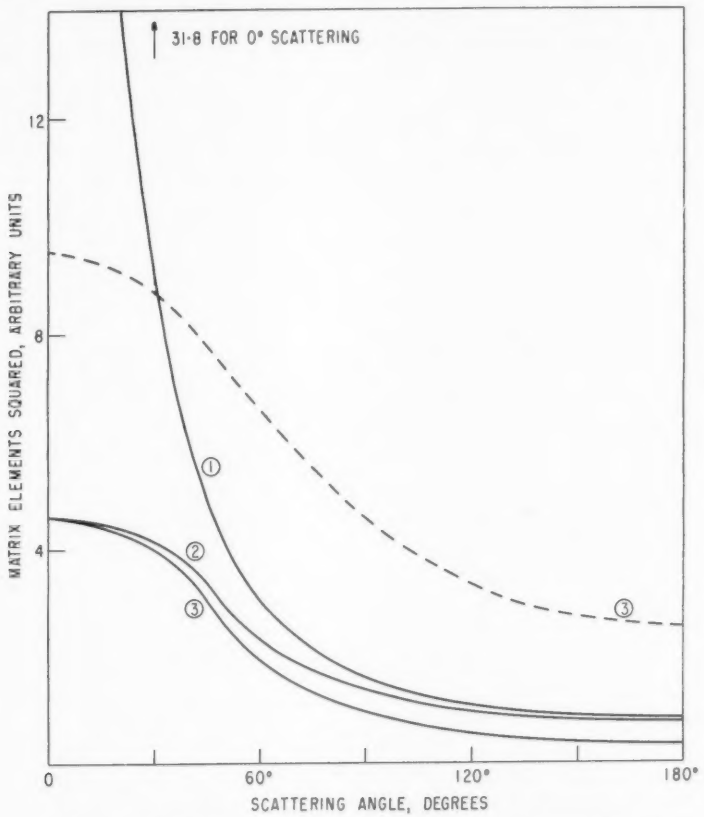

FIG. 1. Absolute square of the matrix element for phonon absorption (arbitrary units) versus scattering angle for an electron having energy KT ($T = 400°K$) in the conduction band of InSb. For further explanation, see text.

effect on the mobility. It should be emphasized that the effect of the p-function admixture becomes considerably larger at higher temperatures.

4. ELECTRON–HOLE SCATTERING

Since electron–hole scattering is an important mechanism in the temperature range of interest in these calculations, we shall have to incorporate this scattering mechanism in the collision term of the Boltzmann equation. Here we shall also have to take into account the effect of the p-function admixture on the scattering.

The matrix element is given by equation (51) of I.* In calculating the absolute square of the matrix element, the degenerate spin states are treated in the same manner as in the preceding section. The result can be expressed in a form analogous to equation (6):

$$|H_{k'k}|^2 = \mathscr{H}^2 \mathscr{F}(|\boldsymbol{k}-\boldsymbol{k}'|)\mathscr{G}(\beta) \tag{14}$$

with

$$\mathscr{H}^2 = (n/4k^4V)(4\pi e^2/\epsilon)^2 \tag{15}$$

$$\mathscr{F}(|\boldsymbol{k}-\boldsymbol{k}'|) = \{2k^2/(a^2+|k-k'|^2)\}^2$$

$\mathscr{G}(\beta)$ is obtained by deleting the $\pm$ superscripts in equations (10). Since electron–hole scattering is elastic, the energy of the electron in the initial and final states is the same in our approximation, which assumes the hole mass to be infinitely larger than the electron mass. As in the preceding section, $0 \leqslant \mathscr{G}(\beta) \leqslant 1$. The effect of the p-function admixture is therefore such as to reduce the probability of electron–hole scattering. For forward scattering $\mathscr{G}(0) = 1$. This result follows directly from the fact that the wave functions used here are normalized to unity.

5. BOLTZMANN EQUATIONS

There are three types of external fields that we wish to consider in the present calculations. The first type consists of a uniform electric field and/or thermal gradient, the second type of crossed uniform electric and magnetic fields, and the third type of a uniform electric field oscillating in time. The first type gives rise to a Boltzmann equation whose solution will enable calculation of the mobility and thermoelectric power, the second type permits calculation of the Hall coefficient, and the third of the far-infrared optical reflectivity.

In this section the Boltzmann equations corresponding to these three situations will be set up. The following sections will be devoted to calculating and discussing the physical quantities just mentioned for intrinsic InSb.

We shall write the Boltzmann equation in the form:

$$(\partial f/\partial t = (\partial f/\partial t)_{\text{coll}} + (\partial f/\partial t)_F. \tag{16}$$

The term depending explicitly on the time will contribute only in case (3).

The postulated solutions of the Boltzmann equation and the collision terms will be very similar for the three cases just described. We postulate

$$f(k) = f_0 - \boldsymbol{k}\cdot\boldsymbol{c}(E)f'_0 \tag{17}$$

for cases (1) and (2) and

$$f(k) = f_0 - kc(E)f'_0 e^{i\omega t}\cos\theta \tag{18}$$

for case (3). Here $f'_0 = df_0/dE$, ω is the frequency of the applied electric field, and θ is the angle between $\boldsymbol{k}$ and the electric field.

The collision term of equation (16) contains two contributions: a part arising from lattice scattering (to be denoted process A) and another due to electron–hole scattering (process B). The term due to lattice scattering is:

$$(\partial f/\partial t)^A_{\text{coll}} = -(\mathscr{H}^2 m_n{}^2 Vs/\pi\hbar^5\lambda)f'_0 L_A(\boldsymbol{k}\cdot\boldsymbol{c}/k)$$

$$= -[4\pi(e^*e)^2 m_n f'_0/\hbar^2 M v_a \omega_l \lambda s E_g{}^*]L_A(\boldsymbol{k}\cdot\boldsymbol{c}/k) \tag{19}$$

in cases (1) and (2). The operator $L_A(c)$ is defined by (I, 30). However, since we here take into account screening and the p-function admixture, the definitions of the quantities $R_\pm$ and $S_\pm$ which appear in that equation must be modified to read:

$$R_\pm = \lambda\lambda_\pm(s_\pm/s)\int_{-1}^{+1}\mathscr{F}_\pm(q)\mathscr{G}_\pm(\beta)dx$$

$$S_\pm = \lambda\lambda_\pm\int_{-1}^{+1}\mathscr{F}_\pm(q)\mathscr{G}_\pm(\beta)dx, \tag{20}$$

where $x = \cos\beta$ and λ, defined by (I, 8), is proportional to the conduction-band density of states. These integrals are readily evaluated provided that $A_q{}^{(s)}$ is taken to be constant. When screening and

* Again there are quantum-mechanical screening effects that are ordinarily neglected in treatments of Coulomb scattering. This is entirely justified at temperatures greater than about 20°K.

VOL 9 195

the p-function admixture are neglected, equations (19) and (20) reduce to (I, 29) and (I, 31).

For case (3) we simply multiply equation (19) or (I, 29) by $e^{i\omega t}$.

The collision term due to electron–hole scattering is obtained from equations (I, 53), (I, 54), and (14). Since the effect of the p-function admixture must also be included in the treatment of electron–hole scattering, equation (I, 54) becomes:

$$\mathcal{H}^2 = \mathscr{H}^2 \int_{-1}^{+1} dx(1-x)\mathscr{F}(|\boldsymbol{k}-\boldsymbol{k}'|)\mathscr{G}(\beta)$$
$$= \mathscr{H}^2(s/\lambda)^2\mathscr{S}. \tag{21}$$

Using equation (I, 53), we find the collision term in question to be

$$(\partial f/\partial t)^B_{\text{coll}} = (\pi e^4 n/\hbar\epsilon^2 E_g^* s\lambda) f'_0 \mathscr{S}(\boldsymbol{k}\cdot\boldsymbol{c}(E)/k). \tag{22}$$

The total collision term will be written in the form (19), with $L_A(\boldsymbol{k}\cdot\boldsymbol{c}/k)$ replaced by

$$L(\boldsymbol{k}\cdot\boldsymbol{c}/k) = L_A(\boldsymbol{k}\cdot\boldsymbol{c}/k) - \eta\mathscr{S}(e^\vartheta-1)^{-1}KT(\boldsymbol{k}\cdot\boldsymbol{c}/k),$$
$$\equiv (L_A+L_B)(\boldsymbol{k}\cdot\boldsymbol{c}/k), \tag{23}$$

where

$$\eta = (\hbar M v_a \omega_l n/4m_n\epsilon^2 KT)(e/e^*)^2(e^\vartheta-1).$$
$$\vartheta = \Theta/T. \tag{24}$$

The field term of the Boltzmann equation in case (1) is given by equation (I, 32). For case (2) it may be written in the form

$$(\partial f/\partial t)_F = ef'_0[\mathscr{E} - (hc)^{-1}\mathscr{H}\times\boldsymbol{c}(E)]\cdot\boldsymbol{v} \tag{25}$$

where $\boldsymbol{v} = \nabla_k E/\hbar$. The external electric field in case (3) will be assumed of the form $\mathscr{E} = \mathscr{E}_0 e^{i\omega t}$. The field term in this case is

$$(\partial f/\partial t)_F = (f'_0 \cos\theta/\hbar)(dE/dk)e\mathscr{E}_0 e^{i\omega t}. \tag{26}$$

The Boltzmann equations to be solved in the following sections may now be written down. It will be convenient to introduce the dimensionless variables

$$\mathscr{L} = (e^\vartheta-1)(KT)^{-1}L$$
$$x^3 = -s^3 E_g^{*\frac{3}{2}}/(KT)^{\frac{3}{2}} = -s^3/\beta^{*\frac{3}{2}}. \tag{27}$$

The variable $c(E)$ will also be replaced by a dimensionless quantity $\gamma(E)$. Its definition, however, will vary in the three cases under consideration.

In case (1) we separate the Boltzmann equation in the same manner as (I, 33). Writing $\boldsymbol{k}\cdot\boldsymbol{c}/k = c(E)\cos\theta$ and

$$c^{(n)} = (KT)^{n-\frac{1}{2}}(e^\vartheta-1)\gamma^{(n)} \tag{28}$$

in place of the $c^{(n)}$ introduced in equation (I, 34), we obtain the equations (I, 35) now written in the form:

$$\mathscr{L}\gamma^{(1)} = -x^3$$
$$\mathscr{L}\gamma^{(2)} = -x^3(y-z), \tag{29}$$

where $z = \zeta/KT$, $y = E/KT$. The solutions of equation (29) by the variational technique used in I will be discussed in Section 6.

In case (2) we assume the magnetic and electric fields involved to be given by $\mathscr{H} = (0, 0, \mathcal{H})$ and $\mathscr{E} = (\mathscr{E}_1, \mathscr{E}_2, 0)$. It follows that $\boldsymbol{c}(E)$ can then be represented by the vector $\boldsymbol{c} = (c^{(1)}, c^{(2)}, 0)$. We now separate the Boltzmann equation obtained by using equations (19) (with L_A replaced by L) and (25) into x and y components. Further we introduce the dimensionless variables defined by equation (27) and also†

$$\theta = \mathscr{E}_2/\mathscr{E}_1,$$
$$c^{(n)} = (\alpha\hbar c(e^\vartheta-1)/\mathcal{H})\mathscr{E}_n\gamma^{(n)}, \tag{30}$$

where

$$\alpha = Mv_a\hbar\omega_l\mathcal{H}(KT)^{\frac{1}{2}}/(2m_n)^{\frac{3}{2}}\pi e e^{*2}c. \tag{31}$$

The resulting equations are

$$\mathscr{L}\gamma^{(1)} + (e^\vartheta-1)x^3\theta\alpha\gamma^{(2)} = -x^3$$
$$\mathscr{L}\gamma^{(2)} - (e^\vartheta-1)x^3\theta^{-1}\alpha\gamma^{(1)} = -x^3. \tag{32}$$

These are generalizations of the equations given by LEWIS and SONDHEIMER[12] in that they apply to non-parabolic bands and hold for arbitrary effective ionic charges e^*. In Section 7 we shall solve these to lowest order in $\mathcal{H}$ by a variational technique to obtain the zero-field Hall coefficient.

Equations (32) may be written in a more compact form which is of interest because of its analogy to the Boltzmann equation for high-frequency conduction (case (3)) which we shall discuss below.

† The different definitions of γ used here should cause no confusion, since the three cases under discussion here will be considered separately. The advantage of the notation will be recognized when it is seen that some of the equations arising in different cases have great similarity.

We introduce the complex form:

$$\bar{\gamma} = (\theta^{-1}\gamma^{(1)} + \theta\gamma^{(2)}) + i(\gamma^{(1)} - \gamma^{(2)}) \tag{33}$$

and find after some elementary manipulations that the equation

$$[1 - i(e^{\vartheta} - 1)^{-1}(x^3\alpha)^{-1}\mathscr{L}]\bar{\gamma} = i(\theta + \theta^{-1})/\alpha(e^{\vartheta} - 1) \tag{34}$$

is equivalent to the coupled set (32). In the relaxation-time approximation $\mathscr{L}$ is no longer an operator. When the band is parabolic, we then find:

$$(e^{\vartheta} - 1)^{-1}(x^3\alpha)^{-1}\mathscr{L} = m_n c/e\mathscr{H}\tau \equiv (\omega_0\tau)^{-1}, \tag{35}$$

where ω_0 is the cyclotron frequency and τ is the relaxation time. For large magnetic fields or small collision cross-sections, the term in equation (34) involving the collision operator $\mathscr{L}$ will therefore be small.

We turn next to case (3). The explicitly time-varying term of equation (16) must now be considered. Using equations (18), (19), (26), and (27) and introducing the dimensionless quantities γ and δ defined as:

$$c(E) = [\hbar^2 M v_a \omega_l \mathscr{E}_0 (KT)^{\frac{1}{2}}(e^{\vartheta} - 1)/(2m_n)^{\frac{1}{2}}\pi e^{*2} e]\gamma$$
$$\delta = 2^{\frac{1}{2}}\pi m_n^{\frac{1}{2}}(e^* e)^2 KT/\hbar M v_a \omega_l \omega E_g^{*\frac{1}{2}}\lambda s^2(e^{\vartheta} - 1), \tag{36}$$

we find a Boltzmann equation having the form

$$(1 + i\delta\mathscr{L})\gamma = -i\delta x^3. \tag{37}$$

In the relaxation-time approximation

$$\delta\mathscr{L} = (\omega\tau)^{-1}. \tag{38}$$

We observe that equations (34) and (37) have the same form and that the collision terms given by equations (35) and (38) are also similar. As one would expect, the cyclotron frequency ω_0 appearing in the magnetic-field problem is replaced by the frequency of the oscillating electric field in the case of high-frequency conduction. When the frequency is large and the scattering small, the term $\delta\mathscr{L}$ is much smaller than unity and a solution of equation (37) by the perturbation theory is possible. These conditions are well satisfied in InSb around room temperature when ω corresponds to frequencies in the far infrared. The solution of equation (37) will be discussed in Section 8.

In the magnetic-field case when $(e^{\vartheta} - 1)^{-1}(x^3\alpha)^{-1}\mathscr{L} \ll 1$, the Boltzmann equation (34) may not be valid, since it is no longer legitimate to think of free carriers in the effective mass approximation. Instead, the carriers must be considered to be in harmonic oscillator states.† This qualification does not apply to equation (37) when $\delta\mathscr{L} \ll 1$, since the strength of the perturbing field is determined by $\mathscr{E}_0$ which can be small even though ω is large.

6. MOBILITY AND THERMOELECTRIC POWER

This section is devoted to a discussion of equations (29), whose solution leads directly to the mobility and thermoelectric power. The treatment presented in this section will apply when both processes A and B are operative. In addition, the scattering mechanisms will be properly combined. Process B has, in the preceding discussion, been associated exclusively with electron–hole scattering, since this is the process of interest for the temperature range considered here. It should be recognized, however, that this treatment is immediately applicable to ionized-impurity scattering, since it has been assumed that the hole mass is much larger than the electron mass. It is only necessary to replace the number n of holes by the number of impurities.

We begin with the simple observation that when process B acts alone, these equations can be solved immediately:

$$\gamma^{(1)} = -x^3/\mathscr{L}_B \equiv \chi_B{}^{(1)} \tag{39}$$
$$\gamma^{(2)} = -x^3(y - z)/\mathscr{L}_B \equiv \chi_B{}^{(2)}.$$

This is possible because the relaxation-time approximation obtains in the case of electron–hole scattering. Further we observe that for process A the asymptotic solutions $\chi_A{}^{(1)}$ and $\chi_A{}^{(2)}$ of equation (36) for large temperatures ($T \gg \Theta$) are especially simple since in that limit

$$\mathscr{L}_A \sim -\beta^*(e^{\vartheta} + 1)(S - R). \tag{40}$$

In general, however, we must use KOHLER's variational principle[4] as discussed in I. Since this principle has not been applied previously to a material where the band structure is known at least for a portion of k-space, some care must be taken in its application. In particular, we must make sure that the integrals D_{ij}, defined in (I, 46), do not have appreciable contributions in a region of the band where the band structure is uncertain.

† See, for example, P. N. ARGYRES.[13]

In the case of InSb, the known region of the conduction band lies between the band edge and an energy equal to the band gap.

A second point, not previously investigated, which has to be considered in a quantitative transport calculation, is the sensitivity of the calculated physical quantities, such as the mobility and thermoelectric power, to the choice of the trial function. It follows from the statement of the variational principle that the current, and hence the mobility, is stationary, but that the thermoelectric power is not. One would therefore expect the mobility to be relatively insensitive to the choice of the trial function. No such *a priori* statement can be made about the thermoelectric power.

In order to investigate these points, a number of different trial functions $\gamma^{(n)}$ will be considered. We shall write

$$\gamma^{(n)} = \chi^{(n)} + \Delta^{(n)} \tag{41}$$

where $\chi^{(n)}$ is a known function and $\Delta^{(n)}$ is a trial function to be used in a variational principle, described below, which is very similar to KOHLER's form. We might, for example, let $\chi^{(n)}$ represent the asymptotic solution (40) when process A alone is operative. Alternatively, when process B predominates, as for instance at low temperatures when ionized impurity scattering is the most important mechanism, we would choose $\chi^{(n)}$ to be given by equation (39).

It is convenient to introduce auxiliary quantities $\gamma^{(0)}$, $\Delta^{(0)}$, and $\chi^{(0)}$ defined by the equations:

$$\left.\begin{aligned} \Delta^{(2)} &\equiv \Delta^{(0)} - z\Delta^{(1)} \\ \gamma^{(2)} &\equiv \gamma^{(0)} - z\gamma^{(1)} \\ \chi^{(2)} &= (y-z)\chi^{(1)} \equiv \chi^{(0)} - z\chi^{(1)}. \end{aligned}\right\} \tag{42}$$

The equations to be solved, which replace equations (29), are then

$$\left.\begin{aligned} \mathscr{L}\Delta^{(1)} &= -x^3 - \mathscr{L}\chi^{(1)} \equiv l_1(\chi) \\ \mathscr{L}\Delta^{(0)} &= -yx^3 - \mathscr{L}\chi^{(0)} \equiv l_0(\chi). \end{aligned}\right\} \tag{43}$$

We also define*

$$\left.\begin{aligned} \langle \psi, \mathscr{L}\phi \rangle &= \int_0^\infty \psi \mathscr{L}\phi (df_0/dy)\, dy \\ \langle \psi, l \rangle &= \int_0^\infty \psi l (df_0/dy)\, dy. \end{aligned}\right\} \tag{44}$$

* The notation here differs from that used in I.

These functions satisfy the relations $\langle \psi, \mathscr{L}\phi \rangle = \langle \phi, \mathscr{L}\psi \rangle$ and $\langle \psi, \mathscr{L}\psi \rangle \geqslant 0$ for the operator $\mathscr{L}$ defined by equation (27). These are the conditions needed to prove the variational principle for $\Delta^{(n)}$.

In brief, the principle states that the solution of equations (43) is the function $\Delta^{(n)}$ that maximizes $\langle \Delta^{(n)}, \mathscr{L}\Delta^{(n)} \rangle$ subject to the subsidiary condition $\langle \Delta^{(n)}, \mathscr{L}\Delta^{(n)} \rangle = \langle \Delta^{(n)}, l_n \rangle$. Formally this principle is the same as that stated more precisely in I. In the present case, however, we can consider $\Delta^{(n)}$ to be a correction to the function $\chi^{(n)}$ which may already by itself represent a good approximation to the true solution. It is easy to show that the Boltzmann equations (43) are obtained upon performing the variation with respect to $\Delta^{(n)}$, taking account of the subsidiary condition by the technique of Lagrange multipliers.

We introduce a complete set of functions $\psi_i^{(n)}$ and write:

$$\Delta^{(n)} = \sum_{i=0}^{\infty} \Delta_i^{(n)} \psi_i^{(n)} \tag{45}$$

where $\Delta_i^{(n)}$ are numbers to be determined by the variational method. The possibility that the set $\psi_i^{(n)}$ may be different for the equations (43) corresponding to $n = 0$ and 1 is contained in equation (45). Application of the variational principle yields the algebraic equations:

$$\sum_{i=0}^{\infty} \Delta_i^{(n)} \langle \psi_i^{(n)}, \mathscr{L}\psi_j^{(n)} \rangle = \langle \psi_j^{(n)}, l_n \rangle \tag{46}$$

which determine $\Delta_i^{(n)}$. The steps leading to expressions for the conductivity σ and thermoelectric power Q are analogous to those given in I and earlier references. We shall give only the results. Both σ and Q can be expressed in terms of integrals:

$$G_n = -\langle \gamma^{(n)}, x^3 \rangle. \tag{47}$$

Thus

$$\sigma = (2/3\pi^2)(Mv_a\nu/\hbar^2 e^{*2})(KT)^2(e^\vartheta - 1)G_1 \tag{48}$$

$$Q = -(K/e)[(G_0/G_1) - z]. \tag{49}$$

From equation (54) and the subsidiary condition one can show that

$$G_1 = -2\langle \chi^{(1)}, x^3 \rangle - \langle \chi^{(1)}, \mathscr{L}\chi^{(1)} \rangle + \langle \Delta^{(1)}, \mathscr{L}\Delta^{(1)} \rangle. \tag{50}$$

Therefore the conductivity is stationary, since

$\langle \Delta^{(1)} \mathscr{L} \Delta^{(1)} \rangle$ is stationary. We find:

$$\langle \Delta^{(n)}, \mathscr{L}\Delta^{(n)} \rangle = \frac{\langle \psi_0^{(n)}, l_n \rangle^2}{\langle \psi_0^{(n)}, \mathscr{L}\psi_0^{(n)} \rangle} + \sum_{i=2}^{\infty} \frac{\{(\mathscr{L}, l_n)_{i-1}^{(n)}\}^2}{(\mathscr{L})_i^{(n)} (\mathscr{L})_{i-1}^{(n)}} \tag{51}$$

where

$$(\mathscr{L})_m^{(n)} = \begin{vmatrix} \langle \psi_0^{(n)}, \mathscr{L}\psi_0^{(n)} \rangle & \cdots & \langle \psi_0^{(n)}, \mathscr{L}\psi_{m-1}^{(n)} \rangle \\ \cdot & & \cdot \\ \cdot & & \cdot \\ \cdot & & \cdot \\ \langle \psi_{m-1}^{(n)}, \mathscr{L}\psi_0^{(n)} \rangle & \cdots & \langle \psi_{m-1}^{(n)}, \mathscr{L}\psi_{m-1}^{(n)} \rangle \end{vmatrix}$$

$$(\mathscr{L}, l)_{m-1}^{(n)} = \begin{vmatrix} \langle \psi_0^{(n)}, \mathscr{L}\psi_0^{(n)} \rangle & \cdots & \langle \psi_0^{(n)}, \mathscr{L}\psi_{m-2}^{(n)} \rangle & \langle \psi_0^{(n)}, l_n \rangle \\ \cdot & & \cdot & \cdot \\ \cdot & & \cdot & \cdot \\ \cdot & & \cdot & \cdot \\ \langle \psi_{m-1}^{(n)}, \mathscr{L}\psi_0^{(n)} \rangle & \cdots & \langle \psi_{m-1}^{(n)}, \mathscr{L}\psi_{m-2}^{(n)} \rangle & \langle \psi_{m-1}^{(n)}, l_n \rangle \end{vmatrix}$$

Since in general $(\mathscr{L})_i^{(n)} \geqslant 0$, all terms in the series in equation (51) are positive. We therefore retain the feature that the conductivity calculated by using only a finite number of terms of the series is always less than the exactly evaluated conductivity in this modified version of the variational principle.

Explicit expressions for the integrals appearing in the preceding equations are easily obtained from the definitions (51). One can show that:

$$\langle \psi_i^{(n)}, \mathscr{L}_A \psi_j^{(n)} \rangle = \beta^{*-1} \int_0^{\infty} dy [e^{y-z} + e^{-y}]^{-1} [1 + e^{-(y-z)}]^{-1} \times$$

$$\times [S_+ \{\psi_i^{(n)} \psi_j^{(n)} + (s_+/s)^2 \psi_{i+}^{(n)} \psi_{j+}^{(n)}\} - R_+ \{\psi_{i+}^{(n)} \psi_j^{(n)} + \psi_{j+}^{(n)} \psi_i^{(n)}\}]. \tag{52}$$

This integral represents the generalization of D_{ij} defined by (I, 27). An analogous expression obtains for $\langle \chi^{(1)}, \mathscr{L}_A \chi^{(1)} \rangle$. The corresponding integrals involving $\mathscr{L}_B$ present no difficulty.

Turning now to G_0, we find that this cannot be expressed in terms of $\langle \Delta^{(0)}, \mathscr{L}\Delta^{(0)} \rangle$. This is a manifestation of that fact that G_0 is not stationary. Direct use of equation (47) shows that:

$$G_0 = -\left[\langle \chi_0, x^3 \rangle + \frac{\langle \psi_0^{(0)}, l_0 \rangle \langle \psi_0^{(0)}, x^3 \rangle}{\langle \psi_0^{(0)}, \mathscr{L}\psi_0^{(0)} \rangle} + \right.$$

$$\left. + \sum_{i=2} \frac{(\mathscr{L}, x^3)_{i-1}^{(0)} (\mathscr{L}, l_0)_{i-1}^{(0)}}{(\mathscr{L})_i^{(0)} (\mathscr{L})_{i-1}^{(0)}} \right]. \tag{53}$$

We note that G_1 could have been written in this form, but without assurance that successive corrections obtained by considering more terms in the series in equation (53) are all positive. Further comment on this point will be made later.

The choice of the trial functions $\chi^{(n)}, \psi_i^{(n)}$ must now be considered. In earlier applications of this variational principle to polar semiconductors, the choice $\psi_i^{(1)} = \psi_i^{(2)} = y^i$, $\chi^{(n)} = 0$ was made. In the present paper we shall consider three trial functions and compare the results retained. They are:

$$\gamma^{(n)} = \gamma_\infty^{(n)} + \Sigma_i \Delta_i^{(n)} \psi_i^{(n)} \tag{54.1}$$

$$\gamma^{(n)\prime} = \Sigma_i \Delta_i^{(n)} \phi_i^{(n)} \tag{54.2}$$

$$\gamma^{(n)\prime\prime} = \Sigma_i \Delta_i^{(n)} \psi_i^{(n)} \qquad n = 0, 1. \tag{54.3}$$

In the first trial function, $\gamma_\infty^{(n)}$ corresponds to the asymptotic solution obtained by properly combining $\chi_A^{(n)}$ and $\chi_B^{(n)}$:

$$\chi^{(n)} = \gamma_\infty^{(n)} = \chi_A^{(n)} \chi_B^{(n)} / (\chi_A^{(n)} + \chi_B^{(n)}). \tag{55}$$

The functions $\psi_i^{(n)}$ must then be chosen so that for large

y, $\psi_i^{(n)} \to 0$. Accordingly we shall choose:

$$\psi_i^{(1)} = e^{-\alpha y} y^i$$
$$\psi_i^{(0)} = e^{-\alpha y} y^{i+1}. \tag{56}$$

The extra factor y in $\psi_i^{(0)}$ is introduced because of the appearance of a corresponding factor on the right-hand side of the second of equation (43). This choice of trial function takes advantage of the known asymptotic solutions, and tends to confine the principle contribution of the integrals in equations (51) and (53) to a region near the band edge where the band structure is known. However, the form of $\gamma_\infty^{(n)}$ still depends on the band structure at larger energies.

For the second trial function (54.2) we choose $\chi^{(n)} = 0$ and

$$\phi_i^{(1)} = y^i; \quad \phi_i^{(0)} = y^{i+1}. \tag{57}$$

Except for the extra factor y in $\phi_i^{(0)}$, this trial function corresponds to that used in earlier treatments. The absence of the damping factor $e^{-\alpha y}$ tends to shift the contribution of the transport integrals to larger energies. In the third trial function (54.3) we put $\chi^{(n)} = 0$, but retain the damping factor. For a sufficiently large value of α this solution will therefore make use of only the known portion of the band.

Some comments concerning the choice of α are in order. It is of course most desirable to let α differ for the two functions (56), by putting $\alpha = \alpha_n$, and to determine the values variationally. A general treatment is difficult, but it is possible to achieve a limited variational determination fairly simply. As a trial function we take $\chi^{(n)} = \gamma_\infty^{(n)}$ and $\Delta^{(1)} = \rho_1 e^{-\alpha_1 y}$; $\Delta^{(0)} = y\rho_0 e^{-\alpha_0 y}$, where ρ_n and α_n are to be determined. As a result of the present form of the variational principle, one finds α_n from the equation

$$(\mathscr{L}, l_n)_1^{(n)} = 0. \tag{58}$$

The quantity on the left-hand side is a determinant appearing in equations (51) and (53) with $\psi_i^{(n)}$ given by equation (56) but with α_n replacing α. Thus if we assume the value of α_n given by equation (58) and use the trial function (54.1), carrying through the variational procedure as before, we obtain the results (51) and (53) with the term corresponding to $i = 2$ in the series missing. The maximum of the variational function used to determine α_n is not very sharp. For the temperature range of interest here, $\alpha_n \lesssim 1$. In view of the difficulty associated with solving equation (58), it is therefore simplest to choose a value of α_n that is reasonably close to the maximum which will still damp out the integrands discussed earlier in the desired way. We have chosen $\alpha_n = 0{\cdot}988$* $(n = 0, 1)$.

One can consider several limiting cases for G_0 and G_1. It is easily seen that equations (51) and (53) reduce properly when processes A and B act alone. In the latter case one obtains a result which corresponds to setting $\gamma^{(n)} = \chi_B^{(n)}$ in equation (39). For large temperatures the proper asymptotic form, with $\gamma^{(n)} = \chi^{(n)}$ as given by equation (55), is obtained.

The low-temperature case, where we associate process B with ionized-impurity scattering, deserves more detailed comment. In this temperature region process A is less important than B. It is desirable to choose a trial function which will give the correct result for process B acting alone as $T \to 0$ in a simple manner. This is accomplished by setting $\chi^{(n)} = 0$ in equations (50), (51), and (53) and choosing $\psi_i^{(1)} = \chi_B^{(1)} y^i$, $\psi_i^{(0)} = \chi_B^{(1)} y^{i+1}$. G_1 is then given by equation (51), the first term reducing to the correct low-temperature solution, and subsequent terms providing small corrections. These latter terms all vanish in the limit $\mathscr{L}_A \ll \mathscr{L}_B$, since then $(\mathscr{L}, l_n)_{i-1}^{(n)} = 0$. For G_0, the first term of equation (53) vanishes and the second gives the limiting value. This procedure provides a simple and accurate way of combining polar lattice scattering and ionized-impurity scattering when the latter is the more important. Alternatively one can use a perturbation expansion like that described in Section 8. One writes, for example, the first of equations (29) in the form:

$$\mathscr{L}_B[1-(\mathscr{L}_A/\mathscr{L}_B)]\gamma^{(1)} = +x^3.$$

The formal solution, when $\mathscr{L}_A \ll \mathscr{L}_B$, is then given by:

$$\gamma^{(1)} = -[1+(\mathscr{L}_A/\mathscr{L}_B)]^{-1}\mathscr{L}_B^{-1}x^3, \tag{59}$$

where the right-hand side must be interpreted as an operator expansion. A detailed treatment of the low-temperature case is beyond the scope of the present paper.

We turn now to a discussion of the results. In the calculations of the G_n, it was possible to consider only a finite number of terms of the infinite series contained in these expressions. In general we shall denote $G_n^{(N)}$ as the approximation when just N terms of the infinite series $\sum_{i=2}^{\infty}$ are retained. It should be recognized that this statement can be made independently of the trial function under consideration. Some of the results of the numerical calculations for combined polar and electron–hole scattering are presented in Table 1 for the G_n obtained with the use of the three trial functions (54). It should be emphasized that these results contain parameters peculiar to InSb and are applicable only in that case. The results for $G_n^{(1)}$ correspond to the lowest reliable approximation. This approximation was used in I for a trial function similar to $\gamma^{(n)\prime}$, and also by HOWARTH and SONDHEIMER[14] for most of their results. The columns labeled $G_n^{(3)}$ show the cumulative effect of adding two more correction terms. In the case

* There is no reason worth stating why 0·988 was chosen in preference to unity.

Table 1

T(°K)	$G_1^{(1)}(\gamma)$	$G_1^{(1)}(\gamma')$	$G_1^{(1)}(\gamma'')$	$G_1^{(3)}(\gamma)$	$G_1^{(3)}(\gamma')$	$G_1^{(3)}(\gamma'')$
200	0·01140	0·01066		0·01171	0·01146	
300	0·2376	0·2369		0·2381	0·2369	
400	0·7970	0·7935	0·5321	0·7972	0·7960	0·7584
500	1·369	1·365		1·369	1·368	
700	2·288	2·287	1·456	2·288	2·287	2·154

T(°K)	$G_0^{(1)}(\gamma)$	$G_0^{(1)}(\gamma')$	$G_0^{(1)}(\gamma'')$	$G_0^{(3)}(\gamma)$	$G_0^{(3)}(\gamma')$	$G_0^{(3)}(\gamma'')$	A_q	$G_1^{(3)}(\gamma, \alpha_q)$	$G_0^{(3)}(\gamma, \alpha_q)$
200	0·02930	0·02046		0·02763	0·02262		0·40	0·01146	0·02257
300	0·7296	0·6812		0·7080	0·6931				
400	2·821	2·768	1·939	2·786	2·779	2·631			
500	5·348	5·290		5·313	5·308		0·90	1·355	5·261
700	10·20	10·10	6·984	10·17	10·16	9·585	0·94	2·274	10·11

of G_1, it is seen that the result for $\gamma^{(1)}$ is always a little larger than that obtained from the other trial functions. Hence $\gamma^{(1)}$ is the best of the three choices. Nevertheless, the difference between the results for $\gamma^{(1)}$ and $\gamma^{(1)'}$ is sufficiently small that, as can now be seen, there is no particular advantage in using the more complicated form of G_1 that is associated with the trial function (54.1). Were one, however, to obtain by some other means an expression for $\chi^{(n)}$, by itself already a good approximation to the true solution over the entire energy range, the form (54.1) would possess definite advantages. In addition we observe that the values of $G_1^{(1)}$ obtained from (54.1) and (54.2) are already quite reliable. The largest corrections occur for $T = 200$°K. This is not the case for $G_1^{(1)}(\gamma'')$. The agreement, however, improves markedly upon considering $G_1^{(3)}(\gamma'')$. Thus if one insists upon confining the principal contributions of the integrals in G_1 to a region around the band edge. one is forced to consider more terms in the series $G_1^{(N)}$ in order to obtain reliable results.

Similar comments concerning G_0 can be made. Even though it is not a stationary quantity, G_0 appears to be little more sensitive to the choice of trial function than was G_1. Successive corrections in this case are not required to be positive. It is interesting that these corrections are positive for $G_0(\gamma')$ and negative for $G_0(\gamma)$. The series for both cases appear, at each approximation, to represent lower and upper bounds, respectively. It is, however, difficult to make a general statement concerning this point.

The last three columns of Table 1 attempt to correct the screening constant for time-dependent but not quantum-mechanical effects, as discussed in Section 2. As mentioned in Section 2, we assume A_q constant and take its value from the typical scattering process corresponding to $q = (2m_nKT)^{1/2}/\hbar$. The correction is seen to be largest in the temperature region where screening is unimportant and to be small in the region where screening contributes significantly. The total effect on the mobility and thermoelectric power is therefore small. The quantum-mechanical effect, which becomes more pronounced with increasing temperature, tends to reduce A_q further. A crude estimate shows the values of G_1 and G_0 to be affected by at most 10 per cent if this effect is taken into account.

We turn now to a discussion of the mobility in the temperature range extending from 200 to 700°K. In I, where no attempt was made to combine scattering mechanisms, we determined a value of the effective ionic charge by requiring the magnitudes of the theoretical and experimental mobilities to agree, assuming polar scattering as the dominant mechanism. The justification of this procedure depends on the fact that e^{*2}, according to equation (I, 23) is proportional to $\epsilon_0 - \epsilon_\infty$. Since $\epsilon_0 - \epsilon_\infty \ll \epsilon_0$ and ϵ_∞, it follows that a small error in the determination of either dielectric

constant will produce a large change in e^*. Specifically, an error of only 5 per cent in the experimental reflectivities obtained by SPITZER and FAN[6] would lead to a value of e^* consistent with the value used in I, rather than the value $e^* = 0{\cdot}13$ which one calculates from their data.

Since it was our purpose in I simply to establish the order of importance of the various scattering mechanisms in InSb, we did not correct the mobility determined by HROSTOWSKI *et al.*[5] for the fact that deformation potential scattering is not the dominant mechanism. They used the relationship $\mu = (8/3\pi)R_H\sigma$ instead of $\mu = R_H\sigma/b$, where b should be calculated for the correct scattering mechanisms.† The proper determination of b is discussed in the following section and results are presented in Fig. 5. Using these results, it was possible to calculate better values of the drift mobility. These values are represented by the dashed curve, labeled "experiment", in Fig. 2.

We also show, in the same figure, the results of the present calculation. The curves given are determined using the experimental effective ionic charge $e^* = 0{\cdot}13$ for polar scattering alone as well as for properly combined polar and electron–hole scattering. In addition, a curve for $e^* = 0{\cdot}20$ and combined scattering is shown. It is seen that the temperature-dependence of the mobility determined from polar scattering alone is in considerably greater disagreement with experiment than the results presented in I. This disagreement results from the fact that we have here considered the effects of screening and the p-function admixture in the wave function, both of which decrease the scattering probability at higher temperatures. The combination of scattering mechanisms, however, leads to results that are in good agreement with experiment except at the two ends of the temperature range under consideration. It should be emphasized that the results shown correspond to an absolute determination of the mobility, there being no adjustable parameters in the theory.

The disagreement at 200°K arises at least in part because charged-impurity scattering has been neglected. The modified experimental data shown in Fig. 2 derive from an n-type sample having an impurity concentration $n_t \approx 7{\cdot}7\times10^{14}$. The number of intrinsic holes present at 200°K can be shown to be $n_h \approx 4\times10^{14}$. It is seen from the effect of electron–hole scattering on the mobility at this temperature that the contribution from scattering by charged-impurity centers may lower the curve for combined scattering to a value approximating 2×10^5 cm²/Vsec. At higher temperatures, $n_h \gg n_t$, so that the impurities may be neglected.

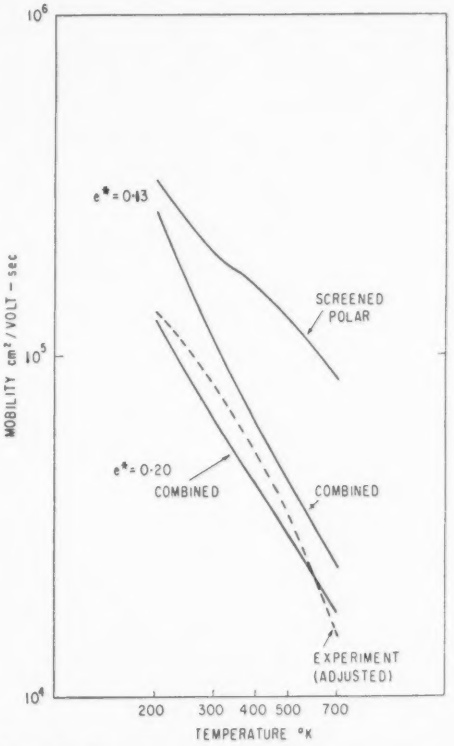

FIG. 2. Electron mobility versus temperature for screened polar scattering and for combined screened polar and electron–hole scattering. $e^* = 0{\cdot}13$ and $0{\cdot}20$. The dashed line refers to Hall mobility data of HROSTOWSKI *et al.*[5] adjusted according to the results of Section 7.

The lack of agreement at 700°K may be associated principally with three features that are inadequately treated by the present calculations. The most serious of these is the neglect of electron–electron scattering. This mechanism will have the most pronounced influence when electron–hole scattering becomes dominant, as it practically does at 700°K. The calculations of SPITZER and

† This point has also been made by C. HILSUM (private communication).

HÄRM[15] for a non-degenerate electron gas show that the mobility due to electron–hole scattering alone is reduced by as much as 40 per cent. The importance of electron–electron scattering is directly related to the rapidity of the variation of the relaxation time with electron velocity.[16] One would therefore not expect this mechanism to influence the mobility in any significant way at lower temperatures where polar scattering predominates, because the relaxation time for this mechanism, where it exists for high and low temperatures, is but weakly dependent on velocity. The relaxation time resulting from proper combination of the two scattering mechanisms is accordingly also weakly dependent on velocity for temperatures below 700°K. It is to be noted, however, that the corrections introduced by electron–electron scattering are in a direction to improve agreement of the theory using the experimentally determined effective ionic charge with experiment.

The remaining features producing disagreement at 700°K are the fact that portions of the band having $E > E_g$, where KANE's calculations no longer apply, are appreciably populated and also that the approximation (I, 12) used to determine the Fermi level becomes unreliable.

From the curve for combined scattering and $e^* = 0{\cdot}20$, it is seen that this value of the effective ionic charge must represent an upper limit. The corresponding static dielectric constant would then have the value $\epsilon_0 = 19{\cdot}9$ rather than 17·5. However, our calculations now appear to be quite consistent with the experimental value of SPITZER and FAN.[6] It is likely that much of the remaining discrepancy, which amounts roughly to 20 per cent over most of the temperature range, can be accounted for by the small contributions arising from deformation potential and piezoelectric scattering, our over-estimate of screening effects, as well as electron–electron scattering.

The results for the thermoelectric power are shown in Fig. 3. They are seen to be quite insensitive to the choice of e^*. This is to be expected, since for purely polar scattering the ratio G_0/G_1 is entirely independent of the effective ionic charge. The curves for both $e^* = 0{\cdot}13$ and $0{\cdot}20$, taking into account combined scattering, agree with the data of WEISS[8] within experimental error. The results for polar scattering alone agree less well. Again electron–electron scattering will affect the results at high temperatures. As pointed out by HERRING,[17] the transport term for pure electron–hole scattering in the non-degenerate limit is reduced from 4·0 to 3·2. The correction introduced at lower temperatures will be considerably smaller for the reasons mentioned earlier. However, at 700°K the effect is probably significant and in a direction to improve the agreement between theory and experiment. The kink in the data at 500°K is not explained by the present theory.

7. HALL EFFECT

As has been stressed repeatedly in this and the preceding paper, the factor b in the conventional expression for the Hall coefficient, $R_H = -b/nec$, must be correctly evaluated in order to be useful in a quantitative theory. This problem is not simple in the case of polar scattering. LEWIS and SONDHEIMER[12] have given a theory which is an extension of the earlier work of HOWARTH and SONDHEIMER.[14] As they point out, however, their treatment is not a complete variational one, and only reduces to a variational calculation in the limit of vanishing magnetic field. In this section we shall give a variational treatment of the Hall coefficient in the limit of *small* (but not vanishing) magnetic fields. This will be sufficient for the interpretation of experimental values of R_H that are ordinarily used to obtain the carrier concentration and Hall mobility.

We wish, then, to find the variational solution of equations (32) to lowest order in the magnetic field $\mathcal{H}$. The equations may be simplified in this approximation. Introducing a new quantity $\gamma^{(3)}$, defined by the equation

$$\gamma^{(2)} = \gamma^{(1)} + (e^{\vartheta} - 1)\alpha\theta^{-1}\gamma^{(3)}, \tag{60}$$

we find that equations (32) may be approximately replaced by

$$\mathscr{L}\gamma^{(1)} = -x^3 \tag{61.1}$$

$$\mathscr{L}\gamma^{(3)} = x^3\gamma^{(1)}. \tag{61.2}$$

Equation (61.1) describes the transport in the direction of the applied electric field. This equation is the same as the first of equation (29) which holds when the only applied field is $\mathscr{E}$. Equation (61.2) describes the transport in the direction of the Hall field. It is independent of $\mathcal{H}$ only because we have made the substitution (60).

Our variational solution of equations (61) depends on the fact that (61.1) may be solved independently of (61.2). This has, in fact, been already done in Section 6. It is therefore only necessary to find a variational principle whose solution will give equation (61.2). If one is willing to assume $\equiv \phi_i = y^i$. The results of the more general treatment will be discussed briefly.

One comment concerning the preceding variational principle is in order. A variational calculation does not necessarily determine the solution $\gamma^{(1)}$ accurately. Only integrals involving $\gamma^{(1)}$ which are at the same time

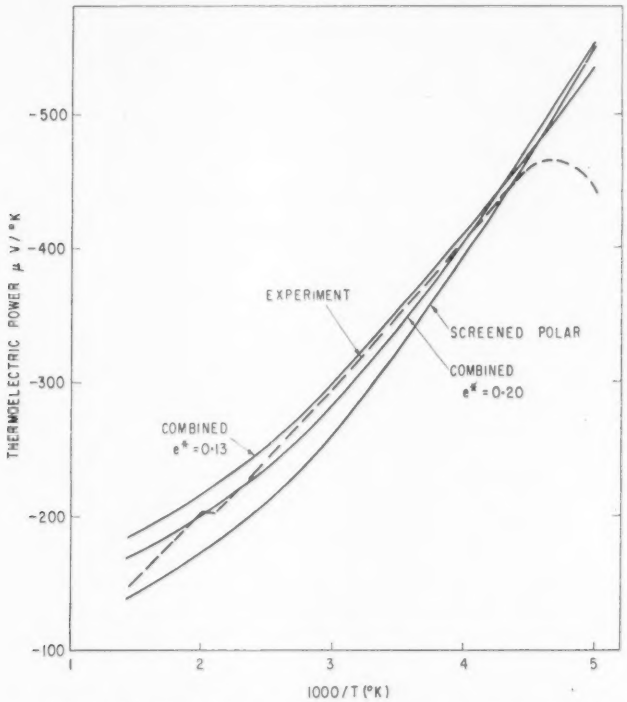

FIG. 3. Thermoelectric power versus reciprocal temperature for screened polar scattering and for combined screened polar and electron–hole scattering. $e^* = 0{\cdot}13$ and $0{\cdot}20$. The "screened polar" curve is independent of e^*. The dashed curve corresponds to the experimental data of WEISS.[7]

$\gamma^{(1)}$ exactly determined by the solution of equation (61.1) already given, then a variational principle having the required properties is the following: the solution of (61.2) is the function that maximizes $\langle \gamma^{(3)}, \mathscr{L}\gamma^{(3)} \rangle$, subject to the subsidiary condition $\langle \gamma^{(3)}, \mathscr{L}\gamma^{(3)} \rangle = \langle \gamma^{(3)}, x^3\gamma^{(1)} \rangle$. This principle has the same form as that used in Section 6. The conditions required for its validity are, of course, also satisfied. In view of the complications in notation, we shall not introduce the function $\chi^{(3)}$ in the present treatment. The trial function to be used here will then take the form (54.2) with $\phi_i^{(n)} \equiv$

stationary quantities are guaranteed to have some quantitative significance. We have seen, however, in the treatment of the thermoelectric power of the last section that even nonstationary quantities appear to be rather stable to changes in the trial function. In view of this fact one might hope that quantities of the type $\langle \gamma^{(3)}, x^3\gamma^{(1)} \rangle$ are also stable. This expectation is fulfilled rather well for the calculation to be described.

It can be easily shown that the Hall coefficient in the present case is given by:

$$R_H = -(nec)^{-1}(3/2)\Phi(G_3/G_1^2), \qquad (62)$$

where G_i is defined by equation (47) for the values i involved in equation (62). The factor Φ depends on the

statistics. For InSb it corresponds to the term in square brackets in equation (I, 13). In the case of parabolic bands and Fermi statistics, $\Phi = F_{1/2}(z)$. Equation (62) is obtained in the usual way from the longitudinal and transverse currents, which, because of equation (30), are here given by:

$$j_i = (\alpha c/3\pi^2\mathcal{H})(e^{\vartheta}-1)(e\mathscr{E}_i)(2m_nKT/\hbar^2)^{\frac{1}{2}}G_i \qquad i=1,\ 2. \tag{63}$$

Because of the great similarity of the present variational principle with that discussed in Section 6, it is evident that the detailed steps in computing a formal expression for G_3 are the same as those used in finding G_0 and G_1.

$$+\sum_{i=2}^{1+N}\frac{(\mathscr{L}, x^3\gamma^{(1)})_{i-1}{}^{(M)}(\mathscr{L}, x^3)_{i-1}}{(\mathscr{L})_i(\mathscr{L})_{i-1}}\Bigg]. \tag{64}$$

This is very similar to the expression for G_0 given by equation (53).

In the present application to InSb, we have taken $M = 2$ and $N = 1$. The results are shown in Fig. 4. We have plotted $(-nec)R_H$ as a function of temperature for polar scattering alone as well as for combined scattering. It is evident from equa-

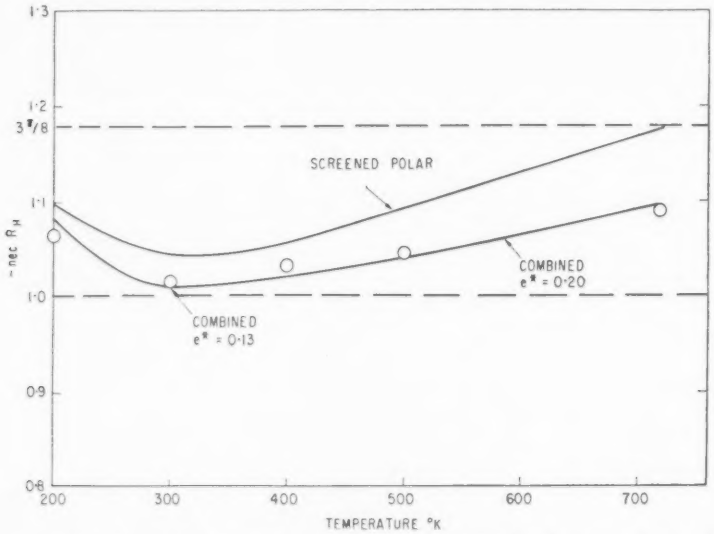

FIG. 4. $-necR_H$ versus temperature for screened polar scattering and combined screened polar and electron–hole scattering. The open circles correspond to results for $e^* = 0{\cdot}13$; the line to results for $e^* = 0{\cdot}20$. The "screened polar" curve is independent of e^*.

One finds that G_3 involves integrals $\langle\phi_i, x^3\gamma^{(1)}\rangle$ which are themselves infinite series of the same type as, say, G_1. It is possible only to include a finite number of terms in a feasible calculation. The degree of approximation may be represented in the way discussed in Section 6 by writing

$$\langle\phi_i, x^3\gamma^{(1)}\rangle^{(M)}.$$

The final approximate result is:†

$$G_3^{(N,M)} = -\Bigg[\frac{\langle\phi_0, x^3\gamma^{(1)}\rangle^{(M)}\langle\phi_0, x^3\rangle}{\langle\phi_0, \mathscr{L}\phi_0\rangle}+$$

† It is to be noted that the superscript (M) here refers to the degree of approximation in contrast to the superscript (n) used in earlier equations, such as (51), which dentifies the trial function.

tion (62) that in the former case R_H is independent of e^*. However, just as in the case of the thermoelectric power, the result will depend on e^* once scattering mechanisms are combined. It is interesting that the curves representing combined scattering for $e^* = 0{\cdot}13$ and $0{\cdot}20$ practically coincide. Both G_3 and G_1 vary appreciably when the effective ionic charge is altered, but the ratio $G_3/G_1{}^2$ remains practically constant. We also show on Fig. 4 the straight line corresponding to $(-nec)R_H = 3\pi/8$ obtained in the case of simple lattice scattering by acoustical modes, parabolic bands, and Boltzmann statistics. It is seen that for intrinsic InSb $1 < -(nec)R_H < 3\pi/8$. The minimum in the

curves at $\vartheta \approx 1$ is similar to that obtained by LEWIS and SONDHEIMER[12] (cf. Fig. 1) for the simpler situation of parabolic bands and Boltzmann statistics.

The present discussion has referred only to results obtained by use of the trial function (54.2). Values of G_3 have also been calculated for the trial functions (54.1) and (54.3). In the temperature range 400–700°K, $G_3^{(1,2)}(\gamma^{(3)})$ and $G_3^{(1,2)}(\gamma^{(3)\prime})$ agree to better than 1 per cent. $G_3^{(1,2)}(\gamma^{(3)\prime\prime})$, however, is smaller by about 15 per cent for combined scattering. This is not unexpected when one recalls the results of Section 6 for the corresponding approximation. At lower temperatures the agreement between $G_3^{(1,2)}(\gamma^{(3)})$ and $G_3^{(1,2)}(\gamma^{(3)\prime})$ is not as good. At 300°K the two values differ by 5 per cent and at 200°K by almost 40 per cent. This indicates that $G_3^{(M,N)}$ must be calculated to a higher approximation at this temperature. In view of the amount of numerical work required, higher approximations have not been investigated.

8. HIGH-FREQUENCY CONDUCTION

This section will be devoted to a discussion of the conductivity and susceptibility of electrons under the influence of an oscillating but uniform electric field. These quantities will be used to calculate the reflectivity of InSb in the far infrared, the results being compared with the experiments of YOSHINAGA and OETJEN.[8] The calculation under consideration is a classical one, for we shall use the Boltzmann equation (37) that has already been briefly discussed. The modifications introduced by quantum-mechanical effects will be mentioned.

We have already pointed out that it is possible to use a perturbation technique to solve equation (37) when $\delta\mathscr{L} \ll 1$. The magnitude of $\delta\mathscr{L}$ for InSb for the temperature and frequency range considered by YOSHINAGA and OETJEN may be estimated roughly from equation (38) and the relationship $\mu = e\tau/m_n$, where μ is the experimental mobility at that temperature. One finds $|\delta\mathscr{L}| \approx 0{\cdot}1$. The expectation is therefore that the perturbation method should yield reasonable results for InSb in the wavelength range 50–150 μ and for temperatures around 300°K.

The γ involved in equation (37) is clearly complex. We accordingly introduce real and imaginary parts:

$$\gamma = \gamma^{(1)} + i\gamma^{(2)}. \tag{65}$$

The formal solution of equation (37) is easily obtained. We find:

$$\begin{aligned} \gamma^{(2)} &= [1+(\delta\mathscr{L})^2]^{-1}(-\delta x^3) \\ \gamma^{(1)} &= \delta\mathscr{L}\gamma^{(2)} \end{aligned} \tag{66}$$

where the quantity

$$[1+(\delta\mathscr{L})^2]^{-1} = [1+(\delta\mathscr{L})(\delta\mathscr{L})]^{-1}$$

is to be interpreted as an operator expansion. From equations (66) we may in principle calculate the conductivity σ and the susceptibility α. Introducing the G_n defined by equation (47), we find:

$$\alpha = (2/3\pi^2)(Mv_a v/\hbar^2 e^{*2})(KT)^2(e^{\vartheta}-1)\omega^{-1}G_2 \tag{67}$$

and σ as given by equation (48). It is to be emphasized that the $\gamma^{(n)}$ appearing in G_n are now those defined by equation (65).

The susceptibility (67) is that due to free carriers alone; the susceptibility due to the lattice is not included. Using (47) and (67), we can find the real and imaginary parts of the dielectric constant $\epsilon_1 + i\epsilon_2$ from the relationships

$$\begin{aligned} \epsilon_1 &= \epsilon + 4\pi\alpha \\ \epsilon_2 &= 4\pi\sigma/\omega. \end{aligned} \tag{68}$$

Here ϵ is the dielectric constant of the crystal. This permits calculation of the reflectivity. For light at normal incidence the reflectivity is given by:

$$R = [(N-1)^2+K^2]/[(N+1)^2+K^2], \tag{69}$$

where

$$\begin{aligned} N^2 &= \tfrac{1}{2}[\epsilon_1 + (\epsilon_1^2+\epsilon_2^2)^{\frac{1}{2}}] \\ K^2 &= \tfrac{1}{2}[-\epsilon_1 + (\epsilon_1^2+\epsilon_2^2)^{\frac{1}{2}}]. \end{aligned} \tag{70}$$

For light at oblique incidence, the expression for R is more complicated. The general form is given by KÖNIG.[18]

The preceding discussion forms an outline of the calculation that needs to be done. In practice, of course, it is necessary to approximate the expressions for G_n. These will involve an infinite sum arising from the expansion of the operator $[1+(\delta\mathscr{L})^2]^{-1}$ as well as an integration over energies. We shall avoid problems associated with interchanging the summation and integration in the usual manner by truncating the series for $\gamma^{(1)}$ and $\gamma^{(2)}$ before integrating. In the present case, since $|\delta\mathscr{L}| \ll 1$, we shall use only the lowest terms in the operator expansion.

From equations (66) it is then found immediately that:

$$\gamma^{(2)} \approx -\delta x^3$$
$$\gamma^{(1)} \approx -\delta \mathscr{L} \delta x^3. \tag{71}$$

In this limit the expression for the susceptibility becomes

$$\alpha = -(2^{\frac{1}{2}}/3\pi^2)(m_n^{\frac{1}{2}} e^2 E_g^{*\frac{1}{2}}/\hbar^3\omega^2) \int_0^\infty (s^4/\lambda) f_0(1-f_0) dy. \tag{72}$$

it was not thought worthwhile to complicate the presentation by considering this more general treatment.

The calculated reflectivity as a function of wavelength, as well as the experimental data of YOSHINAGA and OETJEN, are shown on Fig. 5. We have considered only two temperatures, $T = 298$ and 316°K, since at higher temperatures the intrinsic carrier concentration becomes so large that

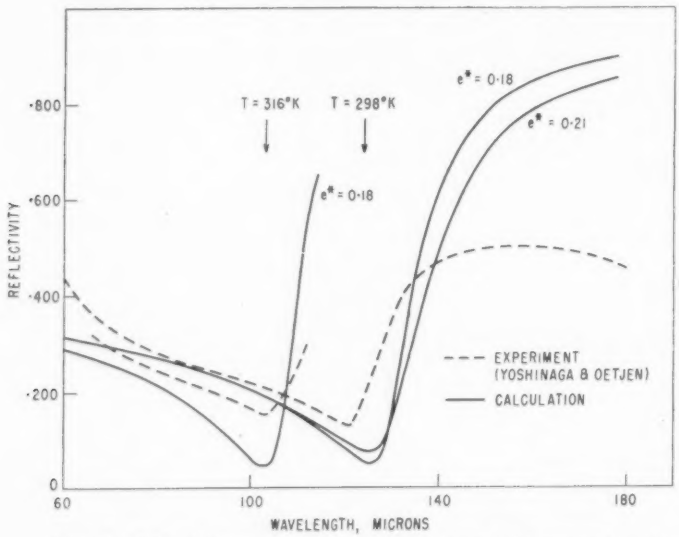

FIG. 5. Reflectivity versus wavelength (microns) for screened polar scattering with $e^* = 0{\cdot}18$ and $0{\cdot}21$ and temperature $T = 316$ and 298°K. The dashed curves refer to data of YOSHINAGA and OETJEN.[8]

This is independent of e^*, in complete analogy with the case when the relaxation-time approximation is valid, where α is found to be independent of τ in the limit $\omega\tau \gg 1$. In fact in the limiting case when Boltzmann statistics are valid and the approximation of parabolic bands applies,

$$\alpha = -ne^2/m_n\omega^2. \tag{73}$$

This is the same result as that obtained with the relaxation-time approximation. On the other hand, the result for σ, which depends explicitly on e^* and the operator $\mathscr{L}$, is more complicated than that obtained using the relaxation-time approximation. One finds that σ is proportional to the integral $\langle (s/\lambda), \mathscr{L}(s/\lambda) \rangle$ which is given explicitly by an expression analogous to (52).

The foregoing perturbation treatment can be improved somewhat by introducing explicitly the asymptotic solution in the manner of Section 6. The results to be presented make use of this fact. The effect on the results, however, turned out to be sufficiently small that

the minimum in the reflectivity shown in the figure shifts into a wavelength region where its position and shape are appreciably perturbed by the *rest-strahlen* peak occurring at 54μ.

The minimum just mentioned is due to free carriers. When $\omega\tau \gg 1$ and the absorption is small one can neglect K in equation (69). It is then clear that R will have a minimum when $N = 1$. For parabolic bands the position of the minimum will then depend only on the effective mass and the number of carriers. Since the latter can be determined from the Hall coefficient, one can use the position of the minimum to estimate the effective mass. This idea, proposed by SPITZER and FAN,[19] has been shown by them to yield very useful experimental information concerning effective masses. When σ and hence K can be neglected, the

expression for R, as we have just seen, is the same regardless of whether the relaxation-time approximation applies or not. It is clear from equation (72), however, that the non-parabolic nature of the bands can affect the position of the minimum considerably. In the present calculations the position of the minimum turns out to be rather insensitive to the value of K, as is evidenced by the curves shown in Fig. 5 corresponding to $e^* = 0{\cdot}18$ and $0{\cdot}21$ for $T = 298°\text{K}$. The value of R, however, depends fairly sensitively on K.

It should be emphasized that the calculated curves shown in Fig. 5 take into account the non-parabolic conduction band of InSb as well as the fact that Fermi statistics must be used for the temperatures under consideration. Only the screened polar interaction together with the p-function admixture is included, electron–hole scattering having been neglected. The viewpoint toward the scattering mechanism that we take here is therefore that used in I, namely that at 300°K polar scattering with $e^* = 0{\cdot}18$ gives an adequate description of the transport properties. Since the results do not depend very sensitively on the scattering mechanism, it was not thought worthwhile to introduce the more complicated description used in Section 6. The agreement with experiment obtained can be regarded as another confirmation of the correctness of the conduction-band structure[2] used in the present calculations. One should note further that these results apply only to intrinsic InSb, no account having been taken of the fact that the sample used in the present experimental data had an extrinsic electron concentration of 6×10^{15} carriers. Finally, these calculations consider the fact that the light in YOSHINAGA and OETJEN's experiment was not normal to the crystal but incident at an angle of 45°. The formula for R used was not equation (69) but the generalization given in Ref. (15). It turns out, however, that these results do not differ significantly from those obtained using equation (69) for normal incidence.

The calculated and observed minima are seen from Fig. 5 to occur at practically the same wavelength for $T = 316°\text{K}$. The agreement for the room-temperature data is not quite as good because the extrinsic carrier concentration present in the sample was not considered in these calculations. Because the number of carriers increases exponentially with temperature, the effect of the extrinsic concentration is still noticeable at 298°K, when there are $1{\cdot}8\times10^{16}$ intrinsic carriers, but less so at 316°K, when there are $2{\cdot}8\times10^{16}$ intrinsic carriers. The effect of these additional carriers is to shift the minimum to smaller wavelengths.

The absolute values of R obtained from the present calculations are in fair agreement with experiment for wavelengths shorter than that at which the minimum occurs. For longer wavelengths, however, the agreement is rather poor. While this may very well be due to an inadequacy of the theory, one should remember that in this range there are extremely difficult experimental problems associated with the production of a monochromatic beam and the elimination of scattered light.

As already pointed out, the calculation just described is a classical one. In this picture all the electrons are accelerated by the electric field and the entire distribution function is altered. On the other hand, according to the quantum-mechanical view, a single electron absorbs the incident photon, leaving the remaining distribution unaltered. BARDEEN[20] has shown that in this case one obtains formulas similar to the classical one in the relaxation-time approximation except that the relaxation time is replaced by an average value corresponding to the excited electron. Since in the present case the photon energy is smaller than KT, one would expect the classical approximation to be fairly adequate. In fact, as the wavelength increases the classical limit is approached. This effect therefore is probably unable to explain the discrepancy just described.

The present calculation has also ignored the effect of intrinsic holes. The holes do not produce another reflectivity minimum, but simply shift the minimum that corresponds to the electrons alone. For the simple theory that yields equation (73) for the susceptibility, the effect of the holes is to replace m_n^{-1} by $m_n^{-1}+m_p^{-1}$, where m_p is the hole mass. Since $m_p \gg m_n$ for InSb, the intrinsic holes clearly will not affect the minimum appreciably.

Finally, it should be clear that for carrier concentrations of the order of 10^{16} encountered here, problems associated with the anomalous skin effect are of no significance. An estimate for the conditions encountered here shows that the electron mean free path is several orders of magnitude smaller than the skin depth.

Acknowledgements—The author is indebted to P. V. GRAY for programming the machine calculations and also to DORIS OLECHNA for considerable help with the numerical work involved in this paper. Some discussions with F. S. HAM and E. O. KANE and comments from C. HERRING are also gratefully acknowledged.

GLOSSARY OF SYMBOLS

Because there are a number of separate problems treated in this paper, each involving mathematical notation, it has occasionally been necessary to use the same symbol in different contexts. The following list, including the more important quantities that occur in the paper, should prove helpful. The numbers in parentheses refer to equations where the symbols are defined. Those preceded by I refer to equations in ref. (1).

a(I, 52) reciprocal screening length; a_q, a_q^* phonon annihilation and creation operators ; $A_q^{(s)}(3)$; b factor of order unity in Hall coefficient; c velocity of light; $c(E)$ (17) function proportional to perturbing part of distribution function; e^* (I, 23) effective ionic charge; E electron energy; E_g band gap; E_g^* (I, Section 2) effective mass band gap; $\mathscr{E}$ electric field; $\mathscr{E}_0$ amplitude of oscillating electric field; $\mathscr{E}_1$, $\mathscr{E}_2$ longitudinal and transverse electric field (Hall effect); $f(k)$ perturbed distribution function; f_0 unperturbed distribution function; $f_0' = df_0/dE$; $\mathscr{F}(q_\pm)$ (7) for polar scattering; $\mathscr{F}(|k-k'|)$ (15) for electron–hole scattering.

$g_i^\pm$ (11); G^3 number of unit cells in volume V; G_n(47) transport integrals; $\mathscr{G}_\pm(\beta)$ (7), (10); $H_{k'\mu', k\mu}$ (5) matrix elements for phonon scattering; $\mathscr{H}$ (21) matrix element for electron–hole scattering; $\mathscr{H}$ magnetic field; $\mathscr{H}$ (7) for polar scattering; (15) for electron–hole scattering; $j_i (i = 1, 2)$ (63); k electron wave number; K Boltzmann constant; l_n (43); L_A (I, 30) and L_B (23) collision operators for polar and electron–hole scattering; L (23) total collision term; $\mathscr{L}_A, \mathscr{L}_B, \mathscr{L}$ (27) dimensionless collision operators.

m_n electron effective mass; M reduced mass of atoms in unit cell; n number of phonons q in field; n number of electrons or holes; N index of refraction; P (I, 3) matrix element; q phonon wave number; Q (49) thermoelectric power; R (69) reflectivity; $R_\pm$ (20); R_H Hall coefficient; $s(\xi)$ (I, 11) quantity proportional to k; $S_\pm$(20); $\mathscr{S}$ (21); T temperature; v_a volume of unit cell; $v_q^\pm$ (2); V volume of crystal; $V_q^\pm$ (1); x^3(27); $y = E/KT$; $z = \zeta/KT$.

α (31) magnetic field problem; α (56) parameter in trial function; α (67) electric susceptibility; β-angle between k and $k_\pm$; $\beta^* = KT/E_g^*$; γ dimensionless quantity related to $c(E)$;

$\gamma^{(n)}$ (28) for uniform electric field and/or temperature gradient; (30) for crossed uniform electric and magnetic fields; (36), (65) for oscillating electric field; $\gamma^{(n)}$, $\gamma^{(n)'}$, $\gamma^{(n)''}$ (54) trial functions used to calculate mobility and thermoelectric power; $\bar{\gamma}$ (33); $\gamma^{(0)}$ (42); $\gamma^{(3)}$ (60); δ (36); Δ spin-orbit splitting; $\Delta^{(n)}$ (41) trial function; $\Delta^{(0)}$ (42); $\Delta_i^{(n)}$ (45) expansion coefficients determined by variational method; ϵ dielectric constant; ϵ_0, ϵ_∞ static and dynamic dielectric constants; ϵ_1, ϵ_2 (68) real and imaginary part of dielectric constant; $\epsilon_\pm$ (12); ζ Fermi level; η (24); θ (30); θ angle between k and $\mathscr{E}$; $\Theta = \hbar\omega_l/K$; $\vartheta = \Theta/T$ (24); λ (I, 8) proportional to conduction-band density of states; λ_D Debye length; λ, general screening length; μ mobility; $\mu = m_n/m_0$; μ spin index; $\upsilon = \omega_l/h$; $\xi = E/E_g^*$ (I, 9); $\xi_\pm = E_\pm/E_g^*$; $\pi_{\nu\lambda^\mu}$ (θ, ϕ) (9); ρ_i parameter in trial function; σ (48) conductivity; $\sigma_{\lambda^\mu}(\theta, \phi)$ (9); τ relaxation time; $\phi_i^{(n)}$ (54.2); Φ (62); $\chi^{(n)}$ (41); $\chi^{(0)}$ (42); $\chi_{k\mu}$(4); $\psi_{k\mu}$(4) Bloch function; $\psi_i^{(n)}$ (45); $\langle\psi, \mathscr{L}\phi\rangle$ (44); $\langle\psi, l\rangle$ (44); $\Psi_{k\mu,n}$(5) total wave function for electron–phonon system; ω frequency of oscillating electric field; ω_0 cyclotron frequency; ω_l longitudinal optical frequency.

REFERENCES

1. EHRENREICH H., *J. Phys. Chem. Solids* **2,** 131 (1957).
2. KANE E. O., *J. Phys. Chem. Solids* **1,** 249 (1957).
3. LONG D., *Phys. Rev.* **99,** 388 (1955).
   KEYES R. W., *Phys. Rev.* **99,** 490 (1955).
4. KOHLER M., *Z. Phys.* **125,** 679 (1949).
5. HROSTOWSKI H. J., MORIN F. J., GEBALLE T. H., and WHEATLEY G. H., *Phys. Rev.* **100,** 1672 (1955).
6. SPITZER W. G. and FAN H. Y., *Phys. Rev.* **99,** 1893 (1955).
7. WEISS H., *Z. Naturf.* **11a** 131 (1956).
8. YOSHINAGA H. and OETJEN R. A., *Phys. Rev.* **101,** 526 (1956).
9. FRÖHLICH H., *Proc. Roy. Soc.* **A160,** 230 (1937).
10. CALLEN H. B., *Phys. Rev.* **76,** 1394 (1949).
11. EHRENREICH H. and COHEN M. H. To be published.
12. LEWIS B. F. and SONDHEIMER E. H., *Proc. Roy. Soc.* **A227,** 241 (1954).
13. ARGYRES P. N. *Phys. Rev.* **109,** 1115 (1958).
14. HOWARTH D. J. and SONDHEIMER E. H., *Proc. Roy. Soc.* **A219,** 53 (1953).
15. SPITZER L. and HÄRM R., *Phys. Rev.* **89,** 977 (1953).
16. DEBYE P. P. and CONWELL E. M., *Phys. Rev.* **93,** 693 (1954).
17. HERRING C., *Phys. Rev.* **96,** 1163 (1954).
18. KÖNIG W., *Handbuch der Physik* Vol. 20, p. 243. Julius Springer, Berlin (1928).
19. SPITZER W. C. and FAN H. Y., *Phys. Rev.* **106,** 882 (1957).
20. BARDEEN J., *Phys. Rev.* **79,** 216 (1950).

VOL
9
195

J. Phys. Chem. Solids Pergamon Press 1959. Vol. 9. pp. 149–152. Printed in Great Britain.

ENERGY TRANSFER IN ZnS:Cu:In PHOSPHORS

N. T. MELAMED

Westinghouse Research Laboratories, Pittsburgh 35, Pennsylvania

(*Received* 25 *July* 1958)

Abstract—Transport of energy between luminescence centers has been observed in ZnS:Cu:In phosphors at room temperature and at 77°K. The results support a photoconductive transfer mechanism. Energy transfer at low temperatures can be interpreted as resulting from a process in which a given wavelength is capable of putting an electron into an impurity level from the valence band, as well as exciting it from the same impurity level to the conduction band.

1. INTRODUCTION

In a recent paper[1] dealing with energy transfer in ZnS:Cu:Cl phosphors, we observed that, from 300° to 4°K, irradiation into the excitation band of the blue emitting centers resulted in an emission from the green luminescence centers. We inferred that excitation energy was transported from blue centers to green centers, and came to the opinion that the most likely mechanism of transfer was photoconductive.

An important feature in a photoconductive transfer process was the assumption that optically induced transitions can take place between an impurity level and either band. It was thought possible to test this assumption, as well as several other possible transfer mechanisms which could not be entirely eliminated, by observing the transport of energy in phosphors similar in composition to ZnS:Cu:Cl, but in which the chlorine is replaced by a different coactivator. Indium was chosen because glow-curve data indicate that, of the known coactivators, it forms the deepest level and therefore differs most in this respect from the chlorine it replaces.

2. EXPERIMENTAL RESULTS

The phosphors were prepared from luminescence-grade zinc sulfide and were fired 1 hr at 950° in H_2S. The impurities were added as copper acetate and indium sulfide. Emission and excitation spectra were obtained in a manner described for ZnS:Cu:Cl.[1]

Fig. 1 shows the emission spectrum of a sample of ZnS:Cu:In. The blue emission band, attributed to zinc vacancies, lies at about 4600 Å. The green copper band is at 5200 Å, and the orange

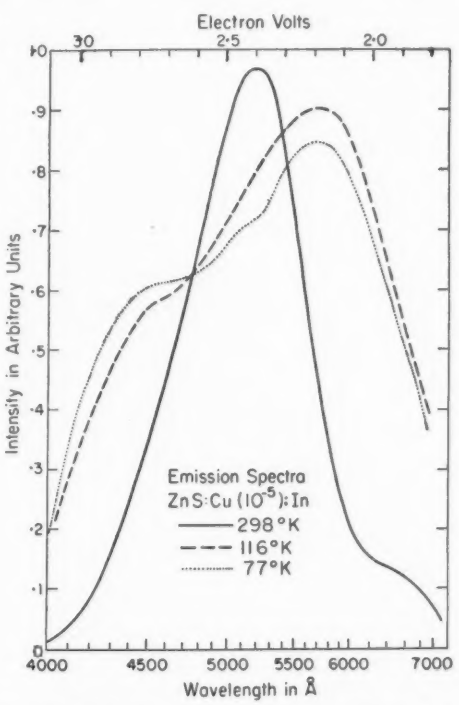

FIG. 1. Emission spectrum of ZnS:Cu(10^{-5}):In at 298°, 116°, and 77°K. Because of their large half-widths, the individual blue, green, and red emission bands are not clearly distinguishable.

emission band of indium has its peak at 5850 Å. The positions of the emission bands agree with the data obtained by KRÖGER and DIKHOFF.[2] The presence of a blue emission in ZnS:Cu:In suggests that indium, like chlorine, can give rise to zinc vacancies at low copper concentrations, apart from its role as charge compensator for copper.[2]

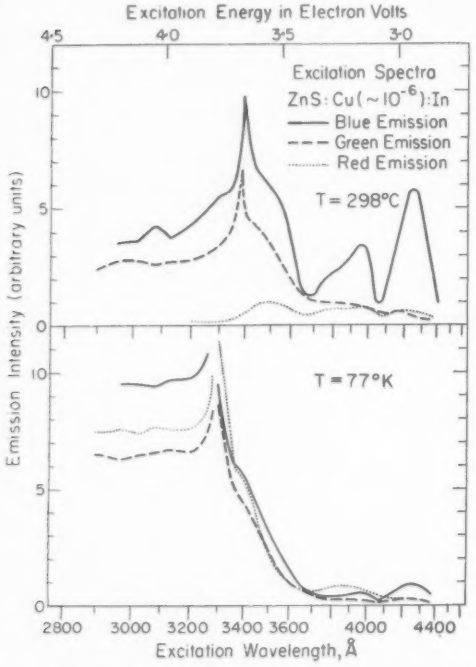

FIG. 2. Excitation spectra for the blue, green, and red emissions of ZnS:Cu(10^{-6}):In at 298° and 77°K.

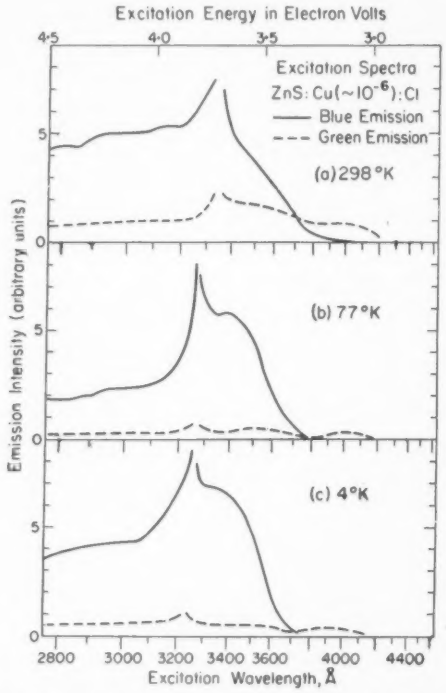

FIG. 3. Excitation spectra for the blue and green emissions of ZnS:Cu(10^{-6}):Cl at 298°, 77°, and 4°K.

Fig. 2 shows the excitation spectra for the blue, green, and orange emissions of ZnS:Cu (0·0001 per cent):In at room temperature and at 77°K. For purposes of comparison the excitation spectra of ZnS:Cu(0·0001 per cent):Cl are shown in Fig. 3.

Considering first the excitation bands of ZnS:Cu:Cl, we find an excitation band for the blue emission at 3450 Å, which we believe corresponds to the absorption band for blue centers. We find two excitation bands for the green emission, at 3850 and 3450 Å. The 3850 Å excitation band corresponds to the absorption band of the green centers; the 3450 Å excitation band arises from the absorption of radiation at blue centers with a subsequent transfer of energy to green centers.[1]

In ZnS:Cu:In, the excitation bands are most numerous, due in part to the greater number of emission bands. The orange emission of indium is excited in three bands: at 4250, 3850, and 3450 Å. The 4250 Å band we attribute to the absorption band of indium. The two bands at shorter wavelengths we believe result from a transfer of energy from green and from blue centers to orange centers. The blue and green emissions of ZnS:Cu:In show excitation bands similar to those found in ZnS:Cu:Cl, with, however, several additional excitation bands which are not present in ZnS:Cu:Cl. For the blue emission, these additional bands lie at 3850 and 4250 Å.

The appearance of two new excitation bands for the blue emission in ZnS:Cu:In has significance towards establishing the mechanism of energy transfer in ZnS. These bands, lying at 3850 and

4250 Å, coincide with what we believe are the excitation peaks for direct absorption in copper and indium. They indicate that in the ZnS:Cu:In phosphor a transfer of energy takes place from the copper and indium centers to the zinc vacancies.

In Fig. 4 is shown an energy-level diagram for ZnS:Cu:In, which we deduce from our optical measurements.

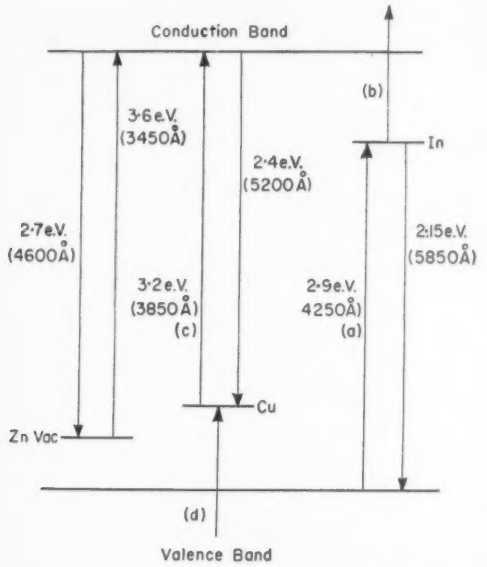

FIG. 4. Energy-level diagram for the ZnS:Cu:In phosphor deduced from measurements of excitation and emission spectra. The excitation spectra for transitions (*b*) and (*d*) are assumed to extend from the near-infrared through the visible to the near-ultraviolet region.

3. DISCUSSION

There is evidence in various phosphors that energy can be transported from one luminescence center to another by three mechanisms: by resonance, by cascade, or by a photoconductivity process. The presence of the 3850 and 4250 Å excitation bands for the blue emission in ZnS:Cu:In strongly supports a photoconductive transfer mechanism. Both resonance transfer and cascade transfer require that the emission band of the absorbing center (or sensitizer) overlaps the absorption band of the emitting center.[3] Since the emission bands of both copper and indium lie too far to the long-wavelength side of the 3450 Å blue excitation band for overlap to occur, it is not likely that either a resonance or a cascade process can play an important role in the transfer from red or green centers to blue.

To account for a photoconductive transfer which results from excitation with energy of less than the band gap, two processes have been proposed.[1] In the first process, an electron is excited from the valence band into an unoccupied donor, leaving a free hole (for example, transition *a*, in Fig. 4). In addition, an electron is excited into the conduction band from an occupied acceptor level (*c* in Fig. 4). Energy transfer results from the recombination of the electron and the free hole at a third center. Such a process requires an overlap in the excitation spectra of a particular set of donor and acceptor impurity levels; it predicts an eventual depletion of one or both of these levels, with a consequent diminution of transfer. Because we have not been able to observe any evidence of exhaustion, we do not think this process, taken by itself, is the major cause of transfer.

As an alternative process we proposed one which is more general, and of which the first process may be regarded as a special case. In this, the more general process, optical transitions can take place between an impurity level and either band. In particular, the same radiation which can fill vacant indium levels from the valence band, can also excite electrons from occupied indium levels to the conduction band (transitions *a* and *b*, Fig. 4) or, by analogy, radiation which excites electrons from occupied copper levels to the conduction band can also partially fill vacant copper centers from the valence band (transitions *c* and *d*). Such a process leads to a photoconductive transfer which requires no overlap in the excitation spectra of donors and acceptors, predicts no depletion of impurity centers, and can occur to a significant extent at low temperatures.

We believe the more general photoconductive process to be the explanation for the energy transfer in ZnS. It is consistent with our observation that no reduction in transfer occurs with time. It is further supported by evidence which indicates that electron traps can be emptied by near-ultraviolet radiation. The emptying of traps by short-wavelength radiation had been previously proposed by ANTONOV–ROMANOVSKII and SHUKEN to explain the increased absorption at 4500 Å which results from excitation in ZnS:Cu:Co,[4] by

SMITH and TURKEVICH to account for the emptying of traps in copper activated ZnS by visible and near-ultraviolet radiation[5] and by HOOGENSTRAATEN and KLASENS to explain the intensity-dependence of the light sum of ZnS:Cu:Co under 3650 Å excitation.[6] Transitions such as (*b*) and (*d*) also can be used to explain the increase in absorption throughout the entire visible range that has been observed in a number of other sulfide phosphors during excitation.[7]

The proposed photoconductive mechanism further suggests that transfer can occur from any one center to any other. That this indeed appears to be the case is seen in the excitation spectrum for the orange emission. This consists of three excitation bands: the long-wavelength band, resulting from direct excitation of orange centers, and two at shorter wavelengths which correspond respectively to the excitation bands for the green centers and for the blue centers, and result from a transfer of energy from these to the indium centers. The green emission in ZnS:Cu:In is also seen to include an excitation band at 4250 Å which is not present in ZnS:Cu:Cl and which suggests that a transfer of energy takes place from indium to copper. The presence of these kinds of multiple-transfer processes favors a photoconductive mechanism.

In discussing the transfer of energy in ZnS:Cu:Cl,[1] several possible complications were described. We considered the presence within the blue excitation band, of either an exciton band or of an excited state for the copper emission. If excited states or excitons exist, it is not likely they would contribute to the long-wavelength excitation bands in ZnS:Cu:In. A further complication was the possibility that dissimilar centers associate. If this were the case, one might assume that in ZnS:Cu:In all three centers are mutually associated. While such a situation could result, for example, from segregation at grain boundaries or at stacking faults, there appears to be no direct evidence at present that association of this kind takes place.

4. CONCLUSIONS

The results obtained on ZnS:Cu:In indicate that a photoconductive energy transfer takes place in ZnS, which can account for the transfer observed at low temperatures and for low impurity concentrations. The detailed process appears to be one in which particular wavelengths are capable of both filling and emptying impurity levels. We believe such processes occur quite generally in sulfide phosphors. They will be most in evidence at low temperatures, where the available thermal energy is insufficient to supply the additional energy needed to empty traps, and at low concentrations, where competing processes and added complications are least likely to occur.

Acknowledgements—The author wishes to thank Dr. E. N. ADAMS for his critical comments and Miss SALLY WARNER for assistance in obtaining the measurements. He is grateful to Mr. A. WACHTEL of the Westinghouse Research Laboratory, Bloomfield, New Jersey, for supplying the specimens.

REFERENCES

1. MELAMED N. T., *J. Phys. Chem. Solids* **7**, 146 (1958).
2. KRÖGER F. A. and DIKHOFF J. A. M., *Physica* **16**, 297 (1950).
3. DEXTER D. L., *J. Chem. Phys.* **21**, 836 (1953).
4. ANTONOV-ROMANOVSKII V. V. and SHUKEN I. P., *Dokl. Akad. Nauk. SSSR* **71**, 445 (1950).
5. SMITH A. W. and TURKEVICH J., *Phys. Rev.* **87**, 306 (1952).
6. HOOGENSTRAATEN W. and KLASENS H. A., *J. Electrochem. Soc.* **100**, 366 (1953).
7. *Final Rep. Polytech. Inst. Brooklyn, Contract*, NObsr 39045 (June 1949).

J. Phys. Chem. Solids Pergamon Press 1959. Vol. 9. pp. 153–164. Printed in Great Britain.

SPIN FLUCTUATION SCATTERING OF NEUTRONS IN MAGNETITE*

TORMOD RISTE, KONRAD BLINOWSKI† and JERZY JANIK‡

Joint Establishment for Nuclear Energy Research, Kjeller, Norway

(*Received* 6 *January* 1958; *revised* 17 *June* 1958)

Abstract—Observations on the peak widths and intensities of inelastically scattered neutrons from Fe_3O_4 are found to agree with spin-wave theory over a wide range of temperatures. The quadratic dispersion relation for ferrimagnetic spin waves is verified, and the value of $J_{AB} = 2 \times 10^{-3}$ eV is in agreement with an earlier result by BROCKHOUSE (*Phys. Rev.* **106**, 859 (1957)). The statistical behaviour of spin waves (magnons) is found to be well described by Bose–Einstein statistics. The maximum temperature for the validity of the spin-wave approximation is seen to be a function of the magnon energy. At higher temperatures fluctuations are also found to exist in the z-component of the spins.

1. INTRODUCTION

A RECENT paper by BROCKHOUSE[1] on the spin-wave scattering of neutrons in magnetite (Fe_3O_4) has led us to take up and extend some work one of us had done earlier on this substance.[2] The aim of the work has been to see if this observed inelastic scattering can be interpreted in terms of spin-wave theory and if the results obtained could determine the proper dispersion law for spin waves in ferrites.

In Section 2 we review the theory of spin-wave scattering of neutrons and the possibilities of experimental verification. We also mention the existing theories of spin waves in ferrites. In Sections 3 and 4 we give our experimental methods and results. In Section 5 we compare experiments and theory.

2. THEORY

If a neutron with mass m_0 undergoes inelastic scattering by quantized waves in a crystal whereby its energy is changed by an amount $\hbar\omega$ and its momentum by $\hbar(2\pi(\boldsymbol{\tau})+\boldsymbol{q})$, the following equations must be satisfied:

$$\frac{\hbar^2}{2m_0}(k'^2-k^2) = \pm\hbar\omega(q) \tag{1a}$$

$$\boldsymbol{k}-\boldsymbol{k}'+2\pi\boldsymbol{\tau}+\boldsymbol{q}=0. \tag{1b}$$

Here $\boldsymbol{k}$ and $\boldsymbol{k}'$ denote the incoming and outgoing wave vectors of the neutron and $\boldsymbol{\tau}$ is a reciprocal lattice vector with magnitude $1/d$, where d is the interplanar spacing. The quantum which gives rise to the inelastic scattering has wave vector $\boldsymbol{q}$ and angular frequency ω; $\omega(q)$ denotes the dispersion relation or the connection between the frequency and the wave vector. The above equations define a scattering surface in reciprocal space on which the end point of $\boldsymbol{k}'$ must lie. SEEGER and TELLER[3] have shown that in the case of scattering of slower-than-sound neutrons by waves which have the dispersion relation:

$$\omega = cq \tag{2}$$

where c is a constant, the scattering surfaces are ellipsoids. In the case of scattering by lattice waves, c is the velocity of sound, and in the case of scattering by antiferromagnetic spin waves, c is the velocity of propagation of the spin disturbance.

* A part of this work has been presented earlier as JENER Report No. 53 (1957).

† On leave from the Institute of Nuclear Research, Warsaw, Poland; now back there.

‡ On leave from the Institute of Nuclear Research, Krakow, Poland; now back there.

Ferromagnetic spin waves have the dispersion relation:

$$\omega = \alpha(\hbar/2m_0)q^2 \tag{3}$$

where α is a constant. MOORHOUSE[4] and ELLIOTT and LOWDE[5] have shown that in this case the scattering surfaces are close to being spheres.

The most direct experimental method of investigating the dispersion relation is the one which has been applied by BROCKHOUSE,[1] in which he analyses the energy spectrum of the scattered neutrons as a function of q. Such an experiment requires a high-flux reactor.

Another method of establishing the proper dispersion relation, not limited to a high-flux reactor, has been discussed by MOORHOUSE,[4] ELLIOTT and LOWDE,[5] and PEIERLS.[6] The method consists of measuring the width of successive peaks arising from inelastic scattering as the crystal is rotated away from the position for Bragg reflection.

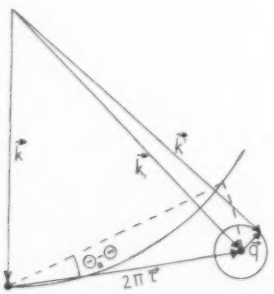

FIG. 1. A two-dimensional geometrical representation of equation (1b). The construction is for energy absorption by the neutron. The scattering surface on which $\boldsymbol{k}'$ ends is here drawn for the case of ferromagnetic spin-waves.

In Fig. 1 we have given the geometrical representation of equation (1b). If we introduce:

$$\boldsymbol{k}_1 = \boldsymbol{k}' - \boldsymbol{q}, \tag{4}$$

then equation (1a) can be written

$$k'^2 = k^2 + \frac{2m_0}{\hbar}c|\boldsymbol{k}' - \boldsymbol{k}_1| \tag{5}$$

in the case where equation (2) applies and

$$k'^2 = k^2 + \alpha(\boldsymbol{k}' - \boldsymbol{k}_1)^2 \tag{6}$$

in the case where equation (3) is valid. The graphical solution of equations (5) and (6) is represented in Fig. 2. The left-hand side of the equations gives the parabola a and the right-hand sides of (5) and (6) give the cone b and the parabola c respectively.

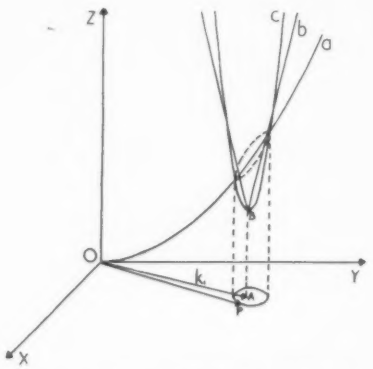

FIG. 2. A construction giving the graphical solution of equations (5) and (6), as explained in the text.

The length of OA is k_1 and the length of AB is k^2. The curve a should be regarded as the section through a paraboloid with rotational axis OZ and b and c as surfaces of revolution with axis along AB. The curve of intersection of the paraboloid a with the surfaces b and c, when projected down on the $(x$–$y)$ plane, gives possible values of the end point of k'. One of the possible vectors is denoted by OP. The maximum value of the angle AOP is the angular width of the diffuse peak associated with the scattering surface. It is seen that if k_1 increases the width of the diffuse peak will also increase. Fig. 1 shows that the increase of k_1 is obtained by increasing $(\theta_B - \theta)$ with the relationship:

$$k - k_1 \simeq 2\pi\tau(\theta - \theta_B)\cos\theta_B \tag{7}$$

The sharpness of the peaks of different values of $(\theta - \theta_B)$ measures the width of the dispersion curve in Fig. 2 at different heights. The ways in which the peak width increases with $(\theta - \theta_B)$ are, however, quite different for the linear and the quadratic dispersion laws. The analytical expressions given by ELLIOTT and LOWDE[5] (E. and L.) for the total semi-angle i of the peaks versus missetting $(\theta - \theta_B)$ are

$$i = \left(\frac{c^2}{v^2} - 1\right)^{-\frac{1}{2}} |\theta - \theta_B| \sin 2\theta_B \tag{8}$$

(v is the neutron velocity) for a linear dispersion law and

$$i = \sin^{-1}\{\alpha^{-1}[1-(1+\epsilon\alpha)(1-k^2k_1^{-2})]^{\frac{1}{2}}\} \quad (9)$$

for a quadratic dispersion law. $\epsilon = +1$ for magnon emission and -1 for magnon absorption.

E. and L. also show that there is a marked difference between the total cross-sections as a function of $(\theta-\theta_B)$ in the two cases. In the former case the cross-section remains constant as $(\theta-\theta_B)$ is varied, whereas in the latter case the cross-section attains a peak as the Bragg setting is approached.

When $v < c$, LOWDE[7] gives the following formula for the vibrational scattering cross-section, integrated over the whole scattering surface:

$$\sigma_V = \left(\frac{k_B}{2m_nc^2}\right) Ce^{-2W}\tau^2\lambda^2 T \tan h^{-1}\left(\frac{v}{c}\right) \quad (10)$$

k_B is the Boltzmann factor, m_n the mass of the nucleus, C the coherent scattering cross-section, e^{-2W} the Debye–Waller factor, and T the temperature of the crystal. The equivalent cross-section for scattering by ferromagnetic spin waves, as given by E. and L. is (for the main branch)

$$\sigma_{SW} = \frac{\pi}{k^2} Sq^2\left[N(q)+\frac{1}{2}+\frac{\epsilon}{2}\right]\left(\frac{e^2\gamma}{mc^2}\right)^2 f^2e^{-2W}\times$$
$$\times[1+(e\varkappa)^2]+\cos h^{-1}[(\alpha|\theta-\theta_B|\sin 2\theta_B)^{-1}+1] \quad (11)$$

S is the spin per magnetic atom, $N(q)$ is the statistical factor for the spin wave, e^2/mc^2 is the classical electron radius, γ the magnetic moment of the neutron, f the magnetic form factor, e the scattering vector, and $\varkappa$ is a unit vector in the direction of the magnetic moments.

The formulae (10) and (11) are for lattices with one particle per cell. For more complicated lattices a structure factor has to be added. The relevant factor to be inserted in (11) in the case of ferrimagnetic substances will be given below. Formula (10) is here given for nuclear vibrational scattering. E. and L. have also introduced the term "magneto-vibrational scattering". This is the scattering connected with the thermal vibration of spins which retain their orientation in the domain. The total cross-section corresponding to equation (10) is obtained by replacing C by the magnetic scattering cross-section. In addition one has to add the factors

$$[1-(e\varkappa)^2]\left(\frac{I_T}{I_0}\right)^2 \quad (12)$$

since the scattering is magnetically elastic. Here I_T is the magnetization of the domain at temperature T and I_0 the same quantity at absolute zero temperature.

Formulae (9) and (11) are for the region where exchange effects predominate. E. and L. have also considered the influence of magnetic dipole forces. The effect is to make peak widths and intensities more asymmetric around the Bragg setting; in addition the dipole term gives a response to an external field more like $[1-(e\varkappa)^2]$. The influence of non-exchange forces is, however, restricted to settings very close to the Bragg position.

It has generally been assumed that spin-wave quanta (magnons) obey Bose–Einstein statistics. Thus E. and L. put

$$N(q) = \left[\exp\left(\frac{\hbar^2}{2m_0}\alpha q^2/k_BT\right)-1\right]^{-1} \quad (13)$$

and made the approximation

$$N(q)+1 \simeq N(q) \simeq \frac{k_BT}{\hbar^2\alpha q^2}2m_0 \quad (14)$$

in order to simplify the scattering formulae. In some recent papers by FRANK[8] and by MEYER,[9] the validity of equation (13) has been questioned. In the case $S = \frac{1}{2}$ they find that magnons obey Fermi–Dirac statistics. Although the case of arbitrary S has not been treated rigorously, MEYER indicates that the magnons should be expected to follow intermediate forms of statistics with maximum occupation number $2S$ per energy state.

Recently the problem of neutron scattering by ferromagnons has also been treated by MALEEV.[10] In the case of $\alpha \sim 100$, as is the case for iron and Fe_3O_4, his formula for the peak width is identical to equation (9). His cross-section formula is given without the approximation (14), but shows the additional difference that the cross-section for magnon emission increases with $|\theta-\theta_B|$.

It has generally been assumed that the spin-wave theory is valid only for temperatures up to $\sim 0{\cdot}1T_c$; at higher temperatures the spin-waves start to interact and the picture breaks down. DYSON[11] has shown, however, that the importance of these interactions is less than had been assumed and that the picture is also valid for higher temperatures. In the same temperature region multiple-quantum-scattering processes will occur. In our experiments the influence of these processes is small, because neutrons scattered in this way give much more diffuse peaks[12] and these merge into the background.

The behaviour of the scattering at general temperatures was first discussed by VAN HOVE,[13] who introduced the correlation function between spin directions in the scattering formulae. Spin-waves describe the time-dependent correlations or the coherent motions of the x- and y-components of the spins, i.e. the components normal to the magnetization. His theory for the critical region, i.e. for $T \sim T_c$, where the spin-wave approximation is no longer valid, has been worked out in more detail by ELLIOTT and MARSHALL[14] and by DE GENNES.[15] They show that fluctuations in the (x, y) components generally respond to a magnetic field according to the formula $[1+(\boldsymbol{e}\cdot\boldsymbol{\varkappa})^2]$, whereas fluctuations in the z-components respond according to $[1-(\boldsymbol{e}\cdot\boldsymbol{\varkappa})^2]$. The latter kind of fluctuations are expected to occur only in the critical region.

Neutron-diffraction studies by SHULL *et al.*[16] have revealed the magnetic structure of magnetite. The magnetic ions are found on tetrahedral (A) sites and octahedral (B) sites. On the A sites there are 8 Fe^{3+} ions in each unit cell, whereas on the B sites there are 8 Fe^{3+} and 8 Fe^{2+} ions in disordered arrangement. Within each of the sub-lattices A and B the spins are aligned parallel and the spins on A are aligned anti-parallel to those on B. The three different magnetic interactions are expressed by the exchange integrals J_{AA}, J_{BB}, and J_{AB}. It is usually assumed that J_{AB} is the dominant one of these and that J_{BB} is very small, but when the NÉEL theory of ferrimagnetism is applied to the data on susceptibility and magnetization curves, it gives J_{AA} only slightly smaller than J_{AB}.[17] A fairly complete list of values of J_{AB} is given by BROCKHOUSE.[1]

It is to be expected that the spin-wave theory is applicable to ionic solids like magnetite. The quantitative treatment is, however, difficult because of the complex crystallographic and magnetic structure, and the results differ. H. KAPLAN,[18] using the semi-classical theory of spin waves, obtained a quadratic dispersion law. The energy of the main branch is

$$\hbar\omega = \frac{|\frac{11}{8}J_{AB}S_AS_B+J_{AA}S_A{}^2+2J_{BB}S_B{}^2|}{4|S_A+2S_B|}a^2q^2 \quad (15)$$

where S_A and S_B are the ionic spins on A and B sites and a is the lattice constant. From this expression one sees that, even if NÉEL's values of the exchange integrals are correct, the dominating term in the dispersion relation is the one containing J_{AB}. KAPLAN's formula is obtained after averaging the values of the spins on the B sites. KOUVEL[19] has studied the effect of ordering of the spins on the B sites and found that the effect is to make the constant-energy surfaces ellipsoidal. In the case of magnetite, however, the difference in the spin values of the iron ions is so small that the surface is close to being a sphere. Furthermore the spins on the B sites in magnetite are disordered for $T > > 120°$K. The quadratic dispersion relation for ferrimagnetic spin-waves has also been found by KONDORSKII *et al.*[20] and by VAN KRANENDONK and VAN VLECK.[21] A conflicting result has been obtained by VONSOVSKII and SEIDOV,[22] who found an essentially linear dispersion relation. T. A. KAPLAN[23] has discovered an error in their calculation, however, and verified the quadratic law. In another paper[24] he discusses the relative structure factor to be inserted in equation (11). For acoustic modes and small enough values of q, he finds that S should be replaced by

$$g^2 = \frac{1}{8|S_A+2S_B|}\times$$

$$\times|S_A\,\Sigma\exp 2\pi i\,\boldsymbol{\tau}\boldsymbol{r}_A+S_B\,\Sigma\exp 2\pi i\,\boldsymbol{\tau}\boldsymbol{r}_B|^2, \quad (16)$$

where $\boldsymbol{r}_A$ and $\boldsymbol{r}_B$ are the position vectors in the unit cell of the A and B ions. Here, as in (15), S_B is negative.

3. EXPERIMENTAL METHODS

In this work we have used an experimental method developed by LOWDE.[7] The complete spectrum of neutrons from the reactor is incident

upon an Fe_3O_4 crystal which is mounted with the [1$\bar{1}$0] axis vertical. The crystal and the counter are set to give neutrons of $\lambda = 1{\cdot}52$ Å by Bragg or Laue reflection. Neutrons of other wavelengths being inelastically scattered by the same set of planes will then develop a diffuse ridge of intensity along the equatorial plane. If neighbouring peaks are similar, the profile of a diffuse peak of a single wavelength can be studied by moving the counter in the vertical direction at a constant angle of longitude. Thus we shall obtain the width in degrees latitude of the counter angle. If we wish, for example, to follow the peak of neutrons of $\lambda = 1{\cdot}52$ Å from the (111) reflection for a specific values of $(\theta - \theta_B)$ (see Fig. 1), we leave the counter at 18° longitude and take the vertical contour for the proper crystal setting. If the peaks are sufficiently narrow, the area under such a curve represents the integrated intensity over the whole scattering surface, because the spectrum of the pile neutrons is broad in comparison. When the cross-section reaches a peak on approaching the Bragg setting, the above statement is not strictly true, but we will assume that the error is small.

To obtain the true width of the diffuse peaks, we have to correct for instrumental broadening. The instrumental width is obtained by surveying the Bragg peak. In our case the collimation was such as to give a Bragg peak with a Gaussian contour and full width at half maximum (or half-width) of 1·7°. From the shape of the elastic peak, it was found that the elastic component was negligible for $|\theta - \theta_B| > 1°$.

The crystals used were cut from a natural geological specimen of Fe_3O_4. The crystal used for observation on peak widths was a cylinder of 8 mm diameter, the axis being the [1$\bar{1}$0] crystallographic direction. To establish the cross-section on an absolute scale, the intensity of a diffuse peak was compared with that of a Bragg peak for a crystal of only 2 mm thickness to reduce extinction effects. In the cases where a magnetic field was applied, a parallel-epipedic sample was used to get a homogeneous field along the scattering vector.

The spectrometer is built for automatic recording in the vertical plane. The counter with its heavy shield climbs in steps along a toothed arc. The arc is part of a circle with centre at the crystal. The angular steps are 0·3° and the recording time is adjustable up to 15 min.

The first series of experiments was performed at room temperature. In the second series the crystal was mounted in a quartz furnace with electrical-heating windings. The temperature uncertainty due to gradients and drifting was measured and found to be less than 5° at T_c. When a magnetic field was applied, the intensity was recorded for field both on and off in each point before moving the counter, to avoid any greater uncertainty due to drifting of the temperature and the pile level. Instead of using a monitor, which is difficult in the white-beam method, the intensity in the Bragg peak was checked at regular time intervals.

The magnetic field applied in the first series of the experiments had a maximum strength of 4500 Oe. In the second series, where the crystal was mounted in a furnace, the field strength was 2000 Oe.

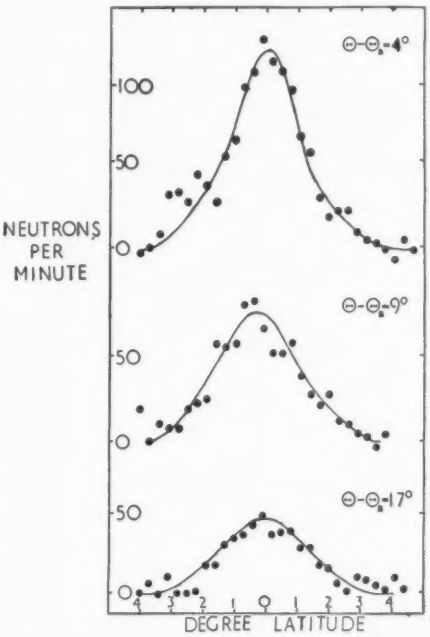

FIG. 3. Typical experimental curves obtained at room temperature when the background is subtracted. All three curves are for 1·52 Å neutrons incident on (111) in Fe_3O_4.

4. EXPERIMENTAL RESULTS

The measurements were made mostly on the (111) reflection, which is known[16] to give a Bragg peak of almost pure magnetic origin. Fig. 3 shows room-temperature curves for three different angles. Within experimental accuracy these curves are all Gaussian, and the true widths of the diffuse peaks are easily obtained within the same accuracy from the widths of the experimental and instrumental curves.

The data on (111), together with a few values for (222) and (220), which are also strongly magnetic,

are given in Fig. 4. The abscissa represents the angle of missetting for the (111) reflection; the data on the other two reflections are brought to the same scale by means of equation (7). Each point

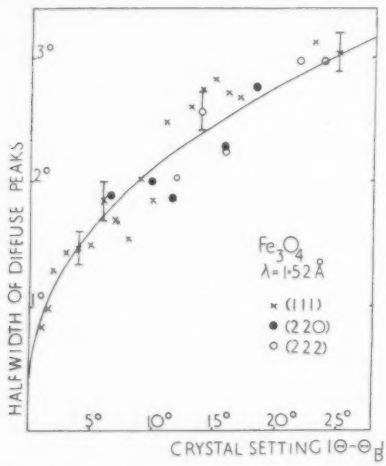

FIG. 4. The half-width of the diffuse peaks when corrected for instrumental broadening. The abscissa is for (111), the data on (220) and (222) being brought to the same scale by means of equation (7).

plotted in the figure represents the average of usually three experimental points. The errors indicated are the standard errors of the arithmetic mean. The experimental points in Fig. 4 definitely support the variation of peak width with missetting given by equation (9), and this indicates that the quadratic dispersion relation is correct. The experimental points extend to $\hbar\omega = 9\times10^{-3}$ eV on the dispersion curve. The theoretical curve indicated in the figure is calculated from equation (9), putting $\alpha = 80$. For refinement of this value, however, see below.

Fig. 5 shows a similar curve for the (440) reflection, which is of almost pure nuclear origin. The linear curve is in contrast to the parabola of Fig. 4 and confirms the behaviour predicted by equation (8).

From equations (10) and (11) we find that the vibrational component, which is mainly of magnetic origin, should be more than an order of magnitude smaller than the spin-wave component. It is therefore to be expected that an external field oriented along the scattering vector (i.e. $\boldsymbol{H}\|\boldsymbol{e}$) will

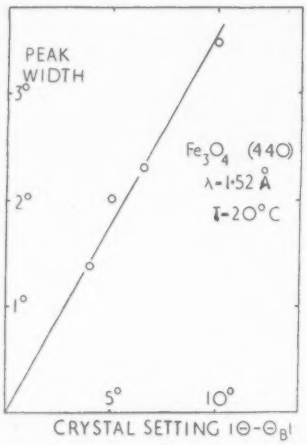

FIG. 5. The half-width of the diffuse peaks connected with the nuclear (440) reflection as a function of the crystal setting.

increase the intensity by 50 per cent. Fig. 6 shows, however, that the field has no effect on the diffuse peak at $\theta-\theta_B = 3°$, even though it reduces the elastic peak in the way expected. Additional data were at first taken at other temperatures and angles with a high slit to integrate the peak intensity, but with the same negative result. The reason these experiments showed no effect is explained by Fig. 7, which is taken with a narrow slit in the same way as Fig. 6, but at a greater missetting and higher

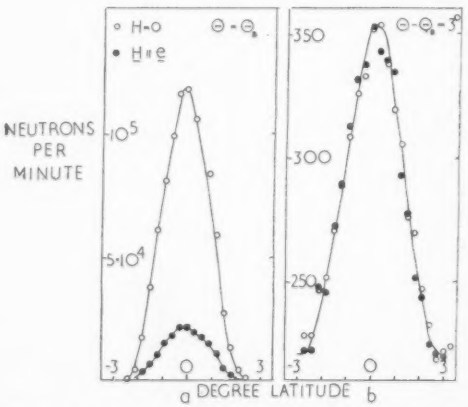

FIG. 6. The effect of magnetizing the crystal along the scattering vector. In (*a*) the elastic Bragg peak is seen to decrease violently. In (*b*) the diffuse peak at 3° misset of the crystal is seen to be unaffected by the same field.

temperature. We now see that the central part of the peak is clearly enhanced on applying the field; the slight change in the peak shape and the background make the changes in the integrated cross-section hard to observe, however, unless the background is measured very carefully. If the vibrational components are negligible, we should expect an increase of 50 per cent if the field is strong enough and has an ideal geometry so as to make $e\varkappa = 1$. By extrapolating the intensity of the Bragg peaks at $T > T_c$ down to room temperature and comparing the values with the residual elastic intensity when the field is applied at room temperature, we find that 90 per cent, of the magnetic intensity is effectively removed by the field. For pure spin-wave peaks we can therefore expect a maximum increase of 42·5 per cent when applying the same field. The intensity at any angle of observation in Fig. 7 is now easily broken down into the spin-wave and the magnetovibrational components. We then find that the magnetovibrational part is higher than estimated above (see Fig. 10).

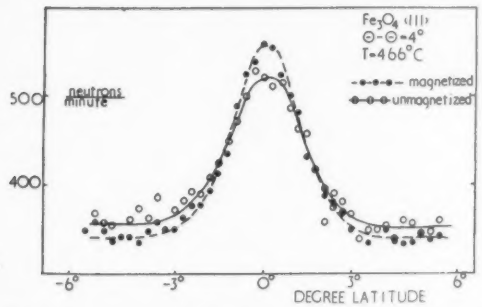

FIG. 7. A test of the field effect as in Fig. 6b, but now the missetting has been increased to 4° and the temperature to 466°C.

The lack of influence by an external field at small missettings and room temperature, as seen in Fig. 6b, must be due to an accidental cancellation of opposite effects. In the discussion of this question which follows, we quote some experimental results which are not shown in any of the present curves.

One can expect the following different components to contribute to the scattered intensity at settings close to the Bragg angle:

(*a*) spin wave (exchange-type),
(*b*) magnetovibrational (and a much weaker nuclear vibrational),
(*c*) elastic contaminant,
(*d*) spin-wave connected with dipole forces,
(*e*) some kind of fluctuations due to the spin disorder on the *B* sites.

If we label the corresponding intensities by the same letters, theory predicts (*a*) to follow the factor $[1+(e\varkappa)^2]$ and (*b*), (*c*), (*d*) to follow $[1-(e\varkappa)^2]$. BROCKHOUSE[25] has checked our observations at $\theta-\theta_B = 3°$ and found the same null effect. By analysing the energy of the scattered beam, he finds that there is a small but definite shift of the energy. He also adds a different mechanism which can make the field effect disappear. When the field is applied, the spin-wave energy is raised and thus the population factor will be lower. This could be an important mechanism for low-energy spin-waves. We have found that the cross-section for $|\theta-\theta_B| < 4°$ exceeds the theoretical spin-wave value by a large amount; there is also a pronounced asymmetry around the Bragg setting both in peak widths and intensities. This would seem to indicate that anisotropy forces affect the scattering for $|\theta-\theta_B| < 4°$, in which case the intensity and the peak width would also have to depend upon the direction of propagation of the spin-waves. To check this point, another crystal with the shape of a circular disc, the face being (111), was rotated around the [111] axis. It was then found that both peak width and intensity remained constant. In addition we have found that the intensity at these small missettings does not show the same temperature variation as at higher $|\theta-\theta_B|$ values. Instead it either remains constant or decreases with increasing temperature. This would then support (*c*), though it seems improbable that independent experiments should have the same elastic contamination. To find out whether (*e*) is effective, one would have to cool the crystal below the ordering temperature of 120°K for the *B* ions.

In iron, the magnetovibrational and spin-wave components are such that the magnetic-field effect nearly cancels out, yet the first demonstration of the effect was given by LOWDE[26] on iron. Simultaneously with our experiments, BROCKHOUSE[25] has also given a clear demonstration of the effect in Fe_3O_4.

As was apparent from Fig. 7, at higher temperatures the peak shape is better defined, and by applying a magnetic field the spin-wave peaks could be studied in isolation. The preliminary value of α given above was obtained by a straightforward application of equation (9), putting the half-width equal to the total semi-angle. A more accurate value of α is obtained in the following way: In the appendix of reference (26), LOWDE has calculated the theoretical shape of the spin-wave peaks for the experimental technique used here. For $|\theta-\theta_B| = 10°$, our peaks should have the shape shown by

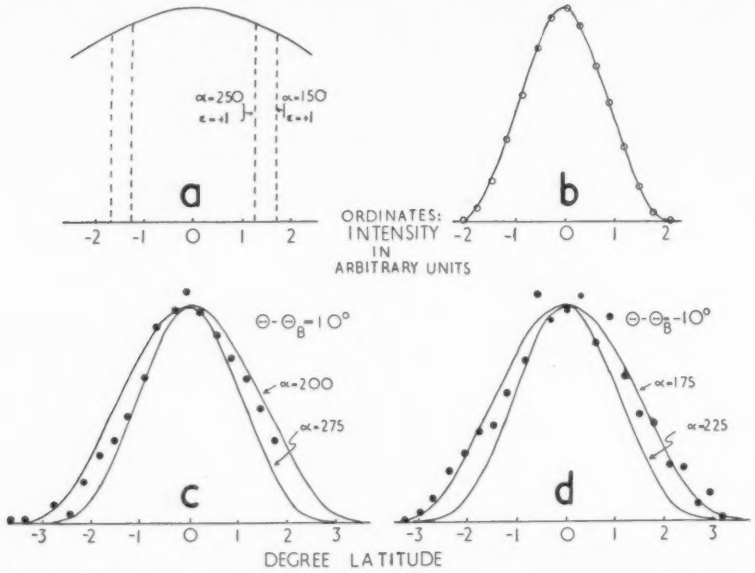

FIG. 8. Curve *a* is the theoretical shape of a spin-wave peak with the white-beam technique. The curve is drawn for (111) of Fe_3O_4 and $|\theta-\theta_B| = 10°$. The width is determined by α and the sign of $(\theta-\theta_B)$. Curve *b* is the instrumental function or the observed shape of a Bragg peak. The curves *c* and *d* are obtained by folding curves such as *a* and *b*. Experimental points are denoted in the figures.

curve *a* of Fig. 8, when observed with infinitely good resolution. The width of the curve is determined by α. Curve *b* shows our experimental function (the Bragg peak) and curves *c* and *d* are obtained by folding (convolution) of curves such as *a* and *b*. The folding was performed by using Beevers and Lipson strips. It is seen that each of the experimental curves determines α within surprisingly narrow limits. The asymmetry of the width around the Bragg setting is not quite verified, but the average value of $\alpha = 225$ is in excellent agreement with the value given by BROCKHOUSE.[1] This value is used in the calculation of the cross-section below and also gives $J_{AB} = 2\times10^{-3}$ eV. KOUVEL[27] has obtained the value $4{\cdot}5\times10^{-4}$ from specific-heat measurements.

The same method of analysis has been applied to the vibrational peaks of Fig. 5. It gives $c = 7{\cdot}7\times10^5$ cm sec^{-1}, which is higher than the value of $4{\cdot}9\times10^5$ cm sec^{-1} derived from a Debye temperature of 670°K. This temperature is derived from the specific-heat data[28] at half the Dulong–Petit value.

After correction for 15 per cent magneto-vibrational scattering, the room-temperature data gave the crosses on the cross-section curve of Fig.

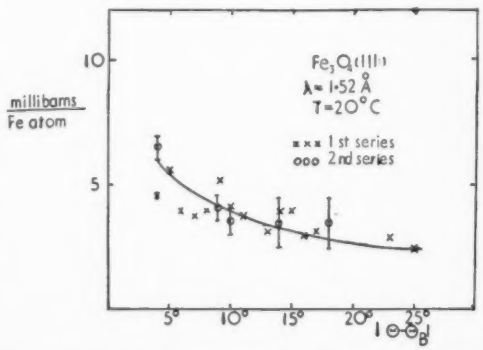

FIG. 9. Experimental points and theoretical curve for the total spin-wave cross-section at different crystal settings.

9. A few more accurate data are given by the solid circles, derived from curves such as those in Fig. 10. The errors indicated are mostly due to the

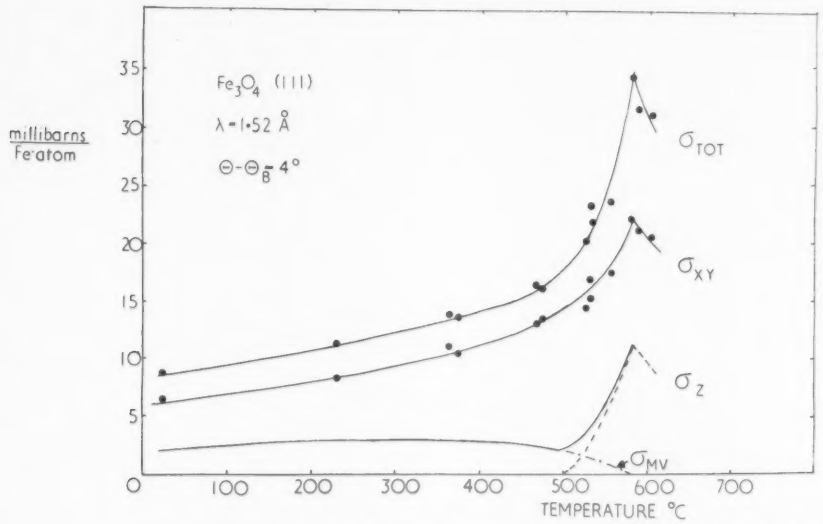

FIG. 10. Temperature variation of the total cross-section at $\theta - \theta_B = 4°$. The upper curve is obtained without applying an external field. The curve marked σ_{xy} is obtained by making $e\boldsymbol{\varkappa} = 1$; the linear part of the curve represents the spin-wave scattering. σ_z is critical scattering due to fluctuations in the z-components of the spins. σ_{MV} is magnetovibrational scattering which continues as the solid curve below 400°C. The cross-section scale is not strictly valid in the critical region.

uncertainty in reducing the data to an absolute scale.* The theoretical curve is calculated from the formulae (11), (14), and (16). The agreement is seen to be quite good, in contrast to the differential cross-section data of BROCKHOUSE, which are lower than the theoretical value by a factor of five[24] when using equation (16).

Optical modes in the spin-wave spectrum have been calculated by T. A. KAPLAN.[23] He finds that the energy of these modes is $\sim 10^{-2}$ eV, which means that they are only weakly excited at room temperature. Our room-temperature data of the intensity of the diffuse peaks from (222) (not included here) give good agreement with a calculation of the cross-section based on acoustic modes only, as was also the case for (111), thus supporting the theoretical predictions. We feel, however, that this point should be checked by using monochromatic neutrons, since in the Laue technique the problem of second-order reflections is more acute.

The temperature variation of the cross-section when broken down into its various components by means of an external field is shown in Figs. 10 and 11. The σ_{xy} data have been reduced to the case $(e\boldsymbol{\varkappa})^2 = \frac{1}{3}$. The σ_{xy} curve represents the spin-wave scattering and the critical scattering in the x- and y-components of the spins. The experimental points are given in each figure; the lower curve is obtained by subtracting the upper two. It has exactly the temperature variation predicted for magnetovibrational scattering, and the curve is extended to T_c by means of the theoretical formula. The width of these peaks corresponds to $c = 6{\cdot}6 \times 10^5$ cm sec^{-1}, thus being about 15 per cent lower than indicated by the (440) peaks. We feel, however, that the data are not good enough to indicate whether the magnetic electrons vibrate differently from the nuclei. The magnitude of σ_{MV} is higher than predicted and c would have to be as low as $2{\cdot}5 \times 10^5$ to give agreement. Comparing Figs. 10 and 11, we see that σ_{MV} is higher at 4° than at 10°, although according to equation (10) it should be constant with the angle of misset. The difference is greater than could be explained by any

* An error in the ordinate of the corresponding curve in JENER Report No. 53 (1957) has been corrected for.

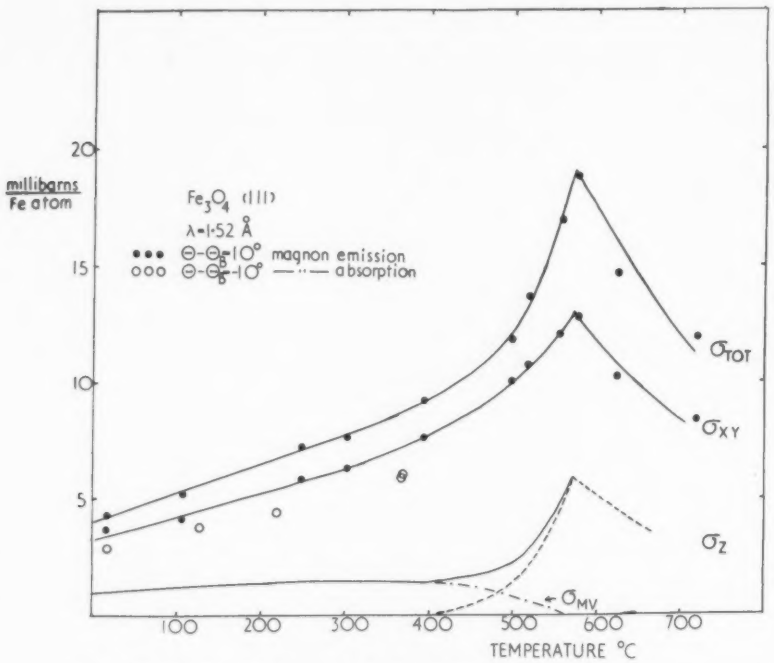

FIG. 11. As Fig. 10, but with $\theta-\theta_B = 10°$. The circular points represent spin-wave scattering for $\theta-\theta_B = -10°$.

elastic contaminant scattering allowed by the temperature variation and is probably connected with the anomalously strong diffuse components at lower missettings discussed above.

Up to $T \sim 400°C$ the temperature variation of σ_{SW} is well explained by formula (13) or (14). At higher temperatures the cross-sections start to increase sharply. This is due to the onset of the critical scattering, which will be discussed in a forthcoming paper. The energy changes corresponding to $\theta-\theta_B = 4°$ and $10°$ are 18·5 and 40°K, respectively, and the curves show that an eventual Fermi temperature would have to be much lower than these temperatures. σ_{SW} is high enough that $N(q) > 2S$, and the statistical behaviour observed therefore contradicts the calculations by FRANK and by MEYER quoted above and strongly supports the validity of equation (13). According to (11), the cross-section at $\theta-\theta_B = -10°$ should be $\sim$ 90 per cent of that at $\theta-\theta_B = 10°$, if equation (13) is valid. In Fig. 11 the open circles denote σ_{SW} for $\theta-\theta_B = -10°$ and the figure of 90 per cent is seen to be roughly correct. From the cross-section formulae given by MALEEV,[10] this ratio should be only 50 per cent; furthermore his prediction for the

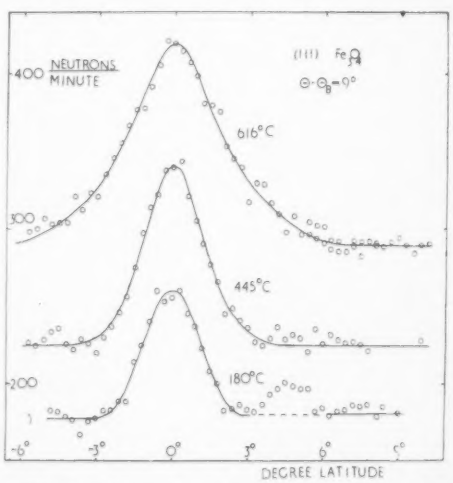

FIG. 12. Experimental peaks when the crystal is unmagnetized and $\theta-\theta_B = 9°$. The extra peak in the lower curve is due to elastic scattering from a misoriented crystallite and disappears at higher temperatures.

magnon emission cross-section mentioned in Section 2 is in marked disagreement with the present data.

The peaks at higher temperatures are very clear and well defined, as shown in Fig. 12. When corrected for instrumental broadening, the half-width

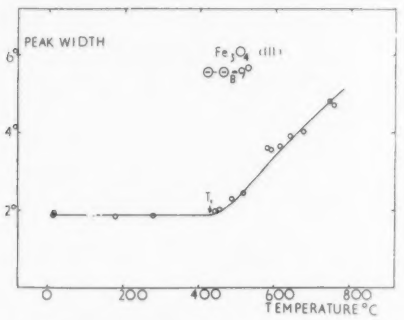

FIG. 13. Temperature variation of the peak width of curves such as those in Fig. 12. Instrumental broadening has been corrected for by assuming Gaussian profiles. The temperature T_1 gives the maximum temperature of the spin-wave approximation.

has the temperature variation shown in Fig. 13. At a well-defined temperature (T_1), the width increases suddenly and it is at this point that the critical scattering sets in. Observations at other missettings revealed the same behaviour, though with T_1 changing regularly with the misetting.

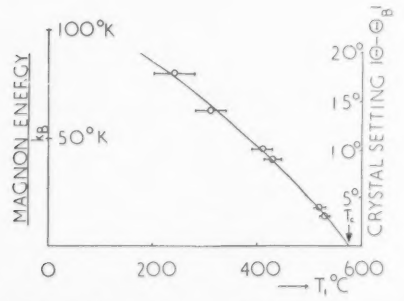

FIG. 14. Shows the temperature T_1 of the previous figure as a function of the angle of misset. The ordinate also gives the mean energy of the magnons which are active.

Fig. 14 shows the connection observed between T_1 and $\theta-\theta_B$. In addition to the angle of misset, we have shown the temperature corresponding to the energy of the magnons scattered at this angle. The curve shows the temperature range for the validity of the spin-wave approximation, as determined from neutron scattering.

5. CONCLUSION

From the experimental results presented here one can conclude that the magnetic inelastic scattering of neutrons from Fe_3O_4 is well described by spin-wave theory over a wide temperature range. The relevant formulae to use are those obtained by ELLIOTT and LOWDE,[5] supplemented by the structure factor calculated by T. A. KAPLAN.[24]

Earlier experiments[2] failed to show any changes in the inelastic intensities when an external field was applied. This led us to use a physical picture where the "wrong" spins are released from the influence of the spontaneous magnetization and form sub-domain regions of fluctuating spins. This picture has also been used by WILKINSON and SHULL[29] as a result of similar observations on iron. The picture is invalidated by the present experiments, which also show why our earlier experiments were unsuccessful. The response to a magnetic field is in agreement with the established idea that spin waves describe the fluctuation in the x- and y-components of the same spins that contribute to the spontaneous magnetization and give rise to the elastic reflection of neutrons.

The maximum temperature for the validity of the spin-wave approximation is defined surprisingly sharply by the temperature variation of the peak width. Above this temperature there are in addition fluctuations in the z-components. For $T > T_1$ the spin-wave theory is not able to describe the fluctuations in any of the three components; a closer analysis of the neutron scattering (the critical scattering) will be given in another publication. The spin-wave approximation breaks down when the waves start to interact. Our observation that T_1 is highest for low-energy magnons is in agreement with the finding by DYSON[11] that the interaction is weaker at longer wavelengths. Our data at $\theta-\theta_B = 4°$ show that the fluctuations of very low energies [$(E/k_B) \simeq 20°$K] have the spin-wave character up to $T_1 = 0{\cdot}9T_c$. The proportionality with temperature of the cross-section for these low-energy magnons demonstrates the validity of Bose–Einstein statistics.

In Section 4 we have mentioned that the magnetovibrational cross-section does not remain

constant with the crystal setting as it should. This discrepancy is most likely due to the presence of other diffuse components at the smallest missettings. All that one is able to say at this point from the present experiments is that the magnetic electrons do not vibrate radically differently from the nuclei.

The validity of the quadratic dispersion law for ferrites is clearly demonstrated by Fig. 4. When applying the formula for peak width directly to this curve, the exchange integral was seen to come out with a large systematic error. This does not alter the conclusion about the quadratic law, however, and the relevant value of J_{AB} is found by the procedure demonstrated in Fig. 8. The value we found must be correct, since it agrees with the more direct measurement by BROCKHOUSE.

Acknowledgements—The authors wish to thank Dr. J. A. GOEDKOOP for many stimulating discussions during the work. We are also indebted to Dr. A. W. MCREYNOLDS for co-operation at an early stage of the work and to Dr. T. A. KAPLAN and Dr. R. D. LOWDE for a useful correspondence.

REFERENCES

1. BROCKHOUSE B. N., *Phys. Rev.* **106,** 859 (1957).
2. MCREYNOLDS A. W. and RISTE T., *Phys. Rev.* **95,** 1161 (1954).
3. SEEGER R. J. and TELLER E., *Phys. Rev.* **62,** 37 (1942).
4. MOORHOUSE R. G., *Proc. Phys. Soc.* A**64,** 1097 (1951).
5. ELLIOTT R. J. and LOWDE R. D., *Proc. Roy. Soc.* A**230,** 46 (1955).
6. PEIERLS R. E., *Quantum Theory of Solids.* Oxford University Press (1955).
7. LOWDE R. D., *Proc. Roy. Soc.* A**221,** 206 (1954).
8. FRANK D., *Z. Phys.* **146,** 615 (1956).
9. MEYER K., *Z. Naturf.* **11a,** 865 (1956); **12a,** 797 (1957).
10. MALEEV C. V., *Zh. eksp. teor. fiz.* **33,** 1010 (1957).
11. DYSON F. J., *Phys. Rev.* **102,** 1217, 1230 (1956).
12. ELLIOTT R. J., LOWDE R. D. and MARSHALL W., *Proc. Phys. Soc.* A**63,** 939 (1956).
13. VAN HOVE L., *Phys. Rev.* **95,** 1374 (1954).
14. ELLIOTT R. J. and MARSHALL W., *Rev. Mod. Phys.* **30,** 75 (1958).
15. DE GENNES P. G. Private communication.
16. SHULL C. G., WOLLAN E. O. and KOEHLER W. C., *Phys. Rev.* **84,** 912 (1951).
17. NÉEL L., *Ann. Phys., Paris* **3,** 137 (1948).
18. KAPLAN H., *Phys. Rev.* **86,** 121 (1952).
19. KOUVEL J. S., *Tech. Rep. No.* 210, *Cruft Lab. Harvard Univ., Cambridge, Mass.* (1955).
20. KONDORSKII E. J., PAKHOMOV A. S. and SHIKLOSH T., *Soviet Phys. Doklady* **1,** 501 (1956).
21. VAN KRANENDONK J. and VAN VLECK J. H., *Rev. Mod. Phys.* **30,** 1 (1958).
22. VONSOVSKII S. V. and SEIDOV Y. M., *Izvest. Akad. Nauk. SSSR, Ser. fiz.* **18,** 319 (1954).
23. KAPLAN T. A., *Phys. Rev.* **109,** 782 (1958).
24. KAPLAN T. A., *Tech. Rep. No.* 1, Penn. State Univ., unpublished (Jan. 1958).
25. BROCKHOUSE B. N. To be published.
26. LOWDE R. D., *Proc. Roy. Soc.* A**235,** 305 (1956).
27. KOUVEL J. S., *Phys. Rev.* **102,** 1489 (1956).
28. *International Critical Tables* Vol. 5, p. 98. McGraw-Hill, New York (1927).
29. WILKINSON M. K. and SHULL C. G., *Phys. Rev.* **103,** 516 (1956).

J. Phys. Chem. Solids Pergamon Press 1959. Vol. 9. pp. 165–175. Printed in Great Britain.

ANALYSIS OF THE SEMICONDUCTING PROPERTIES OF COBALT FERRITE

G. H. JONKER

Philips Research Laboratories, N.V. Philips' Gloeilampenfabrieken, Eindhoven, Netherlands

(*Received* 13 *May* 1958; *revised* 12 *August* 1958)

VOL. 9 1959

Abstract—From measurements of resistivity, activation energy, and Seebeck effect, an energy-level scheme is derived by which the semi-conducting properties of $CoFe_2O_4$ can be described. These properties differ considerably from those of normal semiconductors, as the charge carriers are not free to move through the crystal lattice but jump from ion to ion.

1. INTRODUCTION

As a result of the increasing importance of the microwave properties of ferrites, it has proved necessary to improve the dielectric properties of these materials. It has been found that the value of the electrical resistivity is one of the main quality factors in this respect. In a number of papers VAN UITERT[1] has described a method for obtaining very high resistivities in spinel ferrites by the incorporation of small amounts of manganese or cobalt oxide and of copper ferrite. According to his explanation the presence of small amounts of ions with differing valency (Fe^{II}, Ni^{III}) which give rise to the semiconductivity, is suppressed by the different valency states of manganese or cobalt:

$$Fe^{II} + Mn^{III} \rightarrow Fe^{III} + Mn^{II}$$

$$Ni^{III} + Mn^{II} \rightarrow Ni^{II} + Mn^{III}.$$

Copper ferrite, on the other hand, acts as a flux, so that dense products can be obtained at fairly low temperatures.

From a theoretical point of view, it is an astonishing result that the resistivity of a pure compound should be increased by the addition of impurities. For this reason we started a more general investigation of a number of two- and three-component oxide systems containing phases with a spinel structure in order to study the valency equilibria of the ions of the iron group of transition elements. In general one would expect ferrites with a simple composition $MeFe_2O_4$, where Me represents a small divalent ion, to show a high resistivity which can be lowered by the formation of solid solutions with excess iron oxide in the form of Fe_3O_4 or with excess Me oxide in the form of Me_3O_4.

However, we encountered this simple behaviour only in the case of cobalt ferrite, and for this reason we have studied first the system iron oxide–cobalt oxide more extensively. Although the present paper deals only with the results of this investigation, it is interesting to mention here that the maximum resistivity found in this system near the composition $CoFe_2O_4$ cannot be increased by addition of manganese oxide.

We have investigated the semiconducting properties of a series of mixed crystals $Co_{3-x}Fe_xO_4$ near the composition $CoFe_2O_4$. For values of $x > 2$ such mixed crystals can be considered as consisting of $(3-x)$ molecules $Co^{II}Fe_2^{III}O_4$ and $(x-2)$ molecules $Fe^{II}Fe_2^{III}O_4$; thus $x-2$ represents the Fe^{II} content per molecule. For values of $x < 2$, the compositions can be split into $(x-1)$ molecules $Co^{II}Fe_2^{III}O_4$ and $(2-x)$ molecules $Co^{II}Co^{III}Fe^{III}O_4$ and now $(2-x)$ represents the Co^{III} content per molecule.

In this way we can introduce electrons (Fe^{II}) or electron holes (Co^{III}) and obtain *n*- or *p*-type semiconductivity. This gives double the amount of information about the energy-level picture as compared with the investigations of MORIN[2] on the properties of $\alpha-Fe_2O_3$ and NiO and the investigations of HEIKES[3] on the influence of Li_2O on the properties of divalent metal oxides. By an analysis

of the resistivities, the activation energies, and the Seebeck effect of the mixed-crystal series, we can describe the semiconducting properties by a fairly simple model.

2. EXPERIMENTAL

A number of samples with compositions between $Co_{0.90}Fe_{2.10}O_4$ and $Co_{1.30}Fe_{1.70}O_4$ were prepared from Fe_2O_3 and $CoCO_3$. The mixtures of these materials were ball-milled, fired first at 1000°C in air, milled again, and fired for a second time in the form of rods 5 cm long at various temperatures between 1300 and 1400°C in air or in pure oxygen. Two similar series of rods were prepared containing 1 per cent MnO and 5 per cent CuO, respectively. A number of samples were analyzed for the Co^{III} or Fe^{II} content. As shown in Table 1, the results of the analysis were in remarkably good agreement with the stoichiometric ratio of metal to oxygen ions.

Table 1. *Chemical analysis of samples* $Co_{3-x}Fe_xO_4$. *Positive values of active oxygen represent the oxidation capacity of the samples and thus the* Co^{III} *content, which must be equal to* $2-x$; *negative values represent the reduction capacity and thus the* Fe^{II} *content, which must be equal to* $x-2$ (*see text*)

Composition $Co_{3-x}Fe_xO_4$	Active oxygen in eq./mol.	
	Calculated	Experimental
$Co_{1.050}Fe_{1.950}O_4$	0·050	0·048
$Co_{1.020}Fe_{1.980}O_4$	0·020	0·022
$Co_{1.008}Fe_{1.992}O_4$	0·008	0·012
$Co_{1.002}Fe_{1.998}O_4$	0·002	0·003
$Co_{0.990}Fe_{2.010}O_4$	−0·010	−0·012
$Co_{0.930}Fe_{2.070}O_4$	−0·070	−0·073

This means that the valencies of the metal ions in the present system are determined by the tendency to form an ideal spinel structure with a ratio of metal to oxygen ions of 3 : 4, and that probably the numbers of lattice vacancies are small enough to be neglected in the theoretical consideration. This is not the case with other binary ferrite systems, e.g. $(Ni, Fe)_3O_4$ and $(Mn, Fe)_3O_4$, where it is difficult to obtain the stoichiometric metal : oxygen ratios of 3 : 4.

From a microscopic examination of polished surfaces of the rods, we found that in a series fired at 1350°C in oxygen single-phase spinel compounds were formed in samples with compositions between $Co_{0.90}Fe_{2.10}O_4$ and $Co_{1.10}Fe_{1.90}O_4$. These results are in fairly good agreement with those of SMILTENS.[4] Only the rods having these compositions were used for the physical investigations. The surface layer of the rods was ground off and the resulting rods, about 45 mm long and about 3 mm thick, were used for the physical measurements. These dimensions were chosen in order to minimize the influence of electrode resistances. According to VAN UITERT,[1] indium–mercury and graphite form the best electrodes on ferrites. For our measurements we simply coated the ends of the rods with graphite by rubbing with a pencil and then pressed metal contacts against the ends. We applied a high d.c. voltage to the electrodes (up to 1800 V in the case of the high resistivities), measured the current, and calculated the values of the resistivity. Some of the measurements were compared with the results obtained by a four-electrode method and others with measurements on rods of different lengths. In general the differences were negligible. The effect of temperature on the resistivity was measured by immersing the rods in an oil bath and heating to temperatures between room temperature and 160°C. From the plots of $\log \rho$ against $1/T$, the activation energies q were calculated by the formula $\rho = \rho_0 e^{q/kT}$.

For a better understanding of the conduction mechanism, the Seebeck effect was measured. One end of the rods was immersed in an oilbath at 70–100°C and the other end kept in air at room temperature. The emf between copper wires pressed against the electrodes was measured with the aid of a Philips p_H measuring apparatus in which the emf is transformed into an a.c. current by a vibrating plate condenser. With this apparatus rods having a resistance as high as $10^{11}\Omega$ could be measured. For the sign of the Seebeck effect, we have used the sign of the cold electrode, as the charge carriers diffuse from the hot to the cold part of the rods.

Fig. 1 shows the room-temperature values of the d.c. resistivities of a series of $(Co, Fe)_3O_4$ mixed crystals fired at 1350°C in oxygen. Near the composition $CoFe_2O_4$ a relatively high and sharp peak appears in the resistivity. The series containing MnO or CuO gave similar results.

Most of the compositions showed a simple exponential temperature-dependence of the resistivity. The activation energies calculated from

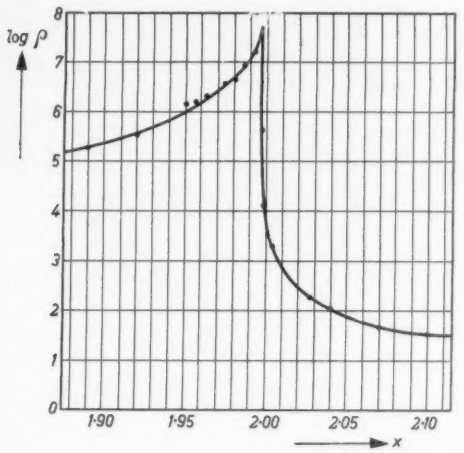

FIG. 1. Room-temperature values of the log resistivity for a series of mixed crystals of $Co_{3-z}Fe_zO_4$ near the composition $CoFe_2O_4$.

these measurements are given in Fig. 2. For samples with compositions near $CoFe_2O_4$, the temperature-dependence was more complex, and for them values of the activation energy at a higher

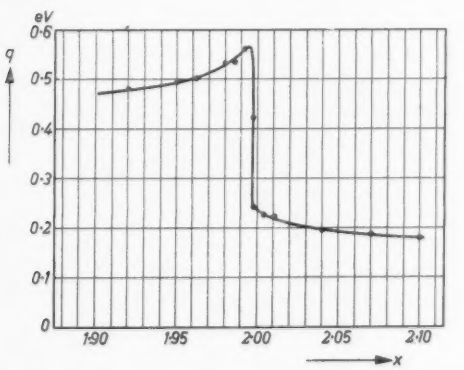

FIG. 2. Activation energies of the conductivity of mixed crystals $Co_{3-z}Fe_zO_4$.

temperature (150°C) are plotted. This quantity also is hardly influenced by manganese oxide or copper oxide.

In Fig. 3 the results of Seebeck-effect measurements are given. As might be expected, the sign of the Seebeck effect is positive for samples with excess cobalt and negative for samples with excess iron, a sharp transition being found near the composition $CoFe_2O_4$. From the sharpness of this transition and also from the sharpness of the peak

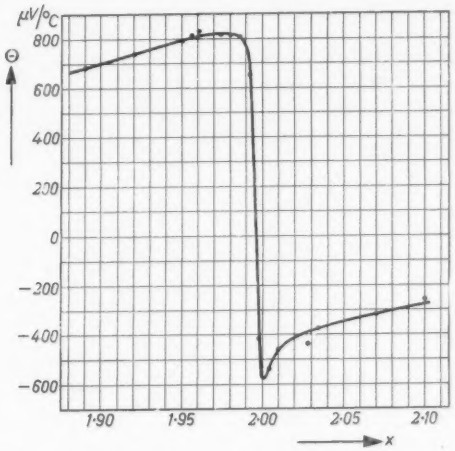

FIG. 3. Thermoelectric or Seebeck effect in mixed crystals $Co_{3-z}Fe_zO_4$.

of the resistivity, it can be concluded that the samples were fairly homogeneous in composition, at least better than 0·2 per cent. In the positive part of the curve it is easy to estimate the maximum value of the Seebeck effect. On the negative side, however this is difficult as the maximum is very sharp.

In general the values of the Seebeck effect are independent of temperature between room temperature and 160°C. Only samples with compositions near $CoFe_2O_4$ show a strong temperature-dependence. For two of these latter samples the Seebeck effect has been measured up to 800°C. The results are shown in Fig. 4.

Generally speaking, the results of all these measurements are qualitatively in agreement with the expected transition from *p*-type to *n*-type conductivity. There is, however, a very peculiar quantitative difference in the values of the physical constants in these two regions.

3. THEORETICAL

At first sight the $(Co, Fe)_3O_4$ mixed crystals show

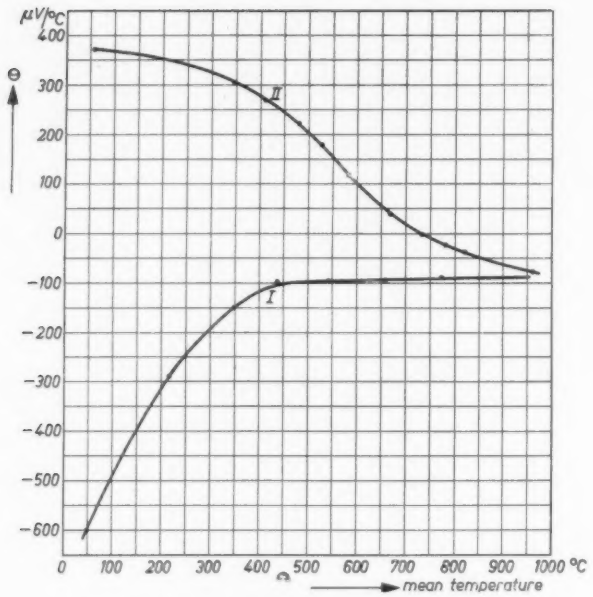

FIG. 4. Variation of the Seebeck effect with temperature for two samples: (I) $CoFe_2O_4$, (II) $Co_{1.01}Fe_{1.99}O_4$.

normal semiconductor behaviour: *n*- and *p*-type conductivity can be related to the presence of Fe^{II} and Co^{III} ions respectively. In this respect they belong to the group of controlled-valency semiconductors such as have been described by VERWEY *et al.*[5] This group is characterized by the presence of ions of a given element in different valency states on equivalent sites in the crystal lattice. Whereas, however, these combinations of valencies are usually obtained by the introduction into the crystal lattice of foreign ions with a different valency, there is here the possibility of obtaining this result by preparing mixed crystals between $Co^{II}Fe^{III}O_4$ and $Fe^{II}Fe_2^{III}O_4$ or $Co^{II}Co^{III}Fe^{III}O_4$, so that no foreign ions are present.

The mixed crystals studied here crystallize in the spinel structure, where two different groups of lattice sites are available for metal ions. The simple compound $CoFe_2O_4$ has the so-called inverse spinel structure, with one-half of the iron ions on tetrahedral sites and the rest, together with the cobalt ions, on octahedral sites. As Fe^{II} and Co^{III} also occupy octahedral sites preferentially, only ions on these sites are of interest in the description of the semiconducting properties. In the restricted group of mixed crystals described here, the tetrahedral sites contain only Fe^{III} ions. From the cell constant of $CoFe_2O_4$, $a = 8{\cdot}39$ Å, it follows that the number of both cobalt and iron ions on octahedral sites is $N = 1{\cdot}35 \times 10^{22}\text{cm}^{-3}$.

It is interesting to note that in compounds of elements of the transition group the possibility exists of changing the valency of a considerable fraction of the metal ions and in some cases even of doing this completely, e.g. in the mixed-crystal series $LaMn^{III}O_3$, $CaMn^{IV}O_3$, where the whole range from 100 per cent Mn^{III} to 100 per cent Mn^{IV} has been prepared.[6] In the case of $CoFe_2O_4$, we have restricted ourselves to changing the valency of a maximum of 10 per cent of the cobalt or iron ions.

If we proceed now to a closer examination of the semiconductor properties, we find a number of peculiarities. Assuming the number of electrons contributing to the conductivity to be equal to the number of Fe^{II} ions, and the number of electron holes to be equal to the number of Co^{III} ions, we calculate from the resistivity data extremely low

values of the mobilities, $\mu_1 \approx 10^{-4}$cm^2/Vsec for electrons and $\mu_2 \approx 10^{-8}$ cm^2/Vsec for holes. Further, even for samples with a large concentration of Fe^{II} or Co^{III} ions, we find a fairly strong exponential dependence of the resistivity on temperature. From the ordinary band theory of conduction one would expect metallic behaviour for such high concentrations of carriers, i.e. a high mobility with only a slight temperature-dependence. Such behaviour is indeed found in some cases e.g. for the ferromagnetic part of the mixed-crystal series $LaMnO_3$–$SrMnO_3$ and $LaCoO_3$–$SrCoO_3$.[6,7] In the present compounds the experimental findings are, as already mentioned, quite different, and we believe therefore that, just as in the case of NiO and Fe_2O_3, the ordinary transport theory based on the simple band picture does not apply. For the equilibrium lattice there is little overlap between the wave functions of ions on adjacent octahedral sites, with the result that the electrons or holes are not free to move through the crystal but are fixed at the metal ions. In the presence of lattice vibrations, however, the ions occasionally come close enough together for transfer to occur with a high degree of probability. Thus the conduction is induced only by the lattice vibrations, and in consequence the carrier mobilities show a temperature-dependence characterized by an activation energy. For such a process of jumping electrons and holes, the mobilities μ are given by:

$$\mu_1 = \frac{ed^2\nu_1 e^{-q_1/kT}}{kT} \qquad (1a)$$

$$\mu_2 = \frac{ed^2\nu_2 e^{-q_2/kT}}{kT}. \qquad (2a)$$

Here the indices 1 and 2 relate to electrons and holes respectively; d represents the jump length for which we will take simply the distance between neighbour octahedral sites: $d = \frac{1}{4}a\sqrt{2} = 3{\cdot}0$ Å; ν_1 and ν_2 are the lattice frequencies active in the jumping process; and q_1 and q_2 are the activation energies involved in the required lattice deformations.

In the case of sufficiently small mobility the localization of the electrons may be increased by additional influences, such as the self-trapping effect of LANDAU,[8] which consists of polarization of the crystal lattice around the charged particles. There may also be an effect of an unknown nature from the magnetic interaction between the metal ions. An indication of this is the fact that particularly antiferromagnetic and ferrimagnetic oxide compounds of the transition elements show properties similar to those described in this paper (JONKER,[9] HEIKES[10]). These considerations lead to a picture (Fig. 5) of the localized levels belonging to the metal ions such as has been used by MORIN.[2] Following the usual convention, the energy levels are denoted by symbols representing the valency states of the metal ions in the cases where these levels are occupied (Fe^{II} and Co^{II}). The energies needed to remove electrons from these levels are determined by the third ionization

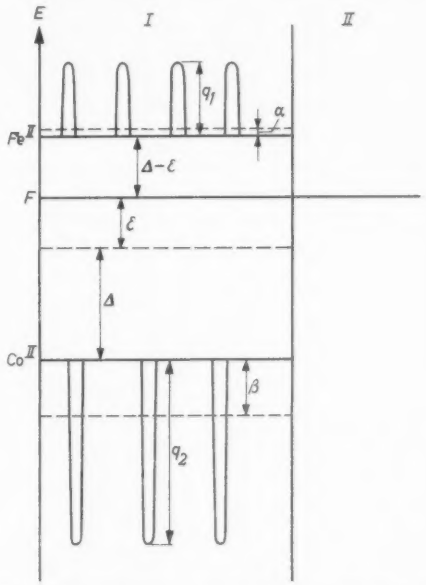

FIG. 5. (I) Energy-level scheme for $Co_{3-x}Fe_xO_4$. For pure $CoFe_2O_4$ at low temperature the Fe^{II} level is empty and only Fe^{III} ions are present, whereas the Co^{II} level is filled and only Co^{II} ions are present. F represents the Fermi level for a special case where excess electrons are introduced. q_1 and q_2 are the activation energies needed for jumps of electrons or electron holes. The distance between the Fe^{II} and Co^{II} level is 2Δ. α and β represent extra contributions to the transport levels of electrons and holes respectively.

(II) A metal in contact with the semiconductor I shows the same Fermi level which is here also the transport level of the electrons.

potentials. In the simplest compound of our series, $CoFe_2O_4$, we may expect that at 0°K all cobalt ions are in the divalent state and all iron ions in the trivalent state, in accordance with the difference in their third ionization potentials, which are, according to the list given by FINKELNBURG and HUMBACH,[11] 33·49 and 30·64 eV, respectively. So in a picture of free ions we would expect a fully occupied Co^{II} level at a distance 2·85 eV below a completely empty Fe^{II} level, all iron ions being Fe^{III}. In a crystal lattice, however, the influence of the crystal field and covalent bonds may cause a considerable change in the distance between the ionic levels.

In Fig. 5 the gap width is called 2Δ and the position of the Fermi level is at a height ϵ above the middle of the forbidden zone. The activation energies needed for the electron jumps are also shown. Strictly speaking these activation energies belong not to the energy picture of the electrons, but to that of the crystal lattice around the sites of the electrons. Further it introduces a simplification to place all the localized levels on one line. The Co^{II} and Fe^{III} ions are randomly distributed, and therefore there will be a certain spread in the individual ionic levels.

Quite a different approach would be to consider the metal ions as traps for electrons and holes and to introduce other, normal, bands, e.g. those belonging to oxygen ions, containing a small part of the charge carriers with normal mobilities. This picture has also been used by MORIN. In this case the activation energies q appear as the distances between the metal-ion levels and the oxygen bands and determine the temperature effect on the numbers of electrons and holes contributing to the conductivity.

We shall attempt, however, to use the first simple picture for an analysis of the semiconducting properties shown by the underlying series of samples and shall discuss later the inadequacy of the second picture.

(a) *Analysis of the conductivity*

The general expression for the conductivity is

$$\sigma = n_1 e\mu_1 + n_2 e\mu_2 \tag{2}$$

n_1 and n_2 representing the numbers of electrons and holes, which are taken as equal to the numbers of Fe^{II} and Co^{III} ions per cm³. For small values of n_1 and n_2 we can apply the Boltzmann expressions:

$$n_1 = Ne^{-(\Delta-\epsilon)/kT} \tag{3a}$$

$$n_2 = Ne^{-(\Delta+\epsilon)/kT}. \tag{3b}$$

In these formulae N is equal to the total number of iron or cobalt ions occupying octahedral sites, which can be taken as constant in our restricted series of mixed crystals and equal to $1{\cdot}35\times10^{22}$ cm^{-3}. The difference between n_1 and n_2 is given by the chemical composition of each sample and is thus independent of temperature. Further:

$$n_1 n_2 = N^2 e^{-2\Delta/kT} \tag{4}$$

and

$$n_1/n_2 = e^{2\epsilon/kT}. \tag{5}$$

From these relations it can be seen that in compositions with a Fe^{II} or Co^{III} content which is appreciably larger than $Ne^{-\Delta/kT}$, the main contribution to the conductivity is made by only one term of expression (2) and that the temperature has then only a negligible influence on the value of the n appearing in this single term. The activation energy found from plots of log ρ versus $1/T$ is in such cases the activation energy of the mobility μ_1 or μ_2. Only in the neighbourhood of the composition with intrinsic conductivity also are the changes of n_1 and n_2 with temperature of interest. Thus the flat parts of the q–c curve (Fig. 2) give at once for these compositions with excess iron or cobalt the activation energies q_1 and q_2 of the mobilities. The q values decrease slowly with increasing excess concentrations, which must correspond with slowly increasing mobilities.

A plot of log ρ against concentration of charge carriers (Fig. 1) such as is generally used leads to the false impression that the first amounts of charge carriers have a much greater influence on the semiconducting properties than further additions. On the other hand if we use a σ–c plot (Fig. 6) in accordance with formula (1), we see that the conductivity increases in both directions more than proportionally with increasing excess concentration. This means that the mobilities do in fact increase.

For compositions containing excess iron we find μ_1 values increasing from 0·7 to $1{\cdot}3\times10^{-4}$ cm²/Vsec. This is in accordance with the calculated variation of the mobility if, in formula (1a), we use

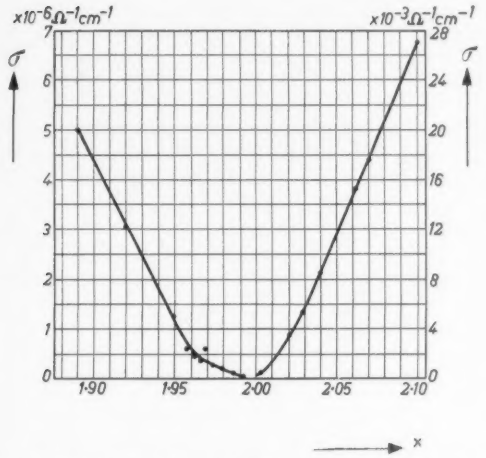

FIG. 6. Values of the conductivity calculated from the measurements given in Fig. 1. For the hole conductivity (excess cobalt) the left ordinate has to be used; for electron conductivity (excess iron) the right ordinate.

the experimental values of q_1, which decrease from 0·205 to 0·175 eV. For compositions with excess cobalt, values for the hole mobility μ_2 are found which increase from 0·6 to $2{\cdot}1\times10^{-8}$ cm²/Vsec, in accordance with the q_2 values, which decrease from 0·51 to 0·475 eV.

Using these μ and q values in formulae (1), we obtain the frequencies $\nu_1 = 6{\cdot}5\times10^{12}$ sec^{-1} and $\nu_2 = 1{\cdot}0\times10^{14}$ sec^{-1}. As these values are very sensitive to the values of q, we can say that the correspondence with the expected value of 10^{13} is reasonably good. In his study on MeO–Li_2O solid solutions (Me = Mn, Fe, Co, Ni), HEIKES[3] found frequency values between 10^{11} and 10^{13}.

The ratio of the electron to hole mobility which is of importance in further calculations is, for comparable concentrations of electrons and holes, roughly 10^4 at room temperature.

From an analysis of equation (2), we find that the extreme value of σ appears at $n_1\mu_1 = n_2\mu_2$ or

$$\epsilon = \frac{-kT}{2}\ln\frac{\mu_1}{\mu_2}.$$

The minimum value of σ is

$$\sigma_{\min} = 2Ne\sqrt{\mu_1\mu_2}e^{-\Delta/kT}. \qquad (6)$$

For a value of $\sigma_{\min} = 10^{-7\cdot6}$ and with the values of μ for low charge-carrier concentrations, this leads to $\Delta/kT = 12$ at room temperature. As at room temperature $kT \sim 0{\cdot}025$ eV, we find by this method that 2Δ has a value of 0·60 eV.

Another result is that, because of the large difference in mobilities, the maximum resistivity is found not at the simple composition $CoFe_2O_4$, but at a composition having a slight excess of cobalt.

(b) *Analysis of the activation energies*

One might expect that the activation-energy maximum would also give some information about the energy-level picture. The activation energy is defined as:

$$q = -k\frac{d\ln\sigma}{d(1/T)}. \qquad (7)$$

Combination with (2), (3a) and (3b) leads to

$$q = Aq_1 + Bq_2 + 2C\Delta, \qquad (8)$$

with

$$A = \frac{n_1\mu_1}{n_1\mu_1 + n_2\mu_2},$$

$$B = \frac{n_2\mu_2}{n_1\mu_1 + n_2\mu_2},$$

and

$$C = \frac{n_1n_2(\mu_1+\mu_2)}{(n_1\mu_1+n_2\mu_2)(n_1+n_2)}.$$

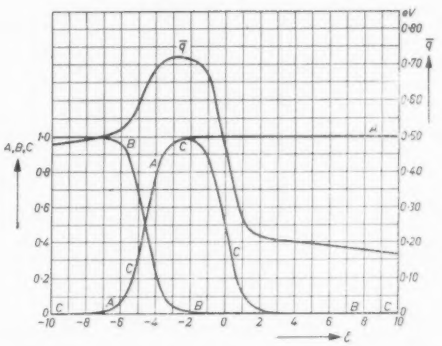

FIG. 7. (a) Values of A, B, and C from equation (8) $q = Aq_1 + Bq_2 + 2C\Delta$, calculated as a function of ε. (b) Values of the activation energy calculated with the corresponding values of A, B, and C.

The easiest way to study this result for room temperature is by calculating A, B, and C as functions of ϵ and using for μ_1/μ_2 a constant ratio of 10^4. The results can subsequently be expressed in concentrations of excess iron and cobalt.

The results are given in Figs. 7 and 8. It is seen that in the case where $\mu_1 \gg \mu_2$ the maximum value of the activation energy is $q_{max} = q_1 + 2\Delta$, which is quite different from the case where the mobilities

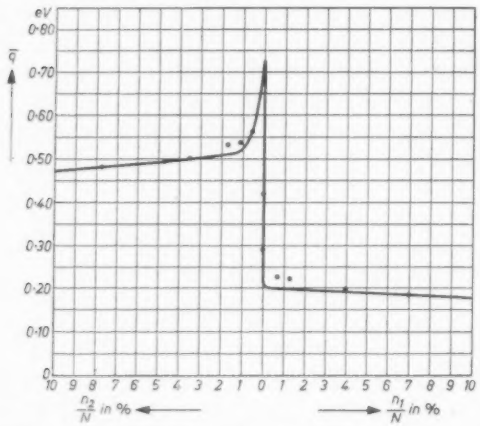

FIG. 8. Values of the activation energy q from Fig. 7 now as a function of the excess concentrations of cobalt and iron on the octahedral sites which correspond roughly with the ratios n_2/N and n_1/N respectively.
... experimental values.

are equal ($q_{max} = q + \Delta$). Unfortunately the theoretical q–c curve has such a sharp peak that it is impossible to prepare samples sufficiently homogeneous to enable this maximum value to be found experimentally. The experimental maximum is much lower and has no special significance. The general form of the theoretical activation-energy curve resembles the experimental one.

(c) *Analysis of the thermoelectric effect*

The Seebeck effect θ is related to the Peltier effect π by the following thermodynamic relation:

$$\pi = \theta T.$$

In Fig. 5 a contact between a semiconductor I and a metal II is represented. The energy levels of the electrons are drawn for both materials. For the semiconductor an example with excess electrons is chosen. For the metal only the Fermi level is given, and in a state of equilibrium this is the same as that of the semiconductor. If now an electric current passes through the contact, we see that this current is transported in the semiconductor by electrons of the Fe^{II} level, but in the metal by electrons near the Fermi level. The energy difference of the electrons appears as a heat effect in the contact. A heat effect of opposite sign appears in the case of a p-type semiconductor in contact with a metal.

In normal semiconductors an additional effect occurs, caused by the thermal distribution of the electrons and holes on the energy levels of the empty and full band. In our case a further effect may also occur, owing to the fact that each electron jump may be accompanied by a transport of energy in excess of the energy indicated by the electron levels. Although the value of the frequency ν in equation (2) confirms the idea that lattice vibrations are indeed involved in the jumping process, it is difficult to predict the contribution of the activation energies q to the transport of energy in the semiconductor and thus to the Peltier effect. Even the sign of this additional effect cannot be predicted, as the lattice activation accompanying the jumps may occur around either the emitting or the receiving ion.

If we assume that parts α and β of the activation energies of electrons and holes respectively are transported, the Peltier effect is described by

$$\pi = \frac{-n_1\mu_1(\Delta - \epsilon + \alpha) + n_2\mu_2(\Delta + \epsilon + \beta)}{n_1 e\mu_1 + n_2 e\mu_2}. \qquad (9)$$

In the case where practically only one type of charge carrier is present, this reduces to

$$e\pi = -\Delta + \epsilon - \alpha \text{ or } e\pi = \Delta + \epsilon + \beta.$$

If we combine these expressions with equations (3a) and (3b), we find the concentration-dependence of the Peltier and Seebeck effects:

$$e\pi = e\theta T = -\alpha - kT \ln \frac{N}{n_1} \qquad (10a)$$

for electrons and

$$e\pi = e\theta T = \beta + kT \ln \frac{N}{n_2} \qquad (10b)$$

for holes.

An analysis of the experimental values of the Seebeck effect for samples with excess iron, where n_1 is practically equal to the Fe^{II} concentration, and the use of a value of $N = 1{\cdot}35 \times 10^{22}$ leads to a value of $\alpha = 0{\cdot}025$ eV at room temperature. As further, the Seebeck effect for these samples is found to be independent of temperature between room temperature and 160°C, it is better to say that $\alpha = 1kT$. The same analysis for samples containing larger excess amounts of cobalt leads to $\beta = 0{\cdot}15$ eV at room temperature, or in general $\beta = 6kT$.

Thus the result is that α is negligible in comparison with q_1 and β is only a fraction of q_2.

At this point of our analysis it is easy to show that the alternative picture containing normal oxygen bands at a distance q_1 above and q_2 below the Fe^{II} and Co^{II} levels respectively is excluded by this last result. The small amount of electrons or holes present in these bands will have practically no influence on the height of the Fermi level. Thus, at a certain minimum distance from the intrinsic state, the values of the Peltier effect would be

$$e\pi_- = -q_1 - kT \ln \frac{N}{n_1}$$

and

$$e\pi_+ = q_2 + kT \ln \frac{N}{n_2},$$

where n_1 and n_2 again represent the numbers of Fe^{II} and Co^{III} ions. The fact that the experimental values are much lower makes this picture useless.

A refinement of the values of the various energies mentioned up till now can be obtained by a further analysis of the Seebeck effect in the region of mixed electron and hole conduction. By differentiating equation (9) with respect to ϵ, expressions can be derived for the extreme values and for the compositions at which these occur.

The negative maximum is determined by

$$e\pi_1 = e\theta_1 T = -\Delta - \alpha + \frac{kT}{2} \times$$

$$\times \left(1 + \ln \frac{4\Delta + 2\alpha + 2\beta - 2kT}{kT} + \ln \frac{\mu_1}{\mu_2}\right) \quad (11)$$

and the positive maximum by

$$e\pi_2 = e\theta_2 T = \Delta + \beta - \frac{kT}{2} \times$$

$$\times \left(1 + \ln \frac{4\Delta + 2\alpha + 2\beta - 2kT}{kT} + \ln \frac{\mu_1}{\mu_2}\right). \quad (12)$$

In our case only the positive maximum can be determined with certainty and this is 0·25 eV. Substituting in equation (12) the preliminary values of Δ, α, and β in the logarithmic term and the value 10^4 for μ_1/μ_2, we find:

$$\Delta + \beta = 0{\cdot}43 \text{ eV} \quad \text{or} \quad 2\Delta = 0{\cdot}56 \text{ eV}.$$

From the location of this maximum at 2 per cent excess cobalt, a value of Δ can be found, since the location of the maximum is given by:

$$kT \ln \left(\frac{n_2}{N}\right)_{\max} = -\Delta + \frac{kT}{2} \times$$

$$\times \left(\ln \frac{4\Delta + 2\alpha + 2\beta - 2kT}{kT} + \ln \frac{\mu_1}{\mu_2}\right). \quad (15)$$

Using again the preliminary values of Δ, α, and β in the logarithmic term and 10^4 for μ_1/μ_2, we find that $2\Delta = 0{\cdot}53$ eV.

4. DISCUSSION

In Table 2 we have chosen a combination of values by which the semiconducting properties at room temperature of the mixed crystals $Co_{3-x}Fe_xO_4$ can be described reasonably well.

Table 2. Values of the various constants needed to describe the semiconducting properties of $Co_{3-x}Fe_xO_4$.

2Δ	$= 0{\cdot}55$ eV
α	$= 0{\cdot}025$ eV $= 1kT$
β	$= 0{\cdot}15$ eV $= 6kT$
q_1	$= 0{\cdot}205 - 0{\cdot}175$ eV
q_2	$= 0{\cdot}51 - 0{\cdot}475$ eV
μ_1	$= 0{\cdot}7 - 1{\cdot}3 \times 10^{-4}$ cm²/Vsec
μ_2	$= 0{\cdot}6 - 2{\cdot}1 \times 10^{-8}$ cm²/Vsec
ν_1	$= 6{\cdot}5 \times 10^{12}$ sec^{-1}
ν_2	$= 1{\cdot}0 \times 10^{14}$ sec^{-1}
μ_1/μ_2	$= 10^4$

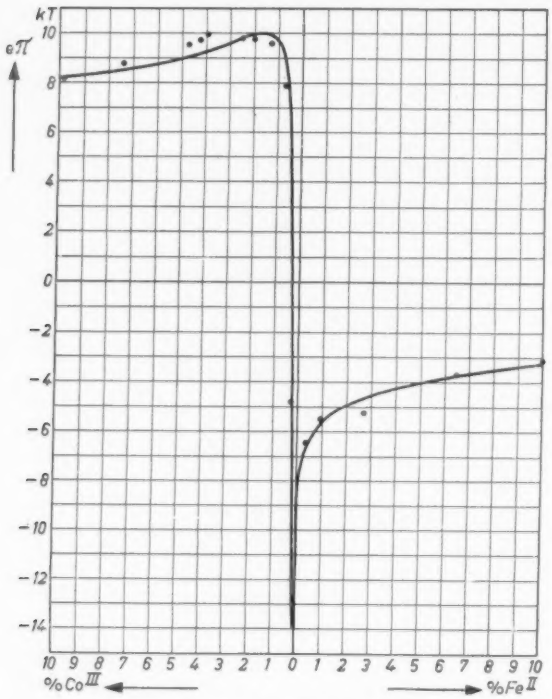

FIG. 9. Values of $e\pi = e\theta T$ calculated with the values of Table 2 as a function of excess concentration of cobalt and iron.
... experimental values.

With these values the Seebeck effect for the whole series of samples has been calculated. As appears from Fig. 9, the line follows the experimental values very closely, only the extreme value in the *n*-region being much larger than was expected. This value is not found experimentally, again probably owing to the inhomogeneity of the samples.

At elevated temperatures the intrinsic dissociation becomes important, so that all samples change their conducting properties gradually to those of intrinsic samples. The Seebeck effect, which is constant as long as the intrinsic dissociation is negligible, decreases at high temperatures. For compositions in the neighbourhood of $CoFe_2O_4$, this already occurs at lower temperatures (Fig. 4). Because of the different mobilities of electrons and holes, the sign of the Seebeck effect becomes negative for all samples. The intrinsic value reached at high temperatures will be

$$e\pi = e\theta T = \frac{\mu_1 - \mu_2}{\mu_1 + \mu_2}\Delta.$$

Experimentally, we find for $e\pi$ at 1000°C a value of $-0{\cdot}025$ eV, which gives, with $\Delta = 0{\cdot}275$ eV, μ_1/μ_2 decreased to 1·2. This is roughly in accordance with a difference between q_2 and q_1 of 0·3 eV, as

$$\frac{(\mu_1/\mu_2)_{T_1}}{(\mu_1/\mu_2)_{T_2}} = \exp\left(\frac{q_2-q_1}{kT_1} - \frac{q_2-q_1}{kT_2}\right).$$

From our analysis we find a rather simple behaviour for the electron conduction caused by the presence of Fe^{II} ions. The energy-level picture we have used is too rough to explain the small extra heat effect of $1kT$ during electron transport. It is in accordance with the idea that the activation of the jumps is caused by lattice vibration that no, or

nearly no, heat effect occurs. With the conduction by holes in the case of excess cobalt ions, more difficulties arise, as the activation energy is very high and the heat effect also is considerable. These effects may be related to the different ionic structures of Co^{II} and Co^{III}. Whereas Fe^{II}, Fe^{III}, and Co^{II} all show the normal magnetic moment in accordance with Hunds' rule, Co^{III} differs. In most compounds Co^{III} is diamagnetic, and this is also found to be the case in compounds with spinel structure by COSSEE.[12] One might expect that the difference in electronic structure causes an extra activation energy which is also found in the extra term in the Seebeck effect. The development of the crystal-field theory does not yet allow us, however, to predict these effects.

Acknowledgements—The author wishes to thank Mr. W. NOORLANDER for his experimental assistance, Mr. J. VISSER for the chemical analysis. Thanks are also due to Dr. D. POLDER for his help in the development of the theory.

REFERENCES

1. VAN UITERT L. G., *J. Chem. Phys.* **23,** 1883 (1955); **24,** 306 (1956).
   VAN UITERT L. G., *Proc. Inst. Radio Engrs.* **44,** 1294 (1956).
2. MORIN F. J., *Phys. Rev.* **83,** 1005 (1951); **93,** 1195 (1954); **93,** 1199 (1954).
3. HEIKES R. R., *J. Chem. Phys.* **26,** 582 (1957).
4. SMILTENS R., *J. Amer. Chem. Soc.* **79,** 4881 (1957).
5. VERWEY E. J. W., HAAIJMAN P. W., ROMEYN F. C. and VAN OOSTERHOUT G. W., *Philips Res. Rep.* **5,** 173 (1950).
6. JONKER G. H. and VAN SANTEN J. H., *Physica* **16,** 337 (1950).
7. VAN SANTEN J. H. and JONKER G. H., *Physica* **16,** 559 (1950).
   JONKER G. H. and VAN SANTEN J. H., *Physica* **19,** 120 (1953).
8. LANDAU L., *Phys. Z. Sowjet* **3,** 664 (1933).
   MOTT N. F. and GURNEY R. W., *Electronic Processes in Ionic Crystals* p. 86. Oxford University Press (1940).
9. JONKER G. H., *Physica* **20,** 1118 (1954).
10. HEIKES R. R., *Phys. Rev.* **99,** 1232 (1955).
11. FINKELNBURG W. and HUMBACH W., *Naturwiss.* **42,** 35 (1955).
12. COSSEE P., Thesis, Leiden (1956).

J. Phys. Chem. Solids Pergamon Press 1959. Vol. 9. pp. 176–180. Printed in Great Britain.

PREPARATION AND CRYSTALLOGRAPHIC PROPERTIES OF THE SYSTEMS $LaMn_{1-x}Mn_xO_{3+\lambda}$ AND $LaMn_{1-x}Ni_xO_{3+\lambda}$ JA-1106*

AARON WOLD and RONALD J. ARNOTT

Mass. Institute of Technology, Lincoln Laboratory, Lexington, Massachusetts

(*Received* 19 *August* 1958)

Abstract—Lanthanum manganese oxides containing varying percentages of Mn^{+4} were prepared and their cell dimensions determined. Lanthanum manganese oxide, prepared under pure nitrogen, contained 0·02 per cent Mn^{+4}. At room temperature it possessed orthorhombic symmetry and was the most distorted member of the series. The orthorhombic-to-rhombohedral transition points for members of this series have been determined, and the shape of the resulting curve interpreted on the basis of an ordering of four, coplanar empty orbitals of the Mn^{+3} ions and steric effects. The system $LaNi_xMn_{1-x}O_{3+\lambda}$ has been prepared and its crystallographic properties studied. La_2NiO_4, $LaNiO_3$ and an intermediate lanthanum nickel oxide were prepared and their X-ray data are given.

1. INTRODUCTION

RECENTLY,[1–4] it has been reported that several rare-earth perovskite-type oxides containing Mn^{+3} ions and another transition metal ($LaMn_xM_{1-x}O_3$) have displayed interesting magnetic and crystallographic properties. JONKER and VANSANTEN[1] first investigated compounds with $M = Mn^{+4}$ and discovered ferromagnetism in the range of compositions 10–50 per cent of the total manganese as Mn^{+4}. JONKER[2] reported ferromagnetism in compounds containing $M = Ti^{+4}$ and Cr^{+3} in a range of compositions about 13 per cent $BaTiO_3$ and 25 per cent $LaCrO_3$. GILLEO[3] has reported ferromagnetism in the systems $LaCo_xMn_{1-x}O_3$ and $LaCr_xMn_{1-x}O_3$; he found no ferromagnetic region in compounds containing $LaFeO_3$. WOLD *et al.*[4] have reported ferromagnetism in the system $LaNi_xMn_{1-x}O_{3+\lambda}$ over the compositional range $0{\cdot}2 \leqslant x \leqslant 0{\cdot}5$.

GELLER[5] has indicated that the rare earth–transition metal perovskites fall into one of two groups. Most of them are orthorhombic and belong to space-group $D_{2h}(16)$—*Pbnm* with four distorted perovskite units in the true crystallographic cell, or they are rhombohedral and belong to space-group $D_{3d}(5)$—$R\bar{3}m$ with two formula units per unit cell. YAKEL[6] and WOLLAN and KOEHLER[7] have shown that $LaMnO_3$ containing 8·9 per cent Mn^{+4} is orthorhombic, and for concentrations of tetravalent manganese up to about 25 per cent, X-ray diffraction patterns indicated that an orthorhombic or monoclinic symmetry is still present. Samples of $LaMnO_{3+\lambda}$ which contained 35·3 per cent Mn^{+4} possessed rhombohedral symmetry. GELLER[5] has indicated that perovskite oxides containing V^{+3}, Cr^{+3}, Mn^{+3} and Fe^{+3} are orthorhombic, whereas Co^{+3} and Al^{+3} perovskite oxides are rhombohedral. He has deduced a set of ionic radii for these ions in perovskite lattices. The radii of the former set of ions range from 0·61 to 0·63 Å, whereas Co^{+3} and Al^{+3} have radii of approximately 0·56 Å. Thus it is implied that the difference in distortion is the result of a difference in size of the transition-element cation.

The orthorhombic distortion from cubic symmetry observed for pure $LaMnO_3$ is larger than that for the other orthorhombic perovskites. GOODENOUGH[4,8] has indicated that this large orthorhombic distortion is due to a particular

* The research in this document was supported by the U.S. Army, Navy, and Air Force under contract with the Massachusetts Institute of Technology.

ordering of the four coplanar, empty orbitals of the Mn^{+3} ions shown in Fig. 1; smaller distortions from cubic symmetry result when this ordering is destroyed. The introduction of ions such as Mn^{+4}, Cr^{+3}, Co^{+3} and Fe^{+3} which do not have an

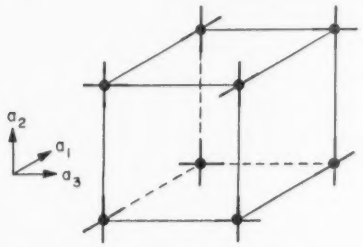

FIG. 1. Simple-cubic array of transition-element ions in perovskite-type lattice, showing the orientations of empty $d_{x^2-y^2}$ orbitals responsible for orthorhombic symmetry.

unequal occupation of d_{z^2} and $d_{x^2-y^2}$ orbitals when located in an octahedral oxygen-ion interstice, reduces the number of ions which are available to participate in the distortion mechanism. Consequently, the magnitude of this distortion and the temperature of the transition from orthorhombic to rhombohedral are expected to decrease with increasing concentration of foreign ions. At a greater concentration than 10–20 atomic per cent, the bond ordering which is responsible for these distortions is completely destroyed. It is a purpose of this paper to investigate the relative magnitude of these effects.

WOLD *et al.*[9] have reported the preparation and structure of $LaNiO_3$. $LaNiO_3$ belongs to space-group $D_{3d}(5)-R\bar{3}m$ with two formula weights per unit cell. The dimensions of the rhombohedral pseudocell are $a = 7{\cdot}676 \pm 0{\cdot}002$ Å, $\alpha = 90°41'$. RABENAU and ECKERLIN[10] have prepared La_2NiO_4, which possesses the K_2NiF_4 structure with $a = 3{\cdot}855$ Å and $c = 12{\cdot}65$ Å.

2. EXPERIMENTAL

Preparation of pure $LaMnO_3$. The samples were prepared by reacting lanthanum oxide with manganese (III) oxide under a pure nitrogen atmosphere at 1300°C for 18 hr. Traces of oxygen were removed by first passing the nitrogen through heated copper gauze and covering the samples with a nickel boat.

Preparation of $LaMn_x^{+3}Mn_{1-x}^{+4}O_{3+\lambda}$. Lanthanum oxide and manganese (III) oxide were heated for 72 hr under an oxygen atmosphere at 1100°C. These samples possessed the maximum amount of Mn^{+4} (30 per cent) obtained in this study. The intermediate lanthanum manganese oxides were prepared by heating portions of these samples under oxygen at various temperatures between 1100 and 1514°C, until equilibrium conditions were obtained. The samples were transferred to sealed Vycor capsules and annealed at 800°C for 72 hr in order to obtain well-crystallized products.

Preparation of $LaMn_{1-x}Ni_xO_{3+\lambda}$. These samples were prepared by reacting lanthanum oxide with varying molar mixtures of nickel (II) oxide and manganese (III) oxide in air at 1100°C and annealing the products at 800°C to improve their crystallinity.

Preparation of $LaNiO_3$ and La_2NiO_4. Lanthanum oxide and nickel (II) oxide, in the molar ratios 1 : 1 and 2 : 1, were heated at 900 and 1350°C respectively to produce $LaNiO_3$ and La_2NiO_4.

Standard analytic techniques were used to determine the total oxidation of the product; excess oxidizing power of the transition-metal cations was attributed to the presence of Mn^{+4} and a deficiency to the presence of Ni^{+2}.

The lattice symmetry and lattice parameters were calculated from spectrometer traces taken with a Philips Norelco diffractometer, using Fe$K\alpha$ and Cu$K\alpha$ radiation. The transition temperatures above room temperature were determined by using a furnace mounted on a Norelco X-ray diffractometer. The instrument is a modified version of that described by PERRI *et al*,[11] and another in the Geology Department, Columbia University. It was adapted for atmospheric control, and during measurements of samples with low Mn–4 content, a nitrogen atmosphere was used. Transition temperatures below room temperature were obtained by passing nitrogen, cooled with liquid nitrogen, over the samples. The instrumentation is a modified version of that described by SCHWARTZ *et al.*[12]

3. DISCUSSION

Lanthanum manganese oxides. Results of chemical and crystallographic analysis are summarized in

Table 1. Chemical and crystallographic analysis of lanthanum manganese oxides

Conditions	Mn^{+4} (per cent)	Symmetry*	Pseudocubic cell dimensions
1300°C PURE N_2	0·02	O	$a_1 = a_3 = 7{\cdot}961$ Å $a_2 = 7{\cdot}699$ Å $\beta = 91° 56'$
1514°C O_2	8·7	O	$a_1 = a_3 = 7{\cdot}895$ Å $a_2 = 7{\cdot}744$ Å $\beta = 90° 57'$
1465°C O_2	9·6	O	$a_1 = a_3 = 7{\cdot}888$ Å $a_2 = 7{\cdot}746$ Å $\beta = 90° 54'$
1281°C O_2	12·4	O	$a_1 = a_3 = 7{\cdot}865$ Å $a_2 = 7{\cdot}768$ Å $\beta = 90° 28'$
1350°C AIR	19·8	O	$a_1 = a_3 = 7{\cdot}804$ Å $a_2 = 7{\cdot}790$ Å $\beta = 90° 20'$
1100°C O_2	24·0	R	$a = 7{\cdot}784$ Å $\alpha = 90° 36'$
1100°C O_2	26·6	R	$a = 7{\cdot}777$ Å $\alpha = 90° 35'$
1100°C O_2	30·0	R	$a = 7{\cdot}777$ Å $\alpha = 90° 35'$

* O = Orthorhombic.
R = Rhombohedral.

Table 1. Pure lanthanum manganese oxide, prepared under pure nitrogen, contained 0·02 per cent Mn^{+4} and at room temperature was the most distorted member of the series. The maximum percentage of Mn^{+4} (30 per cent) was obtained by heating the samples at 1100°C in oxygen for six days. In order to illustrate the various distortions of the perovskite structure, reported in Table 1, the pseudocubic cell dimensions have been given for all cases. For the orthorhombic distortion, the pseudocubic lattice is monoclinic, and for the rhombohedral distortion it is a non-primitive rhombohedron. Fig. 2 was plotted using the monoclinic cell dimensions listed in Table 1. It is assumed that when the two cell edges become equal, the transformation to the rhombohedral structure occurs. As Fig. 2 shows, at room temperature, this transformation takes place when 21 per cent Mn^{+4} is present in the sample.

The variation of transition temperature with Mn^{+3} content for the various lanthanum manganese oxide samples is plotted in Fig. 3, the room-temperature transition point being obtained from Fig. 2.

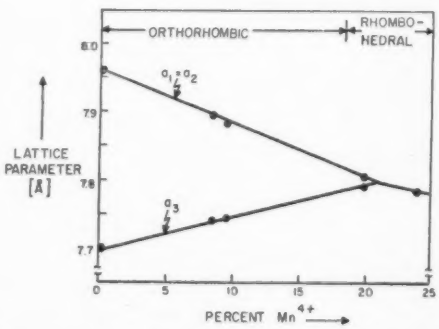

FIG. 2. Room-temperature lattice parameters for pseudo-cubic cell of $LaMnO_{3+\lambda}$ as a function of Mn^{+4} concentration. The rhombohedral phase for sample with 24 per cent Mn^{+4} undergoes a martensitic transformation through the temperature range $175°C \leqslant T \leqslant -45°C$, the low-temperature phase being orthorhombic. At $-160°C$, $a_2/a_3 = 0{\cdot}963$ for pure $LaMnO_3$. By analogy with MnF_3, this should correspond to an average axial ratio in distorted octahedra of $\sim 1{\cdot}15$.

It should be noted that the curve plotted in Fig. 3 has an inflection point at about room-temperature. The higher-temperature portion of the curve

can be explained by the bond-ordering concepts of GOODENOUGH. Perovskite oxides containing percentages of Mn^{+3} greater than approximately 75 will show an orthorhombic distortion because of the ordering of four coplanar empty orbitals of the

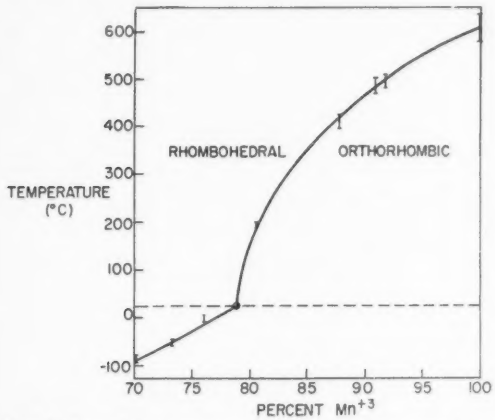

FIG. 3. Transition temperature of $LaMnO_3$ versus Mn^{+3} content.

Mn^{+3} ions (Fig. 1). This distortion is largest ($a_2/a_1 = 0{\cdot}97$) for pure $LaMnO_3$. The introduction of other ions, e.g. Mn^{+4}, which do not have an unequal occupation of d_{z^2} and $d_{x^2-y^2}$ orbitals when located in an octahedral oxygen-ion interstice, reduces the magnitude of the distortions due to bond ordering of the Mn^{+3} ions and in concentrations greater than 10–20 atomic per cent, destroys the bond ordering to eliminate lattice distortions from this effect. Smaller distortions would, therefore, result. At 21 per cent Mn^{+4}, there are sufficient foreign ions present to destroy this ordering, and the residual distortion is due to some other effect. As shown by WICKHAM and CROFT,[13] a similar effect is present in spinel oxides containing Mn^{+3}, where the critical concentration is about 60 per cent Mn^{+3}. Below that percentage, the tetragonal distortion is not present down to −180°C. The magnetic data indicate its probable absence down to liquid-helium temperature. The abrupt change in transformation temperature with composition at a critical composition is characteristic of long-range bond ordering.

Fig. 3 also shows that perovskite oxides, containing less than the critical amount of Mn^{+3} (79 per cent), still transform to the orthorhombic structure below room temperature. However, there is a marked change in the slope of the curve. As mentioned previously, it would be expected that $LaMnO_3$ would be orthorhombic on the basis of its ionic size alone. The presence of considerable amounts of the smaller Mn^{+4} ion should favor the formation of the rhombohedral perovskite. The change of the slope of the curve in Fig. 3 is due to the disappearance of the bond-orienting effect leaving the size effect as the predominant one.

Lanthanum nickel oxides. Lanthanum nickel oxide ($LaNiO_3$) was reported previously by WOLD *et al.*[8] Samples of $LaNiO_3$ are stable up to 900°C. Above this temperature, appreciable amounts of Ni^{+2} form. At 1300°C, pure La_2NiO_4 can be prepared and has been reported to possess the K_2NiF_4 structure. When $LaNiO_3$ is heated to 1100°C, some Ni^{+2} is formed and appears as NiO. The remaining phase cannot be indexed as either $LaNiO_3$ or La_2NiO_4, but is apparently a much distorted perovskite (Table 2). Attempts to prepare this phase pure, by heating lanthanum oxide and nickel (II) oxide were unsuccessful because of the greater stability of the La_2NiO_4 compound which formed. Evidently, the perovskite lattice will

Table 2. Comparison of unidentified lanthanum nickel oxide phase at 1100°C *with* $LaNiO_3$ *and* La_2NiO_4

$LaNiO_3$ (Perovskite)		Unidentified Phase		La_2NiO_4 (K_2NiF_4)	
d	*I*	*d*	*I*	*d*	*I*
				6·30	5
3·82	40	3·79	20		
				3·69	35
		3·49	10		
				3·16	15
				2·85	100
		2·77	100		
2·73	100	2·73	40	2·73	60
2·69	90	2·70	40		
2·22	30				
2·19	10	2·15	15	2·12	25
		1·996	6	2·06	35
1·917	60	1·921	40	1·932	40
1·722	10				
1·706	10			1·712	10
		1·676	10	1·673	15

Table 3. X-ray lattice constants for the system $LaMn_{1-x}Ni_xO_3$

Sample	Mn^{+4} (per cent)	a_0(Å)	b_0(Å)	c_0(Å)	Vol. (Å^3)
$LaMnO_{3+\lambda}$	19·8	5·501	5·536	7·786	237·0
$LaMn_{0.8}Ni_{0.2}O_{3+\lambda}$	13·0	5·495	5·530	7·782	236·5
$LaMn_{0.7}Ni_{0.3}O_{3+\lambda}$	6·2	5·487	5·523	7·773	235·6
$LaMn_{0.6}Ni_{0.4}O_{3+\lambda}$	6·8	5·474	5·515	7·754	234·1
$LaMn_{0.5}Ni_{0.5}O_{3+\lambda}$	2·1	5·463	5·512	7·740	233·1

accommodate a considerable deficiency of nickel and persist as a metastable phase.

The system $LaNi_xMn_{1-x}O_{3+\lambda}$. The system $LaNi_xMn_{1-x}O_{3+\lambda}$ consists of a single orthorhombic phase from $0 \leqslant x \leqslant 0{\cdot}5$ (Table 3). Where $x > 0{\cdot}5$, two phases appear: an orthorhombic phase which resembles $LaMn_{0.5}Ni_{0.5}O_3$ and the metastable lanthanum nickel oxide phase previously mentioned. Nickel oxide lines appear in increasing intensity as x increases.

Acknowledgements—The authors wish to acknowledge the invaluable and enlightening advice of Dr. J. B. GOODENOUGH and helpful discussions with Dr. D. G. WICKHAM. They also would like to thank Mr. J. FITZGERALD for carrying out the numerous chemical analyses and Mr. A. FERRETTI for assistance in the design and construction of the low- and high-temperature units.

REFERENCES

1. JONKER G. H. and VANSANTEN J. H., *Physica* **16,** 337, 559 (1950).
2. JONKER G. H., *Physica* **22,** 707 (1956).
3. GILLEO M. A., *Acta Cryst.* **10,** 161 (1957).
4. WOLD A., ARNOTT R. J., and GOODENOUGH J. B., *J. Appl. Phys.* **29,** 387 (1958).
5. GELLER S., *Acta Cryst.* **10,** 248 (1957).
6. YAKEL H. L., *Acta Cryst.* **8,** 394 (1955).
7. WOLLAN E. O. and KOEHLER W. C. *Phys. Rev.* **100,** 545 (1955).
8. GOODENOUGH J. B., *Phys. Rev.* **100,** 564 (1955).
9. WOLD A., POST B., and BANKS E., *J. Amer. Chem. Soc.* **79,** 4911 (1957).
10. RABENAU A. and ECKERLIN P., *Acta Cryst.* **11,** 304 (1958).
11. PERRI J. A., BANKS E., and POST B., *J. Appl. Phys.* **28,** 1272 (1957).
12. SCHWARTZ R., POST B., and FANKUCHEN I., *Rev. Sci. Instrum.* **22,** 218 (1951).
13. WICKHAM D. G. and CROFT W. J. To be published.

Antwort auf die Bemerkung von M. Balkanski zu der Arbeit „Über den Mechanismus der Energiewanderung in Kadmiumsulfid-Kristallen"

(*Received* 20 *September* 1958)

M. BALKANSKI hat kürzlich[1] einige Bemerkungen über unsere Arbeit „Über den Mechanismus der Energiewanderung in Kadmiumsulfid-Kristallen"[2] in dieser Zeitschrift veröffentlicht, aus denen hervorgeht, dass er mit der von uns vorgeschlagenen Deutung der Ausbreitung von Photoleitung über grössere Entfernungen durch Streuung und Reabsorption von Lumineszenzlicht bzw. von anregendem Licht nicht einverstanden ist. Die von ihm angeführten Argumente gegen einen derartigen Mechanismus der Energieausbreitung in Photohalbleitern sind jedoch unserer Meinung nach nicht geeignet, eine Revision unserer Vorstellungen herbeizuführen. Zu den einzelnen Punkten bemerkt:

(1) Der hier von HERRN BALKANSKI behandelte Reflexionsmechanismus, trägt in der Tat nur wenig zu einer Weiterleitung von Lichtenergie bei. Licht, das von aussen in eine planparallele Platte eintritt, wird nämlich nicht total reflektiert, sondern tritt auf der Rückseite wieder aus. Bei dem von uns beobachteten Effekt handelt es sich dagegen um Licht, dessen Richtungsverteilung im Innern des Kristalles geändert worden ist, sei es — wie bei Anregung mit kurzwelliger Strahlung — durch den Prozess der Lumineszenzerzeugung oder sei es durch kohärente Streuung des durchgehenden Lichtes an idealen oder gestörten Gitterpunkten. In diesem Fall ist die Weiterleitung von Lichtenergie über grosse Strecken möglich (vgl. z.B. die Anwendung dieses Effektes bei den „Lichtleitern"), da auch bei einer mehrfachen Wiederholung der Totalreflexion stärkere Verluste nicht auftreten. Die Einbettung der Kristalle in Stoffer von hohem Brechungsindexes sollte zwar eine Verminderung der gestreuten Lichtenergie ergeben, jedoch wirkt sich dies auf den Wert der „Diffusionslänge" erst dann aus, wenn der Wert des Brechungsindexes von Kadmiumsulfid nahezu erreicht wird.

(2) Die Idee, dass das gemessene Licht durch Zerfall von Exzitonen erst am Ort der Leitfähigkeitsmessung entsteht, erscheint im Fall des langwelligen monochromatischen Lichtes wenig sinnvoll. Aus unserer Abb. 4[2] geht hervor, dass das durchgehende Licht keinerlei Struktur in seiner Wellenlängenabhängigkeit zeigt, wie dies im Falle von Exzitonenanregung der Fall sein sollte. An Hand von neueren Messungen[3] konnte auch einwandfrei gezeigt werden, dass keine Veränderung der Wellenlänge der monochromatischen Strahlung beim Durchgang durch den Kristall eintritt. Erfolgt die Anregung der Leitfähigkeit im langwelligen Gebiet aber durch Lichtstreuung, so lässt sich das Ergebnis der Abb. 2 nur dann sinnvoll deuten, wenn man annimmt, dass im kurzwelligen Gebiet die Anregung der Photoleitung durch Reabsorption des durch den Kristall gestreuten Lumineszenzlichtes verursacht wird (vgl. Diskussion zu Abb. 2 unserer Arbeit).

(3) Ganz offensichtlich entsteht durch jede Abweichung von der Planparallelität (z.B. durch Kratzen) für das totalreflektierte Licht die Möglichkeit, aus dem Kristall auszutreten, was zu einer Verminderung der durch den Kristall gestreuten Lichtintensität und damit zu einer Verkleinerung des Wertes der „Diffusionslänge" führt.

(4) Aus unserer Abb. 4 entnimmt man deutlich den Grund für das Auftreten weiterer Maxima bei der Photoleitung. Wir brauchen unseren diesbezüglichen Ausführungen in der Arbeit[2] nichts hinzuzufügen.

(5) Neuere Messungen haben eindeutig gezeigt, dass die Zunahme der durch „Diffusion" erzeugten Leitfähigkeit mit abnehmender Temperatur durch Veränderungen von Intensität und Wellenlänge des Lumineszenzlichtes hervorgerufen wird.[3] Dabei bleibt aber die „Diffusionslänge" selbst praktisch unverändert (vgl. BALKANSKI und BROSER[4]), was deutlich gegen die Existenz einer Exzitonenleitfähigkeit spricht.

(6) Wir sind weiterhin davon überzeugt, dass die „Transportzeit" vom Ort der Anregung zum Ort der Leitfähigkeitsmessung sehr kurz ist und dass sie durch die Lichtgeschwindigkeit im Kristall gegeben ist. Dies gilt im besonderen auch für den Fall $\nu < \nu_g$ wo lediglich eine Streuung des auffallenden Lichtes erfolgt. Die früher berechnete „Diffusionskonstante" für Exzitonen wird durch

das relativ langsame Anklingen der Photoleitung vorgetäuscht.

(8) Es besteht unserer Meinung nach kein Grund, Ueberlegungen über die Wechselwirkung von Strahlungsfeld und Exzitonenwellen für ein Experiment anzustellen, das sich ohne Widerspruch durch die viel einfachere Annahme der Reabsorption von gestreutem Licht erklären lässt.

(9) Eigene kürzlich durchgeführte Untersuchungen mit zerteilten und wieder gekitteten Kristallen zeigen deutlich, dass die Abnahme der Photoleitung nach dem Zerbrechen mit einer Abnahme der Streulichtintensität verbunden ist.[3] Dabei bleibt der Zusammenhang zwischen Photostrom und Lichtstrom am Ort der Leitfähigkeitsmessung in quantitativer Weise erhalten. Dies spricht eindeutig für den Mechanismus der Lichtstreuung in den von uns untersuchten Kristallen.

(10) Die hier erwähnten Messungen können sinnvoll erst diskutiert werden, wenn auch optische Messungen in der von uns vorgeschlagenen Art durchgeführt worden sind. Es erscheint schwer verständlich, dass die Diffusion von Exzitonen durch die optisch sichtbaren Störungen (Korngrenzen) der polykristallinen Schicht weniger gestört werden soll als die Ausbreitung des Lichtes.

(11) Die Frage, warum DIEMER und HOOGENSTRAATEN an *einem* Kristall eine Diskrepanz zwischen Photostrom und Lichtstrom gefunden haben,[5] kann unseres Erachtens nur auf Grund weiterer sorgfältiger Messungen geklärt werden. DIEMER und HOOGENSTRAATEN fanden im übrigen bei den meisten der von ihnen untersuchten Kristalle ebenfalls, dass der indirekt erzeugte Photostrom durch Reabsorption des gestreuten Lumineszenzlichtes erzeugt wird.[5]

Institut für Elektronenmikroskopie am Fritz-Haber-Institut der Max-Planck-Gesellschaft, Berlin-Dahlem

I. BROSER
R. BROSER–WARMINSKY

LITERATUR

1. BALKANSKI M., *J. Phys. Chem. Solids* **6**, 401 (1958).
2. BROSER I. und BROSER–WARMINSKY R., *J. Phys. Chem. Solids* **6**, 386 (1958).
3. BROSER I. und BROSER–WARMINSKY R., *J. Phys. Chem. Solids* **8**, 177 (1959).
4. BALKANSKI M. und BROSER I., *Z. Elektrochem., Ber. Bunsenges. physik. Chem.* **61**, 715–723 (1957).
5. DIEMER G. und HOOGENSTRAATEN W., Private Mitteilung.

Phase coexistence and hysteresis

(*Received* 15 *September* 1958)

THE strain that arises from the coexistence of two phases in the solid state has been used to provide explanations of the hysteresis that accompanies solid-state transitions. DINICHERT[1] assumed that strain displaced the ammonium chloride transition according to the Clausius–Clapeyron equation. However, THOMAS and STAVELEY[2] showed that on the basis of the Turnbull theory of nucleation the transition rates would be extremely sensitive to temperature, and that the temperatures at which the rates become significant are displaced by the effects of strain and surface energy on the growing nuclei.

Assuming an equilibrium theory of hysteresis, the strain terms can be regarded as perturbations on the bulk free energies of the two phases.[3] If χ_{I} is the value of the strain contribution to the free energy of the low-temperature phase and χ_{II} the contribution to that of the high-temperature phase, then for the I $\rightarrow$ II transition $\Delta\chi^1 = \chi_{\mathrm{II}} - \chi_{\mathrm{I}}$ will determine the displacement of the point of intersection of the free-energy curves. $\Delta\chi_m{}^1$ is regarded as the maximum strain contribution that can be attained before mechanical breakdown occurs, after which the transition will proceed isothermally. Assuming $\Delta\chi_m{}^1$ is small,

$$\Delta\chi_m{}^1 = \left[\left(\frac{\partial G_{\mathrm{I}}}{\partial T}\right)_p - \left(\frac{\partial G_{\mathrm{II}}}{\partial T}\right)_p\right]\Delta T^1,$$

where ΔT^1 is the displacement of the transition from the temperature at which the bulk phases would be in equilibrium. Similar reasoning for the II $\rightarrow$ I transition gives:

$$\Delta\chi_m{}^1 + \Delta\chi_m{}^2 = \Delta S_t \cdot \Delta T_h,$$

where ΔS_t is the entropy change associated with the transition and ΔT_h is the temperature range of the hysteresis.

Hysteresis can also be obtained by varying the

Table 1. *The transitions occurring in certain ammonium salts*

(Data taken largely from ref. (2))

	T_t(°K)	ΔT_h	ΔV_t (cm³/mole)	ΔS_t (cal/mole-deg.)	ΔP_h (atm) calcd.
NH_4Cl	242·6	0·35	0·15	1·3	120
NH_4Br	234·4	0·06	0·03	1·3	110
ND_4Br	214·9	0·11	0·08	1·3	70
$(NH_4)_2SO_4$	223·4	1·2	0·35	4·0	570
NH_3DCl	244·6	0·12	0·11	1·3*	60
ND_3HCl	247·9	0·07	0·07	1·3*	50

* Assuming that these transitions have the same mechanism as that in the ammonium chloride.

pressure at constant temperature. If this process is carried out under similar initial conditions, we may assume that the maximum strain will not be significantly changed. Therefore

$$\Delta\chi_m{}^1+\Delta\chi_m{}^2=\Delta P_h\cdot\Delta V_t,$$

where ΔP_h is the range of the pressure hysteresis and ΔV_t is the volume change accompanying the transition. The extent of the coexistence, and hence the hysteresis, will be governed by an equation of the Clausius–Clapeyron type:

$$\frac{\Delta T_h}{\Delta P_h}=\frac{\Delta V_t}{\Delta S_t}.$$

In the case of the gradual transitions which occur in ammonium salts, all the factors in the above equation have been measured with the exception of the range of pressure hysteresis. This is known to occur, but no quantitative results have been reported.

Apart from any assumptions made, the calculations of the pressure hysteresis are limited by the accuracy of the measurements of ΔT_h and ΔS_t. However, they provide an estimate of the range of pressure hysteresis to be expected from a theory of this type. It seems improbable that these small pressure changes will affect the nucleation process considered by THOMAS and STAVELEY.(2) Thus, experimental measurements of ΔP_h will help test the validity of the two approaches and provide valuable evidence on the mechanism of phase transitions in the solid state.

Acknowledgement—Thanks are due to Dr. B. J. ALDER for valuable comments and suggestions on this topic.

Department of Chemistry E. BRIAN SMITH
University of California
Berkeley 4, California

REFERENCES

1. DINICHERT P., *Helv. Phys. Acta* **17**, 389 (1944).
2. THOMAS D. G. and STAVELEY L. A. K., *J. Chem. Soc.* 2572 (1951).
3. UBBELOHDE A. R., *Nature, Lond.* **169**, 832 (1952).

The antiferromagnetic transformations of the alloy AuMn

(*Received* 29 *September* 1958)

ACCORDING to the results of magnetic and electrical measurements on a bulk specimen of AuMn reported from this Institute in 1955, the compound undergoes an antiferromagnetic transformation at about 230°C.(1,2) From magnetic measurements on a powder specimen, MORRIS and PRESTON(3) later reported an antiferromagnetic transformation of this alloy at 92°C (but not one at 230°C). In a recent publication BACON and STREET(4) give the results of measurements on one bulk specimen and one powder specimen of the same compound. These investigations confirm the results of GIANSOLDATI(1) and of MORRIS and PRESTON.(3) For the powder specimen, BACON and STREET obtained the transformation at 92°C very distinctly. (The transformation at 230°C also appears on their curves for

that specimen, but this fact is not discussed by the authors.) For the bulk specimen they obtained the antiferromagnetic transformation at about 230°C distinctly and a weak indication of a transformation at 92°C.

The bulk specimen investigated in our Institute in 1954 (as reported in papers in 1955) was reinvestigated magnetically later after having been preserved at room temperature for five months. The results of these measurements (which have not been reported before) are given in Fig. 1. From the figure it is seen that the transformation at the lower Néel point ($T_N = 365$°K) proceeds to its full extent during long-time ageing at room temperature. After renewed heating above the higher Néel point, the specimen shows the same properties as before the ageing process. (Only the transformation at 230°C occurs with "finite" speed.) Apparently the "magnetically hard character" of the bulk specimen as compared with a powder specimen presents certain difficulties which prevent the transformation at the lower Néel point (365°K) from occurring with reasonable speed in the temperature range studied.

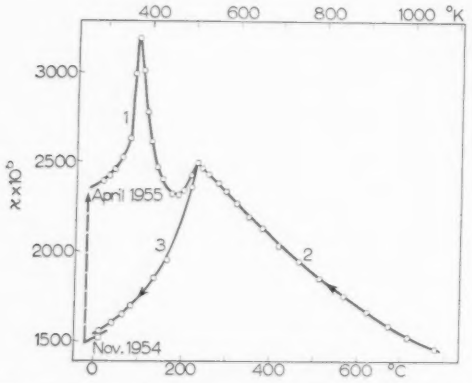

FIG. 1. Magnetic molar susceptibility of a bulk AuMn specimen showing dependence on temperature and long-time ageing at room temperature.

Acknowledgement—The investigation has been supported by a grant from The Swedish Natural Science Research Council.

Department of Physics
The Royal Institute of Technology
Stockholm

A. GIANSOLDATI,
J. O. LINDE,
and
G. BORELIUS

REFERENCES

1. GIANSOLDATI A., *J. Phys. Radium* **16,** 342 (1955).
2. GIANSOLDATI A. and LINDE J. O., *J. Phys. Radium* **16,** 341 (1955).
3. MORRIS D. P. and PRESTON R. P., *Proc. Phys. Soc.* B**69,** 849 (1956).
4. BACON G. E. and STREET R., *Proc. Phys. Soc.* **72,** 470 (1958).

J. Phys. Chem. Solids Pergamon Press 1959. Vol. 9. pp. 185–197. Printed in Great Britain.

THE TEMPERATURE-DEPENDENCE OF THE FLUORESCENCE OF PHOTOCONDUCTORS

H. A. KLASENS

Philips Research Laboratories, N.V. Philips' Gloeilampenfabrieken, Eindhoven, Netherlands

(*Received* 8 *August* 1958)

Abstract—In a previous paper (*J. Phys. Chem. Solids* **7**, 175 (1958)), the effects of exciting intensity on the behaviour of a fluorescent photoconductor were discussed, using a two-state model with one level near the conduction band and occupied by an electron in the dark and one state near the conduction band and not occupied in the dark. In the present paper the effect of temperature in the stationary state for such a model is discussed. The lower level is assumed to be an activator level giving rise to a fluorescent transition, whereas the other level is attributed to a killer centre. The phosphor is excited with long wavelengths bringing electrons from the activator level to the conduction band.

It is shown that the nature of the temperature-dependence curve can be strongly affected by the capture cross-sections for electrons and holes of the two centres. A plot of $\log(I_0/I-1)$ versus T^{-1} will in general not produce straight lines as in the case of non-photoconducting phosphors, and no conclusions can be drawn from such a plot regarding the positions of the impurity levels.

The best way to determine the position of the activator level is to excite the phosphor at high intensities. A plot of $\log\{(I_0/I)^{\frac{1}{2}}-(I/I_0)^{\frac{1}{2}}\}$ versus T^{-1} will then have a slope corresponding to the thermal-energy difference between the activator level and the top of the highest occupied band.

1. INTRODUCTION

THE fluorescence of phosphors is usually quenched when the temperature is raised at relatively low temperatures. MOTT[1] and SEITZ[2] have provided a theory for this phenomenon of temperature quenching by showing how a fluorescent centre can return from an excited state to the ground state in two ways. They treat the centre as a vibrator in the same way as is usual for diatomic molecules. The potential energy of such a vibrator can be given as a function of the positions of the constituent atoms. To simplify matters, the energy is shown schematically as a function of one generalized coordinate.

Two typical cases are illustrated in Figs. 1(a) and 1(b). According to the FRANCK–CONDON principle, optical absorption and emission occur without change in configuration. In Fig. 1(a) absorption brings the system from M to N. The centre rearranges itself gradually from N to O as the result of emission of phonons. From O the centre may return on emission of a photon to P ("radiative transition") and from there on further phonon emission to M. A "radiationless" transition to the ground state, e.g. a transition whereby only phonons are produced, may occur, however, via Q.

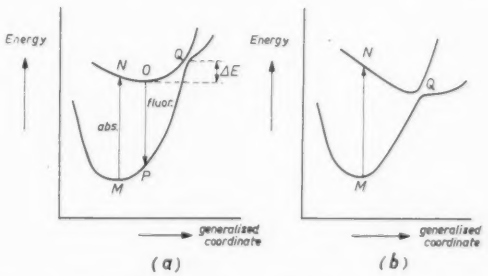

FIG. 1. Schematic drawing showing the potential energy curves versus a generalized coordinate for a fluorescent centre (a) and a killer (b).

In Fig. 1(b) a situation is shown where the return to the ground state is not accompanied by photon emission and all energy is dissipated as heat. Such a centre is often called a "killer".

Returning to Fig. 1(a), the stationary state, when

U centres are excited per second, is described by:

$$U = p_l a^* + p_r a^*, \tag{1}$$

where a^* is the number of excited centres and p_l and p_r represent the probabilities per second for an excited centre to return to the ground state with emission of a photon or without radiation, respectively.

The quantum efficiency is given by:

$$I/U = p_l/(p_l + p_r). \tag{2}$$

Since the probability of finding the excited centre in a vibrational state ΔE above the minimum O in Fig. 1(a) is proportional to a Boltzmann factor $\exp[-\Delta E/kT]$, p_r contains the same factor which is mainly responsible for the observed temperature-dependence because of its rapid change with temperature. Assuming that p_l is not affected by the temperature, the temperature-dependence of the fluorescence intensity I is thus described by:

$$I = \frac{U}{1 + \text{constant.}\ \exp(-\Delta E/kT)}. \tag{3}$$

Since, in this model, both processes, fluorescence and quenching, are proportional to a^*, the rate of excitation has no effect on the temperature-dependence.

The temperature-dependence of the luminescence of many phosphors, such as silicates and phosphates activated with manganese, cerium, lead, and other activators, is adequately described by equation (3). However, for other phosphors, in particular those of the zinc sulphide type, which show photoconduction during excitation, this relation does not hold.

This is illustrated in Fig. 2, where the temperature-dependence of the fluorescence intensity I is shown for a copper-activated (ZnCd)S phosphor with a low cadmium content, commonly used for long-afterglow screens in radar tubes, at various intensities of the exciting 3650 Å radiation. One notices that the curves shift with increasing intensity U to higher temperatures—a typical property of sulphide phosphors.[3–5] Furthermore, as shown in Fig. 3, no straight lines are obtained

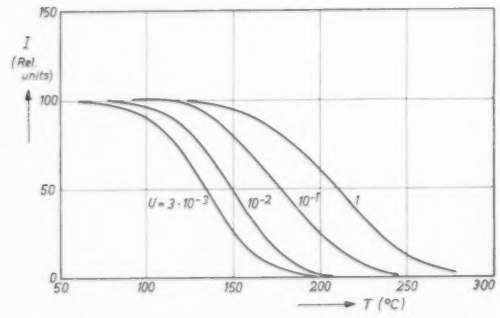

FIG. 2. Temperature-dependence of $(Zn_{0.85}, Cd_{0.15})S$–Cu at various intensities (in arbitrary units) of the exciting 3650 Å radiation. The wavelength of excitation is just on the long-wave side of the fundamental absorption edge for this phosphor.

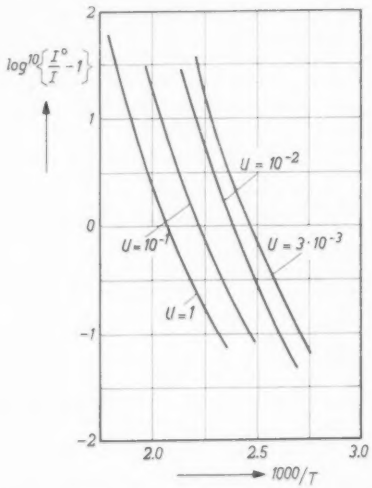

FIG. 3. Curves from Fig. 2 replotted on the basis $\log(I_0/I-1)$ versus T^{-1}.

when $\log(I_0/I-1)$, where I_0 = the maximum value of I for $T \to 0$, is plotted against $1/T$, as would be expected from equation (3).

Empirical formulae including factors containing powers of U have been proposed[6,7] in order to account for the shift with intensity, but they do not explain satisfactorily a deviation as shown in Fig. 3 and moreover do not give an insight into the physical nature of the quenching process.

The nature of the exciting radiation very often has a marked effect on the temperature-dependence. LEVERENZ[8] observed a difference of 100–150° in the quenching temperature of sulphide phosphors between excitation with ultraviolet radiation and that with cathode rays. GARLICK and

GIBSON[9] and KRÖGER[5] found different temperature-dependence curves for different wavelengths of the exciting radiation.

When killers such as cobalt, nickel, and iron are added in minute quantities to sulphide phosphors, the temperature-dependence curves are generally shifted to lower temperatures and the shape of the curves sometimes undergoes a marked change.[3,9,10] To explain the effects of intensity and killer content, the present author[3] has assumed that light emission and quenching in zinc sulphide-type phosphors are processes which occur at different places in the lattice, the first process being due to a recombination between electrons and holes at an activator centre and the latter process being related to such a recombination at a killer centre of the type described above (Fig. 1(b)).

In the transport from one process to the other migration of free electrons and holes takes a part, and it was shown that this migration may in fact be responsible for the observed temperature-dependence and the effect on it of the exciting intensity.

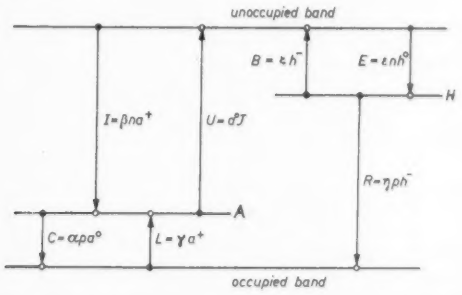

FIG. 4. Two-state model used in discussing the temperature-dependence of sulphide-type phosphors: —●— electrons —O— holes; the arrows indicate electron transitions.

The same mechanism had already been proposed by SCHÖN[11] for the energy transport between different fluorescent centres in a zinc sulphide phosphor.

Activators such as silver or copper give rise to occupied levels A in the forbidden gap between the highest occupied band and the next unoccupied band above it (Fig. 4). Incorporation of killers such as cobalt or nickel produces levels H which are nearer the conduction band and are usually unoccupied when the phosphor is not excited.[12]

During excitation a stationary state will be reached at which electrons and holes are captured by both levels (processes E, I, C and R in Fig. 4). Holes captured by activator levels A may escape again to the full band (process L), whereas electrons may be thermally liberated from H to the unoccupied band (process B). The stationary state of such a two-state model has been analysed in a previous paper,[13] using DUBOC's[14] method of approximations. The effect of the exciting intensity at constant temperature was discussed in more detail. In this paper the effect of temperature will be considered.

2. ANALYSIS OF THE STATIONARY STATE

In the previous analysis it was assumed that the excitation was a band-to-band transition producing a free hole and a free electron. In the present paper it will be assumed that the exciting radiation brings an electron from the activator level to the conduction band (process U in Fig. 4). Such a situation will arise when the energy of the absorbed quantum is smaller than the band gap or when an exciton is formed first which then dissociates near the activator centre into a trapped hole and a free electron.

In analysing the stationary state, it will be assumed, as previously, that A is completely occupied and H completely empty in the dark. It should be kept in mind, however, that temperature quenching can equally well be explained by a different model, in which A and H are partly or completely occupied in the dark. The latter model has been adopted by HILL and KLASENS[10] in explaining the temperature-dependence of the fluorescence of ZnS–Ag, Co.

As it has since been established that cobalt does not produce an occupied level near the occupied band, but instead an empty level about 0·5 eV below the conduction band in zinc sulphide,[15] their results will be analysed again in terms of the new model.

The phosphor was excited with a wavelength of 3650 Å, which is longer than the edge of the fundamental absorption spectrum. It is mainly for this reason that the present model with direct excitation of the fluorescent centre was chosen.

(a) *Mathematical analysis of the two-state model*

The equations describing the stationary state for

the two-state model of Fig. 4 with direct excitation from A are:

$$a = a^0 + a^+ \tag{4}$$

$$h = h^0 + h^- \tag{5}$$

$$a^+ + p = h^- + n \tag{6}$$

$$U = I + R \tag{7}$$

$$L = C + R \tag{8}$$

$$E = B + R, \tag{9}$$

where

a = total density of A centres
a^0 = density of occupied A centres
a^+ = density of unoccupied A centres
h = total density of H centres
h^0 = density of unoccupied H centres
h^- = density of occupied H centres
n = density of free electrons
p = density of free holes.

The meaning of the symbols U, I, R, C, E, L, and B is shown in Fig. 4. Since the rate of excitation is proportional to the absorption coefficient of the exciting radiation and the latter is proportional to the density of the absorbing centres (a^0), the density of excitation is given as $U = a^0 J$, where J represents the intensity of the exciting radiation falling on the phosphor, multiplied by the absorption cross-section of the occupied activator centres.

Table 1

Code	a^0	a^+	h^0	h^-	n	p	I	R
111111	a	$\frac{\epsilon^{\frac{1}{2}} a^{\frac{1}{2}} h^{\frac{1}{2}} J^{\frac{1}{2}}}{\beta^{\frac{1}{2}} \zeta^{\frac{1}{2}}}$	h	$\frac{\epsilon^{\frac{1}{2}} a^{\frac{1}{2}} h^{\frac{1}{2}} J^{\frac{1}{2}}}{\beta^{\frac{1}{2}} \zeta^{\frac{1}{2}}}$	$\frac{\zeta^{\frac{1}{2}} a^{\frac{1}{2}} J^{\frac{1}{2}}}{\epsilon^{\frac{1}{2}} \beta^{\frac{1}{2}} h^{\frac{1}{2}}}$	$\frac{\epsilon^{\frac{1}{2}} \gamma h^{\frac{1}{2}} J^{\frac{1}{2}}}{\zeta^{\frac{1}{2}} \beta^{\frac{1}{2}} \alpha a^{\frac{1}{2}}}$	aJ	$\frac{\gamma \epsilon \eta h J}{\alpha \beta \zeta}$
111112	a	$\frac{\alpha^{\frac{1}{2}} \epsilon^{\frac{1}{2}} h^{\frac{1}{2}} a^{\frac{1}{2}} J^{\frac{1}{2}}}{\gamma^{\frac{1}{2}} \beta^{\frac{1}{2}} \eta^{\frac{1}{2}}}$	h	$\frac{\alpha^{\frac{1}{2}} \epsilon^{\frac{1}{2}} h^{\frac{1}{2}} a^{\frac{1}{2}} J^{\frac{1}{2}}}{\gamma^{\frac{1}{2}} \beta^{\frac{1}{2}} \eta^{\frac{1}{2}}}$	$\frac{\eta^{\frac{1}{2}} \gamma^{\frac{1}{2}} a^{\frac{1}{2}} J^{\frac{1}{2}}}{\alpha^{\frac{1}{2}} \epsilon^{\frac{1}{2}} \beta^{\frac{1}{2}} h^{\frac{1}{2}}}$	$\frac{\epsilon^{\frac{1}{2}} \gamma^{\frac{1}{2}} h^{\frac{1}{2}} J^{\frac{1}{2}}}{\alpha^{\frac{1}{2}} \beta^{\frac{1}{2}} \eta^{\frac{1}{2}} a^{\frac{1}{2}}}$	aJ	$\frac{\epsilon^{\frac{1}{2}} \eta^{\frac{1}{2}} \gamma^{\frac{1}{2}} a^{\frac{1}{2}} h^{\frac{1}{2}} J^{\frac{1}{2}}}{\alpha^{\frac{1}{2}} \beta^{\frac{1}{2}}}$
111121	a	$\frac{\epsilon^{\frac{1}{2}} a^{\frac{1}{2}} h^{\frac{1}{2}} J^{\frac{1}{2}}}{\beta^{\frac{1}{2}} \zeta^{\frac{1}{2}}}$	h	$\frac{\epsilon^{\frac{1}{2}} a^{\frac{1}{2}} h^{\frac{1}{2}} J^{\frac{1}{2}}}{\beta^{\frac{1}{2}} \zeta^{\frac{1}{2}}}$	$\frac{\zeta^{\frac{1}{2}} a^{\frac{1}{2}} J^{\frac{1}{2}}}{\epsilon^{\frac{1}{2}} \beta^{\frac{1}{2}} h^{\frac{1}{2}}}$	$\frac{\gamma}{\eta}$	aJ	$\frac{\epsilon^{\frac{1}{2}} \gamma a^{\frac{1}{2}} h^{\frac{1}{2}} J^{\frac{1}{2}}}{\beta^{\frac{1}{2}} \zeta^{\frac{1}{2}}}$
111122	a	$\frac{\epsilon^{\frac{1}{2}} a^{\frac{1}{2}} h^{\frac{1}{2}} J^{\frac{1}{2}}}{\beta^{\frac{1}{2}} \gamma^{\frac{1}{2}}}$	h	$\frac{\epsilon^{\frac{1}{2}} a^{\frac{1}{2}} h^{\frac{1}{2}} J^{\frac{1}{2}}}{\beta^{\frac{1}{2}} \gamma^{\frac{1}{2}}}$	$\frac{\gamma^{\frac{1}{2}} a^{\frac{1}{2}} J^{\frac{1}{2}}}{\epsilon^{\frac{1}{2}} \beta^{\frac{1}{2}} h^{\frac{1}{2}}}$	$\frac{\gamma}{\eta}$	aJ	$\frac{\epsilon^{\frac{1}{2}} \gamma^{\frac{1}{2}} a^{\frac{1}{2}} h^{\frac{1}{2}} J^{\frac{1}{2}}}{\beta^{\frac{1}{2}}}$
111211	a	$\frac{\alpha^{\frac{1}{2}} a J^{\frac{1}{2}}}{\eta^{\frac{1}{2}} \gamma^{\frac{1}{2}}}$	h	$\frac{\alpha^{\frac{1}{2}} a J^{\frac{1}{2}}}{\eta^{\frac{1}{2}} \gamma^{\frac{1}{2}}}$	$\frac{\alpha^{\frac{1}{2}} \zeta a J^{\frac{1}{2}}}{\epsilon \eta^{\frac{1}{2}} \gamma^{\frac{1}{2}} h}$	$\frac{\gamma^{\frac{1}{2}} J^{\frac{1}{2}}}{\alpha^{\frac{1}{2}} \eta^{\frac{1}{2}}}$	$\frac{\alpha \beta \zeta a^2 J}{\epsilon \eta \gamma h}$	aJ
111212	a	$\frac{\alpha^{\frac{1}{2}} a J^{\frac{1}{2}}}{\eta^{\frac{1}{2}} \gamma^{\frac{1}{2}}}$	h	$\frac{\alpha^{\frac{1}{2}} a J^{\frac{1}{2}}}{\eta^{\frac{1}{2}} \gamma^{\frac{1}{2}}}$	$\frac{aJ}{\epsilon h}$	$\frac{\gamma^{\frac{1}{2}} J^{\frac{1}{2}}}{\alpha^{\frac{1}{2}} \eta^{\frac{1}{2}}}$	$\frac{\beta \alpha^{\frac{1}{2}} a^2 J^{\frac{3}{2}}}{\epsilon \eta^{\frac{1}{2}} \gamma^{\frac{1}{2}} h}$	aJ
111221	a	$\frac{aJ}{\gamma}$	h	$\frac{aJ}{\gamma}$	$\frac{\zeta a J}{\epsilon \gamma h}$	$\frac{\gamma}{\eta}$	$\frac{\beta \zeta a^2 J^2}{\epsilon \gamma^2 h}$	aJ
111222	a	$\frac{aJ}{\gamma}$	h	$\frac{aJ}{\gamma}$	$\frac{aJ}{\epsilon h}$	$\frac{\gamma}{\eta}$	$\frac{\beta a^2 J^2}{\epsilon \gamma h}$	aJ
112111	a	$\frac{a^{\frac{1}{2}} J^{\frac{1}{2}}}{\beta^{\frac{1}{2}}}$	h	$\frac{\epsilon h a^{\frac{1}{2}} J^{\frac{1}{2}}}{\zeta \beta^{\frac{1}{2}}}$	$\frac{\alpha^{\frac{1}{2}} J^{\frac{1}{2}}}{\beta^{\frac{1}{2}}}$	$\frac{\gamma J^{\frac{1}{2}}}{\alpha \beta^{\frac{1}{2}} a^{\frac{1}{2}}}$	aJ	$\frac{\eta \epsilon \gamma h J}{\beta \alpha \zeta}$
112112	a	$\frac{a^{\frac{1}{2}} J^{\frac{1}{2}}}{\beta^{\frac{1}{2}}}$	h	$\frac{\alpha \epsilon a h}{\eta \gamma}$	$\frac{\alpha^{\frac{1}{2}} J^{\frac{1}{2}}}{\beta^{\frac{1}{2}}}$	$\frac{\gamma J^{\frac{1}{2}}}{\alpha \beta^{\frac{1}{2}} a^{\frac{1}{2}}}$	aJ	$\frac{\epsilon h a^{\frac{1}{2}} J^{\frac{1}{2}}}{\beta^{\frac{1}{2}}}$
112121	a	$\frac{a^{\frac{1}{2}} J^{\frac{1}{2}}}{\beta^{\frac{1}{2}}}$	h	$\frac{\epsilon h a^{\frac{1}{2}} J^{\frac{1}{2}}}{\zeta \beta^{\frac{1}{2}}}$	$\frac{a^{\frac{1}{2}} J^{\frac{1}{2}}}{\beta^{\frac{1}{2}}}$	$\frac{\gamma \zeta}{\epsilon \eta h}$	aJ	$\frac{\gamma a^{\frac{1}{2}} J^{\frac{1}{2}}}{\beta^{\frac{1}{2}}}$
112122	a	$\frac{a^{\frac{1}{2}} J^{\frac{1}{2}}}{\beta^{\frac{1}{2}}}$	h	indefinite $ph^- = \frac{\gamma a^{\frac{1}{2}} J^{\frac{1}{2}}}{\beta^{\frac{1}{2}} \eta}$	$\frac{a^{\frac{1}{2}} J^{\frac{1}{2}}}{\beta^{\frac{1}{2}}}$	indefinite $ph^- = \frac{\gamma a^{\frac{1}{2}} J^{\frac{1}{2}}}{\beta^{\frac{1}{2}} \eta}$	aJ	$\frac{\gamma a^{\frac{1}{2}} J^{\frac{1}{2}}}{\beta^{\frac{1}{2}}}$
112211	a	$\frac{\zeta^{\frac{1}{2}} \alpha^{\frac{1}{2}} a J^{\frac{1}{2}}}{\epsilon^{\frac{1}{2}} \gamma^{\frac{1}{2}} \eta^{\frac{1}{2}} h^{\frac{1}{2}}}$	h	$\frac{\alpha^{\frac{1}{2}} \epsilon^{\frac{1}{2}} h^{\frac{1}{2}} a J^{\frac{1}{2}}}{\gamma^{\frac{1}{2}} \zeta^{\frac{1}{2}} \eta^{\frac{1}{2}}}$	$\frac{\zeta^{\frac{1}{2}} \alpha^{\frac{1}{2}} a J^{\frac{1}{2}}}{\epsilon^{\frac{1}{2}} \gamma^{\frac{1}{2}} \eta^{\frac{1}{2}} h^{\frac{1}{2}}}$	$\frac{\gamma^{\frac{1}{2}} \zeta^{\frac{1}{2}} J^{\frac{1}{2}}}{\alpha^{\frac{1}{2}} \epsilon^{\frac{1}{2}} \eta^{\frac{1}{2}} h^{\frac{1}{2}}}$	$\frac{\beta \alpha \zeta a^2 J}{\epsilon \gamma \eta h}$	aJ

Table 1—(continued)

Code	a^0	a^+	h^0	h^-	n	p	I	R
112212	a	$\frac{aJ}{\epsilon h}$	h	$\frac{\alpha\epsilon ah}{\gamma\eta}$	$\frac{aJ}{\epsilon h}$	$\frac{\gamma J}{\alpha\epsilon h}$	$\frac{\beta a^2J^2}{\epsilon^2h^2}$	aJ
112221	a	$\frac{aJ}{\gamma}$	h	$\frac{\epsilon ahJ}{\gamma\zeta}$	$\frac{aJ}{\gamma}$	$\frac{\gamma\zeta}{\eta\epsilon h}$	$\frac{\beta a^2J^2}{\gamma^2}$	aJ
112222	a	$\frac{aJ}{\epsilon h}$	h	indefinite $ph^- = \frac{aJ}{\eta}$	$\frac{aJ}{\epsilon h}$	indefinite $ph^- = \frac{aJ}{\eta}$	$\frac{\beta a^2J^2}{\gamma^2}$	aJ
121111	a	h	$\frac{\beta\zeta h^2}{\epsilon aJ}$	h	$\frac{aJ}{\beta h}$	$\frac{\gamma h}{\alpha a}$	aJ	$\frac{\eta\gamma h^2}{\alpha a}$
121112	a	h	$\frac{\beta\eta\gamma h^3}{\alpha\epsilon a^2J}$	h	$\frac{aJ}{\beta h}$	$\frac{\gamma h}{\alpha a}$	aJ	$\frac{\eta\gamma h^2}{\alpha a}$
121121	a	h	$\frac{\beta\zeta h^2}{\epsilon aJ}$	h	$\frac{aJ}{\beta h}$	$\frac{\gamma}{\eta}$	aJ	γh
121122	a	h	$\frac{\beta\gamma h^2}{\epsilon aJ}$	h	$\frac{aJ}{\beta h}$	$\frac{\gamma}{\eta}$	aJ	γh
121211	a	h	indefinite $nh^0 = \frac{\zeta h}{\epsilon}$	h	indefinite $nh^0 = \frac{\zeta h}{\epsilon}$	$\frac{\gamma h}{\alpha a}$	indefinite	$aJ = \frac{\gamma\eta h^2}{\alpha a}$
121212	a	h	indefinite $nh^0 = \frac{\gamma\eta h^2}{\alpha\epsilon a}$	h	indefinite $nh^0 = \frac{\gamma\eta h^2}{\alpha\epsilon a}$	$\frac{\gamma h}{\alpha a}$	indefinite	$aJ = \frac{\gamma\eta h^2}{\alpha a}$
121221	a	h	indefinite $nh^0 = \frac{\zeta h}{\epsilon}$	h	indefinite $nh^0 = \frac{\zeta h}{\epsilon}$	$\frac{\gamma}{\eta}$	indefinite	γh
121222	a	h	indefinite $nh^0 = \frac{\gamma h}{\epsilon}$	h	indefinite $nh^0 = \frac{\gamma h}{\epsilon}$	$\frac{\gamma}{\eta}$	indefinite	γh
122111	a	$\frac{a^{\frac{1}{2}}J^{\frac{1}{2}}}{\beta^{\frac{1}{2}}}$	$\frac{\zeta\beta^{\frac{1}{2}}h}{\epsilon a^{\frac{1}{2}}J^{\frac{1}{2}}}$	h	$\frac{a^{\frac{1}{2}}J^{\frac{1}{2}}}{\beta^{\frac{1}{2}}}$	$\frac{\gamma J^{\frac{1}{2}}}{\alpha\beta^{\frac{1}{2}}a^{\frac{1}{2}}}$	aJ	$\frac{\eta\gamma hJ^{\frac{1}{2}}}{\alpha\beta^{\frac{1}{2}}a^{\frac{1}{2}}}$
122112	a	$\frac{a^{\frac{1}{2}}J^{\frac{1}{2}}}{\beta^{\frac{1}{2}}}$	$\frac{\eta\gamma h}{\epsilon\alpha a}$	h	$\frac{a^{\frac{1}{2}}J^{\frac{1}{2}}}{\beta^{\frac{1}{2}}}$	$\frac{\gamma J^{\frac{1}{2}}}{\alpha\beta^{\frac{1}{2}}a^{\frac{1}{2}}}$	aJ	$\frac{\eta\gamma hJ^{\frac{1}{2}}}{\alpha\beta^{\frac{1}{2}}a^{\frac{1}{2}}}$
122121	a	$\frac{a^{\frac{1}{2}}J^{\frac{1}{2}}}{\beta^{\frac{1}{2}}}$	$\frac{\zeta\beta^{\frac{1}{2}}h}{\epsilon a^{\frac{1}{2}}J^{\frac{1}{2}}}$	h	$\frac{a^{\frac{1}{2}}J^{\frac{1}{2}}}{\beta^{\frac{1}{2}}}$	$\frac{\gamma a^{\frac{1}{2}}J^{\frac{1}{2}}}{\eta\beta^{\frac{1}{2}}h}$	aJ	$\frac{\gamma a^{\frac{1}{2}}J^{\frac{1}{2}}}{\beta^{\frac{1}{2}}}$
122122	a	$\frac{a^{\frac{1}{2}}J^{\frac{1}{2}}}{\beta^{\frac{1}{2}}}$	$\frac{\gamma}{\epsilon}$	h	$\frac{a^{\frac{1}{2}}J^{\frac{1}{2}}}{\beta^{\frac{1}{2}}}$	$\frac{\gamma a^{\frac{1}{2}}J^{\frac{1}{2}}}{\eta\beta^{\frac{1}{2}}h}$	aJ	$\frac{\gamma a^{\frac{1}{2}}J^{\frac{1}{2}}}{\beta^{\frac{1}{2}}}$
122211	a	$\frac{\alpha a^2J}{\eta\gamma h}$	$\frac{\eta\gamma\zeta h^2}{\alpha\epsilon a^2J}$	h	$\frac{\alpha a^2J}{\eta\gamma h}$	$\frac{aJ}{\eta h}$	$\frac{\alpha^2\beta a^4J^2}{\eta^2\gamma^2h^2}$	aJ
122212	a	$\frac{\alpha a^2J}{\eta\gamma h}$	$\frac{\eta\gamma h}{\alpha\epsilon a}$	h	$\frac{\alpha a^2J}{\eta\gamma h}$	$\frac{aJ}{\eta h}$	$\frac{\alpha^2\beta a^4J^2}{\eta^2\gamma^2h^2}$	aJ
122221	a	$\frac{aJ}{\gamma}$	$\frac{\gamma\zeta h}{\epsilon aJ}$	h	$\frac{aJ}{\gamma}$	$\frac{aJ}{\eta h}$	$\frac{\beta a^2J^2}{\gamma^2}$	aJ
122222	a	$\frac{aJ}{\gamma}$	$\frac{\gamma}{\epsilon}$	h	$\frac{aJ}{\gamma}$	$\frac{aJ}{\eta h}$	$\frac{\beta a^2J^2}{\gamma^2}$	aJ

The analysis according to DUBOC consists of considering all possible combinations between one of each of the following six groups of equations, which are simplifications of equations (4)–(9):

$$\left.\begin{array}{llll} (1) & a = a^0 & (2) & a = a^+ \\ (1) & h = h^0 & (2) & h = h^- \\ (1) & a^+ = h^- & (2) & a^+ = n \\ (1) & a^0 J = I & (2) & a^0 J = R \\ (1) & L = C & (2) & L = R \\ (1) & E = B & (2) & E = R \end{array}\right\} \quad \left.\begin{array}{ll} (3) & p = h^- \\ (4) & p = n \end{array}\right\} \qquad (10)$$

The selected combination will be indicated by a code number consisting of six digits. Each digit corresponds to one row of equation (10) and indicates which equation of the corresponding row has been selected. For example, a situation described by 111111 indicates $a = a^0$(or $a^+ \ll a^0$), $h = h^0$, $a^+ = h^-$, $a^0 J = I$, $L = C$, and $E = B$. These selections of simplified equations can be solved very easily. In Table 1, for example, the values of a^0, a^+, h^0, h^-, n, p, I, and R are given as functions of J for 32 of the more commonly occurring situations in sulphide phosphors. The solutions for C, L, B, and E have been omitted from this table for brevity, but they can be derived immediately from the values of a^0, a^+, h^0, h^-, n, and p. (The meaning of the parameters α, β, &c. is shown in Fig. 4.)

Combinations with $a = a^+$ (saturation) and with $p = n$ or $p = h^-$ have been left out for brevity. Situations with $a = a^+$ may, however, arise at low temperatures when $a < h$ or at high exciting densities. With materials showing complete or partial p-type photoconduction (e.g. PbO), the condition $p = h^-$ would be more appropriate.

The escape rates of holes from A and electrons from H are determined by the parameters γ and ζ, respectively, where:

$$\gamma = \alpha N_p \exp(-E_a/kT) \qquad (11)$$

and

$$\zeta = \epsilon N_c \exp(-E_h/kT) \qquad (12)$$

E_a = energy difference between A and the top of the occupied band.

E_h = energy difference between H and the bottom of the conduction band.

N_p = effective density of the states in the occupied band

$$= 2(2\pi m_h^* kT/h^2)^{\frac{3}{2}}.$$

N_c = effective density of the states in the empty band

$$= 2(2\pi m_e^* kT/h^2)^{\frac{3}{2}}.$$

m_e^* and m_h^* are the effective masses of the free electrons and holes, respectively.

In considering the effect of temperature on the stationary state, we shall make the simplifying assumption that changes in the parameters α, β, ϵ, and η, which represent capture cross-sections multiplied by the thermal velocities of electrons or holes, can be neglected in comparison with the rapid change with temperature of the exponential factors in γ and ζ. This means that zero or very small activation energies are involved in the corresponding recombination processes. For a radiationless transition this is generally the case if the potential energy curves for the initial and final states are similar to those shown in Fig. 1(b).

It is generally accepted that transitions C, E, and R and the radiating transition I can occur at all temperatures, down to very low ones. If this were not the case, it might, for example, be possible to prevent trapping of electrons or holes by cooling. The effects of such "heat barriers" have been discussed by ADIROWITSCH.[16]

Although such effects are not taken into account in the present analysis, one could easily extend the analysis to include such temperature-dependent recombination processes and to see what effect they would have on the variation with temperature of the fluorescence intensity.

Support for the assumption that at least some of

the recombination coefficients are not strongly temperature-dependent comes from the analysis[13] of the photocurrent in a CdSe crystal at various temperatures, as determined by BUBE.[17] It was found that at very low light intensities the density of free electrons is given by $U/\epsilon h$ and at very high intensities by either $U/\beta h$ or by $\alpha a U/\beta\eta h^2$. No marked effect of the temperature was found in these two extreme ranges, showing that the temperature has little effect on the capture cross-sections involved. The intermediate, superlinear range, however, shifted considerably with temperature, the intensity at which n is superlinear with U being equal to $\eta\gamma h^2/\alpha a$ which contains the term $\exp(-E_a/kT)$.

Since N_p and N_c vary only with the 3/2 power of T, their change with temperature is sufficiently slow in the temperature range of interest for it to be assumed that they are substantially constant.

(b) *Graphical representation*

The study of the effect of temperature on the stationary state is greatly aided by a graphical representation of all relevant quantities simultaneously. To draw such a representation, one has first to establish which situation arises for $T \to 0$.

If $h < a$, all H levels will become occupied at low temperatures even at low excitation densities. On the other hand, with $h > a$, all activator levels become empty and a state of saturation will be reached in which there could be no excitation at all in our model, since $a^0 J$ would become zero too. We shall limit ourselves to the first case only.

Since $\gamma \to 0$ for $T \to 0$, very few holes will escape from A and consequently $p \ll a^+$, and at the same time $R \ll I$ at sufficiently low temperatures. Also, at sufficiently low exciting intensities, $n < h^-$ and therefore $a^+ = h^-$. With $h^- = h$ and $aJ = I$, $n = aJ/\beta h$. If one increases J, n will thus increase linearly with J at low temperatures until it becomes of the same order of magnitude as h at $J = \beta h^2/a$. With $aJ > \beta h^2$, the appropriate approximation of equation (6) is: $n = a^+$.

At still higher intensities a^+ may become of the same order of magnitude as a, but we shall not consider this case here.

It follows from the above that for $aJ \ll \beta h^2$, the first four digits of the code number, characterizing the low-temperature conditions, are 1211, and for $aJ \gg \beta h^2$, 1221.

The last two digits are fixed as follows: according to equation (8) with $a^+ = h^- = h$ and $a^0 = a$:

$$\gamma h = \alpha p a + \eta p h.$$

Now $C/R = \alpha a/\eta h$ and the fifth digit is therefore determined by this ratio.

If $\alpha a/\eta h > 1$, $L = C$ and if < 1, $L = R$.

To select the last digit, one deduces from Table 1 that for the situations 1211 . . the ratio B/R contains the factor ζ/γ and thus the term $\exp[(E_a - E_h)/kT]$. This exponential term approaches zero for $T \to 0$ if $E_h > E_a$ and becomes infinite for $T = 0$ if $E_h < E_a$. The last digit is therefore 1 ($E = B$) if $E_h < E_a$, or 2 if $E_h > E_a$.

Summarizing, we conclude that for $h < a$ and $a^+ < a$ there are eight possible initial conditions for $T \to 0$ dependent on the choice of parameters as shown in Table 2.

Table 2. Initial situations for $T \to 0$

Code number	$aJ/\beta h^2$	$\alpha a/\eta h$	E_a/E_h
121111	< 1	> 1	> 1
121112	< 1	> 1	< 1
121121	< 1	< 1	> 1
121122	< 1	< 1	< 1
122111	> 1	> 1	> 1
122112	> 1	> 1	< 1
122121	> 1	< 1	> 1
122122	> 1	< 1	< 1

Let us assume, for example, that the parameters are chosen such that the initial situation is characterized by 121112. When the temperature is

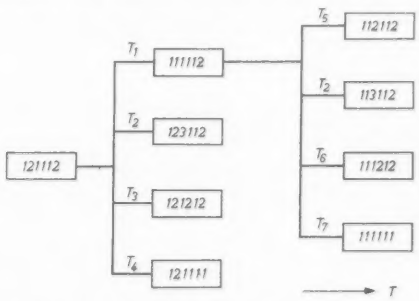

FIG. 5. Pedigree of code numbers indicating which situations may possibly arise out of the low-temperature situation 121112 when the temperature is raised.

raised, various new situations may arise, as illustrated in Fig. 5.

The quantities which are mainly affected by a change in temperature are those depending on ζ and γ, viz. h^0, p, R, B, C, E, and L. One sees from Table 1 that $h^0 = \beta\eta\gamma h^3/\alpha\epsilon a^2 J$. The situation 121112 may therefore change into 111112 if h^0 gets an opportunity to become equal to h when γ has increased to the value $\alpha\epsilon a^2 J/\beta\eta h^2$ or, with equation (11), at the temperature T_1 where

$$T_1 = \frac{E_a}{k \ln\left\{\dfrac{\beta\eta N_p h^2}{\epsilon a^2 J}\right\}}.$$

Similarly one finds:

$$T_3 = \frac{E_a}{k \ln\left\{\dfrac{\eta h^2 N_p}{a^2 J}\right\}} \quad \text{and} \quad T_4 = \frac{E_h - E_a}{k \ln\left\{\dfrac{\epsilon a N_c}{\eta h N_p}\right\}}.$$

Temperature quenching of the fluorescence (121112 → 121212) will occur at T_3 if $T_3 < T_1$, T_2, T_4.

Now let us assume that of the four temperatures T_1 is the lowest. Consequently the situation changes at that temperature to 111112. In this situation the quantum efficiency is still unity, but from this situation a new one, 111212, may arise, where the fluorescence is quenched. To reach this

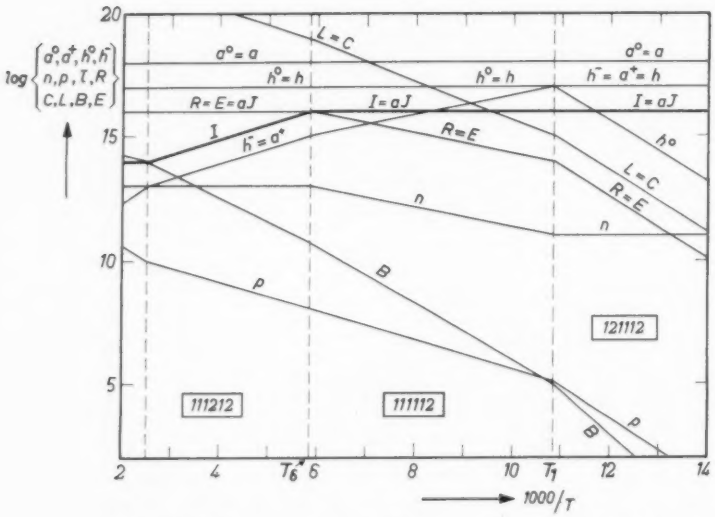

FIG. 6. First-approximation behaviour chart of a model with parameters: $a = 10^{18}$, $h = 10^{17}$, $J = 10^{-2}$, $\beta = 10^{-12}$, $\epsilon = 10^{-14}$, $\eta = 10^{-8}$, $\alpha = 10^{-8}$, $N_p = N_c = 10^{19}$, $E_a = 0{\cdot}24$ eV and $E_h = 0{\cdot}32$ eV.

For the transition to be possible at all, $\beta\eta N_p h^2/\epsilon a^2 J$ must be greater than unity.

With increasing temperature p also increases, however, and the situation may change instead to 123112 at

$$T_2 = \frac{E_a}{k \ln\left\{\dfrac{N_p}{a}\right\}}$$

if $T_2 < T_1$.

situation, T_6 (Fig. 5) must be lower than T_2, T_5, or T_7, where:

$$T_5 = \frac{E_a}{k \ln\left\{\dfrac{\eta N_p J^{\frac{1}{2}}}{\epsilon h a^{\frac{1}{2}} \beta^{\frac{1}{2}}}\right\}} \qquad T_6 = \frac{E_a}{k \ln\left\{\dfrac{\epsilon^2 \eta h^2 N_p}{\beta^2 a^2 J}\right\}}$$

$$T_7 = \frac{3E_h - 2E_a}{k \ln\left\{\dfrac{\beta\epsilon^2 a N_c^3}{\eta^2 h J N_p^2}\right\}}.$$

The conditions $T_1 < T_2$, T_3, T_4 and $T_6 < T_5$, T_2, T_7 are, for example, satisfied by the following choice of parameters:

$a = 10^{18}\,\mathrm{cm}^{-3}$; $h = 10^{17}\,\mathrm{cm}^{-3}$; $J = 10^{-2}\,\mathrm{sec}^{-1}$;* $\beta = 10^{-12}\,\mathrm{cm}^3\mathrm{sec}^{-1}$; $\epsilon = 10^{-14}\,\mathrm{cm}^3\mathrm{sec}^{-1}$; $\eta = 10^{-8}\,\mathrm{cm}^3\mathrm{sec}^{-1}$; $\alpha = 10^{-8}\,\mathrm{cm}^3\mathrm{sec}^{-1}$; $N_p = N_c = 10^{19}\,\mathrm{cm}^{-3}$; $E_a = 0{\cdot}24\,\mathrm{eV}$; and $E_h = 0{\cdot}32\,\mathrm{eV}$.

In Fig. 6 the logarithms of all relevant quantities are plotted against $1/T$. Straight lines are thus obtained with a slope of $-E_a/k$ for h^0, L, C, R, E, and p and a slope $-E_h/k$ for B in the lowest temperature range (121112).

On raising the temperature practically all H levels are emptied at $T = 92°\mathrm{K}(T_1)$, since at that temperature the line representing $\log h^0$ crosses the line $h^- = h$. The situation now changes to 111112. The line representing $\log R$ and having a slope $-E_a/3k$ cuts the line $I = aJ$ at $T = 170°\mathrm{K}(T_6)$. Temperature quenching sets in, and on further increase of temperature the fluorescence intensity falls proportionally to $\exp(E_a/2kT)$.

The lines shown in Fig. 6 give only approximate values. They are in fact asymptotes to the curves representing the real values. The difference between the asymptotic and real values will be largest in the transition range between two situations. In such a transition range two terms on the right-hand side of one of the equations (4)–(9) become of the same order of magnitude. In order to obtain a more satisfactory approximation, this particular equation must not be simplified. In the case of the transition $111112 \rightarrow 111212$, for example, the complete equation (7) should be used:

$$aJ = \beta n a^+ + \eta p h^-.$$

One can easily check with the aid of Fig. 6 that little would be gained by taking into account the other neglected terms.

Solving the new set of equations (including the complete equation (7)), one finds that I in the transition (quenching) range is represented with satisfactory accuracy by:

$$aJ = I + \frac{\epsilon^{\frac{1}{2}}\eta^{\frac{1}{2}}\gamma^{\frac{1}{2}}h^{\frac{3}{2}}}{\alpha^{\frac{1}{2}}\beta^{\frac{3}{2}}a^{\frac{1}{2}}} I^{\frac{3}{2}}. \qquad (13)$$

With this equation I can be calculated as a function of T, and the result is shown by curve a of Fig. 7.

We shall now repeat the same procedure, keeping all parameters the same except ϵ, which will be increased from 10^{-14} to 10^{-10}.

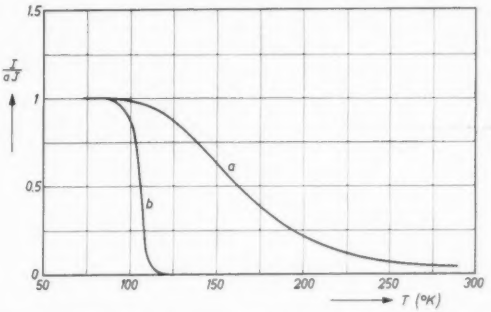

FIG. 7. Accurate calculation of I for: (a) the transition range $111112 \rightarrow 111212$ of Fig. 6 and (b) the transition range $121112 \rightarrow 121212 \rightarrow 111212$ of Fig. 8.

The low-temperature situation 121112 no longer changes to 111112, but instead to 121212 at $T = 109°\mathrm{K}(T_3)$, as shown in Fig. 8. This new situation is a special one in which the simplified equations do not lead to a definite expression for n, h^0, and I. Only the product nh^0 is defined $(= \eta\gamma h^2/\alpha\epsilon a)$.

This means that in our first approximation n, h^0, and I jump discontinuously, while a^0, a^+, h^-, and p remain constant. Since I cannot increase—having already its maximum value aJ—it can only decrease at this temperature, in the same way as n.

Since nh^0 must remain constant, h^0 will increase until it reaches the value h, when the situation changes to 111212. Because in this case not only I and R become of the same order of magnitude over a short temperature range but also h^0 and h^-, the complete equations (5) and (7) should now be used in order to obtain a satisfactory representation of the change of I with temperature in the quenching range. In Fig. 9 the result is plotted as $\log I$ against $1/T$, together with the asymptotes calculated from a complete set of simplified equations, while curve b in Fig. 7 shows I as a function of T.

Fig. 7 clearly demonstrates how a change in one

* This value corresponds to $U = 10^{16}\,\mathrm{cm}^{-3}\mathrm{sec}^{-1}$. Such a density of excitation would be obtained approximately with the 3650 Å radiation from a 125-W high-pressure mercury-discharge lamp at a distance of a few metres, assuming the absorption cross-section of the absorbing activator centres for the exciting radiation to be $10^{-15}\,\mathrm{cm}^2$.

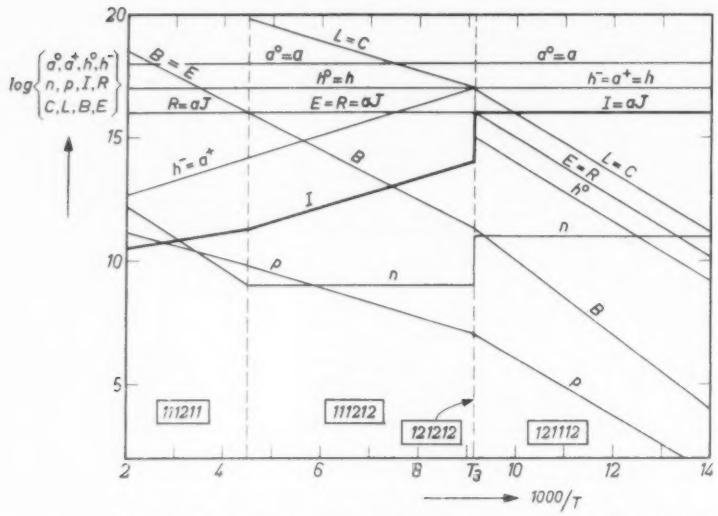

FIG. 8. First-approximation behaviour chart of a model with the same parameters as those of Fig. 6, except $\epsilon = 10^{-10}$.

of the capture cross-sections may alter completely the character of a temperature-dependence curve of the fluorescent intensity. When the curves of Fig. 7 are plotted in the conventional way as

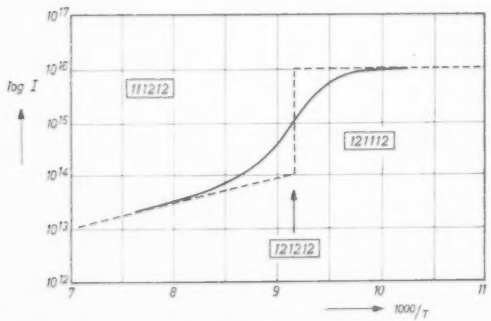

FIG. 9. Section of Fig. 8 showing the actual behaviour of I near the "indefinite" situation 121212.

$\log (I_0/I-1)$ versus T^{-1}, no straight lines are obtained and no conclusion can be drawn at all regarding, for example, the position of the impurity levels.

The above theory of temperature quenching by hole migration has sometimes been criticized[18] by pointing out that no p-conductivity has so far been found in the quenching range of a phosphor. One can immediately verify, however, from Figs. 6 and 8, that, although free holes are indeed necessary to shift the recombination process from A to H, the density of free holes may well remain some orders of magnitude below the density of free electrons. The reason is that β in our example, as well as in actual phosphors,[15] is small compared with α and η.

It is furthermore not surprising that a change in the density of excitation by changing the intensity of the exciting radiation or its wavelength may alter the character of the temperature-dependence completely.

3. CORRECT FORMULAE FOR THE TEMPERATURE-DEPENDENCE OF SULPHIDE PHOSPHORS

In the previous section it has been demonstrated that a temperature-dependence curve of a photoconducting phosphor, if analysed in the same way as is commonly done for non-photoconducting phosphors, will not give any information regarding the position of the impurity levels. In this section we shall consider how a temperature-dependence curve should in fact be analysed in order to obtain such information.

In the temperature range where the fluorescence is quenched from $I = U$ to a lower value, a change takes place, in terms of our code system, in the

fourth digit of the code number describing the situation. In this range, as has been argued above, the complete equation (7) should be used in combination with the appropriate simplified forms of the other equations. From the latter equations, giving simple relations between the six unknowns a^0, a^+, h^0, h^-, n, and p, five of the unknowns can be expressed as a simple power of the remaining sixth. By inserting these values in the complete equation (7), a relation of the following nature is then found:

$$U = I + DI^r \exp(-E/kT), \tag{14}$$

where D and r are constants and E is a function of E_a and E_h.

A particular example has already been worked out in the previous section for the transition 111112 → 111212.

Since, at low temperatures, $I = U = I_0$, also

$$I_0 = I + DI^r \exp(-E/kT).$$

The value of the "activation energy" E can thus be obtained by plotting $\log\{(I_0/I)^r - (I/I_0)^{1-r}\}$ versus T^{-1}. The value of r has to be estimated separately as follows.

In the high-temperature part where $I \ll R$, the relation between I and U is, from equation (14):

$$I = U^{1/r} D^{-1/r} \exp\{E/rkT\}. \tag{15}$$

By observing how I changes with U at constant temperature in the high-temperature range, the values of r can be estimated.

This was done, for example, for the (ZnCd)S–Cu phosphor of Fig. 2. At 270°C the fluorescence intensity was found to increase with the square of the exciting intensity, indicating that $r = \frac{1}{2}$. When plotting $\log\{(I_0/I)^{\frac{1}{2}} - (I/I_0)^{\frac{1}{2}}\}$ against $1/T$, straight lines were indeed obtained with slopes corresponding to $E = 0{\cdot}73$ eV.

However, from this value of E no definite conclusion can still be drawn regarding the position of A or H. To do this, the actual conditions during the transition have to be known or, in other words, the relevant code numbers must be determined. When they are known, the value of E can be read from Table 1.

For example, when the transition is from 111111 to 111211, we see from Table 1 that in the high-temperature range where $I \ll U$:

$$I = \alpha\beta\zeta a^2 J/\epsilon\gamma\gamma h = \beta N_c a U \eta^{-1} N_p^{-1} h^{-1} \exp\{(E_a - E_h)/kT\} \tag{16}$$

or $E = E_a - E_h$.

For four cases of Table 1, where the situations 1212 . . are involved, the relation between I and R is more complex.

Such cases can be recognized in practice by a more than quadratic dependence of I upon J in the quenching range. In these cases an approximate value of E_a can be deduced from the low-temperature part of the temperature-dependence curve which can be described by one of the four code numbers 1211.

Since $I = I_0 - R$ and, from Table 1, $R = N_p \eta h^2 a^{-1} \exp(-E_a/kT)$ for the situations 121111 and 121112, or $\mathbf{N}_p \alpha h \exp(-E_a/kT)$ for the situations 121121 and 121122, E_a can be obtained by plotting $\log(I_0 - I)$ versus T^{-1}. A curve will be obtained whose slope in the low-temperature range corresponds to $-E_a/k$. No very accurate values will be thus obtained, since only the initial, high-temperature part of the temperature-dependence curve can be used.

In all other cases, where not such a strongly superlinear relation between I and J is found in the range $I \ll R$, the complete curve can be used, but other measures have to be taken to determine the actual nature of the transition.

This has been done in the case of ZnS–Ag, Co, where the effect of the cobalt concentration on the temperature-dependence was studied.[10]

4. TEMPERATURE-DEPENDENCE OF ZnS–Ag, Co

On excitation with 3650 Å radiation at temperatures above the quenching temperature, the fluorescence intensity was found to be proportional to the square of the intensity of the exciting radiation,[19] indicating that $r = \frac{1}{2}$.

It has furthermore been shown[10] that the temperature-dependence of this phosphor is strongly dependent on the cobalt content above a certain minimum concentration of about 10^{-7} atoms per mole ZnS.

When $\log\{(I_0/I)^{\frac{1}{2}} - (I/I_0)^{\frac{1}{2}}\}$ was plotted against $1/T$, straight lines were obtained in accordance with equation (14) for $r = \frac{1}{2}$. The slope of these lines corresponded to an activation energy of 0·36

eV. Finally, the constant D in equation (14) was found to be proportional to the cobalt content. From these data it is indeed possible to establish the relevant code numbers and the actual position of the silver level in ZnS.

This is done with the aid of Table 3, where the values of r and E are shown for all possible quenching transitions between the situations of Table 1 except for those cases where an "indefinite" situation is involved, as discussed above, and where the fluorescence intensity increases very strongly with the exciting intensity in the quenching range ($r < \frac{1}{2}$). Also given in this table is the power m in the relation between the constant D and h (= cobalt concentration).

The quenching transitions 112112 → 112212 and 112122 → 112222 cannot occur. In the situations 112112 and 112212, I and R are not affected by the temperature. The situations 112122 and 112222 can occur only at one particular temperature in our first approximation where $\gamma = \epsilon h$. If such a situation does occur, p and h^- will change rapidly at this temperature, with I and R remaining unaltered until a new situation has been established.

Table 3

Transition	r	m	E
111111 → 111211	1	1	$E_a - E_h$
111112 → 111212	$\frac{2}{3}$	$\frac{2}{3}$	$\frac{1}{3}E_a$
111121 → 111221	$\frac{1}{2}$	$\frac{1}{2}$	$E_a - \frac{1}{2}E_h$
111122 → 111222	$\frac{1}{2}$	$\frac{1}{2}$	$\frac{1}{2}E_a$
112111 → 112211	1	1	$E_a - E_h$
112121 → 112221	$\frac{1}{2}$	0	E_a
122111 → 122211	$\frac{1}{2}$	1	E_a
122112 → 122212	$\frac{1}{2}$	1	E_a
122121 → 122221	$\frac{1}{2}$	0	E_a
122122 → 122222	$\frac{1}{2}$	0	E_a

We see from Table 3 that the combination $r = \frac{1}{2}$ and $m = 1$ occurs for only two transitions, 122111 → 122211 or 122112 → 122212, each giving for the activation energy the actual distance between the silver level and the top of the occupied band.

At cobalt concentrations above 10^{-5} atoms per mole ZnS, a different type of temperature-dependence curve was observed, although r was still found to be $\frac{1}{2}$. When $\log\{(I_0/I)^{\frac{1}{2}} - (I/I_0)^{\frac{1}{2}}\}$ was plotted for those phosphors against T^{-1}, a slope was found which was approximately half the slope at low cobalt concentrations. Since at high values of h higher exciting intensities are required to reach the conditions $n \gg h$, the third digit of the initial situation is more likely to be 1, indicating that $a^+ \sim h^-$. Where E was found to be $E_a/2$, the transition at high cobalt contents may well be from 111122 to 111222.

Returning to Table 3, one notices that for all cases where $n = a^+(\ldots 2 \ldots)$, the value of r is $\frac{1}{2}$ and $E = E_a$ except for one case (112111 → 112211), where $r = 1$ and $E = E_a - E_h$. The latter transition can immediately be recognized, since the temperature-dependence curve would not shift with the exciting intensity in such a case with I and R both proportional to J. In all other cases a plot of $\log\{(I_0/I)^{\frac{1}{2}} - (I/I_0)^{\frac{1}{2}}\}$ versus T^{-1} immediately gives the value of E_a.

The best way to proceed, when endeavouring to establish the position of the A level, is to avoid the first five transitions of Table 3 and to measure therefore the temperature-dependence at high exciting intensities—though not so high that saturation occurs—of phosphors with a sufficiently low content of deep traps to ensure that $n = a^+$.

Since this condition was probably fulfilled in the case of the $(Zn_{0.85}, Cd_{0.15})S$–Cu phosphor of Fig. 2—supported by the fact that r was found to be $\frac{1}{2}$—one can conclude fairly safely that the copper level in this phosphor is 0·73 eV above the top of the occupied band.

An examination of Table 2 of ref. (13) will show that the same conclusion holds with band-to-band excitation.

When exciting a ZnS phosphor with short-wave ultraviolet radiation having a wavelength shorter than that corresponding to the edge of the fundamental absorption, it has been observed[5] that the fluorescence was quenched at a lower temperature than that at which the same phosphor was excited with longer wavelengths corresponding to the tail of the absorption curve. From the fact that the rate of excitation is higher in the first case because of the strong absorption of such a radiation, one would have expected a shift of the temperature-dependence curve to higher temperatures.

That the opposite occurs may well indicate that surface states which naturally are of more importance when the excitation takes place in a thin

layer near the surface, may well outnumber the quenching states in the bulk of the material.

5. CONCLUSIONS

(1) It has been shown that the two-state model, with one state below the dark Fermi level, giving rise to a fluorescent transition, and the other an empty level, giving rise to a radiationless transition, can satisfactorily explain the temperature-dependence of sulphide-type phosphors and such effects as, for example, its change with exciting intensity, the incorporation of killers, and the nature of the exciting radiation.

(2) The best way to analyse the temperature-dependence curves of sulphide phosphors is to plot $\log\{(I_0/I)^r - (I/I_0)^{1-r}\}$ versus T^{-1}, where $1/r$ is the power of the intensity-dependence of the fluorescence at temperatures where the fluorescence is quenched for the greater part. One must be certain, however, that at low temperatures $I = U$, i.e. the quantum efficiency of the fluorescence must be near unity.

(3) From the activation energy thus determined, information regarding the position of the activated level can be obtained only by determining the nature of the transition, for example by studying the effect of the killer or activator content. The activation energy may well be found to be a combination of E_a and E_h and possibly even of activation energies for the recombination process themselves. E_h can often be measured separately, e.g. from a study of glow curves.

(4) The best way to determine the position of the activator level is to use a phosphor with a relatively high activator content and a low killer content and to measure its temperature-dependence at high excitation intensities. A plot of $\log\{(I_0/I)^{\frac{1}{2}} - (I/I_0)^{\frac{1}{2}}\}$ versus T^{-1} will then give a straight line with a slope of $-E_a$.

REFERENCES

1. Mott N. F., *Proc. Roy. Soc.* A**167,** 384 (1938).
2. Seitz F., *Trans. Faraday Soc.* **35,** 74 (1939).
3. Klasens H. A., *Nature, Lond.* **158,** 306 (1946).
4. Nail N. R., Pearlman D., and Urbach F., *Cornell Symposium on Solid Luminescent Materials*, p. 190. John Wiley and Sons, New York (1948).
5. Kröger F. A., *Some Aspects of the Luminescence of Solids* pp. 181–182. Elsevier, New York (1948).
6. Garlick G. F. J. and Gibson A. F., *J. Opt. Soc. Amer.* **39,** 935 (1949).
7. Vergunas F. I. and Gavrilov F. F., *Zh. eksp. teor. fiz.* **20,** 224 (1950).
8. Leverenz H. W., *R.C.A. Rev.* **7,** 199 (1946).
9. Garlick G. F. J. and Gibson A. F., *Nature, Lond.* **161,** 359 (1948).
10. Hill C. G. A. and Klasens H. A., *J. Electrochem. Soc.* **96,** 275 (1949).
11. Schön M., *Z. Phys.* **119,** 463 (1942); *Ann. Phys.* **3,** 333 (1948).
12. Hoogenstraaten W., *J. Electrochem. Soc.* **100,** 356 (1953).
13. Klasens H. A., *J. Phys. Chem. Solids* **7,** 175 (1958).
14. Duboc C. A., *Brit. J. Appl. Phys.* **6,** Suppl. **4,** 107 (1955).
15. Hoogenstraaten W. and Klasens H. A., *J. Electrochem. Soc.*, **100,** 366 (1953).
16. Adirowitsch E. I., *Einige Fragen zur Theorie der Lumineszenz der Kristalle* pp. 261–268. Akademie Verlag, Berlin (1953).
17. Bube R. H., *Proc. Inst. Radio Engrs.* **43,** 1836 (1955).
18. Garlick G. F. J., *Progr. Semiconductors* **1,** 109 (1956).
19. Klasens H. A., Ramsden W., and Chow Q., *J. Opt. Soc. Amer.* **38,** 60 (1948).

J. Phys. Chem. Solids Pergamon Press 1959. Vol. 9. pp. 198–213. Printed in Great Britain.

A HEAT-CAPACITY FUNCTION WITH VELOCITY DISPERSION FOR ISOTROPIC SOLIDS

S. W. BARBER and B. MARTIN

Owens-Illinois Glass Company, Toledo, Ohio

(*Received* 12 *April* 1958; *revised* 11 *September* 1958)

Abstract—Structural interpretation of the low-temperature heat capacities of glass has required the derivation of a new function for the lattice heat capacities of isotropic solids. The new formulation permits estimates to be made of acoustic cut-off frequencies and corresponding limiting wavelength. The latter is twice the effective mean distance between centers of primitive cells.

No primitive cells are known for glasses from independent evidence. Consequently, the function is verified by comparison with the lattice heat capacities of monatomic crystals having one-atom primitive cells. Deviations from the function are expected because of the unavoidable anisotropies of the crystals, but these are surprisingly small and easily recognizable. Except for these deviations and uncertainties in experimental lattice heat capacities, the function appears to agree well with experiment at all values of C_v up to its classical limit.

The function is applied to diamond, which has a two-atom primitive cell, to illustrate the manner in which wrong choices of the cell become evident. For both diamond and NaCl, it is shown that this scheme of calculation yields results in good accord with published calculations on lattice dynamics.

Application of the function to glasses involves unique considerations and is reserved for a separate paper. The function can be used to make approximate calculations for moderately anisotropic crystals (see Appendix II).

VOL
9
195

INTRODUCTION

ONE of the first triumphs of quantum statistics was a theory to account for the low-temperature heat capacity of solids.(1) Following EINSTEIN's basic function for the energy of an isolated oscillator, first published in 1906, the first quantitative function to represent the temperature-dependence of the heat capacities associated with the broad array of acoustic frequencies in solids was proposed by DEBYE in 1912. Almost simultaneously, a more accurate discussion based on lattice dynamics by BORN and VON KARMAN made evident some of the shortcomings of the Debye "continuum" treatment. There followed a data-collecting period during which no decisive advances in theory appeared, but which yielded many important deviations from Debye theory. After more than twenty years, BLACKMAN,(2) in an extensive criticism of the Debye function, concluded that "a perfect Debye curve is an extremely rare and probably accidental occurrence" (I, p. 382). Of particular interest in this discussion is his judgment that the Debye T^3 law holds only at $T < \Theta/50$ rather than at $T < \Theta/10$ as indicated by Debye theory (III, p. 122). For most crystals, this corresponds to temperatures lower than any existing measurements, and observed apparent conformity with the T^3 law at higher temperatures must be "spurious". BLACKMAN's judgment (ref. (2), III) is amply justified by the present work.

Since BLACKMAN, there have been many discussions of various crystal lattices.(3) In general, the limitation of the Debye function for any but very approximate or restricted uses is accepted. Probably because most of the later work emphasizes the dependence of the frequency spectra on the many different lattice symmetries, no generalized function superior to Debye's has been generally adopted. (See, however, footnote re equation (13).) The convenience of published tables of the Debye function has led to its continued wide use in spite of its known limitations. It has become customary to portray the experimental low-temperature specific heats of solids by plotting Debye thetas as functions of temperature as done,

VOL. 9 1959

for instance, by DeSorbo,[4] and theoretical functions relating the Debye theta to temperature have been derived from lattice dynamics.[3] As pointed out by Brillouin,[5] the Debye theory neglects the effect of frequency on phase velocity (it assumes constant phase velocity), assumes the "shape of the first zone" to be spherical, and, in spite of quite different velocities of longitudinal and transverse acoustic waves, assumes a common cut-off frequency for them. We shall derive an approximate formula based on a plausible dispersion relation for the elastic waves, and separate cut-off frequencies for longitudinal and transverse waves. The latter is based on the assumption that a common limiting wavelength rather than a common cut-off frequency characterizes the two types of acoustic waves. Since we are ultimately concerned with glasses, we shall assume the first zone to be spherical.

As part of a comprehensive study of glass structure, the low-temperature heat capacities of a series of oxide glasses and related crystals were measured.[6] In the case of crystals, the study of structure is best done by taking advantage of the well-defined planes of atoms, the related symmetries, and the directional properties of single crystals rather than by attempting the analysis of a property such as heat capacity in which the measured quantities involve integrations over all frequencies of thermal motion and over all directions in invariably anisotropic materials. In the case of glass there are no detectible atomic planes, and such advantage is lost. Furthermore, the nearly perfect macroscopic isotropy of glass makes application of a Debye-like function uniquely appropriate. Such an approach can yield only average structural parameters, but this is no serious objection because even diffraction techniques can yield only average configurations involving but few interatomic distances. With some reservations not considered important here, only those frequencies which can propagate through the nonmetallic solids as sound waves make measurable contributions to heat capacity (C_v) at T near 0°K. Consequently, it is possible to approximate some of the details of the low-frequency part of the spectrum of thermal oscillations from details of the C_v versus T curve near 0°K. In the case of oxide glasses, because of limited applicability of more direct methods of study, the heat capacity in the "acoustic" range of temperatures remains as one of a relatively few means of investigating structure in dimensions between first-neighbor distances and polymer cross-sections.

Preliminary attempts to discuss the low-temperature C_v versus T curves for glasses based on published values of the Debye and similar[7] functions led only to suggestive results[8] which, on further consideration, had to be rejected. The assumption of frequency-independent sound velocities in the derivations of such functions is not permissible in this application. As will be shown, the frequency-dependence of sound velocities has easily detectible effects on the shapes of C_v versus T curves, and incorporation of such dependence in our derivation yields a function remarkably faithful to the observed C_v versus T curves of many monatomic crystals, having no optical branches in their spectra, at all values of C_v up to its classical limit. As should be expected, observation indicates that the more isotropic a crystal is with respect to its acoustic frequency limits, the better is its conformance to the function. The application to glasses involves unique considerations and is reserved for a separate paper.

THE FUNCTION

Let r be the wave number of an elastic wave. Assuming isotropy, the number of modes, dn, with wave numbers between r and $r+dr$ is proportional to the volume of a spherical shell, $4\pi r^2\,dr$. Multiplying this volume in reciprocal space by a volume, V, in direct space yields

$$dn = 4\pi V r^2\,dr. \tag{1}$$

This is for one wave type, say longitudinal. The maximum number of modes possible in the volume V for a given wave direction (i.e. one degree of freedom per oscillator) is:

$$\int_0^{r_m} 4\pi V r^2\,dr = N, \tag{2}$$

where N is the number of oscillators in V. Integrating (2),

$$r_m = \left(\frac{3N}{4\pi V}\right)^{1/3} = 0{\cdot}6205\left(\frac{N}{V}\right)^{1/3}. \tag{3}$$

In a cubic lattice with spacing a, the maximum

wave number along a cubic axis would be:

$$\frac{1}{2a}=\frac{1}{2}\left(\frac{N}{V}\right)^{1/3}. \tag{4}$$

It is convenient to define an effective mean distance, $\bar{a}$, between the particles of an isotropic solid such that, from equation (3):

$$r_m=\frac{1}{2\bar{a}}. \tag{5}$$

It follows from equation (4) that

$$a=1{\cdot}241\bar{a}. \tag{6}$$

For our purposes, it is adequate to consider interactions between nearest neighbors only. Following BRILLOUIN'S[5] discussion (p. 31) of a one-dimensional lattice of identical particles, it is plausible to express the phase velocity, W, as

$$W=W_0\frac{\sin \pi r a'}{\pi r a'}, \tag{7}$$

in which W_0 is the limiting velocity as $r\to 0$, and a' is an effective distance to be ascertained. Examination of the secular equations for various three-dimensional solids indicates that the dispersion of acoustic waves in them is more complicated than formula (7), but that (7) is nevertheless a valuable approximation (see Appendix I). It does not seem useful at this stage of our study to investigate more complicated dispersion formulae such as, for instance, sums of such terms over distributions of a'.

The frequency is

$$\nu=Wr=W_0\frac{\sin \pi r a'}{\pi a'}. \tag{8}$$

At the boundary of the first idealized spherical zone, the group velocity $d\nu/dr$, must be zero. Thus

$$\cos \pi r_m a'=0$$

$$a'=\frac{1}{2r_m}.$$

Then from equations (5) and (6)

$$a'=\bar{a}=a/1{\cdot}241, \tag{9}$$

which identifies a' as the mean distance between attice points and a as the equivalent cubic lattice spacing. Then the cut-off frequency, ν_m, and the corresponding Θ are:

$$\nu_m=W_0/\pi\bar{a};\ \Theta=h\nu_m/k=hW_0/k\pi\bar{a}. \tag{10}$$

From equations (8) and (9)

$$r=\frac{1}{\pi\bar{a}}\sin^{-1}\left(\frac{\pi\nu\bar{a}}{W_0}\right) \tag{11}$$

$$dr=\frac{d\nu}{W_0\left[1-\left(\frac{\pi\nu\bar{a}}{W_0}\right)^2\right]^{\frac{1}{2}}}. \tag{12}$$

Putting equations (11) and (12) into (1), assigning three degrees of freedom to each oscillator, and using $V=6N\bar{a}^3/\pi$ as required by equations (3) and (5),

$$dn=g(\nu)\,d\nu=\frac{72N\bar{a}\left[\sin^{-1}\left(\frac{\pi\nu\bar{a}}{W_0}\right)\right]^2}{\pi^2W_0\left[1-\left(\frac{\pi\nu\bar{a}}{W_0}\right)^2\right]^{\frac{1}{2}}}\,d\nu. \tag{13}$$

The authors are indebted to Dr. O. L. ANDERSON, Bell Telephone Laboratories, for pointing out that SCHRÖDINGER[1c] has derived a function for *dn* which, in our notation, is one-third of formula (13). SCHRÖDINGER did not, however, formulate the corresponding heat-capacity function. Consequently, no corresponding table of C_v versus Θ/T values, such as Table 1, existed, and his formula could not be used conveniently for quantitative calculations.

The energy, E, associated with this distribution of frequencies is:

$$E=\int_0^{\nu_m}\frac{g(\nu)h\nu\,d\nu}{\exp\left(\frac{h\nu}{kT}\right)-1}. \tag{14}$$

The corresponding heat capacity is:

$$C_g=\frac{\partial E}{\partial T}=\frac{h^2}{kT^2}\int_0^{\nu_m}\frac{g(\nu)\nu^2\exp\left(\frac{h\nu}{kT}\right)d\nu}{\left[\exp\left(\frac{h\nu}{kT}\right)-1\right]^2}, \tag{15}$$

in which the subscript g distinguishes equation

(15), which is derived for one wave type, from any observable heat capacity, C_v.

Introducing the customary substitution,

$$x = \frac{h\nu}{kT} \tag{16}$$

$$\frac{C_q}{3R} = \frac{24}{\pi^3 x_0} \int_0^{x_0} \frac{x^2 e^x [\sin^{-1}(x/x_0)]^2 \, dx}{(e^x - 1)^2 [1-(x/x_0)^2]^{\frac{1}{2}}} \tag{17}$$

in which $x_0 = \Theta/T$. This Θ is not to be confused with the Θ_D calculated from Debye theory, but is related to it by

$$\Theta = \frac{2}{\pi} \Theta_D. \tag{18}$$

Equation (17) cannot be conveniently integrated, but it can be put into a form suitable for numerical integration by setting

$$\left.\begin{aligned} x &= x_0 y \\ dx &= x_0 \, dy. \end{aligned}\right\} \tag{19}$$

Then

$$\frac{C_q}{3R} = x_0^2 \left[\frac{e^{x_0}}{(e^{x_0}-1)^2} - \frac{8}{\pi^3} \times \int_0^1 \frac{(\sin^{-1} y)^3 e^{x_0 y} [(2y - x_0 y^2) e^{x_0 y} - (2y + x_0 y^2)] \, dy}{(e^{x_0 y} - 1)^3} \right] \tag{20}$$

Corresponding values of $C_v/3R$ and Θ/T are given in Table 1, and $C_v/3R$ versus Θ/T is plotted as equation (20) in Fig. 1 for comparison with the Debye curve for identical values of $\bar{a}$ and W_0.

COMPARISON OF THIS FUNCTION WITH THE DEBYE FUNCTION

For very small values of ν, the quantity $\sin^{-1}(\pi\nu\bar{a}/W_0)$ in equation (13) can be replaced by $\pi\nu\bar{a}/W_0$, and $[1-(\pi\nu\bar{a}/W_0)^2]$ approaches unity. Then, remembering that the Debye cut-off is $W_0/2a = \nu_D$, equation (13) leads to:

$$g(\nu) = \frac{72N\bar{a}^3\nu^2}{W_0^3} = \frac{9N\nu^2}{\nu_D^3}. \tag{21}$$

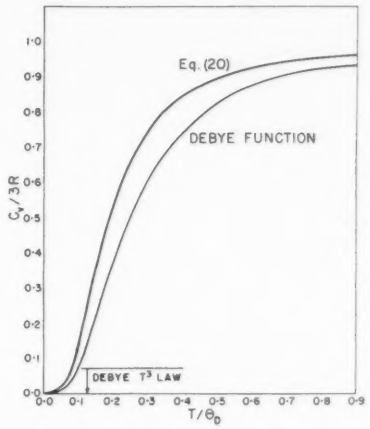

FIG. 1. Comparison of equation (20) with the Debye function for C_v versus T. The difference is due to the neglect of dispersion in the latter.

This is the distribution used in the Debye derivation. It follows that equation (20) is identical with the Debye function of ν_D at the very lowest temperatures where only very long elastic waves contribute to C_v. According to equation (13), however, $g(\nu)$ rises much faster than ν^2, especially as it approaches $\nu_m = (2/\pi)\nu_D = W_0/\pi\bar{a}$. Thus, as a consequence of equation (7), the density of energy states is much greater near the real cut-off, ν_m, than

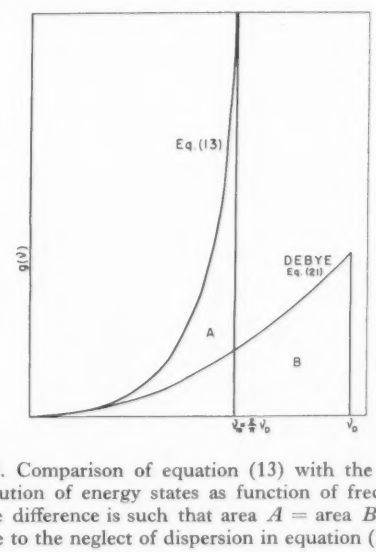

FIG. 2. Comparison of equation (13) with the Debye distribution of energy states as function of frequency, ν. The difference is such that area A = area B and is due to the neglect of dispersion in equation (21).

Table 1.

$$\frac{C_g}{3R}=\frac{24}{\pi^3 x_0}\int_0^{x_0}\frac{x^2e^x[\sin^{-1}(x/x_0)]^2\,dx}{(e^x-1)^2\sqrt{1-(x/x_0)^2}},\quad \text{where } x_0=\frac{\Theta}{T}$$

x_0	0·0	0·1	0·2	0·3	0·4	0·5	0·6	0·7	0·8	0·9
0	1·000000	0·999342	0·997371	0·994098	0·989538	0·983715	0·976658	0·968402	0·958986	0·948457
1	0·936865	0·924263	0·910710	0·896267	0·880998	0·864968	0·848246	0·830898	0·812994	0·794603
2	0·775793	0·756632	0·737184	0·717515	0·697687	0·677759	0·657789	0·637831	0·617936	0·598153
3	0·578526	0·559097	0·539904	0·520983	0·502365	0·484078	0·466147	0·448596	0·431442	0·414703
4	0·398391	0·382518	0·367093	0·352120	0·337606	0·323551	0·309957	0·296821	0·284142	0·271915
5	0·260134	0·248794	0·237886	0·227403	0·217336	0·207674	0·198408	0·189528	0·181022	0·172880
6	0·165089	0·157640	0·150520	0·143717	0·137221	0·131020	0·125103	0·119459	0·114077	0·108946
7	0·104056	0·993966*	0·949584*	0·907315*	0·867066*	0·828746*	0·792269*	0·757549*	0·724506*	0·693061*
8	0·663139*	0·634667	0·607576	0·581799	0·557272	0·533934	0·511726	0·490592	0·470480	0·451338
9	0·433117	0·415771	0·399256	0·383529	0·368552	0·354286	0·340694	0·327742	0·315398	0·303630
10	0·292409	0·281707	0·271498	0·261757	0·252459	0·243582	0·235104	0·227006	0·219267	0·211871
11	0·204799	0·198035	0·191563	0·185370	0·179440	0·173762	0·168322	0·163109	0·158111	0·153318
12	0·148720	0·144307	0·140071	0·136003	0·132095	0·128339	0·124729	0·121256	0·117915	0·114700
13	0·111605	0·108624	0·105752	0·102985	0·100316	0·977430†	0·952604†	0·928645†	0·905515†	0·883177†
14	0·861599*	0·840746	0·820588	0·801096	0·782242	0·763998	0·746340	0·729244	0·712687	0·696646
15	0·681102					0·610166				
x_0		x_0		x_0		x_0		x_0		
16·0	0·549040†	20·5	0·245550†	25·0	0·130285†	29·5	0·780605‡	34·0	0·520607‡	
16·5	0·496024	21·0	0·227280	25·5	0·122383	30·0	0·742486	34·5	0·500655	
17·0	0·449769	21·5	0·210768	26·0	0·115127	30·5	0·707158	35·0	0·481984	
17·5	0·409189	22·0	0·195807	26·5	0·108457	31·0	0·674385	35·5	0·464490	
18·0	0·373411	22·5	0·182222	27·0	0·102318	31·5	0·643951	36·0	0·448077	
18·5	0·341721	23·0	0·169863	27·5	0·966612‡	32·0	0·615662	36·5	0·432658	
19·0	0·313534	23·5	0·158596	28·0	0·914444	32·5	0·589339	37·0	0·418154	
19·5	0·288367	24·0	0·148309	28·5	0·866282	33·0	0·564819	37·5	0·404490	
20·0	0·265818	24·5	0·138901	29·0	0·821775	33·5	0·541954			

* Multiply by 10^{-1}. † Multiply by 10^{-2}. ‡ Multiply by 10^{-3}.

VOL. 9 1959

near ν_D according to equation (21), as shown graphically in Fig. 2. This means that C_g in equation (20) approaches the limit, $3R$, at much lower temperatures than in the corresponding Debye function as shown graphically in Fig. 1.

Inspection of Fig. 1 shows that equation (20) is considerably higher than the Debye function except at $T < 0{\cdot}02\Theta_m$, in accord with BLACKMAN's calculation.[2] In the region of $T = 0{\cdot}1\Theta_m$, which embraces part of the Debye T^3 region, it is about twice as high. Thus it is shown that easily detectable effects due to dispersion of sound waves must be expected even at quite low temperatures, where it has sometimes been assumed that they could be neglected.

CALCULATION OF C_v FROM ELASTIC CONSTANTS

Our function is based on the assumption of isotropy with respect to acoustic waves, as is appropriate for glasses. No glass structure is known well enough, however, to permit verification of the function by the behavior of glasses alone. We shall first apply it to monatomic crystals exhibiting various degrees of anisotropy. The values of Θ for each wave type in such solids are calculated from means of the cut-off frequencies, $\bar{\nu}_m$, over all directions. Values of $\bar{\nu}_m$ are calculated from mean velocities of acoustic waves according to equation (10).

Following BRILLOUIN[5] (p. 162), one can define two values of $\bar{\nu}_m$ corresponding to the mean velocities of longitudinal and shear waves, $\bar{W}_l$ and $\bar{W}_s$, respectively. Thus

$$\bar{W}_l = \sqrt{\frac{\bar{c}'_{11}}{\rho}} \qquad \bar{W}_s = \sqrt{\frac{\bar{c}'_{44}}{\rho}}, \tag{22}$$

in which $\bar{c}'_{11}$ and $\bar{c}'_{44}$ are the mean elastic constants over all directions, as defined by MASON,[9] and ρ is the density.

For cubic crystals:

$$\bar{c}'_{11} = c_{11} - 0{\cdot}4(c_{11} - c_{12}) + 0{\cdot}8c_{44} \tag{23}$$

$$\bar{c}'_{44} = 0{\cdot}6c_{44} + 0{\cdot}2(c_{11} - c_{12}). \tag{24}$$

For hexagonal crystals:

$$\bar{c}'_{11} = \frac{8}{15}c_{11} + \frac{3}{15}c_{33} + \frac{4}{15}(c_{13} + 2c_{44}) \tag{25}$$

$$c'_{66} = \frac{7}{30}c_{11} - \frac{1}{6}c_{12} - \frac{2}{15}c_{13} + \frac{1}{5}c_{33} + \frac{2}{5}c_{44}. \tag{26}$$

It has been found in good accord with experiment to calculate separate values of Θ for longitudinal and shear waves. From equation (10):

$$\Theta_l = \frac{h\bar{W}_l}{k\pi\bar{a}} \qquad \Theta_s = \frac{h\bar{W}_s}{k\pi\bar{a}}. \tag{27}$$

There are two degrees of freedom associated with Θ_s for every one associated with Θ_l. Thus, the combined heat capacity is

$$C_v = \frac{1}{3}C_g\left(\frac{\Theta_l}{T}\right) + \frac{2}{3}C_g\left(\frac{\Theta_s}{T}\right), \tag{28}$$

in which $C_g/3R[(\Theta_l/T)]$ and $C_g/3R[(\Theta_s/T)]$ can be read from a suitable plot of Table 1.

ASSIGNMENTS OF DEGREES OF FREEDOM

The function (20) applied according to equation (28) constitutes a method of calculation which is intermediate with respect to detail between the completely detailed method of lattice dynamics and the classic Debye method. It is as detailed as the available parameters for oxide glasses permit. Therefore, it is correspondingly specific with respect to assignment of degrees of freedom to the various branches of the spectrum of thermal motions. Consequently, although its superficial resemblance to the Debye method suggests its similar application, it cannot be applied with the classic disregard for detail of the spectrum except at temperatures approaching 0°K, where, as shown by equation (21) and Figs. 1 and 2, equation (20) becomes identical with the Debye function.

The purpose of this work was to formulate the heat capacity of isotropic solids as precisely as possible without specifying the exact positions of atoms and the force constants of interactions between them, because these are not available for glasses. If these parameters were available, it would be theoretically possible to calculate the complete spectrum of thermal motions. The ordinate of the spectrum at any frequency would be proportional to the degrees of freedom associated with that frequency.

The motivation of the present work was to develop an approximate means of taking into account dispersion beyond the range of validity of

the Debye spectrum. We propose a function which can be used in the temperature ranges where dispersion is important, but which extrapolates to Debye theory when dispersion is not important. For example, if the primitive cell contains more than one atom, that is if the solid has optical modes, our treatment indicates that dispersion becomes important at a much lower frequency than would be implied by using a modified Debye function based on a monatomic lattice. In this sense the present theory takes into account structural effects to some degree, essentially by making a proper assignment of degrees of freedom between acoustic and optical modes. It has become the practice to apply the Debye function with a $3R$ limit to the total number of atoms in the crystals. This assignment always agrees with our formula in the limit of sufficiently low temperatures. Thus no contradiction with the classical Debye treatment is involved in any of our assumptions.

EXPERIMENTAL VERIFICATION

Aluminum is one of the most elastically isotropic of monatomic cubic crystals. Fortunately, all data required to verify equation (28) by its behavior are known as functions of temperature. First, it will be shown that equation (28) deviates only trivially from the behavior of aluminum and that such deviations as occur are the result of the modest deviations from isotropy except at temperatures where uncertainties in the corrections for electronic heat capacity and $C_p - C_v$ can be important. Then, it will be shown by examination of all monatomic crystals for which sufficient data are available that the deviations of their behavior from equation (28) can be understood heuristically either as consequences of their anisotropy or uncertainties in the data.

Uncertainties in elastic constants are often met. Most of these arise because no measurements near 0°K have been made, but they also occur in aluminum for which all measurable needed data are known. One needs elasticities for frequencies near the cut-offs, $\bar{\nu}_l$ and $\bar{\nu}_s$, i.e. about 10^{12} c/s. Experimentally, however, measurements can be made only at frequencies which are orders of magnitude lower than this. Consequently if there exist mechanical relaxations which can occur in times between the periods used in the measurement and about 10^{-12} sec, the measured elasticities will be too low for the calculation of C_v. Such relaxations may be expected in metals because of the mobilities of electrons which contribute very noticeably to the elastic constants (see Sections 18 and 19 of Ref. 3). The extent of error can be easily evaluated and corrections made by the following procedure:*

(*a*) For each experimental value of C_v find a corresponding value of x_0 from a graph of Table 1. Then $x_0 T$ will give an apparent characteristic temperature, $\bar{\Theta}$, corresponding to each observed value of C_v.

(*b*) Calculate C_v versus T from elasticities by equation (28) and find the corresponding value of $\bar{\Theta}'$ for each data point, as in (*a*).

(*c*) Plot $\bar{\Theta}$ versus T and $\bar{\Theta}'$ versus T on the same graph. Then, if the elastic constants used are a little low, it will be easily noticed that multiplication of $\bar{\Theta}'$ by a factor slightly larger than 1·00, say 1·05, yields $\bar{\Theta}$ versus T except for the usually small deviations expected because of anisotropy. Assuming the ratio between $\tilde{c}'_{11}$ and $\tilde{c}'_{44}$ is correct, this procedure is justified for small corrections because, as shown by equations (22) and (27), Θ_l and Θ_s and therefore $\bar{\Theta}$ are directly proportional to the square roots of the elastic constants.

The value of $\bar{\Theta}'_0$, at 0°K, can be calculated using the limiting value of equation (20):

$$C_g = 119{\cdot}8\left(\frac{T^3}{\Theta^3}\right) = A\left(\frac{T^3}{\Theta^3}\right). \qquad (29)$$

Applying equation (28)

$$C_v = \frac{AT^3}{3}\left(\frac{1}{\Theta_l{}^3} + \frac{2}{\Theta_s{}^3}\right),$$

$\bar{\Theta}'_0$ is found from equation (29) by setting

$$C_v = A\left(\frac{T}{\bar{\Theta}'}\right)^3.$$

* The effect of the electron gas on the elastic constants of a metal is reviewed by DE LAUNAY.[3] For free electrons having a spherical Fermi surface, there is no effect on the velocity of transverse waves, but for complex energy surfaces, such as occur in aluminum, it has been shown by LEIGH (*Phil. Mag.* **42**, 139 (1951)), that the kinetic energy of the electrons makes a significant contribution to the elastic constants and indeed can account for the observed elastic isotropy of aluminum. It may be expected that very fast mechanical relaxations can arise from the suggested influence of mechanical stress on the kinetic energy of the electrons.

Equating these two expressions for C_v

$$\bar{\Theta}'_0 = \Theta_s \left[\frac{3}{(\Theta_s/\Theta_l)^3 + 2} \right]^{1/3}. \qquad (30)$$

Usually $\bar{\Theta}'_0 \sim 1{\cdot}1\Theta_s$, in accord with equation (28), which requires that $\bar{\Theta}'_0$ be near to, but a little larger than, Θ_s at low T and increase toward an intermediate value between Θ_l and Θ_s which is somewhat dependent on their ratio. A close connection, such as this, between Θ at 0°K, and c_{44} is required by lattice dynamics. According to DE LAUNAY's[3] equation (11·40), c_{44} is the only elastic constant occurring in Θ_0. As shown in Table 2, equation (30) is in good accord with the more precise calculations for nearly isotropic crystals. Deviations from isotropy cause most experimental values of $\bar{\Theta}$ for crystals near 0°K to be a little lower than $\bar{\Theta}'_0$ calculated by equation (30). This is so because elastic waves in directions for which v_m is small are preferentially excited especially near 0°K.

Aluminum

In Fig. 3, $\bar{\Theta}'$ versus T is compared with $\bar{\Theta}$ versus T for the various face-centered cubic crystals for which sufficient data exist. Table 2 summarizes related observations and calculations. For aluminum the elastic constants as functions of temperature from 63°K are given by SUTTON[10g] and thermal expansions from 82°K to high temperatures are given by NIX and MACNAIR.[10e]) These data have permitted precise calculation of $\bar{\Theta}'$ versus T in the whole range up to 300°K.

The obvious parallelism of $\bar{\Theta}'$ versus T and $\bar{\Theta}$ versus T at $T < 80$°K should be noted, as should also the excellent agreement of $\bar{\Theta}'_0 = 273{\cdot}4$°K with DE LAUNAY's[10h] calculation $(2/\pi)\Theta_D = 271{\cdot}6$°K. The latter shows that equation (30) is equivalent to his calculation except for the small anisotropy which he takes into account. This close agreement is associated with the fact that the isotropy index

$$s = \frac{c_{11} - c_{12}}{2c_{44}} = 0{\cdot}85$$

is almost 1·00, which corresponds to elastic isotropy. Values of s for other crystals are given in Table 2.

The curves for $\bar{\Theta}'$ and $\bar{\Theta}$ do not coincide for aluminum, however. The nearest coincidence is for 1·08 $\bar{\Theta}'$ versus T, which indicates that the true value of $\bar{\Theta}'_0 \sim 295$°K. This indicates, in accord with remarks above, that the experimental

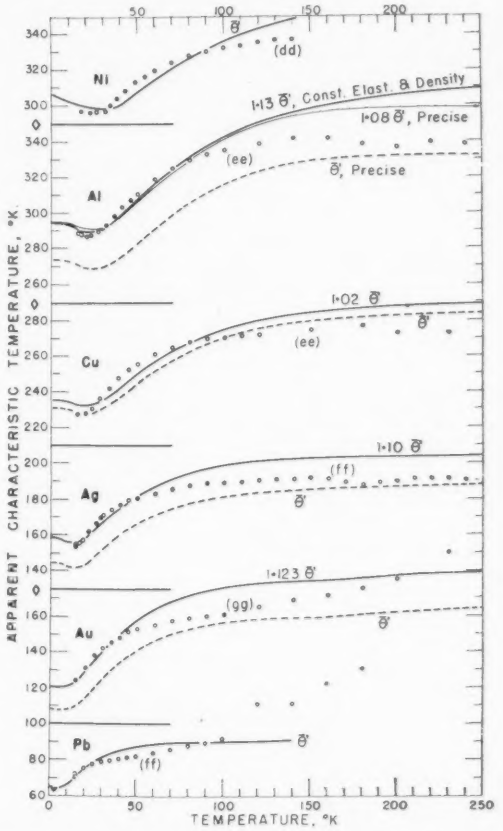

FIG. 3. Apparent characteristic temperatures, $\bar{\Theta}$ (data points) and $\bar{\Theta}'$ (calculated from elastic moduli) as functions of temperature for face-centered cubic crystals. All but the "precise" calculations of $\bar{\Theta}'$ are based on constant elasticities and densities. Letters in parentheses relate to reference (10).

elasticities used in both this calculation and DE LAUNAY's are about 17 per cent [i.e. $100(1{\cdot}08^2 - 1{\cdot}00)$] lower than those needed to calculate C_v.

It is clearly shown that $\bar{\Theta} < 1{\cdot}08\bar{\Theta}'$ at $T < 30$°K and $\bar{\Theta} > 1{\cdot}08\bar{\Theta}'$ for $T = 30°-80$°K. This small difference in the slopes of the two curves seems best regarded as due to the small deviation

Table 2. Calculated values of Θ_l, Θ_s, and $\bar{\Theta}'_0$ from elasticity and density data

Material		Symmetry	Mean elastic constants (10^{11} dynes cm^{-2}) $\bar{c}'_{11}$	$\bar{c}'_{44}$	Density (g. cm^{-1})	Vol. per GFW (cm^3)	a (Å) $(V/N)^{\frac{1}{3}}$	Θ_l	Θ_s	$\bar{\Theta}'_0$	$(2/\pi)\Theta_D$ at 0°K	$\gamma \times 10^4$ (cal. deg.$^{-2}$ atom^{-1})	s
Ni	(R.T.)	FCC	30·85 (a)	8·9 (a)	8·90 (b)	6·60	2·215(c)*	504°	270°	308°	263 (d)	1·744(d)	0·38(a)
			30·14 (f)	9·46 (f)	8·90 (f)		2·22	497°	278°	309°	262 (e)		0·41(f)
Al	(R.T.)	FCC	11·20 (a)	2·62 (a)	2·702	9·970	2·546(c)*	479°	232°	260°		3·484	
	(0°K)		12·64 (g)	2·875(g)	2·734 (h)	9·863	2·539	507°	242°	273°	272 (h)		0·85(g)
Cu	(R.T.)	FCC	21·14 (a)	5·46 (a)	8·92 (b)	7·13	2·273(c)*	405°	206°	231°			
			22·11 (i)	5·942(i)	9·018 (h)	7·049	2·270	413·3°	214·3°	239·9°	219·8(h)		0·31(h)
											220 (j)		
											213 (k,n)	1·777(k,n)	
Single crystal			(21·14)	(5·46)	8·9528(m)	7·1006	2·275	404·8°	206°	231°	200 (l)		
Annealed wire					8·9209(m)								
Cold-rolled bar					8·91 (m)								
Hard-drawn wire					8·9140(m)								
											143·4(k)		
Ag	(R.T.)	FCC	14·21 (a)	3·21 (a)	10·5 (b)		2·570(c)*	271°	129°	144°	145·8(o)	1·54 (k)	0·33(h)
	(0°K)									(158)	146 (j)		
											143 (p,q)		
Au	(R.T.)	FCC	21·38 (h)	3·10 (h)	19·32 (b)	10·21	2·569	245°	93·4°	103°			0·35(h)
	(0°K)		21·76 (h)	3·37 (h)	19·32 (b)	10·21	2·569	248°	97·4°	110°	105 (k)	1·78 (k)	0·35(h)
Pb	(R.T.)	FCC	5·67 (a)	1·02 (a)	11·34 (b)	18·27	3·112(c)*	136°.	57·9°	65·5°			0·26(h)
	—(0°K)		7·8 (h)	1·33 (h)	11·34 (b)		3·112(c)*	158°	65°	74°	61·3(r)	7·48 (r)	0·26
W	(R.T.)	BCC	50·2 (a)	15·15 (a)	19·3 (b)	9·530	2·507(c)*	385°	212°	236°	159 (s)	1·8±0·7(s)	1·00(h)
											108 (t)	51·1 (t)	
Na	(R.T.)	BCC	1·03 (a)	0·384(a)	0·97 (b)	23·7	3·40	182°	111°	122°		4·3 (u)	
	(90°K)		1·37 (h)	0·404(h)	0·97 (b)		3·40	206°	114°	126°	102 (u)		0·13(h)
K	(R.T.)	BCC	0·593(a)	0·175(a)	0·86 (b)		4·23	118°	64°	72°		none	0·17(h)
	(77°K)		0·635(h)	0·175(h)	0·86 (b)		4·23	122°	64°	72°			
Mo	(R.T.)	BCC	44 (h)	12·1 (h)	10·2 (b)	9·41	2·50	497°	261°	292°	283 (s)	5·1±0·4(s)	1·29(h)
Co	(R.T.)	(?)	30·31 (v)	8·45 (v)	8·836 (v)	6·670	2·225	492·9°	260°	291°	282 (w)	12·0 (w)	
Mg	(R.T.)	(?)	5·88 (a)	1·77 (a)	1·745 (x)	13·94	2·849	286·1°	211·8°	235°	248 (y)	none	
	(0°K)									(246°)	258 (z)		
C	(R.T.)	Diamond	107 (h)	37·0 (h)	3·51 (aa)	3·42	1·78	1480°	866°	962°			0·65(h)
	(R.T.)		115·6 (cc)	53·57 (cc)	3·51 (aa)	3·42	1·78	1536°	1043°	1140°	1132 (mm)		

(Letters in parentheses relate to Reference 10.) * From X-ray.

VOL. 9 1957

of aluminum from isotropy because expected preferential excitation of the lower-velocity sound waves would be revealed in this way. It is most pronounced in the least isotropic crystals examined e.g. sodium. There is also the possibility that second-neighbor interactions, which are neglected in our derivation, make the dispersion larger than our function provides for. This, however, would be expected to make $\bar{\Theta}$ lower than $\bar{\Theta}'$ at all values of T except those very near 0°K, and such an effect, if present, is overshadowed by other effects.

The fairly large negative deviation of $\bar{\Theta}$ from $\bar{\Theta}'$ at $T > 100$°K is best regarded as due to uncertainties in the corrections of observed values of C_p for electronic heat capacity, which may not be reliably given by γT at these temperatures, and $C_p - C_v$. While the difference, $\bar{\Theta}' - \bar{\Theta}$, looks large in Fig. 3, it represents less than 4 per cent difference in C_v.

Comparisons of calculated with observed values of $C_v/3R$ for a series of temperatures from 15 to 300°K are shown in Table 3. At $T < 50$°K, the actual data points of BUSEY and GIAUQUE[10dd] are taken. At other temperatures their smoothed values are used. As shown in the last column, the largest deviation is only 6 per cent, and if corrections for anisotropy were made, agreement would be even closer at $T < 80$°K and probably at all other temperatures as well.

The behavior of aluminum shows that equation (28) is a very good approximation in spite of the small anisotropy and the simplifying assumptions in the derivation, and this justifies the formulation in terms of Θ_l and Θ_s rather than an average Θ. The

Table 3. Comparison of equation (28) with experiment for aluminum

Temp. (°K)	This method of calculation				Debye function $\Theta_D = 464$*	
	$1{\cdot}08\,\bar{\Theta}'$	$\frac{C_v}{3R}$(Calc.)	$\frac{C_v}{3R}$(Exp.)	$\frac{\text{Calc.}}{\text{Exp.}}$	$\frac{C_v}{3R}$(Calc.)	$\frac{\text{Calc.}}{\text{Exp.}}$
15·29	292	0·00308	0·0032	0·96	0·00278	0·87
17·68	292	0·00493	0·0052	0·95	0·00432	0·83
20·08	290·5	0·00770	0·0081	0·95	0·00629	0·78
22·67	290·0	0·01183	0·0122	0·97	0·00928	0·76
27·01	290·8	0·02215	0·0228	0·97	0·0153	0·67
31·61	292·0	0·03937	0·0389	1·01	0·0246	0·63
35·94	295·0	0·06055	0·0582	1·04	0·0362	0·62
40·68	297·5	0·09025	0·0852	1·06	0·0520	0·61
45·98	302·0	0·1271	0·1208	1·05	0·0741	0·61
50	306·0	0·1562	0·1501	1·04	0·0933	0·62
60	314·0	0·2343	0·2271	1·03	0·151	0·66
70	322·5	0·3091	0·3056	1·01	0·216	0·71
80	329·5	0·3802	0·3808	1·00	0·284	0·75
90	335·5	0·4441	0·4500	0·987	0·350	0·78
100	341	0·5008	0·5131	0·976	0·414	0·81
120	349	0·5966	0·6143	0·971	0·523	0·85
140	354	0·6720	0·6904	0·973	0·612	0·88
160	358	0·7303	0·7515	0·972	0·680	0·90
180	358	0·7785	0·7984	0·975	0·734	0·92
200	358	0·814	0·8335	0·977	0·776	0·93
220	358	0·843	0·8590	0·981	0·810	0·94
240	358	0·866	0·8798	0·984	0·835	0·95
260	358	0·885	0·8966	0·987	0·857	0·96
280	358	0·900	0·9100	0·989	0·886	0·97
300	358	0·912	0·9215	0·990	0·890	0·97

* $\Theta_D = 1{\cdot}08 \cdot \pi/2 \cdot \bar{\Theta}'_0$.

calculations imply that equation (30) would be quite exact for complete isotropy with respect to ν_m, which is not quite the same as the elastic isotropy indicated by s because ν_m involves a, which is also a function of direction in crystals. Indeed there must be a variation of ν_m due to directional dependence of a in aluminum,but Table 3 shows that this does not lead to large errors. This may be so because the percentage error in C_g is not as sensitive to variations in $g(\nu)$ near ν_m as to those at lower frequencies where $g(\nu)$ is not sensitive to a modest spread in ν_m. At temperatures for which the highest frequencies make major contributions, C_v is approaching its limiting value and is relatively less sensitive to frequency. Thus it may be expected that equation (28) will be within experimental limitations for glasses at temperatures for which the Einstein functions of ν_m are less than, say, 50 per cent of their classical limits.

Other monatomic crystals having one-atom primitive cells

In the calculations on the various other crystals listed in Table 2, only constant elasticities and densities were used. Such calculations for aluminum differ only trivially from the more precise calculations. One may compare, in Fig. 3, the solid heavy line representing 1·13 $\bar{\Theta}'$ as calculated from room-temperature properties with the solid light line for 1·08 $\bar{\Theta}'$ obtained from the exact calculations. These differences are small because ν_m depends on the ratios of elastic constants to density and these two properties change similarly with T.

A wide variation in the isotropy index, s, is represented. Inspection of Table 2 reveals that low values of s are associated with relatively large differences between $\bar{\Theta}'_0$ and $(2/\pi)\Theta_D$ found very near 0°K, or calculated for 0°K by others. Notable cases are sodium and lead, for which $s = 0{\cdot}13$ and $0{\cdot}26$, and $\bar{\Theta}'_0 = 1{\cdot}24[(2/\pi)\Theta_D]$ and $1{\cdot}21[(2/\pi)\Theta_D]$ respectively. Tungsten, for which $s = 1{\cdot}00$, shows even larger deviations from $\bar{\Theta}'_0$, but, because of the widely discordant values of $(2/\pi)\Theta_D$, this is not reliable. Some of the intermediate values of s, such as those for copper, silver and gold, are associated with close agreements of $\bar{\Theta}'_0$ and $(2/\pi)\Theta_D$, while others such as nickel show greater disagreement. This is because s alone does not determine the reliability of $\bar{\Theta}'_0$. For molybdenum s exceeds 1·00 by 0·29 and the agreement is about like that for values 0·3–0·7 less than 1·00. The variation of $(2/\pi)\Theta_D$ for copper is probably related to the variation of density.[10m] The hexagonal crystals, cobalt and magnesium, are nearly isotropic, as indicated by the small differences between $\bar{c}'_{11}$ and c_{11} (see equations (30 and (31)):

	(In 10^{11} dyn cm^{-2})	
	$\bar{c}'_{11}$	c_{11}
Co	30·31	30·7
Mg	5·88	5·86

Judging from the temperature correction for aluminum, $\bar{\Theta}'_0$ for magnesium should be corrected to 246°K, in excellent accord with 248°K found by KOHLER.[10y]

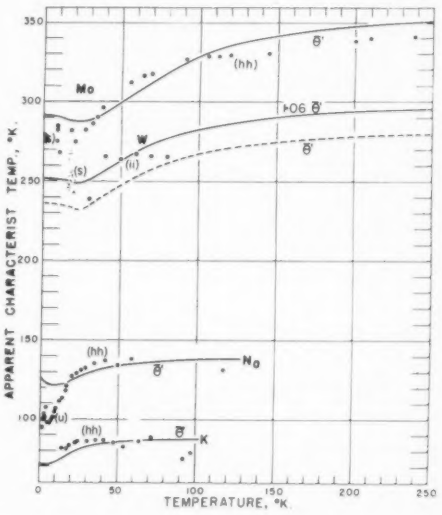

FIG. 4. Apparent characteristic temperatures, $\bar{\Theta}$ (data points) and $\bar{\Theta}'$ (calculated from elastic constants) as functions of temperature for body-centered cubic crystals. Letters in parentheses relate to reference (10).

Inspection of Figs. 3, 4, and 5 shows that the lowest values of s are also associated with the largest deviations of $\bar{\Theta}'$ from Θ at low values of T. Again sodium is the obvious example. In spite of their relatively low values of s, however, lead and silver show exceptionally good agreement in this respect. This indicates again that a low value of s does not necessarily mean narrow distributions of ν_m. Again the nearly isotropic cobalt and magnesium show good agreement between $\bar{\Theta}'$ and $\bar{\Theta}$.

The results on cobalt and magnesium are interesting in another way. WYCKOFF[10c] reports a hexagonal close-packed and a cubic close-packed (f.c.c.) form for cobalt. The sample used in the heat-capacity measurements[10ll]

Note added in proof: The correction of $\bar{\Theta}'$ to 1.10 $\bar{\Theta}$ in the case of silver is well justified by the new measurements of elastic constants by ALERS and NEIGHBORS [*Bull. Amer. Phys. Soc.* **3**, 70 (1958)]. Using their data, $\bar{\Theta}'_0 = 156°$ which is 1·09 times the value in Table 2. This means that $\bar{\Theta}'$ versus T calculated from their data would be within one per cent of 1·10 $\bar{\Theta}'$ as shown in Fig. 3. Their measurements on gold confirmed the curve for $\bar{\Theta}'$ in Fig. 3.

is not identified in this respect. If it had also been hexagonal close-packed, the calculations in Table 2 and the curves in Fig. 5 would have been inappropriate, because they are based on a one-atom primitive cell rather than the two-atom cell required for h.c.p. lattices. Such an error would be expected to lead to a deep minimum in the $\bar{\Theta}$ versus T curve like that shown for diamond in curve B of Fig. 6. The parallelism of the $\bar{\Theta}$ versus T and $\bar{\Theta}'$ versus T curves for cobalt clearly indicates that the one-atom primitive cell was not too small for the heat-capacity data. On the other hand, the $\bar{\Theta}$ versus T curve based on the assumption of a two-atom cell is discordant with the corresponding $\bar{\Theta}'$ versus T curve and descends precipitously at $T > 40°$K. Ideally the two crystal phases have identical volumes. This undoubtedly means that their mean elastic constants over all directions are very similar. Thus the similar magnitudes of $\bar{\Theta}$ and $\bar{\Theta}'$ are not surprising. Furthermore, X-ray studies are reported for the cubic form in liquid nitrogen, showing that it is stable in the temperature range of the heat-capacity measurements.[10c] All these considerations show how application of equation (28) to the heat-capacity data clearly indicates a choice between the two possible crystal forms of the sample. Only the hexagonal form of magnesium is reported by WYCKOFF, but some X-ray

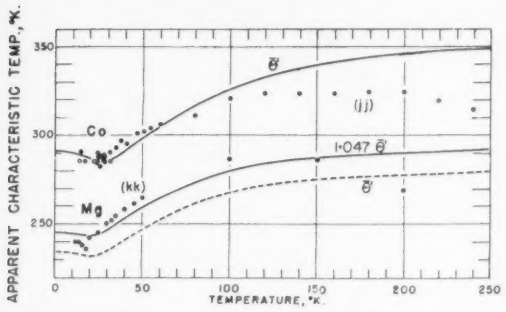

FIG. 5. Apparent characteristic temperatures, $\bar{\Theta}$ (data points) and $\bar{\Theta}'$ (calculated from elastic constants) as functions of temperature for cobalt and magnesium crystals. Letters in parenthesis relate to reference (10).

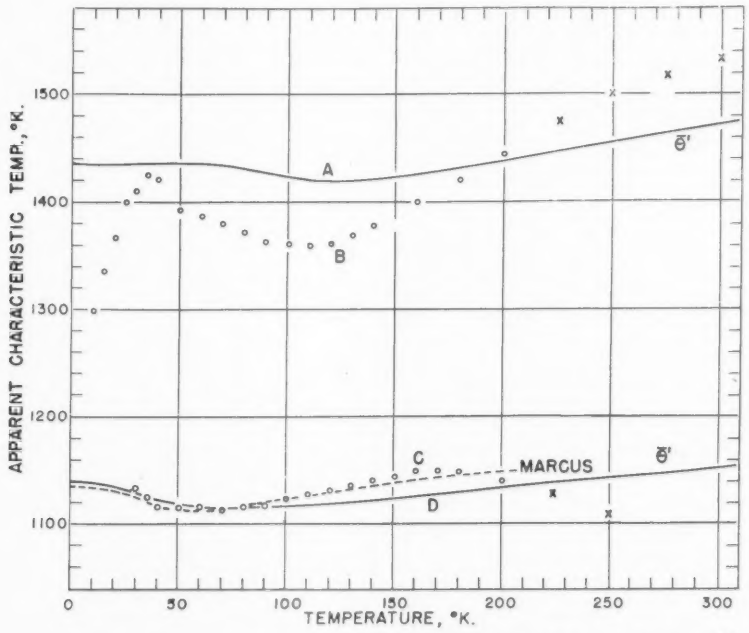

FIG. 6. Apparent characteristic temperatures, $\bar{\Theta}$ (data points) and $\bar{\Theta}'$ (calculated from elastic constants), as functions of temperature for diamond. Curves A and B are for a 1-atom primitive cell and curves C and D are for a 2-atom primitive cell. The circular data points are from reference 10(mm) and the x's are from reference 10(ll). The dashed line was constructed from values of "effective" Θ_p calculated by P. N. MARCUS and reported in reference 10(mm). Deviations of $\bar{\Theta}'$ from this line about like those shown are expected because of the modest anisotropy of diamond.

patterns are not quite characteristic. The identical volumes of the two forms and the existence of both forms mixed in some crystals indicate that its behavior in this respect may be analogous with that of cobalt.

All of these crystals show large deviations of $\bar{\Theta}$ from $\bar{\Theta}'$ at $T > 100°K$. These are partly due to the lack of temperature corrections for elasticity and density, as shown quantitatively for aluminum. Uncertainties in the $C_p - C_v$ and electronic heat-capacity corrections are likely. One may suspect that, in the latter correction, the value of γ found near 0°K is not appropriate above 100°K. These deviations represent small errors in C_v except in the cases of gold, lead, and tungsten, for which the behavior of $\bar{\Theta}$ versus T at $T > 100°K$ requires assumptions outside the scope of this discussion.

Diamond and NaCl

The diamond lattice differs from others considered here in that its frequency spectrum has an optical branch. Consequently, the three translations of the acoustic branch must refer to masses larger than one atom. Its primitive cell contains two atoms. This means that since C_v in equation (28) represents a mole of primitive cells, it must represent the acoustic heat capacity of two moles of carbon rather than one. It will be shown that this scheme of calculation is in accord with the observed heat capacities and reproduces to a good approximation the low-frequency part of the spectra calculated from lattice dynamics.

In order to illustrate an application of equation (28) in structure studies, let us suppose that the dynamics of this lattice are not known. It would be logical then to find $\bar{\Theta}$ versus T corresponding to C_v versus T for one gramatomic weight of carbon. This is curve B in Fig. 6. The corresponding $\bar{\Theta}'$ versus T curve calculated from McSkimin and Bond's[10cc] elasticity data is labelled A. The obvious disagreement in the shapes of the two curves occurs because equation (28), when applied in this way, does not correctly represent the cut-off frequencies or acoustic dispersion in diamond. The rapid fall of $\bar{\Theta}$ as T increases from 35 to 90°K means that important dispersion effects become evident at these temperatures, but the calculations provide for them only at higher temperatures. There are small effects due to second-neighbor interactions, but these should not lead to crossing of A and B at $T = 190°K$. The marked rise of $\bar{\Theta}$ with T above 120°K occurs because the acoustic contribution to C_v is approaching $1{\cdot}5R$ rather than the $3R$ limit assumed, and because the total C_v is being influenced by an optical frequency somewhat higher than the real ν_m. Since diamond is reasonably isotropic ($s = 0{\cdot}65$), $\bar{\Theta}'_0$, which is not influenced by dispersion, is expected to be a little higher than $(2/\pi)\Theta_D$ though in good agreement. This is in accord with the data at temperature near 35°K. The data points below 35°K should be ignored in this connection because they are not accounted for by any existing theories of lattice specific heat.[10mm] This combination of circumstances shows clearly that C_v per mole of carbon is a wrong choice for representation by equation (28).

Curves C and D are based on the known two-atom primitive cell. The expected parallelism of the two curves is seen up to $T = 180°K$ and would be evident to higher temperatures if corrections for thermal expansion were made to $\bar{\Theta}'$. At $T > 200°K$, $\bar{\Theta}$ drops rapidly with increase of T because of contributions to C_v from the optical frequency. This combination of circumstances confirms the choice of the two-atom primitive cell.

The very modest deviations of $\bar{\Theta}'$ from $\bar{\Theta}$ and from the very recent calculations by Marcus[10mm], represented by the dashed line in Fig. 6, are due mainly to the modest anisotropy of diamond ($s = 0{\cdot}65$) which is not taken into account in the calculation of $\bar{\Theta}'$.

The value $\Theta_s = 1043°K$ shown in Table 2 was calculated by assuming a two-atom primitive cell. This corresponds to $\omega_s = 2\pi\nu_s = 1{\cdot}37 \times 10^{14}$ sec^{-1}. Inspection of de Launay's[3] Fig. 36 shows that this value of ω_s is at the center of the first maximum in the diamond spectrum, as calculated from lattice dynamics by Smith. If monatomic primitive cells had been assumed, the clearly unsatisfactory value $\omega_s = 1{\cdot}68 \times 10^{14}$ sec^{-1} would have resulted. Furthermore, the corresponding value $\omega_l = 2{\cdot}54 \times 10^{14}$ sec^{-1} is higher than any frequency in the diamond spectrum, while $\omega_l = 2{\cdot}00 \times 10^{14}$, corresponding to $\Theta_l = 1536°K$ for the two-atom cell, is in good agreement with Smith's calculation. Similar agreement for a lattice with basis is also found in the case of NaCl. Calculations based on the elasticity data of Rose,[11] assuming a two-atom cell, lead to $\Theta_l = 260°$, $\Theta_s = 154°$, and $\bar{\Theta}'_0 = 170°K$. By averaging cut-off frequencies found by Lyddane and Herzfeld[12] along cube edges and diagonals, one finds the very similar values $\Theta_l = 263°$ and $\Theta_s = 148°K$.

VOL. 9 1959

Furthermore, $\bar{\Theta}_0' = 170°$ corresponds to $\Theta_D = 336°$, in excellent agreement with MARTIN's[13] experimental values extrapolated to 0°K.

CONCLUSIONS

The functions (20) and (28) were developed to extract structural information from the low-temperature heat capacities and elasticities of glasses. Since they apply only to the acoustical spectra of solids, it was necessary to verify them with data for the much simpler monatomic crystals which do not have optical branches in their spectra. These crystals involve deviations from the perfect symmetry assumed in the derivation of the functions. Precise calculations on aluminum, which is nearly isotropic, showed that the deviations from isotropy caused only trivial deviations from the functions in the whole range from 0°K up to the classical limit of C_v and that the deviations were of the sort expected. Less exact calculations on various other crystals showed that, where the data were reliable, the most isotropic crystals conformed best to the functions. It appears that for glasses, good conformity can be assumed because of their perfect isotropy. Reservations arise from the unavoidable spread of ν_m because of the amorphous structure and the exclusion of some very long elastic waves by phonon scattering. Evaluation of these effects in glasses is reserved for a separate discussion. The spread of ν_m affects mainly the upper intermediate parts of the C_v versus T curves and may be even less serious in glasses than that caused by the anisotropy of most cubic crystals in the temperature range of anticipated use. Still another reservation arises from possible deviations of real dispersion effects from the simple approximation used here, but these are expected to be no more serious than the spread of cut-off frequencies.

In spite of the limitations related to anisotropy, the fact that its effects are easily identifiable and often small justifies the application of these functions in the study of crystal structures, especially where other techniques yield inconclusive or anomalous results. Such an application was illustrated in the discussion of cobalt and the now well-understood diamond. The comments on diamond and NaCl show that the proposed scheme of calculation, even when applied to crystals, yields good approximations to the acoustic parts of the spectra as calculated by others. Therefore, Θ_s, ν_s, and $\bar{a}$ have significant meanings, and these are the parameters of greatest interest in the intended applications to glass.

A fair evaluation seems to be that equation (20) applied according to equation (28) approximates the acoustic heat capacity of particulate solids at all temperatures about as well as the Debye function does at $T < \Theta/50$.

Acknowledgements—We are indebted to Dr. ARTHUR RUARK for consultations during the development of this work and for criticisms of our presentation. We gratefully acknowledge also the sustaining interest shown by our associates at the Technical Center of Owens-Illinois Glass Company and their many clarifying discussions, especially those of MILTON DANK and B. B. MATHIAS.

APPENDIX I

The intuitively plausible formulae (7) and (8) constitute the basis of our derivation. Their reasonable character can be supported as follows.

It is easily shown that formula (8) is appropriate for a two-dimensional square lattice for which DE LAUNAY (ref. 3, p. 259) gives the secular equation

$$\begin{vmatrix} [2\alpha_1(1-C_1)+2\alpha_2(1-C_1C_2)-\omega^2M] & 2\alpha_2S_1S_2 \\ 2\alpha_2S_1S_2 & [2\alpha_1(1-C_2)+2\alpha_2(1-C_1C_2)-\omega^2M] \end{vmatrix} = 0$$

where α_1 and α_2 are force constants to nearest and next-nearest neighbors, respectively; $C_j = \cos 2\pi r_j a$, $S_j = \sin 2\pi r_j a$, and $\omega = 2\pi\nu$. Since our ultimate interest is glass, let us consider that in a two-dimensional glass, every direction is equivalent. Thus, the direction of a plane wave can be r_1, letting $r_2 = 0$ in the other direction. Then $C_2 = 1$, $S_2 = 0$, and the two solutions of the secular equation are:

$$\omega^2M = 2(\alpha_1+\alpha_2)(1-\cos 2\pi r_1 a)$$

$$\omega^2M = 2\alpha_2(1-\cos 2\pi r_1 a).$$

But $(1-\cos 2\pi r_1 a) = 2\sin^2\pi r_1 a$ and, as shown by DE LAUNAY, $\alpha_1+\alpha_2 = c_{11}$ and $\alpha_2 = c_{44}$. Thus, remembering that $M/a^2 = \rho$, the density, for longitudinal waves:

$$\nu = \frac{\sin \pi r_1 a}{\pi}\sqrt{\frac{c_{11}a^2}{Ma^2}} = \frac{\sin \pi r_1 a}{\pi a}\sqrt{\frac{c_{11}}{\rho}} = \frac{\sin \pi r_1 a}{\pi a}W_l.$$

Likewise for shear waves:

$$\nu = \frac{\sin \pi r_1 a}{\pi a}\sqrt{\frac{c_{44}}{\rho}} = \frac{\sin \pi r_1 a}{\pi a}W_s.$$

Experience with silicate glasses indicates that they may be considered as approximately close-packed "apparent

primitive cells" with an apparent distance between centers of about 6–7 Å. To test the plausibility of equations (7), therefore, it is reasonable to solve DE LAUNAY's secular equation (11.6) for the close-packed face-centered cubic lattice of identical particles. For a plane wave in such a three-dimensional glass, one may set $r_2 = r_3 = 0$. Then one finds:

$$\nu_1 = \frac{1}{\pi}\left(\frac{2\alpha_1 \sin^2\left(\frac{\pi r_1 a}{2}\right) + \alpha_2 \sin^2(\pi r_1 a)}{M}\right)^{\frac{1}{2}}$$

$$\nu_2 = \frac{1}{\pi}\left(\frac{2\alpha_1 \sin^2\left(\frac{\pi r_1 a}{2}\right)}{M}\right)^{\frac{1}{2}} = \frac{\sin\left(\frac{\pi r_1 a}{2}\right)}{\pi}\sqrt{\frac{2\alpha_1}{M}}.$$

For ν_1, the relations between α_1 and α_2 and the elastic moduli are not as simple as in the square lattice above, but, according to DE LAUNAY, $\alpha_1/a = c_{44}$, so that ν_2 is the frequency of shear waves, and its dispersion is expressed by the simple sine function. Since α_1 must be considerably larger than α_2, the dispersion of ν_1 waves very closely approximates the same sine function. Thus, equation (7) is justified not only by the observed rather good conformity of equation (28) with data on monatomic crystals, but also by the dynamics of simple three-dimensional lattices.

APPENDIX II

Formula (20) can be used to calculate the lattice heat capacities of crystals to a better approximation than that afforded by equation (28) if one is willing to calculate the cut-off frequencies for a large sample of directions through the crystal. It was shown in Appendix I that dispersions along certain directions in f.c.c. lattices either follow precisely or approximately the simple sine function. By examination of the secular equation, it can be shown that similar situations exist with respect to other directions and in other lattices. Provided that no serious deviations from the sine functions are found for any direction through the lattice, the contribution of sets of waves in each of the various directions can be read from Table 1. These can then be summed over all directions and normalized to a $3R$ limit. In analogy to equation (28)

$$C_v = \frac{\sum_n C_g\left(\frac{\Theta_l}{T}\right) + 2\sum_n C_g\left(\frac{\Theta_s}{T}\right)}{3n}$$

where n is the number of directions chosen.

REFERENCES

1. For reviews see:
   (a) SEITZ F., *The Modern Theory of Solids* pp. 99–138. McGraw-Hill Book Co., New York (1940).
   (b) KITTEL C., *Introduction to Solid State Physics*. John Wiley & Sons, New York (1953).
   (c) SCHRÖDINGER E., *Handbuch der Physik* Vol. X Chap. 5, pp. 308–18, equation (76). Julius Springer, Berlin (1926–9).
2. BLACKMAN M., (I) *Proc. Roy. Soc.* **A148,** 365–383 (1935); (II) *Ibid.*, **A148,** 384–406 (1935); (III) *Ibid.*, **A149,** 117–126 (1935); (IV) *Ibid.*, **A149,** 126–130 (1935); (V) *Ibid.*, **A159,** 416–431 (1937).
3. For a recent extensive review see: DE LAUNAY J., *Solid State Physics* (Ed. F. SEITZ and D. TURNBULL) Vol. 2, pp. 219–303. Academic Press Inc., New York (1956).
4. DESORBO W., *Acta Met.* **2,** 274 (1954).
5. BRILLOUIN L., *Wave Propagation in Periodic Structures* pp. 161–163. Dover Publications Inc., New York (1946).
6. WESTRUM E. F. Jr., Department of Chemistry, University of Michigan, Ann Arbor, Michigan.
7. (a) TARASSOV V. V., *Zh. fiz. khim.* **24,** 111 (1950).
   (b) DANK M. and BARBER S. W., *Mathematical Tables and Other Aids to Computations* Vol. 9, No. 52 (1952).
8. DANK M. and BARBER S. W., *J. Chem. Phys.* **23,** 597 (1955).
9. MASON W. P., *Piezoelectric Crystals and Their Application to Ultrasonics* pp. 412–419. D. Van Nostrand Co., New York (1950).
10. Sources of data in Table 2 and Figures 3, 4, 5, 6:
   (a) See reference (9), p. 417.
   (b) *Metals Handbook* American Society for Metals, Cleveland (1948).
   (c) WYCKOFF R. W. G., *Crystal Structures* Vol. 1. Interscience Publishers, New York (1951).
   (d) KEESOM W. H. and CLARK C. W., *Physica* **2,** 513 (1935).
   (e) NIX F. C. and MACNAIR D., *Phys. Rev.* **60,** 597 (1941).
   (f) NEIGHBORS J. R., BRATTEN F. W., and SMITH C. S., *J. Appl. Phys.* **23,** 389 (1952).
   (g) SUTTON P. M., *Phys. Rev.* **91,** 816 (1953). See also (h).
   (h) See reference 3, pp. 268, 289.
   (i) OVERTON W. C. Jr and GAFFNEY J., *Phys. Rev.* **98,** 969 (1955). See also (h).
   (j) LEIGHTON R. B., *Rev. Mod. Phys.* **20,** 165 (1948).
   (k) CORAK W. S., GARFUNKEL M. P., SATTERTHWAITE C. B., and WEXLER A., *Phys. Rev.* **98,** 1699 (1955).
   (l) ESTERMAN I., FRIEDBERG S. A., and GOLDMAN J. E., *Phys. Rev.* **87,** 582 (1952).
   (m) GIAUQUE W. F. and MEADS P. F., *J. Amer. Chem. Soc.* **63,** 1897 (1941).
   (n) KOK J. A. and KEESOM W. H., *Physica* **3,** 1035 (1936).
   (o) KEESOM P. H. and PEARLMAN N., *Phys. Rev.* **88,** 140 (1952).
   (p) BHATIA A. B. and HORTON G. K., *Phys. Rev.* **98,** 1715 (1955).

VOL 9 195

(q) KEESOM P. H. and PEARLMAN N., *Phys. Rev.* **98,** 548 (1955).
(r) HOROWITZ M., SILVIDI A. A., MALAKER S. F., and DAUNT J. G. *Phys. Rev.* **88,** 1182 (1952).
(s) HOROWITZ M. and DAUNT J. G., *Phys. Rev.* **91,** 1099 (1953).
(t) SILVIDI A. A. and DAUNT J. G., *Phys. Rev.* **77,** 125 (1950).
(u) PARKINSON D. H. and QUARRINGTON J. E., *Proc. Phys. Soc.* A**68,** 762 (1955).
(v) MCSKIMIN H. J., *J. Appl. Phys.* **26,** 406 (1955).
(w) DUYKAERTS G., *Physica* **6,** 817 (1939).
(x) *Handbook of Chemistry and Physics*, 39th edition. Chemical Rubber Publishing Co., Cleveland, O. (1957–58).
(y) KOHLER M., *Ann. Phys., Lpz.* **36,** 227 (1939).
(z) SMITH P. L., *Phil. Mag.* **46,** 744 (1955).
(aa) HUTCHISON D. A., *J. Chem. Phys.* **13,** 383 (1945).
(bb) See reference (h), p. 300.
(cc) MCSKIMIN H. J. and BOND W. L., *Phys. Rev.* **105,** 116 (1957).
(dd) BUSEY R. H. and GIAUQUE W. E., *J. Amer. Chem. Soc.* **74,** 3157 (1952).
(ee) GIAUQUE W. F. and MEADS P. F., *J. Amer. Chem. Soc.* **63,** 1897 (1941).
(ff) MEADS P. F., FORSYTHE W. R., and GIAUQUE W. F. *J. Amer. Chem. Soc.* **63,** 1902 (1941).
(gg) GEBALLE T. H. and GIAUQUE W. F., *J. Amer. Chem. Soc.* **74,** 2368 (1952).
(hh) SIMON F. and ZEIDLER W., *Z. phys. Chem.* **123,** 383 (1926).
(ii) LANGE F. *Z. phys. Chem.* **110,** 343 (1924).
(jj) CLUSIUS K. and SCHACHINGER L., *Z. Naturf.* **7a,** 185 (1952).
(kk) CRAIG R. S., KRIER C. A., COFFER L. W., BATES E. A., and WALLACE W. E. *J. Amer. Chem. Soc.* **76,** 238 (1954).
(ll) DE SORBO W., *J. Chem. Phys.* **21,** 876 (1953).
(mm) BURK D. L. and FRIEDBERG S. A., *Phys. Rev.* **111,** 1275 (1958).
11. ROSE F. C., *Phys. Rev.* **49,** 50 (1936).
12. LYDDANE R. H. and HERZFELD K. F., *Phys. Rev.* **54,** 846 (1938).
13. MARTIN D. L., *Phil. Mag.* **46,** 751 (1955).

VOL. 9 1959

J. Phys. Chem. Solids Pergamon Press 1959. Vol. 9. pp. 214–216. Printed in Great Britain.

THE SOLUBILITY OF OXYGEN IN SILICON

H. J. HROSTOWSKI and R. H. KAISER

Bell Telephone Laboratories, Inc., Murray Hill, New Jersey

(*Received* 30 *September* 1958)

Abstract—The intensity of the fine structure of the 1100 cm^{-1} silicon–oxygen absorption at 4·2°K has been used to determine the temperature-dependence of the concentration of oxygen in solid solution. Above 1000°C the logarithm of this concentration is a linear function of the reciprocal of the absolute temperature, and the heat of the precipitation reaction is 22 ± 2 kcal/mole.

VOL
9
195

INTRODUCTION

THREE absorption bands have been observed in the infrared spectra of oxygen in silicon.[1] The absorption coefficient, α, of the most intense band, which occurs at 1106 cm^{-1} at room temperature, has been correlated with the oxygen concentration determined by vacuum-fusion gas analysis.[2] Below 125°K this band shows an unusual temperature-dependent fine structure which has been associated with oxygen in solid solution as dispersed Si–O–Si or Si_2O units.[1] After heating near 1000°C, the maximum α at room-temperature decreases as a result of the precipitation of oxygen in SiO_2 clusters.[3] However, low-temperature spectra still show the fine structure of dissolved oxygen superimposed on the absorptions of SiO_2 and the silicon lattice. The intensity of this fine structure provides a direct means of determining the temperature-dependence of the concentration of oxygen in solid solution.

EXPERIMENTAL

Samples were taken from high-resistivity silicon crystals pulled from fused-silica crucibles. Room-temperature values of α varied from 6·5 to 7·4 cm^{-1}, corresponding to oxygen concentrations between 1·4 and $1{\cdot}6 \times 10^{18}/cm^3$. The samples were heated in an inert atmosphere at several high temperatures until further heating produced no change in α. Spectra were obtained at 4·2°K, where the strongest Si_2O band at 1136 cm^{-1} is most intense. The intensity, I, of the Si_2O bands was obtained from the area between the observed absorption and the extrapolated absorptions of SiO_2 and silicon in this region. This extrapolation is somewhat arbitrary and introduces considerable error when the dissolved oxygen concentration is small.

The rate of precipitation of SiO_2 varied considerably with sample history. Although equilibrium was attained in less than 1 hr at 1250°C, the time required at 1000°C ranged from 20 to 100 hr. The long heating times required at lower temperatures limited these measurements to temperatures equal to or greater than 1000°C. Heating for about 100 hr at 450°C decreased the equilibration time at higher temperatures. The introduction of dislocations into one sample by plastic deformation for 15 min at 1200°C decreased α at room-temperature from 6·4 to 3·9 cm^{-1} prior to further heat treatment. However, in all cases the intensities after equilibrium at 1000°C or higher were constant within the limits of experimental error.

OXYGEN CONCENTRATION

Typical spectra for one sample at 4·2°K are shown in Fig. 1 after equilibration at 1000, 1150, and 1250°C. The absorption of oxygen in solid solution increases markedly after heating at successively higher temperatures, while there is little change in the background absorption. Fig. 2 shows the logarithm of the intensity of the Si_2O absorption plotted against the reciprocal of the absolute temperature. The open circles are average values obtained from three samples. The vertical lines indicate the average experimental error (approximately $\pm 2{\cdot}5$ cm^{-2} for each point). The solid circles at 1075 and 1250°C were obtained for one of the samples after the 1000, 1150, and 1250°C

VOL. 9 1959

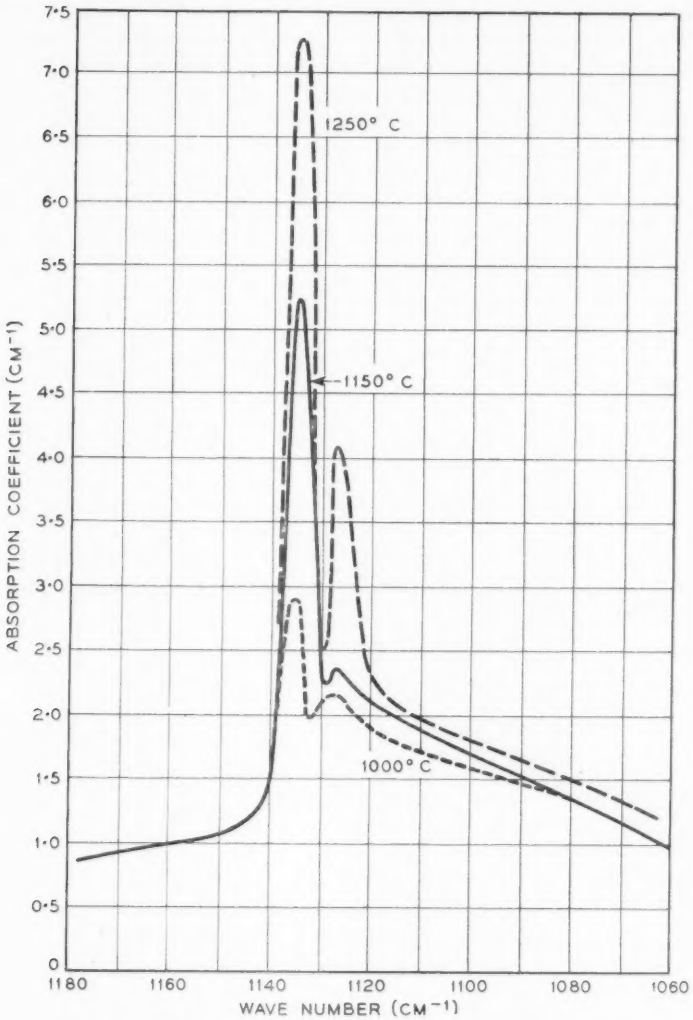

FIG. 1. Infrared absorption at 4·2°K of a silicon sample saturated with oxygen at 1000, 1150, and 1250°C.

points. These results show the reversibility and reproducibility of the measurements. The heating time at 1250°C (8 hr) gave results indistinguishable from those obtained after only 1 hr, indicating that true equilibrium is attained after only 1 hr. Although the total intensity of the fine structure remained constant, only one band was observed at 1136 cm^{-1}, whereas the 1 hr treatment resulted in two absorptions in this region (see Fig. 1). This result supports the assumption that all of the fine structure can be attributed to absorption by Si_2O units.

Within experimental error the intensity of Si_2O absorption satisfies the relation

$$\ln I = -\frac{\Delta H}{RT} + c, \qquad (1)$$

where R is the gas constant and c is a numerical constant. ΔH is the heat of the reaction.

$$\tfrac{1}{2}SiO_2(\text{solid}) = \tfrac{1}{2}Si(\text{solid}) + O(\text{solid solution}). \qquad (2)$$

From the slope of the line in Fig. 2, we find $\Delta H = 22 \pm 2$ kcal/mole. KAISER and KECK[2] have shown that the equilibrium oxygen concentration in solid solution, [O], near the melting point of

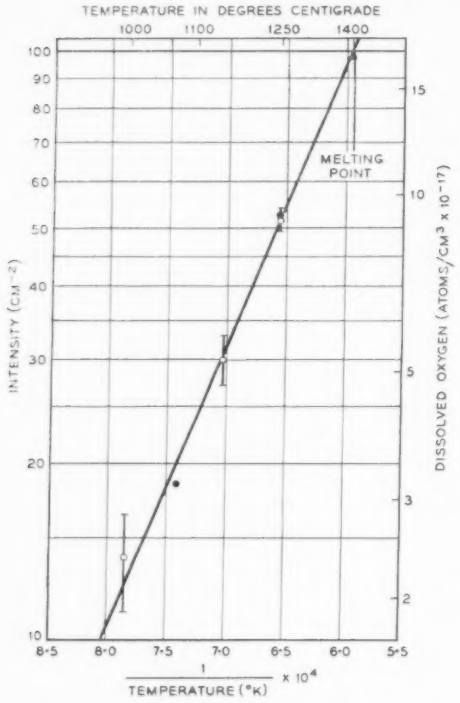

FIG. 2. Logarithm of intensity and oxygen concentration versus reciprocal absolute temperature.

silicon is $1{\cdot}8 \times 10^{18}$/cm^3. Combining this value with the results in Fig. 2 yields the expression:

$$\log[O] = -4{\cdot}83 \times 10^3 T^{-1} + 21{\cdot}2, \qquad (3)$$

where [O] is in atoms/cm^3 and T in °K.

Recently, KAISER and THURMOND[4] have shown from measurements of the diffusion of oxygen in silicon samples of different thicknesses that at 1375°C the solubility of the oxygen is 85 per cent of the solubility at the melting point of silicon. This value is identical with that obtained from Fig. 2.

Although equation (3) may not hold exactly at lower temperatures, some qualitative remarks may be made about heat-treatment processes. From equation (3) the calculated value of [O] in solid solution at equilibrium at 450°C is only $3 \times \times 10^{14}$/cm^3. The observed α for two samples decreased by about 30 per cent after heating for about 200 hr at 450°C, indicating that the aggregation of oxygen occurs after sufficient heating even at this low temperature. This result is in accord with measurements of FULLER and LOGAN,[5] who found that the concentration of heat-treatment donors, n, passes through a maximum value on prolonged heating at 450°C. The decrease in n results from the depletion of oxygen in solid solution. The kinetics of heat treatment have been discussed in detail by KAISER *et al.*[6]

Acknowledgements—We are grateful to W. KAISER, R. A. LOGAN and C. D. THURMOND for profitable discussions and assistance and to M. KOWALCHIK for performing the heat treatments.

REFERENCES

1. HROSTOWSKI H. J. and KAISER R. H., *Phys. Rev.* **107,** 966 (1957).
2. KAISER W. and KECK P. H., *J. Appl. Phys.* **28,** 882 (1957).
3. KAISER W., *Phys. Rev.* **105,** 1751 (1957).
4. KAISER W. and THURMOND C. D. To be published.
5. FULLER C. S. and LOGAN R. A., *J. Appl. Phys.* **28,** 1427 (1957).
6. KAISER W., REISS H. and FRISCH H. L. To be published.

J. Phys. Chem. Solids Pergamon Press 1959. Vol. 9. pp. 217–234. Printed in Great Britain.

OPTICAL ABSORPTION STUDIES OF THE VOLUME PHOTOLYSIS OF LARGE SILVER CHLORIDE CRYSTALS*

F. MOSER, N. R. NAIL and F. URBACH

Research Laboratories, Eastman Kodak Company, Rochester, N.Y.

(*Received* 7 *August* 1958; *revised* 3 *October* 1958)

Abstract—The exposure-induced volume darkening of large AgCl crystals has been studied at very low exposure levels, in both pure crystals and in crystals containing known concentrations of cationic impurities. It has been found that the volume photoproduct that can be produced may be controlled by such impurities, of which cuprous ion is a striking example. The cuprous ion apparently provides deep hole traps at room temperature, thereby allowing the photoprocess to proceed with unit quantum efficiency until these traps have been filled. In the purest crystals grown, the volume darkening saturates at optical densities, measured at the peak of the absorption band, of less than 0·001 per cm thickness. The addition of 5×10^{16} cuprous ions per cm^3 allows the volume darkening to proceed to optical densities 1000 times higher. The shape of the exposure-induced absorption band is approximately constant over this range of densities, suggesting that there is no marked change in the size and distribution of the photoproduct centers as their number increases. In addition to photochemical effects, certain cationic impurities (particularly the elements commonly classed as Group VIIIA) produce impurity absorption bands in the silver halides whose intensity and shape may depend on the valence state of the impurity.

1. INTRODUCTION

THE optical properties of large silver halide crystals and the changes in these properties under various exposure conditions have been the subject of considerable investigation in these Laboratories over the past few years. Various aspects of this study have been reported briefly on several occasions.[1–5] This paper reviews the earlier work, adds new experimental results, and summarizes our present understanding of the effects of certain cationic impurities on the photolysis of large silver chloride crystals.

HILSCH and POHL[6] were the first to investigate the darkening of large silver halide crystals upon exposure to weakly absorbed radiation. In AgCl crystals, they observed the darkening to consist of a broad absorption band in the visible region of the spectrum, with a maximum in the neighborhood of 550 mμ. HILSCH and POHL further showed that they could induce a readily measurable darkening in their crystals with exposures, which, in terms of absorbed quanta per unit volume, were close to the exposures normally used in producing the photographic latent image. They estimated that each absorbed photon led to the formation of one silver atom. Our work suggests that the crystals used by HILSCH and POHL contained a relatively high content of impurities. One cannot form a visible volume darkening in the purest crystals now available.

The rôle of impurities and mechanical imperfections in the photolysis of silver halides has been referred to by many workers. STASIW and TELTOW[7] have studied the optical and photochemical properties of AgCl and AgBr crystals containing additions of silver sulfide, and have also noted the sensitizing effects of other additions such as silver nitrate, silver oxide, and copper chloride.†[8–12]

* Communication No. 1979 from the Kodak Research Laboratories.

† The influence of copper on the photolysis of large AgCl crystals is discussed in considerable detail later in this paper, and some results have been previously published.[5] Study of the literature suggests that HECHT,[8] in 1932, was probably aware of the enhanced darkenability of copper-containing AgCl, and STASIW and TELTOW,[9] in 1944, noted that it was apparently the cuprous ion which conferred sensitivity, while the cupric ion did not. In recent years, several authors in papers dealing with the photolytic behavior of silver halides, have noted the effects of small additions of copper,[10–12] although no quantitative data have been presented.

The influence of strain on the photolysis of AgCl has been referred to by LOHLE.[13]

Much of this earlier work has been summarized by SEITZ.[14] More recently, BROWN and WAINFAN[15,16] have investigated the darkening in nominally pure AgCl crystals, and have reported differences in the initial rate of darkening depending on the atmosphere in which the crystal had been treated. In agreement with our observations,[2] BROWN and WAINFAN suggest that the total amount of darkening that can be produced in the interior of the AgCl crystals may be controlled by impurities. In the present work, we have been able to establish a quantitative relation between the total amount of volume darkening and the concentration of deliberately added cuprous ions.

2. MATERIALS

(a) *Crystal sheets*

Preliminary studies of the photolytic behavior of large AgCl crystals were made on crystal sheets prepared by fairly rapid crystallization of molten silver halide. Techniques for preparing such sheets have been described by HEDGES and MITCHELL.[17] In our work, an appropriate amount of silver halide precipitate was placed on a flat Vycor plate and melted under the desired atmosphere. In the case of AgCl, a protective mixture of chlorine and nitrogen gas was used during the melting operation, and, finally, nitrogen alone. A second preheated plate was then placed on top of the melt, glass spacers determining the sheet thickness. The entire "sandwich" was cooled in a matter of minutes to about 400°C, and then air- or water-quenched to room temperature. Impurities were added to the starting precipitate either in the form of solutions, or where the concentration was high enough to make it possible, directly as a solid. Sheets prepared in this manner, ranging in thickness from 10^{-3} to 10^{-1} cm, had smooth surfaces, were quite polycrystalline, and generally contained some bubbles or voids in their volume.

(b) *"Beaker" crystals*

In addition to the crystal sheets, it was convenient to prepare another type of sample more suited to surveying rapidly a large number of impurities over a large concentration range. For this purpose, samples were prepared by melting 5 g of silver halide precipitate in a 5-cc Pyrex beaker under the desired atmosphere, and cooling to room temperature in about 10 min. Impurities were added in the same manner as to the crystal sheets. These crystal disks, referred to as "beaker" crystals, were highly polycrystalline, contained many bubbles and voids, and had uneven external surfaces. Nevertheless, they proved suitable for both visual and spectrophotometric observation of their optical and photolytic properties.

(c) *Large single crystals*

For quantitative work, large single or nearly single crystals have been prepared by the Bridgman technique. The preparation of these crystals in our Laboratories, their purity, and their physical appearance have been described in detail.[4] Although various atmospheres of growth have been investigated, the large crystals used in the experimental work reported here have all been grown in a nitrogen atmosphere at a rate of 5 mm/hr. Impurities were added to the dry, starting precipitate in the form of solutions. From the final crystal cylinder, sections 1–10 mm thick were cut and polished. The sections so obtained were optically clear, showed several large-angle grain boundaries upon etching with sodium thiosulfate, and appeared strained when viewed between crossed Polaroid filters. By using extremely pure starting precipitate, crystals have been grown which show no spectrochemically detectable amounts of heavy metal impurities, iron excepted. Table 1 gives the results of spectrochemical analyses of a typical starting precipitate, and of top and bottom sections of a nominally pure crystal.

Table 1(A). *Spectrochemical detection limits for some impurities in* AgCl (*expressed as weight of impurity to weight of* AgCl *in parts per million*)

Element	Detection limit	Element	Detection limit	Element*	Detection limit
Cd	0·5	Pb	0·075	Ba	1·0
Cr	0·05	Mn	0·05	Ca	0·1
Co	0·1	Ni	0·05	Li	0·1
Cu	0·05	Sn	0·05	Mg	0·05
Au	1·0	Zn	4·0	Na	0·1
Fe	0·05			Sr	1·0

* For Ba, Ca, Li, Mg, Na, and Sr, the detection limits shown are approximate values only. They are obtained by extrapolation from standards prepared for higher concentrations of these elements.

Table 1(B). *Results of spectrochemical analysis*

Description	Element			
	Cu	Fe	Pb	Au, Cd, Cr, Mn, Ni, Sn, Zn
AgCl precipitate (average of numerous analyses)	N.D.*	0·30	N.D.	N.D.
C–38–B; 1 cm position of pure AgCl Bridgman crystal	N.D.	0·16	N.D.	N.D.
C–38–T; 19 cm position of pure AgCl Bridgman crystal	N.D.	0·10	0·10	N.D.
C–37–12; 4 cm position of AgCl with nominal 10 p.p.m. addition of copper	3·0	0·19	N.D.	N.D.
C–37–14; 16 cm position of AgCl with nominal 10 p.p.m. addition of copper	~ 18	0·19	N.D.	N.D.

* N.D. = not detected. Actually, copper is occasionally detected in the AgCl starting precipitate. Indirect evidence suggests that it may be uniformly present in the starting material to about 0·01 p.p.m.

Spectrochemical data on a crystal with added copper impurity are also given.

Strains that were visible between crossed Polaroid filters could be removed completely by proper annealing. To get such strain-free crystals, it was found sufficient to heat the crystals to 400°C in a nitrogen atmosphere, and to cool them at a rate of about 20°C/hr at 400°C, decreasing to about 10°C/hr by the time the sample was at 50°C. Such a cooling program results in a nearly constant cooling rate when expressed in terms of the fractional change in absolute temperature per unit time. During such an annealing, the crystals rest on a layer of finely divided quartz powder. Similar annealings could be carried out in chlorine atmosphere.

3. EXPERIMENTAL PROCEDURES

As noted in the Introduction, HILSCH and POHL[6] were able to induce a visible volume darkening in their crystals with exposures below those used in producing the photographic latent image. This type of experiment cannot be extended to extremely pure crystals with conventional photometry, since such crystals do not exhibit visible volume darkening, even after long exposure to high-intensity light.[2] However, the study of photolytic darkening in very pure crystals has been made possible by the development in these Laboratories of a photometer capable of measuring changes in optical density of the order of 10^{-5}. The design and performance of this instrument have been reported in detail elsewhere.[18] For changes in optical density smaller than 10^{-3}, this instrument is restricted to monochromatic measurement. At higher levels of darkening, measurements of the spectral distribution of the photoproduct are possible.

In order to extend the measurements of photolytic darkening to the lowest possible levels, it was therefore helpful to characterize the photoproduct by its optical density at some selected wavelength. Measurements of the absorption spectrum of the darkening have shown it to be a broad absorption band with a maximum near 560 $m\mu$, over a large range of photoproduct formation. Consequently, it was meaningful to measure the optical density of this band at one wavelength near the broad maximum. In the present work, 600 mμ was chosen. In practice, a sample was given a series of exposures to actinic radiation, and the total induced optical density was plotted as a function of the total exposure. For convenience and ease of analysis, such plots were generally made on logarithmic scales. In most cases, the measuring light itself produced no detectable change in the photoproduct, although cases have been observed in which the measuring light formed additional photoproduct and others in which it optically bleached the existing product. Neither of these complications was observed in the large single crystals grown in a nitrogen atmosphere, either pure or containing low concentrations of impurity.

The crystal samples were exposed with filtered radiation from a General Electric A–100–H–4 mercury arc lamp. The 365- and 436-mμ spectral lines were particularly suitable for studying the surface and the volume darkening, respectively, in AgCl crystals at room temperature. In AgCl crystals of reasonable purity, the absorption coefficients at room temperature are 1200 and 0·03 cm^{-1} for 365 and 436 mμ, respectively. Thus, crystals up to several centimeters thick will be exposed quite uniformly when irradiated by 436-mμ light; on the other hand, 365-mμ radiation will be attenuated to less than 10^{-4} of its incident intensity in a layer 10^{-2} cm thick. Therefore, exposure of a crystal thicker than, say, 1 mm to 436-mμ light produces a darkening predominantly due to formation of photoproduct throughout the volume if the quantum efficiency of silver formation is comparable in surface and volume regions. In

thinner crystals, intermediate wavelengths may be used to differentiate between surface and volume darkening.

4. RESULTS AND DISCUSSION

(a) *Early observations of photolytic darkening*

Early observations of the darkening upon exposure of AgCl crystals were made on crystal sheets that had been solidified under a nitrogen atmosphere. In these samples, the general progress of the darkening exhibited a characteristic behavior. The darkening, measured by its optical density at 600 mμ, as a function of exposure to 436-mμ light is shown for one such sample in Fig. 1. On this logarithmic plot, the darkening is seen to show an initial region of proportionality between induced density and exposure, followed by a region of virtual standstill. This, in turn, is followed by a region where induced density is approximately proportional to exposure, but with a much lower efficiency or proportionality constant (the term "efficiency" is used here as a measure of optical density produced per unit exposure and not in the sense of quantum efficiency. The latter is discussed in Section 4(f)). It can be shown that a curve of this general shape would result from the superposition of two linear processes of very different efficiencies, the one of higher efficiency saturating after some short exposure. Fig. 2 shows, on a logarithmic plot, two linear darkening processes, the one of higher efficiency (curve 1) saturating after 1 sec of exposure. (Note that a slope of one on this logarithmic plot means proportionality between induced density and exposure. The position of the line represents the "efficiency".) The summed density of these two processes is plotted (curve 3). The experimental points in this figure are obtained from Fig. 1, and illustrate the plausibility of interpreting curves of this type as the superposition of two linear processes. Some factors affecting this idealized curve shape are discussed in the Appendix.

In the next section, experimental evidence is presented which supports the assumption of the existence of two separate processes in the darkening, and shows that the process of higher efficiency is related to the formation of photoproduct throughout the volume of the crystal. Evidence is also given which suggests that the total amount of photoproduct that may be formed in the crystal volume is limited by the concentration of hole traps. The second process of lower efficiency is shown to be related to the formation of photoproduct in a layer near the external surfaces of the crystal. An entirely analogous behavior was observed in large single crystals grown from the melt under an atmosphere of nitrogen. In these pure crystals, however, the saturation level occurred at lower optical densities.

The photoproducts just described are stable in the dark at room temperature; that is, only small amounts of decay were observed after many hours and even days. In samples grown in an atmosphere of hydrogen chloride, however, an additional

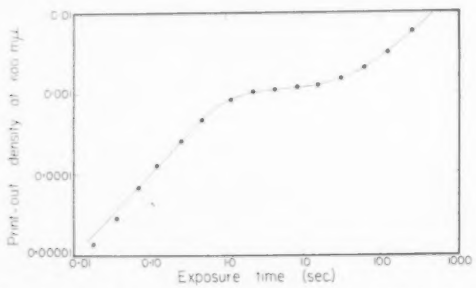

FIG. 1. Print-out density (measured at 600 mμ) as a function of exposure to 405-mμ light. AgCl crystal sheet (M-31) approximately 0·01 cm thick. For this thickness, the exposing intensity is about 6×10^{13} absorbed quanta/cm^2/sec. (Note: The term "print-out density" is used to denote the degree of darkening, measured in optical density units.)

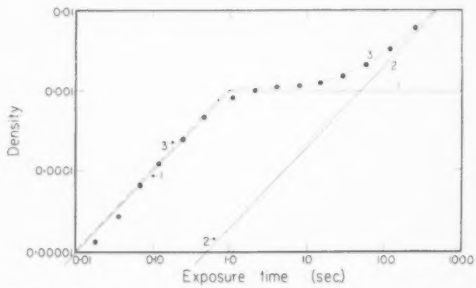

FIG. 2. Curve 1 represents a process of darkening efficiency 0·001 density unit per sec of exposure, which starts at $t = 0$ and terminates after a total of 1·0-sec exposure. Curve 2 represents a process of efficiency 0·00002 density unit per sec of exposure, also beginning at $t = 0$, but continuing for times greater than 1000 sec. Curve 3 is obtained by addition of these two curves. The experimental points are taken from Fig. 1.

VOL
9
195

component of darkening has been observed which decays in a matter of minutes. This transient photoproduct, formed in the crystal volume, can be reformed with less exposure than is required for its initial creation. These more complex photoproducts have not been investigated further.

(b) *Separation of the darkening into a volume and a surface component*

If the first linear rise and saturation level in the darkening curve represent the formation and completion of a photoprocess in the crystal volume, this implies that for similar samples the saturation level measured would be proportional to the effectively exposed crystal thickness. Such thickness variation may be achieved by varying the actual physical thickness of the samples, using for exposure a wavelength which exposes the thickest sample with sufficient uniformity. On the other hand, by varying the wavelength of the exposing light, one may expose to very different depths and in this manner investigate the dependence of the saturation level on sample thickness.

Early observations to check the proportionality between saturation level and thickness were made on crystal sheets, using wavelength variation as a depth probe. While these data showed considerable scatter due largely to lack of reproducible conditions in sheet-making, they are significant because of the large thickness variation possible by this technique. Table 2 summarizes the results of these measurements. It shows that the saturation level, expressed in terms of optical density per cm thickness, is fairly constant over a range of 400 in effectively exposed crystal thickness. This proportionality between saturation level and crystal thickness was verified directly in Bridgman crystals. In this case, samples of varying thickness, but with similar properties, could be obtained by sectioning a single crystal cylinder. Both the initial rate of darkening and the saturation level were measured in samples whose thickness varied from 2·2 to 15·4 mm. Table 3 gives the measured proportionality between sample thickness and the optical density at saturation, and confirms that the first linear rise and saturation represent the formation of photoproduct throughout the volume of the crystal.

Table 3. Saturation density of photolytic darkening, measured at 600 mμ, in nominally pure AgCl *Bridgman crystals. Exposure is to 436-mμ light of intensity approximately* 10^{14} *absorbed quanta/cm³/sec*

Sample thickness (cm)	Measured optical density at saturation	Saturation density per cm thickness
0·22	0·0030	0·014
0·41	0·0048	0·012
0·72	0·0087	0·012
1·05	0·015	0·014
1·54	0·022	0·014

Table 2. Saturation level of volume darkening in AgCl *crystal sheets*

Sample number	Thickness (cm)	Exposing wavelength (mμ)	Absorption coefficient (k cm^{-1})	Optical density at saturation	Saturation density per cm
M–24	0·02	365	1150	0·000069	0·08*
M–25	0·02	365	1150	0·000130	0·15
M–27	0·0125	405	18	0·00100	0·08
M–32	0·0125	405	18	0·00135	0·11
M–33	0·089	436	0·03	0·00520	0·06
M–40	0·10	436	0·03	0·00800	0·08

* In the case of exposure to a wavelength of 365 mμ, the exposed thickness is taken as the reciprocal of the absorption coefficient. For exposure to wavelengths 405 and 436 mμ, the actual physical thickness is used in calculating the optical density per cm at saturation.

The second rise in the darkening curve, which also tended to saturate upon prolonged exposure, exhibited no correlation with sample thickness, and it was suspected to be a process limited to the surface or a shallow subsurface region. This was confirmed by the following experiment, which utilizes the fact that the surface may be exposed without exposing the volume by use of strongly absorbed radiation. Both faces of a AgCl crystal disk were given a prolonged exposure to intense 365-mμ radiation, sufficient to saturate the darkening in the surface layers (since this radiation effectively penetrates less than 10^{-2} cm of the crystal, the volume of the sample remained essentially unexposed). Following this surface exposure, the sample was exposed to 436-mμ light, and the darkening measured as a function of exposure. The darkening curve exhibited the usual first linear rise and saturation, while the second rise was missing even upon prolonged exposure. The results of this experiment are best illustrated

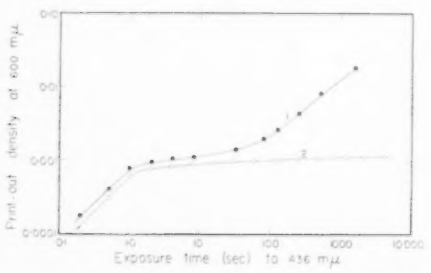

FIG. 3. Print-out density, at 600 mμ, in AgCl Bridgman crystals as a function of exposure to 436-mμ light. The exposing intensity is about 10^{14} absorbed quanta/cm^3/sec. Both samples are approximately 1 cm thick. 1—Crystal C–13–12, no previous exposure; 2—crystal C–13–13, previously exposed to 365-mμ radiation (both sides) in order to saturate the surface component of darkening.

by Fig. 3, in which the darkening upon exposure to 436-mμ light is compared in two samples, one of which received the described pre-exposure to 365-mμ radiation. This result clearly establishes that the second rise in the darkening curve represents a process limited to the crystal surface. It should be noted that the success of this experiment depends on the fact that a low-intensity exposure of the surface (inherent in the exposure to 436-mμ light) will not add to the surface darkening if it has been previously saturated by a high-intensity exposure. This experiment, as well as other qualitative observations, confirms this fact.

These experiments provide clear evidence that the darkening curves are properly interpreted as the superposition of a volume and a surface component. Subsequent work has been directed almost entirely towards an understanding of the factors controlling the rate of formation of the volume photoproduct and of the maximum photoproduct concentration that can be produced by exposure.

(c) *Survey of cationic impurity effects*

The total darkening that could be produced in the volume of AgCl crystals exhibited considerable variation from sample to sample, although crystals believed to be of higher purity showed less darkenability. In the purest AgCl Bridgman crystals studied, the saturation level of volume darkening occurred at values below 0·001 density unit per cm thickness, i.e., well below visually observable values. This volume photolysis which proceeded to a value characteristic of the particular sample, suggested the existence of a concentration of centers in the crystal volume on which the formation of a stable photoproduct depended. On the assumption that each of these centers acted only once in the photolytic process, their concentration would determine the extent to which a crystal could be darkened. Such centers may arise from various crystal imperfections: impurities, lattice defects, and larger-dimensioned crystal defects.

The influence of various anionic impurities on the photolysis of AgCl and AgBr was investigated extensively in 1941 by STASIW and TELTOW[7,19] and more recently by STASIW[20] and by VOLKE.[21] We have chosen to examine the effects of cationic impurities for several reasons: they are easier to incorporate quantitatively in crystals grown slowly from the melt, and they have, to date, been less extensively investigated than the anionic impurities.

Among the various cationic impurities studied, copper has been found to be particularly interesting, and the later sections of this paper deal with the optical and photolytic properties of AgCl crystals containing low concentrations of copper. However, we shall first summarize qualitative

VOL. 9 1959

observations made on other impurities incorporated into the "beaker" crystals described in Section 2. In the beaker work, cationic impurities were generally added as metal chlorides in solution. The samples were prepared under either reducing or oxidizing conditions. Reducing conditions consisted in melting the sample, adding a small amount of metallic silver, under an atmosphere of the appropriate halogen gas, flowing pure nitrogen gas over the melt for several minutes, and cooling the sample to room temperature in the nitrogen atmosphere; to maintain oxidizing conditions, no excess silver was added, and the sample was both prepared and cooled in an atmosphere of halogen gas. Impurity concentrations were in the range 10–1000 p.p.m. Visual, and in some cases spectrophotometric, observations were made of the optical absorption produced by the impurity and of the darkenability upon large exposures to tungsten light.

In AgCl, the metal chlorides of the elements commonly classed as Group VIIIA were soluble and produced characteristic optical absorptions when prepared under oxidizing conditions. Iron produced a brown color, cobalt a blue color, and nickel an orange-red color. Rhodium, platinum, and palladium imparted a yellow color at low concentrations, which shifted to red with increasing concentration of impurity. Ruthenium and osmium produced an absorption which had little selectivity throughout the visible range. In addition to these metals, gold chloride added under oxidizing conditions produced a blue color. Apart from surface darkening, only the addition of gold under these oxidizing conditions was found to promote a strong darkenability upon exposure. There were indications that iron chloride enhanced the darkenability of these samples, but the results were not consistent. Under reducing conditions, arsenic and cadmium produced a weak yellow color, the latter only if the sample was rapidly quenched from the melt. Incorporated in this way, cadmium promoted darkenability. The optical absorption produced by nickel and cobalt, added under oxidizing conditions, could be bleached thermally or optically. Enhanced darkenability of AgCl by copper is discussed later. Experiments with beaker samples showed that this darkenability could be suppressed by simultaneous additions of nickel, and to some extent, of cobalt. A wide variety of other cations* produced no striking effects on the optical or photochemical properties.

In AgBr, the Group VIIIA elements also produced characteristic optical absorptions when added under oxidizing conditions. Nickel particularly, even under reducing conditions, produced an intense red color which could be bleached thermally or optically.[1] Bismuth produced an orange color under both oxidizing and reducing conditions. No cationic impurity has been found which is very effective in producing volume darkenability of AgBr crystals; copper, under reducing conditions, produced some darkenability at very high concentrations, and gold, under oxidizing conditions, also induced some darkenability. Most of the elements listed as having had little effect on the properties of AgCl were found to be similarly ineffective in AgBr. One exception was chromium, which produced an intense green color under both oxidizing and reducing conditions.

Among the few cations that produced interesting effects, copper proved to be particularly amenable to quantitative investigation.

(d) *Sensitization of volume darkening in* AgCl *by cuprous ion*

Copper, added to the crystal sheets under reducing conditions (but with no added metallic silver), caused a large increase in the volume darkenability. Quantitative studies of this sensitization were carried out on large single crystals. Grown under an atmosphere of nitrogen, the copper is believed to be incorporated as a cuprous ion in these crystals (see Sections 4(e) and 4(f)). In Fig. 4 the darkening measured in a nominally pure AgCl large single crystal is compared to that measured in a similar crystal known to contain 0·2 p.p.m. of cuprous ion. The initial darkening rate is comparable, but the sample containing cuprous ion darkens to much higher levels of optical density. The saturation level of volume darkening in AgCl crystals containing cuprous ion has been shown to be proportional to the cuprous-ion concentration over a large range. This is illustrated by Table 4. In a 1-cm-thick AgCl crystal containing 1 p.p.m. of cuprous ion (5×10^{16} ions per cm^3), an

* Li, Na, K, Rb, Cs, Sr, Ba, Mg, Zn, Hg, Y, La, Ce, Pr, Nd, Sm, Eu, Ga, Al, In, Tl, Zr, Ge, Sn, Pb, V, Sb, Cr, Mn.

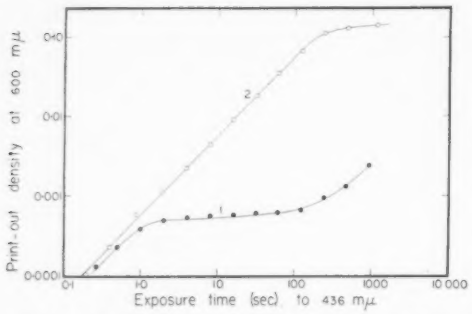

FIG. 4. Print-out density, at 600 mμ, in AgCl Bridgman crystals as a function of exposure to 436 mμ. The exposing intensity is about 3×10^{15} incident quanta/cm². 1—Pure AgCl crystal, 6·8 mm thick; 2—AgCl crystal containing 0·2 p.p.m. of cuprous ion, 8·0 mm thick. Note: For the pure AgCl, the absorption coefficient for 436 mμ is 0·03 cm^{-1} at room temperature; for the copper-containing crystal, the absorption is about 20 per cent greater.

Table 4. *Saturation density of photolytic darkening, measured at* 600 *mμ, in* AgCl *Bridgman crystals with deliberate cuprous-ion additions*

Crystal No.	Crystal thickness (cm)	Cu^+ ion impurity* (ppm)	Measured density†	Density per cm and ppm
C–50–2	1·01	0·04	0·044	1·1
C–48–3	0·80	0·20	0·140	0·9
C–73–12	0·61	2·5	1·22	0·8

* The impurity concentration, determined spectrochemically, is expressed as parts per million, weight of copper to weight of AgCl; 1 p.p.m. is equivalent to $5{\cdot}3 \times 10^{16}$ Cu^+ centers per cm^3. The spectrochemical values are estimated to be reliable to about 15 per cent.

† The density is measured after prolonged exposure to 436-mμ light of about 5×10^{15} incident quanta/cm²/sec.

optical density of about one can be formed in the volume. In a nominally pure crystal prepared in the same way, the optical density formed after prolonged volume exposure is less than 0·001 in a 1-cm-thick sample.

When copper-containing AgCl crystals are grown or annealed under conditions favoring the formation of cupric ions, namely in a chlorine atmosphere, the crystals exhibit no measurable darkening even upon prolonged exposure. Such crystals do, however, develop a characteristic optical absorption described in the next section. Nominally pure crystals annealed in a chlorine atmosphere also show a complete absence of measurable volume darkening upon exposure. No added optical absorption can be detected in such samples. In order to discuss the rôle of the cuprous and the cupric ion, and to make estimates of the quantum efficiency of silver formation in these crystals, it is necessary to have reliable data on the optical absorption of the copper ion in unexposed AgCl crystals.

(e) *Optical absorption of copper-containing* AgCl *crystals*

The optical absorption of AgCl crystals containing small additions of copper was dependent on the atmosphere in which the crystals were prepared.

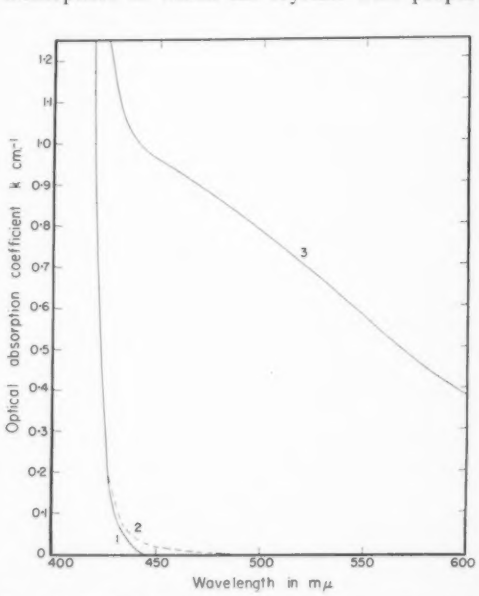

FIG. 5. Optical absorption coefficient as a function of wavelength in AgCl crystals, at 25°C. 1—Pure AgCl: 2—AgCl+1 p.p.m. of cuprous ion; 3—AgCl+1 p.p.m. of cupric ion.

Grown or annealed in nitrogen, these crystals showed a weak yellow color. Annealing in nitrogen with the crystal in contact with metallic silver did not modify this absorption. Under these conditions, the copper ion is almost certainly in its monovalent (cuprous) state. When annealed under chlorine atmosphere, favoring the formation of

cupric ion, a characteristically different and more intense absorption was formed. Heating at 400°C for ½ hr in chlorine or in nitrogen sufficed to form the cupric form or the cuprous form, respectively, independent of the initial state of the crystal. The absorption bands formed by these two copper states have been measured and are shown in Fig. 5. Optical absorption measurements on crystals containing varying concentrations of cuprous ion indicated that the cuprous ion was soluble in AgCl up to concentrations of at least 100 p.p.m. The dark ionic conductivity at room temperature in these crystals containing cuprous ion was not significantly different from that measured in nominally pure crystals. This suggests that the cuprous ion is present substitutionally in the AgCl lattice. Studies of the ionic conductivity of AgBr crystals with copper carried out by TELTOW[22] suggest other possibilities. Optical absorption measurements on crystals containing varying concentrations of cupric ion showed that this ion was much less soluble in AgCl, and remained atomically dispersed only in strain-free crystals: in a sense, one could form a supersaturated solid solution of cupric ions in carefully annealed crystals. Under these conditions, however, the optical data suggested that concentrations up to 100 p.p.m. could be incorporated.

If cupric-ion-containing AgCl crystals were strained, the absorption characteristic of the cupric ion faded and was replaced by a different and less intense band. This band is attributed to cupric ions in some less disperse form, perhaps as colloidal-size particles of cupric chloride. Observations of the light scatter from such samples suggested this possibility. With copper present in either of the two cupric forms, the crystals exhibited no volume darkenability upon exposure, nor could the cupric absorption band be bleached optically. The dark ionic conductivity in the cupric-ion-containing crystals was much higher than that measured for crystals with equivalent cuprous-ion content. This was most pronounced in the strain-free samples. For subsequent discussion, the states of copper in AgCl are designated as dissolved cuprous ion, dissolved cupric ion, and precipitated cupric ion. This latter state has been referred to as the "third state" in an earlier publication.[5] Optical, photochemical, and electrical measurements support this identification. Fig. 6 summarizes the absorption bands of copper, in all three states, in large AgCl crystals.

When AgCl crystals containing several parts per million of dissolved cupric ion were mildly strained, the transition to precipitated cupric ion took place in a matter of hours at room temperature. This

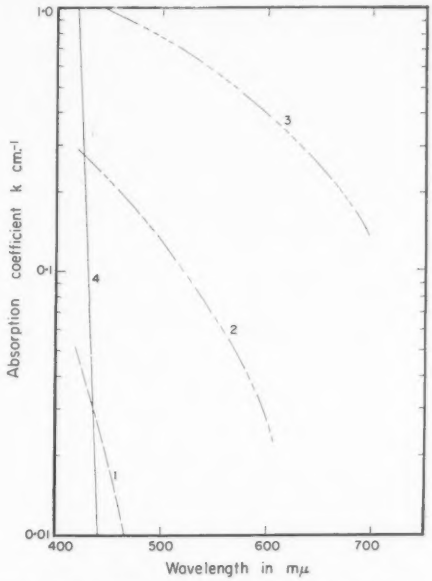

FIG. 6. Optical absorption coefficient (on a log scale) as a function of wavelength for copper ion in AgCl, at 25°C. Absorption coefficients are given for an impurity concentration of 1 p.p.m. 1—Cuprous ion; 2—precipitated cupric ion; 3—dissolved cupric ion. The spectrum shown is for the impurity ion alone. Curve 4, for comparison, shows the absorption edge in a pure AgCl crystal.

transition was not modified by simultaneous exposure; that is, this transition could not be optically enhanced. However, it has been observed that the precipitated cupric ion can be redispersed by mild heating. This phenomenon is best illustrated by the curves of Fig. 7. Curve 1 represents the absorption with copper present as cuprous ion. After annealing in a chlorine atmosphere, the absorption spectrum shown by curve 2 was measured. The annealed crystal was now strained (sufficient to cause several percent deformation) and after approximately 15 hr curve 3 resulted. Now, with the copper supposedly present as precipitated cupric ion, the sample was heated at 200°C for about 1 hr in a nitrogen atmosphere. Curve 4, obtained after this treatment, shows almost complete restoration of the dissolved cupric-ion absorption. Prolonged

heating at 400°C in a nitrogen atmosphere led again to the same absorption spectrum as curve 1.

(f) *Quantum efficiency of photolytic darkening in* AgCl *crystals with copper*

Experimental darkening curves of the type shown in Figs. 1, 3, and 4 reveal an initial region of

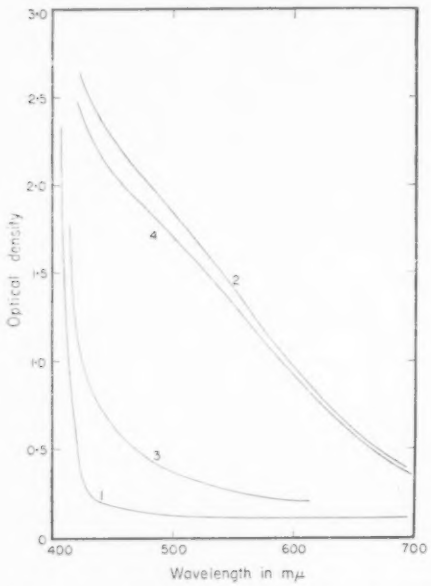

FIG. 7. Total optical density as a function of wavelength in an 8-mm-thick AgCl crystal containing about 7 p.p.m. of copper ion, at 25°C. Curve 1—Initial absorption, copper present as cuprous ion; 2—after anneal at 400°C; 3—15 hr after deliberate strain (this absorption is characteristic of the so-called precipitated cupric ion); 4—after 1 hr at 200°C, in a nitrogen atmosphere, and cooling to 25°C. Prolonged heating, at 400°C in a nitrogen atmosphere, restores the absorption shown by curve 1.

volume photoproduct formation where induced optical density is proportional to the total number of absorbed quanta. It has been implicitly assumed that this optical density is a good relative measure of the total amount of silver formed. This assumption is strongly supported by the fact that the shape of the exposure-induced absorption band is approximately constant over a large range of photoproduct formation (see Sections 4(g) and 4(h)). Therefore, the initial linear region of the darkening curves corresponds to a range of exposure in which silver is formed with constant efficiency. In this section, experimental results are described which enable one to estimate this quantum efficiency of silver formation.

Two experimental observations—the proportionality between induced optical density and absorbed quanta (see, for example, Fig. 4) and the proportionality between cuprous-ion concentration and optical density at saturation (see Table 4)—suggest that cuprous ions are consumed in proportion to the number of absorbed quanta, and that saturation occurs when all of the cuprous ions have been consumed. The total number of quanta required to reach saturation (that is, to use up all of the cuprous ions) can be determined from quanti-

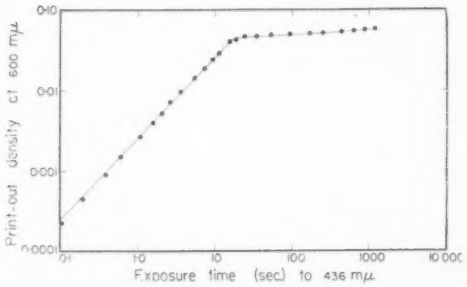

FIG. 8. Print-out density, measured at 600 mμ, as a function of exposure to 436-mμ light, of intensity $1{\cdot}4\times10^{14}$ absorbed quanta/cm³/sec in a AgCl Bridgman crystal, 8·5 mm thick, containing $2{\cdot}2\times10^{15}$ cuprous ions/cc. Measurement of darkening is made at 25°C.

tative measurements of the darkening as a function of the number of absorbed quanta in crystals containing small, but well-defined, cuprous-ion concentrations. The restriction to samples with low copper content is an experimental simplification: in samples that saturate at low levels of darkening, the attenuation of the exposing light by the photoproduct can be neglected (see the Appendix). Darkening curves for such samples have been measured, and the result of one such measurement is shown in Fig. 8, and, on a linear plot, in Fig. 9. According to spectrochemical analysis, this sample contained $2{\cdot}2\pm0{\cdot}4\times10^{15}$ cuprous ions per cm³. The total number of absorbed quanta required to reach saturation was determined, from Fig. 9, and found to be $2{\cdot}2\times10^{15}$ quanta per cm³. It is estimated that this number is accurate to about 10 per cent. Thus, in the linear region of the darkening curve, *the efficiency with which cuprous ions are used up is,*

within the limits of experimental error, equal to unity; and saturation of darkening occurs when one quantum has been absorbed for each cuprous ion present. The

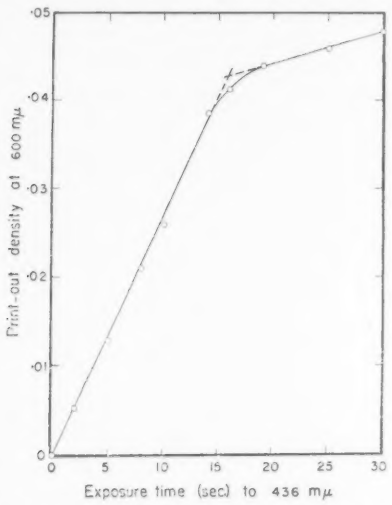

FIG. 9. Plot of the data shown in Fig. 10, on a linear scale. The same numerical values apply. The saturation of the volume photoproduct, taken to occur after 16-sec exposure, corresponds to the absorption of $2{\cdot}2\times10^{15}$ quanta/cm^3.

cuprous ions, whose presence allows the formation of a stable volume photoproduct, are presumed to act as traps for the holes formed by absorbed quanta. Thus, each hole liberated by absorbed photons is trapped by a cuprous ion, producing one cupric ion in some form. The corresponding electron formed by each absorbed photon presumably combines with a silver ion to form one silver atom. The measured one-to-one correspondence between cuprous ions and absorbed quanta at saturation darkening, suggests that each absorbed quantum also leads to the formation of one silver atom; that is, within the limits of experimental error, the quantum efficiency of silver formation is one until nearly all of the possible photoproduct has been formed (see pertinent discussion in the Appendix).

It has already been noted in Table 4, and confirmed in Fig. 8, that 5×10^{16} cuprous ions per cm^3 confer a total volume darkenability of optical density near one in a 1-cm-thick crystal. In accord with the conclusions reached in the preceding paragraphs, this optical density is attributable to 5×10^{16} silver atoms per cm^3 *and* 5×10^{16} cupric ions per cm^3. The absorption strength of photochemically formed cupric ions is not really known. It is nevertheless of interest to observe that *if* the absorption of photochemically formed cupric ions is about the same as that of cupric ions formed by chlorine annealing, then about 80 per cent of the optical density measured at 600 mμ is attributable to photochemical silver.

(g) *Spectrum of the photoproduct in* AgCl *crystals*

Although measurements of the spectrum of the photoproduct at extremely low levels of darkening are difficult to make, several authors have reported such measurements.[13,16] The bands they observed had approximately the same shape as the more intense bands measured earlier by HILSCH and POHL.[6] The lowest-level darkening spectra that have been reliably measured by us are shown

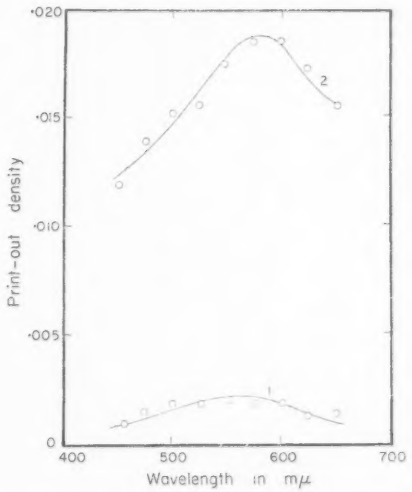

FIG. 10. Spectrum of the photoproduct at low levels of formation in nominally pure AgCl Bridgman crystal, 1·4 cm thick. Exposure is to 436-mμ light. 1—After approximately 10^{14} absorbed quanta/cm^3; 2—after approximately 10^{17} absorbed quanta/cm^3 (saturation).

in Fig. 10, and agree in general shape with the measurements of these authors at somewhat higher levels of darkening. No indications have been found that the darkening spectrum at low levels is a narrow band.

A large number of measurements of the absorption spectrum of the photoproduct have been made on AgCl crystals containing small deliberate additions of cuprous ions. The higher levels of darkening that can be produced in these crystals make measurements of the absorption simpler to obtain, and such spectra may be examined with the question of cupric-ion formation in mind. Fig. 11

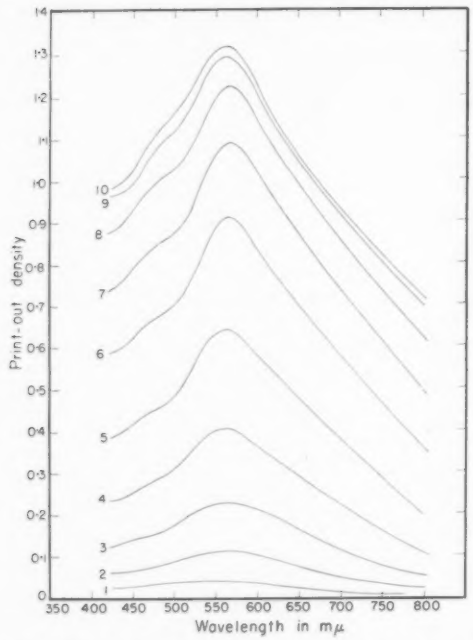

FIG. 11. Print-out density as a function of wavelength for increasing exposures to 436-mμ light of incident intensity about 5×10^{15} quanta/cm²/sec. AgCl Bridgman crystal, 6·1 mm thick, containing 2·2 p.p.m. cuprous ion. 1—After 5-sec total exposure; 2—15-sec total; 3—35-sec total; 4—75-sec total; 5—155-sec total; 6—335-sec total; 7—635-sec total; 8—1235-sec total; 9—2435-sec total; 10—3935-sec total exposure.

shows the spectrum of the photoproduct in an annealed AgCl crystal containing 2·2 p.p.m. of cuprous ion initially, at various stages of exposure to 436-mμ light. Exposure beyond curve 9 of this figure did not produce any significant additional volume darkening; the additional darkening observed occurred on the external surfaces. The broad maximum in the neighborhood of 560 mμ is generally attributed to photolytically formed colloidal silver. The shoulder observed at around 460 mμ may be related to the formation of cupric ions. As the total amount of photoproduct increases, the absorption band becomes somewhat flatter, developing a slightly disproportionate amount of absorption to the long-wavelength side of the maximum. These features of the absorption spectrum have been found to be essentially the same in samples of different cuprous-ion concentrations, and in samples that have been mildly strained, although minor differences in detail have been observed which are not well understood.

The absorption of the photoproduct has been

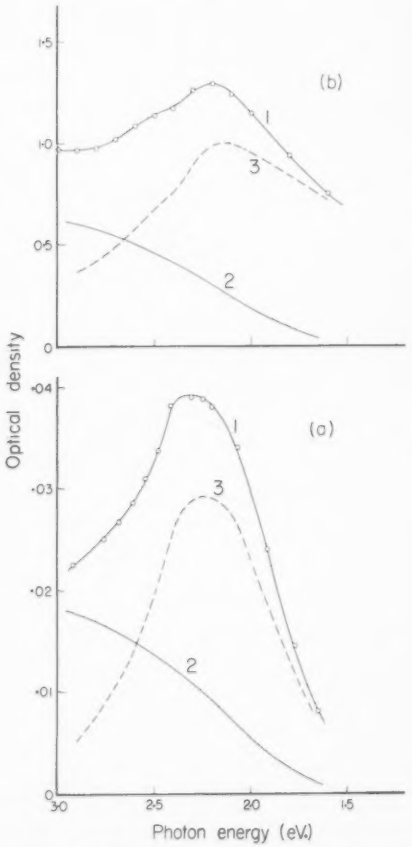

FIG. 12. Possible interpretation of the photolytic absorption spectrum in AgCl–Cu^+ Bridgman crystals. Optical density is plotted as a function of photon energy in electron volts. For each set of curves, number 1 is the total measured darkening, 2 is the calculated absorption of dissolved cupric ions, and 3 is the difference spectrum; (a) is the analysis of curve 1 of Fig. 11; (b) is the analysis of curve 9 of Fig. 11.

assumed to be caused by the photolytically formed silver atoms and cupric ions. The optical absorptions of these photoproducts are not known separately. In particular, it is not known in what state of dispersity and possible association with lattice defects cupric ions are formed by exposure. If one assumes that, upon exposure, cupric ions are formed which have an optical absorption similar to that measured for precipitated cupric ions (see Fig. 6), one can resolve the spectra of Fig. 11 into two components—one due to precipitated cupric ions and one due to the photolytically formed silver. Since the absorption strength of precipitated cupric ions is weak compared to the total measured photoproduct absorption, the resultant calculated curve for the photolytic silver would differ but little from the measured absorption spectrum for the total photoproduct. On the other hand, one can assume that, upon exposure, cupric ions are formed which have an optical absorption similar to that measured for dissolved cupric ions, and see how the spectra of Fig. 11 resolve under this assumption. Such an analysis has been applied to the spectra of Fig. 11, and two cases are shown in Fig. 12. For each set of curves, number 1 is the total measured darkening, and number 2 is the calculated absorption of dissolved cupric ions (this is calculated from the data in Fig. 6, assuming that each absorbed quantum leads to the formation of one silver atom and one cupric ion). Curve number 3 is the difference between 1 and 2, and, under the above assumption, is then attributable to the photolytically formed silver.

The analysis just given proves that the assumption of the formation of cupric ions upon exposure, with an absorption characteristic of cupric ions formed by chlorine annealing, is compatible with the experimental facts. It obviously does *not* prove that such cupric ions are indeed formed by exposure of the crystal volume. On the basis of such optical studies alone, one can obviously not decide in what state of dispersity cupric ions are formed by exposure.* Work is at present underway to obtain a better-founded picture of the exact nature of the photolytic product in these crystals.

(h) *Some considerations on the absorption of silver in* AgCl

Regardless of whether the details of the interpretation of the spectrum of the photoproduct are valid, it is evident that the photochemically formed silver has an absorption band whose broad maximum occurs near 560 mμ and has a half-width of about 150–200 mμ. These general features of the absorption band of photolytic silver appear to be preserved over a large range of silver concentrations; the spectrum shown in Fig. 10, curve 1, results from about 10^{14} silver atoms per cm^3, while that of Fig. 12(b) results from about 10^{17} silver atoms per cm^3. SEITZ[14] several years ago suggested that there appear to be two broad ranges of darkening in the silver halides; in the early stages, the centers responsible for the darkening contain only a few atoms of silver, while in the later stages colloidal aggregates of silver are formed. He further suggested that the early stages of darkening correspond to between 10^{14} and 10^{16} centers per cm^3. If such a transition from atomically dispersed silver to colloidal aggregates occurs, it is apparently not accompanied by a marked change in the shape of the absorption spectrum. Many years ago SAVOST'YANOVA[23] reviewed some of the experimental information available on the absorption of silver metal in silver halide crystals, and compared it to the theory of MIE[24] for the optical absorption of spherical silver particles embedded in a dielectric. More recently, ROHLOFF[25] has published curves of the absorption of silver particles in AgCl, calculated from the MIE theory. Comparison of our experimental curves with these calculated curves suggests that our observed spectra could be interpreted as a distribution of colloidal-size particles with a mean size in the neighborhood of 600 Å.

Quantitative comparison of the curves is compatible with our previous assumption of the formation of one silver atom by each absorbed quantum. It is extremely unlikely that there are silver particles 600 Å in size formed at the lowest darkening levels measured. A particle of this size contains of the order of 10^8 atoms. Thus, at darkening levels of 10^{14} silver atoms per cm^3, the concentration of particles would be only 10^6 per cm^3. This would imply that the particles are separated by distances of the order of 10^{-2} cm in the crystal, which seems rather improbable. BROWN and WAINFAN[15] have published similar considerations on the nature of

* Paramagnetic-resonance studies of copper-doped AgCl crystals carried out by R. F. TUCKER at the University of Illinois suggest that if cupric ions are formed by exposure, they occur in some aggregated form (private communication).

the photoproduct in AgCl crystals, and have reached similar conclusions. Recent unpublished work by DUBOC[26] suggests that absorption bands of the type observed could be produced by random distributions of particles of atomic dimensions which are not spheres but ellipsoids of varying axial ratios. Experimental studies of the type carried out by KAISER[27] may prove to be helpful in differentiating between these various possibilities.

(i) *Optical bleaching of copper-containing* AgCl *crystals*

Optical bleaching of photolytically darkened AgCl crystals was observed many years ago by HILSCH and POHL,[6] and recent experimental studies of this phenomenon have been reported by BROWN and WAINFAN.[15,16] Studies of optical bleaching in AgCl crystals containing small additions of cuprous ion have revealed a behavior which is in essential agreement with these reported observations.

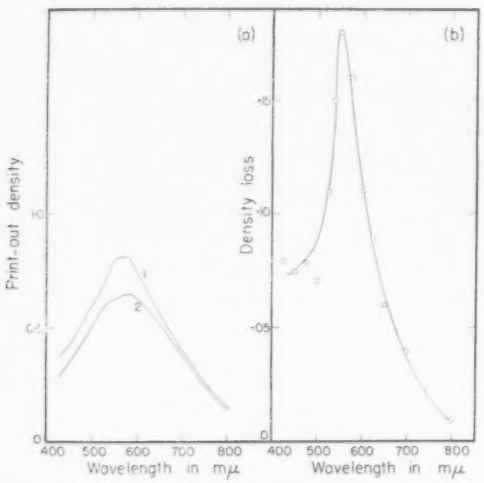

FIG. 13. Bleaching of the photoproduct in a AgCl–Cu^+ crystal. In Fig. 13(a), the absorption after exposure to 436-mμ light is shown by curve 1; after a short exposure to 546-mμ light, curve 2 results. The density difference between these two curves is plotted on an expanded scale in Fig. 13(b), to the right. Quantitative values of the exposing and bleaching light are not available for this sample.

Fig. 13(a) shows the result of an optical bleaching experiment on a copper-containing AgCl crystal. Curve 1 represents the absorption spectrum of the photoproduct formed by exposure to 436-mμ light, the total exposure being sufficient for the saturation of volume darkening. The sample was then given an exposure to 546-mμ light, and the residual density is shown by curve 2. In Fig. 13(b), the density loss produced by the 546-mμ exposure is plotted on an enlarged scale. The fact that the density loss stays high on the short-wavelength side may possibly be associated with changes in the state of the cupric ion. Measurements of density differences near the optical absorption edge are difficult to obtain. An estimate of the quantum efficiency of bleaching has been made by measuring the loss in area of the photoproduct spectrum. Calculated in this manner, the quantum efficiency of bleaching is of the order of 1 per cent. This value, however, seems to depend on the total amount of photoproduct initially present. Striking evidence of such bleaching phenomena has been obtained by use of a slit ultramicroscope,*[28] and one result is shown in Fig. 14.

Related to these observations of optical bleaching are some observations made on the decay of the photoproduct both in the dark and under long-wavelength illumination. The photoproduct formed in these crystals exhibited some decay in the dark, even at room temperature. This decay is slow in well-annealed crystals. Heating to 100°C or above greatly accelerates this regression, and, above 350°C, the photoproduct is rapidly destroyed. Such losses in image, occurring in the dark and with the heating taking place in an inert atmosphere, may be re-formed by re-exposure of the crystal. This photoproduct regression must therefore arise from recombination of thermally released holes with electrons. An example of the dark decay in an unannealed sample is shown in Fig. 15,

* The slit ultramicroscope, now rarely used, but very suitable in the present case, employs a slit and a microscope objective to form a narrow, well-collimated light bundle which is then passed through the crystal being studied. Observation of any scattered light is made by a microscope positioned at right angles to the light beam. Provision has been made for simultaneous observation and photography. The light beam incident on the crystal is itself effective in producing a photoproduct, and the light scattered from this product can be viewed while the photoproduct is being formed. Such an arrangement allows one to resolve, by their light scatter, particles much smaller than are ordinarily observable with a light microscope.

VOL.
9
1959

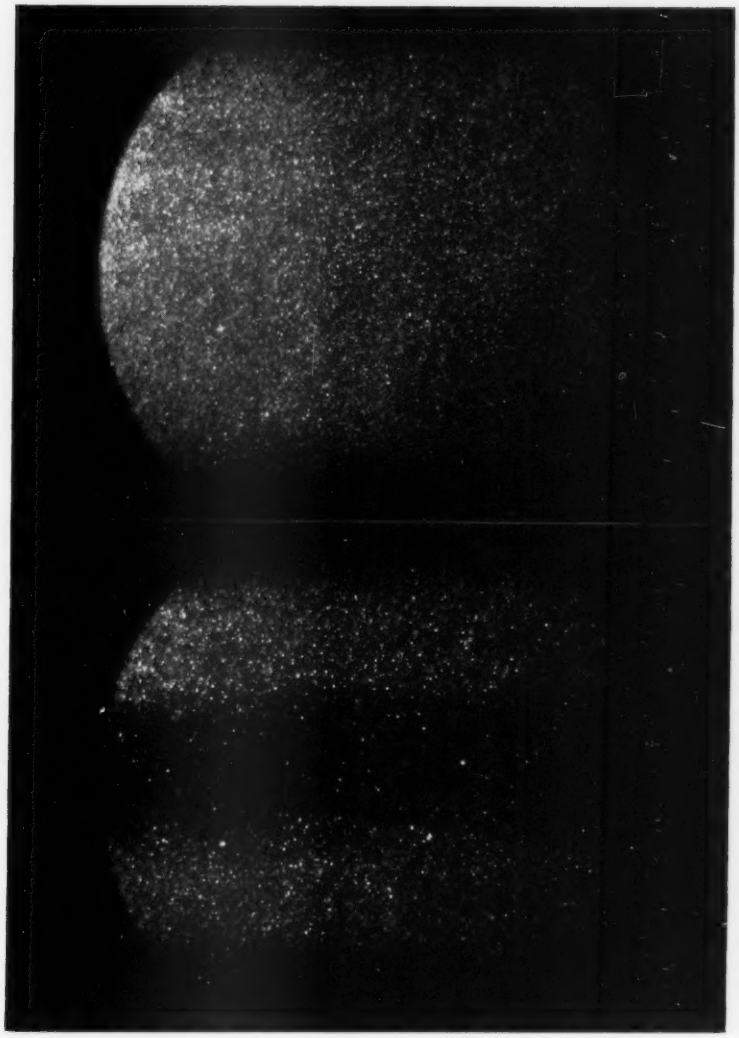

FIG. 14. Photographs of the scattered light from the photoproduct in AgCl–Cu^+ crystals, as viewed in the slit ultramicroscope. Upper photograph: after a long, high-intensity exposure to radiation from a carbon arc (wavelengths shorter than 400 mμ are excluded from the exposure by appropriate filters). Lower photograph: after exposure of the central third of the field to long-wavelength radiation ($>$ 600 mμ). Absolute exposure values are not available for these experiments.

[*facing p.* 230

VOL.
9
195

the decay taking place at room temperature. Curve 1 of this figure shows the optical density before exposure (uncorrected for scatter and reflection losses in the sample). Curve 2 is the absorption after prolonged exposure to 436-mμ light. This absorption band decays rather slowly, but, after

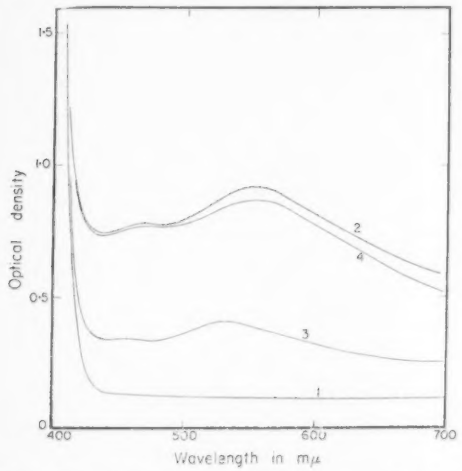

FIG. 15. Optical density (uncorrected for reflection and scatter losses) as a function of wavelength in a AgCl crystal, under various conditions. Sample is 2·4 mm thick, and contains about 3 p.p.m. of cuprous ion. 1—Before exposure; 2—after exposure to 436-mμ light (20 min, incident intensity about 3×10^{15} quanta/cm^2/sec); 3—after 300 hr dark decay; 4—after subsequent re-exposure, as in 2.

several weeks in the dark, the absorption band is much less intense, as shown by curve 3 of this figure. The shape of the absorption band is approximately preserved. As shown by curve 4, this density loss is nearly completely restored by re-exposure. The situation is quite different if the decay does not occur in the dark, as is illustrated by Fig. 16. The same conditions apply here as in Fig. 15, except that the decay took place under low-level tungsten illumination. The curves show that the absorption spectrum after decay has been modified greatly both in intensity *and* in shape. In addition, re-exposure to 436-mμ light is now not effective in restoring the initial photoproduct absorption. Obviously, effects other than simple recombination of electrons and holes are involved here: to some extent, a redistribution of the photoproduct is involved. These results suggest that the optical bleaching that occurs under these conditions has a different mechanism from that occurring when bleaching takes place by monochromatic exposure in a narrow region of the photoproduct band. Density loss occurring by this latter bleaching is known to be restorable by re-exposure.[16] The decay observed in the sample of Fig. 15 is

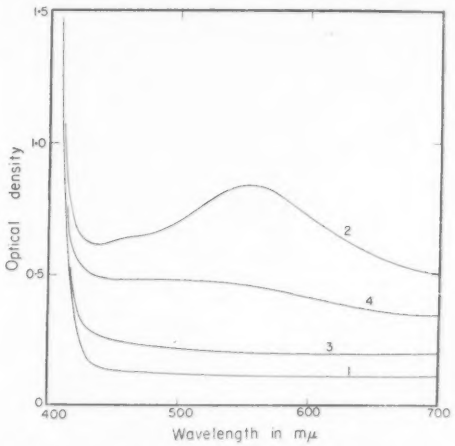

FIG. 16. Optical density (uncorrected for reflection and scatter losses) as a function of wavelength in a AgCl crystal, under various conditions. Sample is 2·5 mm thick, and contains about 3 p.p.m. of cuprous ion. 1—Before exposure; 2—after exposure (same as curve 2 of Fig. 15); 3—after 300 hr decay under low-level tungsten illumination; 4—after subsequent re-exposure, as in 2.

considerably larger than that occurring in well-annealed samples. In such samples, image loss may be of the order of only a few per cent in several weeks. These qualitative observations indicate that a more detailed study of the subject may be worthwhile.

(j) *Influence of exposing intensity and strain on photoproduct formation in copper-containing* AgCl *crystals*

The experimental results reported so far on large single crystals have been obtained on samples with low copper concentrations (below 10 p.p.m.), annealed or only mildly strained, which have been exposed to monochromatic intensities of the order of 10^{14} absorbed quanta/cm^3/sec or higher. Under these restrictions, the efficiency of formation of the photoproduct and the absorption spectrum of the photoproduct have been, within the limits of

experimental error, independent of the particular sample being investigated.

Exposure to lower intensities of actinic radiation, introduction of large amounts of strain, use of higher concentrations of impurity, and non-monochromatic exposures, all act to give results that are considerably more difficult to interpret. Therefore, little experimental work has been done under these conditions. Nevertheless, several qualitative observations on the influence of these factors have been made, and will be reported here.

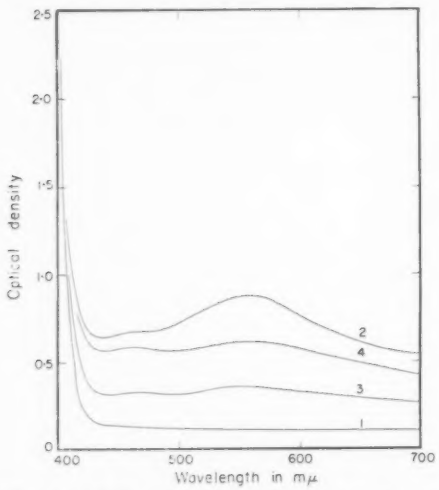

FIG. 17. Optical density (uncorrected for reflection and scatter losses) as a function of wavelength in a AgCl crystal, at two intensities of exposure. Both samples are 2·3 mm thick, and contain about 3 p.p.m. of cuprous ion. 1—Samples before exposure (this initial absorption is essentially identical for the two samples); 2—sample A, after exposure for 30 min to 436-mμ light, intensity about 2×10^{14} absorbed quanta/cm³/sec; 3—sample B, after exposure for 20 hr to 436-mμ light, intensity about 5×10^{12} absorbed quanta/cm³/sec; 4—sample B, after additional exposure for 30 min to the higher-intensity, 436-mμ light.

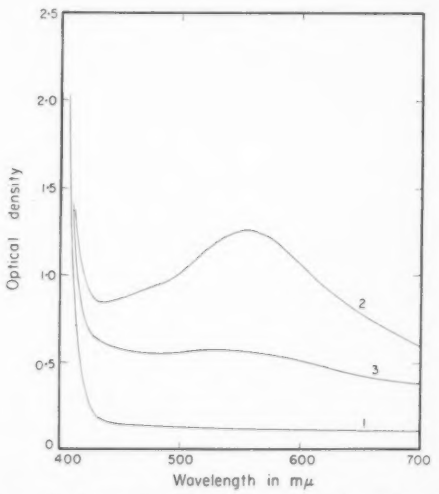

FIG. 18. Optical density (uncorrected for reflection and scatter losses) as a function of wavelength in AgCl crystals. Both samples are about 2·5 mm thick, and contain about 4 p.p.m. of cuprous ion. In both cases, exposure is for 20 min to 436-mμ light, of incident intensity about 3×10^{15} quanta/cm²/sec. 1—Samples before exposure (this initial absorption is essentially identical for the two samples); 2—sample A, no deliberate strain, after exposure; 3—sample B, strained prior to exposure by application of a compressive force sufficient to deform the sample several per cent, after exposure.

Fig. 17 illustrates the effect of a reduction in exposing intensity to a value well below 10^{14} absorbed quanta/cm³/sec. The absorption band produced by exposure to 436-mμ light is shown for a 2·3-mm-thick AgCl crystal containing, initially, approximately 3 p.p.m. of cuprous ion. Sample A (curve 2) was exposed for $\frac{1}{2}$ hr to an intensity of about 2×10^{14} absorbed quanta/cm³/sec; sample B (curve 3) was exposed for 20 hr to an intensity of 5×10^{12} absorbed quanta/cm³/sec. Curve 1 is the optical density before exposure, uncorrected for scatter and reflection losses, and was essentially identical for the two samples. It is seen that the photoproduct formed with low-intensity exposure has an absorption spectrum differing both in shape and in strength from that formed at the higher intensity. The quantum efficiency of silver formation at these low values of exposing intensity has not been estimated. The differences in absorption arise, in part, from differences in the covering power of the photolytically formed silver, and are probably not solely due to a decrease in the quantum efficiency of silver formation. It is interesting to note that subsequent exposure of sample B to the higher intensity causes some increase in total photoproduct, but does not produce the absorption spectrum characteristic of a single, high-intensity exposure. This is illustrated by curve 4 of Fig. 17.

It has been noted (see Section 4(g)) that the absorption spectrum of the photoproduct in these

crystals is not particularly dependent on strain. This conclusion was reached after numerous measurements of darkenability in well-annealed and mildly strained crystals. If, however, the crystal is severely strained (to the extent of several per cent deformation), the photoproduct formed by subsequent exposure is considerably modified. In Fig. 18, the spectrum of the photoproduct in a relatively strain-free crystal is compared with that measured in a crystal that was deformed prior to exposure. The differences are apparent. Interpretation of these results must await further experimental investigations under better-defined conditions.

Acknowledgements—The authors wish to express their appreciation to the following colleagues in these Laboratories: C. A. DUBOC, P. E. GODDARD, and D. PEARLMAN for valuable discussions and direct assistance in many phases of this work; to F. GRUM, E. E. RICHARDSON, and T. WIGHTMAN for their help in obtaining some of the spectrophotometric results, and to D. EASTMAN for the ultramicrographs and for his contribution to the techniques used in preparing them.

APPENDIX

As discussed in detail in Section 4(f), the quantum efficiency of silver formation in the first "linear" region of the darkening curves is estimated to be one. Therefore, at least in the early stages of darkening, there is no effective competition for the photochemical darkening process which entails the trapping of both electrons and holes. As the saturation level is approached, however, some competing process, such as recombination of electrons and holes, must begin to be a factor. Such a competing process would make the volume darkening approach saturation more gradually than the idealized curve described by Fig. 2. The rather good agreement between the constructed curve of Fig. 2 and the experimental curve of Fig. 1, and the sharp transition to saturation normally observed, show that the influence of the competing process or processes on the shape of the darkening curve is small until a large fraction of the possible volume photoproduct has been formed.

Even if the effect of a competing process on the shape of the darkening curve as it approaches saturation is neglected, there are several other experimental factors which would tend to make the measured darkening curve differ in shape from the ideal linear curve described by Fig. 2. If the exposing intensity is considerably attenuated as it passes through the crystal thickness, deeper regions of the crystal will require longer times to saturate, since saturation occurs after the absorption of a certain number of quanta. Where the attenuation of the exposing light is greater than 10 per cent, this will produce a "rounding" in the experimental curve as the saturation level of darkening is approached. With 436-mμ exposing light in AgCl at room temperature, this effect is negligible. When the darkening in the volume proceeds to levels such that the photoproduct itself has appreciable absorption at the exposing wavelength, this also decreases the effective exposing intensity as the light penetrates the crystal depth. This filtering action of the photoproduct on the exposing light also tends to make the approach to saturation more gradual. One may also have to consider the further complication of selective bleaching caused by light absorbed in the photoproduct. The efficiency of the bleaching process, however, appears to be small compared to the efficiency of silver formation (see Section 4(i)). In interpreting our data on the darkening of AgCl crystals, we have been interested primarily in the initial rate of darkening (efficiency) and in the saturation level of darkening in the crystal volume. No attempt has been made to account quantitatively for the shape of the darkening curve as saturation is approached.

REFERENCES

1. URBACH F., A paper entitled *Some Effects of Inorganic Impurities on Silver Halide Crystals* was presented by D. PEARLMAN at a Symposium on Impurity Phenomena, held at the Research Laboratories, General Electric Company, Schenectady, New York, on 16–18 June 1953.
2. NAIL N. R., MOSER F., GODDARD P. E., and URBACH F., *Phys. Rev.* **[2] 102,** 1557(A) (1955).
3. MOSER F. and URBACH F., *Phys. Rev.* **[2] 102,** 1519 (1956).
4. NAIL N. R., MOSER F., GODDARD P. E., and URBACH F., *Rev. Sci. Instrum.* **28,** 275 (1957).
5. MOSER F., NAIL N. R., and URBACH F., *J. Phys. Chem. Solids* **3,** 153 (1957).
6. HILSCH R. and POHL R. W., *Z. Phys.* **64,** 606 (1930).
7. STASIW O. and TELTOW J., *Ann. Phys., Lzg.* **40,** 181 (1941).
8. HECHT K., *Z. Phys.* **77,** 235 (1932).
9. STASIW O. and TELTOW J., *Nachr. Akad. Wiss. Göttingen* No. 10, 155 (1944).
10. LUCKEY G. W., *J. Chem. Phys.* **23,** 882 (1955).
11. CLARK P. V. McD. and MITCHELL J. W., *J. Phot. Sci.* **4,** 1 (1956).
12. SAUNDERS V. and WEST W., Submitted for publication in *J. Phys. Chem.* (1958).
13. LOHLE F., *Nachr. Ges. Wiss. Göttingen* II, No. 43, 271 (1933).
14. SEITZ F., *Rev. Mod. Phys.* **23,** 328 (1951).
15. BROWN F. C. and WAINFAN N., *Phys. Rev.* **[2] 105,** 93 (1957).
16. WAINFAN N., *Phys. Rev.* **[2] 105,** 100 (1957).
17. HEDGES J. M. and MITCHELL J. W., *Phil. Mag.* **44,** 357 (1953).
18. NAIL N. R., MOSER F., and URBACH F., *J. Opt. Soc. Amer.* **46,** 218, (1956).
19. STASIW O. and TELTOW J., *Nachr. Ges. Wiss. Göttingen* II, S93, 100 (1941).

20. STASIW O., *Z. Phys.* **134,** 106 (1952).
21. VOLKE C., *Z. Phys.* **138,** 623 (1954); *Ann.. Phys., Lzg.* **19,** 203 (1956).
22. TELTOW J., *Z. phys. Chem.* **195,** 197 (1950).
23. SAVOST'YANOVA M. V., *Usp. fiz. nauk* **22** 168, (1939).
24. MIE G., *Ann. Phys., Lzg.* **25,** 377 (1908).
25. ROHLOFF E., *Z. Phys.* **132,** 643 (1952).
26. DUBOC C. A. Private communication.
27. KAISER W., *Z. Phys.* **132,** 497 (1952).
28. SIEDENTOPF H. and ZSIGMONDY R., *Ann. Phys., Lzg.* No. 10, 1–39 (1903).

VOL
9
195

J. Phys. Chem. Solids Pergamon Press 1959. Vol. 9. pp. 235–237. Printed in Great Britain.

THE EFFECT OF DISPERSION CORRECTIONS ON THE REFINEMENT OF THE YTTRIUM–IRON GARNET STRUCTURE

S. GELLER and M. A. GILLEO

Bell Telephone Laboratories Inc., Murray Hill, New Jersey

(*Received* 30 *September* 1958)

VOL. 9 1959

Abstract—The refinement of the structure of yttrium–iron garnet has been recalculated with the inclusion of the previously neglected dispersion corrections on the atomic scattering factors of the metal atoms. No significant change is obtained in the positional parameters of the oxygen ions. Changes occur in the temperature factors of the yttrium and oxygen ions: for Y^{3+} from 0·16 to 0·40 Å^2 and for O^{2-} from 2·05 to 1·19 Å^2. There is also a change in the factor required to put the observed amplitudes on an absolute scale.

THE results of the refinement of the crystal structure of yttrium–iron garnet, $Y_3Fe_2(FeO_4)_3$, were recently reported by the authors.[1] In this analysis, CoK_α appeared to be the optimum radiation to use to obtain the single-crystal data. CuK_α radiation would not only be very highly absorbed (Table 1) by the crystal, but would also cause considerable fluorescence of iron. Unreasonably long exposures would be required to record the reflections needed for the refinement if MoK_α radiation were used. The radiations CrK_α and FeK_α would not only reduce the number of data obtainable, but also would be more highly absorbed than CoK_α (Table 1). However, in the original work, the dispersion

Table 1. *Linear absorption coefficients of* $Y_3Fe_2(FeO_4)_3$

Radiation	$\mu(cm^{-1})$
CrK_α	951
FeK_α	615
CoK_α	481
CuK_α	892
MoK_α	190

of the CoK_α radiation by the metal atoms (it is negligible for oxygen) was neglected. Because the dispersion corrections appear to be significant, we have repeated the least-squares refinement with the same observed data, but have applied the real parts of the dispersion corrections to the atomic scattering factors of yttrium and of iron.

The dispersion corrections were computed in accordance with the procedure described by JAMES[2] which was based on the work of HÖNL.[3] Only dispersion by the K electrons was considered. Contributions from outer shells are probably small. The corrections applied to the atomic scattering factors of Y^{3+} and Fe^{3+} were $-1·3$ and $-3·7$ electrons respectively. These values are near those that would be obtained by the method of PARRATT and HEMPSTEAD;[4] the value for iron particularly is in agreement with experimental values.[5]

In the more recent calculations, the latest values of scattering factors for Y^{3+} and Fe^{3+}, namely those of THOMAS and UMEDA,[6] were used. The values for O^{2-} were the same as those used in the previous work.

The important result of this work is that no significant change is found in the oxygen coordinates, the previously neglected dispersion corrections being taken up in the scale and "temperature" factors.

The calculations were carried out as before on the IBM 704 computer by means of the program

Table 2. Results of last three least-squares iterations

Oxygen co-ordinates			Temperature factors (Å²)			Scale factor, K	Iteration
x	y	z	O^{2-}	Y^{3+}	Fe^{3+}		
−0·0275	0·0571	0·1494	1·26	0·41	0·65	1·169	5
−0·0275	0·0572	0·1495	1·21	0·40	0·67	1·169	6
−0·0274	0·0572	0·1495	1·19	0·40	0·66	1·172	7
−0·0274	0·0572	0·1492	2·05	0·16	0·63		*

* Values obtained when dispersion corrections were neglected.[1]

(NYXR2) devised by Dr. D. SAYRE and the auxiliary program for Ia3d worked out by Miss D. C. LEAGUS of these Laboratories. Seven least-squares iterations were computed. The results of the last three are listed in Table 2.

Although no significant changes occurred in the

Table 3. Observed and calculated amplitudes

(*hkl*)	Obs.	Calc.	(*hkl*)	Obs.	Calc.	(*hkl*)	Obs.	Calc.
121	98	−121	671	< 37	27	581	54	−56
123	68	−86	673	70	−84	583	71	81
125	199	−202	677	31	−40			
127	98	−104	679	112	98	691	101	93
129	65	−70						
1, 2, 11	111	−111	781	30	−29	7, 10, 1	106	98
1, 2, 13	29	−39	783	< 30	−7	7, 10, 3	83	77
			785	< 25	8	7, 10, 5	58	61
233	69	−67						
235	170	−164	891	46	−51	8, 11, 1	< 10	9
237	35	33	893	< 22	−6			
239	86	−91	895	17	25	161	213	237
2, 3, 11	79	76				1, 6, 11	80	75
2, 3, 13	80	−86	9, 10, 1	72	−79			
						277	106	109
341	101	104	147	44	46	279	47	−53
345	< 39	−16	149	60	−64	2, 7, 11	95	94
347	48	48	1, 4, 11	31	−25			
349	45	−44	1, 4, 13	< 10	8	381	< 41	−20
3, 4, 11	28	25						
			255	147	−159	5, 10, 1	150	−123
451	30	−26	257	57	51	5, 10, 3	93	−83
457	69	68	259	72	−82	5, 10, 5	70	−66
459	< 30	−12	2, 5, 11	89	85			
4, 5, 11	< 19	−10				299	107	−108
			361	54	−57			
561	92	100	363	66	−72	3, 10, 1	73	73
563	46	52	369	90	−81	3, 10, 3	87	104
565	141	137	3, 6, 11	137	−128			
567	135	131				5, 12, 1	< 19	−9
569	88	87	479	< 24	−6	5, 12, 3	32	38
5, 6, 11	73	76	4, 7, 11	37	46			

atomic co-ordinates, the "temperature" factors for O^{2-} and Y^{3+} changed considerably. Because the metal atoms are in special positions which allow no degrees of freedom, it is to be expected that neglect of the dispersion corrections will not affect the oxygen co-ordinates to any significant extent. On the other hand, significant changes in temperature and scale factors must then occur. The *sensitivity* of these factors to the dispersion corrections is particularly noteworthy.

The calculated and observed amplitudes of the reflections used in the analysis are given in Table 3. These calculations are based on the parameters resulting from the last least-squares iteration, although differences among the last three would not be significant. Final discrepancy factors, $(\Sigma \mid |F_0| - |F_c| \mid \Sigma |F_0|)$, are 8·8 per cent when (hkl) amplitudes are weighted one-half and the unobserved reflections counted as one-half the minimum observable; and 7·9 per cent when the unobserved reflections are excluded. The discrepancy factor for the sixteen reflections resulting from contributions only from O^{2-} atoms is 8·6 per cent.

Some mention should be made of the imaginary parts of the dispersion correction. For iron, this part will not be large, perhaps about 0·5–1·0. For yttrium it is about 2·5–3·0. The imaginary dispersion component will not affect most of the amplitudes in Table 3 significantly. Furthermore, these have not been considered because, reportedly no computational program has yet been written which takes these easily into account. Neglecting these is unlikely to change the oxygen co-ordinates significantly, if the other more important corrections did not. Thus, it is probable that the scale and "temperature" factors would still be in some doubt.

With regard to the actual values of the real parts of the corrections, these also, within limits, are not extremely important. Errors in these would both be in the same direction. Only eight times the difference of the scattering factors of Y^{3+} and Fe^{3+} comes into the calculations of the amplitudes F_{hkl}, when two of h, k, l are odd and the third is $2n$, n being odd. Therefore the difference between the two corrections is of main significance. However, errors in these values will also to some extent affect the scale and temperature factors.

REFERENCES

1. Geller S. and Gilleo M. A., *J. Phys. Chem. Solids* **3**, 30 (1957).
2. James R. W., *The Crystalline State* Vol. II—*The Optical Principles of the Diffraction of X-rays*. G. Bell and Sons, London (1948).
3. Hönl H., *Z. Phys.* **84**, 1 (1933).
4. Parratt L. G. and Hempstead C. F., *Phys. Rev.* **94**, 1593 (1954).
5. Hönl H., *Ann. Phys. Lzg.*, **18**, 654 (1933).
6. Thomas L. H. and Umeda K., *J. Chem. Phys.* **26**, 293 (1957).

J. Phys. Chem. Solids Pergamon Press 1959. Vol. 9. pp. 238–264. Printed in Great Britain.

EXCITON STATES IN RARE-GAS CRYSTALS*†

ROBERT S. KNOX‡

Institute of Optics, University of Rochester, Rochester 20, N.Y.

(*Received* 5 *August* 1958; *revised* 23 *September* 1958)

Abstract—A formulation of FRENKEL's theory of excitons is given in which a general method of constructing orthonormal one-electron trial exciton functions from atomic functions is outlined, and excitation energies, band structure, effective masses, and integrated absorption cross-sections are computed in an approximation which includes atomic spin-orbit interaction and overlapping of atomic wave functions through terms of the order S^2. A treatment of singlet and triplet states built from the atomic p^5s configuration in a cubic lattice is given as an example which is intended to apply to the lowest excited states of the rare gases themselves or to corresponding states of halide lattices on a simple excitation model. With the omission of momentum-dependent terms, the formalism is applicable to computations of first-order excitation energies in systems involving substitutional impurities.

1. INTRODUCTION

IN two fairly large classes of solids, molecular and ionic crystals, electronic charge distributions are well localized in the vicinity of the lattice sites. In these solids it is thus possible to view the crystal electrons as perturbed atomic or molecular electrons, in the sense that an approximation to the crystal charge density is that of an array of atoms or molecules brought to the lattice sites from infinite separation. Although this picture has limited usefulness within the domain of classical laws, it may be exploited with reasonable success quantum-mechanically and forms the basis of the HEITLER–LONDON[1] model. As a trial wave function for the system under consideration, one uses a normalized antisymmetrized product of atomic or molecular wave functions centered at points situated in an assumed nuclear configuration. The model is used in chemistry as the LCAO (linear combination of atomic orbitals) model, and its application in solid-state physics is not limited to ionic and molecular crystals; it is useful in computing band structures in semiconductors and metals, particularly in the case of narrow bands, which may be shown to be associated with small overlapping of valence electrons (see, for example, the book by SEITZ,[2] Chap. VIII).

First-order ground-state energies of the rare-gas solids and of several ionic crystals have been treated on the HEITLER–LONDON model. The first application of the method to solids appears to be the work of HYLLERAAS[3] on LiH. In 1936 LANDSHOFF[4] treated NaCl and his work was greatly extended and applied to several ionic crystals by LÖWDIN.[5] Recently HOWLAND[6] has extended LANDSHOFF's and LÖWDIN's work, which was primarily concerned with cohesive energy and elastic constants, to include a first-order computation of the KCl valence-band structure.

It is possible to get physically reasonable results in a first-order absolute computation of binding energies in ionic crystals because of the large negative contribution of the essentially classical Madelung energy. Second-order energies, which are much more difficult to compute precisely, are included approximately by the addition of a van der Waals energy. Predicted ionic crystal binding

* Based on part of a thesis submitted to the University of Rochester, Rochester, New York, in partial fulfillment of the requirements for the degree Doctor of Philosophy.

† Research supported in part by the U.S. Air Force through the Air Force Office of Scientific Research of the Air Research and Development Command.

‡ Present address: Department of Physics, University of Illinois, Urbana, Illinois.

energies are in quite good agreement with experiment.[5,6] In molecular crystals the HEITLER–LONDON scheme is also well justified for use in constructing zero-order ground-state functions because of small overlapping of atomic and molecular ground-state charge distributions. However, the absence of a Madelung energy forces one to use second-order energies to account for cohesion, and excited states of the crystal are necessarily drawn into consideration. HEITLER–LONDON excited states in systems consisting of two atoms were first discussed by EISENSCHITZ and LONDON.[7] An exhaustive review of work on the solid rare gases, the simplest of molecular crystals, has recently been given by DOBBS and JONES.[8]

In addition to having an important perturbing effect on binding energies, the excited states of ionic and molecular crystals are of primary importance in connection with optical properties. In the following we shall be concerned principally with their role in the absorption of light. Furthermore, we shall restrict our attention to states of the HEITLER–LONDON type and attempt to build a quantitative basis upon which to evaluate their validity and usefulness. The relationship between these states and states in the Bloch scheme is well known and will not be discussed here (see, for example, the discussion in Chap. XII of SEITZ's book[2]).

FRENKEL[9] first considered the excited states of a solid on the HEITLER–LONDON model. He showed that stationary states of excitation must be characterized by a wave vector $\boldsymbol{k}$ and that optical excitation of the crystal by light of wave vector $\boldsymbol{\varkappa}$ would send it, with highest probability, into a state of wave vector $\boldsymbol{\varkappa}$. Finally, he showed that the eigenvalues $E_{\boldsymbol{k}}$ of the stationary states form bands of energy levels, and attempted to show how a crystal, in a state $\Psi_{\boldsymbol{k}}$, could make a non-radiative transition to the electronic ground state, the energy of excitation going into heat motion of the lattice. FRENKEL's principal contribution, in these 1931 papers, was the construction of proper excited-state HEITLER–LONDON functions for a crystal, since he subsequently revised his conception of the process of conversion of excitation energy into heat. In 1932 PEIERLS[10] published a different and considerably more detailed version of this conversion process, criticizing FRENKEL's dynamical model of the excited crystal. In a rejoinder (1936), FRENKEL[11] criticized a similar portion of PEIERLS's work, but appears to have brought the original FRENKEL–PEIERLS treatment of the problem into its final form. The characterization of a state of excitation by a wave vector $\boldsymbol{k}$, and thus the possibility of forming wave packets, led FRENKEL to coin the term "exciton", thought of as the "particle" of excitation which moves freely from atom to atom throughout the excited crystal. An excellent qualitative review of the FRENKEL–PEIERLS theory, with applications to energy-transfer questions, is given by FRANCK and TELLER.[12]

When a crystal is in an exciton state, it is non-photoconducting, since the transfer of excitation does not imply a transfer of charge. In fact one may think of the FRENKEL exciton as an electron and hole moving simultaneously from atom to atom, a process which obviously involves no net current. The possibility of absorption to non-conducting states of NaCl was investigated experimentally by FERGUSON,[13] who found some absorbing regions with no observable photoconductivity or external photoelectric effect.

SLATER and SHOCKLEY[14] found a formal connection between Bloch functions and exciton functions, the latter generalized to include all possible positions of the excited electron relative to its associated hole. WANNIER[15] showed that when the electron and hole of an exciton do not remain at the same atom, they will behave much like a charged pair moving throughout the lattice, carrying no current, and forming a system whose energy levels are hydrogenic in nature. The WANNIER model of the exciton has been useful in explaining the structure of absorption bands in some divalent ionic crystals and semiconductors (such as BaO, Cu_2O, and germanium[16–18]), and its formalism has recently been extended to include the case of degenerate bands and the computation of absorption coefficients.[19–21] There also exist many important treatments of the exciton which lie between the FRENKEL and WANNIER models in their detailed assumptions of the electronic structure of the excited state.[22–26] We shall confine our attention, however, to the basic FRENKEL–PEIERLS model.

The question of the possibility of energy transfer by excitons in ionic crystals was opened in 1950 by the work of APKER and TAFT,[27] who found photoemission of electrons which apparently had not

received their energy directly from incident photons. At about the same time HELLER and MARCUS[28] re-examined the FRENKEL–PEIERLS formalism and called attention to the fact, already noted by PEIERLS (reference (10), p. 918), that an important interaction which couples the localized excitation states and enables excitation to travel throughout a crystal is mathematically equivalent to the interaction of two dipoles. Thus an appreciable coupling at large distances may occur, since such interactions fall off as r^{-3}, even in the absence of overlapping of the wave functions of the interacting atoms. HELLER and MARCUS estimated that dipole–dipole interactions make an exciton in an alkali halide move through the crystal on the order of ten times as fast as do interactions which depend solely on overlap of wave functions. DEXTER and HELLER[29] made use of exciton states in a quantum-mechanical treatment of the polarizability of an idealized crystal. Needing wave functions in first order of perturbation theory to compute the virtual transition probabilities involved, they mixed double exciton states* into the usual HEITLER–LONDON ground state of the crystal and examined the concept of the Lorentz effective field on a simplified model of the crystal. DEXTER[30] has used similar first-order wave functions in a treatment of integrated absorption cross-sections for exciton absorption bands. His results will be discussed in connection with the present work in Section 6.

In view of the many applications just discussed, it seems desirable to learn more about the applicability of the HEITLER–LONDON model for excited states by applying it, in computations from fundamental principles, to solids in which it is thought to be a good approximation. Previous treatments of the exciton which could, in principle, be used in predicting optical properties of the rare-gas solids on the basis of this model, have been either qualitative or over-simplified with regard to the problem of effecting detailed calculations. The formalism as it presently exists in the literature[9–11,28,30] suffices only for one-electron valence shells, and so disregards the complication introduced by atomic spin-orbit coupling in systems in which excitation proceeds from ground-state closed-shell configurations. It does not include treatment of the general case of overlapping atomic functions, and touches only lightly on the detailed dependence of exciton energy on wave vector. None of these points may be neglected in a computation which is to be regarded as even remotely comparable with experimental data on a real crystal. However, they may be taken into account without spoiling the tight-binding character of the original model.

In the present paper, the FRENKEL–PEIERLS–DEXTER–HELLER formalism is extended to include atomic spin-orbit interactions and normalization of crystal wave functions in the presence of appreciable overlap of trial atomic functions on different atoms, all under the assumption of a rigid lattice. In Section 2, the model and Hamiltonian chosen to represent the crystal are described, and trial exciton functions are constructed in Section 3. Necessary matrix elements are computed in Section 4, and band structures and effective masses are discussed in Section 5. Finally an expression for integrated absorption cross-sections is given in Section 6 and the entire formalism is summarized in Section 7. Certain computational details are reserved for Appendices A and B. In a second paper,† the results of a calculation based on this formalism will be given. It has been applied to excitation energies, band structure, effective masses, and integrated absorption coefficients associated with exciton states arising in solid argon from states in the atomic $3p^5 4s$ configuration.

2. MODEL AND HAMILTONIAN

As a model on which to base our computations we choose a static bravais lattice of N identical neutral atoms of atomic number Z whose ground-state configurations consist of closed shells, and impose BORN–VON KARMAN boundary conditions on the solutions of the Schrödinger equation for the system (equivalently, N is considered infinite). The HEITLER–LONDON or tight-binding approximation is assumed valid; that is, the wave functions which serve as trial solutions are taken as one-electron orthonormalized antisymmetrized products of one-electron functions of free atoms. In particular, the excited states of the system

* A double exciton state is one in which two excitations travel throughout the crystal, each with its own propagation vector. Double exciton states with propagation vectors $(\boldsymbol{k}, -\boldsymbol{k})$ have the translational symmetry of the ground state and may mix with it.

† KNOX R. S., *J. Phys. Chem. Solids* **9**, 265 (1959).

involving bound excited atomic states are constructed using linear combinations of states resulting from the excitation of one or more individual atoms in the lattice. The form of these wave functions will be made explicit in Section 3.

For convenience we shall adopt the following notation for electron co-ordinates: rather than running serially from 1 to NZ, the subscripts on electron position and spin co-ordinates will consist of a pair of indices Ii, where I runs from 1 to N and i from 1 to Z. Moreover, we adopt the convention that all summations over upper-case indices will run from 1 to N and all those over lower-case indices from 1 to Z. In this notation, the Hamiltonian operator for a system of NZ (N times Z) electrons and N fixed nuclei of charge Ze may be written:

$$H=-\frac{\hbar^2}{2m}\sum_I\sum_i\nabla_{Ii}^2+\frac{1}{2}\sum_{I\neq J}\sum_J\frac{(Ze)^2}{|\mathbf{R}_I-\mathbf{R}_J|}+$$
$$+\frac{1}{2}\sum_I\sum_{i}\sum_{Ii\neq Jj}\sum_J\sum_j\frac{e^2}{|\mathbf{r}_{Ii}-\mathbf{r}_{Jj}|}-$$
$$-\sum_I\sum_i\sum_J\frac{Ze^2}{|\mathbf{r}_{Ii}-\mathbf{R}_J|}+$$
$$+\frac{i\hbar}{2m^2c^2}\sum_I\sum_i\boldsymbol{S}_{Ii}\cdot\nabla_{Ii}V(\mathbf{r}_{Ii})\times\nabla_{Ii}. \tag{2.1}$$

The five terms are, respectively, the kinetic energy of the electrons, the potential energy of the system of nuclei, the potential energy of the system of electrons, the potential energy of the electrons interacting with the nuclei, and finally the spin-orbit interactions[31] of the electrons. In equation (2.1) the symbols e, $\hbar$, c, and m have their usual meanings and ∇_{Ii} is the gradient operator of the co-odinate $\mathbf{r}_{Ii}$. The notation $Ii\neq Jj$ means that every term for which both $I=J$ and $i=j$ is excluded from the summation over I and i. The positions of the nuclei are denoted by $\mathbf{R}_I$. $V(\mathbf{r}_{Ii})$ is the potential due to all electrons and nuclei except electron Ii (twice the Ii term of the summations in the third and fourth parts of H). $\boldsymbol{S}_{Ii}$ is the spin operator for electron Ii.

The most important symmetry requirements imposed on the solutions of the Schrödinger equation generated by H arise from the choice of the configuration of the nuclei. We will generally assume that the lattice sites fall into a cubic array and will indicate points at which our formalism would need modification if lattices of lower symmetries were to be considered.

Nuclear kinetic energies are missing from H because the static model is being treated. In Section 6 the role of the solutions of the static problem in forming wave functions of an actual vibrating crystal will be discussed.

3. TRIAL WAVE FUNCTIONS

We wish to find the eigenvalues and eigenfunctions of the Schrödinger equation.

$$H\Psi_\alpha=E_\alpha\Psi_\alpha, \tag{3.1}$$

where H is given by equation (2.1). The method to be used is straightforward and consists in finding the eigenvalues and eigenvectors of the matrix $H_{\beta\beta'}=\int u_\beta^* H u_{\beta'}\,d\tau$, where the functions u_β form a complete set of suitable trial functions, chosen with the HEITLER–LONDON model and convenience of computation in mind.

(a) *Ground state (zero-order)*

An unnormalized HEITLER–LONDON zero-order ground-state crystal wave function may be written

$$\chi_0(\mathbf{r},\boldsymbol{\sigma})=\mathscr{A}_{NZ}\prod_I\prod_i\phi_{Ii}(\mathbf{r}_{Ii},\boldsymbol{\sigma}_{Ii}). \tag{3.2}$$

Here $\mathscr{A}_{NZ}$ is the usual antisymmetrization operator, defined as follows:

$$\mathscr{A}_M=(M!)^{-\frac{1}{2}}\sum_\nu(-1)^{p_\nu}P_\nu, \tag{3.3}$$

where P_ν is one of the $M!$ permutations of M objects, $(-1)^{p_\nu}$ is the parity of P_ν, and the sum runs over all $M!$ permutations. $\mathscr{A}_{NZ}$ operates on the NZ electron co-ordinates in equation (3.2). The function ϕ_{Ii} is taken to be one of the normalized one-electron functions of an atom in its ground state centered at nucleus I, and i stands for the set of central-field quantum numbers nlm_lm_s describing this function. The vectors $(\mathbf{r},\boldsymbol{\sigma})$ here stand for the entire set of electron space and spin co-ordinates

and will often be omitted. The products over I and i run from 1 to N and 1 to Z, respectively. In the latter case, of course, the numbers 1 through Z are assigned in some standard way to the Z sets of central-field quantum numbers.

In order to normalize χ_0, we adopt the well-known symmetrical orthogonalization technique of LÖWDIN.[5.32] In computing $\int|\chi_0|^2 d\tau$, the following overlap integrals are encountered:

$$S_{Ii,Jj}=\int \phi_{Ii}(\mathbf{r},\boldsymbol{\sigma})^*\phi_{Jj}(\mathbf{r},\boldsymbol{\sigma})d\tau-\delta_{Ii,Jj}, \quad (3.4)$$

where $\delta_{Ii,Jj}$ is unity if $I=J$ and $i=j$ but zero otherwise.* LÖWDIN showed that an appropriate normalization constant is automatically introduced into χ_0 if one replaces each function ϕ_{Ii} by the following linear combination of functions:

$$\varphi_{Ii}(\mathbf{r},\boldsymbol{\sigma})=\phi_{Ii}(\mathbf{r},\boldsymbol{\sigma})-\frac{1}{2}\sum_J\sum_j S_{Ii,Jj}\phi_{Jj}(\mathbf{r},\boldsymbol{\sigma})+$$

$$+\frac{3}{8}\sum_J\sum_K\sum_j\sum_k S_{Jj,Kk}S_{Kk,Ii}\phi_{Jj}(\mathbf{r},\boldsymbol{\sigma})-\ldots. \quad (3.5)$$

The conditions for convergence and divergence of this series are discussed in a review by LÖWDIN;[33] we shall assume that it converges. Since one has merely taken linear combinations among the rows of the determinant (3.2), the following function is a simple multiple of χ_0, and it is in fact normalized:[5.32]

$$\Psi_0(\mathbf{r},\boldsymbol{\sigma})=\mathscr{A}_{NZ}\prod_I\prod_i\varphi_{Ii}(\mathbf{r}_{Ii},\boldsymbol{\sigma}_{Ii}). \quad (3.6)$$

Detailed expressions for the first-order ground-state energy

$$E_0=\int\Psi_0^*H\Psi_0\,d\tau \quad (3.7)$$

have been written in various forms.[5.32–34] We shall return to E_0 later in connection with matrix-element computations.

* Throughout we shall use $\int d\mathbf{r}$ to indicate integration over the entire range of each space co-ordinate appearing or implied under the integral sign; when summation over the spin co-ordinates is also to be included, $\int d\tau$ will be written.

(b) *Single exciton states*

We continue in the spirit of the HEITLER–LONDON model by constructing a state of localized excitation in which any atom J of the crystal is in an excited state λ. A normalized state is built in a form analogous to that of the ground state; we write:

$$f_J(\lambda;\mathbf{r},\boldsymbol{\sigma})=$$
$$\mathscr{A}_{NZ}\psi_J(\lambda;\mathbf{r}_{J1}\ldots\boldsymbol{\sigma}_{JZ})\prod_{\substack{I\\\neq J}}\psi_{I(J\lambda)}(\mathbf{r}_{I1}\ldots\boldsymbol{\sigma}_{IZ}), \quad (3.8)$$

where

$$\psi_J(\lambda;\ldots)=\prod_j\varphi_{Jj}^{\lambda}(\mathbf{r}_{Jj},\boldsymbol{\sigma}_{Jj}) \quad (3.9)$$

and

$$\psi_{I(J\lambda)}(\ldots)=\prod_i\varphi_{Ii(J\lambda)}(\mathbf{r}_{Ij},\boldsymbol{\sigma}_{Ii}). \quad (3.10)$$

The LÖWDIN functions φ_{Jj}^{λ} and $\varphi_{Ii(J\lambda)}$ are defined exactly as in equation (3.5), with the exception that wherever an atomic function ϕ_{Jj} at site J appears, a function ϕ_{Jj}^{λ} belonging to the atomic excited state λ is to be used. The notation $\varphi_{Ii(J\lambda)}$ is used only for $I\neq J$. In forming the series analogous to (3.5), there will appear overlap integrals between ground- and excited-state functions, which will be written

$$S^{0\lambda}_{Ii,Jj}=\int\phi_{Ii}(\mathbf{r},\boldsymbol{\sigma})^*\phi^{\lambda}_{Jj}(\mathbf{r},\boldsymbol{\sigma})d\tau$$

($\lambda\neq$ ground state.)

Although we have built the state $f_J(\lambda)$ from single determinants of one-electron functions, i.e. zero-order atomic functions,[35] it is feasible and desirable to use linear combinations of the zero-order functions which diagonalize all or part of the atomic Hamiltonian. Thus the localized excitation states actually used in a computation may be of the form

$$\Phi_J(\mu)=\sum_\lambda(\mu|\lambda)f_J(\lambda), \quad (3.11)$$

where the coefficients $(\mu|\lambda)$ are exactly those obtained from constructing linear combinations of zero-order determinants in the atomic problem.

VOL 9 195

VOL. 9 1959

The states μ and coefficients $(\mu|\lambda)$ which are most convenient in treating p^5s configurations in cubic solids are given in Appendix A. The simplicity of equation (3.11) is a result of the fact that all singly excited states of interest contain only one excited electron, all but two of the crystal electrons thus being necessarily paired in spins. The general extension of the atomic vector model to solids requires a more rigorous discussion.[34]

For every μ it is now possible to form N localized excitation states as J ranges over the crystal. Because of the translational symmetry of the lattice, these N states are degenerate at some energy $E_{J\mu}$ and do not diagonalize H. A set of linear combinations of the Φ_J which does remove the N-fold degeneracy is the set of single-exciton functions

$$\Phi_{\boldsymbol{k}}(\mu;\, \boldsymbol{r},\, \boldsymbol{\sigma}) = C_{\boldsymbol{k}}(\mu) \sum_J \exp(i\boldsymbol{k}\cdot\boldsymbol{R}_J)\Phi_J(\mu;\, \boldsymbol{r},\, \boldsymbol{\sigma}), \tag{3.12}$$

where $C_{\boldsymbol{k}}(\mu)$ is a normalization constant and $\boldsymbol{k}$ is a vector in the reciprocal lattice of the crystal whose N independent values range over the first Brillouin zone. One readily finds that the normalization constant must satisfy the relation

$$N|C_{\boldsymbol{k}}(\mu)|^2 = 1 + \sum_{K\neq J} \exp[i\kappa\cdot(\boldsymbol{R}_K - \boldsymbol{R}_J)]O_{JK}(\mu,\, \mu), \tag{3.13}$$

where O is an "excitation overlap" integral,

$$O_{JK}(\mu,\, \mu') = \int \Phi_J(\mu)^*\Phi_K(\mu')d\tau - \delta_{JK}\delta_{\mu\mu'}, \tag{3.14}$$

and that two exciton functions $\Phi_{\boldsymbol{k}}(\mu)$ and $\Phi_{\boldsymbol{k}}(\mu')$ are not necessarily orthogonal if the corresponding atomic functions are orthogonal. The dependence of the normalization constant on $\boldsymbol{k}$ and μ and the difficulty of non-orthogonality may be eliminated simultaneously by constructing, instead of (3.12), the following set of single-exciton functions:

$$\Psi_{\boldsymbol{k}}(\mu;\, \boldsymbol{r},\, \boldsymbol{\sigma}) = N^{-\frac{1}{2}} \sum_J \exp(i\kappa\cdot\boldsymbol{R}_J)\Psi_J(\mu;\, \boldsymbol{r},\, \boldsymbol{\sigma}), \tag{3.15}$$

where $\Psi_J(\mu)$ is a symmetrically-orthonormalized linear combination of the $\Phi_J(\mu)$:

$$\Psi_J(\mu) = \Phi_J(\mu) - \frac{1}{2}\sum_K \sum_\nu O_{JK}(\mu,\, \nu)\Phi_K(\nu) + \ldots . \tag{3.16}$$

The summation on the index ν runs over all localized excitation states which are taken to mix with $\Phi_J(\mu)$ in a given calculation. It will be shown later that O_{JK} is small of order S^2, which justifies the use of symmetrical orthogonalization. The function (3.15) is normalized and orthogonal to any other state $\Psi_{\boldsymbol{k}}(\nu)$, $\nu \neq \mu$.

By the use of LÖWDIN's symmetric orthogonalization procedure, we have been able to keep our exciton functions in the familiar form originally used by FRENKEL and PEIERLS. All the complications due to non-orthogonality are included in $\Psi_J(\mu)$; if the excitation overlap integrals O_{JK} and all the simple overlap integrals S are set equal to zero, and if each atom in the crystal is assumed to consist of an invariant core and one valence electron, $\Psi_J(\mu)$ has the form assumed by earlier workers,[28–30] i.e. a single determinant of free-atomic functions with the Jth atom in excited state μ.

In Section 4 we will treat the case of excitons built from an atomic p^5s configuration. We write zero-order functions $f_J(\lambda)$ according to (3.8, 9, 10), using a Cartesian form for atomic p functions, and then form the linear combinations (3.11) using the set of coefficients $(\mu|\lambda)$ given in Appendix A. The resulting twelve localized-excitation functions $\Phi_J(\mu)$ do not have the full rotational symmetry properties of the initial atomic set because the lower symmetry of the crystal is imposed on them by the LÖWDIN normalization process. In effect, this means that one cannot expect the set $\Phi_J(\mu)$ to be orthonormal with respect to μ, especially if an arbitrary set of axes of quantization is chosen for the atomic functions. This lack of orthogonality is measured by $O_{JJ}(\mu,\, \nu)$, which is a small quantity, and the orthogonality of the set localized at J is restored by the term $J = K$ in the symmetric orthogonalization (3.16). Hence we may use arbitrary axes of quantization for the basic atomic functions and still rigorously maintain an orthogonalized set of trial (zero-order) exciton functions $\Psi_{\boldsymbol{k}}(\mu)$[equation (3.15)]. The axes of quantization which will be used here form the "$\boldsymbol{k}$-frame (of

reference)" and are illustrated in Fig. 1. The x direction, called "longitudinal," always lies along $\boldsymbol{k}$. The y and z directions, called "transverse," are perpendicular to each other and to $\boldsymbol{k}$ and are fixed by the requirement that y is always to lie in the $x_c y_c$ plane, where x_c, y_c, and z_c refer to the three fourfold axes of a cubic crystal.

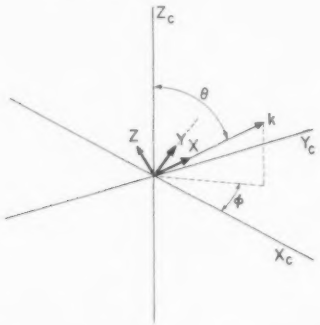

FIG. 1. The connection between the crystal frame of reference and the $\boldsymbol{k}$ frame of reference. Axes in the crystal frame are labeled X_c, Y_c, and Z_c and in the $\boldsymbol{k}$ frame X, Y, and Z. X lies along $\boldsymbol{k}$, Y lies in the X_cY_c plane, and Z is perpendicular to both in the direction shown. When $\theta = 90°$ and $\varphi = 0$, the frames coincide ($X_c = X$, &c.).

The twelve states of the atomic p^5s configuration fall into a set of ^1P and ^3P states in the LS coupling scheme. The three singlet states ($J = 1$) will be called X, Y, and Z, since they transform like the components of a vector. The nine triplet states will be similarly named, viz. R($J = 0$, transforms as a scalar); X', Y', and Z' ($J = 1$, vector); XY, YZ, ZX, $3X^2$–R^2, Y^2–Z^2 ($J = 2$, irreducible tensor). Exciton and localized excitation states built from these atomic states will be written $\Psi_{\boldsymbol{k}}(X')$, $\Psi_J(YZ)$, &c.

(c) *Higher excited states*

Translationally-invariant linear combinations of HEITLER–LONDON functions in which n atoms are in excited states are called "n-fold" excitons. In the case of double excitons, one sets down all possible states of the form

$$\Psi_{\boldsymbol{k},\,\boldsymbol{k}'}(\mu,\mu') = C_{\boldsymbol{k}\boldsymbol{k}'}(\mu\mu')\sum_{J}\sum_{\substack{J'\\ \neq J}}\exp[i(\boldsymbol{k}\cdot\boldsymbol{R}_J+\boldsymbol{k}'\cdot\boldsymbol{R}_{J'})]\Psi_{JJ'}(\mu\mu'), \tag{3.17}$$

where $\Psi_{JJ'}(\mu,\mu')$ is the generalization, to the case of two excited atoms J and J', of the single excitation state (3.8) or (3.11). If the $\Psi_{JJ'}$ constitute an orthonormal set, the exact normalization constant in (3.17) is:[29]

$$C_{\boldsymbol{k}\boldsymbol{k}'}(\mu\mu') = [N(N-1)(1+\delta_{\boldsymbol{k}\boldsymbol{k}'}\delta_{\mu\mu'})]^{-\frac{1}{2}}.$$

When μ and μ' run over a set of m atomic states, there are m^2 possible double exciton states when $\boldsymbol{k} \neq \boldsymbol{k}'$[if $\boldsymbol{k} = \boldsymbol{k}'$, then $\Psi_{\boldsymbol{k}\boldsymbol{k}'}(\mu,\mu') \equiv \Psi_{\boldsymbol{k}\boldsymbol{k}'}(\mu',\mu)$ and there are only $\frac{1}{2}m(m+1)$]. Diagonalization of the crystal Hamiltonian matrix in double exciton states is obviously an enormous task in general, but it can be accomplished for very special cases. We will use double excitons only as perturbing states (Section 6) and will find such a diagonalization unnecessary.

Although Bloch states in the crystals to which this formalism is intended to apply will in all probability have energies which are approximately the same as those of some of the higher single exciton states, they will not be treated here.

4. MATRIX ELEMENTS

(a) *General remarks*

The trial wave functions developed in Section 3 fell into classes according to the number of localized excitations appearing in the determinants. In attempting to diagonalize H by finding proper linear combinations of these trial functions, perturbation theory will be used between states of different multiplicity of excitation. Hence, to first order, the energy of the ground (0-fold exciton) state is given by equation (3.17). Several single exciton states of importance are nearly degenerate and strongly coupled in the systems to which the present formalism applies. Therefore exact diagonalization of parts of the single-exciton submatrix

$$(\mu\boldsymbol{k}|H|\mu'\boldsymbol{k}') = \int \Psi_{\boldsymbol{k}}(\mu)^* H \Psi_{\boldsymbol{k}'}(\mu')\,d\tau \tag{4.1}$$

of the crystal Hamiltonian matrix must be considered.

Because of the translational symmetry of H and the form of our trial functions, we are assured that the matrix element (4.1) is diagonal in $\boldsymbol{k}$, i.e.

$$(\mu\boldsymbol{k}|H|\mu'\boldsymbol{k}') = (\mu\boldsymbol{k}|H|\mu'\boldsymbol{k})\delta_{\boldsymbol{k},\,\boldsymbol{k}'}. \tag{4.2}$$

We may therefore treat each submatrix corresponding to a particular $\boldsymbol{k}$ value separately and search for a set of functions $\Upsilon_{\boldsymbol{k}}(\alpha)$ which complete the diagonalization of H, i.e. those for which

$$\int \Upsilon_{\boldsymbol{k}}(\alpha)^* H \Upsilon_{\boldsymbol{k}}(\alpha') d\tau = \delta_{\alpha\alpha'} W_{\boldsymbol{k}}(\alpha). \quad (4.3)$$

These functions are taken to be linear combinations of the single exciton functions (3.15):

$$\Upsilon_{\boldsymbol{k}}(\alpha) = \sum_{\mu} (\alpha \boldsymbol{k}|\mu \boldsymbol{k}) \Psi_{\boldsymbol{k}}(\mu). \quad (4.4)$$

Coupling coefficients $(\alpha\boldsymbol{k}|\mu\boldsymbol{k})$ and eigenvalues $W_{\boldsymbol{k}}(\alpha)$ are found by solving the standard secular equations

$$\sum_{\mu'} [(\mu \boldsymbol{k}|H|\mu' \boldsymbol{k}) - W_{\boldsymbol{k}}(\alpha)\delta_{\mu\mu'}](\alpha \boldsymbol{k}|\mu' \boldsymbol{k}) = 0. \quad (4.5)$$

In the present section the detailed form of the matrix elements $(\mu\boldsymbol{k}|H|\mu'\boldsymbol{k})$ will be given, and in Section 5 solutions of (4.5) will be discussed.

Using the functions (3.15), one finds that $(\mu\boldsymbol{k}|H|\mu'\boldsymbol{k})$ breaks up into a $\boldsymbol{k}$-dependent and a $\boldsymbol{k}$-independent part:

$$(\mu \boldsymbol{k}|H|\mu' \boldsymbol{k}) = H_{JJ}(\mu, \mu') + \sum_{\substack{K \\ \neq J}} \exp(i\boldsymbol{k} \cdot \boldsymbol{R}_{KJ}) H_{JK}(\mu, \mu') \quad (4.6)$$

where

$$H_{JJ'}(\mu, \mu') = \int \Psi_J(\mu)^* H \Psi_{J'}(\mu') d\tau. \quad (4.7)$$

We have written $\boldsymbol{R}_{KJ} = \boldsymbol{R}_K - \boldsymbol{R}_J$, and J refers to an arbitrary lattice site. We will generally wish to refer energies to the first-order ground-state energy and drop the subscripts on $H_{JJ}(\mu, \mu')$; hence, we make the following definition:

$$E_1(\mu, \mu') = H_{JJ}(\mu, \mu') - E_0\delta_{\mu\mu'}. \quad (4.8)$$

The degree of difficulty experienced in computing $H_{JK}(\mu, \mu')$ depends on the details of the Hamiltonian, the multiplicity of the states μ and μ', and the symmetry of the crystal under consideration. Since $H_{JJ}(\mu, \mu')$ involves excited atomic states at only single lattice site, it may be treated as though the excited atom at J were a center of symmetry for the crystal, and BETHE's work on splitting of atomic terms[37] is applicable. However, the second term of (4.6), which we denote by

$$E_{\boldsymbol{k}}(\mu, \mu') = \sum_{\substack{K \\ \neq J}} \exp(i\boldsymbol{k} \cdot \boldsymbol{R}_{KJ}) H_{JK}(\mu, \mu'), \quad (4.9)$$

may be simplified only by taking into account the behavior of μ and μ' under the operations of the group of $\boldsymbol{k}$,[38] which is generally a much smaller group than the full point-symmetry group of the crystal.

The statements in the preceding paragraph are the most specific one may make with regard to the general problem of mixing of single exciton functions. To illustrate the detailed reduction of equation (4.6) to expressions involving atomic wave functions, we treat the practical case of excitons built from an atomic p^5s configuration in a cubic crystal consisting of atoms normally having closed p^6 shells.[38] It will be explicitly assumed that the spin-orbit term of H[equation (2.1)] is "atomic" in nature, i.e. that the expectation value of $\nabla V \times \nabla$ contributes to $(\mu\boldsymbol{k}|H|\mu'\boldsymbol{k})$ only in the vicinity of the nucleus of excited atom J. This assumption removes the necessity of considering spin-induced splitting by the crystal field, and is quite reasonable, since the atomic spin-orbit interaction is associated with the p^5 hole rather than the more spatially extended s electron. A numerical demonstration of the validity of this assumption in a rare gas has been given elsewhere (reference (38), pp. 40–41). [Its validity should be checked in any application to the excitation model in alkali halides[23] or in any case in which the p function involved in the atomic spin-orbit interaction is not tightly bound to its lattice site.] We thus replace the last term of (2.1) by

$$H_S = \sum_I \sum_i \xi_I(r_{Ii}) \boldsymbol{L}_{Ii} \cdot \boldsymbol{S}_{Ii}, \quad (4.10)$$

where $\boldsymbol{L}_{Ii}$ is the orbital angular momentum operator $i\hbar \boldsymbol{r}_{Ii} \times \nabla_{Ii}$ and ξ_I is defined by

$$\xi_I(r) = (2m^2c^2r_I)^{-1} \partial V(r_I)/\partial r_I, \quad (4.11)$$

in which $r_I = |\boldsymbol{r} - \boldsymbol{R}_I|$.

(b) *Energy parameters diagonal with respect to localized excitation*

The matrix $E_1(\mu, \mu')$ connecting the twelve p^5s states discussed in Section 3 and Appendix A is found to have the following form:

$$\mathbf{E}_1 = \begin{bmatrix} \mathbf{A}_1 & \mathbf{0} & \mathbf{0} \\ \mathbf{0} & \mathbf{A}_2 & \mathbf{0} \\ \mathbf{0} & \mathbf{0} & \mathbf{A}_0 \end{bmatrix} \tag{4.12}$$

where

$$\mathbf{A}_1 = \begin{array}{c} \\ X \\ Y \\ Z \\ X' \\ Y' \\ Z' \end{array} \begin{array}{c} \begin{array}{cccccc} X & Y & Z & X' & Y' & Z' \end{array} \\ \begin{bmatrix} {}^1E & 0 & 0 & -\lambda\zeta/\sqrt{2} & 0 & 0 \\ 0 & {}^1E & 0 & 0 & -\lambda\zeta/\sqrt{2} & 0 \\ 0 & 0 & {}^1E & 0 & 0 & -\lambda\zeta/\sqrt{2} \\ -\lambda\zeta/\sqrt{2} & 0 & 0 & {}^3E+\tfrac{1}{2}\zeta & 0 & 0 \\ 0 & -\lambda\zeta/\sqrt{2} & 0 & 0 & {}^3E+\tfrac{1}{2}\zeta & 0 \\ 0 & 0 & -\lambda\zeta/\sqrt{2} & 0 & 0 & {}^3E+\tfrac{1}{2}\zeta \end{bmatrix} \end{array} \tag{4.13}$$

$$\mathbf{A}_2 = \begin{array}{c} \\ YY \\ YZ \\ ZX \\ XR \\ YY \end{array} \begin{array}{c} \begin{array}{ccccc} XY & YZ & ZX & ZR & YY \end{array} \\ \begin{bmatrix} {}^3E-\tfrac{1}{2}\zeta & 0 & 0 & 0 & 0 \\ 0 & {}^3E-\tfrac{1}{2}\zeta & 0 & 0 & 0 \\ 0 & 0 & {}^3E-\tfrac{1}{2}\zeta & 0 & 0 \\ 0 & 0 & 0 & {}^3E-\tfrac{1}{2}\zeta & 0 \\ 0 & 0 & 0 & 0 & {}^3E-\tfrac{1}{2}\zeta \end{bmatrix} \end{array} \tag{4.14}$$

$$\mathbf{A}_0 = \begin{array}{c} \\ R \end{array} \begin{array}{c} \begin{array}{c} R \end{array} \\ \begin{bmatrix} {}^3E+\zeta \end{bmatrix} \end{array}. \tag{4.15}$$

The submatrices **0** symbolically denote appropriate blocks of zeros, and the abbreviations "XR" $= 3X^2-R^2$ and "YY" $= Y^2-Z^2$ have been used in labeling the rows and columns of $\mathbf{A}_2$. Finally the quantities appearing in the $\mathbf{A}_t$ are defined as follows:

$${}^1E = \int \Psi_J(X)^*(H-H_S)\Psi_J(X)d\tau - E_0 \tag{4.16}$$

$${}^3E = \int \Psi_J(X')^*(H-H_S)\Psi_J(X')d\tau - E_0 \tag{4.17}$$

$$\zeta = 2\int \Psi_J(X')^* H_S \Psi_J(X')d\tau \tag{4.18}$$

$$\lambda\zeta = -\sqrt{2}\int \Psi_J(X)^* H_S \Psi_J(X')d\tau. \tag{4.19}$$

Although the non-zero matrix elements themselves are considerably more complicated, $\mathbf{E}_1$ is seen to have exactly the same form as the corresponding atomic p^5s matrix.[35] One expects, first of all, that the terms of different J values will not mix, regardless of the nature of the interactions in H as long as H has cubic symmetry.[37] This accounts for the null submatrices in (4.12). One further expects the three states X, Y, Z to be degenerate and uncoupled from each other, since they transform as partners in an irreducible representation of the point group of H. The same applies to X', Y', Z'; XY, YZ, ZX; and XR, YY. The fact that ${}^3E$ appears in *each* of the triplet diagonal elements is a result of the assumption that $H-H_S$ involves no spin-dependent interactions. For example, in changing from the matrix element $E_1(Z', Z')$ to $E_1(XY, XY)$, one simply reverses the spin of one of the p^5s electrons of atom J with

respect to its orbital momentum. Aside from the sign of the atomic spin-orbit interaction, nothing changes because the electron "sees" a lattice of paired spins. Hence its electrostatic and exchange interactions are not altered, exactly as in the atomic case. For these reasons the $J=2$ term does not split in this spin-independent cubic field.

The quantities (4.16) through (4.19) have been computed in the S^2 approximation. This means that any quantity which involves more than two products of orthogonal or heterocentric wave functions is dropped. In the case of ^1E and ^3E, one first writes the total energy of the crystal in the form introduced by LÖWDIN[5] with the exception that the Z wave functions associated with atom J belong to appropriate zero-order excited states of the atom. Then the original expression for E_0 is subtracted analytically from this "binding energy", $H_{JJ}(\lambda, \lambda)$, of the excited state λ. The result is:

$$^3E = \mathscr{E}_A + \mathscr{E}_C + \mathscr{E}_X + \mathscr{E}_L + \mathscr{E}_T, \quad (4.20a)$$

where $\mathscr{E}_A$ is the difference between the energies of the pure triplet and ground states of the free atom, and the "Coulomb", "exchange," "LÖWDIN," and "three-center" terms are defined, respectively, as follows:

In the preceding equations the limits on summations are N and Z, according to the convention introduced in Section 2, and a bar over any symbol means that wave functions from the excited (triplet) configuration are to be used when atom J is involved. Elsewhere, ground-state functions are used. The following additional abbreviations have been made:

$$C_L(\boldsymbol{r}) = \sum_l \int |\phi_{Ll}(\boldsymbol{r}', \sigma')|^2 e^2 |\boldsymbol{r}' - \boldsymbol{r}|^{-1} \, d\tau' - Z_L e^2 |\boldsymbol{R}_L - \boldsymbol{r}|^{-1} \quad (4.21)$$

$$C^{L, M, \ldots, T}(\boldsymbol{r}) = \sum_{\substack{K \\ K \neq L, M, \ldots, T}} C_K(\boldsymbol{r}) \quad (4.22)$$

$$(IiJj|g|KkLl) = \int \phi_{Ii}(1)^* \phi_{Jj}(2)^* \frac{e^2}{r_{12}} \phi_{Kk}(1) \phi_{Ll}(2) d\tau_1 d\tau_2. \quad (4.23)$$

$$\mathscr{E}_C = \sum_j [1 + \sum_{K \neq J} \sum_k (\bar{S}_{Kk, Jj})^2] \int |\bar{\phi}_{Jj}|^2 C^J \, d\tau - \sum_j [1 + \sum_{K \neq J} \sum_k (S_{Kk, Jj})^2] \int |\phi_{Jj}|^2 C^J \, d\tau +$$

$$+ \sum_{I \neq J} \sum_i \sum_j [(\bar{S}_{Ii, Jj})^2 \int |\phi_{Ii}|^2 (C^{IJ} + \bar{C}_J) d\tau$$

$$- (S_{Ii, Jj})^2 \int |\phi_{Ii}|^2 (C^{IJ} + C_J) d\tau]. \quad (4.20b)$$

$$\mathscr{E}_X = - \sum_{I \neq J} \sum_i \sum_j [(Ii\bar{J}j|g|\bar{J}jIi) - (IiJj|g|JjIi)]. \quad (4.20c)$$

$$\mathscr{E}_L = - \sum_{I \neq J} \sum_i \sum_j [(\bar{S}_{Ii, Jj})^2 (Ii\bar{J}j|g|Ii\bar{J}j) - (S_{Ii, Jj})^2 (IiJj|g|IiJj)] \quad (4.20d)$$

$$\mathscr{E}_T = - \sum_{I \neq J} \sum_i \sum_j [\bar{S}_{Ii, Jj} \int \bar{\phi}_{Jj} (2C^{IJ} + C_I{}^i + \bar{C}_J{}^j) \phi_{Ii} \, d\tau$$

$$- S_{Ii, Jj} \int \phi_{Jj} (2C^{IJ} + C_I{}^i + C_J{}^j) \phi_{Ii} \, d\tau]. \quad (4.20e)$$

Thus C_L is the classical Coulomb potential due to the entire L atom when its electrons are in states labeled $l = 1, 2, \ldots, Z$, and $C^{L,M,\ldots,T}$ is the combined potential due to all atoms in the lattice *except* $L, M, \ldots, T$. When the kth electron is to be excluded from the sum in $C_L(\mathbf{r})$, we write $C_L{}^k(\mathbf{r})$.

Only one zero-order state need be used to compute ^3E, since the expectation value of $H-H_S$ is the same in each triplet state. Thus, it is convenient to use the zero-order state $\Psi_J(z^-0^+)$. Since ^3E is independent of $\mathbf{k}$, the co-ordinate frame may be chosen so that the pz function involved lies along the z_c axis. The summations over j in equations (4.20) thus run over the configuration $1s^2 \ldots np^6$ in the case of ground-state atoms and over $1s^2 \ldots np^5n's$ in excited atoms; the np functions are $npx+$, $npx-$, $npy+$, $npy-$, and $npz+$ in the latter case. It may be shown[38] that in the S^2 approximation, ^1E differs from ^3E only in that appropriate (singlet) radial wave functions are used in the computation and $\mathscr{E}_A$ is to be taken as the energy difference between the pure-singlet and ground-state energies of the free atom.

The derivation of equations (4.20) has been described in greater detail elsewhere.[38] One point of the derivation should be emphasized: the atomic functions used in computations from equations (4.20) must be solutions of the atomic HARTREE–FOCK equations.[5] If they are not, an exchange correction is necessary.*

Corresponding to ^3E (or ^1E) as defined by equations (4.20) are the quantities $E_{JJ}-E^0$ in the work of HELLER and MARCUS[28] and W_j-W_0 in the work of DEXTER.[30] Expressions for these quantities may be obtained from (4.20) by setting each S equal to zero and assuming that the remaining part of $\mathscr{E}_C$ is zero, since these authors considered only the purely exchange correction $\mathscr{E}_X$ to the atomic energy difference $\mathscr{E}_A$. We have included $\mathscr{E}_L$, which arises from the term LÖWDIN added to LANDSHOFF's work; $\mathscr{E}_T$, a term which consists of three-center interactions and formally similar two-center interactions; and $\mathscr{E}_C$, which is primarily due to classical overlap effects. In a numerical computation to be described in a subsequent paper, it has been found that all of these additional terms are quite important, particularly $\mathscr{E}_T$. This interaction is deceptively simple in appearance; it should be recalled that C^{IJ} involves all electrons on all atoms except I and J, and several hundred small interactions can combine to give a materially important contribution to the excitation energy. In obtaining equation (4.20) we have neglected a term of the form

$$-\sum_K \sum_{\mu'} O_{JK}(\mu, \mu') \int \Phi_J(\mu)^* H \Phi_K(\mu')\, d\tau. \quad (4.24)$$

The evaluation of quantities of this sort is described in the next part and in Appendix B; it turns out that (4.24) is of the order S^4 and is thus excluded from consideration.

The spin-orbit parameters λ and ζ are nearly identical to their atomic counterparts λ_p and ζ_p,[38] and have the following value through terms of order S^2:

$$\zeta \approx \zeta_p[1+\sum_K \sum_k (\bar{S}'_{Jnpz+,Kk})^2] \quad (4.25a)$$

$$\lambda \approx \lambda_p[1+\sum_K \sum_k \bar{S}'_{Jnpz+,Kk}(\bar{S}_{Jnpz+,Kk}-\bar{S}'_{Jnpz+,Kk})]. \quad (4.25b)$$

$\bar{S}$ and $\bar{S}'$ are to be evaluated with singlet and triplet radial functions, respectively.

Since they are based on excitation at a single lattice site, the results of this part may be applied directly to a computation of first-order excitation energies of impurity atoms in a solid. Because of the possibility of strong mixing of these HEITLER–LONDON states with the states of localized excitation of the host crystal, however, the usefulness of such a computation may be limited to the lowest excited states of substitutional impurities in the alkali halides and rare gases.[30] Furthermore, this formalism is not directly applicable to computations of simple configurational co-ordinate (cc) curves, since energy *differences* have been treated. Many interactions which depend on the configuration of the nuclei and which thus help determine the curvature of a cc curve are independent of the

* See reference (33), pp. 95–96.

VOL. 9 1959

electronic state of the impurity atom and do not appear in equations (4.20). One must first restore these interactions if cc diagrams are to be computed on the present model.

(c) *Energy parameters off-diagonal with respect to excitation*

In computing the $\boldsymbol{k}$-dependent part (4.9) of the single exciton matrix element, we shall make explicit use of linear combinations of zero-order functions. We write, for example (cf. Appendix A),

$$\Psi_J(Y) = \sum_\lambda (Y|\lambda)\Psi_J(\lambda)$$

$$= \frac{1}{\sqrt{2}}[\Psi_J(y^-0^-) - \Psi_J(y^+0^+)].$$

Matrix elements between the twelve pure multiplet states are related to the twelve between zero-order states by

$$H_{JK}(\mu, \mu') = \sum_\lambda \sum_{\lambda'} (\mu|\lambda)^*(\mu'|\lambda')H_{JK}(\lambda, \lambda'). \quad (4.26)$$

In Appendix B the computation of $H_{JK}(\lambda, \lambda')$, which involves the single determinant states $f_J(\lambda)$ and $f_K(\lambda')$, is described. The result, to order S^2, and neglecting H_S, is

$$H_{JK}(\lambda, \lambda') = V_{JK}(\lambda, \lambda') + W_{JK}(\lambda, \lambda'), \quad (4.27a)$$

where

In these expressions the abbreviations and conventions used previously have been followed, except that a bar over a quantity now indicates that appropriate excited state functions both on atom J and on atom K are to be used. Also

$$\mathscr{S}_{JK}(\lambda, \lambda') = \frac{1}{2}\sum_I \sum_i [(\bar{S}_{Ii, J\lambda})^2 + (\bar{S}_{Ii, K\lambda'})^2 +$$

$$+ (S_{Ii, J\lambda})^2 + (S_{Ii, K\lambda'})^2]. \quad (4.27d)$$

The quantity δ is a correction term which accounts for the non-orthogonality of excited- and ground-state atomic functions of the same atomic quantum numbers and is defined and computed in Appendix A of reference (38); here, it represents contributions of the terms $I = J$ and $I = K$ which are left out of the first summation of equation (4.27b). Finally, the use of λ and λ' as quantum number designations in equation (4.27) must be explained. In deriving equations (4.27b, c), we have used the fact that an excited zero-order state of the atom contains only a single one-electron function, say $\phi_{J\lambda}$, whose quantum numbers differ from any of those in the ground state. There are $Z-1$ functions ϕ_{Jj} which have quantum numbers corresponding to ground-state quantum numbers. For example, in neon ϕ_{J3} might stand for the function $\phi_{J,\,2s0+}$

$$V_{JK}(\lambda, \lambda') = [1 + 2\delta + \mathscr{S}_{JK}(\lambda, \lambda')](\overline{J\lambda}\,\overline{K\lambda'}|g|J\lambda K\lambda') -$$

$$- \sum_{I \neq J, K} \sum_i [S_{Ii, J\lambda}(\overline{J\lambda}\,\overline{K\lambda'}|g|IiK\lambda') + \bar{S}_{Ii, J\lambda}(J\lambda\,\overline{K\lambda'}|g|IiK\lambda') +$$

$$+ S_{Ii, K\lambda'}(\overline{K\lambda'}\,\overline{J\lambda}|g|IiJ\lambda) + \bar{S}_{Ii, K\lambda'}(K\lambda'\,\overline{J\lambda}|g|IiJ\lambda) +$$

$$+ S_{Ii, J\lambda}\bar{S}_{Ii, J\lambda}(\overline{K\lambda'}Ii|g|K\lambda'Ii) + S_{Ii, K\lambda'}\bar{S}_{Ii, K\lambda'}(\overline{J\lambda}Ii|g|J\lambda Ii)] -$$

$$- \frac{1}{2}\sum_{I \neq J, K} \sum_{\lambda''} [O_{JI}(\lambda, \lambda'')(\overline{I\lambda''}\,\overline{K\lambda'}|g|I\lambda''K\lambda') + \quad (4.27b)$$

$$+ O_{KI}(\lambda', \lambda'')(\overline{I\lambda''}\,\overline{J\lambda}|g|I\lambda''J\lambda)]$$

and

$$W_{JK}(\lambda, \lambda') = -(\overline{J\lambda}J\lambda|g|\overline{K\lambda'}K\lambda') +$$

$$+ \tfrac{1}{2}S_{J\lambda, K\lambda'}\int \bar{\phi}_{J\lambda}(\bar{C}_J{}^\lambda + \bar{C}_K{}^{\lambda'})\bar{\phi}_{K\lambda'}\,d\tau + \quad (4.27c)$$

$$+ \tfrac{1}{2}\bar{S}_{J\lambda, K\lambda'}\int \phi_{J\lambda}(C_J{}^\lambda + C_K{}^{\lambda'})\phi_{K\lambda'}\,d\tau$$

($n = 2$, $l = 0$, $m_l = 0$, $m_s = +\frac{1}{2}$). Then $\bar{\phi}_{J3}$ might stand for $\bar{\phi}_{J,\,2s0+}$, which differs slightly from $\phi_{J,\,2s0+}$, but only in its radial factor. There is one member of the excited set, say $\bar{\phi}_{J,\,3s0-}$, which cannot be paired in this way to a ground state function. The "hole", or ground-state function left unpaired, might be $\phi_{J,\,2px+}$. In equations (4.27), unpaired functions such as these are denoted by $\bar{\phi}_{J\lambda}$ and $\phi_{J\lambda}$, respectively, with a similar convention at atom K.

H_S has been neglected in the computation of $H_{JK}(\lambda, \lambda')$ because this part of the matrix element essentially couples different atoms. The arguments presented earlier in connection with the localized nature of H_S in the case of $H_{JJ}(\lambda, \lambda')$ may be used here, *mutatis mutandis*.

Next we carry out the spin summations in the integrals occurring in $H_{JK}(\lambda, \lambda')$. A computation of this type was done by MERRIFIELD[40] on the simplest possible model, and we shall repeat his considerations in the present context. Suppose that on atom J, an npx_λ electron of spin ξ_λ has jumped to an $n's$ state of spin ξ_λ and on atom K, an $npx_{\lambda'}$ electron of spin $\xi_{\lambda'}$ has jumped to $n's\xi_{\lambda'}$. It is seen by inspection that each term of $V_{JK}(\lambda, \lambda')$ is non-zero only if $\xi_\lambda = \bar{\xi}_\lambda = \pm\xi_{\lambda'} = \bar{\xi}_{\lambda'}$ (i.e. there is no change of spin during the "transition" of either electron). Likewise, $W_{JK}(\lambda, \lambda')$ is nonzero only if $\xi_\lambda = \xi_{\lambda'} = \pm\bar{\xi}_\lambda = \bar{\xi}_{\lambda'}$. These conditions may be expressed analytically as follows:

$$V_{JK}(\lambda, \lambda') = V_{JK}(x_\lambda x_{\lambda'})\delta(\xi_\lambda, \bar{\xi}_\lambda)\delta(\xi_{\lambda'}, \bar{\xi}_{\lambda'}) \quad (4.28)$$

$$W_{JK}(\lambda, \lambda') = W_{JK}(x_\lambda x_{\lambda'})\delta(\xi_\lambda, \xi_{\lambda'})\delta(\bar{\xi}_\lambda, \bar{\xi}_{\lambda'}) \quad (4.29)$$

Here delta functions have their usual meaning and $V_{JK}(x_\lambda x_{\lambda'})$ and $W_{JK}(x_\lambda x_{\lambda'})$ are given by equations (4.27b, c) with all spin functions and summations removed. The original zero-order spatial quantum numbers npx_λ, $n's$ are characterized by x_λ alone for simplicity. We shall generally write $x_\lambda = x, y, z$, the p-functions being referred to the k-frame of reference.

Equation (4.26) may now be applied in specific cases. If μ and μ' are singlet states (X_α, $X_\beta = X, Y, Z$), we obtain [using equations (4.26), (4.27a), (4.28), (4.29), and the coupling coefficients of Appendix A]

$$H_{JK}(X_\alpha, X_\beta) = 2V_{JK}(x_\alpha x_\beta) + W_{JK}(x_\alpha x_\beta). \quad (4.30a)$$

Here V_{JK} and W_{JK} are to be evaluated using radial functions belonging to the singlet term of the atom. If μ' is a triplet state,

$$H_{JK}(X_\alpha, \mu') = 0. \quad (4.30b)$$

Finally, if both μ and μ' are triplet states, we obtain

$$H_{JK}(\mu, \mu') = \sum_{\lambda, \lambda'} c_{\lambda\lambda'}(\mu\mu')W'_{JK}(x_\lambda x_{\lambda'}), \quad (4.30c)$$

where the $c_{\lambda\lambda'}(\mu\mu')$ are constant numerical coefficients and the prime on W_{JK} indicates that radial functions belonging to the triplet term of the atom are to be used. The complete 9×9 matrix (4.30c) has been given elsewhere,[38] but only the following elements are of immediate importance:

$$H_{JK}(Z', Z') = H_{JK}(XY, XY) = \tfrac{1}{2}[W'_{JK}(xx) + W'_{JK}(yy)] \quad (4.31)$$

$$H_{JK}(X', Y') = -\tfrac{1}{2}W'_{JK}(xy) \quad (4.32)$$

$$H_{JK}(Z', XY) = \tfrac{1}{2}[W'_{JK}(xx) - W'_{JK}(yy)]. \quad (4.33)$$

Eight other matrix elements similar to these may be obtained (to within irrelevant phase factors) by the simultaneous cyclic permutations ($X'Y'Z'$), (XYZ), and (xyz).

The quantities $V_{JK}(x_\lambda x_{\lambda'})$ and $W_{JK}(x_\lambda x_{\lambda'})$ may be called "excitation transfer" and "excitation exchange" interactions respectively. They first appeared explicitly in the paper of HELLER and MARCUS[28] who, however, assumed no explicit overlapping of wave functions. Only the first term of V (with $\delta = \mathscr{S} = 0$) and the first term of W are therefore found in their formalism.

Equation (4.27b) contains terms which appear to be of order S^3 and S^4, i.e. those which contain integrations over $\phi_{J\lambda}\bar{\phi}_{J\lambda}$ or $\phi_{K\lambda'}\bar{\phi}_{K\lambda'}$ or both However, for purposes of this computation these products are considered zeroth order in S, since they are involved in atomic transition moments, which we wish to correct to order S^2.

In practice, it is expedient to write V_{JK} in the following form, which is exactly equivalent to equation (4.27b) after spin summations are completed:

$$V_{JK}(x_\alpha x_\beta) = \int \rho_J{}^\alpha(\mathbf{r}_1)\frac{e^2}{r_{12}}\rho_K{}^\beta(\mathbf{r}_2)\,d\mathbf{r}_1\,d\mathbf{r}_2 + \int \rho_J{}^\alpha(\mathbf{r}_1)\frac{e^2}{r_{12}}\Delta\rho_K{}^\beta(\mathbf{r}_2)\,d\mathbf{r}_1\,d\mathbf{r}_2 + \int \Delta\rho_J{}^\alpha(\mathbf{r}_1)\frac{e^2}{r_{12}}\rho_K{}^\beta(\mathbf{r}_2)\,d\mathbf{r}_1\,d\mathbf{r}_2, \quad (4.34)$$

where

$$\rho_J{}^\alpha(\mathbf{r}) = \phi_{Jnpx_\alpha}(\mathbf{r})\bar{\phi}_{Jn's}(\mathbf{r}) \quad (4.35)$$

and

$$\Delta\rho_J{}^\alpha(\mathbf{r}) = \left\{\delta + \frac{1}{2}\sum_{I\neq J}\sum_i [(S_{Ii,Jn's})^2 + (\bar{S}_{Ii,Jnpx_\alpha})^2]\right\}\rho_J{}^\alpha(\mathbf{r}) - \sum_{I\neq J}\sum_i [S_{Ii,Jnpx_\alpha}\bar{\phi}_{Jn's}(\mathbf{r})\phi_{Ii}(\mathbf{r}) + \bar{S}_{Ii,Jn's}\phi_{Jnpx_\alpha}(\mathbf{r})\phi_{Ii}(\mathbf{r}) - S_{Ii,Jnpx_\alpha}\bar{S}_{Ii,Jn's}|\phi_{Ii}(\mathbf{r})|^2] - \frac{1}{2}\sum_{I\neq J}\sum_{\alpha'} O_{JI}(\alpha\alpha')\rho_I{}^{\alpha'}(\mathbf{r}). \quad (4.36)$$

This formal step is useful in connection with the calculation of the $\boldsymbol{k}$-dependence of the matrix elements (4.9). We further simplify (4.34) by introducing

$$P_J{}^\alpha(\mathbf{r}) = \rho_J{}^\alpha(\mathbf{r}) + \Delta\rho_J{}^\alpha(\mathbf{r}). \quad (4.37)$$

Then

$$V_{JK}(\alpha_\alpha x_\beta) = \int P_J{}^\alpha(\mathbf{r}_1)\frac{e^2}{r_{12}}P_K{}^\beta(\mathbf{r}_2)\,d\mathbf{r}_1\,d\mathbf{r}_2 - \int \Delta\rho_J{}^\alpha(\mathbf{r}_1)\frac{e^2}{r_{12}}\Delta\rho_K{}^\beta(\mathbf{r}_2)\,d\mathbf{r}_1\,d\mathbf{r}_2. \quad (4.38)$$

(d) *$\boldsymbol{k}$-Dependence of the matrix elements*

When equations (4.30) are used in computing the $\boldsymbol{k}$-dependent part of the energy from equation (4.9), lattice sums of the following form appear:

$$U_{\boldsymbol{k}}(x_\alpha x_\beta) = \sum_{K\neq J}\exp(i\boldsymbol{k}\cdot\boldsymbol{R}_{KJ})U_{JK}(x_\alpha x_\beta), \quad (4.39)$$

where U is either an excitation transfer interaction V or an excitation exchange interaction W. If the two-center approximation is made[39] and the vectors representing the p-functions are always parallel ($\alpha = \beta$) or perpendicular ($\alpha \neq \beta$) to each other, the following relation holds:[38,39]

$$U_{JK}(x_\alpha x_\beta) = a_\alpha a_\beta[U_\sigma(R_{JK}) - U_\pi(R_{JK})] + \delta_{\alpha\beta}U_\pi(R_{JK}) \quad (4.40)$$

where a_α and a_β are the direction cosines of x_α and x_β with respect to the vector $\boldsymbol{R}_{JK}$, and U_σ and U_π are interactions defined analytically in exactly the same way as $U_{JK}(x_\alpha x_\beta)$ but with the following characteristics: in U_σ the vectors representing the p-functions lie parallel to each other and to the vector $\boldsymbol{R}_{JK}$, while in U_π they are parallel to each other and perpendicular to $\boldsymbol{R}_{JK}$. Because of these fixed orientations, U_σ and U_π depend only on the magnitude of $\boldsymbol{R}_{JK}$. For its simplicity equation (4.40) depends on the vanishing of interactions such as the one in which one p-function is parallel to $\boldsymbol{R}_{JK}$ and the other perpendicular, and on the fact that U_π is independent of the polar orientation of the p-functions about $\boldsymbol{R}_{JK}$. These conditions will obtain in the case of W_{JK} because only two centers are involved [see equation (4.27c)]. However, since several centers are involved in V_{JK}, equation (4.40) is only approximate. It is, however, a good approximation, since the leading term of V_{JK} depends on only two centers. We chose to rewrite V_{JK} in the form (4.34) to make use of the fact that ρ and $\Delta\rho$ constitute effective charge distributions whose moments are principally dipole. In fact ρ has nothing but a dipole moment, and when this dipole lies on one of the fourfold cubic axes, $\Delta\rho$ is also a pure dipole distribution. When R_{JK} is large, e^2/r_{12} may be expanded in a multipole series and only the dipole–dipole interaction contributes to the result (HELLER and MARCUS[28]). In this case, the two-center approximation is manifested in the assumption that $\Delta\rho$ is independent of the orientation of the central dipole, which certainly introduces no serious error. When R_{JK} is small, the multipole expansion breaks down, but a correction to the dipole–dipole interaction which drops off sharply with distance may be computed or estimated and added to W_{JK}, which also drops off rapidly with distance. At small values of R_{JK} the validity of the two-center approximation must be given separate consideration in each specific application of the formalism. In the following we shall treat V_{JK} solely as a dipole–dipole interaction.

When the multipole expansion just discussed is valid, the following expression may be derived from equations

(4.38), (4.39), and related equations:

$$V_{\mathbf{k}}(x_\alpha x_\beta) = \sum_{K \neq J} \exp(i\kappa \cdot \mathbf{R}_K)(M_\alpha M_\beta - \Delta m_\alpha \Delta m_\beta) \times$$

$$\times (\delta_{\alpha\beta} \mathbf{R}_K^2 - 3R_{K\alpha} R_{K\beta}) R_K^{-5}. \tag{4.41}$$

Here $\mathbf{R}_J$ has been set equal to zero for simplicity, $R_{K\alpha}$ is the projection of $\mathbf{R}_K$ in the α direction, and M_α and Δm_α are the magnitudes of the following vectors:

$$M_\alpha = \int r P_J^\alpha(\mathbf{r})\, d\mathbf{r} \tag{4.42a}$$

$$\Delta m_\alpha = \int r \Delta \rho_J^\alpha(\mathbf{r})\, d\mathbf{r}. \tag{4.42b}$$

$$\mathscr{D}_{\mathbf{k}}(x_\alpha x_\beta) = n_0^{-1} \sum_{K \neq J} \exp(i\mathbf{k} \cdot \mathbf{R}_K)(\delta_{\alpha\beta} R_K^2 -$$

$$-3R_{K\alpha} R_{K\beta}) R_K^{-5}, \tag{4.43}$$

where n_0 is the number of lattice points per unit volume and the remaining notation is the same as that used in equation (4.41). HELLER and MARCUS used a continuum approximation in evaluating (4.43), and the result of this device is shown as "C. A." in Figs. 2–4. We shall use the exact lattice sums and will thus have

$$V_{\mathbf{k}}(x_\alpha x_\beta) = n_0(M_\alpha M_\beta - \Delta m_\alpha \Delta m_\beta) \mathscr{D}_{\mathbf{k}}(x_\alpha x_\beta). \tag{4.44}$$

The continuum approximation is not necessarily simpler than the exact lattice sums and may be relied on only for

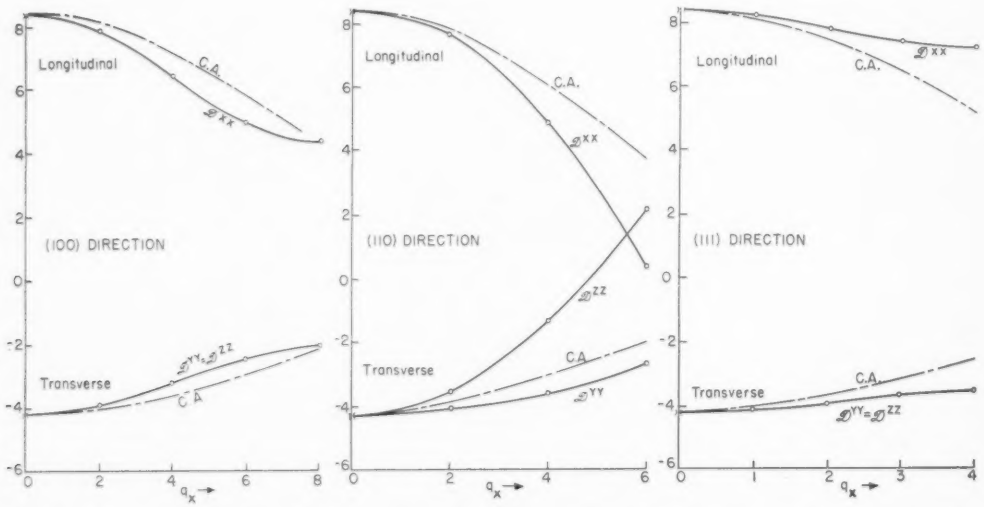

FIGS. 2, 3, and 4. Dipole-wave lattice sums for the (100), (110), and (111) directions in a face-centered cubic crystal. The abscissa in each case is $q_x = (4\sqrt{2}/\pi)k_x a$, where k_x is the component of $\mathbf{k}$ in the crystal x direction, and a is the nearest-neighbor distance. The ordinate is the pure number $\mathscr{D}$, defined by (4.43). The boundary of the first Brillouin zone falls at $q_x = 8$, 6, and 4 in the three respective directions. Circles represent all possible points computed from lattice sums given in reference (41). Lattice sums for an additional point $q_x = 5$ were computed for $\mathscr{D}_{(zz)}$ in the (110) direction to check the interpolation. C. A. stands for continuum approximation (see text, Section 4 (d)).

The subscripts α and β are retained on the magnitudes of these quantities because, although they are not direction-dependent, the atomic states involved might belong to different configurations and some notation to this effect is necessary. Lattice sums useful in treating equation (4.41) in cubic crystals have been computed by COHEN and KEFFER[41] and some useful curves computed from their tables are shown in Figs. 2–4. We have plotted a quantity $\mathscr{D}_{\mathbf{k}}(x_\alpha x_\beta)$, defined by

limiting values of $V_{\mathbf{k}}$ near $\mathbf{k} = 0$, not for curvatures of energy bands.[38]

Lattice sums involving W_{JK} are considerably more simple than the dipole–dipole sums and may be found by direct calculation using equations (4.39) and (4.40), since it is reasonably certain that only a few shells of neighbors will contribute to the result. These sums have been given by SLATER and KOSTER[39] for the various cubic crystals and by MIASEK[42] for the hexagonal

close-packed structure. We have extended SLATER and KOSTER's results for the face-centered cubic crystal to enable summations to be carried out through fourth-nearest neighbors. The only equations necessary for such a summation are these:

$$W_{\boldsymbol{k}}(x_c x_c)_1 = 2(\cos\xi\cos\eta+\cos\zeta\cos\xi)[W_\sigma(a)+W_\pi(a)]+4\cos\eta\cos\zeta W_\pi(a) \tag{4.45a}$$

$$W_{\boldsymbol{k}}(x_c y_c)_1 = -2\sin\xi\sin\eta[W_\sigma(a)-W_\pi(a)] \tag{4.45b}$$

$$W_{\boldsymbol{k}}(x_c x_c)_2 = 2(\cos 2\eta+\cos 2\zeta)W\pi(\sqrt{2}a)+2\cos 2\xi W_\sigma(\sqrt{2}a) \tag{4.45c}$$

$$W_{\boldsymbol{k}}(x_c y_c)_2 = 0 \tag{4.45d}$$

$$3W_{\boldsymbol{k}}(x_c x_c)_3 = 4(\cos\xi\cos 2\eta\cos\zeta+\cos\xi\cos\eta\cos 2\zeta)[W_\sigma(\sqrt{3}a)+5W_\pi(\sqrt{3}a)]+ +2\cos 2\xi\cos\eta\,\mathrm{ccs}\,\zeta[2W_\sigma(\sqrt{3}a)+W\pi(\sqrt{3}a)] \tag{4.45e}$$

$$3W_{\boldsymbol{k}}(x_c y_c)_3 = -16(\cos 2\zeta\sin\xi\sin\eta-\sin 2\eta\sin\zeta\sin\xi-\sin 2\zeta\sin\eta\sin\zeta)\times \times[W_\sigma(\sqrt{3}a)-W_\pi(\sqrt{3}a)]. \tag{4.45f}$$

Here $W_{\boldsymbol{k}}(x_{c\alpha}x_{c\beta})_i$ is the contribution to $W_{\boldsymbol{k}}(x_{c\alpha}x_{c\beta})$ from the ith shell of neighbors, a is the nearest-neighbor distance, $\xi = k_x a/\sqrt{2}$, $\eta = k_y a/\sqrt{2}$, and $\zeta = k_z a/\sqrt{2}$. We have given lattice sums only through third neighbors and only for vectors lying along the crystal x_c and y_c directions for the following reasons: (*a*) By replacing a with $2a$ and ξ, η, and ζ with 2ξ, 2η, and 2ζ in $W_{\boldsymbol{k}}(x_{c\alpha}x_{c\beta})_1$, one obtains $W_{\boldsymbol{k}}(x_{c\alpha}x_{c\beta})_4$. (*b*) The lattice sums for $y_c y_c$, $y_c z_c$, $z_c z_c$, and $z_c x_c$ may be obtained by making the simultaneous cyclic permutations $(x_c y_c z_c)$ and $(\xi\,\eta\,\zeta)$. (*c*) Lattice sums involving p-functions referred to the $\boldsymbol{k}$ frame of reference may be obtained by making the unitary transformation

$$U_{\boldsymbol{k}}(x_\alpha x_\beta) = \mathbf{R}_{\boldsymbol{k}} U_{\boldsymbol{k}}(x_{c\alpha}x_{c\beta})\mathbf{R}_{\boldsymbol{k}}^{-1}, \tag{4.46a}$$

where

$$\mathbf{R}_{\boldsymbol{k}} = \begin{pmatrix} \cos\varphi\sin\theta & \sin\varphi\sin\theta & \cos\theta \\ -\sin\varphi & \cos\varphi & 0 \\ -\cos\varphi\cos\theta & -\sin\varphi\cos\theta & \sin\theta \end{pmatrix} \tag{4.46b}$$

is the transformation which relates the co-ordinates of the $\boldsymbol{k}$ frame to those of the $x_c y_c z_c$ frame of reference. Here θ and φ are the spherical angles of $\boldsymbol{k}$ measured with respect to z_c (see Fig. 1).

(e) *Summary*

The general results of this section are embodied in equations (4.2), (4.6), (4.26), and (4.27a-d). These equations are valid expressions for matrix elements of the crystal Hamiltonian in a single exciton representation independently of the crystal structure and excited atomic configuration under consideration. More specialized results are found in equations (4.12) through (4.15) and (4.30a-c), in which the general energy parameters are applied to the case of $p^5s(^1P, {}^3P)$ atomic states in a cubic lattice with localized spin-orbit interactions. In a more complicated crystal some of the degeneracy in the matrix $\mathbf{E}_1$ equations (4.12) will be lifted, and in a more complicated configuration, equations (4.30) and those in Appendix A must be broadened to include each multiplet. Lattice sums necessary to determine the detailed $\boldsymbol{k}$-dependence of exciton energies in a face-centered cubic lattice have been given [equations (4.44, 4.45)]. Finally, it has been noted that the $\boldsymbol{k}$-independent part of the formalism is applicable to computations of first-order excitation energies associated with impurity centers.

5. EIGENVALUES AND EIGENFUNCTIONS

It will be seen in Section 6 that on the present model the only exciton states which may be reached with high probability by optical excitation from the ground state are those which are mixed with singlet Y and Z states and for which the usual photon–exciton momentum conservation is observed. We would like to examine the entire $\boldsymbol{k}$-dependence of states into which Y and Z are mixed, however, since these bands are of interest in connection with exciton–phonon interactions. It is also of interest to know the curvature of the bands nears $\boldsymbol{k} = 0$, so that effective masses may be assigned to the excitons. Since the 12×12 p^5s matrix presented in Section 4 does not break up into smaller submatrices for a general point in $\boldsymbol{k}$ space, we treat two special situations: first, $\boldsymbol{k}$ lying along directions of high crystal symmetry, and second, $\boldsymbol{k}$ lying in a

general direction but with a very small magnitude. The former case provides only a qualitative picture of the general band structure, but is quantitatively exact as far as the special directions chosen are concerned. The latter case is of interest because it involves states in the region of direct photon–exciton momentum conservation and affords a quantitative picture of the exciton effective masses in this region.

(a) *Special directions of* $\boldsymbol{k}$

We consider $\boldsymbol{k}$ lying in the (100), (110), and (111) directions. We will not study degeneracies associated with special points at the edges of the first Brillouin zone; hence the group of each of these $\boldsymbol{k}$ vectors will generally be the smallest possible associated with the direction of $\boldsymbol{k}$ being considered. Since all of the results which follow may be obtained by direct computation of the lattice sums in Section 4, their group-theoretical justification, given elsewhere,[38] will not be repeated in its entirety. Furthermore, we treat here only those states which are mixed appreciably with the optically-interesting singlet states.

In the (100) and (111) directions, Y and Z are degenerate and uncoupled both from each other and from X, which transforms according to a different irreducible representation. Among the triplet states, Z' and XY mix, as do Y' and ZX. These states are uncoupled from all other triplet states. The crystal field does not mix the singlet and triplet states, but the atomic spin-orbit interaction does. Hence a 3×3 submatrix coupling Y to only two other states results:

$$\begin{array}{c} \\ Y \\ Y' \\ ZX \end{array}\begin{array}{c} \begin{array}{ccc} Y & Y' & ZX \end{array} \\ \begin{pmatrix} {}^1E+E_k(Y,\,Y) & -\lambda\zeta/\sqrt{2} & 0 \\ -\lambda\zeta/\sqrt{2} & {}^3E+\frac{1}{2}\zeta+E_k(Y',\,Y') & E_k(Y',\,ZX) \\ 0 & E_k(ZX,\,Y') & {}^3E-\frac{1}{2}\zeta+E_k(ZX,\,ZX) \end{pmatrix} \end{array} \tag{5.1}$$

A corresponding matrix connecting Z, Z', and XY may be written. Its elements and eigenvalues are numerically equal to those of (5.1) for the directions under consideration. Although (5.1) must be diagonalized exactly for a general magnitude of $\boldsymbol{k}$, it is instructive to analyze it by perturbation theory. According to equations (4.9), (4.33), and (4.39), we have

$$E_k(Y',\,ZX)=\tfrac{1}{2}[W_k(zz)-W_k(xx)] \tag{5.2}$$

and

$$E_k(Y',\,Y')=E_k(ZX,\,ZX). \tag{5.3}$$

The energy difference between the trial states Y' and ZX is thus given by ζ. By applying equations (4.45) to equation (5.2), it may be verified that $E_k(Y'ZX)$ is small of order $(ka)^2$ near $\boldsymbol{k}=0$, so perturbation theory is applicable in at least this region. The coupling of Y and Y' is strong at any value of $\boldsymbol{k}$, so we first diagonalize the upper left 2×2 submatrix of (5.1). The resulting first-order eigenvalues are therefore

$$\left.\begin{matrix} W_k(\mathrm{I}) \\ W_k(\mathrm{II}) \end{matrix}\right\} = {}^3E+\tfrac{1}{2}\Delta+\tfrac{1}{4}\zeta+\tfrac{1}{2}[E_k(Y,\,Y)+E_k(Y',\,Y')]$$

$$\pm\tfrac{1}{2}\sqrt{\{\Delta-\tfrac{1}{2}\zeta+[E_k(Y,\,Y)-E_k(Y'\,Y')]\}^2+2\lambda^2\zeta^2} \tag{5.4a, b}$$

$$W_k(\mathrm{III}) = {}^3E-\tfrac{1}{2}\zeta+E_k(Y',\,Y'). \tag{5.4c}$$

Here $\Delta={}^1E-{}^3E$. Two limiting cases are instructive. When ζ approaches zero, the perturbation process is not valid but the singlet state, Y, is decoupled from the degenerate triplet states and has the energy

$${}^1E+E_k(Y,\,Y)={}^1E+2V_k(yy)+W_k(yy). \tag{5.5}$$

If (5.5) is evaluated with all explicit overlap of atomic functions neglected, this is the Heller–Marcus result except for a factor of 2 multiplying the excitation-transfer interaction, which appears here because of our use of a true singlet state. On

the other hand, if the lattice spacing is allowed to become infinite, the $\boldsymbol{k}$-dependent quantities vanish and the parameters ${}^3E$, Δ, ζ, and λ take on their atomic values $E({}^3P)$, Δ_p, ζ_p, and λ_p, respectively. Thus the atomic excitation energies[43] result:

$$\left.\begin{matrix} W(\mathrm{I}) \\ W(\mathrm{II}) \end{matrix}\right\} = E({}^3P)+\tfrac{1}{2}\Delta_p+\tfrac{1}{4}\zeta_p \pm \sqrt{(\tfrac{1}{2}\Delta_p-\tfrac{1}{4}\zeta_p)^2+\tfrac{1}{2}\lambda_p{}^2\zeta_p{}^2} \qquad (5.6a, b)$$

$$W(\mathrm{III}) = E({}^3P)-\tfrac{1}{2}\zeta_p. \qquad (5.6c)$$

The extent of mixing of the pure singlet exciton state Y into the three states I, II, and III near $\boldsymbol{k}=0$ is given by the following set of coupling coefficients:

$$(\mathrm{I}\boldsymbol{k}|\,Y\boldsymbol{k}) = (1+\zeta^2\mathscr{G}_k{}^{-2})^{-\frac{1}{2}} \qquad (5.7a)$$

$$(\mathrm{II}\boldsymbol{k}|\,Y\boldsymbol{k}) = -(1+\zeta^{-2}\mathscr{G}_k{}^{2})^{-\frac{1}{2}} \qquad (5.7b)$$

$$(\mathrm{III}\boldsymbol{k}|\,Y\boldsymbol{k}) = E_{\boldsymbol{k}}(Y',\,ZX)\zeta^{-1}f_{\boldsymbol{k}} \qquad (5.7c)$$

where $f_{\boldsymbol{k}}$ is a complicated function of the order of unity irrelevant to the discussion and $\mathscr{G}_{\boldsymbol{k}}$ is defined by

$$\sqrt{(2)}\lambda\mathscr{G}_{\boldsymbol{k}} = g_{\boldsymbol{k}}+\sqrt{g_{\boldsymbol{k}}{}^2+2\lambda^2\zeta^2}, \qquad (5.8)$$

where

$$g_{\boldsymbol{k}} = \Delta-\tfrac{1}{2}\zeta+[E_{\boldsymbol{k}}(Y,\,Y)-E_{\boldsymbol{k}}(Y',\,Y')]. \qquad (5.9)$$

Since $E_{\boldsymbol{k}}(Y',\,ZX)\zeta^{-1}$ is very small near $\boldsymbol{k}=0$, the state labeled III is of little optical interest itself. However, its effect on the widths of bands I and II may not necessarily be neglected, since $E_{\boldsymbol{k}}(Y',\,ZX)$ may be fairly large for large values of k.

The bands for $\boldsymbol{k}$ lying in the (110) direction are analytically very similar to those of the (100) and (111) directions, with one important difference. Whereas the states (Y, Z; Y', Z'; ZX, XY) were pairwise degenerate in the latter two directions, the degeneracy is lifted in the (110) direction. This may be seen qualitatively by noting that here a Y function cannot be rotated into a Z function by an operation of the group of the crystal, since the (110) direction is an axis of twofold rotational symmetry. However, Y and Z transform according to different irreducible representations of the group of $\boldsymbol{k}$ and thus represent uncoupled states. All of the discussion related to the diagonalization of equation (5.1) is applicable to the matrices in the (110) case, since the differences between the (Y, Y', ZX) and (Z, Z', XY) solutions manifest themselves only in the detailed form of the lattice sums $E_{\boldsymbol{k}}(\mu,\,\mu')$. In the dipole-wave sums, $V_{\boldsymbol{k}}$, a glance at Figs. 2, 3, and 4 will strikingly convince one of the splitting of transverse states in the (110) direction. This splitting also appears in the excitation exchange lattice sums. In this connection, and to illustrate the use of equations (4.45) and (4.46), we record the three principal lattice sums involved in the (110) direction (first-neighbor contributions only):

$$W_{(110)}(xx)_1 = 2(1+3\cos\tfrac{1}{2}ka)W_\pi(a)+ +2(\cos\tfrac{1}{2}ka+\cos ka)W_\sigma(a) \qquad (5.10a)$$

$$W_{(110)}(yy)_1 = 2\cos\tfrac{1}{2}ka[W_\sigma(a)+3W_\pi(a)]+ +2[W_\sigma(a)+\cos kaW_\pi(a)] \qquad (5.10b)$$

$$W_{(110)}(zz)_1 = 4\cos\tfrac{1}{2}ka[W_\sigma(a)+W_\pi(a)]+ +4\cos^2\tfrac{1}{2}kaW_\pi(a) \qquad (5.10c)$$

Note that these three sums are equal at $k=0$.

(b) *General directions of* $\boldsymbol{k}$ *with* k *small*

We have seen that the ZX state is effectively decoupled from the Y and Y' states in the special symmetry directions when ka is small, unless ζ is also small, in which case the many triplet states are of little concern to us. The argument which led to this conclusion may be extended to the case of general directions of $\boldsymbol{k}$ at small values of ka, and the six exciton states built from atomic $J=0$, 2 terms similarly may be disregarded. Thus the following 6×6 matrix $\mathbf{J}$ remains to be diagonalized (a diagonal matrix ${}^3E\delta_{\mu\mu'}$ has been subtracted):

$$\begin{array}{c} \\ X \\ X' \\ Y \\ Y' \\ Z \\ Z' \end{array}\begin{array}{c} \begin{array}{cccccc} X & X' & Y & Y' & Z & Z' \end{array} \\ \begin{bmatrix} \Delta+E_k(X,X) & -\lambda\zeta/\sqrt{2} & E_k(X,Y) & 0 & E_k(X,Z) & 0 \\ -\lambda\zeta/\sqrt{2} & \frac{1}{2}\zeta+E_k(X',X') & 0 & E_k(X',Y') & 0 & E_k(X',Z') \\ E_k(Y,X) & 0 & \Delta+E_k(Y,Y) & -\lambda\zeta/\sqrt{2} & E_k(Y,Z) & 0 \\ 0 & E_k(Y',X') & -\lambda\zeta/\sqrt{2} & \frac{1}{2}\zeta+E_k(Y',Y') & 0 & E_k(Y',Z') \\ E_k(Z,X) & 0 & E_k(Z,Y) & 0 & \Delta+E_k(Z,Z) & -\lambda\zeta/\sqrt{2} \\ 0 & E_k(Z',X') & 0 & E_k(Z',Y') & -\lambda\zeta/\sqrt{2} & \frac{1}{2}\zeta+E_k(Z',Z') \end{bmatrix} \end{array} \tag{5.11}$$

Let us examine the $\boldsymbol{k}$-dependent parts of this matrix in the limit of small values of k. Two quantities are involved, $V_k(x_\alpha x_\beta)$ and $W_k(x_\alpha x_\beta)$. The former was shown to be proportional to a pure number $\mathscr{D}_k(x_\alpha x_\beta)$ [see equation (4.44)], for which COHEN and KEFFER[41] have obtained the following expression in the limit of small ka:

$$\mathscr{D}_k(x_{c\alpha}x_{c\beta}) = -\left(\frac{4\pi}{3}+B_v k^2a^2\right)\delta_{\alpha\beta}-C_v k_\alpha k_\beta a^2 + D_v k_\alpha{}^2 a^2\delta_{\alpha\beta}+4\pi k_\alpha k_\beta k^{-2}. \tag{5.12}$$

Here $x_{c\alpha}$ and $x_{c\beta}$ are referred to the crystal frame, as are the components of $\boldsymbol{k}$; a is the nearest-neighbor distance, and B_v, C_v, and D_v are numerical coefficients related to COHEN and KEFFER's parameters as follows: $2B_v = \beta+\gamma_{xxyy}$, $2C_v = \alpha$, and $2D_v = \gamma_{xxxx}-\gamma_{xxyy}$. Values of the α, β, and γ are given in reference (41) for cubic lattices. When $\mathscr{D}_k(x_{c\alpha}, x_{c\beta})$ is transformed to the $\boldsymbol{k}$ frame of reference, the three terms in (5.12) which transform as a simple Cartesian tensor are brought to diagonal form at once. The result is

$$\mathscr{D}_k(x_\alpha x_\beta) = \mathbf{R}_k\mathscr{D}_k(x_{c\alpha}x_{c\beta})\mathbf{R}_k{}^{-1} = \begin{bmatrix} \frac{8\pi}{3}-(B_v+C_v)k^2a^2 & 0 & 0 \\ 0 & -\frac{4\pi}{3}-B_vk^2a^2 & 0 \\ 0 & 0 & -\frac{4\pi}{3}-B_vk^2a^2 \end{bmatrix} + D_v\mathbf{G}k^2a^2 \tag{5.13}$$

where $\mathbf{G}$ is the matrix

$$k^{-2}\mathbf{R}_k\begin{bmatrix} k_x{}^2 & 0 & 0 \\ 0 & k_y{}^2 & 0 \\ 0 & 0 & k_z{}^2 \end{bmatrix}\mathbf{R}_k{}^{-1}, \tag{5.14}$$

a purely geometric quantity with cubic symmetry. Three elements of $\mathbf{G}$ which are of interest are

$$\begin{aligned} G_{YY} &= \tfrac{1}{2}\sin^2\theta\sin^2 2\varphi \\ G_{ZZ} &= \tfrac{1}{4}\sin^2 2\theta(1+\sin^4\varphi+\cos^4\varphi) \\ G_{YZ} &= \tfrac{1}{8}\sin\theta\sin 2\theta\sin 4\varphi. \end{aligned} \tag{5.15}$$

The expansions (5.12, 13) are valid for $0 < ka \ll 1$. The first row and column of (5.13) correspond to the X direction in the $\boldsymbol{k}$ frame, and thus represent the longitudinal state.

The excitation lattice sums (4.45) behave much like (5.12) and (5.13) near $ka = 0$. One obtains

$$W_k(x_\alpha x_\beta) = \begin{bmatrix} W_0-(B_w+C_w)k^2a^2 & 0 & 0 \\ 0 & W_0-B_wk^2a^2 & 0 \\ 0 & 0 & W_0-B_wk^2a^2 \end{bmatrix} + D_w\mathbf{G}k^2a^2 \tag{5.16}$$

where $\mathbf{G}$ is defined by equation (5.14). In a face-centered cubic lattice,

$$W_0 = 4W_\sigma(a)+8W_\pi(a)+2W_\sigma(\sqrt{2}a)+ \\ +4W_\pi(\sqrt{2}a)+8W_\sigma(\sqrt{3}a)+16W_\pi(\sqrt{3}a)+ \dots , \tag{5.17a}$$

$$2B_w = W_\sigma(a)+3W_\pi(a)+4W_\pi(\sqrt{2}a)+ \\ +6W_\sigma(\sqrt{3}a)+18W_\pi(\sqrt{3}a)+ \dots , \tag{5.17b}$$

$$2C_w = 2[W_\sigma(a)-W_\pi(a)]+ \\ +16[W_\sigma(\sqrt{3}a)-W_\pi(\sqrt{3}a)]+ \dots , \tag{5.17c}$$

$$2D_w = W_\sigma(a)-W_\pi(a)-4[W_\sigma(\sqrt{2}a)-W_\pi(\sqrt{2}a)]+ \\ +10[W_\sigma(\sqrt{3}a)-W_\pi(\sqrt{3}a)]+ \dots . \tag{5.17d}$$

Returning to the matrix (5.11), let us suppose that a unitary transformation $\mathbf{L}$ has been made which diagonalizes the three 2×2 submatrices lying on the diagonal of $\mathbf{J}$. In the matrix $\mathbf{J}' = \mathbf{L}\mathbf{J}\mathbf{L}^{-1}$, all the zeroes appearing in $\mathbf{J}$ will be filled in with linear combinations of matrix elements $E_k(X_\alpha, X_\beta)$ and $E_k(X_\alpha, X_{\beta'})(\alpha \neq \beta)$, all of which are of order $(ka)^2$. Because of the longitudinal-transverse splitting in V_k, which appears near $k = 0$ as a difference of 4π in the quantity $\mathscr{D}_k$ [see Figs. 2–4 and equation (5.13)], the mixed longitudinal states (X, X') will generally be sufficiently removed in energy from any of the other four (transverse) states that they can be treated as decoupled. An extremely improbable accidental degeneracy is needed to prevent this. We thus restrict our attention to the lower right 4×4 submatrix of $\mathbf{J}$, which we call $\mathbf{j}$ and will write as follows:

$$\mathbf{j} = \mathbf{j}_0+\mathbf{j}_2(\theta, \varphi)k^2a^2, \tag{5.18a}$$

where

$$\mathbf{j}_0 = \begin{bmatrix} \Delta-\frac{4\pi}{3}Q+W_0 & -\lambda\zeta/\sqrt{2} & 0 & 0 \\ -\lambda\zeta/\sqrt{2} & \frac{1}{2}\zeta+W_0' & 0 & 0 \\ 0 & 0 & \Delta-\frac{4\pi}{3}Q+W_0 & -\lambda\zeta/\sqrt{2} \\ 0 & 0 & -\lambda\zeta/\sqrt{2} & \frac{1}{2}\zeta+W_0' \end{bmatrix} \tag{5.18b}$$

and $\mathbf{j}_2(\theta, \varphi)$ is a complicated 4×4 matrix involving the quantities G_{YY}, G_{ZZ}, and G_{YZ} [equations (5.15)]. In equation (5.18b), Q is twice the coefficient of $\mathscr{D}_k$ in equation (4.44) and W_0 is computed from equation (5.17a) with (when unprimed) singlet or (when primed) triplet wave functions. The salient points of the diagonalization of (5.18a) are as follows: a simple unitary transformation $\mathbf{v}$ is made which diagonalizes $\mathbf{j}_0$, changing $\mathbf{j}$ to some new matrix $\mathbf{j}'$. Then, since the diagonal elements of $\mathbf{j}_0'$ are still degenerate in pairs, a final unitary transformation $\mathbf{v}'$ is made which diagonalizes the two 2×2 submatrices of $\mathbf{j}_0'+\mathbf{j}_2'k^2a^2$ coupling these pairs. In the final matrix $\mathbf{j}''$, non-zero elements appear only in positions such that a relatively large, and again assumed not accidentally zero, energy difference exists between the diagonal elements they couple, and they are therefore neglected. The details and results of this process are given in a slightly different

notation on pp. 82–91 of reference (38). The eigenvalues have the following form:

$$^1W+a(\theta,\varphi)k^2a^2\pm b(\theta,\varphi)k^2a^2 \qquad (5.19)$$

$$^3W+c(\theta,\varphi)k^2a^2\pm d(\theta,\varphi)k^2a^2, \qquad (5.20)$$

in which

$$\left.\begin{matrix}{}^1W\\ {}^3W\end{matrix}\right\} = {}^3E+\tfrac{1}{2}\Delta+\tfrac{1}{4}\zeta-\frac{2\pi}{3}Q+\tfrac{1}{2}(W_0+W_0') \pm\left\{\left[\tfrac{1}{2}\Delta-\tfrac{1}{4}\zeta-\frac{2\pi}{3}Q+\tfrac{1}{2}(W_0-W_0')\right]^2+\tfrac{1}{2}\lambda^2\zeta^2\right\}^{\frac{1}{2}}, \qquad (5.21)$$

and a, b, c, and d are functions of θ and φ with cubic symmetry. The quantities ^1W and ^3W may be recognized as the eigenvalues of the 2×2 submatrices of $\mathbf{j}_0$, with ^3E added in, and the splitting of the transverse components represented by $\pm b$ and $\pm d$ is the result of the final unitary transformation $\mathbf{v}'$. Superscripts on the eigenvalues W are not intended to be "good" quantum designations; they denote the character of the states involved as ζ goes to zero.

When $\zeta = 0$, only the singlet states are of interest and the diagonalization of $(\mu\boldsymbol{k}|H|\mu'\boldsymbol{k})$ at small k is considerably simpler. The 3×3 singlet submatrix in this case (except for a constant matrix $\Delta-(4\pi/3)Q+W_0$) is

$$\begin{array}{c} \\ X \\ Y \\ Z \end{array}\begin{array}{c} \begin{array}{ccc} X & Y & Z \end{array} \\ \begin{bmatrix} 4\pi Q-(B+C)k^2a^2 & 0 & 0 \\ 0 & -Bk^2a^2 & 0 \\ 0 & 0 & -Bk^2a^2 \end{bmatrix} \end{array} + D\mathbf{G}k^2a^2, \qquad (5.22)$$

where $B = QB_v+B_w$, $C = QC_v+C_w$, and $D = QD_v+D_w$. The longitudinal state is negligibly coupled to the transverse states which mix with each other whenever G_{YZ} is non-zero [see equations (5.15)]. The eigenvalues of the transverse matrix are

$$^1E-\frac{4\pi}{3}Q+W_0-\tfrac{1}{2}(B+D)g^{\pm}(\theta,\varphi)k^2a^2+\ \ldots\ , \qquad (5.23)$$

where

$$g^{\pm}(\theta,\varphi) = G_{YY}+G_{ZZ}\pm[(G_{YY}-G_{ZZ})^2+2G_{YZ}^2]^{\frac{1}{2}}. \qquad (5.24)$$

The kk component of the reciprocal effective mass tensor is therefore generally different in the two transverse states and is given by

$$[(m^*)^{-1}]_{kk} = \hbar^{-2}\partial^2W/\partial k^2 = -(a/\hbar)^2(B+D)g^{\pm}(\theta,\varphi). \qquad (5.25)$$

In a simple symmetry direction such as (100), where $g^{\pm} = 1$, an exciton effective mass equal to one electron mass is obtained when $B+D$ has the value $-7{\cdot}62a^{-2}$ eV, where a is the face-centered cubic nearest-neighbor distance in Ånström units.

(c) *Discussion*

This section has been devoted entirely to the particular problem of p^5s excitons in cubic crystals, but it may serve as an indication of the type of calculation to be expected in more complicated cases. The mixing of excitons of different polarization has generally been overlooked in previous treatments. Even in a cubic crystal, the two transverse states are usually non-degenerate, and longitudinal states may mix freely with transverse states (except when $\boldsymbol{k}$ lies along a symmetry direction). This mixing is not appreciable when k is small, because of the splitting due to the excitation transfer (dipole–dipole) interaction.

6. INTEGRATED ABSORPTION CROSS-SECTIONS

A group of exciton states of an idealized crystal has been studied in a static approximation in which atomic motion due to thermal energy has been neglected. The stationary states of a real crystal at any temperature depend on nuclear co-ordinates as well as electronic co-ordinates, the former most easily represented by a phonon field. The principal effect of the addition of nuclear

motion to the exciton problem is generally expected to be the same as that encountered in most problems of optical absorption, i.e. broadening of supposedly sharp lines which arise from transitions between states of the static system. In order to obtain detailed predictions of line shape and temperature dependence of the width of "exciton lines", one must quantitatively solve the problem of mixing the exciton and phonon continua. PEIERLS[10] outlined a method for doing this which does not appear to have been exploited, and the basic line-broadening problem has until recently[44] been at a qualitative stage. However, it is possible to compute the zeroth moment (integrated spectrum) of absorption lines associated with transitions from the ground electronic state of the crystal to an excited electronic state.

In computing the integrated absorption coefficient we follow the treatment by DEXTER,[30] which is based on the semiclassical theory of radiation. His work follows the general lines taken by FRENKEL and PEIERLS (reviewed by SEITZ, reference (2), pp. 647 ff.), but differs in the important respect that wave functions in first order of perturbation by the crystal field are used. This refinement is necessary for a consistent formulation of the integrated absorption coefficient if first-order energies are also used. Our starting point is the well-known expression* for the probability per unit time w_{fi} that a system of electrons will make a transition from a state u_i to a state u_f under the influence of an electromagnetic field of polarization direction $\boldsymbol{p}$, wave vector $\boldsymbol{\varkappa}$, angular frequency ω, and complex amplitude $\mathscr{E}_0(\omega)$:

$$w_{fi} = \frac{2\pi e^2\hbar}{m^2 W_{fi}}[\mathscr{E}_0(\omega)]^2 |\boldsymbol{p}\cdot\int\int u_f^* \sum_j \exp(i\boldsymbol{\varkappa}\cdot\boldsymbol{r}_j)\nabla_j u_i \, d\tau d\boldsymbol{x}|^2 \delta(W_{fi}-\hbar\omega). \tag{6.1}$$

In equation (6.1), $\int d\tau$ refers to all electron-co-ordinate summations and integrations, $\int d\boldsymbol{x}$ to those of nuclear co-ordinates, and $W_{fi} = W_f - -W_i$, the difference in the energies of states f and i. The absorption cross-section is defined as the amount of energy absorbed per unit time divided by the incident flux. If the system is in a state u_i before absorption, then the amount of energy lost from the field per unit time because of a transition of the system to a state u_f is simply $w_{fi}W_{fi}$. The incident flux at any point in the medium is given by

$$J(\omega) = n(\omega)c[\mathscr{E}_0(\omega)]^2/2\pi, \tag{6.2}$$

where $n(\omega)$ is the real part of the refractive index and c is the velocity of light. $J(\omega)$ is equal to the energy density multiplied by the energy velocity; although these two quantities may be defined independently and so computed, an explicit atomic model must be assumed. Their product is independent of the model and is given, classically, by equation (6.2). A dielectric constant need not enter our discussion.[45] We do not use an "effective field ratio" in equation (6.2) because the use of first-order crystal wave functions automatically includes it.[29, 30] Hence our final expression for the absorption cross-section due to transitions $i \to f$ is:

$$\sigma_{fi} = \frac{w_{fi}W_{fi}}{J(\omega)} = \frac{4\pi^2 e^2\hbar^2}{n(\omega)cm^2 W_{fi}}|\boldsymbol{p}\cdot\int\int u_f^* \sum_j \exp(i\boldsymbol{\varkappa}\cdot\boldsymbol{r}_j)\nabla_j u_i \, d\tau d\boldsymbol{x}|^2 \delta(W_{fi}-\hbar\omega). \tag{6.3}$$

The approximation we make regarding the specific form of the functions u_j is that they are of the BORN–OPPENHEIMER type,

$$u_j(\boldsymbol{r}, \boldsymbol{\sigma}, \boldsymbol{x}) = \Upsilon_{a_j}(\boldsymbol{r}, \boldsymbol{\sigma}, \boldsymbol{x})\mathrm{X}_{a_j v_j}(\boldsymbol{x}), \tag{6.4}$$

where Υ_{a_j} is a function only of the set of electron co-ordinates $(\boldsymbol{r}, \boldsymbol{\sigma})$ which depends parametrically on $\boldsymbol{x}$. $\mathrm{X}_{a_j v_j}$ is a function only of the set of nuclear co-ordinates $\boldsymbol{x}$ and depends on a_j, the electronic quantum numbers characterizing Υ, and v_j, a set of vibrational quantum numbers. If equation (6.4) is substituted into (6.3), there results:

* See SEITZ, reference (2) §§ 42–44, 148; SCHIFF, reference (31), Chap. X; and references (29) and (30).

$$\sigma_{fi}(\omega) = \frac{4\pi^2 W_{fi}}{c\hbar^2 n(\omega)} \left| \int X_{a_f v_f}(\boldsymbol{x})^* M_{fi}(\boldsymbol{p}, \boldsymbol{x}) X_{a_i v_i}(\boldsymbol{x})\, d\boldsymbol{x} \right|^2 \delta(W_{fi} - \hbar\omega), \tag{6.5}$$

where

$$M_{fi}(\boldsymbol{p}, \boldsymbol{x}) = \frac{e\hbar^2}{mW_{fi}} \int \Upsilon_{a_f}(\boldsymbol{r}, \boldsymbol{\sigma}, \boldsymbol{x})^* \sum_j \exp(i\boldsymbol{\varkappa} \cdot \boldsymbol{r}_j) \boldsymbol{p} \cdot \nabla_j \Upsilon_{a_i}(\boldsymbol{r}, \boldsymbol{\sigma}, \boldsymbol{x})\, d\tau. \tag{6.6}$$

It has been shown by PEIERLS[10] and by LAX[46] that for any complete set of vibrational states $X_{av}(\boldsymbol{x})$, the integrated "spectrum" is independent of the specific form of the $X_{av}(\boldsymbol{x})$ as long as the quantity $M_{fi}(\boldsymbol{p}, \boldsymbol{x})$ is independent of $\boldsymbol{x}$. The assumption that the latter is the case is known as the Condon approximation.[46] We should like to stress that the "spectrum" referred to is actually $[c\hbar^2 n(\omega)/4\pi^2 W_{fi}]\sigma_{fi}(\omega)$, and to obtain the integrated absorption cross-section

$$\sum\nolimits_{fi} = \int \sigma_{fi}(\omega)\, d\hbar\omega \tag{6.7}$$

one must make simplifying assumptions about the dependence of W_{fi} and $n(\omega)$ on ω. If the absorption is confined to a fairly small region about the difference in electronic energies $E_{fi} = E_f - E_i$, and $n(\omega)$ remains close to its value at this energy, we obtain[30,46]

$$\sum\nolimits_{fi} = \frac{4\pi^2 E_{fi}}{\hbar c n(E_{fi})} |M_{fi}(\boldsymbol{p})|^2. \tag{6.8}$$

We now wish to evaluate $M_{fi}(\boldsymbol{p}, \boldsymbol{x})$ using equation (6.6), noting that in the Condon approximation, which has been made in obtaining equation (6.8), no $\boldsymbol{x}$-dependence is considered. We take for the set of electronic states Υ the set which has just been computed (Sections 2–5) for the crystal in the static case. As an initial state, we choose a state which may be represented, in zeroth order, by a ground-state function (3.6), which we write $\Upsilon_i^{(0)}$. As a final state we take any single exciton state of the form

$$\Upsilon_f^{(1)} = \sum_{\mu} (f|\mu) \Psi_{\boldsymbol{k}}(\mu). \tag{6.9}$$

It is possible to restrict the mixing of functions in equation (6.9) to single exciton states without loss of accuracy, because only triple excitons mix with single excitons under the crystal perturbation;[30] it can be shown by simple extension of the analysis which follows that correction terms due to triple excitons contain products of two very small coupling constants. The coupling parameters $(f|\mu)$ in equation (6.9) may result from exact diagonalization of submatrices (as we have done in Section 5) or from the effect of perturbation by other states on those states considered in Sections 4 and 5. Hence, to all practical purposes equation (6.9) is a correct expression for the final state function Υ_f to first order in crystal perturbation. However, it is necessary to obtain a first-order expression for Υ_i. It is readily found that $\Upsilon_i^{(0)}$ mixes with every double exciton $\Upsilon_{\boldsymbol{k}, \boldsymbol{k}'}(\mu\mu')$[see equation (3.17)] through the following matrix element:

$$(i|H|\boldsymbol{k}\boldsymbol{k}'\mu\mu') = \int \Upsilon_i^{(0)*} H \Upsilon_{\boldsymbol{k}\boldsymbol{k}'}(\mu\mu')\, d\tau$$

$$= \delta_{\boldsymbol{k}, -\boldsymbol{k}'} E_{\boldsymbol{k}}(\mu, \mu'). \tag{6.10}$$

$E_{\boldsymbol{k}}(\mu, \mu')$ is defined in equation (4.9). We are thus enabled to write a first-order expression for Υ_i:

$$\Upsilon_i^{(1)} = \Upsilon_i^{(0)} - \sum_{k, \mu, \mu'} [E_{\boldsymbol{k}}(\mu,\mu')/(W_\mu + W_{\mu'})] \Upsilon_{\boldsymbol{k}, -\boldsymbol{k}}(\mu, \mu'). \tag{6.11}$$

Here $W_\mu + W_{\mu'}$ is the zeroth-order energy difference between the state $\Upsilon_{\boldsymbol{k}, -\boldsymbol{k}'}(\mu, \mu')$ and the ground state. It is now possible to compute M_{fi} with

first-order wave functions. Using equations (6.10) and (6.11) in (6.9), we obtain:

$$M_{fi} = \sqrt{N}\delta_{\varkappa,\,k} \sum_{\mu}{}' (f|\mu)(W_\mu/E_{fi})\boldsymbol{p}\cdot e\sqrt{2}\boldsymbol{M}_\mu\left(1+\sum_{\mu'}{}' \frac{E_{\boldsymbol{k}}(\mu,\mu')}{W_\mu+W_{\mu'}}\right). \tag{6.12}$$

Here $\boldsymbol{M}_\mu$ is the dipole matrix element defined by equation (4.42a), W_μ is the zeroth-order energy of the state μ relative to the ground state, and primes on the summations indicate restriction of the sums to ^1P states. Spin-selection rules restrict μ to ^1P states, and thus, according to equations (4.30), μ' needs only run over ^1P states. M_{fi} is seen to be essentially a sum of components of electric dipole moments along the direction of polarization of the incident light wave, corrected by several factors. First of all, $\boldsymbol{M}_\mu$ is an atomic dipole moment corrected to the order S^2 in overlap. The appearance of a dipole moment in equation (6.12) is a result of the use of the general theorem (SEITZ,[2] p. 249) relating the ∇ operator to the $\boldsymbol{r}$ operator. Next, a momentum selection rule appears in (6.12), the factor $\delta_{\varkappa,\,k}$ allowing transitions only to final states whose exciton wave vector is equal to the wave vector of the incident field. Thirdly, the appearance of W_μ/E_{fi} is a result of using the $\nabla \rightarrow \boldsymbol{r}$ theorem on localized excitation functions during the derivation of equation (6.15) and is analogous to the quantity $\epsilon_l/[W_l(\boldsymbol{k})-W_0]$ appearing in equation (28) of reference (30). Finally, the factor in parentheses in equation (6.12) would be unity if zeroth-order ground-state wave functions were used in the computation. The second term in this factor arises from virtual transitions between the states $\Upsilon_{\boldsymbol{k},-\boldsymbol{k}}(\mu\mu')$ and $\Upsilon_{\boldsymbol{k}}(\mu)$; the transition moment involved is exactly the same as that between $\Upsilon_i^{(0)}$ and $\Upsilon_{\boldsymbol{k}}(\mu')$.

To complete the comparison of equation (6.12) with (28) of reference (30), we note that the correction term just discussed corresponds to the quantity

$$-\frac{4\pi}{3}n_0e^2\sum_j r_j{}^2(\epsilon_j/\epsilon_l)/(\epsilon_j+\epsilon_l)$$

which contains the HELLER–MARCUS $V_{\boldsymbol{k}}$ computed near $\boldsymbol{k}=0$ on the continuum model; $W_{\boldsymbol{k}}$ is included in L. Finally the term

$$\frac{4\pi}{3}n_0e^2\sum_{j\neq} r_j{}^2\epsilon_j/[\epsilon_l(\epsilon_j-\epsilon_l)]$$

would arise, in our computation, if we were to include terms in $\sum_\mu$ which lie outside the p^5s configuration.

Restricting μ and μ' to the ^1P state within a single p^5s configuration, we may now obtain the contribution from any state f to the total absorption cross-section by substituting equation (6.12) in (6.8):

$$\Sigma_{fi} = 8\pi^2(e^2/\hbar c)N[E_{fi}/n(E_{fi})](W_\mu/E_{fi})^2\times \\ \times|(f|\mu)|^2|\boldsymbol{p}\cdot\boldsymbol{M}_\mu|^2|1+[E_{\boldsymbol{k}}(\mu,\mu')/2W_\mu]|^2. \tag{6.13}$$

It is understood that f is a state for which the condition of photon–exciton momentum conservation, explicit in equation (6.12), is satisfied.

Probably the most serious approximation made in deriving equation (6.13) is that of keeping n constant during integration over energy. DEXTER has argued[30] that the severity of the approximation may be lessened by cancellation effects on either side of the absorption peak, but even if the approximation is valid, the value of $n(E_{fi})$ is not easy to compute. Other more general limitations and approximations connected with equation (6.13) are the following:

(1) The states of the vibrating crystal are taken to be of the BORN–OPPENHEIMER type, and the CONDON approximation is assumed valid.

(2) It is assumed that the states of a large system of atoms can be used to compute the absorption of a small slab of an actual crystal, so that an integrated absorption coefficient α computed from equation (6.16) has its usual meaning in a differential absorption equation $dI = -\alpha I dx$.

(3) Semiclassical radiation theory is used, i.e. ordinary time-dependent perturbation theory is assumed valid for the description of transitions between the states of the crystal.

Item (1) is probably a good approximation; in an exciton state it is probably even possible to make the harmonic approximation, i.e. retain the vibrational frequencies of the ground state, since little

lattice distortion has chance to take place with the excitation at a completely indefinite position.[11] The assumption (2) is necessitated by the fact that the intensity of light over the whole system was assumed constant in computing the matrix element of the electromagnetic perturbation. For an absorption coefficient of 10^6 cm^{-1}, the intensity will drop to $1/e$ after the incident wave has traversed a path length of 100 Å. Although a sufficiently large number of atoms is involved to validate the use of exciton states, surface effects may render this a serious approximation.[47] Also involved in this assumption is the question of coherence of the light beam and exciton packets in the region of strong absorption. PEKAR[48] has recently treated this problem and finds that a non-local relation exists between the electric vector of the perturbing field and the polarization vector of the crystal. Maxwell equations for the solid considerably more complicated than the usual phenomenological equations obtain in this case. Our neglect of this effect justifies a view that absorption coefficients computed from equation (6.13) may be only rough estimates. Point (3) is reasonable, since it is successful in the case of large lattice constant (atomic absorption) and leads to physically reasonable results in the case of the solid. Relevant to this point are two recent discussions of the problem of perturbations on large quantum systems.[49]

7. DISCUSSION

We have presented a generalization of the FRENKEL exciton theory which takes the basic formalism of the static approximation into as much detail as one will generally need in a practical application. Spin-orbit and electrostatic crystal interactions have been treated, using LÖWDIN orthogonalization methods and the overlap series is terminated at order S^2. The question of convergence of the overlap series may be answered only upon actual computation of overlap integrals in each specific case, but regardless of the convergence of the method, the expressions given here represent the practical limit of calculation on the HEITLER–LONDON model. The inclusion of terms of order S^2 alone adds copiously to the formalism of earlier workers, who neglected all explicit overlapping of heterocentric wave functions.

With practically no modification, the formulas for the $\boldsymbol{k}$-independent part of the exciton energy may be used to obtain first-order excitation energies of low-lying HEITLER–LONDON states of crystals containing impurity atoms.

The principal problem not yet treated quantitatively on the basic FRENKEL–PEIERLS model is that of line shapes and widths, which involves the difficult formal problem of mixing of exciton and phonon continua. Recent work by TOYOZAWA[44] and HOPFIELD[50] may provide a basis on which this gap can be filled.

Acknowledgements—The author is deeply indebted to Professor DAVID L. DEXTER for the suggestion of this problem and for many fruitful discussions. He also wishes to thank Dr. DAVID FOX for his help on the symmetry properties of the exciton.

VOL 9 195

APPENDIX A

The zero-order wave functions used by CONDON and SHORTLEY[35] for p^5s configurations will be rewritten using the Cartesian form of atomic p-functions (characterized by x, y, and z rather than $m_l = 1$, 0, and -1). The relationship between the two forms is given by:

$$\begin{aligned}(x^{\pm}0^{\pm}) &= 2^{-\frac{1}{2}}[(-1^{\pm}0^{\pm})-(1^{\pm}0^{\pm})]\\ i(y^{\pm}0^{\pm}) &= 2^{-\frac{1}{2}}[(-1^{\pm}0^{\pm})+(1^{\pm}0^{\pm})]\\ (z^{\pm}0^{\pm}) &= (0^{\pm}0^{\mp}).\end{aligned} \qquad \text{(A.1)}$$

Using equations (A.1) in conjunction with formula 6[89] of reference (35) and transforming the resulting SLM_SM_L functions to the SLJM scheme by the Clebsch-Gordan series, we express the set of functions $(^{2S+1}L_J{}^M)$ in terms of the zero-order Cartesian set defined in (A.1) and finally take the following set of linear combinations of these SLJM functions:

Singlet ($J = 1$)

$$(X) = 2^{-\frac{1}{2}}[(^1P_1{}^1)-(^1P_1{}^{-1})] = 2^{-\frac{1}{2}}[(x^-0^-)-(x^+0^+)]$$
$$i(Y) = 2^{-\frac{1}{2}}[(^1P_1{}^1)+(^1P_1{}^{-1})] = 2^{-\frac{1}{2}}i[(y^-0^-)-(y^+0^+)]$$
$$(Z) = (^1P_1{}^0) = 2^{-\frac{1}{2}}[(z^-0^-)-(z^+0^+)].$$

Triplet ($J = 0$)

$$(R) = (^3P_0{}^0) = 6^{-\frac{1}{2}}[(x^-0^+)-(x^+0^-)-i(y^-0^+)-$$
$$-i(y^+0^-)-(z^+0^+)-(z^-0^-)]$$

Triplet ($J = 1$)

$$(X') = 2^{-\frac{1}{2}}[(^3P_1{}^1)-(^3P_1{}^{-1})]$$
$$= \tfrac{1}{2}[(z^+0^-)+(z^-0^+)+i(y^+0^+)+i(y^-0^-)]$$

$$i(Y') = 2^{-\frac{1}{2}}[({}^3P_1{}^1)+({}^3P_1{}^{-1})]$$
$$= \tfrac{1}{2}[(x^+0^+)+(x^-0^-)-(z^+0^-)+(z^-0^+)]$$
$$(Z') = ({}^3P_1{}^0) = \tfrac{1}{2}[(x^+0^-)+$$
$$+(x^-0^+)+i(y^+0^-)-i(y^-0^+)]$$

Triplet ($J = 2$)

$$(X^2-Y^2) = 2^{-\frac{1}{2}}[({}^3P_2{}^2)+({}^3P_2{}^{-2})]$$
$$= \tfrac{1}{2}[(x^+0^-)-(x^-0^+)-i(y^+0^-)-i(y^-0^+)]$$
$$i(XY) = 2^{-\frac{1}{2}}[({}^3P_2{}^2)-({}^3P_2{}^{-2})]$$
$$= \tfrac{1}{2}[i(x^+0^-)+i(x^-0^+)+(y^+0^-)-(y^-0^+)]$$
$$(YZ) = 2^{-\frac{1}{2}}[({}^3P_2{}^1)+({}^3P_2{}^{-1})]$$
$$= \tfrac{1}{2}[(z^+0^-)+(z^-0^+)-i(y^+0^+)-i(y^-0^-)]$$
$$i(ZX) = 2^{-\frac{1}{2}}[({}^3P_2{}^1)-({}^3P_2{}^{-1})]$$
$$= \tfrac{1}{2}[i(x^+0^+)+i(x^-0^-)+i(z^+0^-)-i(z^-0^+)]$$
$$(3Z^2-R^2) = ({}^3P_2{}^0) = (12)^{-\frac{1}{2}}[(x^-0^+)-(x^+0^-)-$$
$$-i(y^+0^-)-i(y^-0^+)+2(z^+0^+)+2(z^-0^-)].$$

When the x-axis rather than the z-axis is preferred in a calculation, the following linear combinations of the first and last $J = 2$ functions are convenient:

$$(Y^2-Z^2) = -\tfrac{1}{2}(X^2-Y^2)-\frac{\sqrt{3}}{2}(3Z^2-R^2)$$
$$= \tfrac{1}{2}[i(y^+0^-)+i(y^-0^+)-(z^+0^+)-(z^-0^-)]$$
$$(3X^2-R^2) = \frac{\sqrt{3}}{2}(X^2-Y^2)-\tfrac{1}{2}(3Z^2-R^2)$$
$$= (12)^{-\frac{1}{2}}[2(x^+0^-)-2(x^-0^+)-i(y^+0^-)-$$
$$-i(y^-0^+)-(z^+0^+)-(z^-0^-)].$$

The coefficients of the zero-order functions on the right are the $(\mu|\lambda)$ used in the text. The Cartesian superscript notation on the left indicates the way in which each function transforms under spatial rotations. In the case of triplet functions these transformation properties are not readily apparent upon inspection of the linear combinations on the right because the transformation properties of the spin functions are not made explicit by the notation. The Clebsch–Gordan series reduces the 12 zero-order Cartesian functions in (A.1) to a tensor ($J = 2$ states), axial vector (triplet $J = 1$ states), scalar ($J = 0$ state) and polar vector (singlet $J = 1$ states). The fact that the space parts of X', Y', and Z' transform as an *axial* vector is worth emphasizing; this has been done by adding primes.

APPENDIX B

Quantities of the general form

$$Q_{JK}(\mu, \mu') = \int \Psi_J(\mu)^* Q \Psi_K(\mu')\, d\tau \qquad (B.1)$$

have been called "off-diagonal in localized excitation". They may be written in terms of non-orthogonal localized excitation functions using equation (3.16). The result (to first order of excitation overlap) is

$$Q_{JK}(\mu, \mu') = Q^{JK}(\mu, \mu') - \frac{1}{2}\sum_L \sum_\nu [O_{JL}(\mu, \nu)Q^{LK}(\nu, \mu') + Q^{JL}(\mu, \nu)O_{LK}(\nu, \mu')], \qquad (B.2)$$

where the Q_{JK} are defined by equation (3.14) and

$$Q^{JK}(\mu, \mu') = \int \Phi_J(\mu)^* Q \Phi_K(\mu')\, d\tau, \qquad (B.3)$$

which may in turn be written as a linear combination of matrix elements between zero-order states $f_J(\lambda)$:

$$Q^{JK}(\mu, \mu') = \sum_\lambda \sum_{\lambda'} (\mu|\lambda)^*(\mu'|\lambda')g_{JK}(\lambda, \lambda') \qquad (B.4)$$

where

$$g_{JK}(\lambda, \lambda') = \int f_J(\lambda)^* Q f_K(\lambda')\, d\tau. \qquad (B.5)$$

Since f_J and f_K are single determinants, LÖWDIN's formulas for transition matrix elements[51] are applicable. For brevity we use in the following the terminology and notation associated with equation (49) of reference (51), which we denote by (L49). Our sets u and v are the sets

$$\varphi_{J1}{}^\lambda,\ \varphi_{J2}{}^\lambda,\ \cdots,\ \varphi_{I1(J\lambda)},\ \varphi_{I2(J\lambda)},\ \cdots,$$

and

$$\varphi_{K1}{}^{\lambda'},\ \varphi_{K2}{}^{\lambda'},\ \cdots,\ \varphi_{I1(K\lambda')},\ \varphi_{I2(K\lambda')},\ \cdots.$$

[see the discussion associated with equations (3.9) and (3.10)]. While these sets internally consist of orthonormal functions, a member of the first set is not usually orthogonal to a member of the second. When $Q = 1$, we are computing the determinant D_{UV}. The most efficient way to do this is to arrange it so that the first two rows are associated with $\varphi_{J\lambda}{}^\lambda$ and $\varphi_{K\lambda'(J\lambda)}$ and the first two columns with $\varphi_{J\lambda(K\lambda')}$ and $\varphi_{K\lambda'}{}^{\lambda'}$ (see the discussion of Section 4(c) with regard to using λ and λ' as quantum number designations). By using the Jacobi identity (see reference (32), equation 103, or reference (38), equation 143) on the first two rows and columns, and neglecting all terms of order higher than 2 in overlap, one obtains (for D_{UV})

$$O_{JK}(\lambda, \lambda') = -S_{J\lambda,\, K\lambda'}\bar{S}_{J\lambda,\, K\lambda'}.$$

Here ground-state functions are used on both atoms in $S_{J\lambda,\, K\lambda'}$ and excited-state functions on both atoms in $\bar{S}_{J\lambda,\, K\lambda'}$. As an example, we might have (after spin summations)

$$O_{JK}(xx) = -S_{J2px,\, K2px}\bar{S}_{J4s,\, K4s}.$$

When $Q = H - H_S$, equation (L49) is again employed, with repeated use of the Jacobi identity and a careful search for order-S^2 terms. The zero-order atomic Schrödinger equation is used to eliminate kinetic-energy terms, and when all contributions to equations (B.2) are included, equations (4.27) result. An interesting part of the derivation (unexpected but not surprising) is that in order S^2 one of the terms contributed by $Q^{JK}(\mu, \mu')$ is

$$O_{JK}(\mu, \mu')[\tfrac{1}{2}E^0(\mu) + \tfrac{1}{2}E^0(\mu')],$$

where $E^0(\mu)$ is the total energy of the crystal to zero order in overlap when one atom is in an excited state μ. This apparently divergent quantity is, however, exactly cancelled by two terms in the bracket of equation (B.2); viz., in the first half of the bracket, the term $L = K$, $\nu = \mu'$; and in the second half, the term $L = J$, $\nu = \mu$.

REFERENCES

1. Heitler W. and London F., *Z. Phys.* **44,** 445 (1927).
2. Seitz F., *The Modern Theory of Solids.* McGraw-Hill, New York (1940).
3. Hylleraas E. A., *Z. Phys.* **63,** 771 (1930).
5. Landshoff R., *Z. Phys.* **102,** 201 (1936); *Phys. Rev.* **52,** 246 (1937).
4. Löwdin P.-O., Thesis, Uppsala, Sweden (1948); *Arkiv Mat. Astr. Fys.* **35A,** Nos. 9 and 30 (1948).
6. Howland L. P., *Phys. Rev.* **109,** 1927 (1958).
7. Eisenschitz R. and London F., *Z. Phys.* **60,** 491 (1930).
8. Dobbs E. R. and Jones G. O., *Rep. Progr. Phys.* **20,** 516 (1957).
9. Frenkel J., *Phys. Rev.* **37,** 17, 1276 (1931).
10. Peierls R. E., *Ann. Phys., Lzg.* **13,** 905 (1932).
11. Frenkel J., *Phys. Z. Sowjet.* **9,** 158 (1936).
12. Franck J. and Teller E., *J. Chem. Phys.* **6,** 861 (1938).
13. Ferguson J. N., *Phys. Rev.* **66,** 220 (1944).
14. Slater J. C. and Shockley W., *Phys. Rev.* **50,** 705 (1936).
15. Wannier G. H., *Phys. Rev.* **52,** 191 (1937).
16. Nikitine S., *J. Phys. Radium* **17,** 817 (1956).
17. Gross E. F., *Izv. Akad. Nauk SSSR, ser. fiz.* **20,** 89 (1956).
    Gross E. F., Zakharchenya B. P., and Pavinskii P. P., *Sov. Phys. (Tech. Phys.)* **2,** 2018 (1957).
18. MacFarlane G. G., McLean T. P., Quarrington J. E., and Roberts V., *Phys. Rev.* **108,** 1377 (1957); *Proc. Phys. Soc.* **71,** 863 (1958).
19. Dresselhaus G., *J. Phys. Chem. Solids* **1,** 14 (1956); *Phys. Rev.* **106,** 76 (1957).
20. Elliott R. J., *Phys. Rev.* **108,** 1384 (1957).
21. Haken H., *Nuovo Cim.* **4,** 1608 (1956).
22. Mott N. F., *Trans. Faraday Soc.* **34,** 500 (1938).
23. Dexter D. L., *Phys. Rev.* **83,** 435 (1951); **108,** 707 (1957).
24. Muto T. and Okuno H., *J. Phys. Soc. Japan* **11,** 633 (1956); **12,** 108 (1957).
    Muto T. and Oyama S., *Ibid.* **12,** 101 (1957).
25. von Hippel A., *Z. Phys.* **101,** 680 (1936).
26. Overhauser A. W., *Phys. Rev.* **101,** 1702 (1956).
27. Apker L. and Taft E., *Phys. Rev.* **79,** 964 (1950); **81,** 698 (1951); **82,** 814 (1951).
28. Heller W. R. and Marcus A., *Phys. Rev.* **84,** 809 (1951).
29. Dexter D. L. and Heller W. R., *Phys. Rev.* **91,** 273 (1953).
30. Dexter D. L., *Phys. Rev.* **101,** 48 (1956).
31. Schiff L. I., *Quantum Mechanics* first edn., p. 321. McGraw-Hill, New York (1949).
32. Löwdin P.-O., *J. Chem. Phys.* **18,** 365 (1950).
33. Löwdin P.-O., *Advanc. Phys.* **5,** 1 (1956).
34. Carr W. J., *Phys. Rev.* **92,** 28 (1953).
35. Condon E. U. and Shortley G. H., *The Theory of Atomic Spectra.* Cambridge University Press (1935).
36. Bouckaert L. P., Smoluchowski R., and Wigner E. P., *Phys. Rev.* **50,** 58 (1936).
37. Bethe H. A., *Ann. Phys., Lzg.* **3,** 133 (1929).
38. Knox R. S., Thesis, University of Rochester, Rochester, N.Y. (1958).
39. Slater J. C. and Koster G. F., *Phys. Rev.* **94,** 1498 (1954).
40. Merrifield R. E., *J. Chem. Phys.* **23,** 402 (1955).
41. Cohen M. H. and Keffer F., *Phys. Rev.* **99,** 1128 (1955).
42. Miasek M., *Phys. Rev.* **107,** 92 (1957).
43. Knox R. S., *Phys. Rev.* **110,** 375 (1957).
44. Toyozawa Y., *Progr. Theor. Phys.* **19,** 214 (1958); **20,** 53 (1958).
45. Brillouin L., *Congrés International d'Electricité,* Vol. II, p. 739. Paris (1932).
46. Lax M., *J. Chem. Phys.* **20,** 1752 (1952).
47. Dexter D. L., *Photoconductivity Conference* (Ed. R. G. Breckenridge *et al.*) pp. 617–618. John Wiley and Sons, New York (1956).
48. Pekar S. I., *Zh. eksp. teor. fiz.* **33,** 1022 (1957); *Sov. Phys. (JETP)* **6,** 785 (1958); *J. Phys. Chem. Solids* **5,** 11 (1958).
49. Brout R., *Phys. Rev.* **107,** 664 (1957).
    Hugenholtz N. M., *Physica* **23,** 481 (1957).
50. Hopfield J. J., *Phys. Rev.*, to be published.
51. Löwdin P.-O., *Phys. Rev.* **97,** 1474 (1955).

VOL
9
195

J. Phys. Chem. Solids Pergamon Press 1959. Vol. 9. pp. 265–280. Printed in Great Britain.

EXCITON STATES IN CRYSTALLINE ARGON*†

ROBERT S. KNOX‡

Institute of Optics, University of Rochester, Rochester 20, N.Y.

(*Received* 5 *August*, 1958)

Abstract—The formalism of the preceding paper is applied numerically to exciton states in crystalline argon arising from the atomic $3p^54s$ configuration. Under the assumptions that higher configurations do not perturb the energies and transition probabilities and that the LÖWDIN symmetrical orthogonalization process converges at terms of order S^2, the FRENKEL model predicts two exciton absorption lines at 9 eV ($\pm$1 eV) separated by 0·2 eV and having a combined integrated absorption coefficient of the order of 10^6 cm^{-1} eV. The estimated computational error in excitation energy arises not from the neglect of any important interactions but from difficulties in evaluating two- and three-center integrals and from the natural inaccuracy of the atomic HARTREE–FOCK functions. Exciton effective masses are relatively insensitive to the direction of exciton momentum, are of the order of +5 electron masses, and are found to depend primarily on exchange and overlap interactions rather than the HELLER–MARCUS long-range interaction. It is suggested that closely related overlap and exchange terms may be of considerable importance in the attractive part of crystal binding energies, particularly in the rare gases.

1. INTRODUCTION

IN the classical model of the exciton introduced by FRENKEL and PEIERLS,[1–3] the trial functions used to describe excited states of a crystal are constructed solely from wave functions of free atoms, so their detailed form is assumed known at the outset. Consequently, it is possible in principle to make a numerical computation of excitation energies, exciton band structures, and integrated absorption coefficients once a suitable crystal Hamiltonian has been chosen. No computation based directly on this model seems to have been made, however, and the use of the model, although profuse, has been qualitative or at most semi-quantitative. This situation is understandable in spite of the relative simplicity of the approach, because technical problems such as that of writing usable orthonormalized functions have only recently been solved, making a computation "in principle" possible in actual practice. Also, the enormous amount of arithmetical work involved has now been made feasible by the advent of high-speed computers.

In the preceding paper[4]§ the single-valence-electron FRENKEL model used by HELLER and MARCUS,[5] by DEXTER and HELLER,[6] and by DEXTER[7] was extended to include the necessary complications of the intermediate coupling of singlet and triplet exciton states and overlapping of atomic wave functions in the solid. The purpose of the present paper is to report the results of a numerical application of this formalism to the low-lying excited states of solid argon. The crystalline rare gases have generally been considered best suited for an application of the FRENKEL–PEIERLS theory because they consist of cubic lattices of tightly-bound closed shells of electrons in the ground electronic state and have relatively large lattice constants because of the absence of strong covalent or ionic binding. Argon, rather than another rare gas, was chosen because it has neither a large number of shells

*Based on part of a thesis submitted to the University of Rochester, Rochester, New York, in partial fulfillment of the requirements for the degree Doctor of Philosophy.

†Research supported in part by the U.S. Air Force through the Air Force Office of Scientific Research of the Air Research and Development Command.

‡Present address: Department of Physics, University of Illinois, Urbana, Illinois.

§Throughout, reference (4) will be called "I" and its equations will be referred to as (I.2.1), (I.3.7), &c.

of electrons (such as krypton and xenon have) nor an extremely high fundamental optical excitation energy (as helium and neon have) and because HARTREE–FOCK functions for the ground state of the atom were available.[8] Excited-state atomic HARTREE–FOCK functions were computed for use in this work.[9]

Only those excitons built from the twelve states of argon $3p^54s$ are treated. Nothing quantitative is known about the higher single-exciton states of the solid, since HARTREE–FOCK functions are not available for the atom and would probably not be trustworthy unless computed with explicit configuration interaction.* The neglect of perturbation of the $3p^54s$ configuration by other states is discussed further in Section 5.

In Section 2, the general methods of computation are described, while Section 3 is devoted to a more detailed discussion of the results of computations of particular parameters and the estimated errors in their values. The parameters of Section 3 are used in Section 4 to predict band structures, exciton effective masses, and integrated absorption coefficients. Section 5 contains a general review and appraisal of this calculation, along with a brief discussion of its implications to the rare gas binding energy problem.

2. GENERAL REMARKS ON THE COMPUTATION

The two- and three-center integrals necessary for this computation were evaluated numerically by the α-function method described by LÖWDIN[10] and used in a somewhat different notation by KUNIMUNE.[11] As a lattice constant representative of a real argon crystal, we chose $a = 7{\cdot}10a_0$ (nearest-neighbor distance) in accordance with recent density measurements by DOBBS *et al.*;[12] this value corresponds to the experimental value of the nearest-neighbor distance at about 20°K, at a density of 1·764 g/cm³, and differs only slightly from the experimental value of a at lower temperatures. Ground-state[8] and excited-state[9] argon functions were interpolated and tabulated at constant intervals of $0{\cdot}05a_0$ for use in computing the necessary α-functions. The interval $0{\cdot}05a_0$ was chosen because it was small enough to yield a reasonable picture of the wave functions as they varied rapidly near the nuclei and large enough to keep the functions "short", i.e. to keep them from comprising an excessively large number of tabular entries. Moreover, it was small enough to ensure accuracy in a Simpson's rule computation of α-functions and an even number of intervals could be fitted into the region $r = 0$ to $r = 7{\cdot}10a_0$. In most integrations subsequent to the α-function computations, it was found possible to reduce integration time by a factor of two without loss of accuracy by using an interval of $0{\cdot}10a_0$.

Because of the large spatial extent of the argon singlet and triplet $4s$ functions, it was necessary in many instances to extend the computations out through third neighbors and in through $1s$ functions on the neighbors. Occasionally it was possible to obtain some of the interactions by extrapolation, but this was done only in cases where justified by experience in calculations involving similar wave functions and by the smallness of the contribution. Fig. 1 illustrates the large overlapping of the $4s(^1P)$ function with a $3p$ (ground state) function on a nearest neighbor.

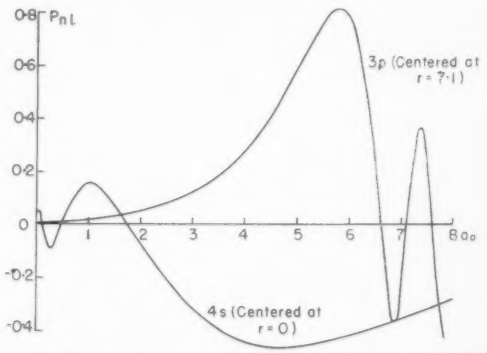

FIG. 1. Comparison of the square root of the radial charge density of a free argon $4s$ electron (from the ^1P term) with that of a $3p$ electron (from the ground state). The $3p$ electron is centered at a distance $a = 7{\cdot}10a_0$ from the center of the $4s$ electron. P_{3p} and P_{4s} are given in units of $a_0^{-\frac{1}{2}}$.

The work described above and below was carried out at the University of Rochester Computing Center, using an IBM type-650 Magnetic Drum Data Processing Machine. Three machine-language programs[13] with identical input and output formats were found sufficient for the basic computations; their jobs were: (1) to compute LÖWDIN α-functions for $l = 0$, 1, 2 and 3; (2) to make a table or perform a single integration of the quantity (const.) $r^m f(r)g(r)$; and (3) to compute the useful double integral

$$\int_0^\infty r^{-1}f(r)\int_0^r (r'/r)^l g(r')dr'dr + \int_0^\infty r^{-1}g(r)\int_0^r (r'/r)^l f(r')dr'dr.$$

*While the $(3p^53d^1P_1)$ and $(3p^55s^1P_1)$ terms of atomic argon are well separated from the $(3p^54s^1P_1)$ term, into which they can be mixed by perturbation methods, they are separated from each other by only 0·1 eV.

The integrations made use of Simpson's rule, and, in case (3), a special adaptation of Simpson's rule for odd numbers of intervals.[14] Finally, in combining all the energy parameters to obtain band structure and effective masses, two programs in BLISS language[15] written by the author and one subroutine for matrix diagonalization (supplied by the Computing Center) were used.

3. COMPUTATION OF BASIC ENERGY PARAMETERS

Localized excitation parameters

The matrix we wish to compute and diagonalize has elements of the form

$$(\mu\mathbf{k}|H|\mu'\mathbf{k}) = E_1(\mu,\mu')+\sum_{K\neq J}\exp(i\mathbf{k}\cdot\mathbf{R}_{KJ})H_{JK}(\mu,\mu') \quad (3.1)$$

(see Section 4(a) of I.). In order to obtain excitation energies one must first compute the localized-excitation parameters which appear in E_1 and which are defined by equations (I.4.16, 17, 18, 19). The "electrostatic" energy ^{2S+1}E is the change in the total first-order energy of the argon crystal when one atom is changed from its normal configuration to a state of definite multiplicity $2S+1$ in the $3p^54s$ configuration. Equations (I.4.20) are used in obtaining ^{2S+1}E from HARTREE–FOCK functions. The quantities ζ and λ are simply related to the matrix elements of the spin-orbit term (I.4.10) of the crystal Hamiltonian and are computed from equations (I.4.25). The lattice sums involved in applying these equations to a face-centered cubic crystal are straightforward and are described in part II.D.3 of the author's thesis.[16] Only the essential features of the numerical work will be presented here.

Table 1 summarizes the results of the computation of the electrostatic energies. The three columns labeled "nth nbrs." show contributions from *entire shells* of nth neighbors; thus the convergence of the contributions with increasingly distant shells is actually better than one might at

Table 1. Contributions to ^1E and ^3E, the electrostatic energy of the pure singlet and triplet crystal states relative to the ground state. $\mathscr{E}_A$ is the atomic electrostatic energy (relative to the atomic ground state) and the other $\mathscr{E}$ represent correction terms (defined in reference 4) which we have called Coulomb, exchange, LÖWDIN, and three-center interactions. Probable computational errors and a discussion of the calculation are given in the text. The last column shows how the atomic energy difference is modified as the crystal corrections are successively added. Energies are measured in electron volts.

Interaction	1st nbrs.	2nd nbrs.	3rd nbrs.	Total	Cum. total
Singlet					
$\mathscr{E}_A$	...	...	...	11·357	11·357
$\mathscr{E}_C$	−4·780	−0·280	−0·204	−5·264	6·093
$\mathscr{E}_X$	−3·329	−0·320	−0·271	−3·920	2·173
$\mathscr{E}_L$	−0·934	−0·059	−0·034	−1·027	1·146
$\mathscr{E}_T$	7·388	0·533	0·372	8·293	9·439
^1E	−1·655	−0·126	−0·137	9·439	
Triplet					
$\mathscr{E}_A$	...	...	...	11·188	11·188
$\mathscr{E}_C$	−4·470	−0·224	−0·138	−4·832	6·356
$\mathscr{E}_X$	−3·360	−0·203	−0·133	−3·696	2·660
$\mathscr{E}_L$	−0·919	−0·052	−0·023	−0·994	1·666
$\mathscr{E}_T$	6·990	0·404	0·234	7·628	9·294
^3E	−1·759	−0·075	−0·060	9·294	

first suppose. The average contribution per neighbor may be found by dividing by 12, 6 and 24 in the respective columns; e.g. the total contributions to ${}^1E$ per neighbor fall off with distance as 0·138, 0·021 and 0·0057. That this is not a regular exponential drop is not surprising, because of several factors such as large overlap of nearest neighbors (which, because of cancellation effects in the case of $4s$-$3p\sigma$ overlapping, behaves irregularly), different behaviors of Coulomb and exchange interactions with increasing distance, and larger probable errors in the third-neighbor computations [for example, one finds ${}^1E$ (third neighbor) $\lesssim {}^1E$ (second neighbor), while the opposite is true of contributions to ${}^3E$]. It is evident, however, that the twelve fourth neighbors would contribute something of the order of 0·02 eV in each term, which is well within the probable numerical error to be discussed shortly. The last column, "cumulative total", will be discussed as we proceed.

We now consider Table 1 according to rows. The quantities $\mathscr{E}_A$ are the computed pure-singlet and pure-triplet energies of the free atom, taken from reference (9), in which a probable error of $\pm 0{\cdot}5$ eV is given for both quantities.

$\mathscr{E}_C$ consists primarily of pure electrostatic Coulomb overlap energy, i.e. it is caused by the breakdown of the formula e^2/R for the interaction between two spherical distributions each of total charge e (one of which may be a charge on a nucleus). The important quantity here [see equation (I.4.20b)] is

$$\int |\phi_{J4s}(\mathbf{r})|^2 C^J(\mathbf{r})\, d\mathbf{r}, \tag{3.2}$$

where $C^J(\mathbf{r})$ is the classical potential at $\mathbf{r}$ due to all atoms, in their ground atomic states, except J. The contributions to (3.2) must be evaluated numerically as the difference between two nearly equal quantities [see equation (I.4.21)], i.e. the parts corresponding to the interaction of the $4s$ electron with the electrons and with the nuclear charge of the neighboring atom. For this reason it was found necessary to demand that the radial functions be normalized to eight decimal places to ensure a consistent computation. A test of this consistency and a means of determining the accuracy of the integration technique was the following: the electrostatic interaction between electrons at centers A and B was evaluated first by expanding the square of B's wave function in spherical harmonics about the center A, and then by expanding A about B. The results of these tests, in which Simpson's rule actually entered three times (once in the α function and twice in the double integral) were found to be surprisingly good, with errors of the order of 0·05–0·1 per cent. This high accuracy was necessary, however, because upon subtracting the electron–nucleus interaction, the probable error of the result was changed to several per cent. For example, in one of the worst cases, one had $(0{\cdot}13412362 \pm 0{\cdot}00008)$–$(0{\cdot}13553361 \pm 0{\cdot}00008)\, e^2/a_0 = (-0{\cdot}00141 \pm 0{\cdot}00016) e^2/a_0$. In addition to the computational errors, the fact that the HARTREE–FOCK free-atomic wave functions are not necessarily accurate at large r must be considered. The actual Coulomb overlap interaction caused by a nearest-neighboring pair, say a $4s$ and $3p$, is small indeed, being about $-0{\cdot}03$ eV, but there are 72 such pairs contributing to the total. The tightly-bound ground-state Coulomb overlap interactions were much smaller than the estimated error in the $4s$ interactions and so could be neglected. In consideration of all the foregoing, the two computed values of $\mathscr{E}_C$ (each of which, incidentally, contains overlap corrections to the extent of about 20 per cent) have an estimated computational error of 8 per cent. They lower the atomic energy to about 6 eV (see the last column of Table 1).

$\mathscr{E}_X$ [equation (I.4.20b)] posed a problem of a completely different nature from that of $\mathscr{E}_C$. Although the numerical integrations involved were accurate, the series expansions for these particular exchange integrals* had poor convergence. It seemed impractical to compute several α-functions for $l > 2$, and since there usually appeared to be a pattern in the convergence of the $l = 0$, 1, 2 terms of the exchange integrals, this pattern was exploited. Often the pattern was simply that the lth term contributed a fraction m^{-l} to the partial sum through the lth term; since in each case m was equal to or greater than 2, the limit of the partial sums for $l \to \infty$ could be computed by elementary means. In a few cases α_3 was evaluated and the $l = 3$ term computed, each time confirming the convergence pattern.

*Reference (16), p. 288.

VOL 9 195

Again a computational error of 7–8 per cent is estimated. Note that after the inclusion of $\mathscr{E}_X$ the atomic energy is "perturbed" to the extent of about -9 eV, according to the cumulative totals in Table 1. Except for the overlap correction embodied in $\mathscr{E}_C$ (about -1 eV), these cumulative totals are the results which would be obtained by computation in the approximation which neglects explicit overlap quantities.

$\mathscr{E}_L$, the LÖWDIN term, is the most accurately determined quantity and has a probable error of some 0·005 eV. Since simple overlap integrals play the leading part here, we take this opportunity to list several for general reference (Table 2).

is involved along with a series expansion of three-center integrals. The problem of series convergence is somewhat lessened here because of cancellation of many terms with $l > 0$ during lattice sums; however, combined computational errors in $\mathscr{E}_T$ are still rather high and are estimated at 10 per cent. The cumulative totals of the two E's are now brought up to the reasonable value of about 9 eV (see Table 1). The contributions to the $\mathscr{E}_T$ are positive, and although each of the three-center interactions is quite small, there is a very large number of them. These large, positive, S-dependent terms have been encountered in previous computations.[17,18]

Table 2. Several representative overlap integrals (computed with the argon wave functions of references 8 and 9). All 4s functions belong to the singlet term except those which are primed (triplet). All other functions belong to the ground state except the one $3p\sigma$, primed, which also belongs to the triplet excited term. These quantities are dimensionless and are functions of the atomic separation R, given at the head of each column ($a = 7{\cdot}10a_0$). Standard nomenclature for p functions in a diatomic configuration is used.

	$R = a$	$R = \sqrt{2}a$	$R = \sqrt{3}a$
$S(4s, 3p\sigma)$	−0·08058	−0·03929	−0·01717
$S(4s', 3p\sigma)$	−0·08466	−0·03796	−0·01337
$S(4s, 3s)$	−0·1282	−0·04556	−0·01850
$S(4s', 3s)$	−0·1234	−0·04163	−0·01549
$S(4s, 1s)$	−0·00272	−0·00092	−0·00039
$S(4s, 4s)$	+0·5494	+0·3435	+0·2063
$S(3p\sigma, 3p\sigma)$	−0·02697	−0·002135	−0·00028
$S(3p\pi, 3p\pi)$	+0·00440	+0·000220	+0·00002
$S(3p\sigma, 2p\sigma)$	+0·00034	+0·000013	...
$S(3p\sigma', 3p\sigma)$	−0·01993	−0·001385	−0·00020

The large positive contribution $\mathscr{E}_T$ comprises a purely three-center part and a two-center part which may be included formally in the equations for the former. It is found that the two-center part actually contributes about half of $\mathscr{E}_T$, since, although it involves many fewer centers, an electron is missing at one of the centers, effectively leaving a full point charge to interact with an overlap charge distribution [see equations (I.4.20b)]. The discussion of errors in $\mathscr{E}_T$ follows closely both that of $\mathscr{E}_C$ and $\mathscr{E}_X$, since Coulomb overlap

Combining the foregoing estimates of percentage error according to the r.m.s. value of the numerical errors, we find

$$\begin{aligned} {}^1E &= 9{\cdot}439 \pm 0{\cdot}995 \text{ eV} \\ {}^3E &= 9{\cdot}294 \pm 0{\cdot}921 \text{ eV} \end{aligned} \tag{3.3}$$

or, more realistically, ${}^1E = 9{\cdot}4 \pm 1{\cdot}0$ eV, ${}^3E = 9{\cdot}3 \pm 0{\cdot}9$ eV. It is immediately evident that one of the important energy parameters, Δ, defined by

$$\Delta = {}^1E - {}^3E, \tag{3.4}$$

is not known accurately. From equation (3.3) we find that Δ has the value 0·145 eV, but with a very large uncertainty. This uncertainty is unfortunate, since a large amount of work went into its computation (each interaction occurring in ^{2S+1}E was done twice, once with singlet and once with triplet functions). Some thought was given to evaluating Δ with differences in wave functions, but this process would not necessarily be more accurate or even easier, since the difference in atomic wave functions on the tail is not extremely well known, and cross terms enter in order-S^2 quantities. In subsequent computations we have used not only the computed value of 0·145 eV, but also other arbitrary values, to test the sensitivity of our final results to changes in Δ.

The spin-orbit parameter, which has the computed value $\zeta_p = 0{\cdot}1157$ eV in the free atom,[9] is changed only slightly in the solid. λ retains its atomic value. Hence we have

$$\begin{aligned} \zeta &= 0{\cdot}1159 \text{ eV}, \\ \lambda &= 1{\cdot}001. \end{aligned} \tag{3.5}$$

These quantities were computed from equations (I.4.25). The calculated values of ζ_p and λ_μ are in excellent agreement with experimental values derived from the atomic argon spectrum.[9]

Excitation transfer and exchange parameters

The $\boldsymbol{k}$-dependent part of the matrix element (3.1) involves the interactions V_{JK} and W_{JK} which we have called "excitation transfer" and "excitation exchange", respectively, defined in equations (I.4.27b, c). The former is essentially the HELLER–MARCUS dipole–dipole interaction which has been generalized in I by the addition of order-S^2 corrections to the atomic transition moments involved. In computing the $\boldsymbol{k}$-dependent quantity

$$V_{\boldsymbol{k}}(x_\alpha x_\beta) = \sum_{K \neq J} \exp(i\boldsymbol{k} \cdot \boldsymbol{R}_{KJ}) V_{JK}(x_\alpha x_\beta) \tag{3.6}$$

(notation and summation conventions are the same as those in I), we first assume that for all values of $\boldsymbol{R}_{JK}$, $V_{JK}(x_\alpha x_\beta)$ is expandible in a multipole series in which only the dipole–dipole term contributes. Then we add a correction term $\delta V_{JK}(x_\alpha x_\beta)$, which is important only at small values of $\boldsymbol{R}_{JK}$. Hence we write

$$V_{JK}(x_\alpha x_\beta) = (Q/2n_0)(\delta_{\alpha\beta}\boldsymbol{R}_K{}^2 - 3\boldsymbol{R}_{K\alpha} \cdot \boldsymbol{R}_{K\beta}) R_K{}^{-5} + \delta V_{JK}(x_\alpha x_\beta). \tag{3.7}$$

We have set $\boldsymbol{R}_J = 0$ for simplicity, and Q is a constant with the dimensions of an energy, defined by

$$Q = 2n_0(M_\alpha M_\beta - \Delta m_\alpha \Delta m_\beta), \tag{3.8}$$

where n_0 is the number of lattice points per unit volume, M_α is a corrected atomic transition dipole moment, and Δm_α is the correction to the atomic transition dipole moment. The last two quantities are defined quantitatively and discussed in Sections 4(c) and (d) of I. Since we are concerned with transition moments associated with a single configuration, the quantitity $(Q/2n_0)$ is given by $M^2 - (\Delta m)^2$, where the leading term of M has the form

$$m = |e \int \phi_{4s0+}(\mathbf{r}) \mathbf{r} \phi_{3px_\alpha+}(\mathbf{r})\, d\mathbf{r}|. \tag{3.9}$$

M and Δm were evaluated using equations (I.4.35, 36, 37, 42) and the detailed lattice sums of reference (16), assuming that the x_α function lay along a cubic axis. The results were

$$\begin{aligned} M &= 0{\cdot}4535\, ea_0 \\ \Delta m &= 0{\cdot}0748\, ea_0, \end{aligned} \tag{3.10}$$

where $a_0 = 0{\cdot}5292 \times 10^{-8}$ cm. We therefore have

$$Q = 0{\cdot}4002\, n_0 e^2 a_0{}^2 = 0{\cdot}04304 \text{ eV}. \tag{3.11}$$

In obtaining (3.11), we have used $n_0 = 4(2^{\frac{1}{2}}a)^{-3}$, where $a = 7{\cdot}10\, a_0$ is the nearest-neighbor distance in the face-centered cubic argon crystal, and $e^2/a_0 = 27{\cdot}21 \text{ eV} = 2$ Ry. If we now substitute equation (3.7) into (3.6) and make use of the lattice sums $\mathscr{D}_{\boldsymbol{k}}$ defined by equation (I.4.43), we obtain

$$\begin{aligned} &V_{\boldsymbol{k}}(x_\alpha x_\beta) \\ &\quad = (0{\cdot}02152 \text{ eV}) \mathscr{D}_{\boldsymbol{k}}(x_\alpha x_\beta) + \delta V_{\boldsymbol{k}}(x_\alpha x_\beta) \end{aligned} \tag{3.12}$$

where

$$\delta V_{\boldsymbol{k}}(x_\alpha x_\beta) = \sum_{K \neq J} \exp(i\boldsymbol{k} \cdot \boldsymbol{R}_{KJ}) \delta V_{JK}(x_\alpha x_\beta). \tag{3.13}$$

Two examples of the first term of equation (3.12) are shown in Fig. 2 for the case of $\boldsymbol{k}$ lying in the (100) direction.

VOL 9 195

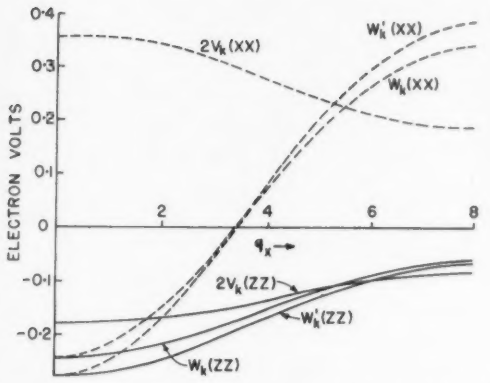

FIG. 2. The k-dependent interactions for k lying in the (100) direction. The ordinate is the value of the interaction concerned in electron volts and the abscissa is $q = (4\sqrt{2}/\pi)ka$, which corresponds to q_x of reference (19). Primed and unprimed sums indicate evaluation with triplet and singlet functions, respectively. $W_k'(xx)$ and $W_k(xx)$ cross and are degenerate with $W_k'(zz)$ and $W_k(zz)$, respectively, at $q = 0$. The exchange interactions W_k contain the correction $2\delta V_k$ discussed in the text, while $2V_k$ is in each case due solely to dipole–dipole interactions.

The "correction" term, defined by equation (3.13), is extremely difficult to evaluate directly from the definition of δV_{JK} [equation (3.7)]. This direct evaluation requires the computation of every interaction appearing in equation (I.4.27b), and even for the one case in which J and K are situated as nearest neighbors, over 60 kinds of three-center interactions are involved. The following approximation is therefore made. When J and K are proximate, even the leading term

$$(V_{JK})_0 = (\overline{J\lambda}\overline{K\lambda'}|e^2/r_{12}|J\lambda K\lambda')$$

of V_{JK} cannot be determined accurately by simply taking the dipole–dipole term of its multipole expansion. However, it is possible to evaluate this leading term exactly with a few integrations, using ordinary methods of classical potential theory.* Then for each $\boldsymbol{R}_{JK}$ the factor by which the dipole–dipole approximation over- or underestimates $(V_{JK})_0$ can be computed. Let us suppose that the true value of the leading term is p times as large as its dipole–dipole part. Our assumption is that the dipole–dipole approximation for the whole quantity V_{JK} breaks down by exactly the same relative amount as it does in the calculable leading term, i.e. we set δV_{JK} equal to $(p-1)$ times the dipole–dipole part of V_{JK}. An approximation of this type seems reasonable and probably gives a more reliable result than would the almost interminable exact computation. It should be emphasized that the validity of the dipole–dipole formalism for V_{JK} is limited only by the two-center approximation when J and K are well-separated (see I, Section 4d); the correction term for which we have just proposed an approximation is only a small fraction ($\sim$0·1) of the total interaction, which further justifies the use of the approximation.

Since δV_{JK} falls off rapidly with increasing $\boldsymbol{R}_{JK}$, the lattice sum in equation (3.13) may be evaluated shell by shell using equations (I.4.45). Computed values will be given later in this section.

We now turn to the excitation exchange interactions. The quantity to be evaluated is

$$W_k(x_\alpha x_\beta) = \sum_{K\neq J} \exp(i\boldsymbol{k}\cdot\boldsymbol{R}_{KJ}) W_{JK}(x_\alpha x_\beta), \quad (3.14)$$

where

$$\begin{aligned} W_{JK}(x_\alpha x_\beta) = &-(\overline{J4s}J3px_\alpha|e^2/r_{12}|\overline{K4s}K3px_\beta) \\ &+\tfrac{1}{2}S_{J3px_\alpha,K3px_\beta}\int \phi_{J4s}(\bar{C}_J{}^{4s}+\bar{C}_K{}^{4s})\phi_{K4s}\,d\mathbf{r} \\ &+\tfrac{1}{2}\bar{S}_{J4s,K4s}\int \phi_{J3px_\alpha}(C_J{}^{3p}+C_K{}^{3p})\phi_{K3px_\beta}\,d\mathbf{r}. \end{aligned} \quad (3.15)$$

Equation (3.15) is the result of applying equation (I.4.27c) to the argon $3p^54s$ problem. The Coulomb potentials $C_J{}^{nl}$ and $C_K{}^{nl}$ are to be regarded as spherically symmetric [because of the use of the atomic HARTREE–FOCK equations in deriving (I.4.27c)], and may in fact be replaced by $e^2/|\boldsymbol{R}_J-\boldsymbol{r}|$ and $e^2/|\boldsymbol{R}_K-\boldsymbol{r}|$, respectively, since the principal contribution to the integrals involved comes from a region of space where the shielding of Z–1 nuclear charges is essentially complete. The numerical evaluation of each of the terms in equation (3.15) posed no difficulties and the results of the computation are shown in Table 3. Examples of the k-dependent sum (3.14) are shown in Fig. 2. Note that the energies associated with exchange-like interactions are of the order

*See, for example, the formalism of reference (10), pp. 15–20 and 96–100.

Table 3. Excitation exchange interactions (in electron volts). Values in parentheses are those which include the correction $2\delta V_{JK}$ to the corresponding excitation transfer interaction. Primes and lack of primes indicate evaluation with triplet and singlet functions, respectively. Values of R are given at the head of each column ($a = 7{\cdot}10a_0$).

	$R = a$	$R = \sqrt{2}a$	$R = \sqrt{3}a$
$W_\sigma(R)$	−0·1042 (−0·08728)	−0·003589	−0·00025
$W_\pi(R)$	0·01600 (0·01384)	0·000382	0·000022
$W_\sigma'(R)$	−0·09796	−0·003788	−0·00027
$W_\pi'(R)$	0·01512	0·000383	0·000026

of magnitude of the dipole–dipole interactions. This is an important departure from the estimate made by HELLER and MARCUS[5] in connection with alkali halides. They felt that exchange interactions would be about one-tenth as great as the dipole–dipole interactions. Here we have an oscillator strength smaller than unity,[9] leading to a smaller dipole–dipole term, and, what is more important, a considerably larger overlap than these authors assumed. It is probable that a numerical computation using the excitation model of an alkali halide would lead to conclusions similar to those of this paper. In Fig. 2, we have included the correction term $2\delta V_k(x_\alpha x_\beta)$ in the W lattice sums corresponding to singlet states; the computed values of $2\delta V_{JK}$ may be inferred from Table 3.

One feature of the numerical calculation based on equation (3.15) is worth special mention. Consider the largest interaction, $W_\sigma(a)$ [see equation (I.4.40) and the associated discussion]. The first term of (3.15) contributing to $W_\sigma(a)$ is seen to be intrinsically positive, since the product of two $3p\sigma$ functions is negative in the important range of the integration variables. Thus, if the latter two terms of equation (3.15) were dropped on the grounds that they involve explicit overlap, we would obtain a positive quantity, and its value is in fact $W_\sigma(a) \approx +0{\cdot}0857$ eV. This would contribute a negative curvature to the exciton energy near $\boldsymbol{k} = 0$. It turns out that the last two terms of equation (3.15) are greater in magnitude than the first, and are intrinsically negative, having the combined value of −0·1899 eV. It will be seen in the next section that the excitation exchange terms are the more important in determining the effective mass of the exciton in argon. It is thus possible to change the computed argon exciton-band structure radically by neglecting explicit overlap terms.

4. NUMERICAL RESULTS

Band structure in directions of high symmetry

The principal results of the band-structure computations based on I and on the parameters computed in the last section are shown in Figs. 5–7. In discussing them, however, it is expedient to look first at some simpler bands. In each of the following reduced-band scheme diagrams, the abscissa is chosen to correspond to the parameter q_x of COHEN and KEFFER.[19] It extends to the edge of the first Brillouin zone in each case. Unless otherwise noted, the ordinate is the energy of the idealized crystal relative to the ground state. The states Y, Y' and ZX of I have been labelled ^1Y, ^3Y and ^3ZX, respectively, here.

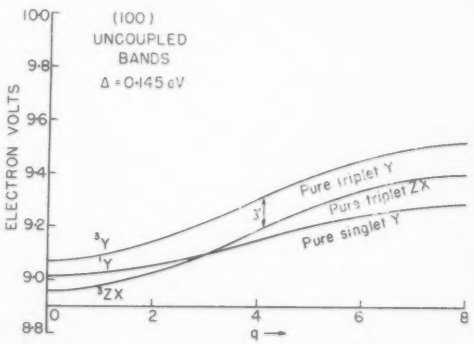

FIG. 3. Pure multiplet transverse bands for $\boldsymbol{k}$ lying in the (100) direction and $\Delta = 0{\cdot}145$ eV neglecting $\boldsymbol{k}$-induced mixing. The abscissa is $q = (4\sqrt{2}/\pi)ka$, and the limit of the first Brillouin zone falls at $q = 8$. The ordinate is the energy of the idealized crystal relative to the ground state.

Fig. 3 shows a band built from a pure singlet Y atomic state along with two triplet bands. The ^1Y band is the band which would actually exist if spin-orbit coupling to ^3Y were negligible. We have retained the spin-orbit splitting between ^3Y and ^3ZX, however, and these two bands run

parallel at a constant separation ζ. The crystal-induced mixing $E_{\boldsymbol{k}}({}^3Y, {}^3ZX)$ is also set equal to zero [see the matrix (I.5.1)]. Hence, Fig. 3 simply shows the diagonal elements of the $({}^1Y, {}^3Y, {}^3ZX)$ matrix as a function of $\boldsymbol{k}$. Especially to be noted is the fact that the singlet state lies below the triplet Y state near $\boldsymbol{k} = 0$; this is caused by the dipole–dipole interaction, which is not present in pure triplet exciton bands. The possibility of this inversion was not considered by other writers in discussions of triplet exciton states.[20,21]

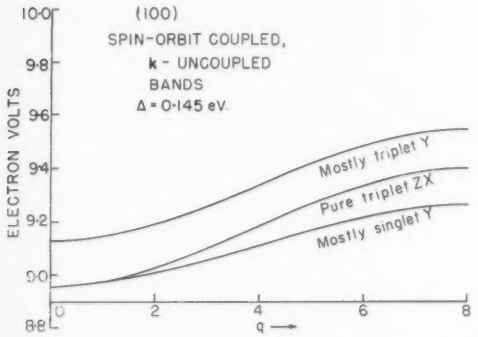

FIG. 4. Spin-orbit coupled transverse exciton bands for $\boldsymbol{k}$ lying in the (100) direction and $\Delta = 0{\cdot}145$ eV, neglecting $\boldsymbol{k}$-induced mixing. Abscissa and ordinate scales are the same as those in Fig. 3.

In Fig. 4 we have "turned on" the spin-orbit interaction between ${}^1Y$ and ${}^3Y$. Note that these two states have repelled each other to such an extent that "${}^1Y$" is nearly degenerate with ${}^3ZX$ at $\boldsymbol{k} = 0$. This is simply an accidental near-degeneracy which cannot be resolved on the scale of Fig. 4 and which also appears in the next three figures. It should not be mistaken for a symmetry-induced degeneracy; the two states are actually separated by several thousandths of an electron volt near $\boldsymbol{k} = 0$.

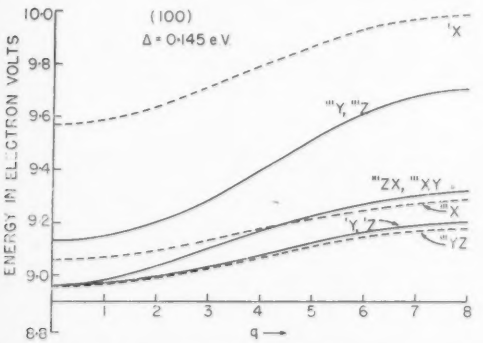

FIG. 5. Exciton bands for $\boldsymbol{k}$ lying in the (100) direction and $\Delta = 0{\cdot}145$ eV. Solid lines indicate transverse states and dashed lines longitudinal states. Abscissa and ordinate scales are the same as those in Fig. 3.

Fig. 5 shows the final form of the transverse bands (heavy lines) and, in addition, the longitudinal bands (dashed lines). Note the marked change in width of the transverse bands from Fig. 4. The band called ${}^1Y$ is a bit narrower, but ${}^{III}Y$, which can participate in optical absorption because it is coupled to the pure singlet state even at $\boldsymbol{k} = 0$, has been considerably broadened.* The ${}^{III}ZX$ band, which at $\boldsymbol{k} = 0$ is pure triplet and therefore optically uninteresting, is nevertheless an important perturbing state in the rest of the band. Regarding the longitudinal states, ${}^1X$ lies above ${}^{III}X$ because of the positive sign of the longitudinal dipole–dipole lattice sum near $\boldsymbol{k} = 0$. ${}^{III}YZ$ is everywhere uncoupled from ${}^1X$ and ${}^{III}X$, but is included as a companion to ${}^{III}ZX$. The fact that these two are degenerate at $\boldsymbol{k} = 0$ is a result of symmetry. Six uninteresting triplet bands are not shown in Fig. 5.

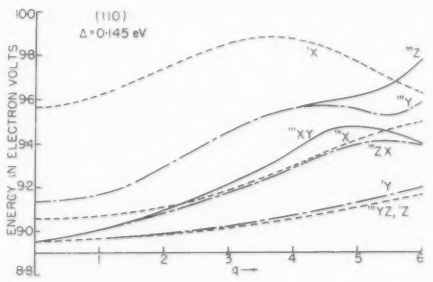

FIG. 6. Exciton bands for $\boldsymbol{k}$ lying in the (110) direction, with $\Delta = 0{\cdot}145$ eV. Solid lines indicate transverse states with excitation parallel to the fourfold crystal axis (Z), alternate dashes and lines indicate transverse states with excitation parallel to the twofold crystal axis (Y), and dashed lines represent longitudinal states (X). The abscissa is $q = (4/\pi)ka$, and the limit of the first Brillouin zone falls at $q = 6$. The ordinate is the same as in Fig. 3.

* The symbols distinguishing a band are intended to suggest the atomic pure multiplet function which is principally mixed into the band near $\boldsymbol{k} = 0$, and are seldom "good quantum numbers".

Fig. 6 shows the rather complex structure of the (110)-direction bands. Here nine generally distinct bands are found because of the splitting of transverse states. ^{III}Y and ^{I}Z happen to lie quite close to one another. It is interesting that the characteristic cosine-like behavior is often missing here; examination of the detailed form of the longitudinal (110) lattice sum reveals that the second Fourier harmonic is at least as important as the first, which helps explain the shape of ^{I}X. This is a complicating factor, too, in ^{III}Y and ^{III}Z, which contain "longitudinal" lattice sums. Another feature is the attempt of ^{III}Z and ^{III}XY to cross, which is impossible because they combine strongly. This also occurs in the case of ^{III}Y and ^{III}ZX. Finally, the (110) direction is not perpendicular to a face of the first Brillouin zone at its boundary, so the bands are not necessarily flat at $q = 6$.

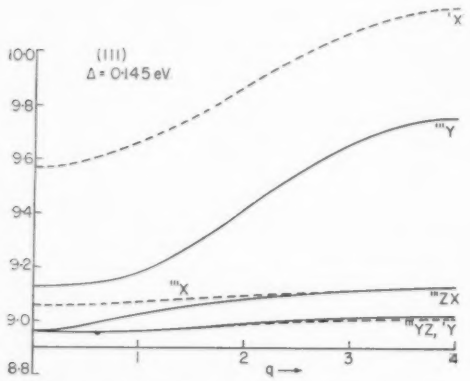

FIG. 7. Exciton bands for $\boldsymbol{k}$ lying in the (111) direction, with $\Delta = 0{\cdot}145$ eV. Solid lines indicate transverse states and dashed lines longitudinal states. The abscissa is $q = \sqrt{2}/3(4ka/\pi)$, and the limit of the first Brillouin zone falls at $q = 4$. The ordinate is the same as in Fig. 3.

Fig. 7 shows the relatively regular (111)-direction bands. Symmetry-wise they follow the pattern of the (100) direction because of the similarity of the irreducible representations of the groups of the two $\boldsymbol{k}$ vectors. The only noteworthy aspect of this structure is the rather broad "longitudinal" lattice sum (^{I}X and ^{III}Y contain "longitudinal" lattice sums).

The entire computation of band structures was repeated for two more values of Δ, in view of the uncertainty connected with the computation of this quantity. The results are typified by the resulting bands in the (100) direction, and these are shown in Figs. 8 ($\Delta = 0{\cdot}00$ eV) and 9 ($\Delta = 1{\cdot}00$ eV). In both of these figures the ordinate is

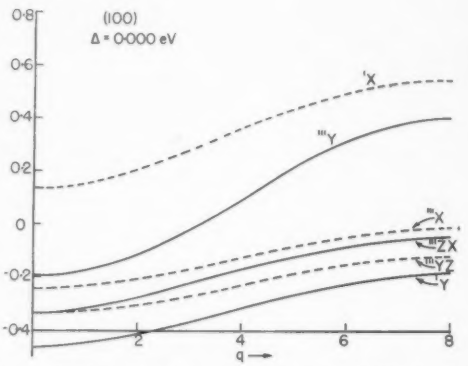

FIG. 8. Exciton bands for $\boldsymbol{k}$ lying in the (100) direction with $\Delta = 0$. The ordinate is energy in electron volts relative to the pure triplet crystal energy ^{3}E. In all other respects the notation is the same as that in Fig. 5.

chosen such that $^{3}E = 0$. In neither case is the shape of the ^{I}Y band appreciably changed. When $\Delta = 1$ eV, the singlet and triplet states resume their normal relative positions, but then LS

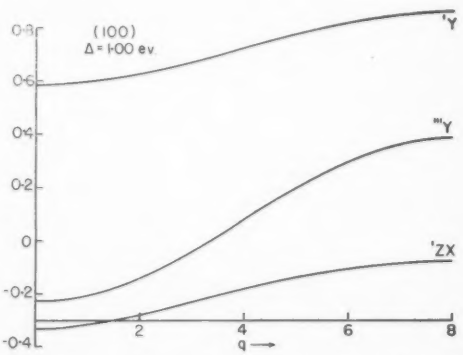

FIG. 9. Transverse exciton bands for $\boldsymbol{k}$ lying in the (100) direction with $\Delta = 1{\cdot}00$ eV. Notation and scales are the same as those in Fig. 8.

coupling is applicable and triplet states are much less important, optically. If Δ were as poorly computed as this case allows, the model would predict only one discernable absorption line.

(100) *direction*

$$W(^{\mathrm{I}}X) = 9{\cdot}568+\tfrac{1}{2}(0{\cdot}121)k^2a^2+ \ldots$$
$$W(^{\mathrm{III}}X) = 9{\cdot}060+\tfrac{1}{2}(0{\cdot}0541)k^2a^2+ \ldots$$
$$W(^{\mathrm{I}}Y) = W(^{\mathrm{I}}Z) = 8{\cdot}956+\tfrac{1}{2}(0{\cdot}0828)k^2a^2+ \ldots$$
$$W(^{\mathrm{III}}Y) = W(^{\mathrm{III}}Z) = 9{\cdot}131+\tfrac{1}{2}(0{\cdot}1009)k^2a^2+ \ldots$$

$$[m^*(^{\mathrm{I}}Y)]^{-1} = \begin{pmatrix} 0{\cdot}153 & 0 & 0 \\ 0 & 0{\cdot}118 & 0 \\ 0 & 0 & 0 \end{pmatrix} \qquad [m^*(^{\mathrm{I}}Z)]^{-1} = \begin{pmatrix} 0{\cdot}153 & 0 & 0 \\ 0 & 0 & 0 \\ 0 & 0 & 0{\cdot}118 \end{pmatrix}$$

$$[m^*(^{\mathrm{III}}Y)]^{-1} = \begin{pmatrix} 0{\cdot}187 & 0 & 0 \\ 0 & 0{\cdot}152 & 0 \\ 0 & 0 & 0 \end{pmatrix} \qquad [m^*(^{\mathrm{III}}Z)]^{-1} = \begin{pmatrix} 0{\cdot}187 & 0 & 0 \\ 0 & 0 & 0 \\ 0 & 0 & 0{\cdot}152 \end{pmatrix}$$

(110) *direction*

$$W(^{\mathrm{I}}X) = 9{\cdot}568+\tfrac{1}{2}(0{\cdot}1092)k^2a^2+ \ldots$$
$$W(^{\mathrm{III}}X) = 9{\cdot}060+\tfrac{1}{2}(0{\cdot}0296)k^2a^2+ \ldots$$
$$W(^{\mathrm{I}}Y) = 8{\cdot}956+\tfrac{1}{2}(0\ 0828)k^2a^2+ \ldots$$
$$W(^{\mathrm{III}}Y) = 9{\cdot}131+\tfrac{1}{2}(0{\cdot}1009)k^2a^2+ \ldots$$
$$W(^{\mathrm{I}}Z) = 8{\cdot}956+\tfrac{1}{2}(0{\cdot}0987)k^2a^2+ \ldots$$
$$W(^{\mathrm{III}}Z) = 9{\cdot}131+\tfrac{1}{2}(0{\cdot}1213)k^2a^2+ \ldots$$

$$[m^*(^{\mathrm{I}}Y)]^{-1} = \begin{pmatrix} 0{\cdot}153 & 0 & 0 \\ 0 & 0{\cdot}088 & 0 \\ 0 & 0 & 0 \end{pmatrix} \qquad [m^*(^{\mathrm{I}}Z)]^{-1} = \begin{pmatrix} 0{\cdot}183 & 0 & 0 \\ 0 & -0{\cdot}029 & 0 \\ 0 & 0 & -0{\cdot}118 \end{pmatrix}$$

$$[m^*(^{\mathrm{III}}Y)]^{-1} = \begin{pmatrix} 0{\cdot}187 & 0 & 0 \\ 0 & 0{\cdot}114 & 0 \\ 0 & 0 & 0 \end{pmatrix} \qquad [m^*(^{\mathrm{III}}Z)]^{-1} = \begin{pmatrix} 0{\cdot}224 & 0 & 0 \\ 0 & -0{\cdot}038 & 0 \\ 0 & 0 & -0{\cdot}152 \end{pmatrix}$$

(111) *direction*

$$W(^{\mathrm{I}}X) = 9{\cdot}568+\tfrac{1}{2}(0{\cdot}1072)k^2a^2+ \ldots$$
$$W(^{\mathrm{III}}X) = 9{\cdot}060+\tfrac{1}{2}(0{\cdot}0254)k^2a^2+ \ldots$$
$$W(^{\mathrm{I}}Y) = W(^{\mathrm{I}}Z) = 8{\cdot}956+\tfrac{1}{2}(0{\cdot}0934)k^2a^2+ \ldots$$
$$W(^{\mathrm{III}}Y) = W(^{\mathrm{III}}Z) = 9{\cdot}131+\tfrac{1}{2}(0{\cdot}1145)k^2a^2+ \ldots$$

$$[m^*(^{\mathrm{I}}Y)]^{-1} = \begin{pmatrix} 0{\cdot}173 & -0{\cdot}014 & 0 \\ -0{\cdot}028 & -0{\cdot}069 & 0 \\ 0 & 0 & 0{\cdot}039 \end{pmatrix} \qquad [m^*(^{\mathrm{I}}Z)]^{-1} = \begin{pmatrix} 0{\cdot}173 & 0{\cdot}014 & 0 \\ 0{\cdot}028 & 0{\cdot}254 & 0 \\ 0 & 0 & -0{\cdot}117 \end{pmatrix}$$

$$[m^*(^{\mathrm{III}}Y)]^{-1} = \begin{pmatrix} 0{\cdot}212 & -0{\cdot}018 & 0 \\ -0{\cdot}036 & -0{\cdot}088 & 0 \\ 0 & 0 & 0{\cdot}051 \end{pmatrix} \qquad [m^*(^{\mathrm{III}}Z)]^{-1} = \begin{pmatrix} 0{\cdot}212 & 0{\cdot}018 & 0 \\ 0{\cdot}036 & -0{\cdot}013 & 0 \\ 0 & 0 & -0{\cdot}152 \end{pmatrix}$$

(*b*) *Energies and effective masses near* $\boldsymbol{k} = 0$

Equations of the form (I.5.19) and (I.5.20) have been used to determine the behavior of the various optically interesting exciton states near $\boldsymbol{k} = 0$ [for details, see pp. 82–91 of reference (16)]. For the three symmetry directions just discussed, the following expressions result. Energies are given in electron volts and reciprocal effective mass tensors in units of reciprocal electron mass. Complete tensors are shown only for transverse states, and the rows and columns correspond to the k, θ, φ directions (the X, $-Z$, and Y directions in the $\boldsymbol{k}$ frame; see Fig. 1 of I.).

These energy expressions are, of course, the asymptotic forms of the corresponding bands near $\boldsymbol{k} = 0$ (Figs. 5, 6 and 7). Again, as a check on the sensitivity of our computation to the value of Δ, we have made a comparison of four cases. Complete effective mass tensors were computed and the numbers given in Table 4 are the $(\partial^2/\partial k^2)$ components of these tensors for various states of transverse polarization and directions of $\boldsymbol{k}$. We see from this table that changing Δ over a range of 1·5 eV results in a variation of the effective masses of only 5–20 per cent. Two other hypothetical cases were also considered: in one, the contributions from second and third neighbors to the $W_{\boldsymbol{k}}$ (excitation exchange lattice sums) were set equal to zero, and in the other, all the $W_{\boldsymbol{k}}$ were set equal to zero (both with Δ held at 0·145 eV). The results are shown in the last two columns of Table 4. It is seen that the second- and third-neighbor contributions to $(m^*)^{-1}$ are about 5–8 per cent of the total, which demonstrates that these contributions were indeed necessary to include, but that convergence in the sum over neighbors is quite good. The last column of Table 4 essentially indicates the contribution to $(m^*)^{-1}$ of the HELLER–MARCUS excitation transfer interaction. This contribution ranges from about 12–20 per cent.

In summary: the computed effective masses of tightly-bound excitons in the lowest set of excited states of argon lie in the range 4·45–6·55 electron masses, the lighter ones generally being associated with the "mostly-triplet" states. Probable computational errors in these quantities are smaller than those in the energy computation, being

Table 4. *Reciprocal effective masses of transverse excitons in solid argon. Unit: reciprocal electron mass.* θ *and* ϕ *are spherical co-ordinates of* $\boldsymbol{k}$ *with respect to the* (001) *axis. The designations* Y *and* Z *simply distinguish between transverse states and do not refer to pure states of polarization except in the three simple symmetry directions. See the discussion in the text for an explanation of the last two columns.*

State	Direction of $\boldsymbol{k}$	Δ(eV)				$W(a)$ only	All $W = 0$
		0·145	0·000	1·000	−0·05		
		$\partial^2/\partial k^2$ component of $(m^*)^{-1}$					
$^{I}Y = {}^{I}Z$	(100)	0·153	0·132	0·123	0·122	0·149	0·0282
$^{III}Y = {}^{III}Z$	,,	0·187	0·208	0·218	0·217	0·176	0·0095
^{I}Y	(110)	0·153	0·132	0·123	0·123	0·149	0·0282
^{I}Z	,,	0·183	0·156	0·144	0·145	0·172	0·104
^{III}Y	,,	0·187	0·208	0·218	0·217	0·176	0·0095
^{III}Z	,,	0·224	0·252	0·263	0·263	0·214	0·0355
$^{I}Y = {}^{I}Z$	(111)	0·173	0·148	0·137	0·137	0·164	0·0794
$^{III}Y = {}^{III}Z$	,,	0·212	0·237	0·248	0·248	0·202	0·0269
^{I}Y	$\theta = 90°, \phi = 30°$	0·153	0·132	0·123	0·122	0·149	0·0282
^{I}Z	,,	0·175	0·150	0·139	0·139	0·166	0·0858
^{I}Y	$\theta = 80°, \phi = 30°$	0·156	0·150	0·139	0·139	0·151	0·0348
^{I}Z	,,	0·175	0·134	0·125	0·125	0·166	0·0847
^{I}Y	$\theta = 60°, \phi = 30°$	0·167	0·150	0·139	0·139	0·159	0·0605
^{I}Z	,,	0·174	0·143	0·132	0·132	0·165	0·0858

VOL. 9 1959

estimated at 2–4 per cent. None of the masses depends strongly upon the direction of propagation. At least 80 per cent of the reciprocal effective mass is due to the exciting exchange interaction whose negative sign, which leads to a positive effective mass, is due exclusively to terms which are purely "overlap" in character, i.e. involve a factor which is an actual overlap integral S [see the second and third terms of equation (3.15)]. It is because of the large overlapping of nearest-neighboring excitations that this exchange-like interaction is much more important, quantitatively, than the HELLER-MARCUS dipole–dipole interaction. The latter is responsible for the splitting off, at $\boldsymbol{k} \approx 0$, of the longitudinal exciton states and thus it maintains considerable qualitative importance.

(*c*) *Integrated absorption coefficient*

We now turn to equation (I.6.13), which consists in an expression for the integrated absorption cross-section Σ_{fi} due to states in a single p^5s configuration participating in absorption of light. We repeat this equation for reference:

$$\Sigma_{fi} = 8\pi^2 N(e^2/\hbar c)[E_{fi}/n(E_{fi})](W_\mu/E_{fi})^2 \times \times |(f|\mu)|^2 |\boldsymbol{p}\cdot\boldsymbol{M}|^2 |1+[E_{\boldsymbol{k}}(\mu,\mu)/2W_\mu]^2|. \quad (4.1)$$

Here N is the number of atoms in the crystal, E_{fi} is the peak absorption energy associated with a transition from state i to state f, $n(E_{fi})$ is the index of refraction of the crystal at this photon energy, W_μ is the first-order energy of the singlet state μ which is mixed into f according to the coupling coefficient $(f|\mu)$, $\boldsymbol{p}$ is a unit vector describing the polarization of the incident light wave, $\boldsymbol{M}_\mu$ is the dipole matrix element computed earlier, and $E_{\boldsymbol{k}}(\mu,\mu)$ is the $\boldsymbol{k}$-dependent part of the energy of the state μ. Since the transverse exciton states are nearly degenerate in the vicinity of $\boldsymbol{k}=0$ and are energetically distinct from the longitudinal states, we may consider excitation simply of the transverse states under a transverse perturbing field. We replace $|\boldsymbol{p}\cdot\boldsymbol{M}_\mu|^2$ by M^2 two states with a probability of one half.* We shall evaluate the integrated absorption coefficient,

$$\mu'_{fi} = \int \mu_{fi}\, dE = n_0(\Sigma_{fi}/N), \quad (4.2)$$

which is equal to the number density of lattice points n_0 times the integrated absorption cross-section per atom, (Σ_{fi}/N). The various quantities appearing in (4.1, 2) have been evaluated in connection with the band-structure computations. Since we necessarily deal with $\boldsymbol{k} \approx 0$ because of the momentum selection rule, and there are no striking directional effects in the transverse bands in this vicinity, it is possible simply to take for an energy E_{fi} a limiting value as $\boldsymbol{k}\to 0$; likewise, coupling coefficients in the limit $\boldsymbol{k}\to 0$ may be used with high accuracy. This automatically excludes "$J=2$" states such as $^{\mathrm{III}}ZX$, since $|(f|^1Y)|^2$ vanishes as $(ka)^4$ for such states (see I., Section 5a). Thus we shall be interested in only two possible final states, ^1Y and $^{\mathrm{III}}Y$ (or ^1Z and $^{\mathrm{III}}Z$). The following computed values are used in equations (4.1) and (4.2): $V_{\varkappa}(yy) = -0{\cdot}0902$ eV, $W_{\varkappa}(yy) = -0{\cdot}246$ eV, $^1E(=W_\mu) = 9{\cdot}44$ eV, $M^2-(\Delta m)^2 = 0{\cdot}200\ a_0^2$, and $n_0 = 4(2^{\frac{1}{2}}a)^{-3}$, where $a = 7{\cdot}10\ a_0$. Atomic constants used are $e^2/\hbar c = 1/137{\cdot}0$ and $e^2/a_0 = 27{\cdot}21$ eV. If E_{fi} is measured in eV, the result is

$$n(E_{fi})\mu'_{fi} = |(f|^1Y)|^2(0{\cdot}777\times 10^6)(9{\cdot}44/E_{fi})\mathrm{cm}^{-1}\,\mathrm{eV}. \quad (4.3)$$

It is not possible to give a computed value for $n(E_{fi})$ because of its dependence on the details of the higher excited states of the argon crystal, which are not considered in the present computation. However, coupling coefficients and energies corresponding to each of the three values of Δ have been used in equation (4.3) with the following results (n is taken arbitrarily as unity):

$$\Delta = 0{\cdot}145\ \mathrm{eV}\begin{cases} ^{\mathrm{III}}\mu'(9{\cdot}13\ \mathrm{eV}) = 0{\cdot}263\times 10^6\,\mathrm{cm}^{-1}\,\mathrm{eV} \\ ^{\mathrm{I}}\mu'(8{\cdot}96\ \mathrm{eV}) = 0{\cdot}550\times 10^6\,\mathrm{cm}^{-1}\,\mathrm{eV} \end{cases} \quad (4.4)$$

since: either $\boldsymbol{p}$ is fixed and can excite only one transverse state; or, $\boldsymbol{p}$ is randomly distributed in the transverse plane and can excite either of the

*In actual fact, we use $M^2-(\Delta m)^2$ rather than M^2, in order to eliminate fourth-order overlap terms, exactly as in the evaluation of $V_{\boldsymbol{k}}(x_\alpha x_\beta)$.

$$\Delta = 0{\cdot}000 \text{ eV} \begin{cases} {}^{III}\mu'(9{\cdot}25 \text{ eV}) = 0{\cdot}087 \times 10^6 \text{ cm}^{-1} \text{ eV} \\ {}^{I}\mu'(8{\cdot}99 \text{ eV}) = 0{\cdot}726 \times 10^6 \text{ cm}^{-1} \text{ eV} \end{cases} \tag{4.5}$$

$$\Delta = 1{\cdot}000 \text{ eV} \begin{cases} {}^{I}\mu'(9{\cdot}02 \text{ eV}) = 0{\cdot}796 \times 10^6 \text{ cm}^{-1} \text{ eV} \\ {}^{III}\mu'(8{\cdot}21 \text{ eV}) = 0{\cdot}009 \times 10^6 \text{ cm}^{-1} \text{ eV} \end{cases} \tag{4.6}$$

The "I" and "III" superscripts correspond to the superscripts on the transverse exciton bands of Figs. 4.9. The energy in parentheses following μ' is the energy of the optically preparable exciton state.

A quantitative or even elaborate qualitative analysis of line shape and breadth following PEIERLS[2] and FRENKEL[3] is outside the scope of the present work, but we shall speculate briefly on the possible absorption lines arising from transitions to our exciton states. It is fully realized that these lines are in all probability not simple,[2] but let us assume that they are, and that their half-widths are roughly half the total exciton band width. Then, if one could possibly prepare a single argon crystal and irradiate in the (111) direction, the absorption lines for $\Delta = 0{\cdot}145$ eV [equations (4.4)] should be resolved (see Fig. 7). Their widths would be such that the peak absorption would exceed 7×10^6 cm^{-1} at 8·96 eV and $0{\cdot}6 \times 10^6$ cm^{-1} at 9·13 eV. Roughly the same picture would hold for the lines in the case $\Delta = 0$ [equations (4.5)] but for $\Delta = 1$ eV [equations (4.6)] the line at 8·21 eV would be very weak. In a random crystal direction and with Δ in the vicinity of zero, one expects in this simplified picture at most two moderately overlapping bands, the less energetic of which has at least twice the integrated absorption coefficient of the other. The total integrated absorption coefficient, regardless (within reason) of the positions and relative sizes of the lines, will be $0{\cdot}78 \times 10^6$ cm^{-1} eV for lines in the vicinity of 9 eV. If absorption characteristic of the pure crystalline solid can be observed, it will be quite interesting to see whether two components exist and whether the intensity ratio is consistent with the splitting.*

*The only data on optical absorption of solid argon appears to be contained in unpublished work of J. R. NELSON and P. L. HARTMAN (Cornell University, 1957). Professor HARTMAN has kindly granted permission to quote from a letter in which he notes that structureless absorption bands appear at 980 and 1380Å (12·8 and 9·0 eV).

Finally, it might be noted that explicit overlap corrections contribute some 30 per cent of the integrated absorption coefficient and double exciton mixing causes a reduction of 5 per cent in the value computed with zero-order ground-state wave functions.

5. DISCUSSION

The exciton formalism of FRENKEL[1] and subsequent workers[2–7] has been applied to the low-lying states of solid argon, i.e. those states built from the atomic $3p^5 4s$ configuration. Complicated exciton bands with energy minima at $\boldsymbol{k} = 0$ in the region of 9 eV (± 1 eV) relative to the ground state result, the various excitons having effective masses of from 4·5 to 6·5 electron masses ($\pm 0{\cdot}2$ electron masses). Optical absorption to these states should take place with a total integrated absorption cross-section of the order of $0{\cdot}8 \times 10^6$ cm^{-1} eV. Large overlap of the excited argon wave functions with neighboring free-atomic functions necessitated summing interactions over 42 neighbors (the first three shells). The estimated error of 1 eV in the position of the exciton band is not a result of neglecting any of the contributions to the interactions involved; it is partly due to difficulties in numerical evaluation of two- and three-center integrals and partly to the inherent inaccuracy of the HARTREE–FOCK functions. Because of the latter, the estimated error could probably never be brought below 5 per cent, the error which obtains in excitation energies computed for the free atom.[9] The only experimental data entering the computation of energies and effective masses are the Rydberg and the lattice constant of solid argon,[12] the latter of which could in principle be computed by a second-order treatment of the argon binding energy. In addition, the fine-structure constant is used in computing absorption coefficients.

The approximations and assumptions inherent in the formalism used have been discussed in

VOL. 9 1959

I, and in most cases we shall merely list them here. The HEITLER–LONDON model is assumed valid for the ground and excited states, and to test its validity in the latter case is in fact one purpose of this calculation. Energies are computed in a static approximation and integrated absorption coefficients are computed on the assumptions that BORN–OPPENHEIMER wave functions are applicable to the vibrating crystal and that the CONDON approximation is valid. The crystal to which our results apply is assumed to contain a very large number of atoms. This is a serious limitation only if absorption properties of very thin films or fine polycrystals are to be studied. Aside from the effects of surface states, which become relatively more important in these cases,[22] the dipole–dipole interaction here no longer provides as effective a splitting of longitudinal and transverse states in the optical region of exciton momentum space. Semiclassical radiation theory is assumed valid in computing transition probabilities in absorption.

Finally, three points pertaining to this particular computation must be discussed. They are: (1) the assumed validity and accuracy of the HARTREE–FOCK functions for atomic argon, (2) the neglect of perturbations on the pure $3p^54s$ exciton states by other single exciton states, and (3) the question of convergence of the LÖWDIN orthonormalization series at terms of order S^2. Of these, (1) has been discussed in reference (9), where it is shown, on the basis of computed energies and oscillator strengths, that the HARTREE–FOCK solutions are reasonably good descriptions of the free argon atom in the $3p^54s$ terms.

As to (2), perturbations by higher states in the free atom appear not to affect the general details of the mixing within the $3p^54s$ configuration, as far as a KING–VAN VLECK spectrum analysis can indicate.[9,23] If perturbations by higher states within the free argon atom amount to as much as 1 per cent in the $3p^54s$ term splittings, the corresponding crystal perturbations could be a factor of ten greater than those in the free atom without upsetting the picture drawn by the present calculation. Although overlap effects would be enormous for higher atomic trial states, it is not *a priori* true that the energy of the corresponding crystal state would be lowered so much as to cause thorough mixing of higher states with those of $3p^54s$. We have seen that there is a considerable positive overlap energy which effectively cancels much of the negative overlap energy. With regard to second-order corrections contributed by double excitons: only a $4\frac{1}{2}$ per cent correction to the absorption coefficient is made by these states, so the corresponding energy correction is expected to be relatively much smaller. Such corrections would be classed as of the "van der Waals" type.

With regard to (3), it is possible to infer from the overlap integral $S(3s, 4s)$ alone (see Table 2) that neither the sufficient condition for convergence nor that for divergence of the orthonormalization series* can be met in the argon states under consideration. Summing over nearest-neighbor $3s$ shells only (indicated by the prime), we have the following result:

$$\sum_{\alpha}{}' S_{4s,\alpha} = 12(-0{\cdot}1234) = -1{\cdot}481. \quad (5.1)$$

It is evident that the completion of the sum over all the lattice has little chance of bringing this sum above $+1$, which would prove divergence, since the overlap of $4s$ with p functions contributes nothing to the sum and each of the other sets of s shells contributes very little. On the other hand, when absolute value signs are included on $S_{4s,\alpha}$, the partial sum (5.1) becomes $+1{\cdot}481$ and a condition for convergence can never be obtained by adding more terms (the sum over absolute values must be less than 1). The application of LÖWDIN's rigorous criterion for convergence [equation (3.44), reference (10)] is difficult for such a large number of highly overlapping functions. Hence, it is not possible to decide whether the S^2 approximation is good. An evaluation of the HEITLER–LONDON model by comparison of our computed results with experiment must therefore be made regarding the S^2 approximation as an important qualifying restriction.

In the introduction to I, we discussed the role of excited states in the formulation of a HEITLER–LONDON computation of binding energies. Briefly, the results of the present calculation have the following bearing on this formulation. The energy of a system in a state μ has the following form in second order of perturbation:

*Reference (10), equations (3.29) and (3.68), respectively.

$$(\mu|H|\mu) - \sum_{\alpha} \frac{|(\mu|H|\alpha)|^2}{E_\alpha - E_\mu}. \qquad (5.2)$$

If μ is the trial ground-state function, an appropriate trial double exciton or doubly excited localized excitation state α will mix with μ. If α involves two excited states of the same multiplicity, $(\mu|H|\alpha)$ will be non-zero and of the form $2V_{JK}+W_{JK}$ (α singlets), W_{JK}' (α triplets), &c. In conventional treatments of second-order terms in the binding energy of a solid, the W_{JK} are neglected and $2V_{JK}$ contributes the common "van der Waals" energy. It is not possible for us to make even a numerical estimate of second-order contributions in argon using the present data, since states built from atomic configurations higher than $3p^54s$ must certainly be included in the expression (5.2). However, it is clear that two important points must be recognized. First, the part of the conventional van der Waals energy due to $3p^54s$ states will be $[(M^2-\Delta m^2)/m^2](E_{\text{atomic}}/E_{\text{crystal}}) = 1{\cdot}72$ times as great as that which would be computed using atomic transition probabilities or polarizabilities alone. Second, we have found that the quantities W_{JK} are of the same order of magnitude as $2V_{JK}$ in the $3p^54s$ configuration. Both of these effects are due primarily to large overlapping of atomic wave functions, and there is every reason to believe that the corresponding overlap effects are no smaller in higher configurations. It therefore seems that the traditional van der Waals energy accounts for only part of the HEITLER–LONDON attractive binding energy of crystalline argon. The attractive potential due to excitation exchange terms contributes a sizable negative energy decreasing exponentially with distance (because of the overlap nature of the interactions W_{JK}). Thus the effective two-body potential in solid argon may be best represented by a mixture of Morse and exp-6 potentials. Although no essentially different kind of lattice sum is introduced, the existence of a sizable Morse attraction term may have some bearing on the current problem of relative stability of lattice types in the crystalline rare gases.[24]*

*While all of the rare gases except helium crystallize in the face-centered cubic lattice, theory predicts a hexagonal closed-packed lattice. Discussions of this discrepancy and of attempts to remove it are given in reference (24).

Acknowledgements—The author is indebted to Professor D. L. DEXTER, who suggested this computation, provided many helpful discussions, and kindly read the manuscripts of this and the preceding paper. The assistance of Mr. M. P. RIMMER in writing several computer programs and in executing parts of the calculation is gratefully acknowledged.

REFERENCES

1. FRENKEL J., *Phys. Rev.* **37,** 17, 1276 (1931).
2. PEIERLS R. E., *Ann. Phys., Lzg.* **13,** 905 (1932).
3. FRENKEL J., *Phys. Z. Sovjet.* **9,** 158 (1936).
4. KNOX R. S., *J. Phys. Chem. Solids* **9,** 238 (1959).
5. HELLER W. R. and MARCUS A., *Phys. Rev.* **84,** 809 (1951).
6. DEXTER D. L. and HELLER W. R., *Phys. Rev.* **91,** 273 (1953).
7. DEXTER D. L., *Phys. Rev.* **101,** 48 (1956).
8. HARTREE D. R. and HARTREE W., *Proc. Roy. Soc.* A**166,** 450 (1938).
9. KNOX R. S., *Phys. Rev.* **110,** 375 (1958).
10. LÖWDIN P.-O., *Advanc. Phys.* **5,** 1 (1956).
11. KUNIMUNE M., *Progr. Theor. Phys.* **5,** 412 (1950).
12. DOBBS E. R., FIGGINS B. F., JONES G. O., PEIRCEY D. C. and RILEY D. P., *Nature, Lond.* **178,** 483 (1956).
13. RIMMER M. P. and KNOX R. S., Unpublished report, Institute of Optics, University of Rochester, Rochester, N.Y. (1958).
14. PIPER W. W., *Trans. Amer. Inst. Elect. Engrs.* **75,** I, 152 (1956).
15. WOLONTIS V. M., *IBM Tech. Newsletter* No. 11 (March, 1956, unpublished).
    NICKLES M. L., ROMBERG B., and KEENAN T. A., *University of Rochester Computing Center Rep.* No. 1 (Jan. 1957, unpublished).
16. KNOX R. S., Thesis, University of Rochester, Rochester, N.Y. (1958).
17. LANDSHOFF R., *Z. Phys.* **102,** 201 (1936); *Phys. Rev.* **52,** 246 (1937).
18. LÖWDIN P.-O., *Arkiv. Mat. Astr. Fys.* **35**A, Nos 9 and 30 (1948).
19. COHEN M. H. and KEFFER F., *Phys. Rev.* **99,** 1128 (1955).
20. SLATER J. C., *Tech. Rep.* No. 6, *Solid State and Molecular Theory Group, Massachusetts Institute of Technology, Cambridge, Mass.* pp. 3–21. (Apr. 15, 1956, unpublished).
21. TAKEUTI Y., *Progr. Theor. Phys.* **18,** 421 (1957).
22. DEXTER D. L., *Photoconductivity Conference* (Ed. R. G. BRECKENRIDGE *et al.*) pp. 617–618. J. Wiley, New York (1956).
23. KING G. W. and VAN VLECK J. H., *Phys. Rev.* **56,** 464 (1939).
24. DOBBS E. R. and JONES G. O., *Rep. Progr. Phys.* **20,** 516 (1957).

J. Phys. Chem. Solids Pergamon Press 1959. Vol. 9. pp. 281–284. Printed in Great Britain.

HALL EFFECT IN COPPER AND Cu_3Au AT LOW TEMPERATURES*

W. F. LOVE

Physics Department, University of Colorado, Boulder, Colorado

(*Received* 9 *September* 1958)

Abstract—The Hall coefficient in single crystals of copper and Cu_3Au in the ordered and disordered states has been measured at temperatures down to 4°K. No dependence of the Hall coefficient on orientation in copper has been found. In all cases the Hall coefficient is found to be appreciably temperature-dependent.

VOL. 9 959

1. INTRODUCTION

KOMAR and SIDOVOV[1] have reported that the Hall coefficient in ordered Cu_3Au is positive, while in disordered Cu_3Au it is negative. The natural interpretation of this phenomenon is that upon ordering a new Brillouin-zone boundary is formed, corresponding to the superlattice reflections, which is just sufficient to contain the one electron per atom present in this alloy. Because of overlapping of electrons across this boundary, both electrons and holes will be present, and the holes predominate in determining the sign of the Hall coefficient. Presumably the electron energies in the disordered alloy will be far removed from a zone boundary and the Hall coefficient will then be negative. If only one type of carrier is present, simple theory predicts a temperature-independent Hall coefficient in a metal. With both electrons and holes present, the two-band theory applies and the Hall coefficient will then depend on the mobilities in both bands as well as the concentration of carriers. Consequently, one would expect to see an appreciably greater temperature-dependence of the Hall coefficient in ordered Cu_3Au compared to disordered Cu_3Au. For this reason measurements of the Hall coefficient in Cu_3Au have been made.

The temperature-dependence of the Hall coefficient in copper was also studied for comparison with Cu_3Au.

2. EXPERIMENTAL

The circuit for measuring the Hall coefficient is essentially the same as that outlined in a previous publication.[2] To ensure thermal equilibrium, measurements were made with the sample immersed in a liquid. Hall leads were soldered to the specimens with Wood's metal. The magnetic field used was approximately 9 kG. No field-dependence of the Hall coefficient was found in these experiments.

The oriented single crystals of copper used in this investigation were grown from spherical oriented seeds in a graphite crucible by the Bridgman technique in a vacuum electric furnace. The copper used was provided by the American Smelting and Refining Co., and was stated to have a purity of 99·999 per cent or better. The resulting crystals were in the form of plates $1\frac{1}{4} \times \frac{3}{8} \times 0{\cdot}020$ in. They were then milled to a uniform thickness with an uncertainty of 0·0002 in. The milling was carried out under liquid nitrogen with cuts not exceeding 0·001 in. to minimize any strains or deformation as a result of the process. After machining they were annealed at 450°C for 30 min and then etched. No visible change in structure or orientation was revealed on the etched specimens. The samples were oriented in an optical goniometer.

The Cu_3Au samples were prepared by melting the two ingredients together in a graphite crucible in a vacuum, using induction heating to ensure thorough mixing. The resulting slug was then

* This research was supported by the United States Atomic Energy Commission and by the Council on Research and Creative Work of the University of Colorado.

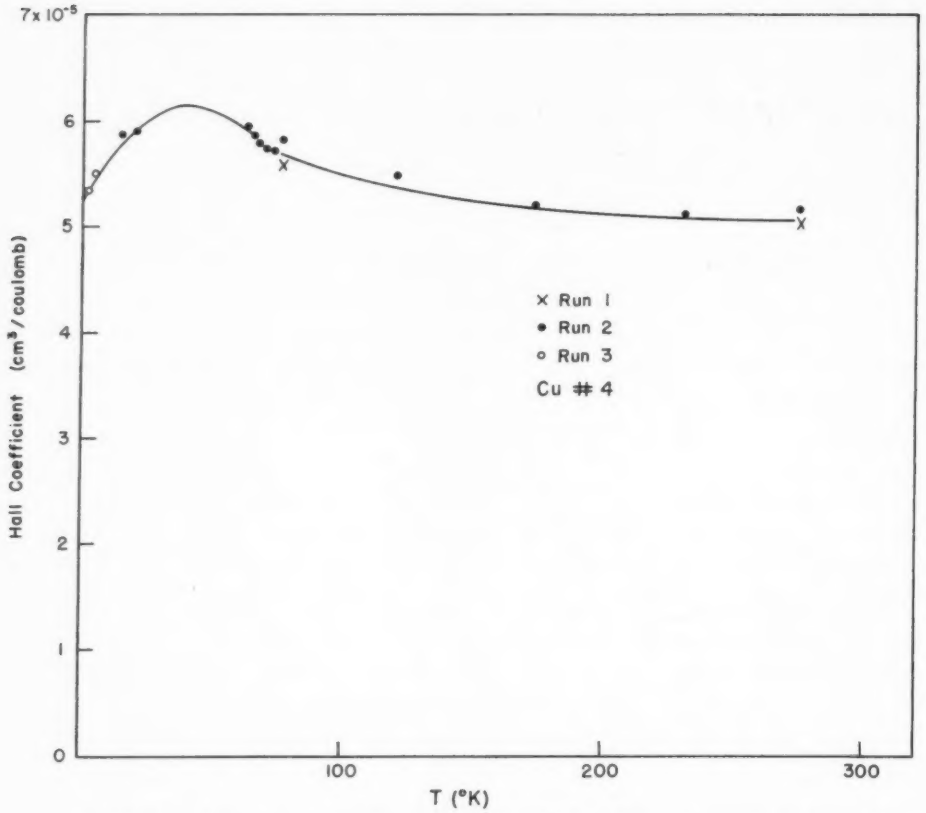

FIG. 1. Plot of the temperature-dependence of the Hall coefficient in a pure single crystal of copper.

remelted in a vacuum single-crystal furnace and grown as a single crystal by the Bridgman technique. No attempt was made at orienting the crystal, since no anisotropy was expected in the Hall coefficient. Two specimens were cut from this single crystal and machined to uniform thickness by the technique mentioned above. One specimen was ordered by a heat treatment extending over a 15-day period. The other specimen was annealed at 550°C for 2 hr in a vacuum and quenched in water. The resistivities in Ω-cm $\times 10^{-6}$ of the annealed and quenched specimens were 5·14 and 12·7, respectively, as compared to the values 4·69 and 11·3 reported by SYKES and JONES.[3]

3. RESULTS

Fig. 1 shows a plot of the temperature-dependence of the Hall coefficient in a single crystal of copper, Cu 4. The orientation of this crystal is given in Table 1. Similar results have been reported by other workers.[4–7] The maximum shown has been reported previously by ALTERTHUM.[4] This maximum can only be inferred from the slopes in the liquid-hydrogen and liquid-nitrogen regions, since not even reasonably accurate measurements with the present apparatus are possible in the intermediate region. It has been observed also in a sample of commercial copper. The points between the ice point and liquid-nitrogen temperatures were obtained in air as the dewar was slowly cooled down. The accuracy is poorer in this region due to thermal fluctuations. The appreciable temperature-dependence of the Hall coefficient in pure copper suggests that two

types of carriers are present even in pure copper, since a metal with a single-type carrier should have no temperature-dependence. The presence of both electrons and holes in copper would require considerable deviations of the Fermi surface from spherical symmetry. For this reason, it was decided to measure the Hall coefficient in oriented single crystals to see if there were any anisotropy.

Four different crystals of copper were studied, and the results are shown in Table 1. The directions of the measuring current and magnetic field with respect to the crystalline axes are given by the angles θ and ϕ shown in the diagram.

The maximum variation of the Hall coefficient in these different crystals is 6 per cent. Variations of 5 per cent have been observed in measurements on the same sample for separate runs, possibly due to the influence of re-soldering the Hall contacts. Consequently, one can only conclude that no anisotropy greater than 6 per cent exists in the Hall coefficient. However, PIPPARD[8] has shown recently that the Fermi surface overlaps the Brillouin-zone boundary in the (111) direction, which would account for the presence of holes in copper. The magnetoresistance experiments of OLSON and RODRIGUEZ[9] confirm this result.

Table 1. *Compilation of Hall-coefficient data on oriented single crystals of pure copper*

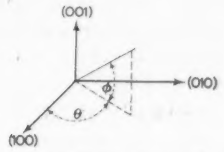

Specimen	Crystal orientation θ	ϕ	Hall coefficient ($cm^3/C \times 10^{-5}$)	Temperature (°K)
Cu 1	I: 0°	2°	5·07	273
	H: 90°	− 2°	5·51	76
Cu 2	I: 0°	2°	5·23	273
	H: 90°	−48°	5·60	76
Cu 3	I: −38°	20°	4·90	273
	H: 2°	44°	5·43	76
Cu 4	I: 0°	− 3°	5·05	273
	H: 90°	− 2°	5·58	76

There is also the possibility that the scattering

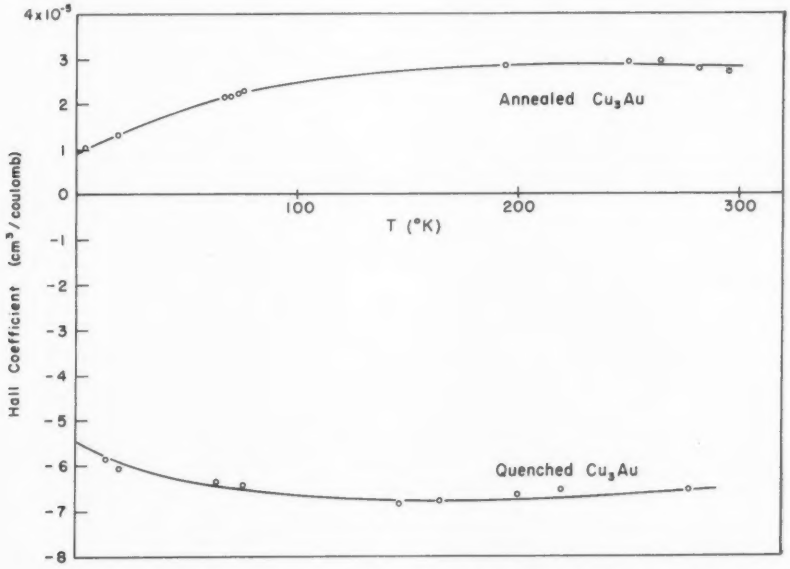

FIG. 2. Plot of the temperature-dependence of the Hall coefficient in ordered and disordered Cu_3Au.

mechanism may produce a temperature-dependent Hall coefficient even for only one type of carrier.

The temperature-dependence of the Hall coefficient in ordered and disordered Cu_3Au is shown in Fig. 2. The change in sign reported by KOMAR and SIDOROV[1] is observed. Their values at room-temperature are $+1{\cdot}72\times10^{-5}$ cm^3/C for the ordered and $-6{\cdot}40\times10^{-5}$ cm^3/C for disordered Cu_3Au. The appreciably greater value which is obtained in these results for the ordered Cu_3Au is possibly due to a somewhat higher degree of order in this specimen.

4. DISCUSSION

The Hall coefficient for a two-band model of a metal containing n_1 electrons and n_2 holes per unit volume is given by:

$$R_H=\frac{1}{ec}\cdot\frac{n_1\mu_1^2-n_2\mu_2^2}{(n_1\mu_1+n_2\mu_2)^2},$$

where μ_1 and μ_2 are the mobilities of electrons and holes respectively. Because of the unknown factors in this equation, it is difficult to reach any conclusions on the effects of ordering on the band structure in Cu_3Au, since ordering will cause significant changes in all the parameters. The change of the Hall coefficient of ordered Cu_3Au on cooling to low temperatures is consistent with the notion that n_1 and n_2 are of the same order of magnitude. Since ordering changes both μ and n, it is difficult to draw any conclusions as to which factor accounts for the change in sign of the Hall coefficient upon ordering. The relatively small changes in the Hall coefficient of disordered Cu_3Au on cooling indicate that any holes present have much smaller concentrations than the electrons.

Acknowledgement—The author is indebted to Mr. E. CRAIG for valuable assistance in the measurements and in the preparation of the single-crystal specimens.

REFERENCES

1. KOMAR A. and SIDOVOV S., *J. Phys. U.S.S.R.* **4,** 552 (1941).
2. TEUTSCH W. B. and LOVE W. F., *Phys. Rev.* **105,** 487 (1955).
3. SYKES C. and JONES F. W., *Proc. Roy. Soc.* **A157,** 213 (1936).
4. ALTERTHUM H., *Ann. Phys., Lzg.* **39,** 933 (1912).
5. ONNES K. and BECKMAN B., *Proc. Roy. Acad. Sci. Amsterdam* **15,** 649 (1912); *Leiden Comm.* 132a (1912).
6. BERLINCOURT T. G., *Bull. Amer. Phys. Soc.* **2,** 136 (1957).
7. CHAMBERS R. G., *Proc. Roy. Soc.* **A238,** 344 (1957).
8. PIPPARD A. B., *Phil. Trans. Roy. Soc.* **A250,** 325 (1957).
9. OLSON R. and RODRIGUEZ S., *Phys. Rev.* **108,** 1212 (1957).

VOL
9
195

J. Phys. Chem. Solids Pergamon Press 1959. Vol. 9. pp. 285–295. Printed in Great Britain.

THE HEAT CAPACITIES OF SEVEN RARE-EARTH ETHYLSULPHATES AT LOW TEMPERATURES

HORST MEYER* and P. L. SMITH†

The Clarendon Laboratory, Oxford University

(*Received* 29 *September* 1958)

VOL. 9 1959

Abstract—Heat-capacity measurements on the ethylsulphates of lanthanum, cerium, praseodymium, neodymium, dysprosium, ytterbium, and yttrium between 1·4 and 20°K are described. In addition, specific-heat results for the cerium salt between 0·6 and 1·2°K are presented. For the salts of lanthanum and yttrium, the specific heat is entirely due to lattice vibrations, while for those of neodymium and ytterbium, there is a small contribution from magnetic interaction, negligible above 2°K.

For the salts of cerium, praseodymium and dysprosium, a Schottky anomaly indicating the presence of excited electronic energy levels was found, and it was possible to determine the position of these levels with accuracy. The maximum of the Schottky anomaly of cerium and praseodymium ethylsulphates was found to be somewhat larger than the one calculated from statistical mechanics, and this specific-heat excess is discussed.

1. INTRODUCTION

THE series of the rare-earth ethylsulphates has been the object of numerous experiments. Cerium ethylsulphate, for example, was one of the first salts to be cooled by adiabatic demagnetization.[1] The magnetic properties of these salts have been extensively investigated by susceptibility measurements and Faraday rotation[2] and by paramagnetic resonance at hydrogen and helium temperatures.[3] ELLIOTT and STEVENS[4] made a thorough theoretical investigation of the magnetic properties and the energy levels of certain salts of this series. Although the specific heat of the paramagnetic spin system of several salts has been measured by the paramagnetic-relaxation method,[5] direct calorimetric measurements have not been published so far. In this paper, we shall give an account of heat-capacity measurements on the ethylsulphates of lanthanum, cerium, praseodymium, neodymium, dysprosium, ytterbium, and yttrium between 1·4 and 20°K.

Heat-capacity measurements on all these salts seemed interesting, since it was possible to investigate systematically an isomorphous series of crystals; in particular for the salts of certain elements such as praseodymium, where the energy levels of the ground state lie very close together, it seemed possible to gain information on the energy and degeneracy of these levels. The advantage of specific-heat measurements at low temperatures is that the contribution of the Schottky anomaly, which accompanies the process of populating higher energy levels, can be of the same order of magnitude as the lattice specific heat. Hence, by estimation of this lattice contribution from neighboring salts such as those of lanthanum, neodymium, or ytterbium, which have no such anomaly, and subtracting it from the total specific heat, the anomalous contribution can be accurately obtained. The position of the energy levels can then be determined by fitting a Schottky function to the results.

It is well known that the Schottky anomaly can be derived from the partition function $Z = \Sigma g(\Delta_i)e^{-\Delta_i/T}$, where $g(\Delta_i)$ is the degeneracy of the energy level having an energy Δ_i (expressed in degrees K).

The specific heat is then obtained from the relation

* Now at the Gordon McKay Laboratory, Harvard University, Cambridge, Mass.

† Now at the National Physical Laboratory, Teddington, England.

$$C_S = RT\frac{\partial^2}{\partial T^2}T \ln Z. \qquad (1)$$

From the value of the experimental specific-heat maximum, one can decide, for example, if one is in the presence of two doublets separated by an energy gap, or a singlet lying above a doublet, since from equation (1) $C_{S_{max}}$ is approximately 0·87 cal/mole-degree in the first case and 0·45 cal/mole-degree in the second one, irrespective of the splitting.

On certain occasions, specific-heat measurements give more direct information about the levels than magnetic measurements. Paramagnetic-resonance experiments, for example, made on the "concentrated" salt are sometimes difficult to interpret because of the broad absorption lines. In the substance "diluted" with an isomorphous diamagnetic salt, where the resonance lines are well defined, the distribution of the levels may have changed[6] because the crystalline electric field is no longer the same.

Specific-heat measurements can be used to confirm the splittings determined from absorption spectra such as those obtained by HELLWEGE and co-workers on rare-earth salts.[7] While the determination of the Schottky anomalies was the main interest in the present work, it was also hoped to gain some information about the variation of the lattice specific heat of this series of salts as one rare-earth ion is replaced by another in the lattice.

2. GENERAL PROPERTIES AND PREPARATION OF THE SALTS

The ethylsulphates form a homologous series of salts with the general formula $M(C_2H_5SO_4)_3{\cdot}9H_2O$ where M is the trivalent rare-earth ion. The crystals grow in hexagonal prisms parallel to the trigonal axis. Their detailed structure has been investigated by KETELAAR[8] and reviewed by ELLIOTT and STEVENS.[4] Yttrium does not belong, strictly speaking, to the rare-earths. Several chemical and physical properties of its salts, however, place it among the rare earths. In fact, the dimensions of the yttrium ion are between those of holmium and dysprosium, and the ethylsulphate of yttrium is isomorphous with those of the rare-earths.

The thermal and magnetic properties of the paramagnetic ions at very low temperatures can often be expressed in terms of a spin Hamiltonian.[9] The total heat capacity of the paramagnetic salts is the sum of the lattice contribution which roughly follows a T^3 law, and the magnetic contributions C_M. To a good approximation:

$$C_M = C_S + C_{\text{h.f.s.}} + C_{\text{dip}} + C_{\text{add.}} \qquad (2)$$

Here $C_{\text{h.f.s.}}$ is the effect of the interaction between the electrons and the nuclear spin of the paramagnetic ion and C_{dip} is due to dipolar interactions between these ions. In addition, there might be a term C_{add} resulting from another type of coupling between the rare-earth ions. At temperatures above 2°K, the three last terms in equation (2) are often small. In several cases, they can be determined by the method of paramagnetic relaxation. $C_{\text{h.f.s.}}$ and C_{dip} can also be calculated from paramagnetic-resonance data.[10,11]

The chemical preparation of these salts was from rare-earth oxides except for cerium, which was obtained as the nitrate. The source of the rare earths and their purity are given in Table 1.

The crystals were grown over a period of several weeks by slow evaporation of a saturated aqueous solution of the ethylsulphate. From a batch of

Table 1. *Source and purity of rare earths*

Element	Provenance	Standard and impurities
La	Johnson, Matthey	0·1 per cent Pr_2O_3, 0·02 per cent Nd_2O_3
Ce	British Drug House	< 0·1 per cent other rare earths
Pr	Dr. J. Marsh	0·1 per cent Nd_2O_3
Nd	Johnson, Matthey	"Specpure"
Dy	Dr. J. Marsh	< 0·5 per cent other rare earths
Yb	Dr. J. Marsh	< 0·5 per cent other rare earths
Y	Johnson, Matthey	"Specpure"

VOL. 9 1959

crystals only the most perfect and transparent ones having an average weight of about 0·5 g, were selected for the measurements. For each salt, the density ρ of several crystals was measured by the elementary gravitation method and found to be the same within $\frac{1}{2}$ per cent. The results are compared to those from X-ray data of KETELAAR[8] in Table 2. It will be seen that the density from our measurements is consistently lower by about 1–2 per cent in comparison to the X-ray data, possibly because of the presence of some water inclusions in spite of the slow rate of crystallization.

Table 2. Densities of rare-earth ethylsulphates

Element	Molecular	ρ (g/cc)	$\rho_{\text{X-ray}}$ (g/cc)
La	676·4	1·81	1·823
Ce	677·6	1·82	1·839
Pr	678·4	1·81	1·857
Nd	681·8	1·84	1·872
Dy	700·0	1·93	1·958
Yb	710·5	1·98	—
Y	626·4	1·73	1·753

3. EXPERIMENTAL

The heat-capacity measurements were made in a low-temperature cryostat described by SMITH and WOLCOTT.[12] About 30 g of crystals were put in the small thin-walled copper calorimeter, and special care was taken to prevent the crystals from losing their water of crystallization during the operation of sealing-off the calorimeter. The mass of the sample was checked after the experiment and no change of mass could be detected. The thermal contact between the crystals was made by helium exchange gas at a pressure of about 0·2 mm Hg at helium temperatures, which was introduced into the calorimeter through a thin German-silver tube. The specific heat of the crystals was obtained by subtracting that of the empty calorimeter from the total. The temperature was measured with a carbon thermometer between 1·3 and 4°K and with a constantan thermometer above these temperatures. No difficulties were experienced from temperature inhomogeneities in the calorimeter; the temperature drifts, about 1 min after the heating, were very small and linear with time. For some of the specimens, several series of measurements were carried out, which were reproducible within the limits of experimental scatter—about 1 per cent.

No account was taken in the final results of the somewhat low density of the crystals. The error introduced by the presence of other rare-earth impurities in a certain sample was found to be smaller than 2 per cent, the experimental error in the measurements.

To analyse the data into contributions from lattice and spins, it was necessary to assume that the lattice specific heats of the salts varied only a little from one rare-earth ion to the next. At temperatures where the Schottky anomaly is large compared to the lattice heat capacity, any error from this assumption is relatively small. On the other hand, at temperatures above the Schottky maximum, the error may be quite important.

Consequently, the energy splittings were

Table 3. Specific heats of the ethylsulphates of lanthanum, neodymium, ytterbium, and yttrium (in cal/mole-degree)

T(°K)	La^{3+}	Nd^{3+}	Yb^{3+}	Y^{3+}
1·5	0·0118	0·0063	0·00550	0·00490
2·0	0·0184	0·0127	0·0117	0·00975
2·5	0·0295	0·0233	0·0202	0·0173
3·0	0·0479	0·0391	0·0334	0·0289
3·5	0·0750	0·0631	0·0561	0·0480
4·0	0·110	0·0980	0·0905	0·0765
4·5	0·173	0·150	0·1480	0·128
5·0	0·253	0·218	0·216	0·195
5·5	0·371	0·312	0·305	0·281
6·0	0·518	0·435	0·431	0·381
6·5	0·685	0·570	0·580	0·505
7·0	0·875	0·735	0·735	0·650
8·0	1·340	1·175	1·175	1·035
9·0	1·91	1·705	1·705	1·53
10·0	2·53	2·330	2·32	2·05
11·0	3·30	3·02	2·99	2·68
12·0	4·10	3·78	3·72	3·29
13·0	4·94	4·55	4·50	3·95
14·0	5·85	5·42	5·35	4·70
15·0	6·80	6·33	6·20	5·50
16·0	7·90	7·35	7·10	6·34
17·0	9·05	8·42	8·10	7·22
18·0	10·20	9·52	9·12	8·20
19·0	11·45	10·68	10·25	9·20
20·0	12·65	11·78	11·30	10·29

determined from the low-temperature "tail" of the anomaly by comparing the experimental Schottky anomaly with equation (1). For $T/\Delta < 0{\cdot}25$, the specific heat is very dependent on the value of Δ, and therefore Δ can be determined with accuracy. If we consider, for example, a system of two doublets separated by a splitting Δ, then, for an error of 6 per cent in the Schottky specific heat, Δ will be known to better than 3 per cent.

In a system of three doublets, the determination of the splittings will be unambiguous too, provided that the two excited doublets do not lie too close together. At the lowest temperatures the specific heat will then be due to the process of populating only the doublet with the smaller energy, Δ_1. One first obtains this splitting from data at the lowest temperatures and later the larger energy, Δ_2, by fitting the theoretical curve to the experimental one at higher temperatures.

Table 4. *Specific heat and entropy of cerium ethylsulphate* (*in cal/mole-degree*)

T(°K)	C_{total}	C_{Schottky}	S'_{Schottky}
0·70	0·0190	0·0132	0·00130
0·80	0·0376	0·0323	0·00376
0·90	0·067	0·0638	0·00858
1·00	0·113	0·108	0·0235
1·25	0·262	0·257	0·0600
1·50	0·425	0·419	0·1205
1·75	0·585	0·575	0·1925
2·00	0·765	0·752	0·282
2·50	1·045	1·021	0·480
3·00	1·092	1·053	0·673
3·50	1·038	0·975	0·833
4·0	0·957	0·859	0·957
4·5	0·887	0·737	1·057
5·0	0·850	0·632	1·118
5·5	0·850	0·538	1·176
6·0	0·900	0·475	1·214
7·0	1·100	0·370	1·280
8·0	1·46	0·290	1·327
9·0	1·97	0·25	1·363
10·0	2·55	0·22	1·385
11·0	3·20	0·18	1·403
12·0	3·97	0·25	1·418
13·0	4·825	—	—
14·0	5·70	—	—
15·0	6·62	—	—
16·0	7·63	—	—
17·0	8·66	—	—
18·0	9·75	—	—

4. RESULTS

The experimental points of some of the measurements are presented in Figs. 2–5. In each figure, the heat capacity of a salt with a Schottky anomaly is compared with that of a salt having none. Smoothed values of molar heat capacities and Schottky entropies $S' = S - R \ln 2$ are given in Tables 3–6.

Table 5. *Thermal properties of praseodymium ethylsulphate* (*in cal/mole-degree*)

T(°K)	C_{total}	C_{Schottky}	S'_{Schottky}
1·5	0·0810	0·0037	—
2·0	0·0750	0·0220	0·0038
2·5	0·1020	0·0531	0·0118
3·0	0·1702	0·113	0·0260
3·5	0·254	0·178	0·0484
4·0	0·369	0·261	0·0774
4·5	0·490	0·333	0·110
5·0	0·605	0·382	0·144
5·5	0·730	0·419	0·185
6·0	0·880	0·440	0·225
6·5	1·035	0·465	0·261
7·0	1·220	0·478	0·290
7·5	1·410	0·480	0·331
8·0	1·670	0·50	0·357
9·0	2·23	0·53	0·415
10·0	2·86	0·53	0·470
11·0	3·54	0·52	0·520
12·0	4·27	0·49	0·560
13·0	5·05	0·47	0·598
14·0	5·87	0·45	0·629
15·0	6·70	0·37	0·660
16·0	7·68	0·33	0·679
17·0	8·70	0·28	0·700
18·0	9·72	0·20	0·718
19·0	10·84	0·16	0·733
20·0	11·98	0·12	0·740

The splittings of the energy levels were determined from measurements at a temperature below 2·5°K for cerium ethysulphate and below 7°K for the praseodymium and dysprosium salts.

La^{3+}, Nd^{3+}, Yb^{3+}, *and* Y^{3+}

Since the salts of lanthanum and yttrium are diamagnetic, their total heat capacity is due to lattice vibrations. Nd^{3+} and Yb^{3+} have only one magnetic doublet populated at low temperatures.[4,13] Their lattice specific heats were obtained by subtracting the magnetic specific heats,

Table 6. Specific heat and entropy of dysprosium ethylsulphate (in cal/mol-degree)

T(°K)	C_{tota}	$C_{Schottky}$	$S'_{Schottky}$
1·5	0·0165	—	—
2·0	0·0215	0·0034	0·0004
2·5	0·0434	0·0190	0·002
3·0	0·1000	0·0630	0·00743
3·5	0·201	0·143	0·0248
4·0	0·352	0·259	0·0513
4·5	0·535	0·387	0·0711
5·0	0·742	0·526	0·1348
5·5	0·991	0·686	0·1918
6·0	1·28	0·850	0·2590
6·5	1·54	0·960	0·3305
7·0	1·81	1·060	0·407
7·5	2·12	1·170	0·483
8·0	2·35	1·25	0·567
9·0	3·05	1·35	0·714
10·0	3·69	1·38	0·859
11·0	4·32	1·33	0·989
12·0	5·03	1·31	1·093
13·0	5·72	1·26	1·200
14·0	6·50	1·15	1·284
15·0	7·22	1·07	1·360
16·0	8·08	0·98	1·420
17·0	8·95	0·85	1·474
18·0	9·90	0·78	1·531
19·0	10·90	0·65	1·560
20·0	12·0	0·56	—

respectively $CT^2/R = 1{\cdot}13\times10^{-3}$[14] and $CT^2/R = 4{\cdot}40\times10^{-4}$[13] from the total. No Schottky anomaly was detected for these two salts, showing that the next excited level lies at least about 60°K above the ground doublet (see Section 5).

The lattice specific heat of the four salts can best be presented by a plot of C_{latt}/T^3 as a function of T (Fig. 1), since the order of magnitude of this ratio does not change at low temperatures. It will be seen that there is a systematic decrease of C_{latt} with increasing molecular weight from La^{3+} to Yb^{3+} and that the temperature variation of C_{latt} is very similar for these salts. Yttrium ethylsulphate, however, which has the smallest mass per mole has the smallest specific heat.

Ce^{3+}

The ground state of the cerium ion is $^2F_{5/2}$ and it is split by the crystalline field of the lattice into three Kramers doublets. At low temperatures, only the two lowest doublets, characterized to a first approximation by the quantum number $J_z = \pm 5/2$ and $J_z = \pm 1/2$, are populated.[4] Measurements of the magnetic susceptibility, paramagnetic resonance, and magnetic specific heat[15] showed that in the concentrated salt the doublet $J_z = \pm 5/2$ lies lowest, separated from $J_z = \pm 1/2$ by an energy

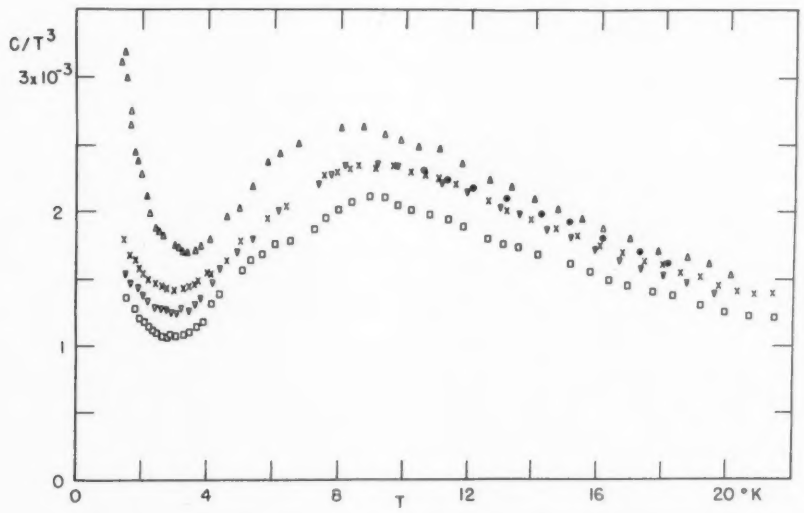

FIG. 1. Lattice specific heat of several rare-earth ethylsulphates, plotted as C/T^3, in cal/mole-degree.[4] △ La^{3+}; ● Ce^{3+}; × Nd^{3+}; ▽ Yb^{3+}; □ Y^{3+}.

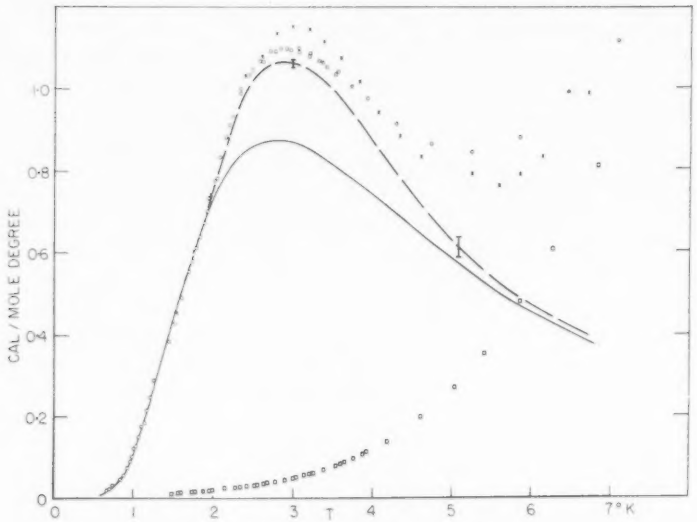

FIG. 2. Specific heat of cerium ethylsulphate and lanthanum ethylsulphate: × Ce^{3+} as measured by SMITH: ○ Ce^{3+} present work. The drawn curve is the Schottky anomaly calculated for a splitting of 6·7°K. The dashed curve is the experimental Schottky anomaly obtained by subtracting the lattice contribution of Nd^{3+} from the total specific heat. □ = La^{3+}.

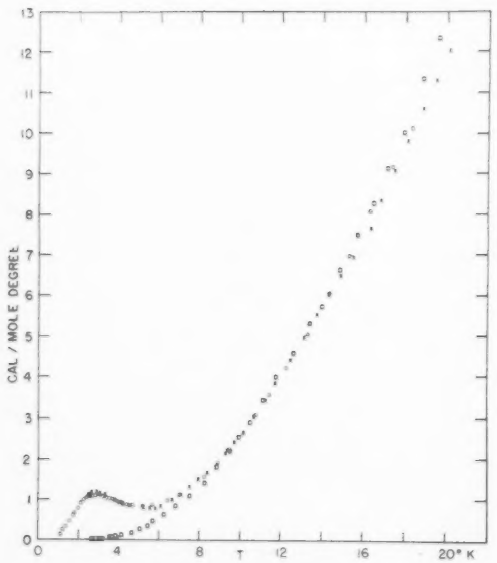

FIG. 3. Specific heat of cerium ethylsulphate and lanthanum ethylsulphate: × Ce^{3+} as measured by SMITH: ○ Ce^{3+} present work; □ La^{3+}.

$\Delta = 6{\cdot}6°K$. The calorimetric measurements are presented in Figs. 2 and 3, together with earlier unpublished measurements by SMITH on a less carefully prepared sample. They show the expected maximum of the heat capacity near 3°K and are compared to the Schottky anomaly calculated for a splitting of 6·7°K, which gives the best fit at low temperatures. Below about 2·5°K the lattice contribution is almost negligible in comparison to C_s. In order to cover completely the low-temperature tail of the Schottky anomaly, the measurements were extended down to about 0·6°K. Two single crystals of cerium ethylsulphate were suspended on cotton threads in a special cryostat, cooled by adiabatic demagnetization below 1°K, and heated up by a small constantan heater as described elsewhere.[16] The temperature was measured from the magnetic susceptibility, which obeys Curie's law down to about 0·5°K.[17] The results from these measurements are presented in Fig. 4 and agree with the splitting of $(6{\cdot}7 \pm 0{\cdot}1)°K$.

The departure at temperatures below 0·8°K from the calculated curve is due to the contributions

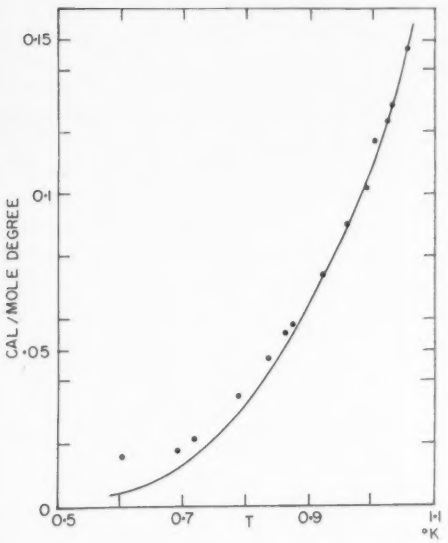

FIG. 4. Specific heat of cerium ethylsulphate below 1°K. The drawn curve is the Schottky anomaly calculated for a splitting of 6·7°K.

of dipole–dipole interaction and of the electric quadrupole–quadrupole coupling between the cerium ions, C_{qq}.[18] While C_{dip} was calculated to be $1{\cdot}93\times10^{-4}R/T^2$,[18] C_{qq} was experimentally found to be $(1{\cdot}2\pm0{\cdot}1)\times10^{-3}R/T^2$, in agreement with the data of COOKE *et al.*[15] Here $C_{\mathrm{h.f.s.}}=0$, since the stable cerium ions present in the salt have no nuclear spin.

The experimental Schottky anomaly, obtained by subtracting C_{latt} of the neodymium salt from the total specific heat, is appreciably larger at the maximum than the one calculated from statistical mechanics (Fig. 2). This excess specific heat, which was also observed for the salt of praseodymium, will be discussed in Section 5. At temperatures above 9°K, the Schottky specific heat is expected to be very small compared to the lattice contribution. After subtracting the "high-temperature tail" of the Schottky anomaly which is given by $C_s=R\Delta^2/4T^2$ cal/mole-degree, the lattice specific heat was plotted in Fig. 1 as C/T^3, and was found to agree very closely with that of the neodymium and ytterbium salts.

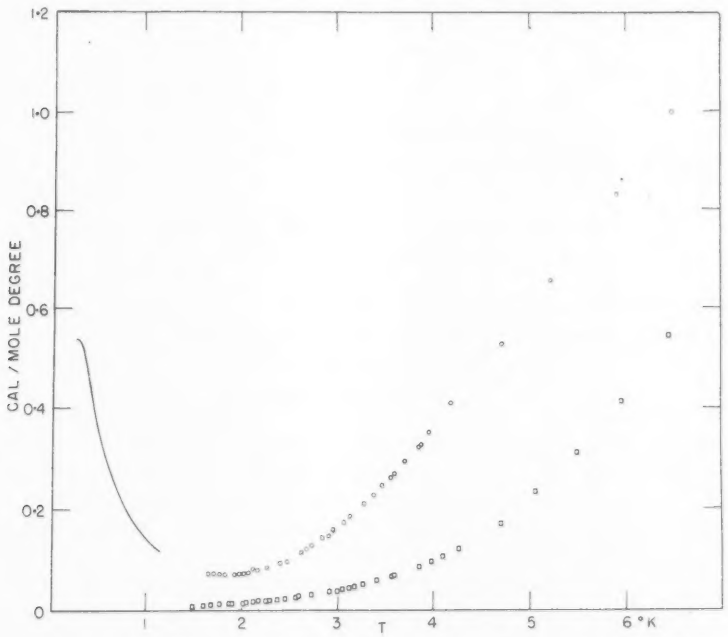

FIG. 5. Specific heat of praseodymium and neodymium ethylsulphates: ○ Pr^{3+} present work. Drawn curve: measurements below 1°K. □ Neodymium ethylsulphate.

Pr^{3+}

The praseodymium ion Pr^{3+} has an even number of electrons and so does not show a Kramers degeneracy. The ground state, $^3H_4$, is split by the crystalline field into three doublets and three singlets.[19] The nuclear spin of the only isotope present, ^{141}Pr, also gives an h.f.s. splitting. BAKER and BLEANEY[20] observed paramagnetic resonance of the lowest doublet of Pr^{3+} in the salt diluted with yttrium ethylsulphate. Because of the distortion of the crystalline lattice, this lowest doublet is resolved into two singlets separated by an average splitting Δ_0. The heat capacity due to this splitting and to the nuclear h.f.s. was found to be $0{\cdot}16/T^2$ cal/mole-degree above $1{\cdot}5$°K, giving a splitting of $\Delta_0 = 0{\cdot}53$°K, in reasonable agreement with measurements below 1°K.[16]

The present calorimetric measurements (Fig. 6) showed also that a singlet becomes populated at temperatures above 2°K. The Schottky anomaly was again obtained by subtracting the lattice specific heat of the neodymium salt and $0{\cdot}16/T^2$ cal/mole-degree from the total specific heat. The splitting between the singlet and the lowest doublet was found to be $(16{\cdot}7 \pm 0{\cdot}3)$°K, in excellent agreement with the value $\Delta = 17{\cdot}0$°K obtained from the absorption spectrum of this salt by HELLWEGE *et al.*[21] It is also in qualitative agreement with the value $\Delta = 23$°K calculated by BAKER and BLEANEY[20] from susceptibility and paramagnetic-resonance data.

It would have been gratifying if our measurements below 4°K could have been confirmed by the paramagnetic-relaxation method, and such an experiment was attempted by us. It is unfortunate that for practical reasons this method was not suitable for such a large specific heat, but it gave an order of magnitude for the heat capacity which agreed with the value obtained calorimetrically.

Dy^{3+}

The ground state $^6H_{15/2}$ of the dysprosium ion is split into five Kramers doublets by the crystalline field. The presence of the ions $^{161}Dy^{3+}$ and $^{163}Dy^{3+}$ which possess a nuclear spin $I = 5/2$ causes, in addition, hyperfine structure splittings. From susceptibility and paramagnetic-relaxation specific-heat measurements below 3°K,[22] it was found that only one doublet, characterized by approximately $J_z = \pm 9/2$,[4] was populated at the lowest temperatures. The experiments of COOKE *et al.*[22] gave $C_{\text{dip}} + C_{\text{h.f.s.}} = 0{\cdot}0150R/T^2$, while our present measurements gave $0{\cdot}013_4 R/T^2$. The theory of ELLIOTT and STEVENS[4] predicts an excited doublet $J_z = 0{\cdot}84|\pm 7/2\rangle + 0{\cdot}54|\mp 5/2\rangle$ lying close above the lowest one, and recent preliminary measurements of the absorption spectrum of this salt by GRAMBERG and KAHLE[23] even show the presence of two doublets close to the ground state, the splittings being respectively $\Delta_1 = 20{\cdot}0$°K and $\Delta_2 = 30{\cdot}0$°K.* Our experiments confirmed the presence of these two doublets, and the calculated

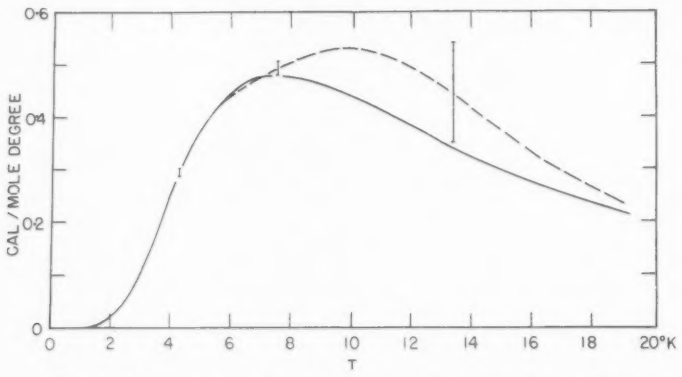

FIG. 6. Schottky anomaly of praseodymium ethylsulphate. Dashed curve: observed. Full curve: calculated for a splitting of 16·7°K.

Note added in proof: More recent data of the absorptionspectrum[23] give $\Delta_1 = 23{\cdot}0$ °K and $\Delta_2 = 29{\cdot}1$ °K.

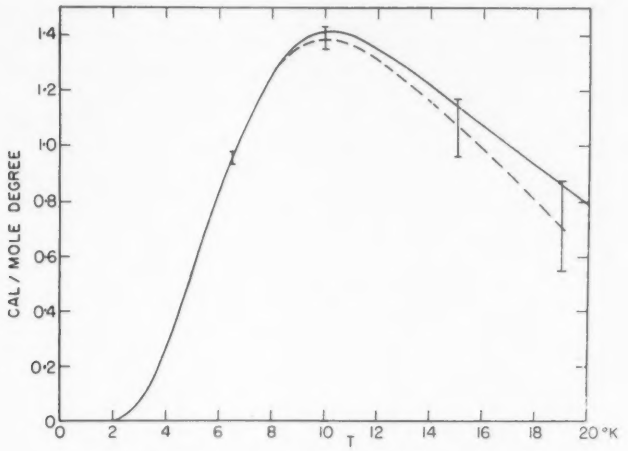

FIG. 7. Schottky anomaly of dysprosium ethylsulphate. Dashed curve: observed. Full curve: calculated for splittings $\Delta_1 = 22{\cdot}5°K$ and $\Delta_2 = 33{\cdot}7°K$.

Schottky anomaly could be fitted within experimental error to the calorimetric data by taking the value $\Delta_1 = (22{\cdot}5 \pm 0{\cdot}5)°K$ and $\Delta_2 = (33{\cdot}7° \pm \pm 1{\cdot}0)°K$ (Fig. 7), which agrees satisfactorily with the optical data. C_M was obtained here by subtracting C_{latt} of ytterbium ethylsulphate from the total.

5. DISCUSSION

The lattice specific heats of many hydrated salts as described in recent papers[24] show departures from a T^3 law at temperatures below 20°K. In particular there is a maximum of the ratio C/T^3 around 10–15°K. The same behaviour is observed with the series of the ethylsulphates. Here, in addition, there is a minimum at about 2°K. It is interesting to note that even near 1°K, the true Debye T^3 region has not been reached.

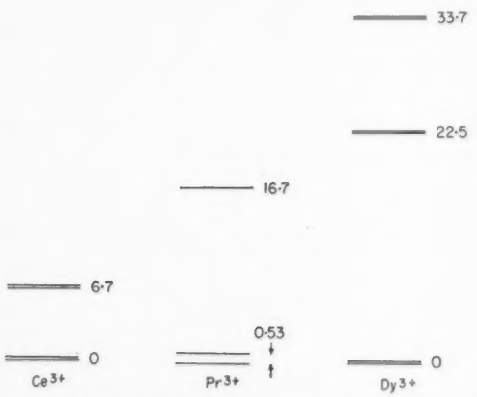

FIG. 8. Energy levels of cerium, praseodymium, and dysprosium ethylsulphates, expressed in °K.

The energy levels determined from the Schottky anomaly are summarized in Fig. 8. There is evidently an upper limit in the size of the splitting which can be determined from heat-capacity measurements because the Schottky anomaly, which is only of the order of 1 cal/mole-degree, shifts with larger splittings to higher temperatures where the lattice specific heat is of the order of 10 cal/mole-degree. The Schottky anomaly is then only a comparatively small effect, as opposed to λ-type anomalies which are easily detectable at high temperatures.[25] The upper limit of a measurable splitting should be therefore about 70°K.

The most unexpected result in this series of measurements is the excess specific heat in the Schottky anomaly of the cerium and praseodymium salts which occurs near the maximum of the anomaly. As a result, the entropy increase S' due to the population of the excited levels may become larger than the theoretical values $R \ln 2$, respectively $R \ln 3/2$ (Fig. 9). These results are difficult to explain. Assuming for example, that an interaction between the lattice waves and the paramagnetic electrons broadens the energy levels, one would indeed obtain another specific-heat distribution as a function of T, but with a maximum

smaller than for the ordinary Schottky anomaly. At high temperatures, S' would again tend to $R \ln 2$ and $R \ln 3/2$, since N new doublets or singlets are fully populated. There is the possibility of a new degree of freedom in the lattice created at the temperature of the Schottky maximum, but it salts showing a Schottky specific-heat maximum between 2 and 10°K. In particular, holmium ethylsulphate might be suitable, since from paramagnetic-resonance data,[20] a splitting of about 8°K is to be expected between the two lowest levels.

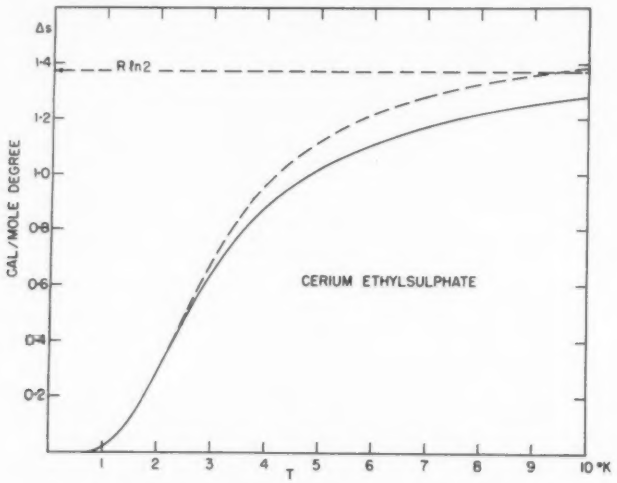

FIG. 9. Schottky entropy $S' = S - R \ln 2$ of cerium ethylsulphate. Dashed curve: experimental. Full curve: calculated for a splitting $\Delta = 6{\cdot}7$°K.

is hard to explain the connection between this effect and the population of excited electronic levels. This excess in entropy and specific heat cannot be attributed to the population of even higher levels, since one would in this case expect a different temperature variation of C_S and S'.

The discrepancy above $T/\Delta = 0{\cdot}3$ between the theoretical and experimental specific heat may throw doubt on the value of the splittings, particularly in the case of praseodymium ethylsulphate, where the maximum of C_S is shifted to higher temperatures. All that can be said here, however, is that the splittings were determined from measurements below about 7°K with an accuracy of about 3 per cent. For praseodymium ethylsulphate, it is difficult to explain the discrepancy between the splitting obtained from calorimetric data and that from the calculations of BAKER and BLEANEY.[20]

As both authors have now left the Clarendon Laboratory, further calorimetric measurements on the ethylsulphates have to be postponed, but clearly it would be interesting to investigate more

Acknowledgements—The authors are indebted to Professor B. BLEANEY, Dr. A. H. COOKE, and Dr. R. W. HILL for several discussions on these experiments, and to Dr. J. MARSH of the Dyson-Perrin Laboratory in Oxford for lending several rare-earth oxides. They also thank Dr. H. G. KAHLE for communicating the data on the optical absorption prior to their publication.

The low-temperature specific-heat measurements described in this report were carried out at the Clarendon Laboratory, Oxford in 1957. The results were then evaluated partly at Harvard, where this project was supported by Contract No. Nonr–1866(33) and AF 19(604)–1084.

REFERENCES

1. DE HAAS W. J. and WIERSMA E. C., *Physica* **2,** 335 (1935).
2. VAN DEN HANDEL J., *Encyclopedia of Physics. Low Temperatures* II. Springer Verlag, Berlin (1956).
3. For a review, see BOWERS K. D. and OWEN J., *Rep. Progr. Phys.* **18,** 304 (1955).
4. ELLIOTT R. J. and STEVENS K. W. H., *Proc. Roy. Soc.* A**215,** 437 (1952); **219,** 387 (1953).
5. DE HAAS W. J. and DU PRÉ F. K., *Physica* **6,** 705 (1939).
6. BOGLE G. S., COOKE A. H., and WHITLEY S., *Proc. Phys. Soc.* A**64,** 931 (1951).

7. HELLWEGE A. M. and HELLWEGE K. H., *Z. Phys.* **130,** 549 (1951).
8. KETELAAR J. A. A., *Physica* **4,** 619 (1937).
9. See, for example, BLEANEY B. and STEVENS K. W. H., *Rep. Progr. Phys.* **16,** 108 (1953).
10. BLEANEY B., *Phys. Rev.*, **78,** 214 (1950).
11. DANIELS J. M., *Proc. Phys. Soc.* A**66,** 673 (1953).
12. SMITH P. L. and WOLCOTT N., *Phil. Mag.* **1,** 854 (1956).
13. COOKE A. H., MCKIM F. M., MEYER H., and WOLF W. P., *Phil. Mag.* **2,** 928 (1957).
14. MEYER H., *Phil. Mag.* **2,** 521 (1957).
15. COOKE A. H., WHITLEY S., and WOLF W. P., *Proc. Phys. Soc.* B**68,** 415 (1955).
16. MEYER H., *J. Phys. Chem. Solids* **9,** 296 (1959).
17. JOHNSON C. E. and MEYER H. To be published.
18. FINKELSTEIN R. and MENCHER A., *J. Chem. Phys.* **21,** 472 (1953).
19. JUDD B. R., *Proc. Roy. Soc.* A**232,** 458 (1955).
20. BAKER J. M. and BLEANEY B., *Proc. Roy. Soc.* In the press.
21. Private communication.
22. COOKE A. H., MCKIM F. M., and WOLF W. P. To be published.
23. Private communication.
24. KAPADNIS D. G. and HARTMANS P., *Physica* **22,** 173 (1956).
25. SIMON F. E., *Ann. Phys., Lzg.* **68,** 264 (1922).

VOL.
9
1959

J. Phys. Chem. Solids Pergamon Press 1959. Vol. 9. pp. 296–301. Printed in Great Britain.

THERMAL AND MAGNETIC PROPERTIES OF PRASEODYMIUM ETHYLSULPHATE BELOW 1°K

HORST MEYER

The Clarendon Laboratory, Oxford University and Gordon McKay Laboratory, Harvard University, Cambridge, Mass.

(*Received* 29 *September* 1958)

Abstract—Single crystals of praseodymium ethylsulphate have been cooled below 1°K by adiabatic demagnetization and the susceptibility, expressed in terms of the magnetic temperature T^*, was measured as a function of T, using cerium magnesium nitrate as a thermometer. The specific heat was measured by electrically heating the sample. A systematic departure of the susceptibility from Curie's law and an anomaly in the specific heat were found. The results were interpreted and confirmed the existence of a variable splitting of the ground doublet, as predicted from paramagnetic-resonance experiments, with a root-mean-square value of $\Delta_0 = (0{\cdot}53 \pm 0{\cdot}04)$°K, which is much larger than the one in the diluted salt.

1. INTRODUCTION

PRASEODYMIUM ethylsulphate (abbreviated to PES) is a member of the isomorphous and paramagnetic series of the rare-earth ethylsulphates. Most of these salts are magnetically anisotropic, and their magnetic properties can be expressed in terms of a tensor with its principal directions parallel and perpendicular to the trigonal crystalline axis. In PES, the $^3H_4$ ground state of the free praseodymium ion is split by the crystalline field into three doublets and three singlets.[1] At temperatures below about 3°K only one doublet, characterized by $\cos\theta|J_z = \pm 2\rangle - \sin\theta|J_z = \mp 4\rangle$,[2,3] is populated. This is not a Kramers doublet, since Pr^{3+} has an even number of electrons, but it is actually split into two singlets separated by a small energy Δ. Probably because of the random fluctuations in the crystalline field, this splitting is not sharply defined, but obeys a certain distribution as described below.

BAKER and BLEANEY[4] observed paramagnetic resonance of these two lowest levels in the salt diluted with yttrium ethylsulphate and, in addition, the nuclear hyperfine structure absorption lines of ^{141}Pr, the only isotope present. They were able to represent their results by the spin Hamiltonian:

$$\mathscr{H} = g_{\parallel}\beta H_z S_z + A S_z I_z + \Delta_x S_x + \Delta_y S_y \qquad (1)$$

with $S = 1/2$, $I = 5/2$, $g_{\parallel} = 1{\cdot}52_5$, $A = 0{\cdot}107$°K. β is the Bohr magneton, $g_{\parallel}$ is the splitting factor parallel to the crystalline axis z and H_z is the magnetic field applied parallel to this axis. $g_{\perp}$, the splitting factor perpendicular to the axis, is zero and therefore the susceptibility varies with the temperature only along the direction of the crystalline axis. Δ_x and Δ_y are parameters to account for the small splitting Δ, and one has the relation: $\Delta^2 = \Delta_x{}^2 + \Delta_y{}^2$.

The energy levels of Pr^{3+} in a magnetic field $H = H_z$ are then:

$$W_m = \pm\tfrac{1}{2}[\Delta^2 + (g_{\parallel}\beta H + Am)^2]^{\frac{1}{2}}, \qquad (2)$$

where m is the nuclear magnetic quantum number and $-I \leqslant m \leqslant I$.

BAKER and BLEANEY[4] interpreted the asymmetrical line shape in their experiments by assuming a Gaussian distribution P of Δ_x and Δ_y

$$P(\Delta_x) = \frac{1}{\Delta_0 \pi^{\frac{1}{2}}} \exp(-\Delta_x{}^2/\Delta_0{}^2);$$

$$P(\Delta_y) = \frac{1}{\Delta_0 \pi^{\frac{1}{2}}} \exp(-\Delta_y{}^2/\Delta_0{}^2) \qquad (3)$$

and found for their sample the root-mean-square splitting $\Delta_0 = 0{\cdot}16$°K. From specific-heat measurements on the concentrated salt above 1°K,[5] a

much larger splitting, $\Delta_0 = 0{\cdot}53°K$, was calculated. Recent resonance measurements by BAKER and BLEANEY[3] also gave evidence that Δ_0 was larger in the concentrated salt than in the diluted one. It seemed of interest therefore to measure the thermal and magnetic properties of this substance at very low temperatures, where a large effect from Δ_0 was to be expected. In this report an account is given of the determinations of these properties on single crystals of undiluted PES below 1°K, using the technique of adiabatic demagnetization.

2. EXPERIMENTAL

In most paramagnetic salts investigated below 1°K so far, the absolute temperature scale has been determined from the relation

$$T = \left[C^* \Big/ \left(\frac{\delta S}{\delta T^*} \right) \right]_H = 0$$

where C^* is the magnetic specific heat dQ/dT^*. T^* is the magnetic temperature defined by extrapolation of Curie's law for a spherical sample, and S is the entropy.[6] S is generally calculated as a function of the magnetic field and the temperature, from which the sample is demagnetized,[7] and account is taken of the splittings in the lowest states.[8] Since, for Pr^{3+} in the ethylsulphate, the disposition of the lowest levels was not well known, this method could not be used. Instead, the magnetic temperature T^* was determined directly as a function of the absolute temperature, using as a thermometer cerium magnesium nitrate (CMN) which obeys Curie's law down to about 0·006°K.[9] This double-sample thermometry has been used before on powdered specimens,[10] but since it was essential to make the measurements on single crystals, a somewhat different technique had to be developed.

In our arrangement, PES, in the form of four single crystals shaped to a rough ellipsoid of 4 cm length and 1·5 cm diameter, was thermally connected by thin annealed silver ribbons to two single crystals of CMN (see Fig. 1). Since the PES crystals have $g_\perp = 0$ and the CMN crystals have $g_\parallel \simeq 0$,[11,12] they were suspended with the crystallographic axis respectively parallel and perpendicular to the sample axis, so that their susceptibilities could be measured by two pairs of concentric coils. The bonding substance between the salts and the ribbons was Apiezon Oil J, and ordinary cotton thread was used to press the ribbons against the salts. A small resistance heater was wound on the ribbon. The sample, which formed a quite rigid unit, was suspended on cotton threads inside a long cylindrical holder which was then fixed inside a demagnetization apparatus described earlier.[13] At temperatures between 4·2 and 1·2°K the susceptibilities were measured as a function of temperature (calculated from the vapor pressure of the liquid helium in the cryostat), and a graph of the susceptibility against $1/T$ was plotted to provide a calibration of the magnetic temperature measurements below 1·2°K. The specimen was then magnetized in fields up to 20 kG at 1·2°K, the field being parallel to the crystal axis of PES. After about 10 min, the helium "exchange" gas in the chamber of the cryostat containing the specimen was pumped away and the cryostat temperature lowered to 0·85°K. This "baking-out process"[14] gave a satisfactory thermal insulation, the rate of heating after the demagnetization being of the order of 50–60 ergs/min. While PES cooled only to about 0·25°K, CMN cooled to an appreciably lower temperature because of its small specific heat, but it warmed up very quickly, and thermal equilibrium in the sample was reached within 1 min. The problem of heat transfer in a similar sample at temperatures below 1°K has been experimentally investigated,[15] and it could be shown that for the same heat leak as quoted above, the temperature difference between CMN and PES above 0·2°K was less than 0·002°, which is within the experimental error of the measurement. From these susceptibility measurements, the relation between T and T^* was obtained.

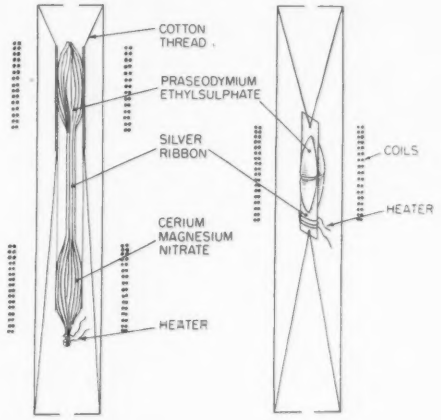

FIG. 1. Sketch of the specimen holder showing the specimen and the coils. The helium cryostat surrounding the holder is not shown. Left side: Arrangement for the determination of the T–T^* relation. Right side: Set up for the specific-heat measurement.

For the specific-heat measurements, the four single crystals, weighing 7·65g, were glued onto a thin silver ribbon 0·1 mm thick, on which a small electrical Constantan heater of 1200 Ω was attached. The heater was

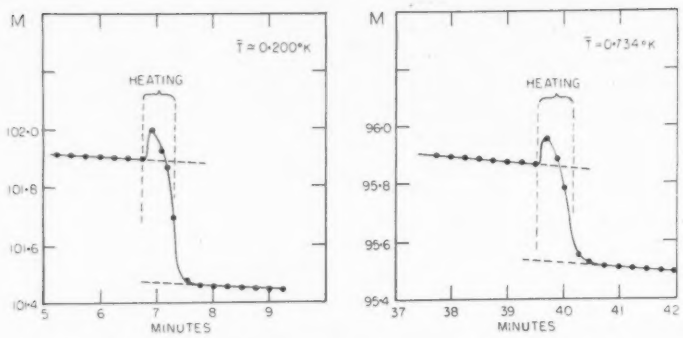

FIG. 2. Warming-up curves during the measurement of the specific heat. The susceptibility $\chi_{\parallel}$, which is a measure of the temperature, is expressed in arbitrary units of the coil mutual inductance M.

connected to the leads outside the cryostat through very thin, tinned Constantan wires which became superconducting at low temperatures and had therefore a nigh thermal and a negligible electrical resistance. The sample was then suspended in the same demagnetization cryostat as described before. After cooling the sample, the temperature was measured again through the parameter T^*. Heat of the order of 2×10^{-5} W was supplied for periods

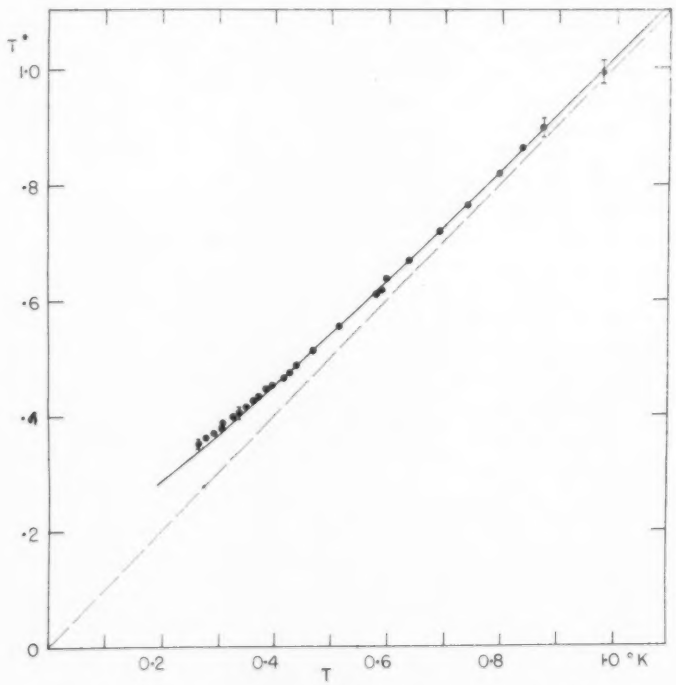

FIG. 3. The relation between T^* and T for praseodymium ethylsulphate. ● Experimental points. The full curve is calculated from equation (8) for a splitting $\Delta = 0{\cdot}55°\text{K}$. The dashed line represents Curie's law.

of about 30 sec by passing current through the Constantan resistance. Immediately after switching on the heat, a particular phenomenon already observed by DUGDALE and MACDONALD[16] was in evidence: the specimen "cooled" down at first and then warmed up. This phenomenon, which occurred near 1°K as well as at about 0·2°K, is shown for two typical heating-up processes in Fig. 2, where, for convenience, the susceptibilities in arbitrary units are plotted rather than the temperatures. No explanation could be given for this mysterious effect. The heat, however, seemed to be quickly distributed inside the sample, since the drift rates 1 min after the heating were small and linear with time.

From these measurements, $C^* = dQ/dT^*$ was obtained, and was then converted into the true specific heat by virtue of the relation $C = C^* \cdot dT^*/dT$. The specific heat of the silver, calculated from the data of CORAK *et al.*,[17] was found to be negligible in comparison with that of the salt.

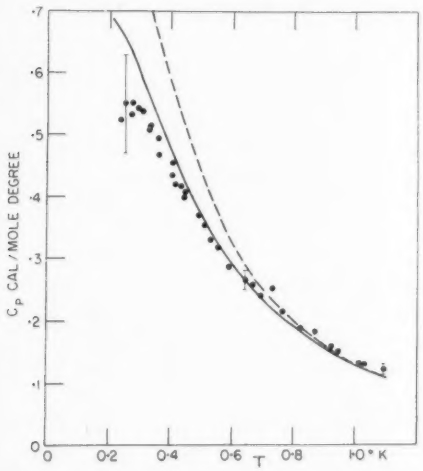

FIG. 4. Specific heat of praseodymium ethylsulphate. ● Experimental points. The full curve is calculated from equation (8) for a splitting $\Delta_0 = 0{\cdot}5$°K. The dashed curve is obtained from equation (6) and $\Delta = 0{\cdot}5$°K, assuming no gaussian distribution.

The most important limitation of the accuracy of our measurements was the small paramagnetic susceptibility of PES, and for practical reasons it was not possible to increase the sensitivity of the measuring coils or the size of the sample. The correlation between T and T^* was determined to about ± 4 per cent at the lowest temperatures, while C^* was found with an error of ± 3 per cent at the lowest temperatures and about 6 per cent at the highest ones. The largest error at low temperatures was introduced when calculating C. This was because the ratio dT^*/dT, obviously less accurately known than the T–T^* relation, drops rather sharply below about 0·5°K. The errors in C are indicated in Fig. 4.

3. RESULTS

Between 4·2 and 1·2°K, the susceptibility was found to obey Curie's law with $g_{\|} = 1{\cdot}55$, in good agreement with BAKER and BLEANEY's results. Between 1·2 and 0·85°K, where CMN was used as a thermometer instead of the vapor pressure of helium in the cryostat, the susceptibility started to deviate slightly from Curie's law. The results below 1°K are given in Table 1, and the experimental points are shown in Figs. 3 and 4. There is a large specific-heat anomaly and also a strong deviation from Curie's law.

Table 1. *The relation between* T^*, T, C^*, *and* C *for praseodymium ethylsulphate* (C *and* C^* *are expressed in cal/mole-degree.* C_{calc} *is obtained from equation* (8), *assuming* $\Delta_0 = 0{\cdot}5$°K)

T	T^*	C^*	C	C_{calc}
—	0·300	1·00	—	—
—	0·320	$0{\cdot}87_5$	—	—
0·250	0·340	$0{\cdot}78_5$	0·54	0·655
0·300	0·375	$0{\cdot}68_5$	0·54	0·600
0·350	0·415	$0{\cdot}59_4$	0·50	0·540
0·400	0·452	$0{\cdot}51_2$	0·45	0·480
0·450	0·498	$0{\cdot}44_5$	0·40	0·415
0·500	0·543	$0{\cdot}39_5$	0·36	0·365
0·550	0·588	$0{\cdot}34_5$	$0{\cdot}32_0$	0·325
0·600	0·635	$0{\cdot}30_9$	$0{\cdot}29_0$	0·385
0·650	0·680	$0{\cdot}27_7$	$0{\cdot}26_0$	0·255
0·700	0·728	$0{\cdot}25_0$	$0{\cdot}23_5$	0·234
0·750	0·776	$0{\cdot}22_8$	$0{\cdot}21_8$	0·210
0·800	0·820	$0{\cdot}20_8$	$0{\cdot}29_5$	0·189
0·900	0·920	$0{\cdot}17_2$	$0{\cdot}16_5$	0·154
1·000	1·018	$0{\cdot}13_0$	$0{\cdot}13_3$	0·126

4. DISCUSSION

The susceptibility and specific heat of PES can be obtained by straightforward derivation from the spin Hamiltonian equation (1)). Let us first calculate these properties for a constant splitting Δ. We will neglect in this treatment the effect of the dipole–dipole interactions,[18] which is expected to be negligible in comparison to the other contributions. By expansion of the energy of the levels (equation 2) in powers of H, one obtains

$$W_m = W_{0,m} + W_{1,m}H + W_{2,m}H^2, \qquad (4)$$

where

$$W_{0,m} = \pm\tfrac{1}{2}[\Delta^2+(Am)^2]^{\frac{1}{2}}$$

$$W_{1,m} = \pm\frac{g_{\parallel}\beta Am}{4W_{0,m}}$$

$$W_{2,m} = \pm\frac{g_{\parallel}{}^2\beta^2}{8W^2{}_{0,m}}\left(1-\frac{A^2m^2}{4W^2{}_{0,m}}\right).$$

The susceptibility $\chi_{\parallel}$ is then obtained from VAN VLECK's well-known formula[19]

$$\chi_{\parallel} = \frac{N\sum_{m=-I}^{m=I}\left[\frac{(W_{1,m})^2}{kT}-2W_{2,m}\right]\exp(-W_{0,m}/kT)}{\sum_{m=-I}^{m=I}\exp(-W_{0,m}/kT)}. \tag{5}$$

At high temperatures, this formula gives Curie's law $Ng_{\parallel}{}^2\beta^2/4kT$, as expected for a doublet with spin $S = 1/2$.

The specific heat is derived from the partition function, Z, and

$$\frac{C}{R} = T\frac{\delta^2}{\delta T^2}T\ln Z \tag{6}$$

where

$$Z = \sum_{m=-I}^{m=I}\exp(-W_{0,m}/kT).$$

Now since there is a Gaussian distribution (equation (3)), the probability of having at the same time Δ_x and Δ_y can be written:

$$P(\Delta)\,d\Delta = \frac{2\Delta}{\Delta_0{}^2}\exp(-\Delta^2/\Delta_0{}^2)\,d\Delta. \tag{7}$$

where

$$\Delta^2 = \Delta_x{}^2+\Delta_y{}^2.$$

The parameter Δ_0 can be interpreted as the root-mean-square value of the splitting. The susceptibility and the specific heat are then finally given by

$$\chi_{\parallel}(\Delta_0, T) = \int_0^{\infty}\chi_{\parallel}(\Delta, T)P(\Delta)\,d\Delta,$$

$$C(\Delta_0, T) = \int_0^{\infty}C(\Delta, T)P(\Delta)\,d\Delta, \tag{8}$$

which can be evaluated graphically. $\chi_{\parallel}$ is relatively little influenced by the Gaussian distribution, and the values given by equation (10) are not very different from those derived from equation (5) with $\Delta = \Delta_0$. On the other hand, the specific heat is markedly changed because the distribution of Δ flattens the maximum of the anomaly (Fig. 5). However, at values of $T \gg \Delta_0$, one has with good accuracy

$$\frac{CT^2}{R} = \frac{\Delta_0{}^2}{4}+\frac{35}{48}A^2,$$

which is the same as if there were only one splitting, Δ_0. It is therefore from specific-heat measurements below about 0·6°K that one can tell whether or not there is really a Gaussian distribution of the splitting.

The calculated $\chi_{\parallel}$ and C values were compared to the experiments for different values of Δ_0, and the parameters $\Delta_0 = 0{\cdot}55$ and $0{\cdot}50$°K, respectively gave the best fit with the two experimental curves. They are in satisfactory agreement, considering that the measurements could not be done more accurately and that systematic errors may have been introduced.

At the low-temperature end, the fit with theory becomes less satisfactory, which suggests that a Gaussian distribution of the splitting may not be the correct one. In the resonance experiments of BAKER and BLEANEY on the concentrated salt, the shape of the line did not agree with that of a Gaussian distribution. Therefore, although such a distribution may be a reasonable approximation in a very diluted salt, the situation may be rather different in a concentrated salt because of the possibility of co-operative effects in the distortions.

5. CONCLUSION

Praseodymium in the ethylsulphate is the first rare-earth ion with an even number of electrons to be cooled below 1°K, and was chosen because its particular energy-level distribution deserved some attention. The average value of $\Delta_0 = (0{\cdot}53\pm 0{\cdot}04)$°K was obtained with an accuracy substantially better than from paramagnetic-resonance experiments. The temperatures that can be reached by demagnetizing from our fairly large magnetic fields are not very low, partly because of the large specific heat. This salt offers a good application of the method of direct temperature measurement

VOL 9 195

using CMN, which works best at temperatures above 0·1°K. It would not be suitable for nuclear-alignment experiments on ^{142}Pr, which has been cooled to much lower temperatures in other substances.[20]

Acknowledgements—The author is indebted to Professor B. BLEANEY, Dr. J. M. BAKER, and Dr. A. H. COOKE for their interest in these experiments, their comments, and their helpful suggestions, and to Mr. J. S. HILL for help in the specific-heat measurement. The experiments were carried out at Oxford University during the tenure of a Nuffield Fellowship, while the evaluation of the results was done mainly at Harvard University, where it was supported by Contract No. Nonr-1866(13) and AF19(604)-1084.

VOL. 9 1959

REFERENCES

1. JUDD B. R., *Proc. Roy. Soc.* A**232,** 458 (1955).
2. ELLIOTT R. J. and STEVENS K. W. H. *Proc. Roy. Soc.* A**219,** 387 (1953).
3. BAKER J. M. and BLEANEY B., *Proc. Roy. Soc.* A**245,** 156 (1958).
4. BAKER J. M. and BLEANEY B., *Proc. Phys. Soc.* A**68,** 936 (1955).
5. MEYER H. and SMITH P. L., *J. Phys. Chem. Solids* **9,** (1959).
6. See, for example, GARRETT C. G. B., *Magnetic Cooling*. Harvard Monographs, Cambridge, Mass. (1954).
7. HULL J. R. and HULL R. A., *J. Chem. Phys.* **9,** 465 (1941).
8. See, for example, DANIELS J. M. and KURTI N., *Proc. Roy. Soc.* A**221,** 243 (1954).
9. DANIELS J. M. and ROBINSON F. N. H., *Phil. Mag.* **44,** 630 (1953).
10. COOKE A. H., MEYER H., and WOLF W. P., *Proc. Roy. Soc.* A**233,** 536 (1956).
11. COOKE A. H., DUFFUS J., and WOLF W. P., *Phil. Mag.* **44,** 623 (1953).
12. WHEATLEY J. C. and ESTLE T. L., *Phys. Rev.* **104,** 264 (1956).
13. MEYER H., *Phil. Mag.* **2,** 521 (1957).
14. COOKE A. H. and HULL R. A., *Proc. Roy. Soc.* A**181,** 83 (1942).
15. To be published.
16. DUGDALE P. and MACDONALD D. C. K., *Canad. J. Phys.* **35,** 271 (1957).
17. CORAK W. S., GARFUNKEL M. P., SATTERTHWAITE C. B., and WEXLER A., *Phys. Rev.* **98,** 1699 (1955).
18. DANIELS J. M., *Proc. Phys. Soc.* A**56,** 673 (1953).
19. VAN VLECK J. H., *Theory of Electric and Magnetic Susceptibilities*. Oxford University Press (1932).
20. GRACE M. A., JOHNSON C. E., SCURLOCK R. G., and TAYLOR R. T., *Proc. Internat. Low-Temperature Conference, Madison, Wisconsin* (1957).

J. Phys. Chem. Solids Pergamon Press 1959. Vol. 9. pp. 302–308. Printed in Great Britain.

SPIN-DEPENDENCE OF THE RESISTIVITY OF MAGNETIC METALS

R. J. WEISS and A. S. MAROTTA

Materials Research Laboratory, Ordnance Materials Research Office, Watertown, Massachusetts

(*Received* 10 *July* 1958; *revised* 12 *October* 1958)

Abstract—The magnetic resistivity is separated from the total resistivity for ferromagnetic and antiferromagnetic metals. It is shown that the magnetic resistivity at temperatures above the Curie point is given by $\rho_{MAG} = CS(S+1)$, where S is the spin and C is a temperature-independent constant having a value of 30×10^{-6} Ω-cm for all transition metals and alloys and approximately $7{\cdot}5 \times 10^{-6}$ Ω-cm for the rare-earth metals. The theory of FRIEDEL based on an exchange interaction between the current carriers and the atomic spins is also shown to be applicable to non-half-integral spin metals such as nickel and cobalt.

VOL. 9 1959

1. INTRODUCTION

IN a series of well-known papers, MOTT[1–3] has interpreted the resistivity of nickel in terms of the current carrying *s*-electrons being scattered into the *d*-band, the sharp drop below the Curie point being associated with the filling of half of the *d*-band which makes it unavailable for scattering. In recent years, with the rare-earth metals exhibiting a similar type of resistivity behaviour, the theory has again been investigated, since the *f*-electrons responsible for magnetism in these metals are not considered to have band-type characteristics.

FRIEDEL and DE GENNES[4] have calculated the magnetic resistivity of free electrons in metals of half-integral spin. By using the Born approximation and assuming an exchange interaction of the form $G\delta(\boldsymbol{R}-\boldsymbol{R}_p)\boldsymbol{S}_R \cdot \boldsymbol{S}_p$ between the spin of the atom $\boldsymbol{S}_p$ at position $\boldsymbol{R}_p$ and the spin of the conduction electron $\boldsymbol{S}_R$, they have shown that at temperatures well above the Curie point the resistivity is temperature-independent and is given by:

$$\rho_{MAG} = \frac{k_0\sigma_0}{\hbar e^2\xi} = \frac{k_0(mG)^2}{4\pi e^2\xi\hbar^3}S(S+1) \qquad (1)$$

$$k_0 = (3\pi^2 N)^{\frac{1}{3}},$$

where $\hbar^2k_0/2m$ is the Fermi energy, N is the number of atoms/cm^3, σ_0 the incoherent cross-section per magnetic atom, ξ the number of conduction electrons per atom, S the spin of the magnetic atom, and G the coupling constant. The above expression is valid when the relative energy loss of the electrons on collision is small, and this is approximately correct above the Curie point, T_c. Their derivation applies to metals such as gadolinium of well-defined half-integral spin, and they specifically exclude metals such as nickel and cobalt with nonhalf-integral spins which they contend should be treated in the band approximation (cf. MOTT[1–3]). COLES[5] has recently made an excellent survey of the literature in terms of the temperature-dependence and magnitude of the magnetic resistivity. It is the purpose of this note to extend the analysis in terms of the dependence of ρ_{MAG} on $S(S+1)$ and to show that the FRIEDEL theory can be applied to nonhalf-integral spin metals by simply using the VAN VLECK model for these cases.

2. SEPARATION OF MAGNETIC RESISTIVITY

We begin by assuming the total resistivity, ρ_T, of a magnetic metal to consist of the sum of magnetic, lattice, and residual resistivity, ρ_0. The lattice resistivity is due to the thermal motion of the atoms and is approximated by the well-known Gruneisen function,[6] ρ_G. We thus have

$$\rho_T = \rho_{MAG} + \rho_G + \rho_0$$

$$\rho_G = (AT^5/\theta^5) \int_0^{\theta/T} Z^5 dZ/(e^z-1)(1-e^{-z}), \quad (2)$$

where θ is the characteristic Debye temperature and A is a constant of the metal. The residual resistivity, ρ_0, is due both to impurities and alloy disordering and is assumed independent of temperature. At high temperatures ($T > T_c$ and θ), the Gruneisen function reduces to $AT/4\theta$, the magnetic resistivity becomes ρ_{MAG} (equation (1)), and we have

$$\rho_T = \rho_{MAG} + AT/4\theta + \rho_0. \quad (3)$$

From the slope, $d\rho_T/dT$, at high temperatures we can determine $A/4\theta$ from equation (3) (both ρ_{MAG} and ρ_0 are constant); while, from the low-temperature resistivity where the magnetic and lattice resistivities approach zero, we can determine ρ_0. This allows us to evaluate the sum of lattice, ρ_G, and residual, ρ_0, resistivities as a function of temperature (θ is obtained from specific heat) and the sum is subtracted from the total resistivity, ρ_T, to yield the magnetic resistivity as a function of T.

3. RESULTS

As an illustration, this separation has been performed for α-iron and is shown in Fig. 1. The high-temperature magnetic resistivity is seen to approach a constant, as predicted by FRIEDEL and DE GENNES.[4] Its value of 80 μΩ-cm indicates a large contribution to the total resistivity, while the low-temperature resistivity indicates a negligible contribution of the residual resistivity ($< 0{\cdot}1$ μΩ-cm). Since the spin of iron ($S = 1{\cdot}1$) is quite close to a half-integral value and might be expected to obey the FRIEDEL expression, it was of interest to attempt a similar separation for a metal of nonhalf-integral spin (for the moment disregarding the meaning of S for nonhalf-integral spins). This was done for nickel (Fig. 2). Here again we find the magnetic resistivity approaching a constant, suggesting that the FRIEDEL expression may not be as limited as was stated. We therefore proceeded to make such a separation for all magnetic metals for which we could find data, and the results are indicated in the second and third column of Table 1, where we have tabulated ρ_{MAG} and the experimental high-temperature slope, $d\rho_T/dT$, used to evaluate $A/4\theta$.

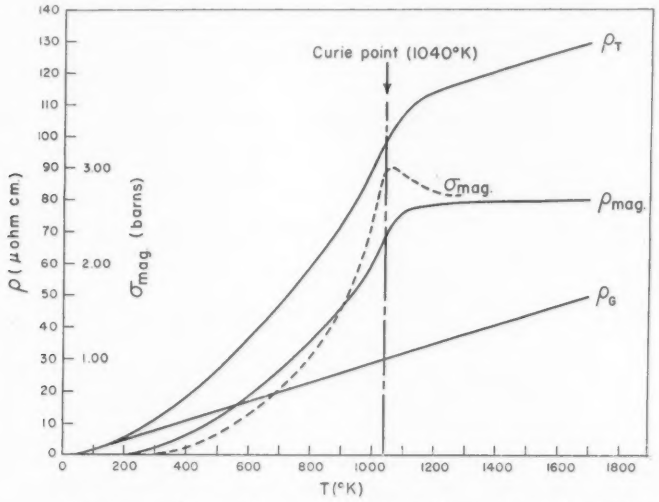

FIG. 1. ρ_T, the total, ρ_{MAG}, the magnetic, and, ρ_0, the lattice components of resistivity for iron as a function of temperature. Included is the total magnetic cross-section for long-wavelength neutrons, σ_{MAG}.

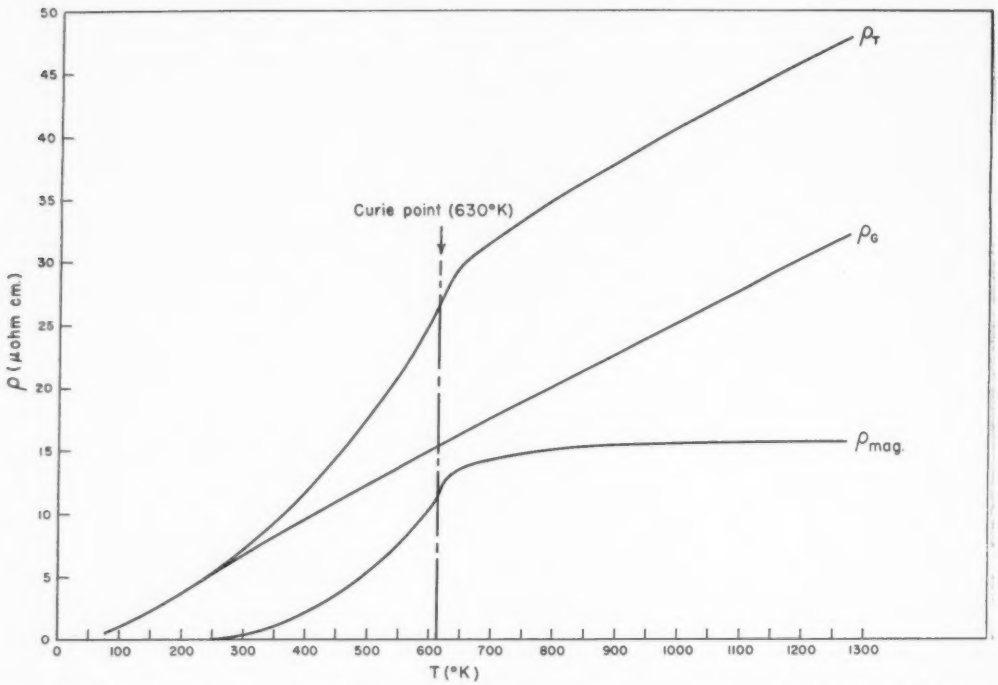

FIG. 2. ρ_T, the total, ρ_{MAG}, the magnetic and, ρ_G, the lattice components of resistivity for nickel as a function of temperature.

Table 1. *The high-temperature magnetic resistivity,* ρ_{MAG}, *the atomic Bohr magneton values,* μ_B, *the high-temperature resistivity slopes,* $d\rho_T/dT$, *the number of conduction electrons per atom,* ξ, *the deduced coupling energy parameter,* G, *and the* VAN VLECK *configurations for the various metals and alloys used for our analysis.**

Substance	ρ_{MAG} ($\mu\Omega$-cm)	μ_B (Bohr magnetons)	$d\rho_T/dT$ ($\mu\Omega$-cm/deg)	ξ	G (eVA^3)	VAN VLECK configuration
Fe[1]	80	2·22	$3{\cdot}0\times10^{-2}$	0·7	16·2	(0·8)$3d^2$ (0·2)$3d^3$
AuMn[2]	75	Au–0[10] Mn–3·5	$1{\cdot}1\times10^{-2}$	0·8	15·1	(0·5)$3d^7$ (0·5)$3d^6$
FeNi[3]	63	Fe–2·7[11] Ni–0·7	$3{\cdot}3\times10^{-2}$	0·7	16·1	(0·7)$3d^7$ (0·3)$3d^8$ (0·7)$3d^9$ (0·3)$3d^{10}$
Co[4]	50	1·7	$2{\cdot}5\times10^{-2}$	0·7	15·7	(0·7)$3d^8$ (0·3)$3d^9$

*The only substance omitted from this analysis is α-Mn, since its high-temperature resistivity decreases rapidly with temperature, making the separation unfeasible.

Table 1 (*continued*)

Substance	ρ_{MAG} ($\mu\Omega$-cm)	μ_B (Bohr magnetons)	$d\rho_T/dT$ ($\mu\Omega$-cm/deg)	ξ	G (eVA^3)	Van Vleck configuration
Au_3Mn[2]	45	Au–0[14] Mn–4·1	$1{\cdot}3\times10^{-2}$	1·0	18·7	$3d^6$
Ni_3Mn[5]	43†	Mn–3·4[11] Ni–0·4	$1{\cdot}8\times10^{-2}$	0·4	11·9	$(0{\cdot}4)3d^6$ $(0{\cdot}6)3d^7$ $(0{\cdot}4)3d^9$ $(0{\cdot}6)3d^{10}$
Ni[6]	15	0·6	$2{\cdot}5\times10^{-2}$	0·6	14·5	$(0{\cdot}6)3d^9$ $(0{\cdot}4)3d^{10}$
Cr[7]	10	0·4[12]	$4{\cdot}2\times10^{-2}$	0·7	16·4	$(0{\cdot}4)3d^1$ $(0{\cdot}6)3d^0$
$Cu_{0{\cdot}15}Mn_{0{\cdot}85}$[15]	34	Cu–0[15] Mn–1·6	$6{\cdot}0\times10^{-2}$	0·7	15·0	$(0{\cdot}4)3d^1$ $(0{\cdot}6)3d^2$
Cu(1·8%Mn)[8]	1·2†	Cu–0[13] Mn–4	$1{\cdot}0\times10^{-2}$	1·0	18·7	$3d^6$
Er[9]	42	3[9]	$44{\cdot}5\times10^{-2}$	2·1	4·9	$4f^{11}$
Dy[9]	74	5[9]	$15{\cdot}0\times10^{-2}$	1·5	3·3	$4f^9$
Gd[9]	120	7[9]	$7{\cdot}5\times10^{-2}$	2·1	3·5	$4f^7$

†See Appendix.

REFERENCES FOR TABLE 1

1. Powell R. W., *Phil. Mag.* **44,** 772 (1953).
2. Giansoldati A. and Linde J. D., *J. Phys. Radium* **16,** 341 (1955).
3. Wakelin R. J. and Yates E. L., *Proc. Phys. Soc.* B**66,** 221 (1953).
   Bozorth R. M., *Ferromagnetism,* pp. 107–108. D. Van Nostrand, New York (1951).
4. Hampel C. A., *Rare Metal Handbook,* p. 117. Reinhold Publishing Corp. New York (1954).
5. Bozorth R. M., *Rare Metal Handbook,* pp. 316–317. Reinhold Publishing Corp. New York (1954).
6. *Nat. Bur. Stand. Circ.* **592,** 21 (1958).
7. Marotta A. S., Tauer K. J., and Weiss R. J. Unpublished work.
8. Coles B. R., *Advanc. Phys.* **7,** 67 (1958).
9. Coles B. R., *Advanc. Phys.* **7,** 44–45 (1958).
10. Bacon G. E. and Street R., *Proc. Phys. Soc.* **72,** 470 (1958).
11. Shull C. G. and Wilkinson M. K., *Phys. Rev.* **97,** 304 (1955).
12. Shull C. G. and Wilkinson M. K., *Rev. Mod. Phys.* **25,** 100 (1953).
13. Myers H. P., *Canad. J. Phys.* **34,** 527 (1956).
14. Meyer A. J. P., *C.R. Acad. Sci., Paris* **242,** 2315 (1956) (Au_4Mn—same value assumed for Au_3Mn).
15. Bacon G. E., Dunmur I. W., Smith J. H., and Street R., *Proc. Roy. Soc.* A**241,** 228 (1957).

4. ANALYSIS OF RESULTS

In order to analyze our results in terms of equation (1), we must extend the Friedel and de Gennes derivation to the case of nonhalf-integral spins. The coefficient $S(S+1)$ in equation (1) arises as the expectation value $\langle S^2\rangle$, where S is the atomic spin. The question simply reduces itself as to the value of $\langle S^2\rangle$ for nonhalf-integral spin metals such as nickel. Van Vleck[7] has proposed that nickel consists of 60 per cent of the atoms in $3d^9$ states (one Bohr magneton) and 40 per cent in $3d^{10}$ states (zero Bohr

magnetons). With this model $\langle S^2\rangle \cong 0{\cdot}6\,\frac{1}{2}(\frac{1}{2}+1)+0{\cdot}4\;0(0+1) = 0{\cdot}45$.* We have used the VAN VLECK model for the metals and alloys in Table 1 of nonhalf-integral spin, and their configurations are given in column 6. We then plotted ρ_{MAG} versus $S(S+1)$ in order to ascertain the values of the coupling constant G. In the case of the alloys, the different atomic species have different values of AuMn, FeNi, cobalt, Au_3Mn, Ni_3Mn, nickel and copper (1·8 per cent manganese), ξ can be determined from the Bohr magneton value. For example, in FeNi the iron atom has 8 electrons outside the argon core and a Bohr magneton number of 2·7. If we require that the $3d$ shell is first filled to maximum multiplicity (5 electrons) and then continue to fill the d shell with paired

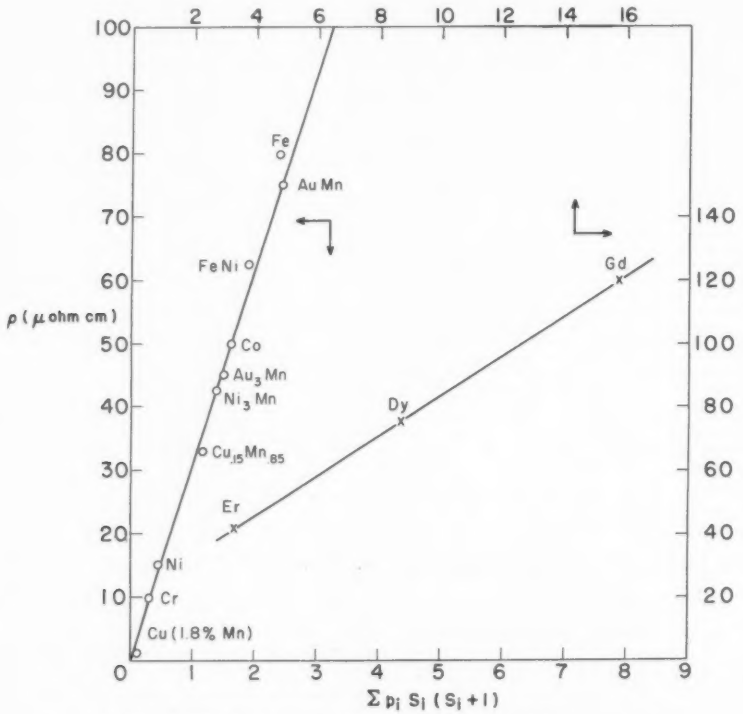

FIG. 3. The high-temperature magnetic resistivity, ρ_{MAG}, versus $S(S+1)$ for various transition metals and alloys and for rare-earth metals.

of spin, and this can be accounted for in the FRIEDEL expression by replacing $S(S+1)$ by $\sum_i p_i S_i(S_i+1)$, where p_i is the fraction of atoms of spin S_i and $S_i(S_i+1)$ is the VAN VLECK expectation value. The results of this plot are given in Fig. 3. In order to ascertain the values of G listed in Table 1, we require values for ξ. In the case of spin, and this can be accounted for in the FRIEDEL expression by replacing $S(S+1)$ by $\sum_i p_i S_i(S_i+1)$, where p_i is the fraction of atoms of spin S_i and $S_i(S_i+1)$ is the VAN VLECK expectation value. The results of this plot are given in Fig. 3. In order to ascertain the values of G listed in Table 1, we require values for ξ. In the case electrons to give the observed Bohr magneton number, the remaining electrons are assumed to be conduction electrons. For iron in FeNi we have 5 electrons with spin up, 2·3 electrons with spin down, leaving 0·7 as current carriers. For nickel in FeNi this same analysis also gives 0·7 current carriers. For gadolinium, erbium and dysprosium, we have used the Hall measurements[8] to determine ξ, while for iron $Cu_{0.15}Mn_{0.85}$, and chromium we have used the value 0·7 which is an average between the high

*This model is strictly applicable only for static configurations of $3d^9$ and $3d^{10}$, but since the effective mass of the holes is large, it is a reasonable approximation.

and low values (1·0–0·4) for the other transition metals. (Since G depends on the square root of ξ, this is not a large source of error.) Table 1 includes the values of ξ and the calculated values of G from equation (1).

5. DISCUSSION OF RESULTS

The most significant point is the surprisingly linear variation over a wide range of spins of ρ_{MAG} for *all* transition metals and alloys (Fig. 3) and the rather narrow range of values of G. The average value of the exchange potential for the transition elements is thus about 1·5 eV/atom. The rare earths also show a linear variation, but with a lower value of G and a lower value of the exchange potential ($\sim 0{\cdot}11$ eV/atom). A second point is that the rare-earth metals are proportional to $S(S+1)$ rather than $J(J+1)$; the respective values of J for gadolinium, dysprosium and erbium are 7/2, 15/2 and 15/2. This lends further support to the idea that the basic interaction is of the exchange type, since the fundamental exchange interaction is only with the spin, S. Recently ANDERSON and LEGVOLD have made a similar analysis for the rare earth metals adding several previously unpublished points. (*Phys. Rev.* Letters **1**, 322, 1958).

The value of the exchange potential of 1·5 eV/atom for the transition metals and 0·11 eV/atom for the rare earths would lead, though, to a marked polarization of the current carriers, and this can be ruled out from the neutron experiments of SHULL on iron in which it is shown that less than $0{\cdot}1\mu_B$ can be due to 4s electrons. Rather than discard the FRIEDEL treatment, which is based on free electrons, we might assume that the current carriers are far from free electrons and an effective mass $m^* \sim 10m$ is not unreasonable, particularly if we assume the current carriers to contain a large d admixture. (In order to explain the anomalous Hall effect in terms of spin-orbit coupling, we must invoke such an argument.[9]) Taking $m^* = 10m$ and a Fermi level of ~ 12 eV, we can reduce the value of the exchange potential to $\sim 0{\cdot}03$ eV/atom, which is surprisingly close to the value of the exchange integral obtained from the Curie temperature ($J = 0{\cdot}01$ eV for iron and nickel). This suggests that the exchange interaction giving rise to ferromagnetism and and antiferromagnetism is intimately connected to that giving rise to the resistance anomaly.* Further support for this comes from the fact that the exchange interaction as determined from resistivity is at least an order of magnitude greater in the transition metals than in the rare earths, as is also found from their Curie temperatures.[10]

Since the resistivity is proportional to the cross-section per atom (equation (1)), it is not too surprising that the correlation of atomic spins is quite similar for conduction electrons as well as for neutrons. This is shown in Fig. 1, where we have included the total magnetic cross-section of iron for long-wavelength neutrons. The neutron and conduction electron cross-sections would agree only if the wavelength of both were the same, and this possibly explains the difference in the vicinity of the Curie point.

6. CONCLUSIONS

(1). The origin of the magnetic resistance of ferromagnetic and antiferromagnetic metals is consistent with an exchange interaction between the current carriers and the atomic spins, and to this extent the s–d scattering mechanism of MOTT appears superfluous.

(2). This exchange interaction may be identical to that giving rise to ferromagnetism and antiferromagnetism and is supported by the fact that the ratio of this interaction between transition metals and rare earths is quite similar for both resistivity and Curie points.

Acknowledgements—We wish to thank Dr. A. PASKIN for his help and advice.

REFERENCES

1. MOTT N. F., *Proc. Phys. Soc.* **47,** 571 (1935).
2. MOTT N. F., *Proc. Roy. Soc.* A**153,** 699 (1936).
3. MOTT N. F., *Proc. Roy. Soc.* A**156,** 358 (1936).
4. FRIEDEL J. and DE GENNES P., *J. Phys. Chem. Solids,* **4,** 71 (1958).
5. COLES B. R., *Advanc. Phys.* **7,** 40 (1958).
6. WILSON A. H., *Theory of Metals,* p. 287. Cambridge University Press (1953).

*The referee has pointed out that the conduction-electron model for magnetism would yield an exchange integral of order G^2/E_F, where E_F is the Fermi energy. However, we choose not to suggest a specific model for magnetism, but merely to point out the magnitude of the two exchange integrals.

7. VAN VLECK J. H., *Rev. Mod. Phys.* **25,** 220 (1953).
8. KEVANE C. J., LEGVOLD S., and SPEDDING F. H., *Phys. Rev.* **91,** 1372 (1953).
9. KARPLUS R. and LUTTINGER J. M., *Phys. Rev.* **95,** 1154 (1954).
10. HOFMANN J. A., PASKIN A., TAUER K. J., and WEISS R. J., *J. Phys. Chem. Solids* **1,** 45 (1956).

APPENDIX

Determination of ρ_{MAG} for Cu(1·8 per cent Mn) and Ni_3Mn

In the case of copper (1·8 per cent manganese), the resistivity at absolute zero consists of the alloy-disorder scattering term plus a magnetic term due to the disordered arrangement of atoms of different spin, and can be represented as:

$$\rho_0(\text{MAGNETIC}) = Cp_{Mn}p_{Cu}(S_{Mn}-S_{Cu})^2 \cong Cp_{Mn}(S_{Mn})^2,$$

since $S_{Cu} \cong 0$ and $p_{Cu} \cong 1$. At temperature above the Néel point ($T_c \sim 18°K$), we have:

$$\rho_{MAG} \cong Cp_{Mn}S_{Mn}(S_{Mn}+1).$$

Therefore

$$\rho_{MAG}-\rho_0(\text{MAGNETIC}) = 0{\cdot}4\ \mu\Omega\text{–cm} = Cp_{Mn}S_{Mn}$$

$$\rho_{MAG} = \frac{S_{Mn}(S_{Mn}+1)}{S_{Mn}} \cdot 0{\cdot}4\ \mu\Omega\text{–cm} = 1{\cdot}2\ \mu\Omega\text{–cm}$$

For Ni_3Mn the Curie point for the ordered alloy and the critical temperature for ordering are quite close and prevent a straightforward separation. The total additional resistivity ($\rho_{MAG}+\rho_0$) is 70 $\mu\Omega$-cm. At 10 per cent manganese, the additional room-temperature resistivity over pure nickel is 19 $\mu\Omega$-cm, and this is due to the ρ_0 term plus the magnetic resistance due to disordering on atomic sites (it is well below the Curie point). We thus have:

$$25 \text{ per cent manganese: } 70\ \mu\Omega\text{–cm} = \rho_0(0{\cdot}75)(0{\cdot}25)+C[p_{Mn}S_{Mn}(S_{Mn}+1)+\rho_{Ni}S_{Ni}(S_{Ni}+1)]$$

$$10 \text{ per cent manganese: } 19\ \mu\Omega\text{–cm} = \rho_0(0{\cdot}9)(0{\cdot}1)+C[p_{Mn}p_{Ni}(S_{Mn}-S_{Ni})^2]$$

Solving for ρ_0 and C, we determine the magnetic resistivity to be $\rho_{MAG} = 43$ $\mu\Omega$-cm.

J. Phys. Chem. Solids Pergamon Press 1959. Vol. 9. pp. 309–319. Printed in Great Britain.

HYPERFINE INTERACTIONS IN *F*-CENTER PARAMAGNETIC-RESONANCE SPECTRA IN LiF AND NaF*

G. J. WOLGA and M. W. P. STRANDBERG

Department of Physics and Research Laboratory of Electronics,
Massachusetts Institute of Technology, Cambridge, Massachusetts

(*Received* 5 *September* 1958; *revised* 15 *October* 1958)

VOL.
9
1959

Abstract—The method of paramagnetic resonance is used to study the magnetic-energy levels of *F*-centers in LiF and NaF. The microwave absorption spectra show a set of nearly resolved transitions; each crystal has an odd number of almost equally spaced lines symmetrically located about a central resonance. The spectra are found to be isotropic with respect to relative orientation of the 100-axis and the applied magnetic field. The scalar magnetic hyperfine interaction and the spectroscopic splitting factor are determined from experimental data.

The experimental results are interpreted on the basis of the DE BOER model of the *F*-center, and determine the probability density of the *F*-electron wave function at the sites of the nearest-neighbor nuclei. The line breadth of the inhomogeneously broadened spin packets is obtained from the dependence of the spectrum on the ratio of line width to hyperfine interaction. The packet breadth is attributed to unresolved hyperfine interaction with further nuclei, and yields an estimate of the scalar hyperfine interaction with the next-nearest-neighbor nuclei.

The observed spectroscopic splitting factors, corrected for the hyperfine interaction shift, are found to be smaller than the free-electron value. This difference is attributed to spin-orbit coupling with excited states of higher orbital angular momentum, and it yields an estimate for the expectation value of $(1/r^3)$.

The predictions of the theory of inhomogeneous broadening on the dependence of the absorption upon microwave power are confirmed.

1. INTRODUCTION

AMONG the major problems in the study of the defect solid state are the obtaining and justifying of a model for the defect. This has also been true for *F*-centers, although, since DE BOER's[1] proposal, there has been general agreement that his is the most likely model. Paramagnetic-resonance techniques afford a very sensitive method for investigating paramagnetic impurities such as the *F*-center. Early resonance studies of *F*-centers[2–6] confirmed their paramagnetic property, and the smallness of the deviation of the spectroscopic splitting factor from the free-electron value seemed to confirm the association of a "free" electron with the *F*-center. However, these studies did not clearly differentiate among possible models for the *F*-center. The DE BOER model is very specific. It puts the electron at a negative (halogen) vacancy in the alkali-halide crystal and thereby implies that there are definite symmetry properties in the magnetic interactions between the paramagnetic electron and the surrounding nuclear moments. Since these early studies did not yield resolved hyperfine splittings, the DE BOER hypothesis was not conclusively verified. Recently, resolved hyperfine interactions have been observed in LiF and NaF.[7–10] The work that will be described is an amplification of earlier results.[7–9] Although the present results are similar in many ways to those given by LORD,[10] we feel that, because of the differences and of the importance of corroborative evidence in a problem of this sort, a detailed presentation of our results is desirable.

* This work was supported in part by the U.S. Army (Signal Corps), the U.S. Air Force (Office of Scientific Research, Air Research and Development Command), and the U.S. Navy (Office of Naval Research).

2. THEORY

(a) *Energy levels and wave functions*

In states in which the electronic wave function has a predominantly S-like character, the major hyperfine interaction is the scalar or contact magnetic hyperfine interaction. That this is the major interaction for F-centers in the alkali halides is shown experimentally by two facts: the effective $\bar{g}$-value is close to the free-electron value; the interaction is isotropic in the sense that the energy levels are independent of the angle between the steady magnetic field and the principal crystalline axes. The first fact points to the smallness of the orbital part of the electronic angular momentum. The second shows that the dipole–dipole term is much smaller than the contact term. For this reason, we shall calculate the scalar interaction between the F-center electron and the set of equidistant nuclei which comprises the nearest neighbors in the DE BOER model. These interactions will account for the gross energy-level splittings. The similar interaction between the F-center and the next-nearest-neighbor nuclei is not resolved by paramagnetic resonance* and is believed to contribute to the broadening of the observed spectrum.

The magnetic energy of the F-electron may be described by:

$$H_{\text{mag}}^{\text{op}} = g_e\beta_e S_z B_z + \sum_{\alpha=1}^{6} g_n\beta_n I_z^{\alpha} B_z + \sum_{\alpha=1}^{6} A_\alpha \cdot \boldsymbol{I}_\alpha \cdot \boldsymbol{S}\delta(\boldsymbol{r}_e - \boldsymbol{r}_n^{\alpha}), \tag{1}$$

where $\boldsymbol{B} = B_z$ is the steady external magnetic field, $A_\alpha = (8\pi/3)g_e\beta_e g_n\beta_n$ is the magnitude of the contact hyperfine interaction,[12] g_e, β_e, g_n, and β_n being the g-factors and Bohr magnetons for electron and nucleus. The summation is over nearest neighbors. Because of the equivalence of neighbors and the isotropic character of the operators, we may choose a system of quantum numbers in which I^2 and I_z are diagonal, where

$$\boldsymbol{I} = \sum_{\alpha=1}^{6} \boldsymbol{I}_\alpha.$$

The corresponding quantum numbers are i and m_i.

We may write the wave function for the F-center electron and the nuclear spins as:

$$\phi = \phi(\boldsymbol{r})_\beta{}^\alpha \chi(i, m;) \tag{2}$$

where $\phi(\boldsymbol{r})$ is the spatial part of the F-center wave function, and α, β are electron spin eigenfunctions. We consider that the n-electron hyperfine interaction has been reduced to the interaction that involves only the F-electron in the manner described by GOURARY and ADRIAN.[13] We may thus write:

$$H_{\text{mag}}^{\text{op}} = \gamma_e S_z + \gamma_n I_z + A(I_z S_z + \tfrac{1}{2}I^+S^- + \tfrac{1}{2}I^-S^+)$$

where

$$\gamma_e = g_e\beta_e B_z;\ I^\pm = I_x \pm iI_y$$
$$\gamma_n = g_n\beta_n B_z;\ S^\pm = S_x \pm iS_y. \tag{3}$$

With the wave functions (2) the operator (1) has the matrix given by:

$$\langle S, i, m_s, m_i | H_{\text{mag}} | S, i', m_s', m_i' \rangle = \delta(m_s, m_s')\delta(m_i, m_i')(\gamma_e m_s + \gamma_n m_i) + A\delta(i, m; i', m')\{\delta(m_s, m_s')m_i\, m_s + \tfrac{1}{2}\delta(m_s', m_s \pm 1)\sqrt{[(i \mp m + \tfrac{1}{2})(i \pm m + \tfrac{1}{2})]}\}, \tag{4}$$

where $m = m_i + m_s$. With $i = 3/2$, this is a 19×19 matrix. However, since it is diagonal in m, it factors into blocks which are at most 2×2 matrices, each characterized by a value of m. The eigenvalues of a typical 2×2 matrix are given by:

* The double-resonance method has revealed the next-nearest-neighbor and dipole–dipole interactions in KCl and has confirmed our assignment of relative magnitudes to the interactions. LORD[26] has recently obtained data on LiF by the double-resonance method.

VOL. 9 1959

$$\epsilon_{\pm} = -\frac{A}{4}+\gamma_n m \pm$$

$$\pm\tfrac{1}{2}[(\gamma_e-\gamma_n)^2+4D^2+A^2m^2+2Am(\gamma_e-\gamma_n)]^{\frac{1}{2}}, \tag{5}$$

where

$$D = \frac{A}{2}\sqrt{[(i-m+\tfrac{1}{2})(i+m+\tfrac{1}{2}]}.$$

The wave functions which diagonalize the submatrices may be written:

$$\left.\begin{aligned}\psi_1 &= \quad T_1\alpha\chi(i,\, m-\tfrac{1}{2})+T_2\beta\chi(i,\, m+\tfrac{1}{2})\\ \psi_2 &= -T_2\alpha\chi(i,\, m-\tfrac{1}{2})+T_1\beta\chi(i,\, m+\tfrac{1}{2})\end{aligned}\right| \tag{6}$$

where

$$T_1 = \sqrt{\left[\frac{Am+(\gamma_e-\gamma_n)+\sqrt{[(\gamma_e-\gamma_n)^2+4D^2+A^2m^2+2Am(\gamma_e-\gamma_n)]}}{2\sqrt{[(\gamma_e-\gamma_n)^2+4D^2+A^2m^2+2Am(\gamma_e-\gamma_n)]}}\right]}$$

$$T_2 = \sqrt{\left[\frac{\sqrt{[(\gamma_e-\gamma_n)^2+4D^2+A^2m^2+2Am(\gamma_e-\gamma_n)}-Am-(\gamma_e-\gamma_n)]}{2\sqrt{[(\gamma_e-\gamma_n)^2+4D^2+A^2m^2+2Am(\gamma_e-\gamma_n)]}}\right]}.$$

We obtain to second order in A

$$\epsilon_+(m) = -\frac{A}{4}+\gamma_n m+\frac{(\gamma_e-\gamma_n)}{2}+\frac{A}{2}m+\frac{A^2}{4(\gamma_e-\gamma_n)}\left[i(i+1)+\frac{1}{4}\right]-\frac{A^2m^2}{4(\gamma_e-\gamma_n)}$$

$$\epsilon_-(m-1) = -\frac{A}{4}+\gamma_n m-\gamma_n-\frac{(\gamma_e-\gamma_n)}{2}-\frac{A}{2}(m-1)-\frac{A^2}{4(\gamma_e-\gamma_n)}\left[i(i+1)+\frac{1}{4}\right]-\frac{A^2(m-1)^2}{4(\gamma_e-\gamma_n)} \tag{8}$$

The energy levels $\epsilon_{\pm}$ given in equation (5) are functions of the three parameters A, B_z, and m. It is convenient to re-express them as a function of A/B_z and thus obtain a set of universal curves. We obtain thereby

$$\eta_{\pm} = -\frac{\theta}{4}+g_n\beta_n m \pm \sqrt{\{(g_e\beta_e-g_n\beta_n)^2+\theta^2[i(i+1)+\tfrac{1}{4}]+2\theta m(g_e\beta_e-g_n\beta_n)\}}, \tag{7}$$

where

$$\eta_{\pm} = \frac{\epsilon_{\pm}}{hB_z}\cdot\ \theta = \frac{A}{hB_z};\ h = \text{Planck's constant};$$

and β_e and β_n are expressed in mc/G. The reduced energies $\eta_{\pm}$ have been plotted over a wide range of values of θ in Fig. 1.

(b) *Transition frequencies*

With the assumption that the interactions contributing to equation (5) sufficiently describe the energy levels, the exact transition frequencies can be obtained from equation (5). Because $\gamma_e \gg \gamma_n$, coupling to the microwave field is effected primarily through the $\boldsymbol{S}\cdot\boldsymbol{B}_{rf}$ interaction, and transitions will occur from the ϵ_+ to ϵ_- levels. Consequently, the most probable transitions will obey the "selection rule" $\Delta m_s = \pm 1$; $\Delta m_i = 0$, and we expect transitions $\epsilon_+(m) \rightleftarrows \epsilon_-(m-1)$. For $A/B_z \ll 1$, it is convenient to compute transition frequencies by expanding the expressions for $\epsilon_{\pm}$ in powers of $A/(\gamma_e-\gamma_n)$.

Rewriting this, we have

$$\Delta E(m_i) = h\nu(m_i) = g_e\beta_e B_z\left[1+\frac{A^2}{2g_e^2\beta_e^2B_z^2}[i(i+1)-m_i^2]\right]+Am_i. \tag{9}$$

The absorption spectrum predicted by equation (9) is easily interpreted. With LiF and NaF as examples, the nearest-neighbor nuclei have spin 3/2, and therefore $i = 9$, and m_i varies from $+9$ to -9. To first order, the hyperfine

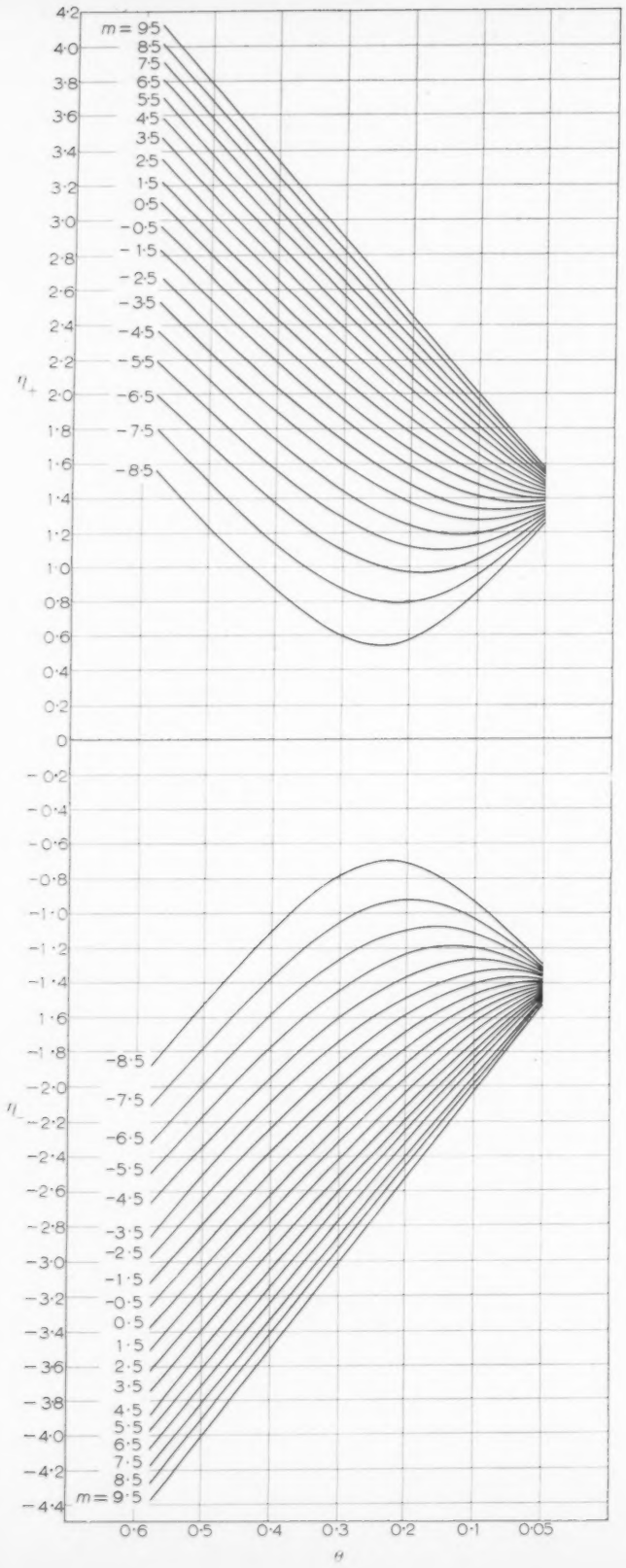

FIG. 1. Reduced magnetic energy as a function of magnetic field and contact hyperfine interaction for $S = \frac{1}{2}$, $I = 9$.

VOL.
9
1959

transitions will be symmetrically located about $g_e\beta_e B_z$, and separated by A, thereby giving 19 resonances. In addition, there is a constant shift and an m_i-dependent shift that are proportional to $(A/B_z)^2$. For $A = 40$ G and $B_0 = 3000$ G, the second-order correction is 0·8 per cent at its maximum value when $m_i = 0$. This correction is appreciable and measurable at microwave frequencies and should be taken into account in g-factor analyses.

(c) *Intensities and line shape in the hyperfine spectrum*

The relative intensities of the 19 nearest-neighbor absorptions that correspond to different m_i values have been interpreted[6] as arising from the relative statistical weights of the m_i states which are determined by the number of arrangements of the m_α that are consistent with

$$m_i = \sum_{\alpha=1}^{6} m_\alpha .$$

The relative statistical weights for the six nearest-neighbor nuclei are listed in Table 1.

Table 1. *Relative statistical weights of the nearest-neighbor* m_I *states*

$m_i = \pm 9$	1	$m_i = \pm 4$	216
$m_i = \pm 8$	6	$m_i = \pm 3$	336
$m_i = \pm 7$	21	$m_i = \pm 2$	456
$m_i = \pm 6$	56	$m_i = \pm 1$	546
$m_i = \pm 5$	120	$m_i = 0$	580

For our crystals, in which only the nearest-neighbor interactions yield resolved lines, all other nuclei contribute to the observed width of the resolved lines. The line width, or spectral distribution, of the resolved lines will depend, for each set of equidistant nuclei, on the relative statistical weights of the total component of nuclear spin of that set. For LiF and NaF, the 12 next-nearest-neighbors of spin $\frac{1}{2}$ have the relative statistical weights listed in Table 2. These statistical weights are determined by simple combinatorial analysis. It is not sufficient to include only the next-nearest neighbors in calculating the line shape, since the following shells are separated by mere fractions of the lattice spacing. However, the width of the resolved lines may be used to give an upper bound to the next-nearest-neighbor interactions, and the actual line shape is best determined by fitting the observed spectrum to theoretical curves.

Table 2. *Relative statistical weights of the next-nearest neighbor* m_I *states*

$m_i = \pm 6$	1	$m_i = \pm 2$	495
$m_i = \pm 5$	12	$m_i = \pm 1$	792
$m_i = \pm 4$	66	$m_i = 0$	924
$m_i = \pm 3$	220		

To facilitate quantitative analysis of the experimental data, a set of charts was prepared showing the spectrum that was obtained by superposing resonances that are spaced according to equation (9) with individual line intensities determined by the statistical weights of Table 1. Normalized charts were prepared for the ratio $0{\cdot}6 \leqslant A/W \leqslant 3{\cdot}0$ (A represents the contact hyperfine interaction with the nearest neighbors, and W, the full width between the peaks of the derivative of the absorption shape, (χ''). The resultant spectrum is quite critically dependent on this ratio. Charts were prepared for Gaussian and Lorentzian line shapes. We found that the Gaussian curves fell off too rapidly in the skirts and could not reproduce the observed spectra. Much better agreement was obtained with the Lorentzian shape. The choice of a Lorentzian line shape is consistent with the findings of other workers.[16,17] Several of the charts are shown in Fig. 2 for values of A/W for which the spectrum is a rapid function of this ratio. It is evident that for $A/W < 1$, the resultant spectrum rapidly blends into one unresolved line, and for ratios that are close to one, the transitions corresponding to $m_i > 5$ are virtually unresolved.

(d) *The theory of inhomogeneous broadening*

It is evident from the discussion of line width and line shape that the F-center absorptions are inhomogeneously broadened. This type of broadening results from the fact that the effective local magnetic field for each F-center, and consequently its paramagnetic-absorption frequency, depends

on the parameters A and m_i of each "shell" of surrounding nuclear moments. The dependence of the paramagnetic-resonance signal on the impressed microwave power level has been discussed by PORTIS.[16] He obtains an equation for $\chi''(\omega)$ with the assumption that the Bloch equations can be used; that the individual spin packets, which we summed in Section 2(c) are much narrower than the over-all spectrum width, and that the individual spin packets have a Lorentzian shape. The relation is:

$$\chi''(\omega)=\frac{1}{2}\chi_0\omega h(\omega-\omega_0)\int_0^\infty \frac{1/T_2}{(\omega-\omega')^2+(1/T_2^2)+\gamma^2B_{rf}^2(T_1/T_2)}\,d\omega', \tag{10}$$

where $h(\omega-\omega_0)$ is the broad over-all line shape; $g(\omega-\omega')$ is the individual spin-packet shape, centered at the value ω' of the spectral distribution of local frequencies; and B_{rf} is the microwave field strength at the sample. Here, T_2 is related to the width of the spin packet, and χ_0 is the static susceptibility. The saturation behavior is easily obtained in the limit $\gamma^2B^2{}_{rf}T_1/T_2 \gg 1/T_2^2$ as long as the spin packets are narrower than the over-all width $(\omega-\omega_0)$. We obtain:

$$\chi''(\omega)\xrightarrow{\text{large } B_{rf}}\frac{\pi}{4}\frac{\chi_0}{\gamma\sqrt{(T_1T_2)}}\omega h(\omega-\omega_0)\left(\frac{1}{B_{rf}}\right). \tag{11}$$

Since the detected resonance signal is proportional to $B_{rf}{}^2\chi''$, the signal will increase as the square root of the microwave power in the saturation region.

3. EXPERIMENTAL METHODS

(a) *Microwave and associated apparatus*

Microwave spectra were obtained with a high-sensitivity spectrometer. The microwave source was a 2K25 klystron frequency-stabilized directly to the cavity containing the sample with a d.c. microwave discriminator. For this reason, only the imaginary part of the r.f. sample susceptibility was detected. The sample absorption was modulated at 6000 c/s by sinusoidally modulating the static magnetic field. The high-Q (loaded $Q = 7000$) reflection microwave cavity, which was made of quartz coated on the inside with a thin silver layer, was operated in the TE_{011} mode. The microwave power that was reflected from the cavity and amplitude-modulated by the sample absorption was linearly detected in a matched IN23B silicon diode. The signal sidebands were linearly translated to a signal with a carrier at 6000 c/s, amplified in a 6000-c/s amplifier, and then detected in a phase-sensitive manner before the final bandwidth narrowing around zero frequency. The final output, which was proportional to $(d\chi''/dB_z)$ for small modulation amplitude, was displayed as a function of the linearly swept magnetic field on a recording milliammeter. The signal-detection system and the apparatus for controlling and sweeping the magnetic field have already been described.[18,19]

The sample crystal was inserted along the longitudinal axis of the microwave cavity, and could be rotated inside the cavity to vary the angle between the 100-axis and the static field. The cavity coupling could be adjusted externally to accommodate the decoupling effect of the high-dielectric-constant sample.

Magnetic-field measurements were made by graphical interpolation from field markers on the spectrum. The field markers were calibrated by a secondary standard, with a proton resonance probe.[20] All experimental values were obtained as an average over many identical runs.

For g-factor determination, the microwave frequency was measured by using the sharp DPPH resonance to establish a field-frequency point in conjunction with a proton-resonance field measurement.

(b) *Optical equipment*

All optical measurements were made on a Beckman Model DU quartz spectrophotometer. Data were taken for each 10 mμ over a range of 200–600 mμ. For uncolored alkali-halide crystals, air was used as the comparison sample in the Beckman spectrophotometer. An uncolored crystal from the same batch was used for comparison with the colored crystals.

(c) *Sample preparation*

The alkali-halide crystals were obtained from the Optovac Company and from the Harshaw Chemical Company in the form of parallelepipeds cleaved along the 100-axes. The size of the crystals was approximately $\frac{1}{2}\times1\times2$ cm. The crystals were colored at room temperature by exposure to 1·2-MeV gamma rays from a ^{60}Co source at M.I.T.

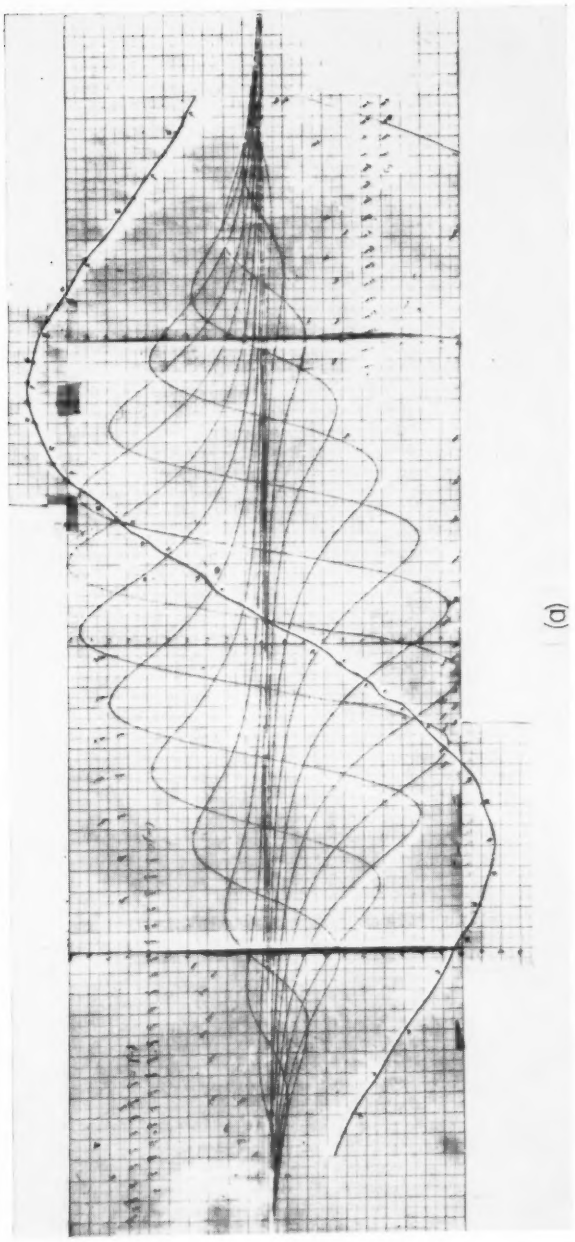

(a)

FIG. 2(a)

[*facing p.* 314

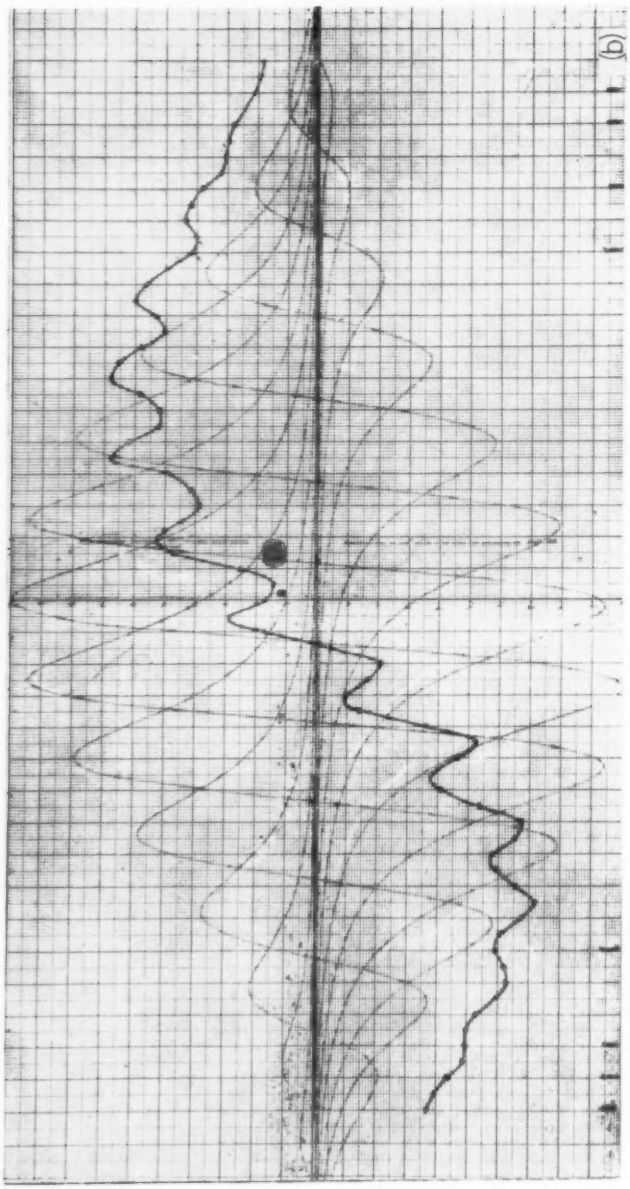

FIG. 2(b)

VOL.
9
1959

VOL. 9 959

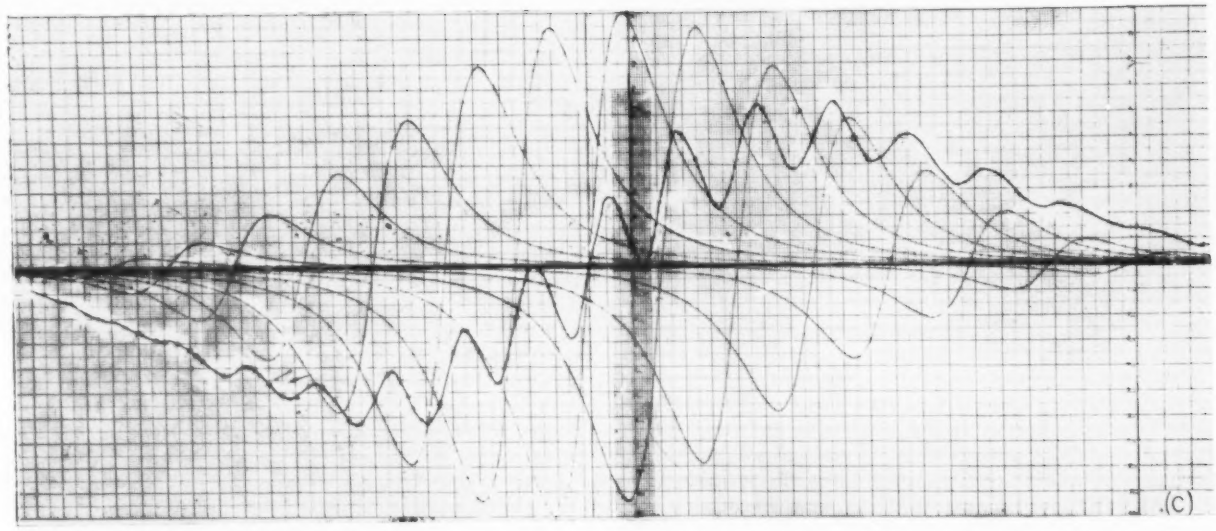

FIG. 2. Expected inhomogeneously broadened line shape for three A/W ratios; (a) $A = 0{\cdot}6W$; (b) $A = 0{\cdot}9W$; (c) $A = W$.

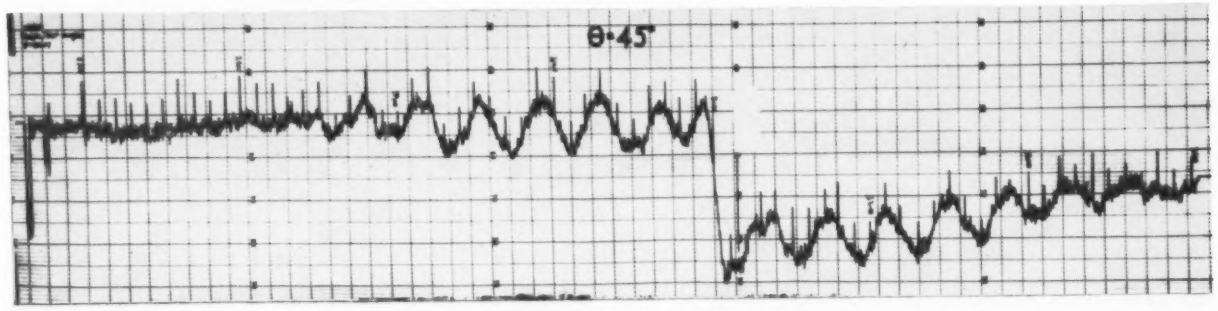

FIG. 3. Microwave absorption spectrum of irradiated NaF.

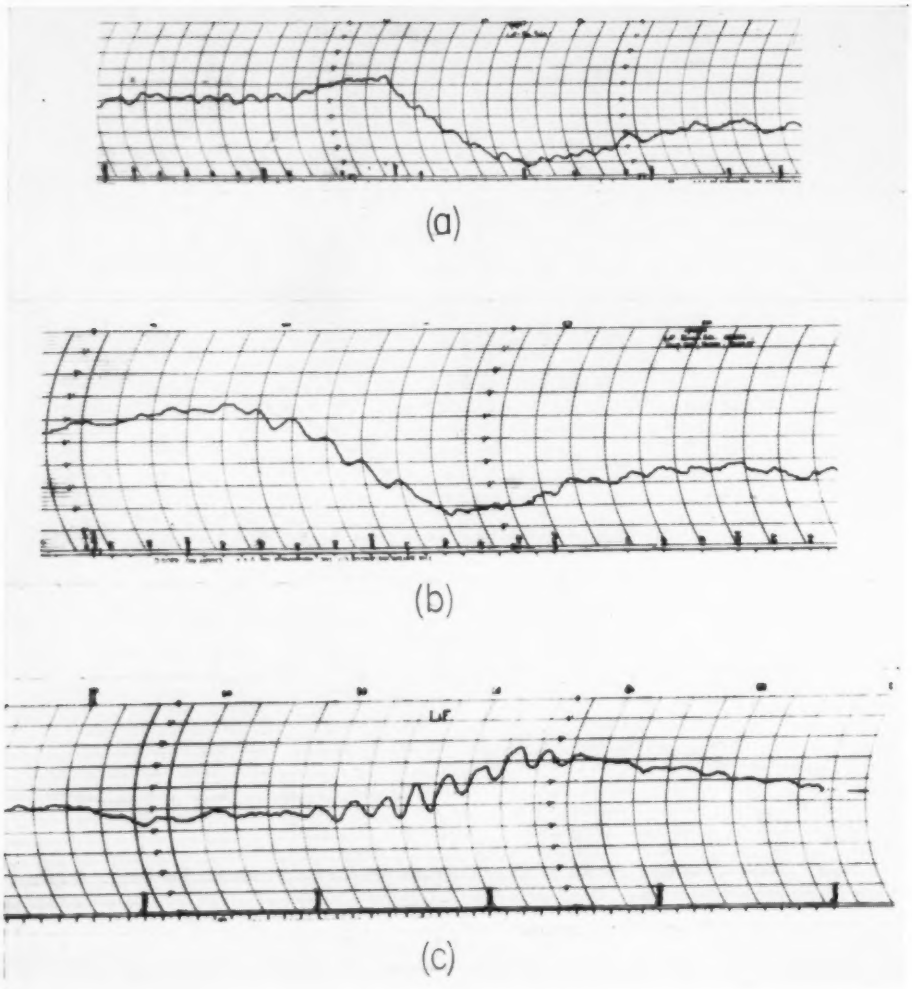

FIG. 4. Microwave absorption spectrum of irradiated LiF for three irradiation dosages: (a) $\frac{1}{2}$ hr; (b) 1 hr; (c) 2 hr.

VOL
9
195

(d) *Experimental procedure*

First, optical and microwave runs were made on unirradiated crystals to determine the presence of prior coloration or of paramagnetic impurities in the range of the *F*-center absorption. The crystals were colored and examined by optical and then by microwave means. As a rule, the spectra were obtained for the first time within 24 hr of irradiation. Samples were prepared and examined for varying irradiation dosages. The microwave runs for each irradiated sample included angular-dependence runs to establish the extent of anisotropy of the absorption.

In addition to determining the shape of the paramagnetic absorption, the magnitude of the hyperfine interactions, and the field-frequency position of the absorption, experiments were conducted to examine the dependence of the absorption signal on microwave field strength. This was done to check the theory of inhomogeneous broadening outlined in Section 2. Consecutive runs for various degrees of attenuation of the microwave power incident on the cavity were made. Microwave power was measured by monitoring the power reflected from the cavity. This was done by measuring the rectified d.c. crystal current from the detector crystal. We assumed that the crystal detection law was constant over the power range that was investigated, and the rectified d.c. crystal current was taken as a linear function of the incident microwave power. For each degree of attenuation, the detector crystal was rematched and the cavity reflection coefficient was determined so that all crystal-current readings could be referred to the same reflection coefficient.

VOL. 9 1959

4. EXPERIMENTAL RESULTS AND INTERPRETATIONS

Fig. 3 shows a typical NaF paramagnetic-resonance spectrum. There are from 13 to 15 well-resolved resonances, almost equally spaced and symmetrically located about the center line. The midpoint of the central line will be referred to as the centroid of the spectrum. The chart that is shown was taken with a 45° angle between the static magnetic field and the 100 crystal direction. The splittings and centroid position were independent of this angle.

Fig. 4 shows paramagnetic-resonance spectra from three different LiF crystals irradiated for $\frac{1}{2}$, 1, and 2 hr. Although different ordinate scales were used because of the different signal strengths, it can be seen that the resonances become more clearly defined with increasing irradiation. The hyperfine splittings were invariant to different irradiation dosages and were isotropic. The 2-hr sample shows 9 (higher-resolution charts showed 11) well-resolved resonances almost equally spaced and symmetrically located about the centroid.

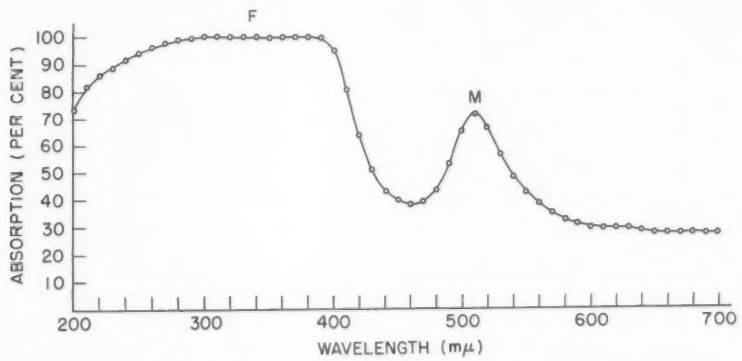

FIG. 5. Optical absorption spectrum of irradiated NaF.

Figs. 5 and 6 show optical spectra from irradiated NaF and LiF samples. Both curves show a very strong absorption in the well-known *F*-band[20–22] at approximately 340 mμ in NaF and at 250 mμ in LiF. The *F*-band absorption is saturated on both charts because the transmission thickness of the crystal in the optical spectrophotometer was quite large ($\frac{1}{2}$ cm). Considerably weaker absorptions in the *M*-band,[20,21,23] at 510 mμ in NaF, and at 440–450 mμ in LiF, are also visible. For the irradiation times used in this study, the integrated area of the *M*-band absorption was always much smaller than the corresponding *F*-band strength, and hence the relative

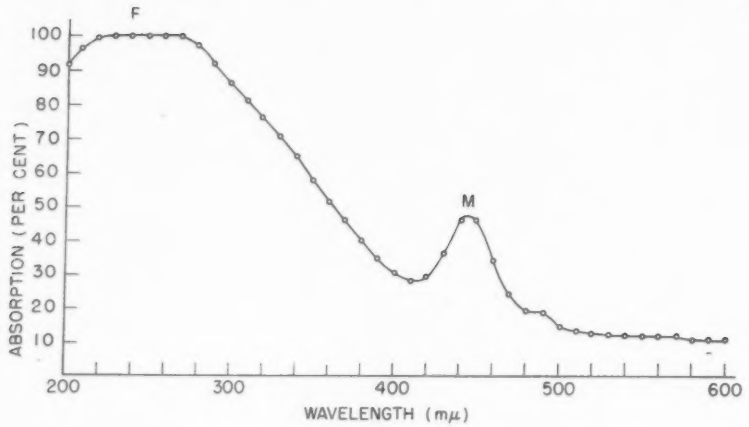

FIG. 6. Optical absorption spectrum of irradiated LiF.

influence of the M-centers on the microwave results was minimized. The NaF optical chart shown and the microwave chart refer to the same sample. The LiF optical chart shown was made from the 2-hr irradiated sample. The symmetry properties of the resonances, their scalar nature, and the odd number of almost equally spaced, symmetrically located resonances are all in agreement with the DE BOER model for the F-center, and with the analysis of the magnetic and hyperfine Hamiltonian in Section 2.

(a) *Evaluation of* A *and* $|\phi(0)|^2$ *for interaction with nearest-neighbor nuclei*

The value of A for nearest-neighbor nuclei was taken as an average of different samples and runs on a given sample. The splitting was measured on the first three lines on either side of the centroid, where the second-order corrections are least, and was adjusted for these corrections. The values that were obtained were the same, within observational error, for different irradiation dosages. The average value was equated with the product $8\pi/3g_e\beta_e g_n\beta_n|\phi(0)|^2$. The collected results are given in Table 3. The indicated spread results from the difficulty of reading the splitting for incompletely resolved lines.

(b) *Evaluation of* A *and* $|\phi(0)|^2$ *for interactions with next-nearest-neighbor nuclei*

The interactions of next-nearest-neighbor nuclei are estimated from the broadening of the nearest-neighbor resolved lines. The assumption is made that the mean-square width of the nearest-neighbor resonances results from unresolved contact hyperfine interactions with the next-nearest-neighbor nuclei. This assumption is plausible, since FEHER's[11] result is that the dipolar

Table 3. *Evaluated results on* NaF *and* LiF

	NaF	LiF
A_{alkali}	38·6±0·5 G	17±0·5 G
$\lvert\phi(0)\rvert^2_{\text{alkali}}$	$6{\cdot}18\times10^{23}$ cm^{-3}	$1{\cdot}9\times10^{23}$ cm^{-3}
A_{halide}	11·8±1·5 G	7·5±1·5 G
$\lvert\phi(0)\rvert^2_{\text{halide}}$	$0{\cdot}52\times10^{23}$ cm^{-3}	$0{\cdot}33\times10^{23}$ cm^{-3}
$\bar{g}$	1·996±0·0004	1·987±0·0004
$\langle 1/r^3\rangle_{\text{alkali}}$	$3{\cdot}14\times10^{24}$ cm^{-3}	
$\langle 1/r^3\rangle_{\text{halide}}$	$0{\cdot}79\times10^{24}$ cm^{-3}	

interactions are smaller than A by a factor of 10 for next-nearest neighbors in KC1. The mean-square width is determined from a statistical averaging of the next-nearest-neighbor interactions, and is compared with the mean-square width obtained from the data.

The statistical analysis has already been given by KIP *et al.*[6] If we neglect the second-order corrections that do not contribute appreciably here, the energy of a particular resonance is given by:

$$E = h\nu = g_e\beta_e B_{\text{eff}} + A\sum_{\alpha=1}^{12} I_z^{\alpha} \tag{12}$$

in which we sum over next-nearest-neighbor halide nuclei, and use a simple product representation of nuclear-spin functions. The mean-square deviation in resonant field is therefore given by:

$$\begin{aligned}\langle(\Delta B)^2\rangle_{\text{av}} &= \frac{A^2}{(g_e\beta_e)^2}\langle(\sum_{\alpha} I_z^{\alpha})^2\rangle_{\text{av}} \\ &= \frac{A^2}{(g_e\beta_e)^2}\frac{1}{3}\sum_{\alpha} i_{\alpha}(i_{\alpha}+1).\end{aligned} \tag{13}$$

For the fluorine nuclei, $i_{\alpha} = 3/2$ and we obtain:

$$\langle(\Delta B)^2\rangle_{\text{av}} = 3A^2, \tag{14}$$

where A is now expressed in gauss. The next-nearest-neighbor contact interaction is therefore given in terms of the mean-square deviation of the resonant field for a given line by:

$$A = (\tfrac{1}{3}\langle(\Delta B)^2\rangle_{\text{av}})^{\frac{1}{2}}. \tag{15}$$

The mean-square deviation, $\langle(\Delta B)^2\rangle_{\text{av}}$, was obtained from the absorption spectrum as follows. The appropriate A/W ratio was determined from comparison between experimental and theoretical charts, and since the nearest neighbor A is taken directly from the spectrum, a value for W which is defined as the full width between the peaks of (dX''/dB_z) is obtained. Since the Lorentzian shape does not have a finite second moment, the Lorentzian line shape that was used was fitted with an exponential tail at the point where the Lorentzian line had fallen to 20 per cent of its peak value. This choice is arbitrary, but the nature of the approximations that were made would appear to warrant it. The Lorentzian shape was fitted to the distribution given in Table 2 for next-nearest-neighbors and had the same area as that distribution. The mean-square width is defined as:

$$\langle(\Delta x)^2\rangle_{\text{av}} = \frac{\int_{-\infty}^{\infty} x^2 f(x)\,dx}{\int_{-\infty}^{\infty} f(x)\,dx}, \tag{16}$$

where $f(x) = 4/(4+x^2)$ for $-4 \leqslant x \leqslant 4$; $f(x) = e^{-4|x|}$ for $-\infty \leqslant x \leqslant -4$; and $f(x) = e^{-4x}$ for $+4 \leqslant x \leqslant \infty$, from which we obtain $(\langle(\Delta x)^2\rangle_{\text{av}})^{\frac{1}{2}} = 0{\cdot}79\times$ [full width at half power of $f(x)$], and since for the Lorentzian shape [full width at half power of $f(x)$] $= \sqrt{3}W$, we obtain:

$$\sqrt{[\langle(\Delta x)^2\rangle]_{\text{av}}} = 0{\cdot}79\sqrt{3}W. \tag{17}$$

Therefore

$$A_{\text{halides}} = \sqrt{[(0{\cdot}79)^2 W^2]}. \tag{18}$$

The values of A/W that were chosen as giving a best approximation to the data were: $A/W = 1{\cdot}8$ for LiF and $A/W = 2{\cdot}6$ for NaF. The results are listed in Table 3.

(c) *Comparison with theoretical calculations*

GOURARY and ADRIAN[13] calculated $|\phi(0)|^2$ for nearest and next-nearest neighbors in LiF with a ground-state F-center wave function obtained through a variational treatment of a modified Hartree equation from which exchange terms are omitted. Their results give the correct order of magnitude for LiF, but are higher than ours. It is possible that the neglect of exchange could account for this, because calculations of atomic Hartree functions for alkali and halide ions give consistently higher values near $r = 0$ to the p-functions that are calculated without exchange, as compared with those calculated with exchange. A larger value of the wave function near $r = 0$ would indicate a larger contact hyperfine interaction.

(d) *Spectroscopic splitting factors and their interpretation*

The spectroscopic splitting factors were obtained by correcting the g-factor of the centroid

of the resonance pattern for the second-order hyperfine correction. The values are averages of many runs and samples and are independent of orientation. The corrected values are given in Table 3. The deviations from the free-electron value $g_0 = 2{\cdot}0023$ fall within the range of measurements on other alkali halides. KIP *et al.*[6] quote the following values for $\bar{g}$: KCl 1·995, NaCl 1·987 and KBr 1·980. It is interesting to note that for the same halide their results show a greater $\Delta g = g_0 - \bar{g}$ for the lighter alkali ion. The same variation is present here for the fluorides. A proper analysis of such systematic shifts would rest on accurate wave functions that are not available.

The small negative shifts, $\Delta g = g_0 - \bar{g}$, in the g-factor are usually attributed to a residual spin-orbit coupling. An analysis of the spin-orbit coupling with applications to the F-center has been given by ADRIAN.[24] He obtains for the contribution to Δg from ion α:

$$\Delta g_\alpha = \frac{4Z_\alpha'\beta^2}{(\Delta E)} \frac{(X_\alpha^2 + Y_\alpha^2)}{R_\alpha^2} \langle u_p(r) \left| \frac{1}{r^3} \right| u_p(r) \rangle, \quad (19)$$

in which the total Δg is given by a sum of equation (19) over all contributing ions. In equation (19) $R_\alpha = X_\alpha \hat{i} + Y_\alpha \hat{j} + Z_\alpha \hat{k}$ is the position vector of ion α with respect to the F-center; Z_α' is the effective charge of ion α; u_p (r) is the spatial dependence of the residual p part of the F-center wave function when it is expanded about the ion α; ΔE is an assumed average excitation energy of the excited states of the F-center. Since at least the nearest and next-nearest ion shells will contribute to Δg, we cannot obtain both $\langle$alkali $|1/r^3|$ alkali$\rangle$ and $\langle$halide $|1/r^3|$ halide$\rangle$ from a single measurement of Δg. In the interest of obtaining an estimate of $\langle |1/r^3| \rangle$ for nearest and next-nearest neighbors, we offer the following suggestions. Independent measurements[11] of $(1/r^3)$ for nearest and next-nearest neighbors have been made for F-centers in KCl. Since the P or nonspherically symmetric part of ϕ determines both Δg and $\langle 1/r^3 \rangle$ and since Δg is practically the same for KCl and NaF, we assume that the ratio of $\langle 1/r^3 \rangle$ for alkali and halide ions is the same (i.e. 4) for both crystals. The effective charges[22] are: $Z'_{N_a^+} = 8$; $Z'_{Li^+} = 1$; and $Z'_{F^-} = 7$. The values for ΔE are taken as the energy of the center absorption in the F-band. With these assumptions, we obtain:

$$\Delta g = \frac{4\beta^2}{\Delta E} \left\langle \frac{1}{r^3} \right\rangle_{N_a^+} \times \times \left(Z_\alpha' \sum_\alpha^{N_a^+} \frac{X_\alpha^2 + Y_\alpha^2}{R_\alpha^2} + \frac{Z_\gamma'}{4} \sum_\gamma^{F^-} \frac{X_\gamma^2 + Y_\gamma^2}{R_\gamma^2} \right). \quad (20)$$

The values of $\langle 1/r^3 \rangle$ for N_a^+ and F^- are given in Table 3.

(e) *Inhomogeneous broadening*

The condition for saturation is that

$$\frac{|\boldsymbol{\mu}_e \cdot \boldsymbol{B}_{rf}|^2}{h^2} T_1 T_2 > 1.$$

Under normal conditions this requirement will be met, as some representative values indicate. For the very conservative condition $T_1 = T_2 = 10^{-6}$ sec, $B_{rf} = 1$ G, we have a saturation factor of $2{\cdot}56 > 1$. Actually, estimates[25] of T_1 and T_2 for KCl at room temperature give $T_1 \approx T_2 \approx 8 \times 10^{-6}$ sec. Under such conditions, and with milliwatts of microwave power incident on the cavity, we expect that the absorption signal, which is proportional to $\chi'' B^2_{rf} Q_L$, will not vary linearly with the microwave power (see Section 2(d)). This was confirmed for our sample by measuring the relative signal that was obtained as the microwave power was varied. A representative series of measurements is given in Table 4 for four consecutive runs with varying power levels. The measured signal was proportional to the square root of the power, which indicated that operation

Table 4. Variation of signal strength with incident power

Run ratio	Signal ratio	Power ratio	(Power ratio)$^{1/2}$
2/1	0·79	0·66	0·81
3/2	0·78	0·60	0·77
4/3	0·72	0·50	0·71

indeed took place well into the region of saturation under conditions of inhomogeneous broadening. For all measurements with varying power level, the line width was constant within measurement error, which, again, is in agreement with theory.

5. CONCLUSIONS

By resolving the hyperfine structure and allowing the symmetry properties of the paramagnetic absorption to be studied, the method of paramagnetic resonance differentiates clearly in favor of the DE BOER model of the *F*-center.

Acknowledgements—We wish to thank Professor G. F. KOSTER for several illuminating conversations. The generous co-operation of members of the M.I.T. Department of Food Technology, in particular, of Professor G. F. FULD and Mr. J. WERTHEIM was greatly appreciated.

REFERENCES

1. DE BOER J. H., *Rec. Trav. Chim. Pays-Bas* **56,** 301 (1937).
2. HUTCHISON C. A., *Phys. Rev.* **75,** 1769 (1949).
3. HUTCHISON C. A. and NOBLE G. A., *Phys. Rev.* **87,** 1125 (1952).
4. SCHNEIDER E. E. and ENGLAND T. S., *Physica* **17,** 221 (1951).
5. TINKHAM M. and KIP A. F., *Phys. Rev.* **83,** 657 (1951).
6. KIP A. F., KITTEL C., LEVY R. A., and PORTIS A. M., *Phys. Rev.* **91,** 1066 (1953).
7. WOLGA G. J. and STRANDBERG M. W. P., *Bull. Amer. Phys. Soc.* **2,** No. 1, 36 (1957).
8. WOLGA G. J. and STRANDBERG M. W. P., *Bull. Amer. Phys. Soc.* **2,** No. 4, 186 (1957).
9. WOLGA G. J., *Microwave Resonance Study of Absorption and Hyperfine Interactions of F-Centers in Alkali Halide Crystals* Ph.D. Thesis, Department of Physics, M.I.T. (1957).
10. LORD N. W., *Phys. Rev.* **105,** 756 (1957).
11. FEHER G., *Phys. Rev.* **103,** 834 (1956).
12. FERMI E., *Z. Phys.* **60,** 320 (1930).
13. GOURARY B. S. and ADRIAN F. J., *Phys. Rev.* **105,** 1180 (1957).
14. ROSE M. E., *Elementary Theory of Angular Momentum.* John Wiley and Sons, New York (1957).
15. BREIT G. and RABI I. I., *Phys. Rev.* **38,** 2082 (1931).
16. PORTIS A. M., *Phys. Rev.* **91,** 1071 (1953).
17. BEHRINGER R. E., *J. Phys. Chem. Solids* **2,** 209 (1937).
18. STRANDBERG M. W. P., TINKHAM M., SOLT I. H., and DAVIS C. F., Jr., *Rev. Sci. Instrum.* **25,** 776 (1954).
19. STRANDBERG M. W. P., TINKHAM M., SOLT I. H., and DAVIS C. F., Jr. *Rev. Sci. Instrum.* **27,** 596 (1956).
20. MOLLWO E., *Z. Phys.* **85,** 56 (1933).
21. MOLNAR J. P., *Absorption Spectra of Trapped Electrons and Alkali-Halide Crystals* Ph.D. Thesis, Department of Physics, M.I.T. (1940).
22. IVEY H. F., *Phys. Rev.* **72,** 341 (1947).
23. DELBECQ J. J. and PRINGSHEIM P., *J. Chem. Phys.* **21,** 794 (1953).
24. ADRIAN F. J., *Phys. Rev.* **107,** 488 (1957).
25. PORTIS A. M., *Phys. Rev.* **104,** 584 (1956).
26. LORD N. W., *Phys. Rev. Letters* **1,** 170 (1958).

J. Phys. Chem. Solids Pergamon Press 1959. Vol. 9. pp. 320–324. Printed in Great Britain.

OSCILLATORY MAGNETO-ABSORPTION IN GALLIUM ANTIMONIDE JA-1149*

SOLOMON ZWERDLING, BENJAMIN LAX, KENNETH J. BUTTON and LAURA M. ROTH

Massachusetts Institute of Technology, Lincoln Laboratory, Lexington, Mass.

(*Received* 2 *October* 1958)

Abstract—High-resolution magneto-absorption measurements made at photon energies just above the intrinsic absorption edge in GaSb have revealed an oscillatory spectrum having a strong resemblance to the corresponding spectrum for direct transitions in germanium. Eight successive transmission minima were observed in magnetic fields up to 38·9 kG at both 1·5 and 4·2°K, using polarized incident radiation. The value of the energy gap found is $\mathscr{E}_g = 0{\cdot}813 \pm 0{\cdot}001$ eV and is shown to be attributable to direct transitions of electrons between the valence and conduction bands. The electron effective mass, $m^* = (0{\cdot}047 \pm 0{\cdot}003)m_0$, was determined by considering transitions from the heavy holes to the conduction band and employing the data of the $\boldsymbol{E} \| \boldsymbol{B}$ spectrum. The existence of fine structure, although not resolved, is indicated by the unsymmetrical character of some of the transmission minima. The first absorption line is believed to contain exciton absorption. The inability to resolve the fine structure and exciton absorption is attributed to line broadening and overlapping due chiefly to scattering by the high impurity density in the sample.

VOL. 9 195

1. INTRODUCTION

MAGNETO-ABSORPTION studies have been used successfully to obtain information about transition processes, band structure, and effective masses of current carriers in semiconductors,[1–3] and the present report concerns the extension of this work to GaSb. This study is the first application of the low-temperature, high-resolution, magneto-spectrophotometric system developed for studying magneto-absorption effects[2] to an intermetallic compound semiconductor. Previous studies of InAs and InSb were made at room temperature with a prism dispersion system of relatively low resolution.[1] The primary aims of the experiment were to measure the low-temperature energy gap and electron effective mass, as well as to determine whether the interband transition is direct or indirect. In addition we attempted the observation of exciton magneto-absorption and the resolution of fine structure of the absorption due to interband Landau-level transitions. The following discussion will describe the achievement of the primary aims and mention some interesting spectral features observed.

2. EXPERIMENTAL

The experiments were performed on a single-crystal sample of GaSb about 4 μ thick, mounted on glass and having 10^{16}–10^{17} impurities/cm^3. Measurements were made at 1·5 and 4·2°K in the spectral region of the intrinsic absorption edge, using constant magnetic field up to 38,900 G. An operating chromatic resolving power up to 20,000 was achieved. Representative transmission curves obtained are shown in Fig. 1, in which the ratio of the transmitted intensity at maximum field to that at zero field is plotted as a function of energy for two orientations of the electric vector of the linearly polarized incident radiation relative to the magnetic field, which was parallel to the [111] axis. The fact that an oscillatory spectrum is found rather than a "staircase" spectrum[2,3] means that the energy gap being observed involves a direct

* The research reported in this document was supported jointly by the Army, Navy, and Air Force under contract with the Massachusetts Institute of Technology.

transition of electrons from the valence to the conduction band.*

The motion of the transmission minima with field is shown in Fig. 2 for several values of the field intensity. The shift of the respective minima to higher energy with increasing field and the associated increase in intensity of the magneto-absorption is clearly evident.

shoulders characteristic of overlapping multiple lines. The second transmission minimum in the spectrum for $\boldsymbol{E}\|\boldsymbol{B}$ is broader than that for $\boldsymbol{E}\perp\boldsymbol{B}$ and the mean position is shifted to higher energy. These characteristics are completely analogous to the earliest observations in germanium.[1] The fine structure was eventually resolved[4] in germanium, using the present apparatus, but for

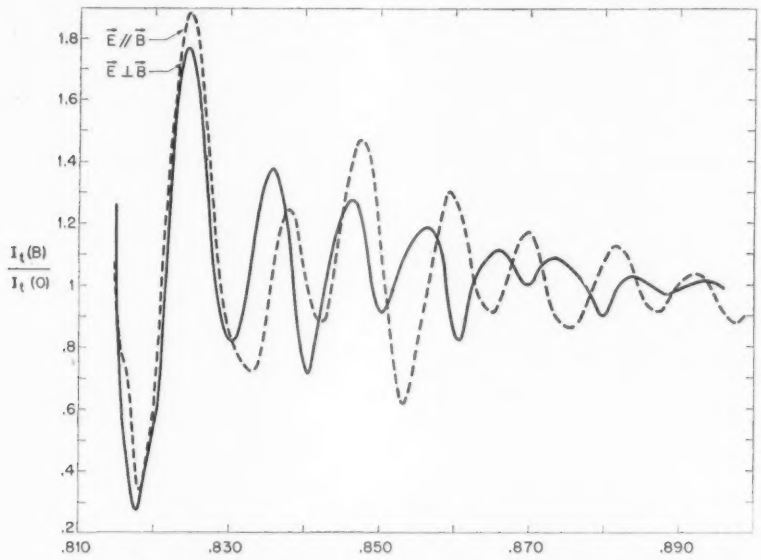

FIG. 1. Oscillatory magneto-absorption in GaSb at photon energies slightly greater than the direct absorption edge. The plot shows the ratio of the transmission of infrared radiation at 38·9 kG to that at zero field versus photon energy. The magnetic field was applied along the [111] crystal direction. The crystal was about 4 μ thick, the temperature was 1·5°K, and the incident radiation was polarized as indicated.

3. RESULTS AND DISCUSSION

The low-temperature transmission curves of Figs. 1 and 2 are very similar to those obtained for the direct transition observed in germanium at room temperature with the lower-resolution prism spectrometer.[1] For both polarizations, the existence of fine structure, although not resolved, is indicated by the unsymmetrical character of some of the transmission minima. The first transmission minimum of Fig. 1 shows two

GaSb the relatively large impurity concentration broadens the lines and prevents the resolution of the fine structure.

Since the transmission minima of Fig. 1 correspond to transitions between Landau (or magnetic) levels of the valence band and the conduction band, a line spectrum of the magneto-absorption data at 38·9 kG, shown in Fig. 3, can be used to obtain the effective mass. The dotted lines refer to the positions of the unresolved shoulders in the first transmission minimum. In order to obtain a value for the electron effective mass, we assume that the fifth, sixth, seventh, and eighth lines in the $\boldsymbol{E}\|\boldsymbol{B}$ spectrum are heavy hole

* It has been shown theoretically[3] and experimentally[2] that the magneto-absorption spectrum exhibits a series of absorption edges for indirect transitions and an oscillatory behavior for direct transitions.

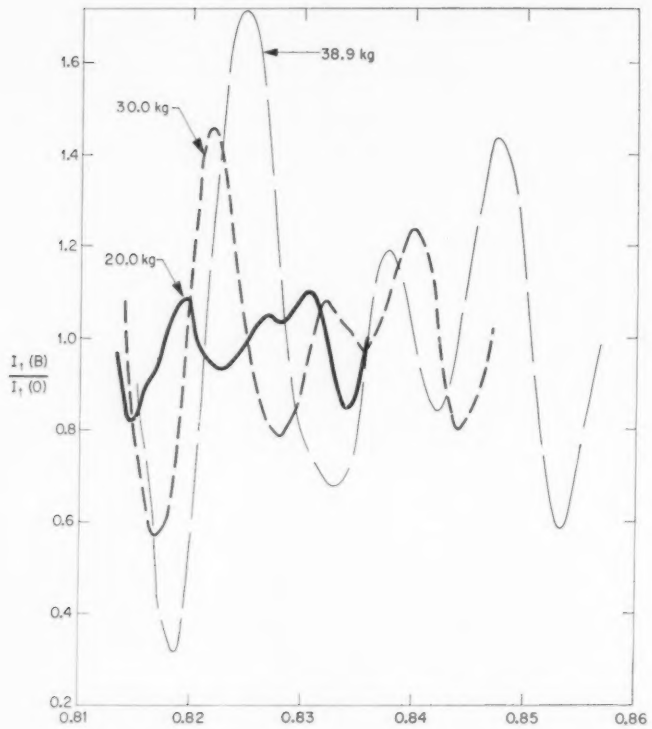

FIG. 2. Oscillatory magneto-absorption for three values of the magnetic field intensity showing the motion of the transmission minima with field. These spectra were observed at 4·2°K with $\boldsymbol{E}\|\boldsymbol{B}$ and with the magnetic field $\boldsymbol{B}$ along the [111] direction.

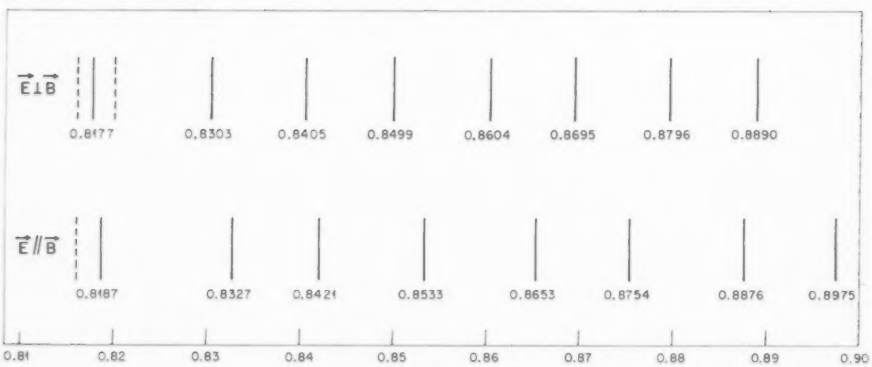

FIG. 3. A line spectrum constructed from experimental data showing the positions of the transmission minima for a temperature of 1·5°K and a dc magnetic field of 38·9 kG oriented along the [111] crystal direction. The dashed lines denote the positions of the unresolved shoulders in the first transmission minimum. The uncertainty in energy values shown is $\pm 0{\cdot}0003$ eV.

transitions having the selection rules $\Delta n = 0, -2$, as was the case for germanium. This assumption is justified by the extraordinary similarity of the spectra of GaSb and germanium except for the position on the energy scale. The average energy difference between these lines in Fig. 3 is $\Delta\mathscr{E} = \hbar(\omega_{c1}+\omega_{c2}) = 0{\cdot}0107$ eV, where $\omega_c = eB/m^*$ is the cyclotron resonance frequency and 1 and 2 that that of silicon. From the expression $1/\mu^* = 1/m_1^*+1/m_2^*$, we find the mass of the electron, $m_1^* = (0{\cdot}047\pm0{\cdot}003)m_0$ in GaSb.

The direct energy gap may be determined accurately from plots such as those shown in Fig. 2. When the photon energy of the transmission minima as a function of magnetic field intensity is extrapolated to zero field, as shown in Fig. 4,

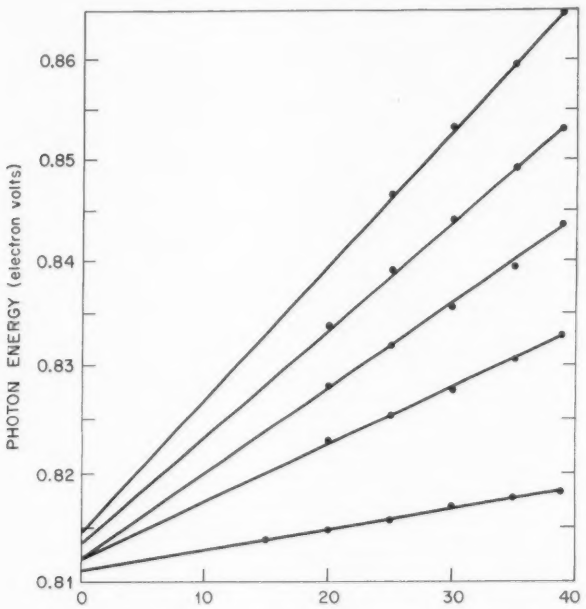

FIG. 4. A plot of the position of the transmission minima in terms of photon energy as a function of dc magnetic field intensity for $\boldsymbol{E}\|\boldsymbol{B}$ at 4·2°K with the magnetic field along the [111] direction. The lines drawn through the points have been extrapolated to zero field to determine the direct energy gap. The lowest line, containing exciton absorption, extrapolates to a point below the gap.

refer to the conduction and valence bands respectively. The combined (or reduced) effective mass for the hole and electron is therefore $\mu^* = (0{\cdot}042\pm0{\cdot}002)m_0$. Although we have no detailed knowledge of the valence bands in GaSb, we can estimate the effective mass of the heavy hole by assuming that the lower and upper bounds are those of germanium and silicon, $m_2^* = 0{\cdot}38\,m_0$ and $0{\cdot}56\,m_0$, respectively. This is reasonable because the reported mobility of holes in GaSb is smaller than that of germanium and larger an accurate value of the energy gap, $\mathscr{E}_g = 0{\cdot}813\pm0{\cdot}001$ eV is obtained. This determination was made without the use of the lowest line of Fig. 4, which we believe to contain exciton lines which would extrapolate to a value below the energy gap.[4] This value of the energy gap is somewhat larger than that estimated by ROBERTS and QUARRINGTON,[5] who gave 0·787 eV. Their measurements of absorption coefficient versus photon energy were made on relatively thick samples (70–300μ), compared to the 4μ thickness

used in the present work. By unsuccessfully attempting to fit their absorption curve to the theoretical results of BARDEEN *et al.*[6] for direct transitions, they concluded that they were dealing with indirect transitions involving a band extremum displaced from $k = 0$ and requiring the emission or absorption of a phonon. It is now apparent that they were studying the same absorption edge as that reported here. Furthermore, their conclusion of an indirect transition from a displaced band is unlikely in view of our oscillatory magneto-absorption results. DUMKE[7] has shown that, even for transitions between two bands with extrema at $k = 0$, an "indirect" process involving an optical phonon is possible. Such a process would account for the finite width of the absorption edge even at very low temperatures. Since DUMKE's theoretical result was not available when the earlier work was done, it was not possible to get a correct estimate of the gap by a curve-fitting procedure. This probably accounts for the discrepancy with our value of the energy gap in GaSb.

Acknowledgements—We wish to acknowledge the assistance of Mr. J. P. THERIAULT in making the measurements and Mr. I. B. LURIE and Mr. G. W. CATUNA for reducing the data. We wish to thank Mr. PAUL MOODY and Dr. H. C. GATOS for providing the single crystal of GaSb and Mr. A. D. JONES for preparing the thin specimen used.

REFERENCES

1. ZWERDLING S. and LAX B., *Phys. Rev.* **106,** 51 (1957).
   ZWERDLING S., LAX B., and ROTH L. M., *Phys. Rev.* **108,** 1402 (1957).
2. ZWERDLING S., LAX B., ROTH L. M., and BUTTON K. J., *Phys. Rev.* To be published.
3. ROTH L. M., LAX B., and ZWERDLING S., *Phys. Rev.* To be published.
4. ZWERDLING S., ROTH L. M., and LAX B., *Phys. Rev.* **109,** 2207 (1958).
5. ROBERTS V. and QUARRINGTON J. E., *J. Electronics* **1,** 152 (1955).
6. BARDEEN J., BLATT F. J., and HALL L. H., *Photoconductivity Conference* (Ed. R. G. BRECKENRIDGE *et al.*) John Wiley, New York (1956).
7. DUMKE W. P., *Phys. Rev.* **108,** 1419 (1957).

VOL
9
195

J. Phys. Chem. Solids Pergamon Press 1959. Vol. 9. pp. 325–329. Printed in Great Britain.

PREPARATION AND PROPERTIES OF HgTe AND MIXED CRYSTALS OF HgTe–CdTe

W. D. LAWSON, S. NIELSEN, E. H. PUTLEY and A. S. YOUNG

Royal Radar Establishment, Malvern, England

(*Received* 16 *October* 1958)

Abstract—The elements mercury, cadmium, and tellurium have been purified, and crystals of the compounds CdTe and HgTe, and of the mixed compounds CdTe–HgTe have been prepared. X-ray and cooling-curve data have established that CdTe and HgTe mix in all proportions to give single-phase crystals. Hall-coefficient and conductivity measurements show that HgTe is a semiconductor with a very low activation energy (~ 0·01 eV) and a high mobility ratio (~ 100). HgTe is opaque to infrared radiation out to a wavelength of 38 μ, but the mixed crystals show absorption edges which vary in position with composition from 0·8 μ in pure CdTe to 13 μ in crystals containing 90 per cent HgTe. Photoconductivity has been observed in filamentary detectors made from the mixed crystals.

VOL. 9 1959

1. PREPARATION

THE compounds HgTe and CdTe were prepared by direct synthesis from the elements *in vacuo*, in sealed silica crucibles. CdTe presented no problem, but the formation, subsequent zone melting, and crystal growth of HgTe had to be carried out in specially prepared thick-walled silica crucibles because of the high vapour pressure of free mercury (22 atm. at 600°C). We used crucibles with an internal diameter of 10 mm and a wall thickness of 3 mm; these were capable of withstanding an internal pressure of about 150 atm.

Preparation involved the following stages: (*a*) purification of the elements, (*b*) synthesis of the compounds HgTe and CdTe, (*c*) zone purification and crystal growth of these two compounds, and (*d*) preparation of mixed crystals from the two compounds.

Mercury was purified by shaking to an emulsion for several minutes with dilute nitric acid (this removes base-metal impurities), filtering and distilling slowly in a quartz apparatus *in vacuo*. It is essential to avoid breaking the surface of the mercury during distillation, by boiling or "bumping", as this causes droplets of the undistilled mercury to be thrown over. It was found, using radiotracers, that most impurities were reduced in concentration to well below 0·1 p.p.m. by this process.* It is worth mentioning in this connection that as little as 0·1 p.p.m. of metals such as sodium lithium, lead, tin, indium and zinc in mercury produce a visible surface scum.

Cadmium was purified by repeated distillation *in vacuo* or in a low-pressure stream of hydrogen (from a palladium leak) as indicated in Fig. 1a. Hydrogen is especially advantageous, as it reduces

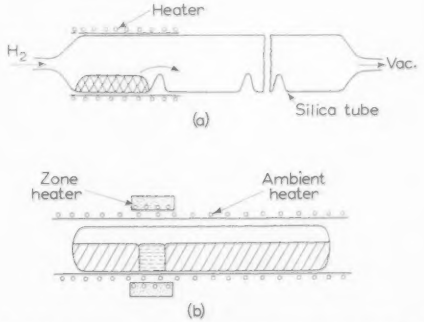

FIG. 1. (*a*) Apparatus for distilling cadmium and tellurium. (*b*) Apparatus for zone melting and growing crystals of the compounds.

* We are indebted to Dr. F. M. REYNOLDS of the National Chemical Laboratory for suggesting this process and for checking its efficiency with radiotracers.

any oxides present and thus prevents the ingots from sticking to the silica crucibles. Tellurium was also processed in this way and was in addition zone-refined *in vacuo* in sealed silica crucibles. The efficiency of the distillation and zone-melting processes was checked by spectrographic methods, using doped specimens to bring the initial impurity concentrations well within the limits of detection of the spectrograph. The purity of our tellurium was also checked by Hall-coefficient measurements, and we obtained material with an extrinsic Hall coefficient of $+40{,}000$ cm^3/C, which corresponds to a carrier concentration of 2×10^{14} positive holes per cm^3. It was discovered during this investigation that the Hall coefficient of a specimen of tellurium is influenced very markedly by the physical nature of its surface, and we found it essential to etch the specimens very carefully in order to achieve consistent results. The Hall coefficient can be reduced by a factor of over a hundred by abrasion or roughening of the surface; even polishing produces a marked reduction.

The compounds CdTe and HgTe were prepared by introducing weighed amounts of the elements into the appropriate silica crucible, which was subsequently pumped to a residual air pressure of 10^{-6} mmHg and sealed off. The crucible was then heated slowly to a temperature just above the melting point of the compound in a furnace which was rocked gently to and fro.

Both compounds were zone-refined in an apparatus of the type shown in Fig. 1b, in which the solid parts of the ingot could be maintained at a uniformly high temperature to prevent undue transfer of material from the molten zone by evaporation. Because of the high vapour pressure of molten HgTe, an ambient temperature within 50°C of the melting point was necessary. A zone rate of 5 cm/hr was used. Single crystals were grown in the same apparatus using a crucible with a tapered end and a zone rate of 1 cm/hr.

The mixed crystals of HgTe–CdTe were prepared by melting together the appropriate weights of the purified compounds *in vacuo*, in sealed, thick-walled, silica crucibles. Preparation directly from the elements usually resulted in explosions, which were probably caused by very high pressures from local pockets of uncombined mercury. Single crystals of the mixtures were grown in the same way as the compounds.

HgTe and CdTe both have the zinc-blende structure with lattice parameters,* i.e. the edge dimension of the unit cube, 6·460 and 6·480Å, respectively, a difference of 0·31 per cent. X-ray examination of the mixed crystals indicated that they were single phase over the whole range from pure CdTe to pure HgTe, and this was confirmed by classical cooling-curve methods. The melting point of CdTe was found to be 1106° C and that HgTe 600°C. The variation of melting point with respect to composition of the mixed compounds was almost linear between these two values.

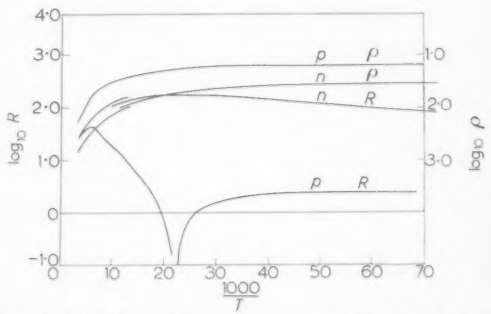

FIG. 2. Variation with temperature of Hall coefficient R and resistivity ρ of one n-type and one p-type crystal of HgTe (R in cm^3/C. ρ in Ω-cm).

2. RESULTS OF ELECTRICAL MEASUREMENTS

Fig. 2 shows Hall-coefficient and resistivity values between 14 and 290°K for two specimens HgTe, one n-type, the other p-type. From the Hall curve for the p-type crystal, the mobility ratio c can be calculated, using the relation

$$\left|\frac{R_{\text{ext}}}{R_{\max}}\right| = \frac{4c}{(c-1)^2}.$$

This gives $\mu_e/\mu_h = c = 70$. Also $R_{\max}/R_i = (1+c)/4c$ at the temperature of $R_{\max}$, 174°K. This gives R_i, and hence the intrinsic carrier concentration $N_i = 6{\cdot}4\times10^{17}$ per cm^3 at 174°K. By assuming that c does not vary with temperature, values of N_i at other temperatures, e.g. at 44·5°K where R is zero, can be obtained. The values at 284 and at 116°K were obtained by solving the general expression for R, again using the same

* We are indebted to Miss A. E. RENNIE for the X-ray measurements.

value of c. The values of N_i are given in Table 1. The activation energy can now be deduced and a value of $\sim 0{\cdot}01$ eV is obtained.

Table 1. *Intrinsic carrier concentration in HgTe*

T(°K)	284	174	116	44·5
$N_i(\div 10^{17})$	6·8	6·4	2·3	0·46

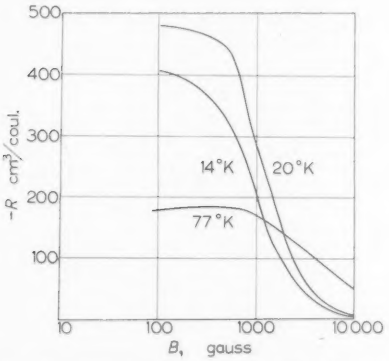

FIG. 3. *P*-type crystal of HgTe. Variation of Hall coefficient with magnetic field at 14, 20, and 77°K.

Fig. 3 shows the variation of Hall coefficient with magnetic field in the *n*-type crystal of HgTe. An analysis of this,* following the method used for InSb,[1] yields the following results at 77°K:

$$c = 120;\quad N_i = 0{\cdot}612\times10^{17} \text{ per cm}^3;\quad \mu_e = 6120;$$

$$\mu_h = 51.$$

It will be seen that the value of N_i obtained by this analysis agrees with the values given in Table 1.

The results of Hall-coefficient and conductivity measurements on one of the mixed crystals, an *n*-type specimen containing 90 mol. per cent mercury, are given in Fig. 4. Similar results were

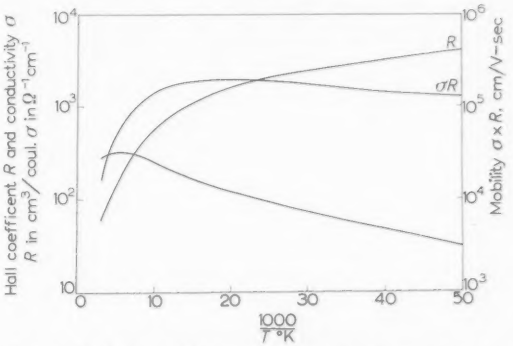

FIG. 4. Variation with temperature of Hall coefficient R, conductivity σ, and Hall mobility $R\times\sigma$, of a mixed crystal of composition $Hg_{0{\cdot}9}Cd_{0{\cdot}1}Te$.

obtained from other crystals containing a high percentage of mercury. The results have not been analysed in detail, but mobility appears to follow a T^{-2} law approximately (values from 1·7 to 2·2 were obtained).

Table 2 gives spot measurements at 77 and at 300°K of R, σ and $R\times\sigma$ for some of the mixed

* Carried out by Dr. D. J. HOWARTH.

Table 2. *Hall coefficient, conductivity, and Hall mobility of mixed crystals of CdTe–HgTe at* 300 *and* 77°K

Composition (mol.–% Hg)	Conductivity $\sigma(\Omega^{-1}\,cm^{-1})$		Hall coeff. R(cm³/C)		$R\times\sigma$ (cm²/V-sec)	
	300°K	77°K	300°K	77°K	300°K	77°K
100	790	109	24	215	19,000	23,400
90(1)	314	261	72	1030	22,600	269,000
90(2)	320	149	71·4	1000	22,800	149,000
84	130	30·4	112	869	14,560	26,400
75	32	9·5	101·5	330	3,250	3,140
50	4·5	4·8	194	37·6	870	180
40	1·5	1·1	52	190	78	209

crystals, all *n*-type specimens. The main feature is that some very high values of Hall mobility were obtained in some of the specimens. These are not necessarily the maximum values obtainable; further work on the preparation of more perfect crystals may yield even higher electron mobilities.

3. OPTICAL RESULTS

Crystals of pure HgTe were opaque to infrared radiation out to a wavelength of 38μ, the limit of our apparatus, and at temperatures down to 4°K. This indicates that the activation energy is lower than 0·03 eV, in line with the electrical results. Crystals of the mixed compounds were, however, found to be transparent at lower wavelengths, and the results of measurements taken at room temperature are given in Fig. 5. The results are

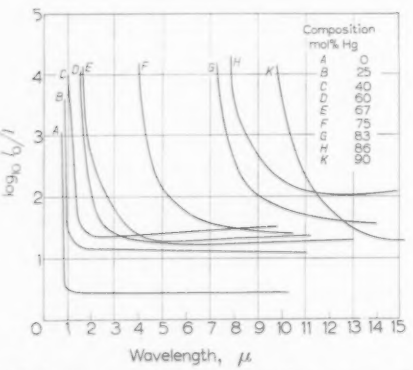

FIG. 5. Room-temperature absorption curves of mixed crystals of HgTe–CdTe. (I_0 = incident energy; I = transmitted energy).

presented as curves of $\log_{10} I_0/I$ against wavelength in microns, where I_0 is the incident and I the transmitted energy; no attempt has been made to calculate absorption coefficients as the refractive index, and hence the reflection loss, is not known. It will be seen that the absorption edge moves from 0·8μ in pure CdTe to 13μ in the mixed crystals as the ratio of mercury increases to about 90 per cent.

The free-carrier absorption beyond the edge tends to increase, and the absorption edges themselves become less steep, as the position of the edge moves to longer wavelengths, thus making the estimation of the exact position of the edge by inspection of the curves progressively more difficult. However, estimates were made by extrapolating those regions of the curves where free-carrier absorption predominates backwards through the absorption edges and subtracting this component, which also includes reflection loss, from the observed total values. The remainder is proportional to the absorption coefficient for electronic transitions across the forbidden gap, and plots of the square root of this quantity against energy E eV, where $E = 1{\cdot}24/\lambda$, give approximately straight lines. The intersects of these on the E axis were taken as the activation energies for the particular crystals, and the corresponding values of λ as their absorption edges.

Fig. 6 shows how the absorption edge calculated in this way varies with composition. The curve cannot be drawn with sufficient certainty at the mercury-rich end to enable an accurate value of

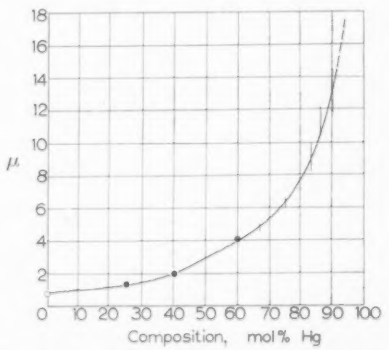

FIG. 6. Mixed crystals HgTe–CdTe. Variation of estimated position of absorption edge with composition.

the activation energy of pure HgTe to be obtained by extrapolation. However, it is evident from Fig. 6 that this series of compounds can provide, by suitable choice of composition, a range of infrared filters and detectors to operate anywhere in the region from 0·8μ to at least 15μ and, probably to much longer wavelengths.

4. PHOTOCONDUCTIVITY

Photoconductivity has been observed in thin filamentary detectors made from these crystals. The filaments were made by polishing and etching thin slices of the crystals, and some of the results are shown in Figs. 7 and 8. Fig. 7 shows the response curve of a crystal containing 86 per

cent HgTe, and also shows that the limit of response moves to longer wavelengths on cooling. At the peak of the response the minimum detectable energy is about 2×10^{-8} W/cycle normalized to 10 mm² area. Fig. 8 gives some results for a crystal containing about 90 per cent HgTe. A measurable photoconductive signal was observed out to 13μ with the detector at room temperature;

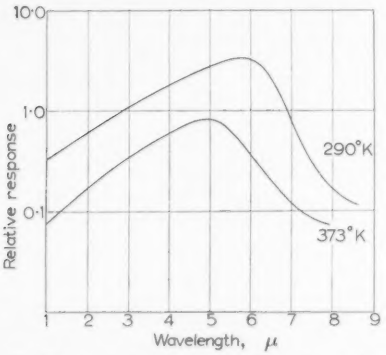

FIG. 7. Photoconductive response of a mixed crystal $Hg_{0.86}Cd_{0.14}Te$, at 290 and 373°K.

at longer wavelengths the signal was lost in noise. A P.E.M. signal was also observed, again with the detector at room temperature, as well as a photovoltaic signal which probably originated from a *p–n* junction in the crystal, near an electrode.

The sensitivity at longer wavelengths of these detectors, when fully developed, may well be higher than that of impurity-doped silicon and germanium detectors; the sensitivity of a CdTe–HgTe detector depends on an intrinsic activation energy, so that its absorption efficiency should be much higher than that of a germanium or silicon impurity detector where the density of absorbing centres (impurities) may be limited.

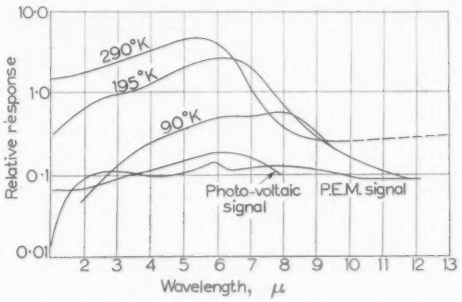

FIG. 8. Photoconductive response at 90, 195 and 290°K of a mixed crystal $Hg_{0.9}Cd_{0.1}Te$. Photovoltaic and P.E.M. signals measured at 290°K.

Acknowledgements—The authors would like to thank G. G. STEEL, R. A. CLAY, R. J. HERITAGE and A. A. BROOKER for assistance with the preparation of specimens and measurements. The paper is published by permission of the Controller, H.M. Stationery Office.

REFERENCE

1. HOWARTH D. J., JONES R. H., and PUTLEY E. H., *Proc. Phys. Soc.* B70, 124 (1957).

J. Phys. Chem. Solids Pergamon Press 1959. Vol. 9. pp. 330–334. Printed in Great Britain.

THE EFFECT OF PRESSURE ON THE NEAR-ULTRAVIOLET SPECTRA OF SOME FUSED-RING AROMATIC CRYSTALS*

S. WIEDERHORN and H. G. DRICKAMER

University of Illinois, Urbana, Illinois

(*Received* 7 *November* 1958)

Abstract—The effect of pressure has been studied on the near-ultraviolet and visible absorption peaks of anthracene, phenanthrene, (*a*, *h*) dibenzanthracene, and (α) benzanthracene. In general, the effect of pressure is to shift the peaks to the red (lower energy) and to broaden them. The greater shift and broadening were found, in general, for the peaks with the larger transition moments. The total shift cannot be accounted for by the increase in density if only dipole–dipole interactions are considered. There seems to be no measurable increase in integrated intensity, and therefore no increase in transition moment. The most likely cause of the shift (in addition to the dipole–dipole interaction) is increased importance of quadrupole and higher interactions at high pressures.

VOL
9
195

THE effect of pressure on the visible and near-ultraviolet absorption spectra of anthracene, phenanthrene, (*a*, *h*) dibenzanthracene, and (α) benzanthracene, has been studied, The chemicals were Eastman Kodak white label recrystallized from absolute alcohol. The high-pressure bomb and optical equipment have been previously described.[1,2] The organic crystals were diluted by mixing with NaCl so that the crystal orientation was random. It was not possible to study polarization effects because of the depolarizing action of the highly strained salt windows. In all cases, an increase of pressure resulted in a red shift of the peak, accompanied by more or less broadening. The individual compounds are discussed below, with emphasis on anthracene since there is most theoretical and experimental information on this compound.

Anthracene

The band system studied was the weak absorption in the region 360–395 mμ. The transition is denoted as ^1L_a by PLATT and KLEVENS[3] and is assigned as $A_g \rightarrow B_{2u}$ by CRAIG and HOBBINS.[4] The shift is shown as a function of pressure to 100,000 atm in Fig. 1. At 1 atm it was possible to obtain four peaks caused by vibrational splitting. At the higher pressures, only two peaks were identifiable due to broadening. The term splitting did not increase significantly with pressure. Fig. 2 shows the shifts plotted against density, using BRIDGMAN's[5] data. The shift cannot be fitted by a single one-term power function of density. If one considers $\Delta\nu \sim \rho^n$, n varies from 1·8 below 10,000 atm to 4·0 near 50,000 atm. Fig. 3 illustrates the change in band shape, and Fig. 4 the change in half-width to 50,000 atm. At higher pressures it was possible to identify the maxima, but not to measure half-widths.

A number of authors[6–11] have discussed the excited states of aromatic crystals as exciton levels in the solid state. The calculations of CRAIG[9] and of CRAIG and HOBBINS[4,8] predict an energy decrease (red shift) for the $A_g \rightarrow B_{2u}$ transition due to excitation exchange between molecules of the crystal. In the dipole approximation the shift is proportional to the inverse cube of the interatomic distance (i.e. $\sim \rho$) and to the square of

*This work was supported in part by U.S. Atomic Energy Commission Contract AT(11-1)-67, Chemical Engineering Project 5.

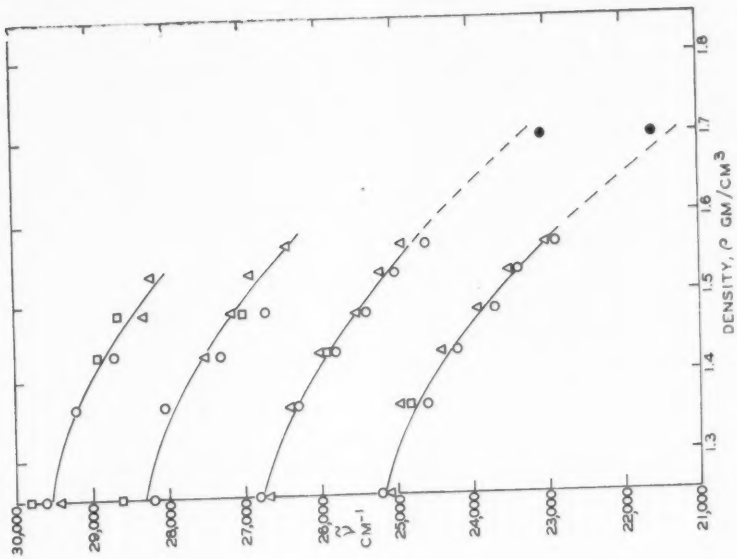

FIG. 2. Frequency shift versus density—anthracene ^1L_a band.

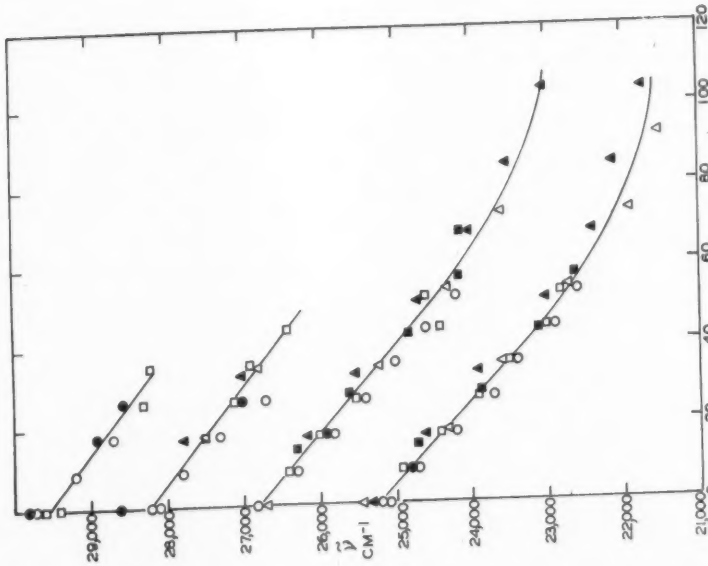

FIG. 1. Frequency shift versus pressure—anthracene ^1L_a band.

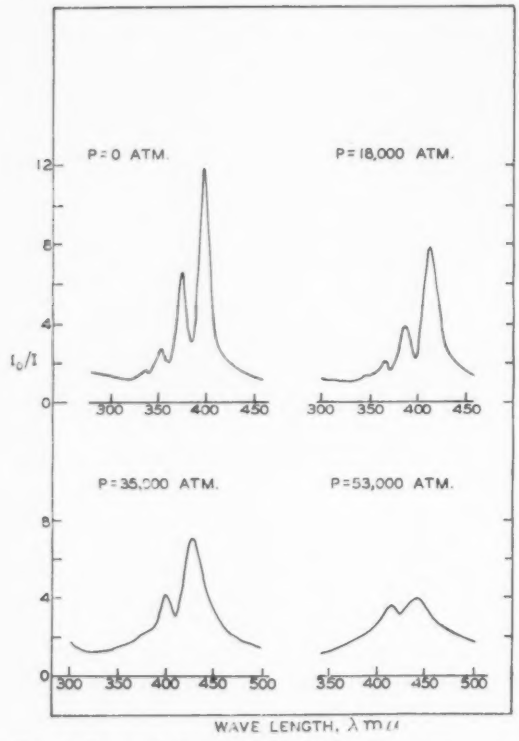

FIG. 3. Shape of absorption band at various pressures—anthracene ^1L_a band I_0/I versus wavelength. $I_0/I = 1$ when $\lambda = 600$ mμ.

the transition moment. The vapor–solid shift is approximately 2130 cm^{-1}. The density increase is 24 per cent in 50,000 atm, accounting for about 20–25 per cent of the shift in the dipole approximation. An increase in transition moment of 25–30 per cent in 50,000 atm could account for the rest of the shift. The measured areas under the curve show no increase (conceivably a small decrease) with pressure, but the broadening and flattening make it impossible to eliminate a 20 per cent increase. Another possible cause of the increase in shift at higher densities is an increase in the relative importance of quadrupole–quadrupole and higher terms. The data for phenanthrene discussed below indicate that, in that case at least, the latter cause is more likely.

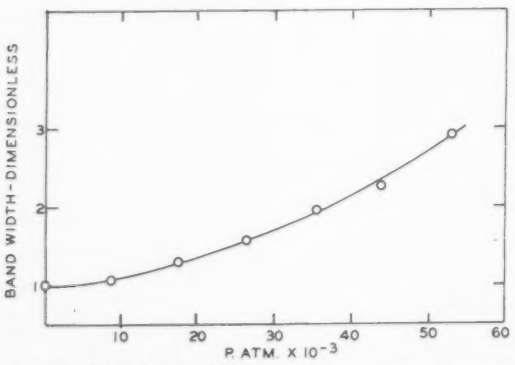

FIG. 4. Half band-width versus pressure—anthracene ^1L_a band. Band-width = (width at given pressure)/(width at zero pressure).

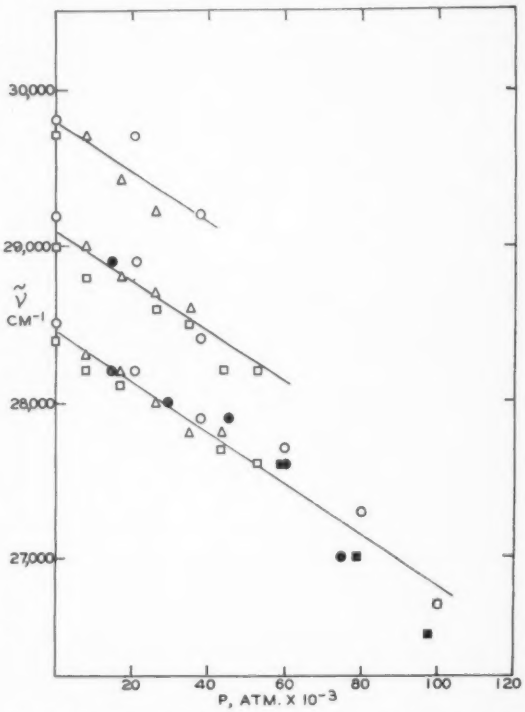

FIG. 5. Frequency shift versus pressure—phenanthrene ^1L_b band.

Phenanthrene

The phenanthrene transition studied occurred with 0–0 transition at 28,500 cm^{-1}. It is the ^1L_b transition discussed by PLATT and KLEVENS.[3] The shift with pressure is shown in Fig. 5. The broadening can be seen in Fig. 6. Both the shift

and broadening are considerably less than for anthracene. These results are qualitatively consistent with the smaller transition moment for the ^1L_b transition and with the results of ROBERTSON *et al.*[12] for anthracene and phenanthrene dissolved in *n*-pentane. The vapor to solid shift is about 680 cm^{-1}. With an estimated 24 per cent density increase in 50,000 atm, the $1/r^3$ term would account for less than one-fourth of the total shift. A 30 per cent increase in transition moment would be needed to account for the rest of the increase through the $|M|^2$ term. This seems clearly inconsistent with the data, as, in fact, a small but consistent decrease in integrated intensity is estimated. Apparently the shift must be accounted for in terms of the increased importance of quadrupole and higher interactions.

In these highly anisotropic crystals, it is also possible that the density change cannot be simply interpreted in terms of a change of r^3, but this effect should not vary with pressure.

(a, h) Dibenzanthracene

Four peaks were observed in this compound—at 24,930, 26,380, 27,620 and 29,000 cm^{-1}, at 1 atm. These are identified as the 0–0 and 0–1 peaks of the ^1L_b transition and the 0–0 and 0–1 peaks of the ^1L_a transition. The shifts with pressure are shown in Fig. 7. The shift is nearly the same for the two transitions and is intermediate between that of the ^1L_a transition in anthracene and the ^1L_b transition in phenanthrene. It should be noted that the apparent intensity of the ^1L_a band is only two to three times that of the ^1L_b band in the crystal. There appeared to be some broadening (less than anthracene but more than phenanthrene) but no significant increase in intensity.

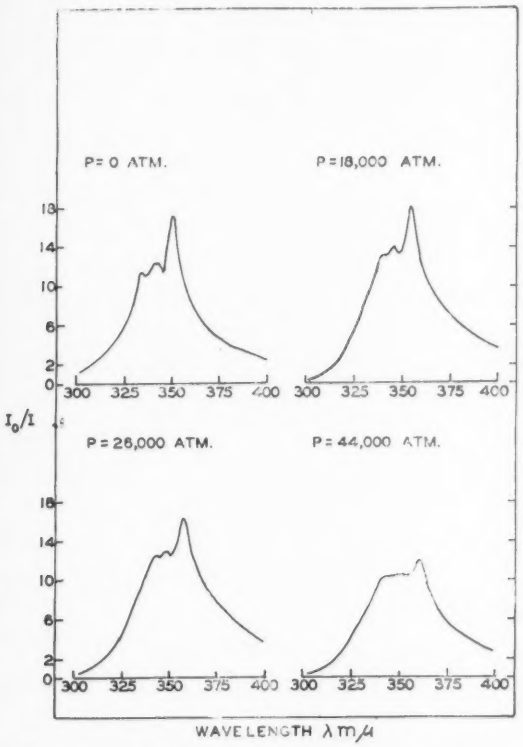

FIG. 6. Shape of absorption band at various pressures—phenanthrene ^1L_b band. I_0/I versus wavelength. $I_0/I = 1$ when $\lambda = 450$ mμ.

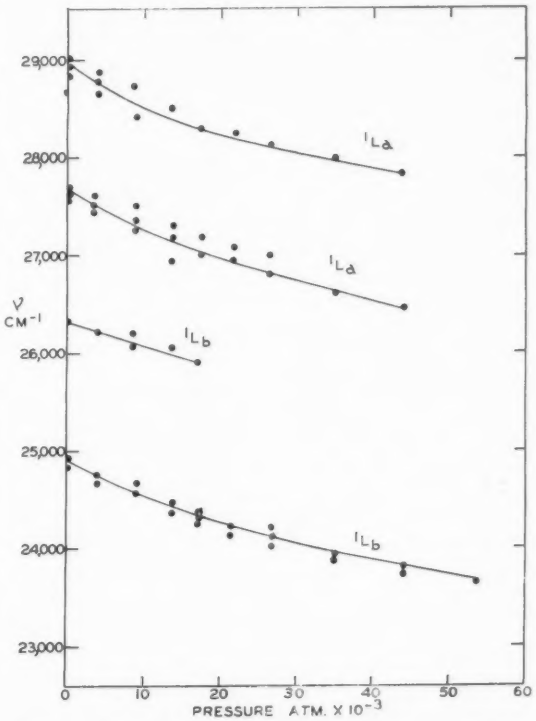

FIG. 7. Frequency shift versus pressure—(*a, h*) dibenzyanthracene ^1L_a and ^1L_b band.

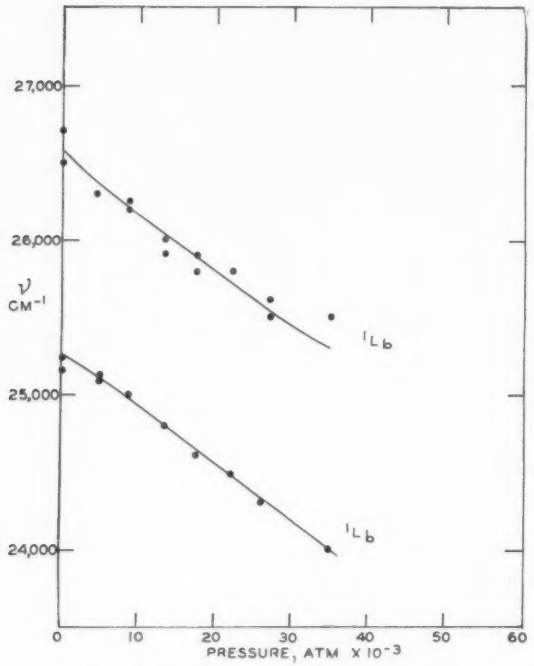

FIG. 8. Frequency shift versus pressure—(α)-benzanthracene.

α-Benzanthracene

A few runs were made on α-benzanthracene (Fig. 8). Two peaks were found at 26,540 and 25,240 cm^{-1}. These are apparently the 0–0 transitions of the ^1L_a and ^1L_b bands. The shift with pressure was the same for the two bands (about two-thirds of the shift for anthracene in the same pressure range). The peaks were comparable in intensity. There was considerable broadening, but apparently no great change in intensity in either band.

It should be pointed out that the large red shift accompanied by considerable broadening will result in ultimate overlap with the conduction band, and some of these fused-ring aromatics would become conductors at a few hundred thousand atmospheres.

REFERENCES

1. FITCH R. A., SLYKHOUSE T. E. and DRICKAMER H. G., *J. Opt. Soc. Amer.* **47,** 1015 (1957).
2. PARSONS R. W. and DRICKAMER H. G., *J. Chem. Phys.* **26,** (1958).
3. PLATT J. R. and KLEVENS H. B., *J. Chem. Phys.* **17,** 470 (1949).
4. CRAIG D. P. and HOBBINS P. C., *J. Chem. Soc.* 2309 (1955).
5. BRIDGMAN P. W., *Proc. Amer. Acad. Arts Sci.* **77,** 115 (1949).
6. DAVYDOV A. S., *Zh. eksp. teor. fiz.* **18,** 210 (1948).
7. MCCLURE D. L., *J. Chem. Phys.* **25,** 481 (1956).
8. CRAIG D. P. and HOBBINS P. C., *J. Chem. Soc.* 539 (1955).
9. CRAIG D. P., *J. Chem. Soc.* 2302 (1955).
10. FOX D. and SCHNEPP O., *J. Chem. Phys.* **23,** 1575 (1955).
11. WINSTON H., *J. Chem. Phys.* **19,** 156 (1951).
12. ROBERTSON W. W., WEIGANG O. E. and MATSON F. A., *J. Mol. Spec.* **1,** 1 (1957).

One-dimensional configurational co-ordinate curves for luminescence centers

(*Received* 5 *October* 1958)

ONE-dimensional configurational co-ordinate curves have been used by many workers to represent the quantitative characteristics of luminescence centers.[1] For instance, WILLIAMS calculated the configurational co-ordinate curves for KC1 : T1, and KLICK and other workers derived those for *F*-centers in alkali halides and for several luminescence centers in phosphors. However, the configurational space describing the center should in principle be many-dimensional. In this note the relations between one- and many-dimensional models are discussed.

To represent the shape of the normalized spectrum, $f(E)$, the semi-invariants will be used. These are defined as the coefficients, Λ_l, in the expansion

$$f(E) = \Phi_0(E) - \frac{\Lambda_3}{6}\Phi_3(E) + \frac{\Lambda_4}{24}\Phi_4(E) + \ldots, \quad (1)$$

where

$$\Phi_0(E) = \frac{1}{\sqrt{2\pi\Lambda_2}} \exp\left\{-\frac{(E-\Lambda_1)^2}{2\Lambda_2}\right\},$$

$$\Phi_m(E) = \frac{d^m}{dE^m}\Phi_0(E).$$

In the many-dimensional model, we assume that the energies of the ground and excited state are described by quadratic forms in the configurational co-ordinates, with different minimum positions, principal-axis directions, and curvatures for the two states. The semi-invariants of the absorption band due to optical transition between these two states are given by KUBO and TOYOZAWA[2] as a first approximation

$$\begin{aligned} \Lambda_{1a} &= \epsilon_0 + \tfrac{1}{2}\Delta\Omega''^2\Delta, \\ \Lambda_{2a} &= \frac{\hbar}{2}\Delta\Omega''^2\Omega'^{-1}\coth\left(\frac{\hbar\Omega'}{2kT}\right)\Omega''^2\Delta. \end{aligned} \quad (2)$$

In a similar way, the semi-invariants of the luminescence spectrum are calculated:

$$\begin{aligned} \Lambda_{1f} &= \epsilon_0 - \tfrac{1}{2}\Delta\Omega'^2\Delta, \\ \Lambda_{2f} &= \frac{\hbar}{2}\Delta\Omega'^2\Omega''^{-1}\coth\left(\frac{\hbar\Omega''}{2kT}\right)\Omega'^2\Delta. \end{aligned} \quad (3)$$

Here, ϵ_0 is the energy separation between the minimum positions of the two electronic states, Δ is the N-dimensional vector denoting the distance between the two minimum positions, and Ω'^2 and Ω''^2 are the N-dimensional tensors denoting the potentials of the ground and excited states respectively. Since units are chosen here so that the mass of the oscillators is unity, each element in Ω' and Ω'' is the vibrational frequency when these tensors are transformed into diagonal form.

If all the vibrational frequencies in the ground state and all those in the excited state are the same, while the former and the latter are not necessarily equal, i.e. $\Omega' = \omega' I$ and $\Omega'' = \omega'' I$, equations (2) and (3) may be simplified to coincide with the corresponding equations for the one-dimensional model. The same activation energy for the non-radiative transition competing with radiative transition is also obtained in both one- and many-dimensional models. Consequently, in this special case, the one-dimensional model represents the nature of the luminescence center correctly.

Although various vibrational frequencies would actually be involved, the experimental results on the temperature-dependence of spectral width can usually be represented by assuming a single frequency. This is one of the reasons why the one-dimensional treatment has been used by many workers. However, the temperature-dependence of the squared spectral width in the many-dimensional model as a sum of several hyperbolic cotangent terms of different vibrational frequencies can be approximately represented by a single hyperbolic cotangent term of suitably chosen frequency. We would not be able to discern experimentally the vibrational frequency spread within a range of magnitude of several times by measurements of spectral width over the usual range of temperature. Consequently, the experimental results themselves cannot be adduced in support of the one-dimensional treatment.

In the one-dimensional analysis of experimental data, the vibrational frequency is determined by the ratio of squared spectral width at 0°K to the rate of broadening at high temperatures. Thus the vibrational frequency in the ground state obtained from the absorption band width is approximately equal to the following average of actual frequencies; we have from equation (2):

$$\omega_g = \frac{2k}{\hbar}\frac{\Lambda_{2a}(0^\circ\mathrm{K})}{\left(\frac{d\Lambda_{2a}}{dT}\right)_{T=\infty}} = \frac{\Delta\Omega''^2\Omega'^{-1}\Omega''^2\Delta}{\Delta\Omega''^2\Omega'^{-2}\Omega''^2\Delta}. \quad (4)$$

In the same way, the vibrational frequency in the excited state obtained from the luminescence band width is, from equation (3),

$$\omega_e = \frac{2k}{\hbar}\frac{\Lambda_{2f}(0^\circ\mathrm{K})}{\left(\frac{d\Lambda_{2f}}{dT}\right)_{T=\infty}} = \frac{\Delta\Omega'^2\Omega''^{-1}\Omega'^2\Delta}{\Delta\Omega'^2\Omega''^{-2}\Omega'^2\Delta}. \quad (5)$$

Equating the expressions of the spectral width at 0°K in the two models to each other, the relations between the various quantities are obtained. We have for the absorption band

$$x^2\frac{\omega_e{}^4}{\omega_g{}^2} = \Delta\Omega''^2\Omega'^{-2}\Omega''^2\Delta, \quad (6)$$

and for the luminescence band

$$x^2\frac{\omega_g{}^4}{\omega_e{}^2} = \Delta\Omega'^2\Omega''^{-2}\Omega'^2\Delta. \quad (7)$$

Here, x is the distance between the two minimum positions in the one-dimensional configurational co-ordinate.

It is clear from these considerations that the value of each quantity in the one-dimensional model does not generally have any direct significance for the actual situation of the luminescence center. Therefore, it depends on a particular center whether or not a one-dimensional model explains various characteristics consistently. In particular, the activation energy of the non-radiative transition can hardly be predicted, since it is the height of lowest intersection point of many-dimensional paraboloidal surfaces with different origins, principal-axis directions, and curvatures. Moreover, the actual situation is more complex, when non-harmonicity of potential and resonance between two states in the vicinity of the intersection point are important.

As an example, one-dimensional configurational co-ordinate curves are determined by an analysis of some spectral characteristics for the luminescence center in $Ca_3(PO_4)_2$: Cu phosphor, which has been extensively studied by UEHARA.[3] The other observed characteristics are compared with the values expected from the determined curves. The absorption band width is calculated giving reasonable agreement with the observed value but the expected value of activation energy of non-radiative transition is much larger than observed. The details of this work will be published later in *J. Phys. Soc. Japan*.

Matsuda Research Laboratory KEIJI MAEDA
Tokyo Shibaura Electric Co.
Kawasaki-shi, Japan

VOL. 9 195

REFERENCES

1. A general review has been given by KLICK C. C. and SCHULMAN J. H., *Solid State Physics* (Editors F. SEITZ and D. TURNBULL), Vol. 5, p. 97. Academic Press, New York (1957).
2. KUBO R. and TOYOZAWA Y., *Progr. Theor. Phys.* **13,** 160 (1955).
3. UEHARA Y., to be published in *J. Electrochem. Soc.* and *J. Phys. Chem. Solids*.

Hall coefficient of molybdenum disilicide*

(*Received* 10 *July* 1958; *in revised form* 3 *November* 1958)

THE Hall coefficient of polycrystalline molybdenum disilicide has been measured from room temperature to 445°C. The thermoelectric power versus temperature relationship for this material has previously been reported.[1] The alloy was prepared[2] by direct synthesis of molybdenum silicon powders of high purity mixed in the stoichiometric ratio of $MoSi_2$, compressed, and sintered. Three samples were used in these experiments. Two were about $0{\cdot}1\times0{\cdot}5\times2$ cm with densities of 85·3 and 82·8 per cent of the X-ray value (6·222 g/cm^3) for an ideal crystal.† The

*This project was assisted by the Research Corporation.

†Obtained from Fansteel Metallurgical Corporation, North Chicago, Ill.

third sample was $0{\cdot}2\times1\times4$ cm, with 72·8 per cent density.*

Hall emf's, v_h, were measured by conventional d.c. methods. The usual precautions were taken to avoid spurious emf's. Thermal emf's were not troublesome. For a sample 1 mm thick in a magnetic field of 10,000 G with a current of 2A through the sample, v_h is about 3 μV. Potentiometer readings were reproducible for increasing and decreasing temperature and for repeated trials on the same sample.

Hall leads were attached by silver soldering. The current leads were silver soldered to platinum strips which were clamped to the ends of the sample. Heat was supplied by a **U**-shaped ribbon heater controlled by a Variac. Sample holder and heater were mounted on a Mycalex base and the whole assembly placed in a Vycor tube which was evacuated by a fore-pump while measurements were being taken. Temperature measurements were made with a platinum/platinum–10 per cent rhodium thermocouple and a Rubicon precision portable potentiometer. The Vycor tube was supported between the poles of a Guoy-type electromagnet. Magnetic field intensity, H, was measured with a fluxmeter having a sensitivity of 125 G/division, using a 10-turn search coil. For values of H up to 13,500 G, the Hall constant was independent of field intensity.

No change in Hall constant with temperature was detected between 25 and 445°C. A coefficient of $10{\cdot}4\pm0{\cdot}2\times10^{-12}$ V-cm/AG was obtained for the Fansteel specimens. Correction has been made for porosity, assuming spherical cavities, according to the equation deduced by JURETSCHKE *et al.*[3] This value is lower than the $13{\cdot}4\pm0{\cdot}2\times10^{-12}$ V-cm/AG found for the American Electro Metal sample. The latter figure is near that of $13{\cdot}7\times10^{-12}$ measured in their laboratory.[4] The Hall constant was positive for all samples. The smaller, more dense samples were more metallic in appearance, which might explain their lower Hall constant. The presence of a small amount of uncombined silicon, or a silicon compound such as the oxide, might account for the higher Hall constant of the Electro Metal sample. However, no free silicon or molybdenum was detected by X-ray analysis.

The resistivity, ρ_0, for samples from the two sources was nearly the same: $26{\cdot}8\times10^{-6}$ Ω-cm (Fansteel) and $26{\cdot}0\times10^{-6}$ Ω-cm (Electro Metal) corrected for porosity. But the temperature coefficients of resistivity were quite different: $4{\cdot}3\times10^{-3}$°C and $7{\cdot}1\times10^{-3}$°C, respectively, for the temperature range 25–160°C. A temperature coefficient of $6{\cdot}4\times10^{-3}$°C for molybdenum disilicide has been reported by ROBINS,[5] who observed no marked variation of the coefficient with density.

Southern Illinois University MARTIN J. ARVIN
Carbondale, Ill. RAY F. TIPSORD†

REFERENCES

1. ARVIN M. J., *J. Appl. Phys.* **24,** 498 (1953).
2. GLASER F. W., *J. Appl. Phys.* **22,** 103 (1951).
3. JURETSCHKE H. J., LANDAUER R., and SWANSON J. A., *J. Appl. Phys.* **27,** 838 (1956).
4. Private communication.
5. ROBINS D. A., *Phil. Mag.* **3,** 313 (1958).

*Obtained from American Electro Metal Division of Firth Sterling Inc., Yorkers, N.Y.

†Present address: Missouri School of Mines, Rolla, Missouri.

BOOK REVIEW

L. R. G. TRELOAR: **The Physics of Rubber Elasticity.** Second Edition. Clarendon Press, Oxford, 1958. 342 pp., 40*s*.

ALTHOUGH at first glance one gets the impression that this second edition of TRELOAR's book is rather similar to the first, closer examination soon reveals that much of the material has been rewritten and several new topics have been covered. Readers of the first edition will remember the clarity and conciseness of the book, and happily the second edition retains these admirable features. Admittedly some of the conciseness arises from the lack of complete derivation of the more complex theories relating to rubber elasticity, but the author is usually careful to point out the location of the original papers.

In the first two chapters, the gross thermodynamic features of rubber elasticity are presented, as well as a short history on the studies of rubber. In the two following chapters the various theories of elasticity of long-chain molecules and molecular networks are reviewed. These two chapters are the heart of the subject, and the author gives a clear presentation of the various theories of FLORY, JAMES and GUTH, TRELOAR, &c. In particular, we were interested in the discussion of the work of JAMES and GUTH, since their papers are a bit difficult.

In Chapter V the theories are confronted with experimental evidence. Reasonable agreement is shown. To explain some of the deviations, the reader is led into a thorough study of non-Gaussian chain statistics and network theory in the following chapter.

An interesting new feature is a chapter on swelling phenomena. A longer review is given of the phenomenological theory of large deformations, with special emphasis on the recent work of RIVLIN and SAUNDERS. One also finds a short new chapter on the determination of cross-linking. The photo-elastic properties of rubber are discussed in great detail, and much new material is included here. Crystallization effects in rubbers are covered in two quite long chapters, but these are rather similar to the first edition. There is also only a slight revision of the material on tensile strength, stress relaxation, and flow.

The last chapter deals with the dynamic properties of rubbers. Here the reviewers feel that the archaic model of springs and dash-pots could have been de-emphasized in favor of inclusion of the more recent molecular theories of such workers as FERRY, BUECHE, ROUSE, &c. One is also disappointed by the lack of discussion of the effect of fillers on rubber properties. Admittedly this field is not well-understood, but in view of its technical importance it can hardly be completely ignored.

The book is printed in easily read type, and appears to have been thoroughly proof-read.

TRELOAR's book provides an excellent introduction to rubber elasticity for the new student and will provide new insights for the advanced worker.

B. H. ZIMM
R. W. KILB

PAPERS TO BE PUBLISHED IN FUTURE ISSUES

A. W. Hornig, R. C. Rempel and H. E. Weaver: Electron paramagnetic resonance in single crystals of $BaTiO_3$.

H. Sato, A. Arrott and R. Kibuchi: Remarks on magnetically dilute systems.

G. Shirane, S. J. Pickart, R. Nathans and Y. Ishikawa: Neutron diffraction study of antiferromagnetic $FeTiO_3$ and its solutions with α-Fe_2O_3.

F. Kettel: Die Wärmeleitfähigkeit von Germanium bei hohen Temperaturen.

Hartmann Kallmann, Bernard Kramer and Peter Mark: Calculation of the photoconductivity from a.c. impedance changes induced in ZnS and ZnCdS phosphors.

John C. Fisher: Antiferromagnetic ground state.

Taira Suzuki and Masao Doyama: Hardening induced by additive coloration in KCl.

Junjiro Kanamori: Superexchange interaction and symmetry properties of electron orbitals.

Jun Kondo and Jiro Yamishita: Nuclear quadrupolar relaxation in ionic crystals.

A. F. Forestieri and L. A. Girifalco: The effect of plastic deformation on self-diffusion in silver.

D. G. Thomas: Infrared absorption in zinc oxide crystals.

J. L. Davis, G. E. Devlin, V. Jaccarino and A. L. Schawlow: Structure sensitivity of the high-frequency NMR in powdered antiferromagnetic MnF_2.

J. J. Hopfield: A theory of edge emission phenomena in CdS, ZnS and ZnO.

Edgar F. Westrum and D. M. Grimes: Low-temperature heat capacities and thermodynamic properties of zinc ferrites—III Effect of copper substitution.

A. Blandin and E. Daniel: Sur le deplacement de Knight dans les alliages.

R. Nathans, C. G. Shull, G. Shirane and A. Andresen: The use of polarized neutrons in determining the magnetic scattering by iron and nickel.

R. J. Weiss and A. F. Freeman: X-ray and neutron scattering from electrons in a crystalline field and the determination of outer electron configurations in Fe and Ni.

E. N. Adams and T. D. Holstein: Quantum theory of transverse galvanomagnetic phenomena.

R. Guccione, M. P. Tosi and M. Asdente: Migration barriers for cations and anions in alkali halide crystals.

Issai Lefkowitz: Radiation induced changes in the ferroelectric properties of some barium titanate type materials.

E. Daniel: Sur le deplacement de Knight des impuretes dans les metaux.

M. A. Gilleo and D. W. Mitchell: The ferrimagnetism and crystal chemistry of substituted manganese–tin spinels.

M. A. Gilleo and S. Geller: The interaction of magnetic ions in $Gd_3Mn_2Ge_2GaO_{12}$ and related garnets.

Pierre Morel: Calcul semi-empirique de la temperature de transition des superconducteurs et de l'effet de la pression sur la transition.

F. D. Rosi, B. Abeles and R. V. Jensen: Materials for thermoelectric refrigeration.

S. H. Koenig and R. D. Brown: Thermal oscillations in *n*-Ge at low temperatures.

M. S. Abrahams, R. Braunstein and F. D. Rosi: Thermal, electrical and optical properties of (In, Ga)As alloys.

J. P. Evans and P. G. Mardon: Some physical properties of neptunium metal—I A determination of the specific heat of α-neptunium.

K. Teegarden and R. Weeks: Trapped charge and the low temperature luminescence of undoped Kl.

G. J. Ogilvie and M. J. Ridge: The cathodic sputtering of silver.

G. J. Ogilvie: The surface structure of silver crystals after argon ion bombardment.

S. J. Pickart: Magnetic properties of solid solutions of Fe_3O_4 and $FeAl_2O_4$.

E. N. Adams and E. I. Blount: Energy bands in the presence of an external force field—II Anomalous velocities.

ERRATA

JOHN B. GOODENOUGH, *J. Phys. Chem. Solids* **6**, 287 (1958).

The figures over the figure captions Fig. 4 and Fig. 5 are reversed. The minor omissions in these figures which were not corrected in proof can be readily detected by the reader.

H. Y. FAN and P. FISHER, *J. Phys. Chem. Solids* **8**, 270 (1959).

The following captions were missing from this paper.

FIG. 1. The absorption spectrum of arsenic-doped germanium at $\sim 4{\cdot}2°$K. Room temperature resistivity $= 2{\cdot}0\ \Omega$-cm.

FIG. 2. The effect of a magnetic field on the transmission spectrum of arsenic-doped germanium at $\sim 4{\cdot}2°$K, with $H \| [100]$. The ratio of transmitted intensity with and without field is plotted against energy. Room temperature resistivity $\simeq 1{\cdot}7\ \Omega$-cm; sample thickness $=$ 1·25 mm.

M. J. STEPHEN and A. B. LIDIARD, *J. Phys. Chem. Solids* **9**, 43 (1959).

The name of the second author was spelt LIDARD throughout the paper and in the Contents List; the correct spelling is as above.

VOL.
9
1959